

# nature

## GLOBAL CLIMATE

Yes, we changed  
rainfall too

## CHILDHOOD

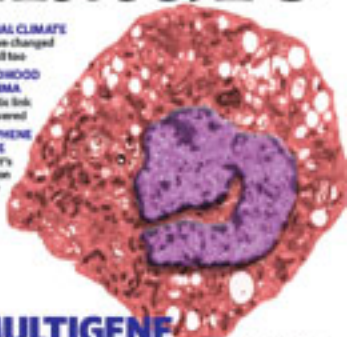
### ASTHMA

Genetic link  
discovered

## GRAPHENE

### OXIDE

Why it's  
good on  
paper



## MULTIGENE DISEASES

Work on inflammatory bowel  
disorders unravels complexity

NATURE JONES

Back to content

# Nuclear test

Japan's response to an earthquake highlights both the promise and the pitfalls of nuclear power at a critical time for its future.

On the face of it, the Japanese government and the Tokyo Electric Power Company seem to have reacted competently when an earthquake occurred some 20 kilometres from a huge nuclear facility on 16 July (see page 392).

The incident, at the Kashiwazaki-Kariwa plant in Niigata prefecture on Japan's western coast, could have been serious. Seven reactors on the largest single-site nuclear-power facility in the world were hit by a quake of magnitude 6.8, exceeding their design capacity of 6.5.

Prime Minister Shinzo Abe responded swiftly to the event, directly instructing the operator to come clean about the full facts of the case. The operator duly grovelled about some incomplete information that was released in the hours after the earthquake.

The nuclear fall-out from the incident was, thankfully, minimal. Despite a few minute leaks into cooling water and the atmosphere, and the upending of some wheelie bins containing low-level nuclear waste, the reactors and their materials seem to have been reassuringly well contained. That's a substantial engineering achievement.

At the same time, questions are being asked about why this facility was built on a seismically active fault line. Japan manages to combine an intense hunger for nuclear-generating capacity with a dearth of seismically inactive sites. But last week's event was the third time in as many years that a nuclear power station in Japan has been subjected to an earthquake more powerful than it was designed to withstand. It would seem that the nuclear regulator, the Nuclear Safety Commission, needs to involve seismologists more fully in its site approval process — and to raise its standards. This need not preclude the construction of new facilities: nuclear power stations in Japan have already been designed and built to deal with earthquakes of magnitude 8.

The power company's response also seemed a little shaky in the immediate aftermath of the quake — saying that emergency-response teams were difficult to assemble because it was the Marine Day holiday, for example, was unlikely to inspire public confidence. But the subsequent flow of information on the situation inside the plant seemed reassuringly complete. Regular updates for the local population

and a comprehensive release of data on the nature of the faults caused by the earthquake combined to suggest that both the operator and the government have learned a lot — including the sublime benefits of transparency — from their shaky track record in this realm in past decades.

A larger pall is cast by the commercial consequences of the inevitable decision to close the seven reactors on the site until there has been a full assessment of the damage done. The loss of eight gigawatts of electrical-generating capacity (enough to power half of Tokyo) is a major blow despite the well-planned nature of Japan's generating system.

In a precautionary move, major industrial corporations have been asked to plan reductions in their peak power consumption to help see the grid through the summer peak in electricity demand.

Global warming and high energy prices have put nuclear power firmly back in the picture around the world. Plans are afoot to build new plants in Britain and the United States, and China and India look set to press ahead with nuclear power on a significant scale.

Investors in planned nuclear plants continue to worry about waste disposal and liability issues, and look to sympathetic governments to provide assurance regarding these. Lurking in the back of their minds, however, is the ever-present risk of accidents of the sort that played havoc with the global industry at Three Mile Island, Pennsylvania, in 1979 and at Chernobyl in 1986. Another such event could undermine political support for nuclear power and so up-end their planned investments altogether, possibly before a single megawatt of power is generated and sold.

On balance, last week's events go some way towards bearing out the industry line that such unfortunate incidents can be averted. For that to remain the case will demand not revolutionary, next-generation technology, but rather a combination of diligent engineering, careful regulation and public transparency. ■

**"The Japanese government has learned about the sublime benefits of transparency regarding nuclear power."**

## Storm brewing

It's the season of discord at US National Oceanic and Atmospheric Administration.

This year's hurricane season in the Atlantic Ocean has so far seen just two named storms: Andrea and Barry. But a much bigger tempest has been brewing in Miami, Florida, for several months — let's call it Hurricane Bill.

In January, Bill Proenza took over as director of the US National Hurricane Center, the forecast facility in Miami, Florida, that aims

to keep the US public safe from storms. At best it was a lateral career move from his previous post at the National Weather Service into a position that Proenza had not applied to fill.

Within weeks of assuming the centre's directorship, Proenza landed himself in hot water (see *Nature* **447**, 514–515; 2007). Among other things, he criticized how much money the centre's parent agency, the National Oceanic and Atmospheric Administration (NOAA), was spending on anniversary celebrations. More pointedly, he publicly bemoaned the lack of a detailed plan to replace the QuikSCAT satellite, which among its many jobs provides data on ocean winds to the team that forecasts hurricanes in the Atlantic.

This criticism did not sit well with his bosses or his employees, many

of whom eventually called for his ousting. On 9 July, in the midst of a special assessment of his performance, Proenza was placed on leave.

Last week, he got his chance to tell his side of the story in Washington DC, to the House Committee on Science and Technology. Democrats on the committee pressed the question of whether Proenza had been sidelined because of his whistleblower activities on QuikSCAT. Meanwhile, Republicans griped about the committee spending its time investigating what they dismiss as a routine personnel matter.

Nick Lampson (Democrat, Texas), who chaired the hearing, got at least one thing right. "The only storms the centre should be dealing with are those that form out in the ocean," he said. At the hearing, both sides acquitted themselves well: Proenza delivered an impassioned defence of his leadership, and Conrad Lautenbacher, NOAA's administrator, gave a lengthy and reasonably convincing explanation of why the agency felt it had to remove Proenza from his position.

The Proenza affair is not something that hurricane researchers and forecasters really need at this point, as the storm season begins to gear up. Government agencies are still reeling from their failure to cope with Hurricane Katrina in 2005, and scientists are dealing with the fall-out from their very public spats over the possible link between hurricanes and global warming (see *Nature* **441**, 564–566; 2006).

So NOAA needs to show coherent and firm management. First, it should find a relatively quiet spot to assign Proenza to — outside of the hurricane centre, where employee resentment is apparently too high for him to continue to function as an effective leader.

Lautenbacher is aware of the need for NOAA to raise its public profile and assert itself as a powerful scientific agency, rather than just a backwater of the Department of Commerce, of which it is part.

But it must make sure that its public-relations efforts don't get in the way of its scientific work. The very existence of a multimillion-dollar anniversary celebration is a cause for concern. And NOAA scientists have also been unhappy in recent months about management decrees suggesting, for example, that they improve the agency's branding by substituting 'NOAA' for 'National' in the names of centres such as the National Weather Service and the National Hurricane Center. Both of these outfits have distinguished histories and identities of their own, and NOAA needs to find ways of asserting itself and its mission in the public eye without diminishing them.

More substantively, the agency needs to address gaps in its satellite systems. Proenza is only the latest to highlight these. The National Academies had already done so, most recently in January, when it set out a national strategy of Earth-observing missions for the federal

**"Spats among staff should not distract from the larger task of focusing Earth-observation priorities."**

government. That plan would include an ocean-winds mission to do much the same job as QuikSCAT. An area of further concern was, the academies said, the level of coordination between NASA, which has customarily developed research satellites, and NOAA,

which takes them into operational use.

NOAA needs to make sure that spats among staff at its hurricane centre do not distract from the larger task of focusing Earth-observation priorities in the coming decades. Researchers have already clarified what they need. Now it's time for the government to follow those recommendations and make sure the next generation of satellites is in place for the storms yet to come. ■

## California dreaming

Universities should draw the line at certain types of support from the drug industry.

California, home to the largest public university system in the United States, is currently a battleground in a struggle over how to police perceived conflicts of interest at its medical schools. The university's campuses are trying to derail a proposal from its central administration that would clamp down on common drug-industry practices, such as the sponsorship of free lunches for medical students and the granting of general purpose, 'unrestricted' money to some faculty members (see page 394).

The campuses argue, for example, that these unrestricted grants can provide important sources of revenue. And some faculty members are also questioning the need for the policy. On behalf of a committee at the University of California, Los Angeles, for instance, Hossein Ziai writes: "With all the myriad problems facing health care in the United States... this issue seems rather trivial in comparison, and we question whether there is any demonstrable harm (as opposed to perceived harm) arising from these practices." The campuses' concerns about their autonomy, and freedom of action for their staff, deserve careful consideration.

But these arguments fall flat against the growing evidence that some

forms of support from drug companies can taint perspectives and practices. Policy analysts such as Lisa Bero at the University of California, San Francisco, have documented how pervasively industrial funding can influence the outcomes of studies, and have shown the inadequacy of measures meant to address these influences, such as disclosure of funding sources. Additionally, one source of the well documented problems of the US healthcare system is the large amount of money spent by pharmaceutical and medical-device vendors on marketing efforts, including some of the types of activity that would be banned under the University of California's proposed policy.

On both ethical and rational grounds the university's policy is worthy of general support. But, as with most things, the broader issue here is a fiscal one. In 2004, the University of California's president, Robert Dynes, signed a deal with Governor Arnold Schwarzenegger that froze state public funding of the university's system, began tuition and fee hikes, and committed the university to seek billions of dollars a year in additional private-sector funding.

In a sense, the latest policy tries to put the brakes on a trend towards heavier reliance on private funding that this fiscal squeeze has unleashed. The university's campuses are understandably concerned about their ability to attract funding from all sources so that they can continue to operate at world-class levels. The best course available to them, nonetheless, is to follow the high standards that have recently been set at other academic medical centres, such as those at Stanford University, and to embrace the proposed policy. ■



# RESEARCH HIGHLIGHTS

## Carbon lost from lakes

*Global Biogeochem. Cycles* **21**, GB3002 (2007)

An assessment of the carbon cycles of 41 lakes on five continents has put new global numbers on lakes' contribution to carbon in the atmosphere. The lakes' net carbon emission, at around 86 million tonnes, is roughly equivalent to Spain's annual carbon emissions.

Simone Alin of the University of Washington in Seattle and Thomas Johnson of the University of Minnesota in Duluth compiled available data for primary production, carbon burial and lake-atmosphere gas exchange for lakes (including Lake Malawi, pictured) representing more than two-thirds of the world's total volume of freshwater and saline lakes.

Overall, the lakes lose an order of magnitude more carbon to the atmosphere than they remove through burial of sediments.



T. JOHNSON

## BIOTECHNOLOGY

### Viral endgame

*Proc. Natl Acad. Sci. USA* doi:10.1073/pnas.0705362104 (2007)

Viruses could be placed in a 'checkmate' position with a strategy that identifies and blocks off all escape routes for evading antiviral agents by mutation.

Richard Lerner, Sydney Brenner and their colleagues at the Scripps Research Institute in La Jolla, California, engineered bacteria-infecting phages to express the surface proteins of other viruses, such as a strain of influenza. They then exposed the phages to libraries of small molecules or antibodies to identify molecules that blocked the viral protein's interaction. Cycles of mutagenesis create phages in which the viral protein evades the blocker, whereupon new blockers can be found that stop that mutated form. In effect, the likely viral mutations in the wild are thus explored and counteracted in advance *in vitro*, so that the antidotes can be prepared in anticipation.

at different points in time.

The proteins are present in the most ancient plant studied, a moss, but don't interact. In spikemosses, which evolved later, the hormone is present and the proteins interact, but they do not control growth. When they looked in the most recently evolved plant, the angiosperm *Arabidopsis thaliana* (or thale cress), they found that the system regulated plant growth.

This suggests that the gibberellin-response mechanism evolved in a step-by-step fashion between around 300 million and 400 million years ago.

## MICROBIOLOGY

### Build-up in the brain

*Mol. Microbiol.* doi:10.1111/j.1365-2958.2007.05837 (2007)

Certain variants of the malaria parasite *Plasmodium falciparum* preferentially accumulate in the brain, researchers have found.

*P. falciparum* manufactures proteins

that make the red blood cells it infects (pictured below) stick to the lining of small blood vessels. In the brain, this can lead to blockages that may ultimately cause the infected person's death.

Jacqui Montgomery of the Malawi-Liverpool-Wellcome Programme of Clinical Tropical Research in Blantyre, Malawi, and her colleagues compared the expression of *var* genes, which encode such proteins, in parasites taken from the brain, lung, heart and spleen of malaria patients. The team identified a couple of *var* genes that are specifically expressed in the brain and could represent targets for future therapies.

## NEUROBIOLOGY

### Release from helplessness

*Neuron* **55**, 289–300 (2007)

Researchers report that a protein called  $\Delta$ FosB may help mice to cope with repeated stress.

When mice experience recurrent, inescapable stress, some simply stop trying to get away. This behaviour, called

'learned helplessness', is relieved by antidepressants and is used to model depression and post-traumatic stress disorder.

Now, Eric Nestler of the University of Texas Southwestern Medical Center in Dallas and his colleagues have found that  $\Delta$ FosB is expressed by neurons that contain a pain-signalling peptide called substance P, in a brain region called the periaqueductal gray. Overexpressing  $\Delta$ FosB in stressed mice diminishes stress-induced release of substance P, and reduces learned helplessness.

## EVOLUTIONARY BIOLOGY

### Interaction over time

*Curr. Biol.* **17**, 1225–1230 (2007)

Researchers have traced the evolution of a mechanism that controls the growth of more recently evolved plants.

The hormone gibberellin acts by promoting the interaction of two proteins. Nicholas Harberd and his colleagues at the John Innes Centre in Norwich, UK, looked for this interaction in plants that diverged



D. SCHARF/SCIENCEFACION/GETTY



## MATERIALS SCIENCE

## Water pores

*J. Am. Chem. Soc.* doi:10.1021/ja073067w (2007)  
Specially designed lipids can polymerize to create a three-dimensional network of pores perfectly tailored to filter salts out of water, researchers in the United States have found. The hope is that such 'nanofilters' could be used for desalination in regions where fresh water is scarce.

The nanofilter developed by Douglas Gin, Richard Noble and their colleagues at the University of Colorado in Boulder has uniform pores that have an effective size of just 0.75 nanometres — around three times as big as a water molecule. This means that water can flow through but larger ions get blocked.

## BIOTECHNOLOGY

## Pick up a prion

*Nature Methods* doi:10.1038/nmeth1066 (2007)  
A new assay may prove quicker than existing techniques for detecting prions — the proteins responsible for brain diseases such as scrapie in livestock and Creutzfeldt–Jakob disease in people.

Currently, researchers monitor the ability of a sample of tissue or neural fluid to convert normally folded prion protein from brain tissue into the infectious, misfolded aggregates characteristic of disease. But the assay takes weeks to reach optimal sensitivity.

Ryuichi Atarashi and his team at the Rocky Mountain Laboratories in Hamilton, Montana, instead tested samples against prion proteins produced by bacteria. These proteins can be engineered to carry probes that make it easy to monitor the structural changes that occur in the protein when aggregates form. The assay, tested on samples from hamsters with scrapie, takes three days or less.

## CELL BIOLOGY

## Quick change

*Cell* 130, 77–88 (2007)  
Our cells may be poised to change fate, reports a team led by Richard Young of the Whitehead Institute for Biomedical Research in Cambridge, Massachusetts.

Young's team looked in embryonic stem cells and two types of adult cell for chemical

signals usually found close to genes that are being actively transcribed. They found these signals near about three-quarters of protein-coding genes in all the cell types. This was a surprise, because less than half of these genes were turned into the complete mRNAs needed to make proteins.

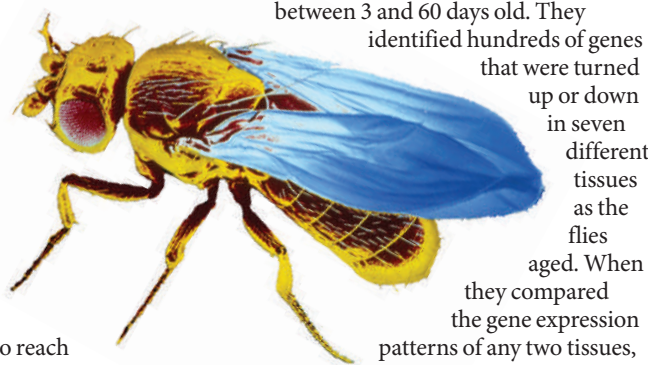
Although the cellular machinery initiates transcription at many genes, it only finishes transcribing some. This may allow the cell to quickly change fate under certain conditions by extending to completion the transcription of key genes.

## GENETICS

## Time waits for no fly

*Genome Res.* doi:10.1101/gr.6216607 (2007)  
Whether you look at brain, gut, muscle or fat, ageing exacts its toll on an animal's body. Now a study of fruitflies (pictured below) has found that gene expression follows different ageing patterns in different body tissues, with little overlap.

Researchers led by Sige Zou at the National Institute on Aging in Baltimore, Maryland, did a genome-wide screen of fruitflies aged between 3 and 60 days old. They identified hundreds of genes that were turned up or down in seven different tissues as the flies aged. When they compared the gene expression patterns of any two tissues, fewer than 10% of the changes were in the same genes.



J. BURGESS/SPL

## PALAEOLOGY

## When dinos hit puberty

*Biol. Lett.* doi:10.1098/rsbl.2007.0254 (2007)  
Many dinosaurs hit puberty before they reached adult size, according to a new study.

Gregory Erickson of Florida State University in Tallahassee and his colleagues studied seven fossilized dinosaurs that were brooding when they died. The specimens' body sizes indicate that they followed a growth and maturation pattern more akin to that of modern crocodilians than their other descendants, birds.

Birds reach their full size long before sexual maturation. The discovery hints that this life-history trait may have emerged relatively recently, and no earlier than the first true bird, *Archaeopteryx*.

## JOURNAL CLUB

**Jon Kleinberg**  
Cornell University, Ithaca, New York

**A computer scientist wonders how much information is really good for us.**

I am interested in understanding how groups of people or computer systems work together to solve complex problems. This is relevant in real-life situations that demand collective problem-solving, ranging from scientific research to military operations, so we hope to learn about the underlying mechanisms through experiment.

Stanley Milgram's famous 'six degrees of separation' studies form one such set of experiments. In these, participants were asked to help send a letter to a far-away stranger by forwarding it to a friend they thought might know the target. That this strategy often succeeded hints at how people lacking a global picture of the social network they inhabit can still jointly solve a difficult search problem.

One of the interesting questions here is how a group's ability to solve a problem is affected by the amount of information available. I expected that if people had a global view of the system, rather than just a local one, their effectiveness at solving the problem would increase.

A fascinating experiment (M. Kearns *et al. Science* 313, 824–827; 2006) shows that this isn't always so. The researchers posed a task in which they deliberately varied how much information was revealed to participants about what others in their group were doing.

For certain settings of the problem, giving participants a global view significantly slowed down progress. People faced with too much information in a time-pressured setting became 'overloaded', and this impaired the group's function.

As we consider designing tools to help people work together effectively, we should remember that increasing everyone's situational awareness might not always lead to improved performance.

Discuss this paper at <http://blogs.nature.com/nature/journalclub>

## NEWS

# Quake shuts world's largest nuclear plant

No one died as a result of Japan's latest nuclear incident and environmental damage seems to have been mostly avoided. But is this testimony to successful plant design or a warning of impending disaster, asks **David Cyranoski** in Tokyo.

**A**fter the stunning revelation that the nuclear power plant damaged in an earthquake last week was built above an active fault line, Japan faces an uphill struggle to convince its citizens, and the rest of the world, that its commitment to nuclear power is safe.

Perched on top of four converging tectonic plates, Japan is one of the most earthquake-prone countries — geological instability causes around 1,000 tremors a year there. And yet, with 55 operating reactors, it has the third largest nuclear generation capacity in the world — behind France and the United States. With few indigenous energy resources, Japan relies on nuclear power for about a third of its needs, and aims to up this to 40% in an ambitious expansion programme that will see 11 new facilities built by 2017.

This tricky dichotomy was brought into stark relief on 16 July when a magnitude-6.8 earthquake caused a shut down of the Kashiwazaki-Kariwa plant, in Niigata prefecture on the west coast. The damage to the facility was relatively minor, no one died and the amount of radiation released was reportedly negligible — well within international safety limits. Nevertheless, the incident has sparked fears that neither Japan's nuclear facilities nor its

nuclear safety evaluation system can handle the seismic activity that plagues the country (see 'The big one').

The quake — which killed ten people and injured more than 1,000 in Niigata — sparked a fire in a transformer that supplies electricity to one of Kashiwazaki-Kariwa's seven reactors and leaked radioactive cooling water into the sea and gas into the atmosphere. The plant — the world's largest in terms of power output — has been shut indefinitely. International observers have described the handling of the incident by its owner, Tokyo Electric Power Company (TEPCO), as a public-relations disaster, especially in light of the country's history (see 'A shaky nuclear record').

## Catalogue of errors

Because the earthquake occurred on a national holiday, only four people were available to fight the transformer blaze, so it took around 90 minutes and the help of local firefighters to put it out. The public were not informed of the incident for seven hours, and the disclosures of leaks and malfunctions trickled out over several days. TEPCO initially said that 100 drums of solid nuclear waste had fallen over, but inspectors later said hundreds had been



Cracks in the ground next to Tokyo Electric Power Company's Kashiwazaki-Kariwa nuclear plant.

knocked over, and the lids of several dozen had opened, spilling their contents.

The list of malfunctions, damages and mistakes rose from an initial 50 to 63 in the ensuing days, and included an admission by the company that the 1,200 litres of contaminated water that poured into the ocean was 50% more radioactive than it had previously stated. Perhaps most worrying was the discovery, nearly three days after the quake, that radioactive iodine gas

AFP/GETTY IMAGES

## A shaky nuclear record

A string of past accidents, safety lapses and cover-ups in Japan have shaken public confidence in the industry.

- July 2007: earthquake damage at the Kashiwazaki-Kariwa nuclear power station run by Tokyo Electric Power Company (TEPCO) results in radioactive leaks, burst pipes and a fire.
- February 2007: TEPCO admits 199 cases of falsifying inspection data at three nuclear power plants, including Kashiwazaki-Kariwa.
- August 2006: negligible

radiation released via radioactive heavy-water steam at TEPCO's Fukushima-Daiichi power plant.

- August 2004: five workers at the Mihama nuclear power station run by Kansai Electric Power Company killed and six injured by boiling water and steam when a corroded pipe bursts.
- February 2004: eight workers exposed to low-level radiation at the Japan Atomic Power Company's plant in Tsuruga when they are accidentally sprayed with radioactive water.

- September 2003: small leak of radioactive water from a reactor at Chubu Electric Power's plant in Hamaoka.

- September 2002: TEPCO ordered to close all its reactors after admitting it falsified data.

- November 2001: Hamaoka plant shut down after two radioactive leaks occurred within days of each other.

- July 2000: more than 100 litres of radioactive water leak from a reactor at the Fukushima plant after an earthquake.

- September 1999: high-level radiation leak at JCO Company's fuel-reprocessing plant in Tokaimura when uranium oxide being mixed went critical because of deviations from prescribed procedure. Two workers die later from radiation exposure.

- March 1997: workers exposed to low doses of radiation after a fire and explosion at another Tokaimura fuel-reprocessing plant (operated by the official Japanese fuel-reprocessing organization Donen).

G.V.





# MANIC MOOD SWINGS CAN KILL GREY MATTER

Bipolar episodes decrease brain size, and possibly intelligence.

[www.nature.com/news](http://www.nature.com/news)

GETTY IMAGES



## The big one

'Genpatsu-shinsai', a term coined by seismologist Katsuhiko Ishibashi at Kobe University in Japan, is the media's post-quake buzzword. An amalgamation of the words for nuclear power and earthquake disaster, it describes a nuclear meltdown caused by a quake. Many fear that genpatsu-shinsai will be realized at the old Hamaoka plant in Shizuoka on the coast southwest of Tokyo, which has become the focus of anti-nuclear protest in the country.

Hamaoka is built directly on top of a major fault line. Just offshore, in the Pacific Ocean, three of the planet's main tectonic plates rub against each other. The

reactors at Hamaoka may be the strongest anywhere in the world — they are encased in massively reinforced concrete bunkers, supposedly able to withstand a quake of up to 8.5 in magnitude. The Tokyo authorities are now working to a disaster plan that assumes an 87% probability of a magnitude 8.0 quake within 30 years.

But the earthquake that triggered the 2004 Indian Ocean tsunami measured more than 9.0.

Kiyoo Mogi of Tokyo University, former chairman of Japan's top authority on earthquake prediction, the Coordinating Committee for Earthquake Prediction, said

the plant poses a serious safety risk and that atomic experts are calling for it to be shut down. Mogi said that it is "hard to say at this stage how many nuclear power plants should be stopped... but I can say Hamaoka power plant in Shizuoka should be stopped immediately".

Lawyer Mitsuei Murata of Tokai Gakuen University, a former diplomat and leading anti-nuclear campaigner told *Nature* that a quake at Hamaoka could smash the reactor. This, he says, could send a radiation cloud across Tokyo within 8 hours, killing hundreds of thousands of people immediately and millions thereafter.

D.C.

— or intentionally avoided — seeing fault lines," Nakata says.

Daisuke Suzuki, TEPCO spokesman for the Kashiwazaki-Kariwa plant, says of new guidelines to govern reactors and quake resistance, "The 2007 guidelines require us to look back 130,000 years, rather than the previous 50,000, so we might find evidence that it was active."

"The new guidelines also require geomorphological techniques to be used now, which may have revealed that the fault was longer if we had used them before," Suzuki says. He admits the earthquake was probably caused by movement of this fault. "If so, it must be longer than seven kilometres to have caused such a large earthquake."

### Blind thrusts

The new guidelines — under which all 55 reactors are being re-evaluated — are an improvement, says Katsuhiko Ishibashi, a seismologist at Kobe University's Research Centre for Urban Safety and Security and a member of a 2006 government subcommittee to revise them. For example, the method to estimate ground shaking is better. But his proposal to reconsider the survey standards for active faults in the guidelines was dismissed by the committee.

The guidelines also failed to factor in the effects of 'blind thrusts' — movements that cannot be seen by seismologists but can cause quakes with magnitudes of greater than 6.5. Ishibashi says that "the committee's misunderstanding leads to a strong underestimation

of powerful earthquakes". On the day of the last committee meeting, Ishibashi resigned in protest.

So is it safe to build a nuclear facility on such shaky ground? Scott Burnell, a spokesperson for the US Nuclear Regulatory Commission in Maryland, argues that they can endure floods, tornadoes, hurricanes, earthquakes and even a tsunami. "They are designed to withstand just about everything short of a meteor strike," he says.

**"This case is close to the worst scenario."**

The worldwide track record in nuclear versus nature has been good. In 1992, a 690-megawatt reactor at Turkey Point in Florida weathered the winds of Hurricane Andrew. And in 2004, the Kalpakkam reactor near Madras, India, emerged unscathed from a massive tsunami that engulfed the city in which it was located. Sensors detected the rising water level and shut down the reactor before the tsunami reached the shore.

Most observers agree that the Kashiwazaki-Kariwa reactor seems to have performed well. Despite being designed for a lower-magnitude quake, the reactor buildings are mostly intact. Mitsuru Uesaka, a nuclear engineer at the University of Tokyo, says that given the difference between the expected shaking and that experienced, "this case is close to the worst scenario. Even so, the leaked radiation was negligible," he says.

**David Cyranoski, with additional reporting from Geoff Brumfiel in Washington DC.**

**See Editorial, page 387.**

was still being vented from one of the reactors.

TEPCO built the facility to withstand a magnitude 6.5 quake — the Japanese safety standard for reactors located on sites not above an active fault line. But it has now emerged that the offshore epicentre of last week's quake is on an active fault line that probably extends directly under the Kashiwazaki-Kariwa plant. A preliminary investigation of the quake and its aftershocks has revealed a fault line of up to 30 kilometres long.

Akira Fukushima, of Japan's Nuclear and Industrial Safety Agency in Tokyo, says that four fault lines were identified at the site in 1980 before the facility was built, but that all were considered inactive. *Nature* has heard claims from Japan's seismologists that data indicating an active fault line was potentially under the site were ignored when the plant was enlarged.

Hiroaki Nakata, a seismologist at the Hiroshima Institute of Technology, says that TEPCO found a seven-kilometre-long fault line in 1996, during investigations as part of its application to install two new reactors on the plant, but failed to investigate it fully.

Nakata has produced a map showing where fault lines taken from TEPCO data should have extended. "When we find an active fault, we check features surrounding it. There's no reason for TEPCO to have stopped when they did. There are many places where they missed



# Darfur lake is a 'mirage'

"Water find may end Darfur war," proclaimed headlines last week, describing a claim by researchers at Boston University in Massachusetts to have identified the site of an ancient lake in northern Darfur that could imply extensive groundwater reserves. But geologists speaking to *Nature* dismissed the hype, pointing out that the lake dried up thousands of years ago and that it will not necessarily be surrounded by aquifers holding ancient water. Furthermore, they say that the lake was identified in the 1800s, and that its size and shape were detailed over a decade ago.

The press release from Boston University — entitled 'Mapping of ancient mega-lake by Boston University scientists catalyst for global humanitarian outreach' — announced a '1,000 Wells for Darfur' initiative to drill around the lake "to create new groundwater resources to help establish peace and economic security in the region."

The initiative was launched by the government of Sudan after a meeting between President Omar al-Bashir and geologist Farouk El-Baz, director of the Boston University Center for Remote Sensing. El-Baz had announced the discovery of the 30,750 square kilometre lake — which would have contained around 2,500 cubic kilometres of water — in April, after scouring Landsat satellite images and sand-penetrating radar data from the Shuttle Radar Topography Mission.

The media's portrayal of a lake that actually contains water now stems from the way the Boston group presented its claims, says Mohamed Abubaker, an official at the Ministry of Irrigation and Water Resources in Khartoum. "The general public in Sudan, and even some very



high-ranking officials, came to believe that what has been discovered is literally a lake — perhaps even with fish in it," he says. "The way El-Baz presented his efforts helped consolidate this misconception. It was like a political rally for a presidency run-up rather than a scientific portrayal of facts."

El-Baz contests this allegation. "It is incomprehensible for anyone to think it is a physical lake," he says, adding that he consistently made it clear that his argument was that the lake's water would have seeped

through the sandstone substrate to accumulate as groundwater, and that drilling the sandstone under and around the ancient lake could yield fresh water.

The Sahara region is known to have been rainy in past millennia, and this ancient water

exists as groundwater in the so-called Nubian sandstone aquifer that stretches across Chad, Libya, Egypt and Sudan. The International Atomic Energy Agency, based in Geneva, has a programme to manage this aquifer.

Geologists argue that the rocks beneath and around the ancient lake are no more likely to hold water than those elsewhere in the Nubian aquifer. "Nearly everywhere it is present in Egypt the Nubian sandstone is water-bearing, so it is a matter of simple common sense that it would be the first place to look for significant groundwater reserves in Sudan," says Neil Sturchio, a geologist at the University of Illinois in Chicago, who describes the lake story as "hype".

There may actually be less chance of finding substantial water in the lake vicinity in northern Darfur than elsewhere on the aquifer. Although the porous, water-retaining sandstone aquifer is up to 3,500 metres thick at its northern fringes in Egypt, it thins to just a few hundred metres in northern Darfur, its southernmost reach.

Alain Gachet, a French geologist who has spent decades exploring for oil and water in the region, says that the configuration of rocks in the vicinity of the lake makes substantial water reserves even more unlikely. The lake is in an uplifted area, which has accelerated the erosion of the Nubian

sandstones underneath, he says, and he claims that the lake is probably underlain by a crust of granite and other impermeable rocks rather than sandstone.

"There is obviously no trace of water at the bottom of this lake. In the best case, it would

**"The general public in Sudan, and even high-ranking officials, came to believe that what has been discovered is literally a lake — perhaps even with fish in it."**

## California campuses resist industry restrictions

Campuses at the University of California are fighting a move to restrict their interactions with industry representatives.

Last year, officials at the University of California proposed a set of draft guidelines to govern how industry representatives can influence students and employees of the university's health sciences facilities and campuses, including medical and pharmacy schools. The measures would ban free gifts

and samples for clinicians, catered lunches for medical students and so-called unrestricted research grants from industry.

But on 12 July, the campuses roundly rejected the proposed guidelines, calling them "unacceptably vague, overbroad, and impinging on academic freedom". Speaking on behalf of the campuses, the system-wide academic council recommended that the university's president ditch

the guidelines altogether.

"The Academic Council... respectfully requests that the [University of California Office of the President's] Office of Clinical Services withdraw this proposal at this time," wrote academic council chair John Oakley, a law professor at the University of California, Davis, in a letter to the University of California president's office.

The president's office will review the recommendations and

decide how to proceed, said office spokesperson Jennifer Ward.

The move bucks a recent trend of medical schools clamping down on the close relationships that industry cultivates with faculty and students. Medical schools across the nation, from Yale University in New Haven, Connecticut, to Stanford University in Palo Alto, California, have passed rules restricting gifts, free lunches and money that often flows freely from pharmaceutical companies,



**LIQUIDS BOUNCE AGAIN**  
Jumping jets move from the bathroom to the kitchen.  
[www.nature.com/news](http://www.nature.com/news)

M. THRASHER



**Sheikas (traditional women leaders) at the south Darfur camp are in urgent need of water.**

ern Darfur, where current needs are greatest, say geologists. The geology of these areas is mainly impermeable rock, with only a few outcrops of sandstone aquifer.

If the Darfur aquifer did yield water it would only be a stop-gap solution as the aquifer is not being replenished by rainfall and the fossil water reserves are finite, says Johanna Kieniewicz, an expert on the Nubian aquifer at Denison University in Granville, Ohio. "It's essentially 'mining' groundwater," she says, adding that many of the oases in Egypt feeding off the Nubian aquifer have only around 50 years of water supply left.

The widespread notion that water is at the origin of the Darfur genocide, and so could be a solution, is also simplistic say experts. That idea has been perpetuated by Ban Ki-moon, secretary-general of the United Nations, who recently painted the genocide as a tragic result of resource scarcity.

But experts on the region argue that the true culprit is the National Islamic Front, which came to power in Khartoum in 1989 and has since expanded its political base through ethnic cleansing (see *Nature* 447, 1038; 2007).

Al-Bashir is himself allied to the National Islamic Front. El-Baz defends obtaining support from such sources, and says his own efforts are apolitical. "This is science in the service of a humanitarian cause."

And even the novelty of the mega-lake 'discovery', which is to be published in the *International Journal of Remote Sensing*, has been questioned. Geologists claim that the palaeolake was identified by German scientists in 1985 and mapped during the 1990s. El-Baz admitted to *Nature* that the ancient lake deposits he claimed to have found had already been discovered, but says that new satellite data allowed his group to map its full extent. ■

**Declan Butler**

be so salty that it would be undrinkable," says Gachet, who uses radar remote-sensing techniques to detect aquifers close to the surface and is working with UN agencies to map potential wells across Darfur.

El-Baz admits there is a real possibility that there may be little sandstone in contact with the lake, but argues that this can be established only by drilling and geophysical surveys. "Gachet is right to say the lake has dried up, but not if he says that some of its water would not be held beneath the desert surface," he says, "No one can paint the subsurface picture with

the available information."

Mike Edwards, of the Centre for Water Research at the University of Oxford, UK, says that it is misleading to suggest that groundwater will be found if the area of a former palaeolake is drilled. He adds that "there is no substitute for drilling as far as groundwater resources are concerned — but there will already be quite a few wells in this area. El-Baz's work is certainly not innovative."

Even if extensive water resources were to be found in northern Darfur, this would do little to alleviate the situation in western and south-

medical device manufacturers and other industry sources to doctors, researchers and students. The bans have been sparked in part by an article published in January last year (T. A. Brennan *et al.* *J. Am. Med. Assoc.* 295, 429–433; 2006). In the article, doctors and researchers called on academic medical centres to tighten their policies to eliminate conflicts of interest between their employees and faculties and industry.

But under president Robert Dynes, the University of California has gone in the opposite direction,

cultivating close relationships with industry that have caused controversy.

For instance, some members of the faculty of the University of California, Berkeley have protested against a \$500 million deal their campus signed with the energy company BP in February (see *Nature* 445, 688–689; 2007). And for several years the university has been embroiled in a debate about

whether it should accept research funding from tobacco companies (see *Nature* 446, 242; 2007).

This worries academics such as Lisa Bero, a professor of clinical pharmacy and health policy at the University of California, San Francisco, who studies the way such 'unrestricted' funding can influence both research and clinical practice (*Br. Med. J.* 326, 1167–1170; 2003). Bero calls the academic council's attempt to

**"Whether they're called unrestricted or not, a lot of these grants do have strings attached."**

derail the university's vendor policy "disappointing". She notes that no University of California school has implemented a comprehensive ban on gifts and other industry influence on campus, and disputes the academic freedom argument cited in opposition to the proposed system-wide policy.

"The evidence we have shows that whether they're called unrestricted or not, a lot of these grants do have strings attached," Bero says.

Erika Check

See Editorial, page 388. ■



## ON THE RECORD

**“The pain was immediate and felt like my body was on fire.”**

Endurance swimmer Lewis Pugh (pictured) after his 19-minute swim at the North Pole, when he braved water temperatures of  $-1.8^{\circ}\text{C}$  to raise awareness of melting polar ice.



REUTERS

## SCORECARD

**Low-sugar water melons**

Diabetics and dieters will be pleased to learn that US geneticists have bred water melons with 50% less sugar than normal.

**High-fat friends**

A 30-year study monitoring some 12,000 Americans concludes that they were 57% more likely to become obese if one of their close friends became obese too, suggesting that social ties help to spread the obesity epidemic.

## ZOO NEWS

**Prolific panda**

Huamei, a US-born giant panda now living at a reserve in Sichuan, China, has delivered her third set of twins, boosting China's captive giant-panda population by nearly 1%.



CHINA DAILY/REUTERS

## NUMBER CRUNCH

**74 watts** is the power needed to display a full-screen version of the Google homepage on a conventional cathode-ray monitor.

**3,000 megawatt-hours**

is the energy that would be saved worldwide each year if everyone switched to blackle.com, a new website that allows users to do Google-powered searches from a dark page that uses only 59 watts.

**25%** is the proportion of computers worldwide that still use cathode-ray monitors. This figure is declining all the time, prompting cynics to argue that 'dark searching' is merely a gimmick.

Sources: *The Times*, USDA, *N. Engl. J. Med.*, *blackle.com*; *ecolron*, Reuters

# Carbon sinks threatened by increasing ozone

Rising levels of ozone pollution over the coming century will erode the ability of plants to absorb carbon dioxide from the atmosphere, a new climate-modelling study predicts.

Ozone is already known to be a minor greenhouse gas, but the new calculations highlight another, indirect way in which it is likely to influence global warming by 2100. High levels can poison plants and reduce their ability to photosynthesize, says Stephen Sitch of the UK Met Office's Hadley Centre for Climate Prediction and Research in Exeter.

Whereas ozone high in the stratosphere shields Earth from solar ultraviolet rays, high levels of ozone closer in are toxic to plants and animals. Ozone is generated when oxides of nitrogen — chiefly from vehicle exhausts and fossil-fuel power stations — react with other chemicals in the air.

Many of the world's most polluted areas routinely endure ozone concentrations higher than 40 parts per billion, enough to damage plant life. By the end of the century, virtually all the world's populated areas are predicted to be above this threshold.

Plant growth is a vital carbon sink, estimated to suck up around a quarter of the  $\text{CO}_2$



R. KRAUSE/REUTERS

Beijing smog is a sign of rising ozone pollution.

emitted into the atmosphere. “This study combines knowledge about ecosystem function with atmospheric chemistry, and that's never been done before,” says Sitch. “No one has considered the detrimental effect of ozone on plants.”

The issue is complicated by the intricate interplay between rising  $\text{CO}_2$  levels, which boost plant growth, and increasing ozone, which stunts it. Some ecosystem models had predicted that the rise in  $\text{CO}_2$  expected over the coming century might be offset by the expected

# Diamonds 'melted' inside an onion

Diamonds may not be for ever: researchers think they have seen, for the first time, the molten form of what is arguably the world's hardest material.

Jianyu Huang of Sandia National Laboratories in New Mexico heated diamond, at high pressure, to more than  $2,000^{\circ}\text{C}$  inside microscopic hollow shells of carbon and watched the diamond soften (J. Y. Huang *Nano Lett.* doi:10.1021/nl0709975; 2007).

Huang describes this as

quasi-melting. It is not true melting, he says, because the diamond particles don't become liquid carbon, but instead flicker between crystal forms by continually melting and instantly refreezing in a different conformation.

This is the closest anyone has ever come to directly melting diamond. No one really knows what molten carbon looks like. One form, graphite, seems to break down into liquid-like blobs when heated to high temperatures, although

they have not been examined while still molten. But until now, molten diamond had not been achieved.

A key problem is that when diamond is heated to very high temperatures, at atmospheric pressure, it turns into graphite rather than melting. To overcome this, Huang's team used structures known as 'carbon onions' to create very high pressures and temperatures.

These roughly spherical concentric shells of graphite-





**MASTODON DNA SEQUENCED**  
Ancient tooth reveals elephants' family tree.  
[www.nature.com/news](http://www.nature.com/news)

L. O'KEEFE/SPL

boost in the growth of forests and swamps. But factoring in ozone means that it looks less likely that this carbon sink will grow fast enough to keep pace with the increasing emissions.

Eva Pell, who studies the effects of ozone on plants at Pennsylvania State University in University Park and who was not involved in the study, finds the results credible. "There is no doubt that ozone reduces CO<sub>2</sub> fixation," she says. "It makes sense that the adverse effects of ozone would be dampened by elevated CO<sub>2</sub>, and the ability of plants to serve as carbon stores in an elevated CO<sub>2</sub> environment would be reduced by elevated ozone."

In 1901, according to the researchers' calculations, plant growth was responsible for storing 113 billion tonnes of carbon worldwide. By 2100, this figure is predicted to be 171 billion tonnes — without ozone it would be more than 200 billion tonnes, they say. Their results are published online this week (S. Sitch *et al.* *Nature* doi:10.1038/nature06059; 2007).

Different plant species vary in their sensitivity to ozone, and these figures reflect predictions based on a fairly high average level of toxicity, says team member Bill Collins of the Met Office. But even in the researchers' low-sensitivity calculations, there's likely to be a dent of around 15 billion tonnes in overall carbon sequestration as a result of the effects of ozone.

"The bottom line is that ozone is a greenhouse gas, so it's known to contribute to the greenhouse effect. Our study says you should double that predicted contribution," says Collins.

Unlike most greenhouse gases, ozone is a short-lived, regional pollutant that can be tackled at an individual level using catalytic converters, for example, to reduce precursors to ozone, Sitch suggests. ■

Michael Hopkin

## Memory seen in the making

The physical changes that occur when the brain makes a new memory have been observed for the first time, say researchers, who hope to go on to map the distribution of memory across brain regions.

Gary Lynch of the University of California, Irvine, and his colleagues examined the junctions between neurons — synapses — in three dimensions using a technique called restorative deconvolution microscopy (RDM). This consists of a sensitive light microscope with computer algorithms that analyse light scattered above and below the focal point, producing a three-dimensional 'trace' of an object's structure.

In previous work, the group developed a fluorescent marker that attaches to synapses in the brain that have recently undergone a certain type of neuron-to-neuron connection believed to be responsible for encoding memory, called long-term potentiation (LTP) (L. Y. Chen *et al.* *J. Neurosci.* 27, 5363–5372; 2007).

The team exposed live rats to a novel environment and allowed them to learn its layout. They then removed the animals' brains to examine the hippocampus — a region involved in memory — using RDM to observe individual synapses. A second group of rats was shown the new environment but not allowed to explore it before their brains were examined.

**"We saw that the synapses had actually changed shape as a result of the new memory."**

Only rats that had undergone learning and memory acquisition showed new synaptic growth, Lynch says (V. Fedulov *et al.* *J. Neurosci.* 27, 8031–8039; 2007). And the hippocampal synapses to which the LTP fluorescent marker attached were 50% larger than other synapses not involved in LTP.

Furthermore, when the group looked at hippocampal slices from a third group of rats, which had been allowed to learn the same new environment but been given

a drug to block LTP, the synapses showed no new growth, and were similar to those of the second group. This indicates that the new synaptic growth observed in the study is a result of LTP, Lynch asserts.

"We saw that the synapses had actually changed shape as a result of the new memory," Lynch says. "They went from oval to circles, which have a greater surface area." He now aims to use the technique to see which other areas of the brain might be involved in memory.

Being able to look at memory at the synaptic level is a major advance, says Mark Bear, a neuroscientist at the Massachusetts Institute of Technology in Cambridge. But he hesitates to accept the conclusions Lynch's team has drawn. "I don't think it's been proven that these [synaptic] changes represent the memory," he says. ■

Kerri Smith



Quick change: molten diamond flickers between crystal forms.

like carbon act as high-pressure cells that shrink when blasted with a beam of electrons. As they contract,

the material in their centres is squeezed to very high pressures. Previous studies by Florian Banhart

of the Institute for Physical Chemistry in Mainz, Germany, and Pulickel Ajayan of the Rensselaer Polytechnic Institute, New York, showed that graphite-like carbon in the onion's centre can be converted to diamond in these chambers (F. Banhart and P. M. Ajayan *Nature* 382, 433–435; 1996).

Huang's team used carbon onions with a carbon nanotube attached to the outside. They wired up the nanotube and heated the tube-onion composite while irradiating it with electrons. Huang estimates that this created temperatures of more than 2,000 °C and pressures of around 400,000 atmospheres at the core.

As the onions shrank, the carbon at the centre was transformed from graphite to diamond. When this got hot enough, it adopted the fluctuating quasi-molten state, Huang explains. Ultimately, he hopes, it will be possible to make fully molten diamond, so that the onions have liquid carbon cores.

But not everyone is confident that the diamond is really melting. Although Banhart says the new work is interesting, he thinks that the carbon may instead be switching between diamond and graphite — each time it returns to diamond, the crystals will look different, he says. ■

Philip Ball

PASIEKA/SPL

# Libyan ordeal ends: medics freed

A French government aircraft carrying six medical workers convicted of deliberately infecting children with HIV touched down in Sofia, Bulgaria, on 24 July, ending their 8-year ordeal in a Libyan prison.

The five Bulgarian nurses and a Palestinian doctor — given life sentences after more than 400 children contracted HIV at the hospital they worked at in Benghazi in 1998 — were immediately pardoned by Bulgarian President Georgi Parvanov. The charges, denied by the six, have been condemned as baseless by scientists, who argued that the outbreak was accidental and caused by inadequate sanitary precautions at the hospital.

Their release is the final scene in meticulously crafted negotiations between the European Union (EU) and Libya, which sought a way for Libya to climb down on the case without being seen to concede to Western pressure. Diplomatic efforts intensified as a result of international public and political outcry after the six medical workers were sentenced to death in a retrial on 19 December 2006.

Then, on 17 July, Libya's highest judicial body commuted their sentences to life imprisonment, over-ruling the death-penalty verdict upheld a few days earlier by the Supreme Court (see *Nature* 448, 230–231; 2007).

That move came after families of the children each received US\$1 million per child in 'compensation' from an international fund set up by the EU, Bulgaria and Libya. *Nature* understands



**Sofia airport: Bulgarian president Georgi Parvanov pardons the medical team convicted of infecting Libyan children with HIV.**

that most of money is in fact likely to have been paid by Libya itself, and that the move allowed Libya to save face. The EU also agreed to provide humanitarian aid for long-term treatment of the infected children.

Libya has long used the six medical workers as bargaining chips and political pawns in its international relations. Right until the final hour of their release, Libya haggled to win further concessions to improve its political and trade ties with the EU.

Benita Ferrero-Waldner, the European commissioner for external relations, was also on the aircraft with the freed health workers. She, the EU and Britain, were the main players working patiently behind the scenes to secure the release. On the Libyan side, the key force in freeing the

workers was Seif al-Islam Gaddafi, son of the Libyan leader Muammar al-Gaddafi, through his charity the Gaddafi Development Foundation. He is thought to be personally convinced that the outbreak was accidental.

More controversial is the role played by another passenger on the plane, French first lady Cécilia Sarkozy. France has not had a prominent role in the negotiations, and her last-minute intervention is widely considered to be a thinly veiled bid by her husband to steal the limelight that may, in fact, have weakened the EU's negotiating position in the talks.

"The efforts to mobilize Western governments to act by increasing international public

opinion have paid off," says Emmanuel Altit, a lawyer from the medical workers' international defence team. The concerted efforts of the scientific community around the case played a "fundamental role" in changing the trajectory of the case and helping to secure today's outcome, he adds.

"It's great news," says Vittorio Colizzi, an AIDS researcher at Tor Vergata University in Rome, Italy, who campaigned for scientific evidence exonerating the medical workers to be considered by the Libyan courts. "But we must not forget the children," he adds, pointing out that the 1998 outbreak was a double tragedy — for the six unjustly imprisoned, and for the infected children and families.

**Declan Butler**

## Stem-cell researcher's move attracts funding

James Thomson has added a part-time position at the University of California, Santa Barbara, to his current position at the University of Wisconsin, Madison. The new post is raising eyebrows because of recent strains between his home institution and the California Institute for Regenerative Medicine (CIRM) in San Francisco.

Thomson, a pioneering stem-cell researcher, expects to spend

around one month per year at his US\$1-million lab in Santa Barbara. But even that limited presence helped the university secure a \$2.3-million grant from the CIRM in June, noted blogger David Jensen on 15 July. And if some of the money granted to the university leads to breakthroughs it might also profit the state of California.

According to CIRM spokesperson Dale Carlson, discoveries made

with CIRM money at such non-profit institutions are owned by the institution. But the state of California can claim a share of revenue of more than \$500,000 generated on any resulting patents.

The prospect of California earning money from a Thomson discovery is noteworthy because researchers and watchdog groups have spearheaded a move to revoke patents for Thomson's work, owned

by the Wisconsin Alumni Research Foundation in Madison, on key human embryonic stem-cell research (see *Nature* 447, 16–17; 2007).

He is not the only researcher to take a job in California that could bring in CIRM funding — his colleague at Wisconsin, Clive Svendsen, has arranged a part-time consultancy at Stanford University in Palo Alto.

**Erika Check**



## US worker charged with stealing nuclear secrets

A labourer at a nuclear site in Tennessee has been charged with attempting to sell uranium-enrichment technology to France.

On 19 July, a federal grand jury indicted Roy Lynn Oakley for illegally possessing and attempting to transfer sensitive nuclear technology. Oakley was working to disassemble part of the K-25 gaseous-diffusion plant near the Oak Ridge National Laboratory that was used to enrich uranium for the nation's first nuclear weapons.

Oakley allegedly tried to sell sections of the plant's diffusion barriers to the French embassy in Washington DC. The embassy refused his offer; France has had gaseous-diffusion technology since the early 1950s.

This is the second recent security breach at a US weapons complex. Last autumn, classified documents from Los Alamos National Laboratory in New Mexico turned up in the trailer of a local drug dealer.

Oakley has pleaded not guilty.

## Abbott drops suit against AIDS activist group

The drug company Abbott Laboratories back-pedalled in its battle against AIDS activists this week, agreeing to drop its lawsuit against the group Act Up-Paris.

Illinois-based Abbott has been increasingly criticized for its decision not to apply to sell new drugs in Thailand after the country began to issue 'compulsory licences' for key drugs. These would allow generic versions to be manufactured without the consent of the patent-holder (see *Nature* 448, 14; 2007). Abbott makes several AIDS drugs, including a heat-stable combination pill called Aluvia.

In April, Act Up-Paris organized an Internet protest that temporarily shut down Abbott's website. In May, the drug firm started legal proceedings against the group.

But on 22 July in Sydney, the International AIDS Society brokered a meeting between the two. Abbott has not changed its mind about applying to market drugs in Thailand.



Protesters demonstrate against Abbott's decision not to market new AIDS drugs in Thailand.

C. R. ARBOGAST/AP

## Cosmology prizewinner sails off to work in virtual life

Last week, the day after astrophysicist Robert Knop decided to quit academia, he and 52 other scientists won the 2007 Gruber Cosmology Prize for discovering that the Universe's expansion is accelerating. "It gave me pause, but not much," says Knop. He is moving on to write code for Second Life, the alternative-reality computer program (right) run by the Linden Lab in San Francisco, California.



In 1998, Knop was part of a team led by Saul Perlmutter of the University of California, Berkeley, that measured distant supernovae to gauge the Universe's growth. Researchers led by Brian Schmidt at the Australian National University in Canberra did the same. Knop later took a faculty position at Vanderbilt University in Nashville, Tennessee, but says he has been unable to get funding and thinks he wouldn't make tenure.

Perlmutter and Schmidt will each receive US\$125,000, with the rest of the \$500,000 prize being split between the co-authors of the seminal papers. "I'll take whatever they give me," says Knop.

## German stem-cell law should change, says ethics council

Germany's advisory committee on medical ethics has recommended easing restrictions on human embryonic stem-cell research.

Current law, which has prompted bitter complaints from the research community, bars German scientists from working on stem-cell lines created after 2001. On 16 July, 14 of the National Ethics Council's 24 members approved a proposal to end the ban and establish mechanisms to approve research plans individually. The country's main funding agency, the DFG, made a similar recommendation last November, reversing its previous stance (see *Nature* 444, 253; 2006). More politicians are also coming out in favour of lifting the ban or shifting the cut-off date for cell lines to 2007.

Parliament is expected to consider revisions to the stem-cell law this autumn. Council member Horst Dreier thinks the federal research minister, Annette Schavan, will oppose ending the ban but may reset the cut-off date.

## US publishing rate slows as Asia's rate grows

American institutions are publishing fewer research papers, and more papers are coming from Asia and Europe, a new US government study finds.

Overall, US scientists are authors of more articles than researchers in other countries. But production started to plateau in the late 1990s, according to a National Science Foundation survey that analysed scholarly output between 1988 and 2003 using article database citations.

China, Singapore, South Korea and Taiwan made the biggest gains, publishing an average of 15.9% more articles per year between 1992 and 2003. Japan and the European Union upped their production by 3.1% and 2.8% per year, respectively, whereas US publications increased by just 0.6%.

American scientists are teaming up more often, the study adds, with more authors on each manuscript and more international collaborations.

## Italy's research council boss departs at last

After a long and public struggle, the Italian government has finally ousted the unpopular president of the CNR, Italy's National Research Council, which runs some 100 institutes. On 20 July, Fabio Pistella, appointed by the previous right-wing government and criticized for his performance (see *Nature* 440, 264–265; 2006), was transferred to a non-scientific government agency.

The current centre-left government has changed the selection procedure for the heads of research agencies to avoid future political patronage. Under the new system, a short list of top scientists is proposed by an expert search committee, and the research minister must select from the list.

Pistella's removal follows several other high-profile departures, including those of Sergio Vetrone from the Italian Space Agency in October 2006 and Piero Benvenuti from the Italian National Institute for Astrophysics in April.

A temporary CNR commissioner is expected to be named by the end of this week.

LINDEN RESEARCH, INC., 2007



## BUSINESS

# The pain game

The safety problems that brought down Vioxx have tainted a whole class of drugs. **Meredith Wadman** examines their chances of a comeback.

Few were surprised this spring when an advisory panel to the US Food and Drug Administration (FDA) trounced Merck's Arcoxia (etoricoxib) in a 20–1 vote. The painkiller was, after all, a 'COX2 inhibitor' — a relative of Vioxx (rofecoxib), the Merck pill that was pulled from global markets in 2004 for increasing the risk of heart attacks and strokes. To pass muster with the FDA, the regulator said ahead of the vote, Arcoxia would have to be more effective than established painkillers in some patients, as well as safe.

That bar proved too high. Despite a trial<sup>1</sup> of nearly 35,000 patients showing that Arcoxia's heart risks were no worse than those of the traditional painkiller diclofenac, the agency took the panel's advice and refused to approve the drug.

"The challenges for a new drug in this class are unparalleled," says Seamus Fernandez, a drug-industry analyst with investment bank Leerink Swann in Boston, Massachusetts. "It's really not worth it for the FDA to approve a drug in this category if it isn't superior." So for most drug companies, he says, the calculation is clear: "The amount of money you have to spend, versus the magnitude of sales you could capture, really wouldn't warrant starting clinical trials with a new COX2 inhibitor."

Because the United States is by far the most lucrative market, FDA reticence has become a major disincentive to companies even considering pressing forward with this new generation of medicines.

## Tummy trouble

Yet only a few years ago, COX2 inhibitors were lauded as much-needed alternatives to conventional painkillers, called non-steroidal anti-inflammatory drugs, or NSAIDs, such as ibuprofen. These are some of the most-used drugs, but they can upset the stomach, making it tough for people to take them for chronic ailments such as arthritis. And in a small but significant proportion of patients they can cause severe, and even fatal, gastrointestinal damage.

There's a reason for these effects: NSAIDs work by blocking the actions of two enzymes, known as cyclooxygenase-1 (COX1) and cyclooxygenase-2 (COX2), both of which catalyse the production of chemical messengers called prostaglandins, which have many

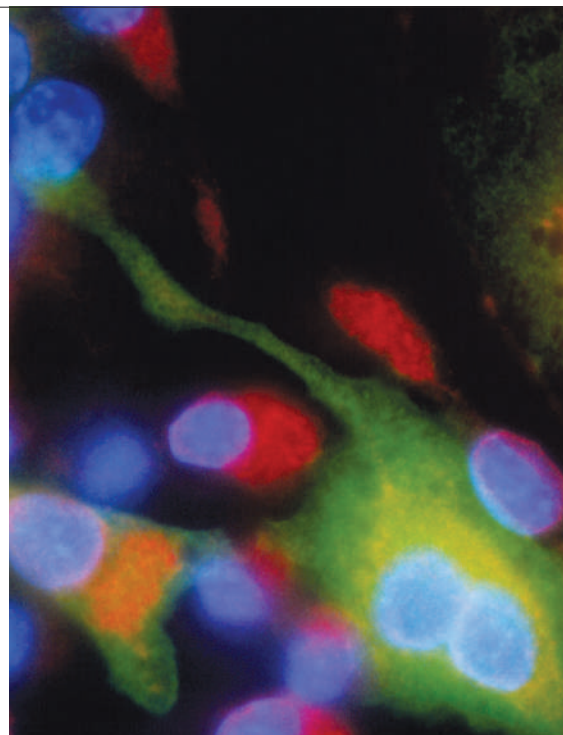
important functions in the body. COX1 protects the stomach and intestines by stimulating production of mucus. Block its action, and ulceration and gastrointestinal bleeding can occur.

By contrast, COX2 is activated only in response to injury, when it causes a prostaglandin called PGE<sub>2</sub> to be pumped out, increasing pain sensitivity. The importance of COX2's discovery<sup>2</sup> in 1991 by Daniel Simmons of Brigham Young University in Provo, Utah, and his colleagues was not lost on drugmakers. They quickly set about developing selective COX2 inhibitors in the hope of producing an effective painkiller that wouldn't cause gastrointestinal harm. And the new drugs did indeed prove gentler on the stomach in clinical trials. In 1999, Merck's Vioxx and Pfizer's Celebrex (celecoxib) were launched and rapidly became blockbusters; by 2002, when Pfizer's Bextra (valdecoxib) joined them on the US market, the three generated a combined revenue there of US\$4.9 billion.

But it was the very selectivity of the COX2 inhibitors that proved to be their undoing. For COX2 also catalyses production of the hormone prostacyclin (PGI<sub>2</sub>), which protects the heart by discouraging blood clotting and relaxing blood vessels. Suppression of this hormone is thought to be the cause of the heart attacks and strokes. Shortly after these risks emerged, Vioxx was withdrawn from global markets. Pfizer withdrew Bextra six months later, leaving Celebrex the only original COX2 inhibitor to remain standing.

Celebrex doesn't seem to be as risky to the heart as Vioxx and Bextra — possibly because it is an order-of-magnitude less selective for COX2 than its cousins — so the FDA has allowed it to be marketed, with clear warnings of its cardiac risks. And Celebrex is undoubtedly benefiting from the withdrawals of Vioxx and Bextra. It had \$2 billion in global sales in 2006 — an 18% increase over 2005 — with \$1.7 billion of that in the United States, according to the drug-information firm IMS Health in Norwalk, Connecticut. Arcoxia, despite the US rebuff, is still being sold in 63 countries. But in 2006 it earned Merck just \$265 million, 1% of the company's global sales.

Because Pfizer has so much at stake, it is spending more than \$100 million on clinical tri-



The COX2 enzyme (red) is activated after injury.

als to test the cardiovascular effects of Celebrex against two common NSAIDs in 20,000 people with pre-existing heart risks. "The COX2 class is under a cloud and whether that cloud lifts or not will depend on the results of this study," says Steven Nissen, a cardiologist at the Cleveland Clinic, Ohio, who is leading the trial.

## Tough markets

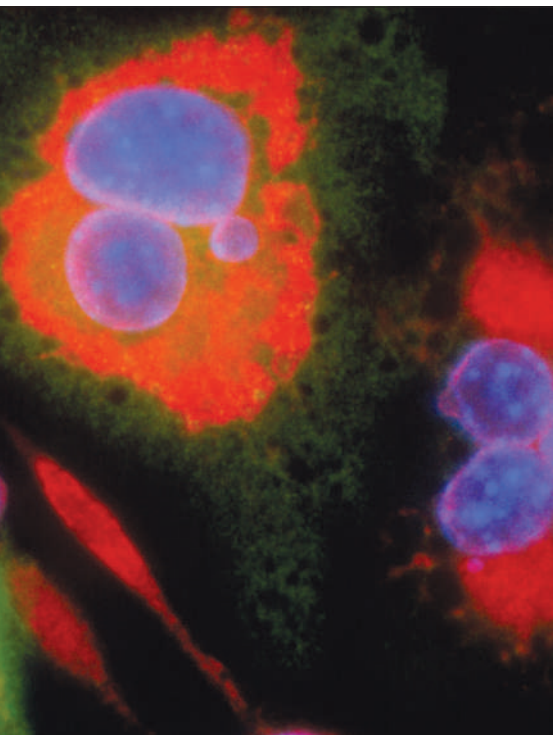
But even if the trial produces stellar results for Celebrex, the pay-off will be limited: it loses patent protection in 2016, and the trial's results are due in 2010 at the earliest. "If you were a company with a new COX2 inhibitor, even if you had a pretty good drug, could you market it in the face of generic Celebrex?" Nissen asks.

That could be a problem faced by Prexige (lumiracoxib), a COX2 inhibitor from Novartis that is now under FDA review, with a decision expected this year. Since its 2005 launch in Brazil, Prexige has been approved in more than 50 countries, including the United Kingdom. Last month, the company trumpeted the results of a trial of 741 people, which showed that the drug is significantly kinder to blood pressure than ibuprofen. Whether that will be enough to convince the FDA remains to be seen. Prexige can elevate liver enzymes, a sign of potential liver toxicity.

Supporters of COX2 inhibitors maintain that deeper study could revive their potential. "It just seems a pity to walk away from them without trying to segregate benefit from risk

**"The challenges for a new drug in this class are unparalleled."**

— Seamus Fernandez



N. KEDERSHA/SPL

in a way much more sensitive than large-scale phase III trials, which are very crude approaches to that question,” says Garret Fitzgerald, director of the Institute for Translational Medicine and Therapeutics at the University of Pennsylvania in Philadelphia, whose mechanistic studies<sup>3,4</sup> in humans and mice first pointed to the cardiovascular risks of COX2 inhibitors. Fitzgerald wants to see more studies of these drugs in humans, to discover whether genetic and other differences can establish which patients can use them without heart risks.

Others are moving beyond COX2, downstream in the biochemical pathway that leads to PGE<sub>2</sub>, to an enzyme called microsomal PGE<sub>2</sub> synthase. Blocking that enzyme, they think, could relieve pain by damping down PGE<sub>2</sub> — without causing stomach problems or suppressing heart-protecting PGI<sub>2</sub>.

“This is based on a much more selective mechanism of action” than COX2 inhibitors, says Charlotte Edenius, chief scientific officer at Biolipox, a small Swedish company founded by scientists from the Karolinska Institute in Stockholm. The company, which signed a major development deal with Boehringer Ingelheim in 2005, is working “intensely” on its project, she says. ■

1. Cannon, C. P. *et al. Lancet* **368**, 1771–1781 (2006).
2. Xie, W. L., Chipman, J. G., Robertson, D. L., Erikson, R. L. & Simmons, D. L. *Proc. Natl Acad. Sci. USA* **88**, 2692–2696 (1991).
3. McAdam, B. F. *et al. Proc. Natl Acad. Sci. USA* **5**, 272–277 (1999).
4. Catella-Lawson, F. *et al. J. Pharmacol. Exp. Ther.* **289**, 735–741 (1999).

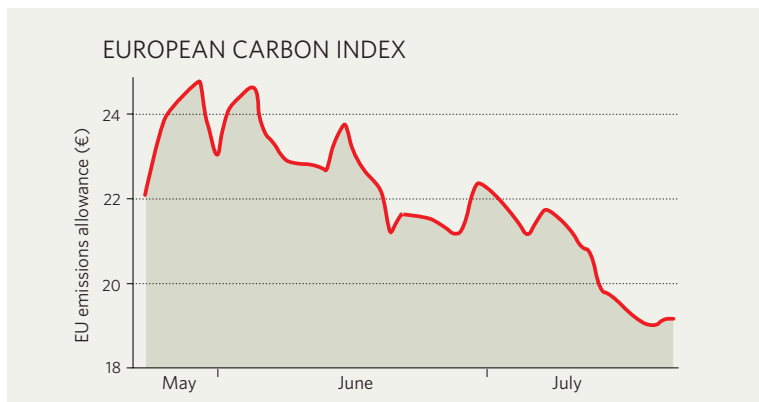
## IN BRIEF

**SMOOTH TRANSITION** Roche says that Severin Schwan, a 40-year-old Austrian lawyer who currently runs its diagnostics division, will succeed Franz Humer as chief executive next March. Humer will stay on as chairman of the Swiss drug company, which has enjoyed an unparalleled run of success since he arrived from GlaxoSmithKline to take over as chief executive 12 years ago. Although some recent changes of senior personnel in the pharmaceuticals industry have been forced, Roche is making this one on a high: it just announced sales up 15% to SFr 23 billion (US\$ 19 billion), and profits up 29%, to SFr 5.9 billion, for the first half of this year.

**PREPARING FOR TAKE-OFF** NASA awarded Rocketdyne — a Californian subsidiary of aeroengine maker Pratt & Whitney — a US\$1.2-billion contract to supply the upper-stage engine of the space shuttle's replacement. The company's engine, known as the J-2X, will propel a crew of six through the final stage of the rocket's ascent. It runs on liquid hydrogen and oxygen and bears a strong resemblance to the Apollo-era engines that took the first astronauts to the Moon. The contract covers design, development and testing. A separate contract for future engines will be awarded after the first test flight in 2012.

**NORTHERN DRIVE** A £12-million (US\$25-million) National Industrial Biotechnology Facility opened in the north of England, with the intention of making it easier for companies there to manufacture enzymes for use in industrial processes. The facility officially opened on 16 July at the Centre for Process Innovation at Wilton, Teeside — a traditional centre of the British chemical industry. It is supported by local development agencies, who hope that it will boost biotechnology innovation in the surrounding area, and will operate in partnership with the Manchester-based Centre of Excellence in Biocatalysis, Biotransformations and Biocatalytic Manufacturing.

## MARKET WATCH



The price of carbon allowances for the second phase of the European Union's emissions trading scheme, which runs from 2008 to 2012, has fallen to less than €20 from a late-May peak of €25.

Under the scheme, emissions trading credits are bought and sold — mainly by energy utilities — at five carbon exchanges, including the European Energy Exchange (EEX) in Leipzig, Germany. Analysts around the world are watching the market closely to see whether it will provide a stable and effective model for global trading in carbon emissions.

They attribute the latest price drop (see graph) to a new technical development. Some businesses are swapping so-called Certified Emission Reductions (CER), generated by approved clean development projects in poor nations, for European trading allowances, leading to

a surplus of the latter on the market.

CERs certify a specific amount of avoided emissions rather than granting permissions to emit extra carbon dioxide. Until recently, businesses were wary of them, because of doubts over whether the projects would deliver emission reductions that could be verified. But Stefan Kleeberg, a carbon asset manager with the 3C Group near Frankfurt, Germany, says that confidence is growing in the projects that are actually approved by the European Commission under the CER scheme.

Trading regular allowances for CERs, which are still 10–20% cheaper, has thus allowed some businesses to profit from emissions trading. However, the market is not yet very transparent, Kleeberg says, with only a handful of companies and brokers aware of its possibilities. ■

**Quirin Schiermeier**

EEX





## Mark of respect

A project that gives Congolese pygmies new ways to tell logging companies about the trees that are important to them, and their own radio station to discuss community issues, is really putting their interests on the map, says **Michael Hopkin**.

In June in the rainforests of the northwest of the Republic of Congo, the trees rain caterpillars. For the Mbendjele pygmies who live there, it's boom time. For a few weeks each year, children climb the 45-metre-tall sapelli trees and shake the branches, sending hundreds of newly hatched caterpillars down to the waiting women, who dry and cook the creatures to eat or sell.

But someone else has their eye on the 'caterpillar trees' of the Congo. Their wood is one of the most valuable of the African mahoganies — a fact that has not escaped the attention of commercial loggers. One tree might yield five sacks of caterpillars per year, potentially fetching US\$500 at the local market, but the timber from the same tree could bring in more than \$1,500 of profit to a logging company.

Now, though, the Mbendjele have a new way to help keep the trees standing. Scientists, conservationists and technicians have put together an innovative set of technologies to allow the forest people to mark trees that are important to them, saving them from the logger's axe.

Logging is a given in these regions. A logging company called Congolaise Industrielle des Bois (CIB) — a subsidiary of the Danish

timber multinational DLH Group — holds logging rights to nearly 10% of the Congo. And although the government has been fastidious in setting aside reserves such as the 4,000-square-kilometre Nouabalé Ndoki National Park (see map) to preserve wildlife, it has not allocated any land to indigenous semi-nomadic people. The Mbendjele are one of these groups, which together constitute about 3,000 people living in the CIB concession.

Activists worry about the collision between local people and logging companies. In a report released after a 2004 fact-finding trip to the country, a band of non-governmental organizations led by the environmental-activist group Greenpeace strongly criticized the CIB's activities in the area, saying that there were "no mechanisms by which the indigenous community as a whole is kept informed about logging plans, or by which they can have an input".

But appealing to loggers' pockets may help resolve these issues, some say. Consumers in the developed world are increasingly demanding

that their wood or furniture comes with a stamp of approval from the Forest Stewardship Council (FSC), an organization based in Washington DC that aims to ensure that the world's timber is harvested in a sustainable, environmentally friendly and socially responsible way. Not engaging with local people means no FSC certification and, potentially, fewer buyers.

Greenpeace's report found that engagement with the local people was one of the main areas in which CIB was wanting. For its part, the company said it had wanted to work on the issue, but didn't know how to go about doing it. "We had no ideas on the issue of traditional people," says Lucas van

der Walt, who oversees the company's environmental management practices. "We looked elsewhere but found no examples of community projects that we thought would work."

So in 2004, CIB turned to the Tropical Forest Trust, an organization based in Crassier, Switzerland, that helps logging companies win FSC certification by fostering more responsible

**"The only successful engagement of local people happens when they start doing the monitoring themselves."**

— Jerome Lewis

N. GAMI



practices. The result, now coming to fruition, blends simplicity with technology to help CIB achieve its aims and at the same time give the Mbendjele a chance to protect their way of life.

The task has not been easy. Pygmies in the Congo have long been disenfranchised from the rest of the population, says Scott Poynton, executive director for the forest trust. Loggers typically pass them over for employment, and even having national parks in the region doesn't always help. "There were incidents where ecoguards with Kalashnikovs beat up pygmies," says Poynton. "Politically, the pygmies are really not a powerful people."

### Inside knowledge

Somehow, the pygmies had to find a way to let the loggers know the locations of forest sites that are important to them, such as hunting and foraging grounds, water sources, burial places and sacred sites. The idea is not new; mapping of valuable sites with global-positioning systems (GPS) has been tried before with Amazonian tribes and elsewhere in the Congo river basin, such as in Cameroon. But these efforts have been hampered by the lack of literacy, both traditional and technological, among the indigenous people.

"Before, it was a question of going around with a notebook and an old-fashioned GPS unit, numbering the important areas and then marking them on a map," says Marcus Colchester of the Forest Peoples Programme, an advocacy group based in the United Kingdom. "It was pretty laborious."

Now, the forest trust has a different approach. With a \$150,000 grant from the World Bank, they enlisted the help of Jerome Lewis, an anthropologist at the London School of Economics, UK, who has lived on-and-off with the Mbendjele for more than a decade. He knew how to go about getting the information the logging company needed.

"I sat down and spoke with Mbendjele friends who were really pissed off when loggers drove bulldozers over cemeteries and water sources," Lewis says. To the loggers, many of the sites look the same as any other part of the forest; their significance is known only to the pygmies, who don't want to share the sites with outsiders. "The only successful engagement of local people happens when they start doing the monitoring themselves," explains Lewis.

How to do that is the tricky part. So Lewis designed a set of electronic icons to help the Mbendjele record the locations of important sites using a portable, palm-pilot-style device. The simple pictorial menu allows the pygmies to identify different types of sites as they wander through the forest; the sites



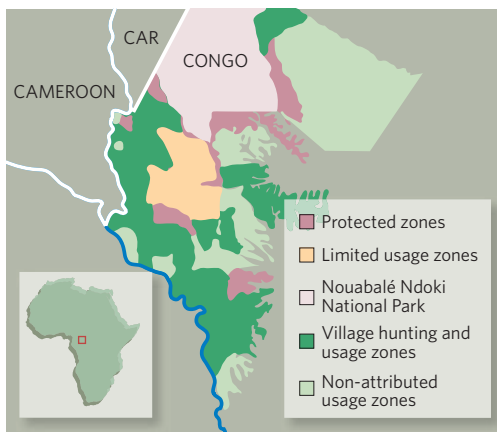
**Roll up:** to gain certification, logging firms must take more interest in the needs of local people.

are then automatically plotted onto a computerized map with GPS. The Mbendjele choose from four categories to classify their important sites: hunting, gathering, social/religion and farming. From there, each category branches off into more specific details.

For instance, to signify the importance of a sapelli tree, one would select 'gathering' and then 'caterpillars' from the next list of choices. Similarly, the system can log areas where yams grow, where herbal medicines are found, and where the Mbendjele camp while travelling through the forest.

The results can easily be plotted on a piece of mapping software such as Google Earth. And the pygmies know the terrain so intimately that they have no problems visualizing it as depicted from a birds-eye view on a map. "People are very quick to understand it," Lewis says. Other groups of pygmies, in regions such as Cameroon, were also quick to adopt the technology, he says. "The younger ones play it like a video game," adds Poynton.

Mapping began on a trial basis in June 2006, and CIB says that it has since mapped all of the area it was planning to survey for this year's



logging activities — in about one-third of the time it would previously have taken with traditional mapping.

Of course, there are trade-offs from the logging company's point of view. CIB has only ever logged the forest selectively — it takes only about 1.5 trees per hectare, which is why its concessions are so large — and it has no plans to change that. But they have pledged not to cut down trees deemed by the Mbendjele to be of value. "They have been able to respect the trees that people want without harming their profit margins," says Lewis.

### Radio pygmy

Meanwhile, the Mbendjele are getting another technical toy: a community radio station that, although still in its preliminary stages, should turn locals into roving reporters, and provide information about CIB's plans for logging. Perhaps inevitably nicknamed 'Pygmy FM' at its inception, the station has now formally been named 'Bisso na Bisso', which means 'between us' in the Lingala language. Only a few pilot programmes have been made, but the plan is to eventually broadcast six to eight hours a day of music and public-service broadcasts, about both logging and wider issues such as AIDS awareness. The pygmies currently get their information about when and where logging is to occur from representatives, called 'animateurs', that CIB sends into the villages — but they usually talk only to men; women and children are kept in the dark.

The station already has its headquarters in the logging town of Pokola, but a planned series of satellite bases and broadcasting towers have not yet materialized. Government broadcasting licences have yet to be finalized, and it must all be done on an annual budget of less than \$90,000, says Lewis. Funding so far has come from the World Bank grant, and CIB has promised to match the funding.

In May 2006, the project plus other engagement with the indigenous peoples earned CIB its FSC certification, at least for one of the five areas of its concession. But its plans to open a sawmill in Loundoungou, one of the remotest parts of its concession, has been condemned by Greenpeace as "unacceptable"; activists say that the mill will raise the number of transient workers in the area and exacerbate the problem of bushmeat hunting. But the Mbendjele are finally getting the chance, over the airwaves and by satellite, to let the loggers know what they think about the impact on their own lives.

Michael Hopkin is a reporter for *Nature*.

**For more on the project and to hear some of Bisso na Bisso's pilot show, go to [www.nature.com/podcast](http://www.nature.com/podcast).**

E. PARKER

## Q&amp;A



## Mmm... Pi

Part of *The Simpsons'* greatness is a willingness to find the humour in absolutely everything — including science. Executive producer **Al Jean**, the show's head writer and a Harvard mathematics graduate, talks to *Nature* about how to get a laugh out of Euler's formula.

**The Simpsons Movie comes out this week — is there much science in it?**

The crisis that precipitates the plot is environmental — Lisa's trying to warn the town about it and she gives a lecture entitled 'An Irritating Truth'. She's often the voice for the writers, even though she's eight years old a lot of us identify with her. But she's also depicted as socially unpopular, and is not always listened to.

**As writers do you set out to satirize public attitudes to science?**

Our general agenda is to show both sides of an issue and to let the viewer make up his or her own mind. In my lifetime I've seen science viewed as the saviour for everything, but now it's almost come full circle, because nothing can completely solve everyone's problems, and the disappointment when that happens is extreme. So now people are casting scientists as villains and not listening to them, which I think is tragic.

But we make fun of everything, so if a scientist appears on the show we make fun of them too. Generally our depiction of scientists is that they're insular and have bad social lives, and say things in an obscure fashion that isn't always comprehensible to the layman. From my limited experience in the scientific world I wouldn't say it's completely off the mark.

**One episode in which the show does take sides is the one in which Lisa protests against creationism in her school.**

What we say is that there are conservatives, like Pope John Paul II, who believe in the theory of evolution, and that it's far from a liberal theory: it's scientific, it's as close to a fact as can be. We did say that Flanders, who opposed the teaching of evolution, is sincere in his beliefs. We tried to take his emotions seriously.

What's really funny is that they had a debate here between the Republican candidates [for the presidential nomination], and the moderator said "so, which of you believe in evolution?" And you could see a couple sort of raising their hands and then changing their minds, and I'm going "how can you not be sure whether you think that's true or not? It's not a matter of opinion."

**You've had several famous scientists, including Stephen Hawking and Stephen Jay Gould, as guest stars on the show.**

People seem thrilled that we've had Stephen Hawking on the show, and no one could be more thrilled than I. Although one joke that

reflects the attitude of the public to science is when he appeared in front of the people of Springfield and told them what they should do, and Homer said, "Yeah, Larry Flynt is right!"

**Do you have a dream scientific guest who you'd love to have on the show?**

Living or dead, it would be Isaac Newton. But living would be a tough question. Fifty years ago, Albert Einstein was the epitome of a scientist as far as the public were concerned, and was regarded as a hero. But there isn't anybody comparable today. I think it shows how science has been made by some to appear in a more ambiguous light.



Stephen Hawking has featured as a guest character on *The Simpsons*.

**The Simpsons also boasts staggeringly obscure mathematical references.**

One that always makes me laugh is in a recent episode in which Homer and Marge are at a baseball game where the public has to guess the attendance, and each of the options is a different mathematical irregularity — one's a perfect number, one's a sum of four squares. They're all in the thousands and they're numbers that nobody except a mathematician would, at face



value, recognize as anything unusual, but if you're really sharp you'll pick it up. I love the fact that we can throw that sort of thing in.

My favourite mathematical reference on the show was when we did an episode where Apu was a witness in a courtroom and the lawyer asked if he had a good memory. He said, yes I do, I've memorized pi to one million decimal places, and Homer said "mmm... pi" and started drooling. We did call Caltech [the California Institute of Technology in Pasadena] to check that whatever we said the millionth decimal place was correct.

My favourite mathematical equation is  $e^{i\pi} + 1 = 0$ , and we threw that into one episode even though not all of our audience would necessarily understand it.

### In one episode Professor Frink shocks a lecture theatre into silence by shouting "Pi is exactly three!"

One thing I always thought was funny was that in the 1890s, I believe, the state of Indiana declared that the value of pi was 22/7. I mean, it's just... the idea that you could change a mathematical concept to suit a legislative whim is nutty.

### So is there a formula for writing good jokes?

I look at comedy writing mathematically, it's sort of like a proof in which you're trying to find the ideal punchline for a setup, and when you get it it's a very elegant feeling. It's a little like the feeling I used to get on completing a proof when I was doing maths at college.

### Several Simpsons writers have backgrounds in maths and science. Are you a bunch of geeks at heart?

When we're alone we talk about maths [chuckles], but we've learned that there's a wider world, so we don't always expose others to it, and we do it in a subtle way.

### Do you ever regret not pursuing your mathematical studies?

I wouldn't have been among the top people in my field; there were guys I knew in maths who were just the best. I don't know if I would ever have achieved what they did, so I'm very happy doing what I'm doing.

### And what does *Nature* have to do to get a mention on *The Simpsons*?

We should mention *Nature*! There's still time, we're only 400 episodes young...

Interview by Michael Hopkin.

Al Jean can be heard on this week's *Nature* Podcast, along with Homer, Lisa, Principal Skinner and Stephen Hawking.

## "IN THIS HOUSE WE OBEY THE LAWS OF THERMODYNAMICS"

### The Top Ten science moments in *The Simpsons*, as chosen by *Nature's* editorial staff

**"Bart's comet":** After sabotaging a weather balloon, Bart accidentally discovers a comet about to hit Springfield. Deep impact miraculously avoided, bartender Moe comes up with a new form of planetary defence: "Let's go burn down the observatory so this will never happen again."

**Inherit my shorts:** In the episode "The Monkey Suit," the Simpsons' pious next door neighbour Ned Flanders is flabbergasted that the science museum's exhibit on the origins of man both highlights evolution and makes light of creationism — and, to top it all, has a unisex bathroom.

**Mmmmm GMOs:** Homer's attempts to be a farmer in "E-I-E-I-(Annoyed Grunt)" involve using plutonium as a fertilizer. DNA from tobacco seeds and tomato seeds blend to produce a fruit that

tastes like ashtray, but is nonetheless "refreshingly addictive".

#### Thank you, Andrew Wiles:

In a Halloween episode two-dimensional Homer travels to the third dimension, which looks a lot like "that movie *Tron*", but with more equations. Writer David X. Cohen was responsible for the funniest and geekiest:  $1782^{12} + 1841^{12} = 1922^{12}$ , an incorrect disproof of Fermat's last theorem produced by a computer program Cohen wrote for the purpose.

**"Bye bye nerdie":** Lisa isolates the element in nerd sweat that makes them irresistible targets for bullies. She presents her data at a conference with luminaries including former surgeon general C. Everett Koop, a scene in which we find the true purpose of a science pole.

#### Better living through chemistry:

"Thank goodness I still live in a world of telephones, car batteries, handguns and many things made of zinc," says Jimmy, a character in an educational film. When confronted with a world without zinc he

attempts suicide but fails, as his zinc-free gun cannot work.

**Piltown angel:** In "Lisa the Skeptic" an almost complete human skeleton with angel's wings pits science — Lisa and guest star Stephen Jay Gould — against faith, as defended by Ned Flanders: "Science is like a blabbermouth who ruins a movie by telling you how it ends. Well I say that there are some things we don't want to know. Important things!"

**Trips to Stockholm:** In another Halloween episode, chemistry Nobel prizewinner Dudley Herschbach appears on the show to present Professor Frink with a Nobel prize of his own. Herschbach won the prize for crossed-molecular-beam techniques with which to study in detail the dynamics of chemical reactions. Frink is rewarded for reanimating his dead father.

**Forensics files:** DNA evidence in "Who Shot Mr. Burns" correctly identifies the assailant as a member of the Simpson family (Maggie, the baby, as it turned out). There were alternative endings, but to accept them would have meant ignoring "the Simpson DNA evidence". "And that," a narrator informs the audience with a nervous laugh "would be downright nutty".

**Perpetually funny:** In "The PTA Disbands", Lisa gets so bored by a lack of schooling she builds a perpetual motion machine. Homer is not pleased: "Lisa, in this house we OBEY the laws of thermodynamics."

Brendan Maher



Professor Frink divides the circumference by the diameter.

# THE MAP MAN

Alan Krensky has been put in charge of a controversial new office responsible for charting the progress of the NIH Roadmap for Medical Research. **Meredith Wadman** catches up with him in his first few days on the job.



**H**urrying in to an interview on his second official day as the de facto roadmap czar at the US National Institutes of Health (NIH), Alan Krensky is absently clutching a piece of paper; he's proud to hand it over for inspection. On it, the physician-scientist has charted a year's worth of trans-NIH 'rounds' — expert talks on cross-agency topics from network theory to pharmacogenomics to health economics. He has scheduled 11 lectures. The first is in two days.

Krensky, a respected paediatric immunologist who spent the past 23 years at Stanford University, has been recruited to institutionalize the Roadmap for Medical Research, a brainchild of NIH director Elias Zerhouni that was launched four years ago to decidedly mixed reviews. The map is intended to foster trans-NIH, large-scale and high-risk research. This year, it will spend \$483 million, roughly

1.7% of the \$29-billion NIH budget.

But Krensky's job — his official title is deputy director for the Office of Portfolio Analysis and Strategic Initiatives (OPASI) — doesn't stop at the map. Krensky will be assessing its effectiveness, trying to come up with ways, for instance, to evaluate whether the coveted Pioneer Awards for high-risk research are delivering the intended spoils. He will be scoping out new scientific opportunities and emerging public health risks, to recommend for future trans-NIH projects. And he and his staff will be completing an exhaustive, unprecedented cataloguing of the NIH's research portfolio aimed, in a tight budget era, at identifying both gaps and redundancies in all the science that the NIH funds.

"The roadmap needed a home and someone to be responsible for it. But OPASI is much bigger than that," says Krensky, whose broad grin

and tousled grey hair belie the earnest energy required of a man squeezing an interview between meetings with senior staff and directors of 27 institutes and centres.

Zerhouni sees Krensky and the new office as lending the roadmap permanence and continuity. "You need a permanent director," he says. "Somebody who will be there through NIH directors and ensure that things are done well, without any temptation of having this dictated from the top."

An outgoing Chicago native, Krensky graduated from the University of Pennsylvania Medical School, trained in Boston in nephrology and immunology and landed at Stanford in 1984, where, along with seeing patients, he shared a lab with his wife, Carol Clayberger, a Yale-educated cell biologist.

During his last six years at Stanford, Krensky was tapped to lead a \$526-million campaign to

M. TEMCHINE



transform the Lucille Packard Children's Hospital. In 2001, Packard was a regional hospital struggling to chart a course after Stanford University Medical Center's failed merger with the University of California, San Francisco. Krensky recruited 47 new faculty, oversaw the growth of the hospital's endowment from \$20 million to \$200 million and earned the hospital thirteenth place last year in *US News and World Report's* national ranking of children's hospitals.

What he achieved at the hospital, says Harvey Cohen, until recently its chief of staff, "is nothing short of astounding." Cohen, along with hospital chief executive Christopher Dawes and Stanford dean of research Ann Arvin, consider Krensky a perfect fit for the NIH job. At the hospital, he developed disease-based centres glued together by cross-cutting functions from imaging to informatics. In the process, they say, he proved himself an outstanding strategist with a vision broad enough to take in the massive complexity of the NIH and deep enough to understand how to tackle the thorny problems involved in incubating trans-institute research.

### Light leadership

Krensky is quick to note that OPASI — a \$3.3 million, 15-person office intended to ramp up to 70 people in coming months — doesn't exercise executive power over individual institutes or roadmap spending. As in the past, roadmap projects will continue to run a gamut of review by senior NIH staff, with Krensky's office one of many participants. He sees his role instead as coordinating, advising, greasing inter-institute wheels and providing information. "A lot of my job is cajoling," he laughs.

Krensky's experience at Stanford went a long way with the hiring committee at the NIH. Top administrators there are scrambling to get into synch with a new NIH-governing law enacted in January that, among other things, enshrines the roadmap as an NIH fixture, backed by a 'common fund' that can comprise up to 5% of the NIH budget in any given year. "We were very impressed with his package of experience and knowledge and vision," says Raynard Kington, the agency's principal deputy director, who until this month was doing Krensky's job in an acting capacity. "He understood that a big part of the responsibility of this office is to integrate sciences that cut across the agency. He got that in a very concrete way."

And by the end of 2008, Krensky's job will grow. In the recent law, Congress created a new NIH division — the Division of Program Coordination, Planning and Strategic Initiatives (DPCPSI) — that is similar to, but not the same as, Krensky's current shop. A sort of OPASI-plus, DPCPSI (which Krensky will direct) will

incorporate offices including OPASI, the Office of AIDS Research and the Office for Research on Women's Health, with a combined annual budget of \$150 million. Although the new law explicitly states that these offices will keep their current powers, it has caused some to complain about reporting to Krensky rather than directly to Zerhouni.

Krensky will also oversee an exhaustively detailed accounting of the agency's science spending that will for the first time allow members of the public — and Congress — at the click of a mouse to examine every NIH project being funded in a given disease area, with dollar amounts and other details attached. This 'portfolio analysis' tool, intended to go public in February 2009, is using sophisticated computer software that will capture elusive disease connections not immediately obvious in research grants, along with a new, pan-NIH set of disease definitions laboriously crafted with input from hundreds of scientists.

"The idea is to identify gaps in funding but also redundancies," Krensky says. "It has the potential to find out that various people are funding similar things." Such talk can be unsettling to institute heads.

"People are worried that the historic independence of individual institutes' leadership could be undermined by having this kind of central analytic and oversight capacity within the NIH director's office," says David Korn, the senior vice-president for biomedical and health sciences research at the Association of American Medical Colleges.

But Korn says that worry is misplaced. A former dean of medicine at Stanford who knew and admired Krensky when he was on the faculty there, Korn contends that Zerhouni "is on exactly the right track" in appointing Krensky to take a more sophisticated and rigorous approach to analysing the research portfolio of the massive agency. In a time of fiscal duress on Capitol Hill, he says, the NIH needs just such numbers to assure the public its money is being spent as wisely and effectively as possible.

Others, including scientists who have spent their lives in the trenches of investigator-initiated research, see Zerhouni, Krensky and the entire enterprise of the new office as well-meaning but misguided. "The function of a

federal agency that funds science is to respond to the innovative, novel and exciting ideas generated by individual scientists," says Gerald Weissmann, a longtime NIH grantee who is the director of the Biotechnology Study Center at the New York University School of Medicine. "Considering the enormous lassitude of large organizations, I tend to doubt that we will get more bang for the buck from big science."

Indeed, senior agency administrators have been perennially tempted to direct science, rather than letting it come to them, says Murray Goldstein, a former director of the National Institute of Neurological Disorders and Stroke who spent 40 years at the NIH. There are many first-class grant applications from individual scientists that are not being funded, he says. "What's the priority?"

Krensky is unapologetic. "Having the kinds of infrastructure that OPASI will develop doesn't take away from individual investigators — it buoys them," he says, "by giving them tools that modern science requires." What's more, he argues, "It's only 1.7% of the budget. Investigator-initiated awards are still the mainstay." As if to remind himself of this, Krensky intends to keep his hand in at the bench, working in the lab his wife will be running at the National Cancer Institute. There, he's hoping to find applications in tuberculosis for the cytolytic molecule granulysin.

But for the moment, he has to dash to a meeting of institute directors. There, he and NIH chiefs will be deciding the fate of \$60 million in unspent 2007 roadmap funds. A top aim is to jumpstart the new epigenetics and microbiome initiatives from the latest phase of

the roadmap, which is rolling out this autumn.

Mark Lively, a biochemist at Wake Forest University in Winston Salem, North Carolina, says he hopes Krensky's priorities stay in the right place. Recalling a recent Krensky speech to the Federation of American Societies for Experimental Biology, he says he has a "good feeling" about Krensky: "He spoke to us all like a scientist and not yet like a government bureaucracy leader. I hope he can maintain his optimism and not find the government rules and regulations too stifling for his ideas." ■

Meredith Wadman writes for *Nature* from Washington DC.



**"The Roadmap for Medical Research needed a home and someone to be responsible for it."**

M. TEMCHINE

## Nobel laureates know what they're talking about

SIR — Your Editorial 'Nobels in dubious causes' (*Nature* **447**, 354; 2007) urges scientists and Nobel laureates to "campaign only where they can truly make a difference". I think you mean that we should use our fleeting fame only in causes that we know something about. Or, as Pliny the Elder put it: "Shoemaker, stick to your last".

A few laureates may sign too many things. However, as a founder and board member of Scientists and Engineers for America, I use my Nobel prize to discuss something I know a good deal about.

Our aim is to make available to society at large the evidence-based science relating to critical issues facing us all. There is a lot of shouting out there and it is hard for the layperson to find reality. Political affiliation does not matter to us. Both Republican and Democratic presidential candidates endorse corn-based ethanol as an energy source. Both are wrong; it is our job to call it mainly a farm subsidy and explain why it is that rather than what it is claimed to be. It is up to the public to decide how much to support it.

We are also educating scientists on how to run for school boards. We hope many of them will win, and in this way improve the poor state of science education in our schools and keep it focused on the real world.

We intend to inform the electorate of the science-based issues that their elected officials have to face, and of what actions these officials have taken. We also intend to summarize the science behind the issues, including what we know and what we don't know. We hope both to draw attention to under-appreciated science issues and provide the advocacy necessary to get things done — not along party-political lines, but scientifically.

**Burton Richter**

Stanford University, SLAC MS 80, 2575 Sand Hill Road, Menlo Park, California 94025, USA

## Nobel: politicians need the insights scientists can give

SIR — As a member of the board of directors for Scientists and Engineers for America (SEA) and president of the Federation of American Scientists, two organizations mentioned in your Editorial 'Nobels in dubious causes' (*Nature* **447**, 354; 2007), I must take exception to your argument that scientists should not overstep their expertise.

In matters of interior decoration you'd be as likely to get good advice from a person pulled at random off the streets of Glasgow as from a gaggle of Nobel laureates. But eminent

scientists bring much-needed perspectives and insight to policy decisions that hinge on scientific facts and methods, and the uncertainties associated with them. Many of the most difficult political issues today — such as climate change, securing nuclear materials, setting priorities in health research and many others — are intimately tied to issues in science.

Given the cacophony of biased and misleading information that dominates many of these debates, the kind of advice and leadership provided by scientists is essential.

How could it be considered 'dubious' for scientists to defend and explain the process of scientific inquiry, when elected officials are making technical decisions based on the advice of novelists and religious extremists? SEA was organized to ensure that candidates' positions on critical science-policy matters are easily available, clearly understood and openly debated.

Your Editorial implies that this essential public service is inappropriate. On the contrary, it would be a terrible mistake if scientists with information critical to the debate retreat to ivory towers. Scientists have a responsibility to bring relevant facts to light, provide early warnings of problems that scientists are uniquely able to see and suggest solutions that might otherwise not enter the debate.

**Henry Kelly**

Scientists and Engineers for America, Federation of American Scientists, Suite 209, 1717 K Street NW, Washington DC 20036, USA

## How a naturalist found safe colours for soldiers

SIR — I enjoyed the Science in Culture article 'Hidden talent' about the London exhibition exploring the art of camouflage and its military implications (*Nature* **447**, 148; 2007). It reminded me of a little-known Englishman who made contributions to both zoology and military camouflage.

Charles Hamilton Smith (1776–1859), a colonel in the British Army, was a naturalist who described several equine species and subspecies — now mostly synonymized with *Equus* — and wrote an important volume in William Jardine's Naturalist's Library series (*The Natural History of Horses* Lizards, Edinburgh, 1841). Charles Darwin cited this work in his *Origin of Species*, in connection with hybridism and equine striping patterns.

Hamilton Smith is also known to military historians for his experiment conducted in 1800 on the colour of soldiers' field uniforms. The experiment involved soldiers firing at targets of different colours, including the conspicuous red of the British soldier's field uniform. This colour was more than twice

as likely as grey to receive a bullet-hole. Hamilton Smith submitted a report concluding that "the question arises whether all riflemen and light infantry should not take the field in some grey unostentatious uniform, leaving the parade dress for peace and garrison duty" (published later in the Royal Engineers' *Aide Memoire to the Military Sciences*, Weale, London, 1853).

Although some sections of the army readily took up Hamilton Smith's recommendations, cryptic coloration in British field uniforms was not fully adopted until the Boer War, at the end of the nineteenth century. Hamilton Smith was born in the year of the US declaration of independence; had someone conducted his experiment before that time — and had the British authorities been more willing to respond — history might have taken a rather different turn.

**James T. Costa**

Highlands Biological Station, 265 N. Sixth Street, Highlands, North Carolina 28741, USA and Department of Biology, Western Carolina University, Cullowhee, North Carolina 28723, USA

## Post-publication review could aid skills and quality

SIR — Shi V. Liu's correspondence, 'Why are people reluctant to join in open review?' (*Nature* **447**, 1052; 2007), struck a chord. Recently, I stayed my hand before submitting a comment to an online article, because the comment included as-yet unpublished research that I was reluctant to reveal in such a forum.

I believe that there are two ways to encourage online commenting. These would require little additional commitment, but would improve journal quality and enhance the development of review skills among young scientists.

First, journals could institute periodic post-publication review, in which the journal would solicit formal review of the article, focusing on how well its methods and results have held up, given the research that has been published in the intervening period. Such reviews would provide valuable historical perspective. Second, young scientists participating in journal clubs could be asked to derive and post a consensus comment on the article under discussion.

**Todd A. Gibson**

University of Colorado at Denver and Health Sciences Center, PO Box 6511, Mail Stop 8303, Aurora, Colorado 80045, USA

### Correction

PLoS One published just over 550 articles during its first six months, not 1,189 as stated in Correspondence 'Why are people reluctant to join in open review?' (*Nature* **447**, 1052; 2007).



## COMMENTARY



W. LAURANCE

## Driving a wedge into the Amazon

Things are heating up in the Amazon as the burning season begins. In Brazil, a 30-year-old study of forest fragments is itself threatened by farming, logging and hunting, say **William Laurance** and **Regina Luizão**.

**H**abitat loss and fragmentation are a pervasive threat to Earth's biodiversity. For those who study such things, the Biological Dynamics of Forest Fragments Project (BDFFP) in central Amazonia has, since 1979, been a scientific Mecca. Two hours north of the city of Manaus in Brazil, this 1,000-square-kilometre study area is home to the world's largest and longest-running experimental study of forest fragments<sup>1–3</sup>. Yet despite assurances from the Brazilian government, the BDFFP is now itself in imminent danger of becoming fragmented by rampant colonization (see map, overleaf). As the agricultural frontier expands, forest burning, logging and hunting are threatening to besiege the study area and drive a wedge deep into a crucial conservation corridor. For the BDFFP, is this the beginning of the end?

The BDFFP is under particular pressure from the Manaus–Venezuela highway. Aside from slicing through the BDFFP, the highway bisects the Central Amazonian Conservation Corridor<sup>4</sup>, a budding network of protected and indigenous lands that is one of the most important conservation areas in the entire Amazon basin. These and other protected reserves in Amazonia are coming under increasing pressure as deforestation activity has spiked over the past decade<sup>5</sup>. For those Brazilian and foreign scientists who have studied at the BDFFP — and there are hundreds — the situation is all the more depressing as they fight against

government bureaucracies that seem either myopically disinterested or determined to push ahead with forest colonization at any cost. The solution, the scientists believe, is to follow a carefully conceived land-use plan for the region that they themselves helped to devise. This plan, inexplicably, has yet to be released by the federal agency that sponsored it.

### Unique insight

When the BDFFP first got going in the 1970s, it took advantage of a government scheme to promote large-scale cattle ranches in the central Amazon. With the cooperation of the ranchers, BDFFP researchers designed a giant project to study experimentally, for the first time, how fragmented habitats might affect tropical wildlife. Because of poor soils and an end to government subsidies, the ranches have been largely abandoned, but the BDFFP has flourished. Operated jointly by Brazil's National Institute for Amazonian Research (INPA) in Manaus and the Smithsonian Tropical Research Institute in Panama, it has been one of the most productive ecological research projects in the Amazon, generating nearly 500 scientific publications and books, and more than 100 graduate theses.

Why is the BDFFP so special? A key advantage is its rigorous experimental design. Within the study area, isolated but comparable fragments of 1, 10 and 100 hectares were created as the surrounding forest was cleared by the

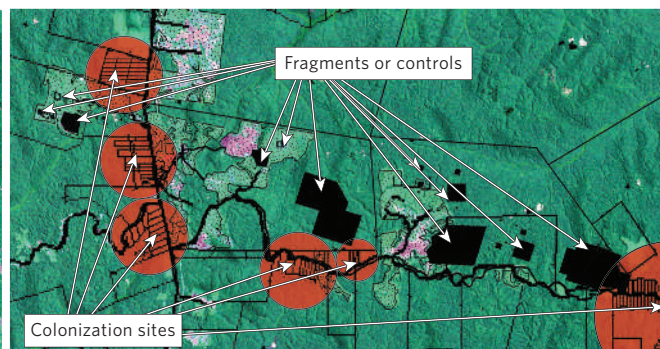
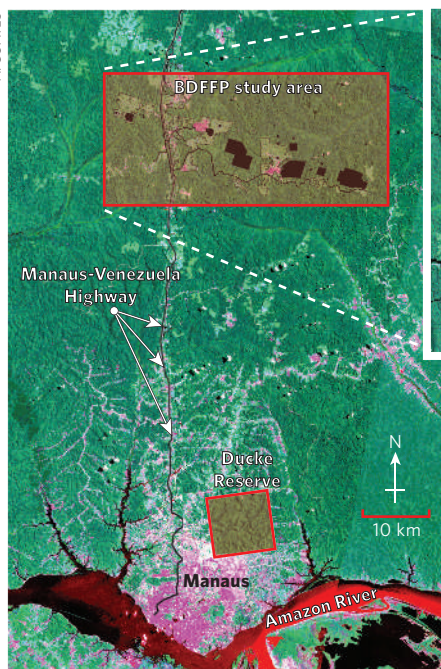
ranchers to create cattle pastures. Because tropical forests are both notoriously heterogeneous and chock-full of rare species, inferring how fragmentation affects such complex communities can be a statistical nightmare. In the BDFFP, however, researchers have surveyed thousands of rainforest species, including trees, birds, mammals, amphibians and various invertebrate groups, both before the forests were fragmented and at regular intervals afterwards. By repeated monitoring of these species and by contrasting them with those in nearby intact forest, BDFFP researchers have gained unparalleled insights into the ecological decay of forest fragments<sup>1–3,6,7</sup>. It is these critical intact forests that are now directly under threat.

In addition to its research mission, the BDFFP has a leading educational role, providing free environmental training courses for up to 100 Latin American students, park managers and political leaders each year. Veterans of these courses now hold strategic positions in many government agencies, universities and conservation organizations in Amazonia. The BDFFP also hosts high-profile visitors, including former US vice-president Al Gore, actor Tom Cruise and numerous members of US Congress and Brazilian officials, who experience the rainforest first hand, trudging to remote field camps and sleeping in the open.

Equally important is that the unfragmented parts of the BDFFP study area feature a fully intact biota, replete with jaguars, pumas, harpy



A. COATES



Urban sprawl and forest colonization north of Manaus, Brazil (left); planned colonization sites near the Biological Dynamics of Forest Fragments Project (right).

eagles, tapirs and other predators and megafauna that have vanished from much of the tropics because of rampant forest destruction and overhunting. Most of the world's leading tropical research centres, such as Barro Colorado Island in Panama, La Selva in Costa Rica, Las Tuxtlas in Mexico and Pasoh in Malaysia, are either isolated forest fragments or islands on which the original megafauna have largely disappeared. Large rainforest predators help to regulate the density of their prey species, and their absence can provoke ecological distortions that reverberate throughout the entire ecosystem<sup>8</sup>.

Regrettably, the days of the BDFFP — at least as a bastion for the species-rich Amazonian ecosystem — could be numbered. To promote colonization of central Amazonia, in the 1970s the Brazilian government decreed the city of Manaus to be a free-trade zone, with minimal taxes to encourage investment. The city has since grown explosively, now totalling around 1.7 million people. Urban sprawl and forest colonization — some of it illegal — are consuming expanses of surrounding forest and, like a giant amoeba, the city has all but swallowed the nearby 100-square-kilometre Dúcke Forest Reserve (see map).

### Mounting danger

Since the late 1990s, the paving of the 1,070-kilometre-long Manaus–Venezuela highway has greatly accelerated forest colonization and logging north of the city. SUFRAMA, a Brazilian federal agency that controls a large expanse of land north of Manaus that includes the BDFFP, has begun settling families in farming plots around the immediate periphery of the study area. At least six SUFRAMA colonization projects involving 180 families are planned for the near future (see map). This could be the beginning of a dramatic influx into the area, especially if a proposed

highway is paved between Manaus and Rondônia, a major deforestation hotspot in southern Amazonia<sup>9</sup>.

The pressures from the farm settlers are already being felt. Roaring chainsaws and shotgun blasts can now be heard from the BDFFP study camps. Last year one of the camps was raided, with research equipment worth thousands of dollars being stolen, and a settler-lit fire destroyed an array of critical study plots. Field researchers are increasingly encountering gun-toting hunters that encroach into the study area, with one plucky graduate student facing down a truckload of armed men. As such conflicts increase, many fear a possible tragedy — such as the recent murder of two park guards by illegal gold miners in French Guiana, or the 2005 assassination of the American nun Dorothy Stang by Amazonian ranchers.

### Time is ticking

Can the BDFFP be saved? The project's staff and researchers are digging in for a fight. They are lobbying SUFRAMA and the Brazilian land-settlement agency INCRA not to establish forest-colonization projects in the area, arguing that the study area is of irreplaceable scientific value, that its nutrient-staturated soils are poorly suited to farming, and that INCRA is violating its own formal policy not to settle people on forested land. They also contend that the BDFFP study area, if protected, would secure the most vulnerable part of the planned Central Amazonian Conservation Corridor, which will ultimately span much of Brazilian Amazonia along an east–west axis. Finally, they are working with partners in the Amazonas state government to help establish new protected areas in the region, and with colleagues at INPA and other organizations whose study areas north of Manaus are also being threatened by rapid encroachment.

The most frustrating aspect of the ongoing battle, say the project researchers (a group that includes both of us), is that SUFRAMA completed a comprehensive ecological-zoning study in 2004, to which a number of BDFFP scientists contributed. SUFRAMA is now ignoring its own study — which would have ensured that critical environmental and scientific areas such as the BDFFP were protected —

and has failed to release it publicly. In response, BDFFP researchers are attempting to enlist the help of IBAMA, Brazil's national environmental agency, to stop SUFRAMA from charging ahead with its environmentally destructive development plans. IBAMA is obliged to intervene, they maintain, because parts of the BDFFP study area are national protected areas, but so far little has happened.

How can people outside the Amazon help? The key, say project researchers, is to focus attention on the alarming and irrevocable land-use decisions being taken in central Amazonia.

**"We have gained unparalleled insights from the intact forests now under threat."**

Anything that generates publicity, such as newspaper stories and letters to the editor, would be useful. Ultimately, they hope, the Brazilian media will take an active interest, highlighting the strategic importance

of this region to the Amazonian conservation corridor and the disappointing response so far from federal officials.

Time is of the essence. The burning season takes off in July and then goes on until November or December. Smoke plumes from forest fires will soon encircle the BDFFP landscape, and settlers, loggers and hunters are drawing ever closer. "We are like the little Dutch boy with his fingers in the leaking dike," says BDFFP researcher José Camargo, "and we are running out of fingers!"

William F. Laurance is at the Smithsonian Tropical Research Institute, Apartado 0843-03092, Balboa, Ancón, Republic of Panama.

Regina C. C. Luizão is in the Department of Ecology, National Institute for Amazonian Research (INPA), C.P. 478, Manaus, Amazonas 69011-970, Brazil.

1. Lovejoy, T. E. et al. in *Conservation Biology: The Science of Scarcity and Diversity* (ed. Soulé, M. E.) 257–285 (Sinauer, Sunderland, Massachusetts, 1986).
2. Pimm, S. L. *Nature* **393**, 23–24 (1998).
3. Laurance, W. F. et al. *Conserv. Biol.* **16**, 605–618 (2002).
4. Ayres, J. M. et al. *Abordagens Inovadoras para Conservação da Biodiversidade no Brasil: Os Corredores das Florestas Neotropicais* (Pilot Program to Conserve the Brazilian Rainforest and Brazilian Ministry of Environment, Brasília, 1997).
5. Laurance, W. F. et al. *Science* **304**, 1109–1111 (2004).
6. Ferraz, G. et al. *Proc. Natl Acad. Sci. USA* **100**, 14069–14073 (2003).
7. Laurance, W. F. et al. *Proc. Natl Acad. Sci. USA* **103**, 19010–19014 (2006).
8. Terborgh, J. et al. *Science* **294**, 1923–1926 (2001).
9. Fearnside, P. M. & Graça, P. M. L. A. *Environ. Manage.* **38**, 705–716 (2006).



## BOOKS &amp; ARTS

## A man of peace

One scientist's journey from the Manhattan Project to the Nobel Peace Prize.

**Joseph Rotblat: Visionary for Peace**

edited by Reiner Braun, Robert Hinde,  
David Krieger, Harold Kroto & Sally Milne  
Wiley: 2007. 371 pp. \$45, £27.50

**War and Peace: The Life and Work of Sir Joseph Rotblat**

edited by Peter Rowlands & Vincent  
Attwood  
University of Liverpool: 2006. 338 pp. £15

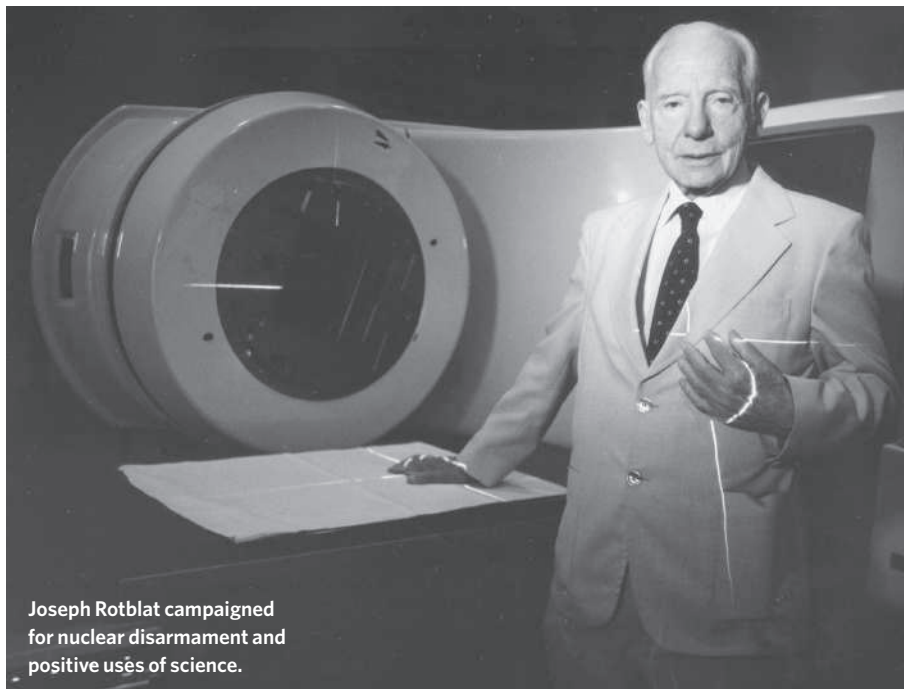
**Malcolm Dando**

Joseph Rotblat, when receiving the honorary degree of Doctor of Science from Bradford University in 1973, described the ongoing build-up of nuclear arms and the underlying doctrine of deterrence: "This doctrine of deterrence is known under the name of mutual assured destruction: M.A.D. It is indeed a mad system in which survival depends on the threat of total annihilation."

Such a system, he believed, was bound to fail sooner or later and so he advocated an alternative: "One in which our survival is based on mutual incentives, on the recognition of the ever-growing interdependence of all members of society all over the world, on the utilization of the vast potential of technology to build and sustain a clean and healthy world."

The two books reviewed here, *Joseph Rotblat: Visionary for Peace* and *War and Peace: The Life and Work of Sir Joseph Rotblat*, celebrate the achievements of the nuclear physicist, who died in 2005 aged 96 (*Nature* **437**, 634; 2005). For much of his long life, Joseph Rotblat advanced the argument that nuclear deterrence was extremely dangerous, but that there were positive alternative uses of our science and technology. Yet rejection of the doctrine of deterrence had not always been Rotblat's position. As one of the first scientists to realize that atomic bombs of incredible destructiveness were possible because of advances in our understanding of physics, he felt it was necessary to develop such bombs in order to deter Hitlerite Germany from using them, should it develop that capability. Thus, he became a member of the Manhattan Project in the United States and went to work at Los Alamos. However, when he realized that Germany could not develop the bomb, he left and returned to the United Kingdom.

Today, life scientists increasingly face the dual-use dilemma that physicists had to confront in the middle of the last century. It is



Joseph Rotblat campaigned for nuclear disarmament and positive uses of science.

becoming ever clearer that the vast new capabilities being generated by the biotechnology revolution for beneficial reasons could also be used for extremely destructive, hostile purposes. As Sir Joseph indicated in his lecture 'Citizenship and the Challenge of Science' in March 2002: "We already know about advances in biological warfare whereby gene manipulation could change some pathogens into terrifyingly virulent agents. But entirely different mechanisms might be developed. We cannot predict the destructive potential of military applications. All we can say is that the danger is real."

Despite the growing attention directed at the potential misuse of benignly intended life-science research by states parties to the Biological and Toxin Weapons Convention and the Chemical Weapons Convention, few practising life scientists have grasped the nature of the problem, let alone considered what might be done to prevent the large-scale hostile use of their technology in future decades.

These two fascinating sets of essays would be a good place for life scientists to begin considering their dual-use problem and what might best be done about it. *War and Peace* is based on a conference held at Liverpool University, UK, in October 2006. It was to the Physics Department of Liverpool University that Rot-

blat moved, from Poland, just before the start of the Second World War, tragically having to leave his sick wife behind. The book contains essays from numerous people who knew him well and casts many different lights on his life: his early career in Poland; his work in Liverpool and then in medical physics at St Bartholomew's Hospital, London; and his decades of work as a campaigner for peace and cooperation. I particularly liked the archivist's story of carrying away some three tonnes of papers from Rotblat's home to the University of Bath, UK, for cataloguing. Rotblat's few 'faults' included an inability to throw away any records.

There is some overlap between this book and *Visionary for Peace*, but the latter deals to a greater extent with Rotblat's international activities for nuclear disarmament and peaceful cooperation, for which he and his creation, the Pugwash Conferences on Science and World Affairs, jointly received the Nobel Peace Prize in 1995. Mikhail Gorbachev, for example, recalls how he came to know Rotblat personally in the 1990s and how, at meetings of Nobel Peace Prize-winners, Rotblat's contribution to discussions of nuclear disarmament was invaluable because he was "the best qualified and perhaps the most passionate participant". Gorbachev also noted that as the 1990s progressed, "concern and alarm in our discussions

M. PELLETIER/CORBIS SYGMA

became more and more prominent". He concluded: "We should not delude ourselves: in the final analysis, the problem can only be solved through the abolition of nuclear weapons. So long as they continue to exist, the danger will be with us."

Rotblat would certainly have agreed, and *Visionary for Peace* has a useful appendix of a set of his writings, which include his 2003 paper, 'The Nuclear Issue: Pugwash and the Bush Policies'. This contains a typically incisive condemnation of the recent lurch to yet more reliance on nuclear weapons in the Western world: "The use of nuclear weapons is seen by the great majority of people in the world as immoral, due to their indiscriminate nature and unprecedented power. Their possession — and therefore likely use — is thus equally unacceptable, whether by 'rogue' or benevolent regimes." Little wonder then that Pugwash scientists have argued against the replacement of Trident by the United Kingdom.

Few of us are able to achieve a mature balance between our many activities and diverse relationships. Yet, despite his hectic work schedule, Joseph Rotblat was universally regarded as an exceptionally kind and generous person. His wife and her mother died in the Holocaust but members of the family joined him in England after the war. An essay by his niece, Halina Sand, demonstrates his humanity so well: "His warmth and kindness to me continued throughout his life, descending through the generations to my two daughters and their children. In his mid-nineties, and in poor health, he was still able to charm his small great-great-niece and twin great-great-nephews, just as he had once enthralled their mother and their grandmother." Joseph Rotblat was indeed a man of peace. ■

Malcolm Dando is professor of international security at the Department of Peace Studies, University of Bradford, Bradford, West Yorkshire, BD7 1DP, UK.

The book's central chapters follow a more conventional selection of examples spanning the development of Western civilization: from the origins of writing in Mesopotamia for keeping commerce and administration records, to the accumulation of books and bibliographic records (at Alexandria, for example), through the Dark Ages in which Irish scribes worked alone outside traditional hierarchies (like today's bloggers, Wright suggests), and into the age of print in the Renaissance.

The author discusses some high points of early modern information management. For example, Giulio Camillo's memory theatre (around 1550) promised access to all knowledge through a system of visual mnemonic cues; in 1751, the *Encyclopédie* of Diderot and d'Alembert established the modern norm for the encyclopaedia as an alphabetized, multi-author, multivolume and illustrated reference work; and at about the same time, Carl Linnaeus devised a precise set of rules for classification in nature. Wright pays special attention to the methods for classifying books between the late seventeenth and early twentieth centuries, which culminated in the development of multi-tiered, expandable hierarchies of standardized headings, such as Melvil Dewey's decimal classification in the late nineteenth century. He points out that libraries and librarians have long been at the forefront of information management techniques.

Finally, Wright considers twentieth-century attempts to form a universal collection of retrievable information, many of which are now forgotten, although their original ambitions are partially realized in the World Wide Web. Paul Otlet, for example, was a Belgian bibliographer who dreamed of guiding users not just to the right books, but to their contents. His *Mundaneum* (1910) eventually consisted of more than 12 million facts kept on index cards to which users could submit queries for a fee. The American engineer Vannevar Bush envisioned a machine called the 'memex', which would retrieve information to match a query from texts stored on microfilm. Although Bush's article 'As we may think' (*Atlantic Monthly*, 1945) is considered seminal today, Wright notes how little current information science

## Too much information

### Glut: Mastering Information Through the Ages

by Alex Wright

Joseph Henry Press: 2007. 296 pp. £16.99, \$27.95

### Ann Blair

'Information overload' is a phenomenon we know well — a Google search on the term retrieves close to 2 million hits. But is it really as new as we think? "We are not the first generation — nor even the first species — to wrestle with the problem of information overload," Alex Wright reminds us in his ambitious new book, *Glut*. He seeks a balanced and historically informed assessment of the digital revolution's impact. As a former librarian now working as an information architect, Wright combines insights from his areas of expertise with a wide range of historical and scientific literature aimed at non-specialist audiences. He does not attempt a synthesis of specialist

debate, but offers a well-informed account of information management across a surprising range of examples.

Information management systems, which typically rely on a combination of self-organizing networks and hierarchical relationships, are central to biological phenomena — from the evolution of multicellular organisms to the dynamics of social insects. Wright draws from sociobiology the suggestion that evolution has favoured the development of particular human cognitive behaviours in managing information, such as the drive to classify and the emotional attachment to symbols. He turns for confirmation to anthropologist Donald Brown's notion of human universals and notes the particular importance of the ice age that began some 40,000 years ago in forcing humans to interact more closely, thus stimulating the development of drawing and symbolic objects. Wright argues that this "ice age information explosion brought humanity to the brink of literacy".



N. STRAUSS/AGF IMAGES

Many information management techniques were first developed in libraries, where hierarchical classification methods have existed for centuries.



has heeded Bush's call for biological as well as mathematical models in computer science or his concerns about the influence of corporations on the growth of the field. Wright shows more generally how the Internet has developed beyond the control or the approval of its early contributors (such as Tim Berners-Lee or Ted Nelson, the conceptual father of hypertext).

The historical perspective of *Glut* is admirable: Wright neither assumes a linear progress nor makes unwarranted claims about the novelty or the indebtedness of current technologies to earlier ones. He doesn't try to predict what the lasting impacts of the Web will be, but notes that the Internet facilitates the formation of small, self-organized communities that have the potential to undermine large hierarchical structures. In this way, he suggests that human culture may no longer be moving unidirectionally as was once thought, towards coalescence into larger entities, but rather multidirectionally. Wright clearly values the growth of grassroots self-organization on the Web, but also acknowledges that bottom-up networks can benefit from some hierarchical structure.

One pay-off of attending to earlier ambitions for information control is to highlight some of the weaknesses of our current system. Wright notes, for example, that our search algorithms and the metadata they create are not transparent but are the work of software engineers operating within a world of commercial secrecy; and our weblinks that carry information about intellectual associations are evanescent and can disappear without leaving a trace. Using the analogy of print's arrival in the mid-fifteenth century, Wright warns of the potential for new technologies to seriously disrupt established structures. However, his interpretation that printing caused the Protestant Reformation is overly reductionist.

Wright's conclusion that "as Internet users continue to congregate in small groups, such behavior harkens back to our deepest rooted social instincts" is less convincing. This type of hasty sociobiological generalization argues from evidence selected to suit its purposes, without weighing counterevidence or other contributing factors. That humans have evolved a desire to communicate and form social groups does not strike me as the most helpful explanation for the complex choices we make among the many means of communication now at our disposal. Indeed, Wright shows throughout his book how the tools that were developed in different historical contexts to cope with information overload continue to shape our options and ambitions today.

This stimulating book offers much opportunity to reflect on the nature and long history of information management as a damper to the panic or the elation we may variously feel as we face ever greater scales of information overload.

Ann Blair is a professor of history at Harvard University, Cambridge, Massachusetts 02138, USA.



Hot seat: archaea thrive in extreme environments.

MOMATUK-EASTCOTT/CORBIS

## Introducing the extremophiles

**The Third Domain: The Untold Story of Archaea and the Future of Biotechnology**  
by Tim Friend

Joseph Henry Press: 2007. 250 pp. \$27.95

**Sean Nee**

Envy the achievement of Carl Woese, who announced his discovery of the third domain of life on Earth a mere 30 years ago. Marvel at the fact that most people are unaware of this three-domain understanding of biodiversity. Admire the journalist Tim Friend who resigned from the newspaper *USA Today* to write this superb book introducing the public to the third domain. Buy it and enjoy the personalities, the adventures, the drama and the science too, all presented in an admirable mix that is a terrific read.

Until recently, our view of life on Earth had changed little over centuries. There were animals, plants and a bunch of little things such as bacteria. One of the many quaint anachronisms of the University of Oxford is that it is still one of the few seats of learning to have separate departments of plant sciences and zoology, reflecting a view of life that is as outdated as snuff after dinner and bulldogs in bowler hats (don't ask). It is probably no coincidence that Oxford's most famous popular writer on biology, Richard Dawkins, notoriously gave only a single page to the third domain of life in his take on biodiversity, *The Ancestor's Tale*, apparently more interested in things like cabbages.

Here are the three domains. Bacteria: you know what they are but you probably have no idea how interesting they are — but that's another book. Eukaryotes: unlike bacteria, eukaryotic cells enclose their genetic material in an internal membrane and have lots of internal membrane-bound organelles. This domain includes multicellular plants and animals, but these are small beer compared with the enormous diversity of single-celled eukaryotes, most of which we know about only because

they cause disease, such as giardia. The third domain, the subject of this book, is the archaea. Although they are single-celled and definitely not eukaryotes, they are not bacteria either. To see this point clearly, know that there are no archaea that cause disease. If anyone has a good idea why this is, please contact me at once. It is not that they are only found in strange places where we do not go — your mouth, for example, is teeming with them. Also, a particular antibiotic that works by disrupting the information-processing machinery in bacteria has no effect on eukaryotes or archaea. The current understanding is that we share the same information-processing genes as archaea.

It had long been conventional wisdom that the phylogeny — the family tree — of bacteria could not be constructed. Until recently, phylogenies had been based on morphology: we look quite like gorillas and chimps, less like gibbons, even less like howler monkeys, not at all like cabbages, and so on. These degrees of similarity reflect the length of our separation in evolutionary time. But morphology is useless for bacteria: they are blobs, squiggles or rods. That tells us nothing.

Soon after the invention of DNA-sequencing technologies, Carl Woese had the insight that comparing sequence similarities between bacteria might allow the construction of their phylogeny, and he got to work. He chose a particular gene that is essential in translating DNA into proteins and so must be found in all life forms — at least, as understood at the time. Having sequenced a segment of the gene in many bacterial species and found reasonably varying degrees of similarity, a colleague down the hall brought him some 'bacteria' with an unusual metabolism: methanogens get their energy by combining hydrogen and carbon dioxide, producing the potent greenhouse gas methane as an end product. These are responsible for swamp gas, for example, and about 50% of you reading this have them in your gut. This is one of the gases that allows you to do

your party trick, bent over, with a lighter in a darkened room. Woese found that the methanogen gene sequence was very, very different to those of other bacteria he had sequenced. What could this mean?

At the time, and before, microbiologists had been looking for life in apparently ridiculous places, and finding it. We now know that archaea can live everywhere: in hot acid fluids that can dissolve steel, in fluids as alkaline as those we use for floor strippers, in pressures and temperatures as high as that in autoclaves that hospitals use to sterilize equipment. It is not just that they can tolerate such environments. These are their natural habitats and species adapted to them die in conditions that we

would consider benign. Sequencing more and more such 'extremophiles' from different environments, Woese found that they all naturally grouped together in the 'bacterial' family tree.

Previous workers, such as the exalted Thomas Brock, had observed that the biochemistry of the cell walls of 'bacteria' was similar in specimens from very different extreme environments and quite different from that of typical bacteria. This had been explained away as convergent evolution — the same adaptation by bacteria to extreme environments, of whatever sort. But Woese pulled all the evidence together and made the intellectual leap that is now accepted: there is a third domain of life — the archaea.

All of this is told, and much more. Friend quite rightly does not restrict himself to archaea. For example, there is a fascinating chapter on the *Titanic*, which is literally being eaten by enormous, macroscopic consortia of symbiotic microbes from all three domains — superorganisms called rusticles with vasculatures and immune systems, ultimately powered by the fact that the sunken passenger liner is functioning like a giant battery. Having learned all about them from the scientists, Friend went down to the *Titanic* to see for himself. I'd quit my job for that as well. ■

Sean Nee is an evolutionary biologist at the School of Biological Sciences, University of Edinburgh, Edinburgh EH9 3JT, UK.

## Mind tricks

Cognitive scientists take a lesson from magicians.

**Susana Martinez-Conde and Stephen L. Macknik**

Teller, the mute half of the magician duo Penn & Teller, apparently pulls a coin out of thin air for the umpteenth time. The audience breaks into applause. It's another great performance in Las Vegas, Nevada — only tonight, Teller is part of a special symposium hosted by the Association for the Scientific Study of Consciousness, bringing together magicians and cognitive scientists.

Vision scientists have often turned to the visual arts to rediscover the principles underlying visual perception, such as how to convey the illusion of depth on a flat canvas. Similarly, cognitive scientists have much to learn from magicians, who have developed cognitive principles and illusions that trick audiences.

The Magic of Consciousness Symposium on 24 June attempted to plumb directly the depths of the intuition of world-class magicians. Magicians are behaviour experts who artfully manipulate attention and awareness. Their wealth of knowledge on cognition and behaviour is now ripe for picking.

James Randi — aka The Amazing Randi — explained that spectators will easily accept unspoken assumptions. He made his point by fooling more than 200 consciousness researchers into thinking that his voice was being amplified by a dummy microphone, and by pretending to read with glasses that were merely empty frames.

Teller pulled coins out of thin air, conference bags and spectacles. He used water from his drinking glass to make a ball disappear. Shedding his normally silent stage persona, he described with eloquence how magicians make their audiences incorrectly link cause and effect. We all infer cause and effect in everyday life. When A



precedes B, we conclude that A causes B. The skilled magician takes advantage of this inference by making sure that A (pouring water on a ball) always precedes B (the ball disappearing). However, A does not really cause B. The magician only makes it look so. Audiences assume that each repetition of a trick is done by the same method. "When a good magician repeats an effect, he varies the method in an unpredictable rhythm," said Teller. "That way, each time observers suspect one method, they find their suspicion disproven by the subsequent repetition." For instance, the disappearing ball is first secretly palmed by the other hand, but in the next repetition it is instead dropped on the magician's lap (allowing the magician to show that the other hand is empty).

Johnny Thompson — aka The Great Tomsoni — refers to this principle as "closing all the doors". That is, a good trick will appear to rule out all possible explanations, except for magic. Mac King illustrated these points by impossibly pulling a melon-sized rock out of his shoe — three times. The first two times he purposely used the same method, making it easier to see the trick the second time around. The third

time he changed the method, deceiving the audience once again. "Much of our lives is devoted to understanding cause and effect," Teller said. "Magic provides a playground for those rational skills."

He also explained that "action is motion with a purpose". In normal social interactions, we constantly search for the purpose motivating other people's actions. An action with no obvious purpose raises questions. However, when the purpose seems crystal clear, we look no further. "Skilled magicians inform every necessary maneuver (motion) with a convincing intention," said Teller. Thus, the real purpose of the motion (hiding the ball) is hidden by the apparent purpose of the action (pouring the water).

Apollo Robbins, a professional thief who once pickpocketed Jimmy Carter's secret service detail, demonstrated the use of interpersonal distance and eye contact to control a target's gaze and attention. In doing so, he looted, undetected, every single pocket of a journalist from the audience.

James Randi tied the evening together by effortlessly escaping ropes knotted by philosopher Dan Dennett. The intuitive insights offered by magicians will frame future cognitive experiments, from measuring the dynamics of attentional blindness to determining the neural correlates of causal inference. Where in the brain is motion perceived as action? Does this same brain area encode the purpose of the action? For cognitive scientists, the second act of the show will take place in the lab. ■

Susana Martinez-Conde and Stephen L. Macknik are at the Barrow Neurological Institute of St Joseph's Hospital and Medical Center, Phoenix, Arizona 85013, USA. They co-chaired the 11th Annual Meeting of the Association for the Scientific Study of Consciousness.



## NEWS &amp; VIEWS

J. FOOTY/DISCOVERY CHANNEL IMAGES/GETTY



Crop protection. Preparations that include phosphinothricin are used as a weed-killer in agriculture.

## BIOCHEMISTRY

# Uncharted route for antibiotics

John P. Quinn

**In their battle for survival, soil microorganisms produce a vast arsenal of toxic molecules. One such toxin contains a unique sequence of atoms, and its biosynthesis includes some unexpected steps.**

Many commercially available antibiotics are products of soil bacteria that belong to the genus *Streptomyces*, or are modified versions of those products. They include several that are vital to medicine, such as vancomycin, rifampicin and clavulanic acid. But some microbial antibiotics are effective against more than just other microbes — they also act as herbicides. Reporting in *Nature Chemical Biology*<sup>1</sup>, Blodgett *et al.* provide fresh insights into the complex route by which the active ingredient of several widely used herbicides is made in *Streptomyces viridochromogenes*. This molecule, phosphinothricin (Fig. 1, overleaf), is unique among naturally occurring amino acids because it contains a carbon–phosphorus–carbon bond; its biosynthesis turns out to be equally unusual.

The term ‘antibiotic’ was first coined by the soil microbiologist Selman Waksman to describe the array of toxins produced by microorganisms in an apparent attempt to kill or suppress the growth of their competitors. Towards the end of his career, Waksman became less convinced that antibiotics were involved in microbial chemical warfare<sup>2</sup>, and their ecological role is still unclear<sup>3</sup>. Nevertheless, most anti-infective drugs used today were found by screening biologically active, naturally occurring compounds — often described as ‘natural products’ by chemists — in extensive

programmes first set up in the 1940s.

Such programmes have been scaled back in recent years. This is partly because the development of high-throughput technologies in the 1990s has facilitated the chemical synthesis and screening of large ‘libraries’ of structurally related molecules with potential biological activity. But the era of natural-product discovery is far from over. It is now recognized that synthetic approaches to finding biologically active compounds are most likely to be successful if they optimize promising structures that occur naturally. Some 12,000 structurally distinct ‘molecular scaffolds’ have been identified in natural-product databases<sup>4</sup>. Further variants can be generated by manipulating the genes that encode the molecules involved in the biosynthetic pathways to these compounds.

Phosphonates and phosphinates comprise a relatively unexplored group of biologically active natural products. They are characterized, respectively, by a direct carbon–phosphorus (C–P) or carbon–phosphorus–carbon (C–P–C) bond<sup>5</sup>. This distinguishes them from the many phosphorylated cellular compounds that contain carbon–oxygen–phosphorus (C–O–P) bonds. Phosphorylated compounds can be broken down by enzymes (which cleave C–O–P bonds), but phosphonates and phosphinates are resistant to this process. Such resistance, coupled with their structural and

chemical similarity to phosphorylated biological molecules, means that many phosphonate and phosphinate natural products can interfere with cellular functions.

This is certainly true of phosphinothricin, which was originally isolated<sup>6</sup> from various species of *Streptomyces* in 1972, and was the first herbicidal natural product to be commercialized. Phosphinothricin inhibits glutamine synthetase — an enzyme central to plant nitrogen metabolism — by mimicking a phosphorylated amino acid (glutamic acid) that acts as the enzyme’s reaction intermediate.

Strangely, our knowledge of phosphinothricin biosynthesis is incomplete. The information we do have is based largely on a patchwork of data collected during the 1980s, and was obtained from the analysis of specially generated mutant bacterial strains that each lacked an individual component of the phosphinothricin biosynthetic machinery<sup>7</sup>. Sequencing of the gene cluster thought to encode the enzymes of the synthetic pathway was completed only in 2004 (refs 8, 9). It then became clear that the roles of just half of the genes’ products had been definitively established. Blodgett *et al.*<sup>1</sup> now use a systematic mutational analysis that integrates chemical, biochemical and molecular-biological approaches to achieve a near-complete dissection of the complex route of phosphinothricin formation.

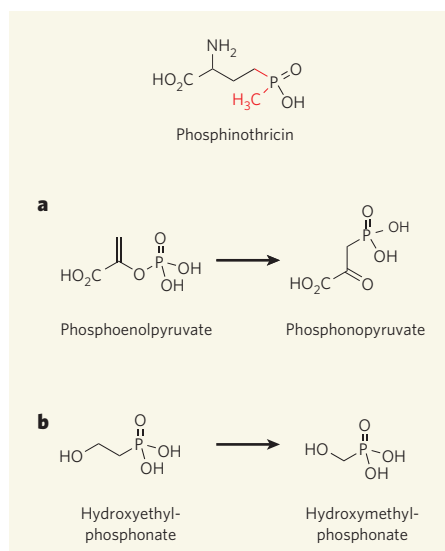


**Figure 1 | Key steps in the biosynthesis of phosphinothricin.** This herbicidal antibiotic is unique among naturally occurring amino acids because it contains carbon–phosphorus bonds (red). Blodgett *et al.*<sup>1</sup> have determined how phosphinothricin is synthesized by the bacterium *Streptomyces viridochromogenes*. Two steps are especially noteworthy. **a**, The first carbon–phosphorus bond is formed by rearranging the atoms of the ubiquitous intermediate molecule phosphoenolpyruvate, in a reaction catalysed by the enzyme phosphoenolpyruvate phosphomutase. **b**, The hydroxyethylphosphonate intermediate is converted in one step to hydroxymethylphosphonate, removing a carbon atom. This seemingly simple reaction is catalysed by an unknown enzyme encoded by the *phpD* gene, and has no biochemical precedent.

It is a tribute to those involved in the early research into phosphinothricin metabolism that so many of their conclusions withstand the scrutiny of modern analytical technologies. For example, the enzyme phosphoenolpyruvate phosphomutase was known to be central to the formation of all phosphonate natural products; it catalyses the transfer of a phosphorus group in the ubiquitous intermediate compound phosphoenolpyruvate. This atomic rearrangement converts a C–O–P bond to a direct C–P bond and leads to the formation of phosphonopyruvate. Blodgett *et al.*<sup>1</sup> confirm that this reaction is indeed the initial step in phosphinothricin biosynthesis (Fig. 1a).

Other previously reported features of phosphinothricin metabolism are also consistent with the new model. These include the formation of the second C–P bond by a methyl transferase enzyme, and the involvement of yet another enzyme (an acetyl transferase) that inactivates phosphinothricin to protect the producer organism from the compound; this acetyl transferase has already been exploited in the construction of herbicide-resistant transgenic crop plants<sup>10</sup>.

Blodgett and colleagues' investigation<sup>1</sup> nevertheless reveals several big surprises. They

identify an unanticipated reaction sequence early in the phosphinothricin biosynthetic pathway (Fig. 1b) that includes the single-step removal of a carbon atom from an intermediate compound. This transformation seems to have no biochemical precedent or readily predictable mechanism. Equally unexpected is the finding that formation of the second C–P bond of phosphinothricin requires an energy input. This comes from the reaction of a phosphinothricin precursor with a cytidine triphosphate molecule (which is closely related to the more widely used energy source, adenosine triphosphate, ATP).

The authors report one more unexpected discovery: mutations in biosynthetic genes do not always totally block phosphinothricin production in *S. viridochromogenes*, nor always lead to the accumulation of metabolic intermediates. This suggests that these steps can be bypassed — albeit with a resulting reduced overall efficiency — by generic cellular enzymes that can bind to several different, structurally related substrates. This complication may be

responsible for some of the ambiguous or confusing results that confounded the efforts of earlier workers in the field. Overcoming such difficulties demanded considerable technical ingenuity by Blodgett and colleagues. Their remarkable achievement lays a firm foundation for the further exploitation of an underappreciated group of natural products. ■

John P. Quinn is at the School of Biological Sciences, Queen's University, 97 Lisburn Road, Belfast BT9 7BL, Northern Ireland.  
e-mail: j.quinn@qub.ac.uk

1. Blodgett, J. A. V. *et al.* *Nature Chem. Biol.* **3**, 480–485 (2007).
2. Waksman, S. *Perspect. Biol. Med.* **4**, 271–272 (1961).
3. Davies, J. J. *Ind. Microbiol. Biotechnol.* **33**, 496–499 (2006).
4. Henkel, T., Brunne, R. M., Mueller, H. & Reichel, F. *Angew. Chemie Int. Edn* **38**, 643–647 (1999).
5. Ternan, N., McGrath, J. W., McMullan, G. & Quinn, J. P. *World J. Microbiol. Biotechnol.* **14**, 635–647 (1998).
6. Bayer, E. *et al.* *Helv. Chim. Acta* **55**, 224–239 (1972).
7. Seto, H. & Kuzuyama, T. *Nat. Prod. Rep.* **16**, 589–596 (1999).
8. Schwartz, D. *et al.* *Appl. Environ. Microbiol.* **70**, 7093–7102 (2004).
9. Blodgett, J. A. V., Zhang, J. K. & Metcalf, W. W. *Antimicrob. Agents Chemother.* **49**, 230–240 (2005).
10. Wohlleben, W. *et al.* *Gene* **70**, 25–37 (1988).

## IMMUNOLOGY

# Narcissistic helpers

Matthew T. Palmer and Casey T. Weaver

**T helper-17 cells, which are involved in immune responses, arise from a pool of precursor cells. It emerges that their differentiation is partly mediated by the IL-21 protein, which originates from the helper cells themselves.**

Over the past 500 million years, vertebrates have evolved an elegant solution to the life-long challenge posed by microbes: adaptive immunity. The adaptive immune response is triggered when a foreign, or non-self, molecule (an antigen) is encountered. This process is partly controlled by several types of T cell, each of which arises from a shared pool of precursor cells that have not previously encountered an antigen. So mechanisms must be in place to enforce the commitment of each 'naïve' T cell to differentiate along one of the lineages.

For their part, the long-recognized T helper type 1 (T<sub>H</sub>1) and type 2 (T<sub>H</sub>2) lineages produce immune mediator proteins called cytokines that advance the development of one lineage to the exclusion of the other. Certain T<sub>H</sub>1 and T<sub>H</sub>2 cytokines act in an autocrine manner — that is, once produced, they bind to cell-surface receptors on new, naïve T cells, thereby activating their own signalling pathways. These cytokines also suppress the development of the recently identified proinflammatory cells of the T<sub>H</sub>17 lineage. However, no cytokines from T<sub>H</sub>17 cells that would promote T<sub>H</sub>17 development had been identified. Three reports — by Nurieva *et al.*<sup>1</sup> and Korn *et al.*<sup>2</sup> on pages 480 and 484 of this issue, and by Zhou *et al.* in *Nature Immunology*<sup>3</sup> — now fill this gap by identifying

the interleukin (IL)-21 protein as the T<sub>H</sub>17-secreted autocrine cytokine.

T<sub>H</sub>17 cells produce cytokines such as IL-17A and IL-17F, which regulate immune responses specially adapted to clearing extracellular bacteria and fungi. Interest in T<sub>H</sub>17 cells has been intense — not just because their discovery shored up a deficiency in our understanding of the arsenal of adaptive responses to microbial pathogens, but also because these cells have been implicated in the pathogenesis of several chronic inflammatory diseases, including inflammatory bowel disease, psoriasis and rheumatoid arthritis<sup>4</sup>.

In an immune response, specialized cells called dendritic cells recruit antigen-naïve helper T-cell precursors. Dendritic cells not only process and present microbial antigens to the antigen receptor on the precursor T cells, but they also produce, or elicit the production of, cytokines that guide the differentiation of these cells. The resultant effector T cells then specifically eradicate the microbial invader initially presented by the dendritic cells.

Differentiation of T<sub>H</sub>17 cells is triggered by a pair of cytokines — transforming growth factor (TGF)-β and IL-6 — which induce the expression of an orphan nuclear receptor known as retinoic acid receptor-related orphan



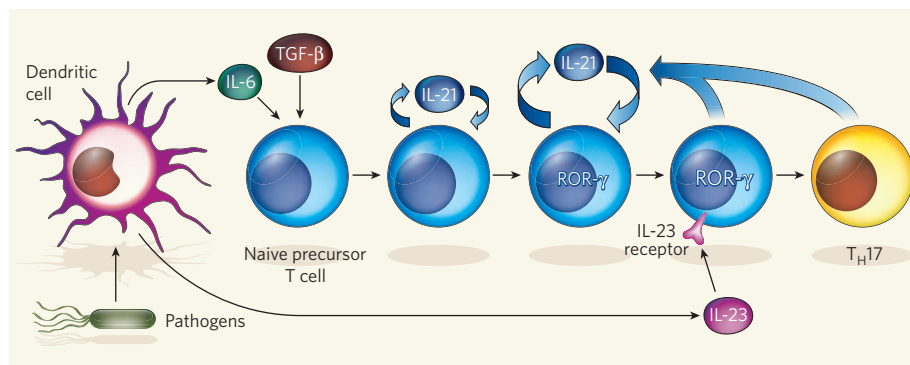


**Figure 1 | Development of the  $T_H17$ -cell lineage.** Some bacterial and fungal pathogens are detected by dendritic cells, which process them and present them as antigens, together with proinflammatory cytokines, to naive T-cell precursors. Three research teams<sup>1–3</sup> now find that dendritic-cell-derived IL-6, and another cytokine, TGF- $\beta$ , then direct the antigen-activated precursor T cell down the  $T_H17$  developmental pathway by inducing the expression of IL-21. This cytokine amplifies its own production by an autocrine feedback loop and drives the expression of the  $T_H17$ -specific transcription factor ROR- $\gamma$ . In turn, ROR- $\gamma$  induces the expression of the receptor for IL-23 — a cytokine that further enforces  $T_H17$ -cell differentiation.

receptor (ROR)- $\gamma$  (refs 5–8). This gene transcription factor prepares  $T_H17$  cells to respond to IL-23, a third cytokine that had already been associated with  $T_H17$  differentiation<sup>9</sup>.

Unlike  $T_H1$  and  $T_H2$  cells,  $T_H17$  cells had not been found to produce cytokines that reinforce their own differentiation, apparently being unable to beget their own kind through an autocrine mechanism. The three new papers<sup>1–3</sup> rectify this misconception, showing that IL-21, whose expression is induced in developing  $T_H17$  cells by dendritic-cell-derived IL-6, could sustain and amplify  $T_H17$ -cell differentiation through an autocrine feedback loop, bypassing any further requirement for IL-6.

In addition to promoting  $T_H17$ -cell differentiation, TGF- $\beta$  promotes the differentiation of a subset of T cells known as induced regulatory T ( $T_{reg}$ ) cells. In contrast to effector T cells,  $T_{reg}$  cells are responsible for maintaining immune tolerance: they limit responses mediated by effector T cells that could injure host tissues. To shift TGF- $\beta$ -induced  $T_{reg}$  development towards  $T_H17$  requires IL-6. So Korn *et al.*<sup>2</sup> predicted that, in IL-6-deficient mice, both the development of  $T_H17$  cells and the induction of a mouse model of multiple sclerosis would be impaired, instead favouring  $T_{reg}$  development. This proved to be the case. However, when the authors depleted IL-6-deficient mice of  $T_{reg}$  cells, the development of  $T_H17$  effector cells was partially restored, indicating an IL-6-independent pathway to  $T_H17$  differentiation. By screening for cytokines that might substitute for the effect of IL-6, they identified IL-21.

In complementary studies, Nurieva *et al.*<sup>1</sup> and Zhou and colleagues<sup>3</sup> compared the total gene expression of T helper cells that had differentiated under different conditions. Both teams found that, under conditions known to promote  $T_H17$ -cell development, levels of messenger RNA for IL-21 were enhanced, indicating induction of its encoding gene. These groups<sup>1,3</sup> also found that IL-21 was as effective in inducing the expression of ROR- $\gamma$  and the

receptor for IL-23 as was IL-6. But, compared with IL-6-deficient T cells, cells deficient in IL-21 were profoundly impaired in inducing IL-23 receptor, ROR- $\gamma$  and IL-17 in response to IL-6. Thus, IL-21, not IL-6, seems to be the main inducer of the IL-23 receptor.

Could IL-21 induce its own expression through a ROR- $\gamma$ -independent pathway? Possibly; ROR- $\gamma$ -deficient T cells expressed normal levels of IL-21, but expressed reduced levels of IL-17A, IL-17F and IL-22 (refs 1, 3). This indicates that, in the molecular-signalling pathway, IL-21 induction is upstream of, and independent of, ROR- $\gamma$ .

Together, these studies support a revised model of  $T_H17$ -cell development. Thus, IL-21 is both necessary and sufficient for the differentiation of  $T_H17$  cells, acting downstream of IL-6 and upstream of ROR- $\gamma$  to promote the expression of the IL-23 receptor. This, in turn, prepares cells for IL-23-mediated completion of  $T_H17$ -cell differentiation (Fig. 1).

It was known that IL-21 suppresses the production of another cytokine, IFN- $\gamma$ , both by cytolytic T cells, which destroy infected cells, and by  $T_H1$  cells<sup>10</sup>. It is therefore plausible that, in promoting the development of  $T_H17$  cells, another function of IL-21 is to suppress IFN- $\gamma$ , which can potentially inhibit  $T_H17$ -cell differentiation.

The possibility that IL-21 is an essential inductive and maintenance factor for  $T_H17$ -mediated immune responses raises the prospect that it will be a target for therapeutic intervention, either to curb the pathogenic (autoimmune) effects of  $T_H17$  or to enhance its protective (anti-pathogen) effects. ■

Matthew T. Palmer and Casey T. Weaver are in the Department of Pathology, University of Alabama at Birmingham, Birmingham, Alabama 35294-2170, USA.  
e-mail: cweaver@uab.edu

1. Nurieva, R. *et al.* *Nature* **448**, 480–483 (2007).
2. Korn, T. *et al.* *Nature* **448**, 484–487 (2007).



## 50 YEARS AGO

The General Board of the Faculties of the University of Cambridge has prepared a report outlining a course whereby students could undertake study of a science subject as well as of an arts subject... The new course would give students the advantages of training in both arts and science. Arts men are trained not only to collect accurate data and to use them systematically, but also to exercise critical judgment upon matters of opinion where scholars may reach quite different conclusions. On the other hand, the conclusions of the scientist are based on precise observations and measurements, involve exact calculations, and must be tested by experiment or controlled observation; agreement on essential issues can therefore ultimately be reached.

From *Nature* 27 July 1957.

## 100 YEARS AGO

We learn with regret of the death of Prof. Egon von Oppolzer at the early age of thirty-seven. Dr. von Oppolzer, who was a son of the celebrated Theodor von Oppolzer, was born at Vienna in 1869, and was educated at the universities of Vienna and Munich. In 1897 he became an assistant in the observatory at Prague, where he discovered in 1901 the variability in the brightness of the planet Eros... Among the subjects on which he wrote are astronomical refraction, solar physics, and the application of physical theory to stellar problems. He also made contributions to meteorology. A new form of zenith telescope was constructed by him, as well as a photometer of novel design. The variability of the minor planets, which has recently become a subject of very great interest, has naturally been investigated with the greatest success by the aid of photography, and it is worthy of note that Dr. von Oppolzer's important discovery in this branch of research was established by visual observations.

From *Nature* 25 July 1907.

50 & 100 YEARS AGO

3. Zhou, L. *et al.* *Nature Immunol.* doi:10.1038/ni1488 (2007).
4. Weaver, C. T. *et al.* *Annu. Rev. Immunol.* **25**, 821–852 (2007).
5. Veldhoen, M., Hocking, R. J., Atkins, C. J., Locksley, R. M. & Stockinger, B. *Immunity* **24**, 179–189 (2006).
6. Mangan, P. R. *et al.* *Nature* **441**, 231–234 (2006).
7. Bettelli, E. *et al.* *Nature* **441**, 235–238 (2006).
8. Ivanov, I. I. *et al.* *Cell* **126**, 1121–1133 (2006).
9. Murphy, C. A. *et al.* *J. Exp. Med.* **198**, 1951–1957 (2003).
10. Mehta, D. S., Wurster, A. L. & Grusby, M. J. *Immunol. Rev.* **202**, 84–95 (2004).

## ASTROBIOLOGY

# Photosynthesis in watercolours

John Raven

**The spectrum of stellar radiation available to an organism is altered by the atmosphere and water on the planet it inhabits. Study of this relationship can outline the limits to photosynthesis.**

Water is essential for life 'as we know it', and the search for life 'as we don't know it' elsewhere in the Universe centres on the search for evidence of water<sup>1</sup>. But the properties of water that make it essential for organisms and their environments can also restrict organisms' activities. An example that has now been re-investigated by Kiang *et al.*<sup>2,3</sup> and by Stomp *et al.*<sup>4</sup> is the wavelength dependence of the absorption of electromagnetic radiation by water, and also by permanent atmospheric gases. Such studies can inform our understanding of the distribution and pigmentation of photosynthetic organisms on Earth<sup>2–4</sup>, and on any life-supporting Earth-like planets in other solar systems.

This biological dark side of water — its absorption of solar electromagnetic radiation — creates habitats that restrict or eliminate the roles of solar radiation in supplying energy for photosynthesis and information to sensory systems. The effective absence of solar radiation deep in large bodies of water such as lakes and oceans has long been recognized, and limits photosynthesis with this energy source to at most the top few hundred metres of water bodies, and to the land surface. The significance of water's wavelength-dependent attenuation of solar radiation for photosynthesis by aquatic organisms has been recognized since the late nineteenth century. Engelmann<sup>5</sup>, with his theory of complementary chromatic adaptation, suggested in 1883 that the depth at which seaweeds with different pigments grow might be related to the spectrum of incident radiation they receive.

Later work showed that Engelmann had underestimated the role of dissolved and suspended material in modifying the radiation attenuation due to water alone, and that, even when this was taken into account, the quantitative significance of complementary chromatic adaptation of seaweeds in nature was small<sup>6</sup>. But Engelmann's perception was a great stimulus to study of the photosynthetic pigmentation and the radiation environment of organisms in relation to the absorption of radiation by water. That work has extended to anoxygenic organisms (photosynthetic bacteria)<sup>2–4</sup> — that

is, those whose photosynthesis does not generate oxygen — as well as being carried out on the oxygenic organisms considered by Engelmann, and also to other planets that might support life<sup>4</sup>. On Earth, the advent of anoxygenic organisms preceded that of oxygenic ones.

Kiang *et al.*<sup>2</sup> surveyed the diversity of photosynthetic organisms, and propose constraints on the evolution of the pigments that harvest and transform radiation. One is the wavelength of the peak photon flux in the environment. Another is the longest wavelength that has sufficient energy per photon to bring about the appropriate photochemical reaction (in which photon energy is converted into chemical energy). Organisms that produce oxygen from water, a very energy-intensive reaction, are constrained to using shorter wavelengths than are those that do not produce oxygen. This is the case despite the oxygen producers using two photochemical reactions in series, rather than a single reaction, as seen in anoxygenic organisms. The sorts of photochemistry that can occur, and the pigmentation of the organisms, are greatly influenced by the absorption of solar radiation by water (and oxygen) in the atmosphere and, for aquatic organisms, in the water body in which they live<sup>2</sup>.

Independent work by Stomp *et al.*<sup>4</sup> emphasizes the photon-absorbing properties of bulk water. Their analysis concentrates on photosynthetic microorganisms living in various bodies of water whose photon-attenuation properties differ because of dissolved and suspended material. Stomp *et al.* also examined the details of the photon absorption of water in the visible and infrared parts of the spectrum, concentrating on the harmonics of the molecular vibrations resulting in the main absorption features.

A major outcome of this work is in defining spectral niches for photosynthetic organisms in different aquatic habitats. Such conclusions for photosynthetic microorganisms do not necessarily conflict with those of Dring<sup>6</sup> for seaweeds. Dring showed that the differences in pigmentation among seaweeds are less quantitatively significant for photosynthetic performance in their natural

habitats than many had previously believed.

Kiang and colleagues' analyses<sup>2</sup> of constraints on pigmentation of photosynthetic organisms on Earth provide the basis for their discussion<sup>3</sup> of astrobiological aspects of photosynthesis. Putative planets associated with stars of the M spectral type are commonly taken to be locations where life might occur, given the abundance of these stars and their longevity. Photosynthetic organisms on an Earth-like planet orbiting an M star would experience stellar radiation with maximum photon fluxes at wavelengths in the infrared spectrum. The 'average' photon would have a lower energy content, and there would also be a much greater absorption by water, than for solar radiation on Earth<sup>2–4,7</sup>.

Significant photosynthesis could nonetheless occur on such a planet<sup>4,7</sup>. But there would be energetic problems in using the relatively low-energy photons to reduce carbon dioxide with electrons from water, with production of oxygen. The mechanism on Earth relies on two photochemical reactions in series; on planets orbiting an M star more than two reactions in series would be required<sup>2,7</sup>. On any such planet, the longer wavelengths at which photosynthetic pigments would absorb would have implications for the remote sensing of pigments by reflectance spectroscopy as an indicator (with appropriate caveats) of photosynthesis, and hence life.

Kiang *et al.*<sup>2,3</sup> and Stomp *et al.*<sup>4</sup> use physics and chemistry to set limits on the mechanisms of photosynthesis that are possible in different habitats on Earth and on any Earth-like planets orbiting other stars. The authors' analyses outline the sorts of photosynthetic mechanism that are possible in a given radiation environment, without defining the chemical nature of the pigments or other components of the photosynthetic system.

Although the evolution of oxygen-producing photosynthesis is a likely outcome of the biogeochemical changes that accompany photosynthesis not involving oxygen production on a planet, this cannot be taken for granted. Accordingly, in the search for life outside our Solar System, an astrobiological niche presents itself. This is the spectroscopic remote-sensing not only of photosynthetically produced oxygen and its derivative ozone<sup>8</sup>, but also of a diversity of photosynthetic pigments<sup>3,7</sup>, on any Earth-like planets that may be detected. ■

John Raven is at the College of Life Sciences, University of Dundee, Invergowrie, Dundee DD2 5DA, UK.  
e-mail: j.a.raven@dundee.ac.uk

1. Tinetti, G. *et al.* *Nature* **448**, 169–171 (2007).
2. Kiang, N. Y., Siefert, J., Govindjee & Blankenship, R. E. *Astrobiology* **7**, 222–251 (2007).
3. Kiang, N. Y. *et al.* *Astrobiology* **7**, 252–274 (2007).
4. Stomp, M. *et al.* *ISME J.* doi:10.1038/ISMEJ.2007.59 (2007).
5. Engelmann, T. W. *Bot. Z.* **41**, 1–29 (1883).
6. Dring, M. J. *Limnol. Oceanogr.* **26**, 271–284 (1981).
7. Raven, J. A. & Wolstencroft, R. D. in *Proc. IAU Symp. 213. Bioastronomy 2002: Life Among the Stars* (eds Norris, R. P. & Stootman, F. H.) 305–308 (Astron. Soc. Pacific, San Francisco, 2004).
8. Lovelock, J. E. *Proc. R. Soc. Lond. B* **189**, 167–181 (1975).



## MATHEMATICS

## Some assembly needed

Ian Stewart

**Origami, the ancient Japanese art of paper folding, is mathematically deeper than it looks. Delving into its complexities allows the construction of elaborate and useful structures from simple, flat templates.**

Saving space is an imperative in commerce, engineering and the structure of living creatures. Furniture and garden equipment come in flat-packs to save storage space in the warehouse and the delivery van — and, it must be said, to make the purchaser do all that time-consuming work of assembly. The solar panels that provide satellites with electrical power have to be folded so that they fit into the bay of a space shuttle. And who could fail to be entranced by the emergence of a butterfly from a pupa, as pulsing blood inflates bedraggled, folded tissue into glorious, gaudy wings?

Over the past two decades, a dedicated band of mathematicians, engineers and computer scientists has been developing a new branch of mathematics to understand the science of folding objects flat. In a contribution<sup>1</sup> to a recent conference<sup>2</sup> that exemplifies these efforts, Taketoshi Nojima details the derivation of a surprising range of geometrical forms from a flat sheet of material, including “tubes, conical shells, circular membranes, movable/shape-changeable models and highly rigid 3-D cores”.

Researchers’ inspiration in this area derives from two quite different sources: ‘biomimetics’, the technological mimicry of biological processes and structures, and the ancient Japanese art of origami. The results have been intriguing and ingenious, and have already found applications in maps, food packaging, folding drinks containers, car airbags and spacecraft antennas. Among future applications could be foldable plastic bottles, lightweight skeletons for aerospace structures and compact light-sails for interplanetary travel. The mathematics developed along the way could also feed back into a better understanding of nature’s own origami: the growth and development of leaves, buds and insect wings.

Origami’s potential as a source of mathematical problems has been recognized for some time. Its patterns of folds can construct geometric forms beyond those possible with Euclid’s traditional rule and compass, such as regular seven-sided and nine-sided polygons. The basic problem of origami is the flat-folding problem: given a diagram of fold lines on a flat sheet of paper, can the paper be folded into a flat shape

without introducing any further creases?

In 1996, two computer scientists, Barry Hayes of Placeware, Inc. and Marshall Bern at Xerox’s Palo Alto Research Center, proved that this question is mathematically equivalent to a famous problem in logic, the 3-SAT problem<sup>3</sup>. This is the ‘satisfiability problem’, and is an example of an NP-hard problem, meaning that the running time required for any algorithm to solve the problem grows rapidly as the problem becomes more complex, so that the calculation takes too long to be feasible. The satisfiability problem asks the question whether there is some assignment of values for boolean expressions — combinations of true-or-false logical statements — built from simple three-component formulas such that the entire expression returns the value ‘true’. Mathematically, therefore, origami is deeper than it looks.

The same is true biologically, and this is where Nojima’s research comes in. By studying natural folding patterns, especially those associated with the growth of plants, he has devised methods for folding remarkable three-dimensional shapes from flat sheets of lightweight material. For example, one class of structures derives from the well-known occurrence of Fibonacci numbers (the sequence of numbers in which each is the sum of the

two preceding numbers: 0, 1, 1, 2, 3, 5, 8, 13, 21, 34, 55 and so on) in various cylindrical or helical plants, such as pine cones and pineapples. The scales of a pine cone, for instance, form two families of helices, one twisting clockwise and the other anticlockwise. The numbers of helices in these families are two adjacent Fibonacci numbers, such as 8 and 13. Folding patterns with a similar form can be used to create rigid helical structures from flat sheets, which are rolled into a cylinder and then folded. If the sheet is first formed into a cone, collapsible conical structures can also be made (Fig. 1).

This idea is only the beginning. Far more elaborate shapes can also be constructed by origami methods. Often these resemble biological forms — flowers, horns, shells. Some of Nojima’s patterns are inspired by the buds of the morning glory and the folds in an earwig’s wings. Another source of inspiration is purely

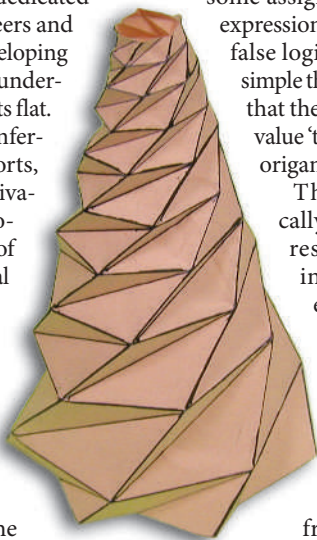


**Figure 1 | Natural inspiration**  
— Nojima’s origami pine cone.

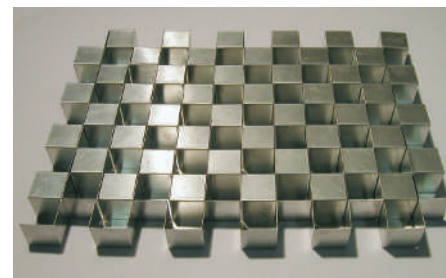


**Figure 2 | Industrial application of origami.**  
The mathematical folding schemes developed by Nojima<sup>1</sup> can be used to stamp out tiled patterns from sheet metal, which can then be folded and welded to form rigid, lightweight materials that might be of use, for example, in the aerospace industry.

mathematical: tiling patterns, or ‘tessellations’, in the plane. Clever folding processes based on tessellations lead to rigid, lightweight materials of a ‘honeycomb’ type (Fig. 2). Some of these can be stamped out from sheet metal, folded and then welded so that they retain the folded shape, providing a simple and reliable way to manufacture apparently complicated materials. The work<sup>1</sup> analyses the precise geometric conditions required for these constructions, putting them on a solid mathematical basis. It also pays attention to practical issues, such as the thickness of the sheet being folded.

The potential of these simple but ingenious ideas is huge. Complex three-dimensional forms could arise from flat, stamped sheets of ‘shape memory’ materials merely by heating them. They could also be made from flat sheets of rubber and inflated, a usefully reversible construction technique. Honeycomb cores are common in the aerospace industry for their rigidity and lightness, and any new, simple manufacturing process is likely to prove valuable. Origami structures, being lightweight and compact, are ‘green’: they can easily be recycled, and even if they’re not, the amount of rubbish they create is reduced.

Nojima ends with a look to the future. He envisages the creation of a new discipline, which I am tempted to name ‘origamics’. This would be a combination of engineering, mathematics and biology, and could lead to significant progress in a variety of fields. Nojima himself cites “plastic buckling, biomimetic robotic modelings, movable origami modeling for education or edutainment... [and] new interpretations of bionic mechanics.” He could well be right.

Ian Stewart is at the Warwick Mathematics Institute, Zeeman Building, University of Warwick, Coventry CV4 7AL, UK.  
e-mail: i.n.stewart@warwick.ac.uk

1. Nojima, T. <http://impact.kuero.kyoto-u.ac.jp/pdf/Origami.pdf>
2. *VIP Symp. Internet Related Res.* Tokyo, 2007 <http://internetconferences.net/ipsi/conference.php?conf=52&past=1>
3. Bern, M. & Hayes, B. *Proc. 7th ACM-SIAM Symp. Discrete Algorithms* 175–183 (SIAM, Philadelphia, PA, 1996).

## DEVELOPMENTAL BIOLOGY

# A ten per cent solution

John Reinitz

**In early embryos, a concentration gradient of the Bicoid protein affects pattern formation. Studies of living embryos reveal a surprising level of accuracy in the Bicoid gradient. But is it accurate enough?**

A central idea in developmental biology is Lewis Wolpert's theory of positional information<sup>1</sup>. This states that a substance present in a concentration gradient induces different developmental fates in cells when present at different concentrations. The first such morphogenetic gradient to be identified was that of the gene transcription factor Bicoid in embryos of the fruitfly *Drosophila melanogaster*<sup>2,3</sup>. This protein is distributed with an exponential profile, with its concentration decreasing towards the posterior pole of the embryo. Although the importance of the Bicoid gradient in specifying cellular fates was established, quantitative puzzles remained. These problems have now been largely solved by Gregor and colleagues<sup>4,5</sup> in two papers in *Cell*.

A previous study<sup>6</sup> had shown that the Bicoid concentration gradient varied far more widely between embryos than did the expression of the *hunchback* (*hb*) gene, which is used as a readout of the effect of Bicoid concentration. This and other studies, however, were performed in fixed tissue, where it is impossible to determine absolute protein concentrations or to follow changes in gene expression over time.

Gregor *et al.*<sup>4</sup> tagged Bicoid with enhanced green fluorescent protein (eGFP), which allowed them to directly observe its gradient in live embryos. For this, the authors constructed a genetic line of fruitflies in which the *bicoid* gene (*bcd*) was replaced by a functional *bcd-egfp* fusion gene. They then monitored the gene's protein product by time-lapse microscopy during the blastoderm stage of early embryonic development.

In early *Drosophila* development, the embryo is a syncytium — it consists of a mass of cytoplasm, with nuclei that are not separated by cell membranes. The nuclei undergo a series of 13 rapid divisions, with the blastoderm forming at about division 10. The authors found that it is at division 9 — before blastoderm formation — that Bicoid-eGFP is first detected. As it is a DNA-binding protein, Bicoid is localized in the nucleus. But as nuclei lose their envelopes during each division, internally stored Bicoid is released into the cytoplasm.

Gregor and colleagues show that there is a remarkable constancy in nuclear Bicoid concentration between nuclear divisions, with peak concentrations varying by less than 10% at any given anterior–posterior position within the embryo. Evolution has thus provided a startlingly precise mechanism for preserving positional information in nuclei, in the face of

repeated dissolutions and restorations of their membranes.

The authors also found that a photo-bleached nucleus regains its fluorescence within a few minutes, indicating that nuclear Bicoid is in tight equilibrium with its cytoplasmic pool. They established a simple model of diffusion-limited active transport and used it to predict the value of a diffusion constant for Bicoid in the cytoplasm. In observing the recovery of fluorescence in the photo-bleached region of the cytoplasm, they confirmed this prediction.

The Bicoid gradient was thought to be exceptional in terms of regulating early patterns of *Drosophila* gene expression because its distribution can be determined using a diffusion equation that assumes there is a constant source of Bicoid at the anterior pole and first-order decay of diffusing Bicoid<sup>7,8</sup>. But Gregor and colleagues' results introduce serious complications in this picture.

The authors found that the Bicoid gradient reaches a steady state in 90 minutes. This implies, using the diffusion equation, that the diffusion coefficient is more than  $2 \mu\text{m}^2$  per second; however, photo-bleaching experiments indicate a value of only  $0.35 \mu\text{m}^2$  per second. It may be that diffusivity varies on different timescales, or perhaps is affected by the nuclei themselves. Although the authors provide some evidence for the second possibility by observing that the Bicoid gradient is altered in unfertilized eggs, a true solution to this problem must await further experiments.

In their second paper, Gregor *et al.*<sup>5</sup> investigate just how precise the readout of the Bicoid effect can be. They find that, by the end of the blastoderm stage, certain gene-expression patterns are specified to a resolution of one nucleus, which corresponds to a 10% difference in Bicoid concentration between adjacent nuclei. Can such small differences be perceived by the embryo?

To be detected by the cell, Bicoid molecules must diffuse to a cellular receptor. The theory of this diffusive process was worked out for bacterial chemotaxis — movement along a chemical concentration gradient — many years ago<sup>9</sup>, when it was established that the limit of detection depends on the square root of the product of the signalling-molecule concentration, its diffusivity, the size of the receptor, and the time period over which the concentration is averaged. This relation is completely general in physical details, as long as the processes involved do not dissipate energy. Thus,

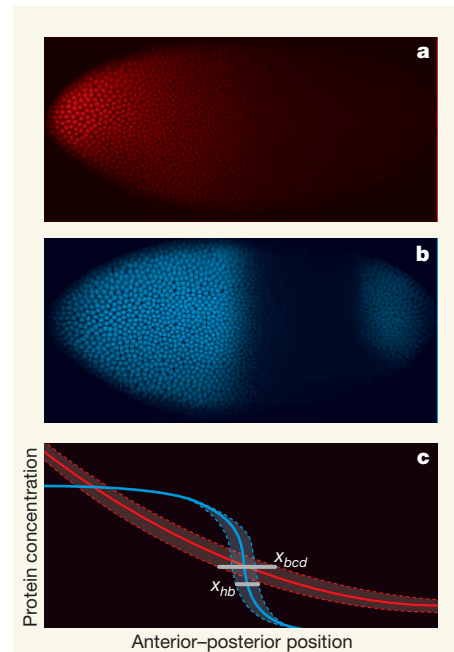


**Figure 1 | The role of Bicoid in dictating levels of gene expression during development.**

**a**, A *Drosophila* embryo at the blastoderm stage of development stained with a fluorescently tagged antibody to Bicoid. **b**, The same embryo stained with a fluorescently tagged antibody to the Hunchback protein, the expression of which is determined by the Bicoid gradient. **c**, Gregor *et al.*<sup>4,5</sup> found that the range of positions of threshold concentrations of Bicoid ( $x_{bcd}$ ) was twice that of the border of *hunchback* gene expression ( $x_{hb}$ ). The mean Bicoid pattern in a population (red solid line) is an average of the range of Bicoid levels in the population (dashed red lines). The mean expression profile of the *hunchback* gene (solid blue line) differs from its upper and lower limits of expression in the population (dashed blue lines) accordingly. (**a** and **b** are from ref. 10.)

the accuracy of detection rises with the square root of the number of molecules sensed.

To apply this formula, Gregor *et al.* measured the absolute concentration of Bicoid by placing embryos expressing Bicoid-eGFP in a bath containing GFP at a known concentration, thus assigning an absolute concentration scale to their measurements. They found that the nuclear concentration of Bicoid was about 8 nanomolar in the centre of the embryo, which amounts to about 700 molecules per nucleus. In this region of the embryo, Bicoid must be averaged over a period of about 2 hours for a 10% difference in concentration to be detectable. The actual timescale is much shorter because boundaries of gene-expression domains form over a period of 7 minutes. These timescales imply a Bicoid discrimination threshold of 20–40% in neighbouring nuclei.

Embryo-to-embryo variations in gene expression also provide information on the actual discrimination threshold. The anomalous positional accuracy described in earlier work<sup>6</sup> had two main components. First, when



measured as a percentage of egg length, the range in position of Bicoid concentration thresholds for activation of the expression of the *hunchback* gene ( $x_{bcd}$ ) was found to be six times that for the *hb* border it nominally controls ( $x_{hb}$ ). Moreover,  $x_{hb}$  correlated with embryo size, whereas  $x_{bcd}$  did not, raising the question of how the Hunchback border scales with the size of the egg.

Gregor *et al.* present *in vivo* data from 15 live embryos imaged side by side. These data indicate that, based on absolute distance — rather than percentage of egg length — the range in  $x_{bcd}$  is about twice that of  $x_{hb}$  (Fig. 1). I think these results indicate that the anomalous positional-accuracy problem still exists, but that the anomaly is smaller than was thought. The small range of  $x_{bcd}$  in absolute distance units may mean that the apparently different scaling properties of  $x_{bcd}$  and  $x_{hb}$  were a fixation artefact, a point that has serious implications for theoreticians.

Gregor and colleagues argue that a 10% change in Bicoid concentration is detectable

and that the Bicoid gradient is sufficiently accurate to be used for specifying the position of the border of *hb* expression in the anterior domain. To make this point, they marshal an intricate set of quantitative arguments that are ultimately unconvincing, because they are based on a picture in which Bicoid is the only input to *hb* expression. This assumption is demonstrably false. The mean position of  $x_{hb}$  is altered in embryos that have mutations in *giant* and other gap genes — genes involved in allocating domains in the insect embryo. Furthermore, the variance of  $x_{hb}$  is doubled when one chromosome arm is removed<sup>6</sup>. Although such effects are much smaller than is seen for other gap genes, it is dangerous to ignore them in a study that aims to obtain a complete quantitative characterization of the control of *hb* expression.

The most radical elements of the authors' conclusions are not well supported. But there is no question that this work is a landmark that may prove to be as revolutionary as were the methods for imaging protein and RNA in fixed tissue that were developed 25 years ago.

Moreover, these findings confirm that it is unlikely that either experimentalists or theoreticians will run out of fascinating phenomena to investigate in the *Drosophila* embryo any time soon.

John Reintz is in the Department of Applied Mathematics and Statistics, Stony Brook University, Stony Brook, New York 11794-3600, USA.  
e-mail: reintz@odd.bio.sunysb.edu

1. Wolpert, L. *J. Theor. Biol.* **25**, 1–47 (1969).
2. Driever, W. & Nüsslein-Volhard, C. *Cell* **54**, 83–93 (1988).
3. Driever, W. & Nüsslein-Volhard, C. *Cell* **54**, 95–104 (1988).
4. Gregor, T., Wieschaus, E. F., McGregor, A. P., Bialek, W. & Tank, D. W. *Cell* **130**, 141–152 (2007).
5. Gregor, T., Tank, D. W., Wieschaus, E. F. & Bialek, W. *Cell* **130**, 153–164 (2007).
6. Houchmandzadeh, B., Wieschaus, E. & Leibler, S. *Nature* **415**, 798–802 (2002).
7. Houchmandzadeh, B., Wieschaus, E. & Leibler, S. *Phys. Rev. E* **72**, 061920 (2005).
8. Gregor, T., Bialek, W., de Ruyter van Steveninck, R. R., Tank, D. W. & Wieschaus, E. F. *Proc. Natl Acad. Sci. USA* **102**, 18403–18407 (2005).
9. Berg, H. C. & Purcell, E. M. *Biophys. J.* **20**, 193–219 (1977).
10. <http://flyex.ams.sunysb.edu/FlyEx>

## INFLAMMATORY DISEASE

# Assault on the guardian

Richard M. Ransohoff

**In multiple sclerosis, the immune system attacks 'self' tissues. Ten years after the discovery of one target of this autoimmunity, work with mice identifies it as a guardian protein produced in response to inflammation.**

On page 474 of this issue, Ousman and her co-workers<sup>1</sup> describe how autoimmunity to a protein known as  $\alpha$ B-crystallin (CRYAB) can contribute to inflammatory injury of the central nervous system. They show that autoimmune attack on CRYAB does not directly cause tissue damage. Rather, it worsens the severity of damage by simultaneously eliminating two of the protein's functions — its action as a restraining element for inflammation, and its ability to inhibit programmed cell death of glial cells in the nervous system.

The clinical context for this research is multiple sclerosis (MS), an inflammatory disorder of the human central nervous system. This disease selectively targets myelin, the complex, lipid-rich membrane that enwraps some nerve axons. Its connection with CRYAB began with an experiment that challenged orthodoxy: in 1995, van Noort *et al.*<sup>2</sup> reported CRYAB to be a predominant target of autoimmunity in MS. They discovered CRYAB's significance by isolating myelin proteins from MS autopsy material, and determining these proteins' ability to act as autoantigens in evoking a reaction from T cells. These are major players in the immune system, and both produce and are stimulated by cytokine messenger molecules.

The group's finding<sup>2</sup> came as a surprise.

During many years of research on autoimmune models of MS (known collectively as experimental autoimmune encephalomyelitis, or EAE), investigators had identified several myelin proteins with encephalitogenic potential. Encephalitogenicity implies that immunization with the protein, or with a peptide derived from it, could elicit an autoimmune reaction, characterized by inflammation, demyelination and weakness of the limbs. Known encephalitogenic agents included the principal proteins of myelin — myelin basic protein and myelin proteolipid protein — as well as minor components, such as myelin oligodendroglial glycoprotein (MOG).

Van Noort and colleagues took the road “less traveled by” and focused on myelin from patients with MS. Previously, the usual assumption had been that any autoantigen present in myelin would be a constituent of the healthy tissue. CRYAB was distinctly an outlier, because it is expressed only at low levels in myelin derived from the non-diseased central nervous system<sup>3</sup>. It belongs to the family of small heat-shock proteins that are produced by all cells in response to stress. CRYAB is also an oddity among heat-shock proteins, however, being expressed selectively in the eye lens, in skeletal and cardiac muscle, and in glial

cells, including oligodendrocytes (the cells that produce myelin) and astrocytes.

It soon emerged that both MS patients and healthy individuals have a strong immune response to CRYAB<sup>4</sup>. As with previous candidate MS antigens, it was assumed that clinically relevant autoimmune targets should themselves be encephalitogenic. Exasperatingly, however, attempts to demonstrate this property in rodents, the most widely used host species for EAE, were unsuccessful. One proposed explanation was that the immune system was ‘tolerized’ to Cryab by destruction, in the thymus, of T cells that recognize the protein<sup>5</sup>. This possibility was addressed in ingenious ways that involved using Cryab to immunize Cryab-deficient mice (*Cryab*<sup>−/−</sup> mice)<sup>6</sup> to uncover an encephalitogenic portion of the Cryab molecule. However, these approaches, which had been successful in other systems<sup>7</sup>, failed to reveal an encephalitogen.

Enter Ousman and colleagues<sup>1</sup>, who also took an unorthodox approach — studying Cryab's functions by immunizing *Cryab*<sup>−/−</sup> mice to develop EAE using a peptide from MOG, a known encephalitogen. These mice developed disease at the expected frequency and time after immunization, but became noticeably sicker, and remained so for longer, than their normal counterparts. This observation became the focal point for the authors' subsequent studies.

The actions of individual components in the EAE model usually occur either in the immune compartment (where autoimmunity or inflammation is made more or less severe), or in the central nervous system (where cells can be more or less susceptible to dying during the inflammatory process). Ousman *et al.* show that Cryab violates this dichotomy

by mediating both the immune and neural functions. On stimulation with the MOG peptide antigen, T cells from *Cryab*<sup>-/-</sup> mice proliferated more and secreted higher levels of inflammatory cytokines than did those from EAE controls. Other immune cells, macrophages, were also hyper-reactive, producing high levels of cytokines after challenge with lipopolysaccharide, a well-characterized macrophage stimulant. In addition, increased numbers of glial cells underwent programmed cell death in the inflamed central nervous system of *Cryab*<sup>-/-</sup> mice with EAE, extending *in vitro* studies<sup>8</sup> that suggested *Cryab* could protect these cells.

Ousman *et al.* then went further. They looked at two cell-signalling pathways (NF- $\kappa$ B and MAP kinase) involved in inflammation, and found that alterations in these pathways in cells from *Cryab*<sup>-/-</sup> mice correlated not only with a heightened immune reaction, but also with the vulnerability of astrocytes to programmed cell death. They also explored the clinical relevance of their findings by testing the cerebrospinal fluid of MS patients, and found CRYAB antibodies to be present. Finally, they injected *Cryab* protein into mice with EAE, and showed that it reduced disease.

Overall, Ousman *et al.*<sup>1</sup> show that *Cryab* is produced early on in response to inflammation associated with EAE (and possibly MS): the protein itself becomes an autoimmune target, its destruction exacerbating inflammatory damage but not directly causing demyelination. In humans, the disease cascade presumably begins with generation of autoreactivity to unknown primary encephalitogens. This is followed by upregulation of CRYAB production as part of the stress response, followed in some patients by the onset of autoimmunity to CRYAB and acceleration of the disease process.

There are several provocative leads for further research. It seems<sup>9</sup> that autoimmunity to CRYAB can be detected early in the course of MS, and an obvious step is to find out whether strategies to restore tolerance can be devised<sup>10</sup>. It is also of interest that infection with Epstein-Barr virus, the agent most strongly associated with MS in epidemiological studies, upregulates CRYAB expression in certain immune cells<sup>11</sup>. Finally, polymorphisms in the promoter genes encoding CRYAB may influence disease severity<sup>12</sup>, and a suspected mediator of damage in MS, known as MMP9/gelatinase B, can use CRYAB as a substrate<sup>13</sup> — offering yet another way in which inflammation could reduce the protein's availability.

Richard M. Ransohoff is in the Neuroinflammation Research Center, Department of Neurosciences, Lerner Research Institute, Cleveland Clinic Foundation, 9500 Euclid Avenue, Cleveland, Ohio 44195, USA.  
e-mail: ransohr@ccf.org

3. Bajramovic, J. J., Lassmann, H. & van Noort, J. M. *J. Neuroimmunol.* **78**, 143–151 (1997).
4. van Noort, J. M. *et al. Mult. Scler.* **12**, 287–293 (2006).
5. van Stipdonk, M. J. B., Willems, A. A., Verbeek, R., Boog, C. J. P. & van Noort, J. M. *Cell Immunol.* **204**, 128–134 (2000).
6. Wang, C. *et al. J. Neuroimmunol.* **176**, 51–62 (2006).
7. Huseby, E. S. *et al. J. Exp. Med.* **194**, 669–676 (2001).
8. Alge, C. S. *et al. Invest. Ophthalmol. Vis. Sci.* **43**, 3575–3582 (2002).

9. Bajramovic, J. J. *et al. J. Immunol.* **164**, 4359–4366 (2000).
10. Verbeek, R., van der Mark, K., Wawrousek, E. F., Plomp, A. C. & van Noort, J. M. *Immunology* **121**, 416–426 (2007).
11. van Sechel, A. C. *et al. J. Immunol.* **162**, 129–135 (1999).
12. Stoevring, B., Frederiksen, J. L. & Christiansen, M. *Clin. Chim. Acta* **375**, 57–62 (2007).
13. Starckx, S. *et al. J. Neuroimmunol.* **141**, 47–57 (2003).

## QUANTUM COMPUTING

# Powered by symmetry

Johannes Hecker Denschlag

**Forces determine how particles move and behave. But so can symmetry, and exchange symmetry can be used to control the interactions of ultracold atoms. This could be a big step towards practical quantum computation.**

Quantum computers promise to solve problems that cannot be tackled by conventional computers<sup>1</sup>. But they make high demands on the machinery from which they are built. The physical entities storing quantum bits — the smallest units of quantum information — must be controlled and coupled to each other with great precision. On page 452 of this issue, Anderlini *et al.*<sup>2</sup> present a very general method, based on a quantum-mechanical phenomenon known as exchange symmetry<sup>3–5</sup>, that allows this degree of precision manipulation in controlled collisions of neutral atoms.

Arrays of trapped ultracold atoms are promising candidates for storing quantum information because of their weak, random coupling to the external world. During a controlled collision, the interaction between two cold atoms each carrying a bit of quantum information

can be used to process that information<sup>6,7</sup>. But this scheme only works if the interaction between the atoms depends on the specific state of their quantum bits, and finding an appropriate atomic system is no trivial matter.

One option is to exploit symmetry. Symmetry is a fundamental concept throughout physics, and is the basis for all conservation laws. Angular momentum, for example, is conserved in isotropic (that is, rotationally symmetric) environments. Another type of symmetry is based on the idea that no measurable quantity should change after the exchange of identical particles. This exchange symmetry classifies particles into two groups: fermions, described mathematically by an overall antisymmetric wavefunction, and bosons, with an overall symmetric wavefunction. The antisymmetry of the fermionic wavefunction leads directly to the famous Pauli exclusion principle, which forbids two or more particles from occupying the same quantum state.

Anderlini *et al.*<sup>2</sup> find a way to make use of a similar symmetry-based constraint. They work with bosonic rubidium atoms, <sup>87</sup>Rb, that have a symmetric total wavefunction. This wavefunction has two components: a spin component describing the internal state of the atoms, and a spatial component describing their locations. Because of the fixed exchange symmetry of the total wavefunction, the symmetries of the spin and spatial wavefunctions are precisely related: if the spin wavefunction for <sup>87</sup>Rb atoms is symmetric, then the spatial wavefunction is also symmetric, and vice versa. Crucially, antisymmetric spatial wavefunctions hinder particles from getting close to each other, whereas symmetric spatial wavefunctions favour it (Fig. 1). Because the atoms interact effectively only when they come into contact, particles in symmetric spatial states interact with each other, whereas particles in antisymmetric spatial states do not.

Anderlini *et al.* stored quantum information in the atoms' spin wavefunction, such that the

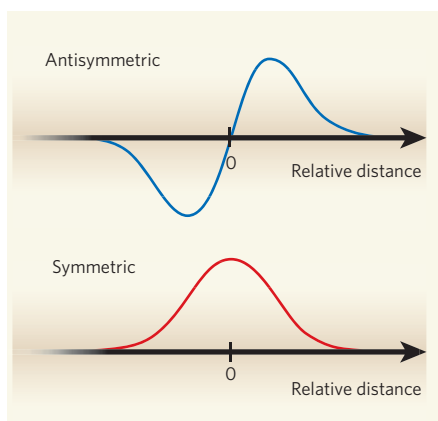


**Figure 1 | Never the twain shall meet.** An antisymmetric spatial wavefunction of two atoms held in a harmonic potential similar to the microscopic traps used by Anderlini *et al.*<sup>2</sup> vanishes at zero distance between the two atoms. As a result, atoms in an antisymmetric state can never be found in the same place. A symmetric wavefunction, by contrast, favours atoms being at the same place. By controlling the symmetry state of atoms, one can therefore control their interactions.

1. Ousman, S. S. *et al. Nature* **448**, 474–479 (2007).  
2. van Noort, J. M. *et al. Nature* **375**, 798–801 (1995).



stored bits determined its symmetry character — symmetric, antisymmetric or a superposition of both. The spin wavefunction also controlled the spatial wavefunction through the direct link between their symmetries, and so determined the collisional properties. Thus, the state of the quantum bits controlled the atoms' interactions.

To prepare, manipulate and detect the atomic states, Anderlini *et al.*<sup>2</sup> used a sophisticated technology developed by them and other groups in recent years. A large number (about 10,000) of isolated pairs of atoms are held in microscopic optical traps formed by interfering laser beams. The atoms in any given pair can be held separately, or brought together to interact.

The authors also developed a procedure to map out the quantum-bit content of each atom of a pair. By carefully switching off the optical trap, and with the help of magnetic-field gradients, the atoms can be distributed in space according to their quantum state. Projections of the quantum bits can then be read from a photographic image of this atomic distribution. The authors obtained a strong signal by simultaneously probing all of the pairs in the atomic ensemble, whose quantum states had undergone an identical evolution in parallel. By taking repeated measurements at different time intervals, they were able to map out this evolution.

In the first experiment with their system, Anderlini *et al.* tested an exchange of quantum information between two atoms. For this 'SWAP' operation, two atoms are initially held at separate sites and their individual quantum-bit states are set to 1 and 0 using radio-frequency radiation. The sites are then merged slowly enough that the two atoms end up in different trap states, but quickly enough that the wavefunction of the atoms is in a quantum superposition of the symmetric and antisymmetric states. These two states have different energies, so a quantum oscillation takes place in which the bit information is repeatedly exchanged between the atoms. To move from a SWAP operation to real quantum-computational operation is not, in principle, a big leap. By letting the atoms interact for only half of the time needed for a SWAP, one creates a quantum-mechanical correlation, known as entanglement, which is the basis for quantum computation.

There are many systems other than cold, colliding atoms that can make use of exchange symmetry for quantum computation: for example, coupled electron spins in a solid-state double quantum dot<sup>3,8</sup>. Here, again, antisymmetric and symmetric wavefunctions lead to different effective interactions between the electrons. Equally, when two identical light particles, photons, arrive from different directions at a beamsplitter — a partially reflecting mirror at which an impinging photon can be either transmitted or reflected — they always end up travelling together as if

strongly attracted to one another. The photons respond to each other not because of interaction forces, but because of their symmetry of state. This effect, first described in 1987 by Hong, Ou and Mandel<sup>9</sup>, is now used in experiments on photon-based quantum computation<sup>10</sup>.

What are the advantages of symmetry-based computation for atoms? Other schemes not involving exchange symmetry could do the job. But as Anderlini *et al.*<sup>2</sup> point out, these schemes place a number of requirements on the atoms that are more stringent than those of the exchange-symmetry scheme. Furthermore, these state-dependent schemes are more likely to suffer decoherence — loss of quantum information — through state-dependent coupling to the environment. In general, exchange-symmetry schemes should be less susceptible to the noise that plagues highly precise apparatus.

So, how far are we from a working quantum computer? A long way: there are still various issues to resolve, including efficiency, fidelity, decoherence and scalability. But scientists all over the world are closing in on this goal from many different directions. New ideas such as

making use of fundamental symmetries could ultimately provide new lines of attack. In view of all of the recent work in the field of quantum computation, we are perhaps experiencing a 'paradigm shift' for controlling the quantum-bit interactions, from schemes controlled by forces to schemes driven by symmetries. ■

Johannes Hecker Denschlag is at the Institute of Experimental Physics, University of Innsbruck, 6020 Innsbruck, Austria.

e-mail: johannes.denschlag@uibk.ac.at

1. Nielsen, M. A. & Chuang, I. L. *Quantum Computation and Quantum Information* (Cambridge Univ. Press, 2000).
2. Anderlini, M. *et al.* *Nature* **448**, 452–456 (2007).
3. Loss, D. & DiVincenzo, D. P. *Phys. Rev. A* **57**, 120–126 (1998).
4. DiVincenzo, D. P., Bacon, D., Kempe, J., Burkard, G. & Whaley, K. B. *Nature* **408**, 339–342 (2000).
5. Hayes, D., Julienne, P. S. & Deutsch, I. H. *Phys. Rev. Lett.* **98**, 070501 (2007).
6. Jaksch, D., Briegel, H.-J., Cirac, J. I., Gardiner, C. W. & Zoller, P. *Phys. Rev. Lett.* **82**, 1975–1978 (1999).
7. Mandel, O. *et al.* *Nature* **425**, 937–940 (2003).
8. Petta, J. R. *et al.* *Science* **309**, 2180–2184 (2005).
9. Hong, C. K., Ou, Z. Y. & Mandel, L. *Phys. Rev. Lett.* **59**, 2044–2046 (1987).
10. Zeilinger, A., Weihs, G., Jennewein, T. & Aspelmeyer, M. *Nature* **433**, 230–238 (2005).

## IMMUNOLOGY

# Sensing the enemy within

Hongbo Chi and Richard A. Flavell

**Damaged or foreign DNA stimulates immune responses by inducing the production of interferon proteins. New evidence indicates that this response is mediated by a cytosolic DNA sensor known as DAI.**

On infection by a pathogen, the immune system rapidly mounts defence mechanisms, characterized by massive production of interferon proteins and other cytokines (immune mediators). This reaction, known as the innate immune response, is mediated by pattern-recognition receptors that detect conserved structures found in a broad range of pathogens. The best-studied receptors of this type are Toll-like receptors (TLRs) — a class of membrane receptor that senses microbes either in the extracellular space or intracellular compartments<sup>1</sup>. So how do host cells fight pathogens that have entered their cytosol? Intracellular sensors that can detect microbial products, including viral RNA and bacterial cell-wall components, in the cytosol have been identified<sup>1</sup>. Now, Takaoka *et al.*<sup>2</sup> report on page 501 of this issue the identification of another cytosolic factor called DAI (also known as DLM-1 or ZBP1) as a DNA sensor.

Although host nucleic acids are normally sequestered in the nucleus and are therefore safe from recognition by cellular receptors, the immunostimulatory activity of DNA and RNA has long been recognized. In 1963, two groups<sup>3,4</sup> — including one led by the discoverer of interferon, Alick Isaacs — reported

that DNA and RNA derived from pathogens or host cells can activate interferon production in chicken and mouse fibroblast cells. But the cellular receptors for nucleic acids remained unknown for almost four decades.

In the early 2000s, specific TLRs that detect immunostimulatory nucleic acids during infection or tissue damage were identified<sup>1</sup>. For example, TLR9 recognizes DNA sequences that contain specific motifs known as unmethylated CpG dinucleotides, features common to microbial, but not mammalian, DNA. In addition, TLR3 and TLR7/TLR8 sense double-stranded RNA (dsRNA) and single-stranded RNA (ssRNA), respectively<sup>1</sup>. Engagement of TLRs initiates a molecular signalling cascade that leads to the activation of essential gene transcription factors, including interferon-regulated factors (IRFs) and NF- $\kappa$ B. This cascade ultimately leads to the production of type I interferon (interferon- $\alpha$  and - $\beta$ ) and proinflammatory cytokines to fight infectious organisms<sup>1</sup> (Fig. 1, overleaf).

Despite the importance of TLRs in recognizing nucleic acids, alternative receptors must exist. This is because nucleic-acid-specific TLRs are localized in intracellular compartments such as endosomes, which

means that they cannot bind to pathogen-released nucleic acids in the cytosol. Moreover, these TLRs are expressed in only a subset of cells, whereas almost all nucleated cells can activate type I interferon in response to viral infection<sup>1</sup>. Thus, the interferon-associated response first described in fibroblasts in 1963 is unlikely to be mediated by TLRs.

The enzymes RIG-I and MDA5 have been shown<sup>1,5</sup> to recognize viral RNA (specifically, dsRNA and 5'-triphosphate ssRNA) in the cytosol, promoting the production of type I interferon and innate immune responses. On binding to their ligands, these cytosolic RNA sensors signal through a set of adaptor molecules. These are distinct from those that mediate TLR signalling, although both pathways converge on IRFs and NF- $\kappa$ B for the production of interferon and other cytokines<sup>1,5</sup> (Fig. 1).

Does a pathway analogous to that of RIG-I/MDA5 that mediates an innate immune response to DNA exist in the cytosol? Accumulating evidence indicates that this is the case. The DNA of herpes simplex virus type 1 elicits the production of type I interferon through both TLR9-dependent and TLR9-independent pathways<sup>6</sup>. Similarly, during infection with the intracellular bacterium *Listeria monocytogenes*, cytosolic DNA stimulates interferon production independently of TLRs<sup>7</sup>. Sensing of cytosolic DNA does not require RIG-I or MDA5 (ref. 8), indicating that some other factor must be involved.

Takaoka *et al.*<sup>2</sup> now show DAI to be a cytosolic DNA sensor that activates the innate immune response. They became interested in DAI when they found that expression of the gene encoding this protein is greatly increased after treatment with interferon- $\beta$ , and because previous reports<sup>9,10</sup> had suggested that DAI can bind to DNA, especially DNA of an unusual configuration known as Z-DNA.

To test whether DAI is a cytosolic DNA sensor, the authors overexpressed it in cell lines and found that, after stimulation with cytosolic DNA, the production of type I interferon in these cells was notably enhanced. In cells lacking IRF3 or IRF7, DAI overexpression did not affect interferon production, indicating that DAI requires both of these factors for interferon production. The authors confirmed their findings using small interfering RNA (siRNA) to reduce DAI expression. This treatment decreased interferon production and led to increased sensitivity to infection with viruses that have DNA as their genetic material, but not those with RNA. The team also found that DAI binds directly to DNA, although the

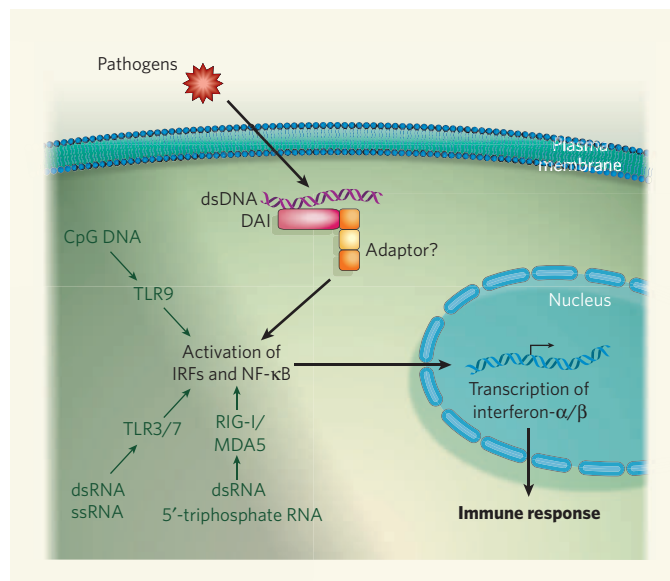


**Figure 1 | Recognition of DNA by DAI.** Infectious pathogens (viruses and bacteria) are often internalized into host cells. There, an immune response is initiated by recognition of the genetic material of the pathogen — DNA or RNA. Takaoka, *et al.*<sup>2</sup> found that pathogenic double-stranded DNA (dsDNA), as well as DNA of damaged host cells released into the cytosol, is recognized by a cytosolic DNA sensor known as DAI. This protein binds to the DNA, possibly with the aid of an adaptor protein, triggering the activation of the gene transcription factors IRFs and NF- $\kappa$ B. These factors are also activated by other DNA sequences, as well as by dsRNA and ssRNA, through independent sensors. In all cases, expression of genes encoding interferon and other cytokines follows, leading to an immune response.

involvement of other protein(s) in this interaction remains unclear. Moreover, DAI was shown to interact physically with the TBK1 enzyme and IRF3 in a DNA-dependent manner, suggesting that these two factors may be recruited to the DNA–DAI complex to facilitate interferon production.

Takaoka and colleagues<sup>2</sup> conclude from these results that DAI is the first cytosolic DNA sensor, which is truly exciting. Their work also raises a number of interesting questions. First, is DAI the sole DNA sensor? Possibly not. In cells in which DAI was depleted with siRNA, interferon levels were reduced but not completely abolished after DNA stimulation. Moreover, DAI does not seem to stringently discriminate among different types of DNA, whereas previous work<sup>8</sup> suggested that cytosolic DNA sensor(s) have a strong preference for the usual configuration of DNA (B-DNA) rather than Z-DNA. A definitive answer to this question will come from detailed analysis of mice genetically deficient in DAI.

Another question is which signalling pathway is activated by DAI. Specifically, does DAI use the same adaptor molecules and signalling intermediates as do RNA sensors such as RIG-I/MDA5? The evidence so far favours this possibility, as both DAI and RIG-I/MDA5 can associate with TBK1 and IRF3. Furthermore, an earlier study suggested that the putative DNA sensor(s) can signal through IPS-1 — an adaptor molecule mediating RIG-I/MDA5 signalling<sup>8</sup>. Future work should verify whether DAI

associates with and signals through IPS-1.

As DAI can be activated by viral, bacterial and mammalian DNA, it poses a potential threat to the host, in that autoreactivity to host DNA could result in interferon-dependent autoimmunity. In mice deficient in the enzyme DNase II, genomic DNA cannot be degraded and therefore accumulates in the immune cells known as macrophages; this leads to TLR9-independent, interferon-mediated autoimmunity<sup>11</sup>. Therefore, cells must have developed strategies to prevent the sensing of self DNA and thus accidental activation of the interferon pathway. Although DAI would normally be excluded from the nucleus, where the host cell's genomic DNA resides, during cell division the nuclear envelope is disrupted, potentially giving DAI access to the host DNA. Precisely how recognition of host DNA by DAI is inhibited awaits further investigation. One possibility is that the packaging of mammalian DNA into high-order complexes of DNA and histone proteins (chromatins) protects host DNA.

The identification of DAI as a cytosolic DNA sensor suggests that DAI has a fundamental function in detecting both microbial products and danger signals such as damaged host DNA. Future studies on this sensor should lead to deeper mechanistic insights into how infection is controlled through effective detection of bacterial and viral DNA in the cytosol, and how tolerance towards host DNA is maintained, preventing its abnormal recognition.

Hongbo Chi is in the Department of Immunology, St Jude Children's Research Hospital, Memphis, Tennessee 38105, USA. Richard A. Flavell is in the Howard Hughes Medical Institute and Department of Immunobiology, Yale University School of Medicine, New Haven, Connecticut 06520, USA.

e-mails: hongbo.chi@stjude.org;  
richard.flavell@yale.edu

1. Akira, S., Uematsu, S. & Takeuchi, O. *Cell* **124**, 783–801 (2006).
2. Takaoka, A. *et al.* *Nature* **448**, 501–505 (2007).
3. Rotem, Z., Cox, R. A. & Isaacs, A. *Nature* **197**, 564–566 (1963).
4. Jensen, K. E., Neal, A. L., Owens, R. E. & Warren, J. *Nature* **200**, 433–434 (1963).
5. Meylan, E., Tschopp, J. & Karin, M. *Nature* **442**, 39–44 (2006).
6. Hochrein, H. *et al.* *Proc. Natl Acad. Sci. USA* **101**, 11416–11421 (2004).
7. Stetson, D. B. & Medzhitov, R. *Immunity* **24**, 93–103 (2006).
8. Ishii, K. J. *et al.* *Nature Immunol.* **7**, 40–48 (2006).
9. Schwartz, T., Behlke, J., Lowenhaupt, K., Heinemann, U. & Rich, R. *Nature Struct. Biol.* **8**, 761–765 (2001).
10. Ha, S. C. *et al.* *Biochim. Biophys. Acta* **1764**, 320–323 (2006).
11. Okabe, Y., Kawane, K., Akira, S., Taniguchi, T. & Nagata, S. *J. Exp. Med.* **202**, 1333–1339 (2005).



## OBITUARY

# Horst Tobias Witt (1922–2007)

Seminal research on photosynthesis.

During the second half of the twentieth century, great strides were made in revealing the molecular details of oxygen-generating photosynthesis, the basis of almost all life on Earth. Horst Witt was one of the prime movers behind this revolution in understanding.

Witt was born in 1922 in Bremen, Germany. From his youth he was interested in physics, and while at school he won a prestigious prize for his high-risk, and literally explosive, experiments on supersonic airfoils. On the outbreak of the Second World War, he entered the Luftwaffe, but his scientific aptitude led to his early (and lucky) release to take up research at the University of Göttingen. He received his PhD in solid-state physics in 1950, and then moved to the Max Planck Institute of Physical Chemistry where — like several other brilliant young scientists, including Manfred Eigen — he began to explore the largely hidden beauties of the molecular life sciences.

Witt chose oxygenic photosynthesis as his lifelong research topic. Inspired by the methods pioneered by George Porter and Ronald Norrish, he embarked on work with the technique of flash spectrophotometry. Using algae, in 1955 he discovered reactions of chlorophylls, carotenoids and cytochromes that occurred in microseconds. By 1961, his work, along with the independent discoveries of Lou Duysens and of Bessel Kok, led to a scheme with two photochemical reaction centres in series. At photosystem II, electrons are removed from water, generating a strong oxidant, oxygen. At photosystem I, the electrons are used to produce a strong reductant, NADPH (and thence sugars). The energy difference between the strong oxidant and the strong reductant powers all oxygen-based life.

At that time the two Nobel laureates in the field, biochemist Otto Warburg and spectroscopist James Frank, were fighting their famous battles from ensconced positions. When confronted with Witt's detailed reaction scheme in 1962, Warburg mused: "Could you tell us how the chemical mechanism of photosynthesis can be described on the basis of your spectroscopic observations?" Witt countered with a well-aimed jibe at his eminent critic, the pioneer of oxygen detection, by observing that "it would be difficult to deduce the mechanism of a combustion engine based only on sniffing the exhaust".

In 1962, Witt moved to the Technical University of Berlin, where he moulded the Max-Volmer-Institute for Physical Chemistry into an internationally renowned laboratory for biophysical studies of photosynthesis. The

scope of research ranged from light absorption and energy transfer to the production of redox equivalents and the synthesis of ATP, the general-purpose fuel of life. His daring ideas, and above all his extraordinary perseverance, attracted a stream of ambitious and able young scientists to work under him.

During the ensuing years, this team of investigators marked off milestones in photosynthesis research. They found that excess light energy is disposed of harmlessly as heat through protective carotenoids. They discovered that the reactive pigment of photosystem II is chlorophyll *a*: its cationic form extracts electrons from the active site of water oxidation, with kinetics that depends on the electrostatics of charge accumulation. And they identified plastoquinone as an electron acceptor in photosystem II, where it functions as a one-to-two electron gate and as a mobile carrier between the two photosystems.

A further success was the use of electrochromic absorption transients from intrinsic photosynthetic pigments. These behave as ultra-rapid 'molecular voltmeters' to show that the primary electron-transfer reactions in both photosystems generate transmembrane voltage, and are thus directed across the photosynthetic coupling membrane. These vectorial reactions, together with associated proton uptake and release at opposite sides of the membrane, as hypothesized earlier by Peter Mitchell, were shown to generate the proton-motive force required for the synthesis of ATP.

But it was the mechanism of water oxidation that remained Witt's career-long preoccupation, his *spröde Geliebte* (prudish beloved). The manganese cluster in photosystem II is charged up with four oxidizing equivalents before it reacts with two water molecules, releasing dioxygen. Witt and his co-workers contributed valuable information on many aspects of the mechanism, including the valence changes of manganese, associated electrostatic changes and effects of extrinsic reductants. Despite these and other contributions from many laboratories around the world, understanding the detailed mechanism has remained a major challenge.

Witt's early attempts to crystallize photosystem II were fruitless, and it seemed that the game would be lost to others. However, crystals of photosystem I proved to be an initial consolation. With colleagues, including his wife Ingrid, Witt fine-tuned the crystallization procedure, and in 1993 produced crystals of photosystem I diffracting to 6 Å. The resolution was gradually improved



to 2.5 Å, revealing a beautiful trimeric structure with multiple subunits, diverse electron-transfer cofactors, about 100 chlorophyll molecules and many carotenoids, all in three-dimensional glory.

In 2001, together with a team led by Wolfram Saenger, also working in Berlin, Witt and his colleagues finally succeeded in crystallizing and analysing photosystem II, with a resolution of 3.8 Å. This structure was followed by the first refined model from James Barber's group, and then by the Berlin groups' further model based on slightly higher resolution. A full understanding of how photosystem II works remains one of the greatest challenges in biology.

Witt received numerous awards and honours, and more than 200 publications carry his name. His co-workers and former students, many of whom remained hooked on photosynthesis research, were fascinated by his seemingly permanent youth. Indeed, instead of growing into a father to his scientific offspring, he remained the ambitious elder brother — with its mix of fraught fraternal relations from time to time, but with spark, fun and high productivity when it came to science.

To those outside the inner circle, Horst Witt was a legendary figure from the early days of photosynthesis research. He had a tendency to divide members of the field into those of whom he approved (with whom he was open and charming, and relished robust argument) and those he did not: he could be intimidating. He was nevertheless universally respected for his sharp intellect and single-minded drive. Witt, who died on 14 May, leaves an unmatched legacy for those many scientists grappling with the intricacies of photosynthesis.

**Wolfgang Junge and A. William Rutherford**

Wolfgang Junge is in the Division of Biophysics, University of Osnabrück, 49069 Osnabrück, Germany. A. William Rutherford is at iBiTec-S, CEA Saclay, 91191 Gif-sur-Yvette, France.  
e-mails: junge@uos.de; alfred.rutherford@cea.fr

# Unravelling the pathogenesis of inflammatory bowel disease

R. J. Xavier<sup>1,2</sup> & D. K. Podolsky<sup>1</sup>

Recently, substantial advances in the understanding of the molecular pathogenesis of inflammatory bowel disease (IBD) have been made owing to three related lines of investigation. First, IBD has been found to be the most tractable of complex disorders for discovering susceptibility genes, and these have shown the importance of epithelial barrier function, and innate and adaptive immunity in disease pathogenesis. Second, efforts directed towards the identification of environmental factors implicate commensal bacteria (or their products), rather than conventional pathogens, as drivers of dysregulated immunity and IBD. Third, murine models, which exhibit many of the features of ulcerative colitis and seem to be bacteria-driven, have helped unravel the pathogenesis/mucosal immunopathology of IBD.

The major forms of idiopathic IBD, ulcerative colitis and Crohn's disease are chronic inflammatory disorders of the gastrointestinal tract that have been empirically defined by clinical, pathological, endoscopic and radiological features<sup>1</sup>. The onset of IBD typically occurs in the second and third decades of life and a majority of affected individuals progress to relapsing and chronic disease. Family aggregation has long been recognized. First-degree relatives of affected individuals have a relative risk of fivefold or greater. The inheritable component seems stronger in Crohn's disease than in ulcerative colitis<sup>2,3</sup>. It is of interest that in several countries with historically low rates of IBD, a pattern of rising incidence in the past one to two decades, particularly for Crohn's disease, has occurred, suggesting that environmental factors are also involved.

Key features of ulcerative colitis include diffuse mucosal inflammation that extends proximally from the rectum to a varying degree. In conjunction with severe inflammation and the coincident production of a complex mixture of inflammatory mediators, extensive superficial mucosal ulceration develops. Histopathological features include the presence of a significant number of neutrophils within the lamina propria and the crypts, where they form micro-abscesses (Fig. 1). Depletion of goblet cell mucin is also common. Crohn's disease is characterized by aggregation of macrophages that frequently form non-caseating granulomas (Fig. 1). Although any site of the gastrointestinal tract may be affected, involvement of the terminal ileum is most common and the earliest mucosal lesions in Crohn's disease often appear over Peyer's patches. Unlike ulcerative colitis, Crohn's disease may be patchy and segmental, and inflammation typically transmural.

## IBD genetics

Genome-wide searches for IBD susceptibility loci performed in the last few years have been highly successful in identifying genes that contribute to disease susceptibility. In initial screening efforts, two groups identified *NOD2* (also designated *CARD15* and *IBD1*) as a susceptibility gene in Crohn's disease, using positional cloning and candidate gene approaches<sup>4,5</sup>. Since then, several additional susceptibility loci have been implicated in inflammatory bowel disease and confirmed by replication: *IBD5*, *IL23R* and *ATG16L1* (refs 6–14).

(See Fig. 2 for the full list of genes validated in multiple studies as well as those genes that require additional confirmation). The genetic variants that have been found to confer Crohn's disease risk point to the importance of innate immunity, autophagy and phagocytosis in Crohn's disease pathogenesis. In particular, a number of genes associated with Crohn's disease (*IL23R*, *PTPN2*) are also associated with other autoimmune disorders, suggesting that a subset of Crohn's disease patients share common triggers with these conditions. In addition, multiple disease-associated intergenic segments have been identified and replicated in genome-wide association studies. These intergenic regions implicate new genes and pathways—possibly including genes that are expressed within these regions and others that are remotely regulated to modify the disease phenotype. Further understanding of regulatory elements within non-coding genomic regions and gene–gene interactions will lead to a better understanding of the underlying mechanisms that cause disease. Despite early linkage analysis suggesting an important contribution of the MHC complex to IBD susceptibility, in contrast to rheumatoid arthritis

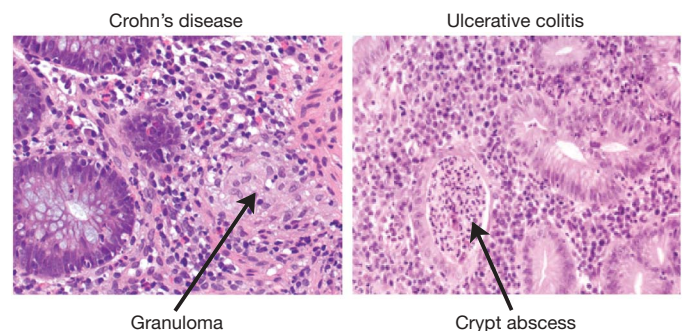


**Figure 1 | Histologic hallmarks of IBD: clues to immunopathogenesis.** Left panel, Crohn's disease—biopsy from a terminal ileum with active disease. The figure illustrates a discrete granuloma composed of compact macrophages, giant cells and epithelioid cells. Surrounding the nodule there is marked infiltration of lymphoid cells, plasma cells and other inflammatory cells, but there is no necrosis. Right panel, Ulcerative colitis—colonic mucosal biopsy taken from a patient with active disease. The crypt abscess is composed of transmigrated neutrophils and the surrounding epithelium exhibits features of acute mucosal injury.

<sup>1</sup>Gastrointestinal Unit and Center for the Study of Inflammatory Bowel Disease, and <sup>2</sup>Center for Computational and Integrative Biology Massachusetts General Hospital, Harvard Medical School, Boston, Massachusetts 02114, USA.



and multiple sclerosis, identification of precise genes within the MHC region that confer susceptibility has been problematic. Individual risk genes are discussed below within the context of a consideration of pathophysiologic mechanisms.

### Microbes control development of IBD in a susceptible host

Accumulating evidence suggests that the dynamic balance between microbes, particularly commensal flora, and host defensive responses at the mucosal frontier has a pivotal role in the initiation and pathogenesis of chronic IBD. Circumstantial evidence for this inference is provided by the observed therapeutic benefits of antibiotic treatment in, at least, subsets of IBD patient and recent findings suggesting that so-called 'healthy bacteria' or probiotic combinations can ameliorate IBD<sup>15,16</sup>. In addition, the enteric flora of IBD patients has been found more commonly than in control patient groups<sup>17,18</sup> to include strains of *Escherichia coli* that are able to adhere to the epithelium, and with low frequency effect epithelial invasion. The importance of the flora is more directly supported by studies in a variety of murine strains in which 'spontaneous' chronic colitis seems to be entirely dependent on the presence of a luminal flora. Thus, colitis is not observed when any of several of these lines are maintained in a gnotobiotic state, but rapidly emerges when they are reconstituted with bacteria that are considered normal constituents of luminal flora<sup>19,20</sup>. In some instances, it has been possible to induce colitis in a susceptible murine strain with a single species of normal bacteria, for example, *Bacteroides vulgatus* in the *Il10*-deficient mouse<sup>21</sup>. These studies provide compelling evidence that the nature of the host defenses, rather than the biological properties of a luminal bacterial species *per se*, may determine the functional outcome of that interaction.

Unfortunately, our understanding of the microbial flora itself is quite incomplete<sup>22</sup>. Insights into the microbial–host interrelationships are hampered by both the limited knowledge of the diversity and complexity of the microbial flora and the limitation

of available tools to delineate these characteristics. Metagenomic and computational analysis of the so-called microbiome may provide a foundation to achieve an understanding of the relevant, functional diversity of the flora in the context of IBD. Understanding the distribution, dynamics and responses to microbial flora in these disease states will probably provide insight into the regional distribution of disease.

### Barrier and mucosal homeostasis

Defending the integrity of the mucosal frontier as a barrier is as essential a function of the mucosa as nutrient and fluid absorption and secretion. The importance of the epithelial barrier in disease predisposition is supported by the finding of abnormal intestinal permeability in some first-degree relatives with Crohn's disease<sup>23–26</sup>. Barrier function is provided by anatomical features that physically impede penetration of macromolecules and intact bacteria. Many molecular details of the pre-epithelial barrier and structure of the epithelial tight junctions that comprise this physical barrier have been defined. The junctions are dynamically regulated in response to cytokines tumour necrosis factor (TNF)- $\alpha$ , interleukin (IL)-17, interferon- $\gamma$ , chemokines and the underlying immune cell network.

Expression analysis in human IBD biopsies has demonstrated downregulation of junctional complexes (E-cadherin and  $\beta$ -catenin), although the mechanisms involved are unknown<sup>27</sup>. A recent genome-wide association study reported that 5p13.1, a Crohn's disease locus contained within a 1.25-Mb gene desert, is associated with disease susceptibility and the associated alleles correlated with quantitative expression of the prostaglandin receptor EP4 (also known as PTGER4)<sup>9</sup>. EP4 is expressed in intestinal epithelial cells and regulates epithelial barrier function; interestingly, EP4 knockout mice are susceptible to dextran sodium sulphate colitis<sup>28</sup> (Table 1).

The epithelium is in constant communication with luminal flora and the underlying dense network of innate and adaptive immune cells. Intestinal epithelial cells express Toll-like receptors (TLRs), NOD1 and 2, and receptors for different chemokines and antibody-specific Fc<sup>29–31</sup>. In this context, epithelial-cell-specific NF- $\kappa$ B activation or suppression seems to be a nodal point in the suppression and/or recruitment of immune responses in IBD. Of note, some bacteria seem to be able to hijack this process to minimize epithelial cell NF- $\kappa$ B activation<sup>32</sup>. These studies imply that commensals actively dampen intestinal inflammation by inhibition of IKB $\alpha$  degradation, protein ubiquitination and enhanced PPAR $\gamma$ -mediated nuclear export of RelA to terminate signal transduction<sup>33</sup>. Mice with conditional deletion of *NEMO* (also known as *IKBK*) in intestinal epithelial cells develop spontaneous colitis and the expression of antimicrobial peptides is significantly attenuated<sup>34</sup>. Deletion of IKK- $\beta$  (encoded by *IKK2*) in intestinal epithelial cells does not trigger spontaneous colitis (as in the case of *NOD2*<sup>-/-</sup> mice); however, these mice are unable to initiate pathogen specific T helper (T<sub>H</sub>)2 responses to parasitic infection<sup>35</sup>. Together, these observations highlight the importance of NF- $\kappa$ B signalling networks within the intestinal epithelium in sustaining normal mucosal homeostasis and in mediating pathogen-specific responses. These studies point to substantial challenges in the development and use of inhibitors of NF- $\kappa$ B signalling pathways in intestinal inflammation as these pathways have protective as well as deleterious effects.

In addition to columnar epithelial cells, specialized cells are interspersed along the crypt villus axis to enhance protection against microbes and promote repair. Paneth cells reside in the base of the crypt where they secrete antimicrobial peptides, including the  $\alpha$ -defensins. Some observations suggest that a reduction in Paneth cell  $\alpha$ -defensins may contribute to the pathogenesis of terminal ileal Crohn's disease in patients with mutant *NOD2* (refs 36, 37).

Goblet cells are also an important component of the epithelium. They are responsible for production of trefoil peptides, key both to defence and epithelial/mucosal repair<sup>38</sup>. Recent studies have demonstrated that RELM $\beta$ , another goblet cell specific protein, is induced

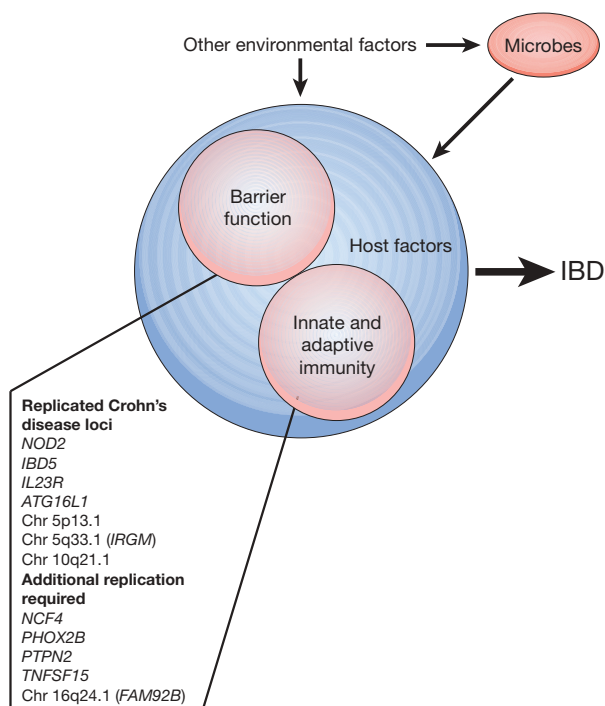


**Figure 2 | Patterns of IBD etiopathogenesis.** Intestinal inflammation in IBD results from alteration in the interaction between resident microbes and the mucosa. This can result from the influence of environmental factors and/or host factors, which vary depending on genetic inheritance at several susceptibility loci. Genetic factors discovered to date affect barrier function, and innate and adaptive immunity. Replicated Crohn's disease loci and Crohn's disease loci that require additional replication are listed below.

on bacterial colonization, and disruption of this gene reduces the severity of colitis in a dextran sodium sulphate model of colonic injury<sup>39</sup>. MUC2, a major goblet-cell-derived secretory mucin, is differentially expressed in human IBD. Consistent with these observations, *MUC2*<sup>-/-</sup> mice are deficient in goblet cells and develop spontaneous colitis<sup>40</sup>. A recent study elegantly demonstrates a contribution of intestinal mucus to the suppression of colitis<sup>41</sup>. Overall these data suggest that Paneth cell deficiency increases the risk of Crohn's disease, whereas goblet cells play a part in protection and pathogenesis in colitis<sup>35,39,42,43</sup>.

## Mucosal monitors

The processes that monitor the luminal contents and titrate the mucosal response are probably central to functional integrity of the mucosa and health. Thus, the mucosal immune system is poised to detect bacteria and antigens at the mucosal surface and to drive an appropriate response. The response must be nuanced between 'tolerant' and 'active' to distinguish between an innocuous commensal (which may even serve as a symbiote) and pathogens, which can invade the epithelium and beyond.

A number of sentinel cell populations in the intestinal mucosa continuously monitor luminal microbes. These include specialized M cells that transport by pinocytosis macromolecules, IgA complexes and microbes that are then picked up by antigen-presenting cells. Peyer's patches, isolated lymphoid follicles and the lamina propria work as inductive sites for the mucosal response, whereas the lamina propria functions as a recognition/effector site<sup>35,44</sup>.

Among the subsets of antigen-presenting cells, myeloid-derived dendritic cells are the dominant subtype in the intestinal lamina propria and show considerable functional plasticity depending on the location, state of maturation, and stage of inflammation. Intravital fluorescent microscopy techniques have demonstrated that dendritic cells form an extensive network beneath the intestinal epithelium and project long processes through the interstices of epithelial cells to sample luminal antigens<sup>45</sup>. Sampling of bacteria by resident dendritic cells is mediated in part by a CX3CR1-dependent mechanism that permits direct dendritic-cell-microbe contact<sup>46</sup>. In response to TLR ligands, the immature CD11c<sup>+</sup> CD11b<sup>+</sup> dendritic cells produce IL-23, which contributes to development of intestinal inflammation in murine models of colitis. Furthermore, studies

using a transgenic *p40* (also known as *IL-12p40* or *IL-12B*) or IL-23 depletion suggest that IL-23 is the dominant driver of regional intestinal inflammation in murine models of intestinal inflammation<sup>47,48</sup>. Recent studies also implicate IL-4, B-lymphocytes and enteric flora in dendritic-cell-mediated granuloma formation in states of chronic intestinal inflammation<sup>49</sup>.

Consistent with a baseline state of hyporesponsiveness, intestinal macrophages show attenuated proliferation and chemotactic activity in response to either microbial ligands or host cytokines/chemokines despite possessing the molecular mechanisms to elaborate strong phagocytic and bactericidal responses<sup>50</sup>. Following an inflammatory signal, circulating macrophages migrate to the intestinal mucosa and these cells, unlike resident macrophages, express TREM1/2, Nod-like receptors (NLRs), TLRs capable of rapid response and functional chemotactic receptors. Direct support for the role of macrophages in the regulation of IBD has been obtained from analysis of mice with selective disruption of *STAT3* in their macrophages<sup>51</sup>. Tumour-necrosis factor (TNF) produced by non-lymphoid cells, mostly macrophages, was found to be essential for the development of colitis using the adoptive T-cell model of colitis induction. Recent studies have also shown that depletion of macrophages in the *Il10*<sup>-/-</sup> mouse prevents development of colitis, which otherwise occurs owing to unregulated production of IL-12 and IL-23 by macrophages<sup>52</sup>.

Migration of innate immune cells such as neutrophils, macrophages, and dendritic cells into target mucosal tissues depends on the expression of cytokines, chemokines and adhesion molecules. Furthermore, these cells generate reactive oxygen species that are key effectors of inflammation and tissue injury and also increase epithelial permeability. Recruitment of activated neutrophils, dendritic cells and macrophages into the lamina propria in general amplifies the local immune response, whereas activated natural killer cell recruitment seems to enhance antimicrobial factors, leading to attenuation of inflammation<sup>53</sup>. This regulated homing of cells into the mucosa is tightly choreographed by integrins, chemokine receptors and microbial signals. Modulation of the expression of regional inflammation-induced adhesion molecules may be a useful method of disease intervention.

It is ironic that attention has only relatively recently turned to the role of the evolutionarily ancient set of innate immune responses, which serve as, figuratively, the first line of immune defence. Although there are many components of innate immunity, they are

**Table 1 | Mouse models of colitis with altered barrier, innate or adaptive immune responses**

Model	Known defects
Multidrug-resistant <i>1α</i> <sup>-/-</sup> (also known as <i>ABCB1</i> <sup>-/-</sup> )	Altered epithelial barrier
<i>Gxi2</i> <sup>-/-</sup> ( <i>GNAI2</i> <sup>-/-</sup> )	Defective epithelial barrier; defective regulatory B cells
Macrophage-PMN <i>Stat3</i> <sup>-/-</sup>	Increased response to lipopolysaccharide (LPS); resistance to IL-10 regulation
Bone marrow <i>Stat3</i> <sup>-/-</sup>	Increased response to LPS; impairment of innate immune function
<i>A20</i> <sup>-/-</sup> ( <i>TNFAIP3</i> <sup>-/-</sup> )	Increased response to LPS
<i>Il10</i> and <i>Il10Rb</i> <sup>-/-</sup>	Lack of Trl (Tr1; T <sub>reg</sub> cells) activity; lack of TGF-β signalling
NF-κB ( <i>Nfkb1</i> <sup>-/-</sup> , <i>Rela</i> <sup>-/-</sup> )	Increased IL-2 production
<i>TGFb1</i> <sup>-/-</sup> , <i>TGFbR2</i> <sup>-/-</sup>	Decreased numbers of regulatory T cells
<i>Cdcs</i> <sup>C3H/HeJBir</sup> mutant mice	Impaired innate responses to TLR ligands; increased numbers of bacterially reactive T cells
<i>SAMP1/Yit</i> mutant mice	Epithelial cell defects; expanded B-cell population; increased numbers of activated T cells
<i>Il2</i> <sup>-/-</sup> and <i>Il2Ra</i> <sup>-/-</sup>	Decreased numbers of CD4 <sup>+</sup> CD25 <sup>+</sup> T cells
<i>TNFA</i> <sup>ΔARE/-</sup> (ARE, AU-rich elements)	Increased TNF-α production
CD4 <sup>+</sup> , CD45RB <sup>high</sup> transfer	Decreased numbers of regulatory T cells
<i>TCRa</i> <sup>-/-</sup> (T-cell antigen receptor mutant)	Loss of a regulatory B-cell function
<i>WASP</i> <sup>-/-</sup> ( <i>WAS</i> <sup>-/-</sup> )	Regulatory T cells
<i>CD40L</i> transgenic mice	Increased numbers of activated T cells
<i>Smad3</i> <sup>-/-</sup>	Decreased numbers of regulatory T cells
Epithelial cell specific deletion of <i>NEMO</i>	Barrier function/innate immunity
Dextran sulphate sodium	Direct damage to epithelial barrier
Dextran sulphate sodium/ <i>Tff3</i> <sup>-/-</sup>	Goblet cell dysfunction; impaired epithelial repair
Dextran sulphate sodium/ <i>Ptger4</i> <sup>-/-</sup>	Altered epithelial barrier
<i>Muc2</i> <sup>-/-</sup>	Barrier function/mucus defect
N-cadherin mutant	Barrier function

Key lessons learned from IBD models include: (a) a compromised epithelial layer has been shown to be sufficient to result in intestinal inflammation; (b) T cells have been implicated in numerous models presumably promoting an inappropriately activated autoreactive effector T-cell population; (c) a variety of other haematopoietic cells have been shown to be able to mediate or regulate intestinal inflammation; (d) many studies have elucidated the roles of the different cytokines at play in the different models of colitis—chemoattractant cytokines may have a unique role in IBD pathogenesis; and (e) although no specific pathogen has been isolated from the intestinal flora of spontaneous colitis models, the resident enteric flora seems necessary for colitis induction.



all 'hard wired': a defining characteristic that contrasts with the acquired specificity of adaptive responses. Immediacy of response is possible, in part because innate immune sensors/receptors recognize stereotypic molecular structures. It seems clear that the innate immune system evolved as a means to monitor the microbial environment and to limit infection by invasive organisms.

Distinct classes of receptors that recognize microbial molecular patterns are central to innate immunity. To date, more than 11 TLRs, 23 NLRs, several C-type lectin-like molecules, and  $\beta$ -glucan receptors have been identified. Although initial studies suggested that TLRs/NLRs were expressed in macrophages and dendritic cells, recent studies have demonstrated that innate immune receptors are broadly expressed in many cell types, including the intestinal epithelium. Many TLRs are probably non-functional at the apical side of intestinal epithelial cells, and, at baseline, NLR (also known variously as NOD or CARD) proteins might be the most important active sentinels for bacterial molecular patterns in these cells. Engagement of TLRs by microbial components triggers the activation of signalling cascades leading to the induction of genes involved in antimicrobial defence. A recent study also proposes that ligands for NOD2 may synergize with TLR2 for the production of IL-12p70 and IL-23 (ref. 54).

In the past few years, mutations in both TLRs and NLRs have been found to be associated with inflammatory bowel diseases, suggesting that each detection system is key for regulating mucosal homeostasis<sup>7,55–57</sup>. As noted above, NOD2 was identified as IBD1, providing the most compelling evidence for the importance of microbial–mucosal interaction in the pathogenesis of IBD. NOD2 protein is expressed in macrophages, dendritic cells, intestinal epithelial cells and Paneth cells, and may have cell-specific functions. Individuals who are either homozygotes or compound heterozygotes for any one of the three 'common' identified germline variations of *NOD2* have as much as a 40-fold increased likelihood of developing ileal Crohn's disease.

Muramyl dipeptide (MDP), found in bacterial peptidoglycan, is recognized by the leucine rich repeat (LRR) domain of NOD2 and leads to the activation of NF- $\kappa$ B through a receptor-interacting serine-threonine kinase-2 (RIPK2)-dependent signalling pathway (Fig. 3a)<sup>58,59</sup>. Recent studies have demonstrated that the signalling pathway is positively and negatively regulated by interacting partners<sup>60–64</sup>. A number of observations point to multiple regulatory steps in NOD2 signal transduction. Analogous to plant R proteins, NOD1 and NOD2 interact with SUGT1 and HSP90, thereby determining the specific transmission of activating and desensitizing signalling outputs that are evolutionarily conserved<sup>62,65</sup>. MDP is also recognized by the NLRP1 inflammasome<sup>66</sup>. Of note, duration of MDP stimulation may regulate tolerance in these pathways. Tissue-specific splice variants could also contribute to signalling outcome.

The mechanism by which NOD2-mediated functions contribute to intestinal immune homeostasis and how dysregulation of these functions in individuals with disease-associated NOD2 polymorphisms contribute to the increased propensity to develop Crohn's disease remain incompletely understood. Antibacterial defensins are expressed in a NOD2-dependent manner and patients with Crohn's disease seem to have diminished defensin production<sup>36,37</sup>. *NOD2*<sup>-/-</sup> mice do not develop spontaneous intestinal inflammation but are more susceptible than control mice to intra-oral *Listeria* infection<sup>67</sup>. The most common Crohn's disease-associated variant has been found to have reduced ability to control intracellular *Salmonella* survival in epithelial cells compared with those expressing wild-type NOD2 (ref. 30). Primary-monocyte-derived macrophages from patients with Crohn's disease who are homozygous for the truncating mutation in the LRR sensor domain (Leu1007fsinsC) have a globally blunted transcriptional response to MDP<sup>68</sup>. In contrast, *NOD2* frameshift-mutation knock-in mice have an enhanced response to MDP and are susceptible to dextran sodium sulphate colitis<sup>69</sup>. Comparative analysis of the colonic flora in *NOD2* knock-in and deficient mice may reconcile the disparate loss-of-function and gain-of-function phenotypes found when studying

the Crohn's disease-associated NOD2. Collectively, studies suggest that NOD2 primarily functions in antibacterial immunity and that persistent bacterial survival might be a driver of persistent inflammatory responses in IBD. However, a more comprehensive understanding of the relationship between NOD2-dependent pathways and cellular processes for handling internalized bacteria is needed.

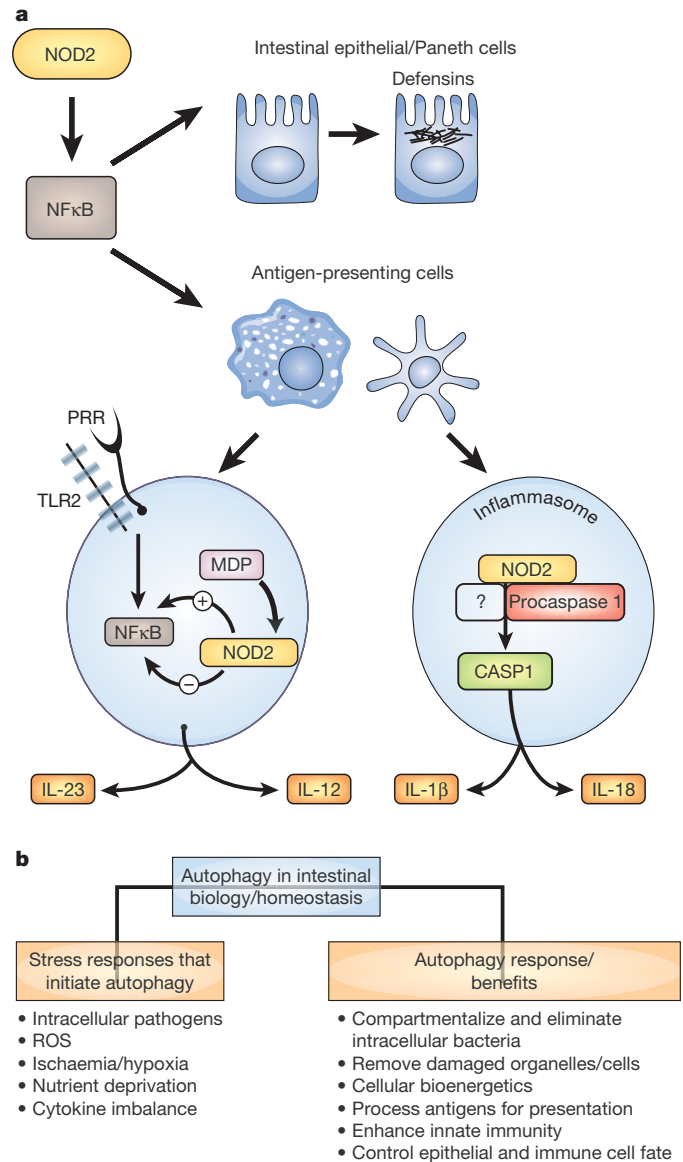
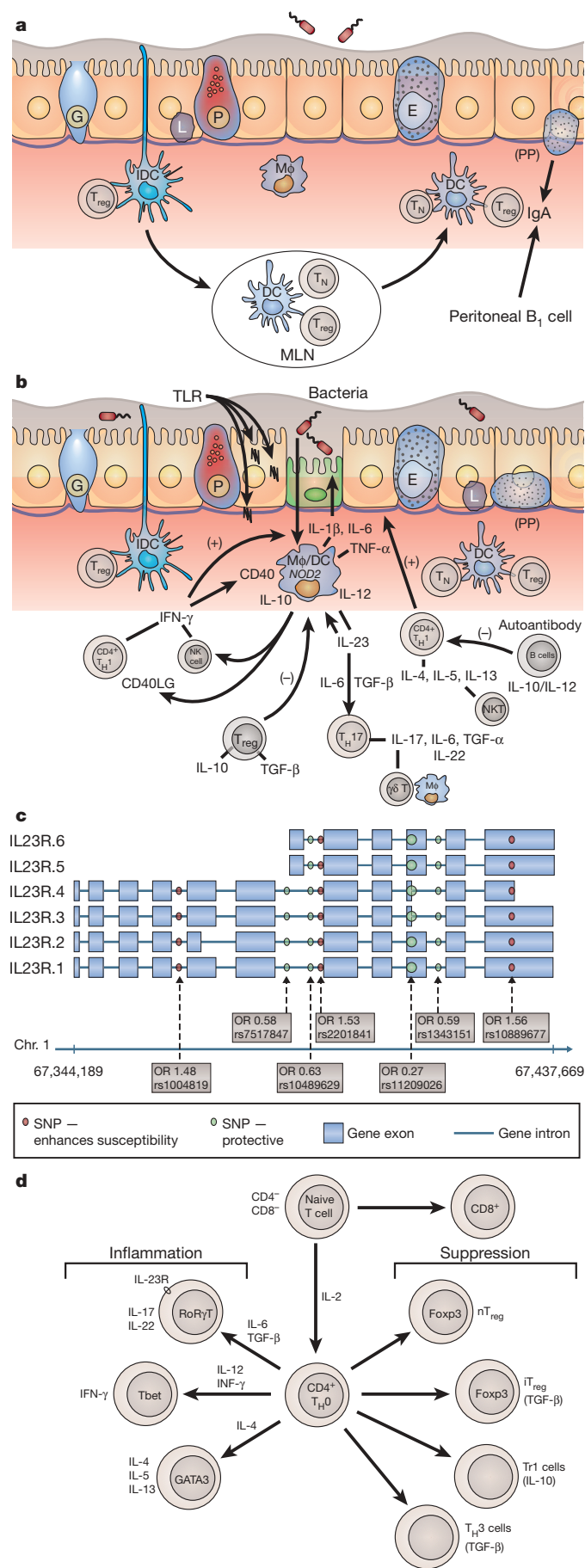


**Figure 3 | Several IBD susceptibility gene products modulate host-cell functional response to microbial flora.** **a**, Schematic representation of cell-specific NOD2/CARD15 signalling pathways. In intestinal epithelial cells/Paneth cells and antigen-presenting cells, muramyl dipeptide (MDP) found in bacterial proteoglycans is recognized by the leucine rich repeats (LRR) domains of NOD2 and leads to the activation of NF- $\kappa$ B. In Paneth cells, NOD2-mediated NF- $\kappa$ B activation leads to the induction of defensins. Mutations in NOD2 attenuate selective  $\alpha$ -defensin production and protect epithelial cells from bacterial infection. In antigen-presenting cells, NOD2 signalling is modulated by TLR signalling inputs and, via interaction with procaspase 1, regulates pro-inflammatory cytokine production. **b**, Potential roles for autophagy in IBD. Autophagy is essential for cellular homeostasis, providing a mechanism of response among all cell types to limit the harmful effects of diverse exogenous and endogenous stresses. The schematic flow diagram depicts the multiple stages at which autophagy may have a role in intestinal physiology, acute stages of inflammatory injury and the resolution phase of IBD. PRR, pattern recognition receptor; ROS, reactive oxygen species.



## The intracellular responses of autophagy and IBD

As noted above, a working model of IBD pathogenesis has evolved from a central focus on adaptive immunity to innate immunity. A constellation of findings, particularly in the last year, suggest a more focused orientation of that model on intracellular responses to low-level invasive bacteria. These include recent findings implicating alterations in autophagy and phagosomal function.

The autophagy pathway plays a part in protecting mammalian cells against various bacterial pathogens and the cytotoxic effect of bacterial toxins<sup>70–72</sup>. Following low-level stimuli or pathogen infection, autophagy could represent a primary attempt to re-establish homeostasis and when autophagic capacity is overwhelmed apoptosis could be triggered. The relevance to IBD is highlighted by the recent discovery that a synonymous SNP in the auto-phagocytic gene *ATG16L1* is associated with increased risk for Crohn's disease<sup>8,12</sup> (Fig. 3b). *ATG16L1* is broadly expressed in the intestinal epithelium, APCs, CD4/8 T cells, B1 cells and memory B cells. Preliminary data have implicated *ATG16L1* in host responses to intracellular bacteria<sup>12</sup>. Recent studies have also implicated a second autophagy gene, *IRGM* in Crohn's disease risk<sup>73</sup>. Short interfering (si)RNA studies have demonstrated that *IRGM* is required for mycobacterial immunity and may have an analogous role in the granulomatous response often observed in Crohn's disease<sup>74,75</sup>. Future studies will need to systematically determine the functional implications of disease variants in a cell- and tissue-specific context with the goal of gaining insight into the pleiotropic mechanisms behind human IBD.

NADPH oxidases and associated accessory proteins are also essential components of cellular response in microbial invasion<sup>76–78</sup>. An SNP within the first intron of *NCF4* (p40<sup>phox</sup>) is associated with enhanced susceptibility to IBD<sup>12</sup>. The presence of mutations within *NCF4* also prompts the hypothesis that altered phagosome function affecting handling of commensal flora may contribute to disease. Functionally altered phagosomes may kill microbes less effectively, resulting in prolonged immune activation or incomplete pathogen clearance.

## Innate signals meet adaptive immunity

Although innate immune responses seem to be a prerequisite for the excessive activation of adaptive immunity, the latter is the more proximate driver of tissue damage that is manifest in IBD patients (Fig. 4a, b). Adaptive responses are effected by a combination of resident and recruited cell populations. These comprise mucosal B cells producing secretory immunoglobulin A and immunoglobulin G, a complex mixture of T cells that are dominated by a T<sub>H</sub>1, T<sub>H</sub>17

**Figure 4 | Mucosal immune responses to luminal flora are multi-dimensional.** **a**, Mucosal immune responses to dietary and microbial antigens. DC, dendritic cell; IgA, immunoglobulin A; E, enterocyte; G, goblet cell; L, lymphocyte; IDC, immature dendritic cell; T<sub>N</sub>, T cell (naive); MLN, mesenteric lymph node; Mφ, macrophage; P, Paneth cells; PP, Peyer's patches. **b**, Mucosal immune response initiated by microbial sensing systems activates adaptive immune responses. Pathogenic bacteria or commensal microbes in genetically susceptible hosts disrupt epithelial barrier function, triggering the recruitment and activation of innate immune responses and colitogenic CD4<sup>+</sup> T cells. Depicted cells and cytokines imply that multiple components are involved in controlling mucosal immune responses in physiological and pathological states of inflammation. NK, natural killer. **c**, Schematic representation of IL23R isoforms and susceptibility loci implicated in Crohn's disease. The SNPs depicted are not all independent associations (the differences in the ORs presented are not necessarily biologically relevant differences). Additional genetics and functional studies will be essential to identify truly functional SNPs and to determine mechanisms by which some confer risk and others protection. Chr., chromosome; OR, odds ratio. **d**, Differentiation of CD4<sup>+</sup> T cells. The relative balance between effector T cells and regulatory T cells determines intestinal immunity and inflammation. T<sub>H</sub>1, T<sub>H</sub>2, T<sub>H</sub>17 and T<sub>reg</sub> cells are present in the intestinal mucosa and their differentiation is determined by cytokines, chemokines, self-ligands and microbial products present in the local and systemic milieu. nT<sub>reg</sub>, natural T<sub>reg</sub>; iT<sub>reg</sub>, induced T<sub>reg</sub>; Tbet, TBX21.



or  $T_H2$  phenotype, and the coincident presence of regulatory T/B cells.  $T_H1$  development is triggered by microbes that stimulate production of interferon- $\gamma$  and IL-12p40, which signal through STAT1, TBX21 and STAT4. STAT6 is essential for enhancement of  $T_H2$  cell differentiation and GATA3 for the induction of IL-4, IL-5 and IL-13 (refs 79–81).

In simplistic terms, ulcerative colitis seems to exhibit a  $T_H2$ -type-like cytokine profile, and Crohn's disease, a  $T_H1$  profile. Recent studies suggest a more complex and significant overlap between the two major forms of IBD. Another CD4 T-cell lineage ( $T_H17$ ) has been recognized that is characterized by the production of the eponymic cytokine IL-17 and the development of which is promoted by IL-23 and suppressed by transcription factors required for  $T_H1$  and  $T_H2$  cells<sup>81,82</sup>. Although the precise mechanism by which IL-23 maintains  $T_H17$  responses *in vivo* is still not well understood, recent studies have shown that  $T_H17$  cell lineage commitment is driven by TGF- $\beta$  in the presence of proinflammatory cytokines, whereas IL-23 seems to expand or maintain  $T_H17$  cell populations<sup>83</sup>. Furthermore, studies have demonstrated that IL-2 signalling using STAT5 inhibits  $T_H17$  differentiation, which by its positive effects on regulatory T ( $T_{reg}$ ) cells (see below) may constrain  $T_H17$ -mediated inflammation<sup>84</sup>. Compelling evidence indicates that ROR $\gamma$ t (retinoic acid-related orphan nuclear hormone receptor gamma-t) is necessary for  $T_H17$  commitment and differentiation<sup>85</sup>.

Recent studies have demonstrated that an IL23R coding variant is associated with reduced risk of IBD<sup>6</sup> (Fig. 4c). Further analysis suggests that there are multiple variants in the region independently associated with risk of IBD and establish that IL23R signalling is central to IBD. IL-23 is predominantly produced by activated dendritic cells and phagocytic cells, further suggesting that there may be distinct populations of dendritic cells expressing IL-12 and IL-23. IL-23 signals via the constitutive association of JAK2 in a STAT3/STAT4-dependent pathway, and IL-23-stimulated cells express IL-17A, IL-17F, IL-6, IL-22, TNF and CXCL1. Many microbial signals, CD40 and PGE2 (also known as PTGES2) receptors enhance the expression of the IL-23 subunits<sup>82,86</sup>.

Mechanistic studies also suggest the potential importance of the IL-23 axis in IBD pathogenesis. Anti-IL-12p40 (common to both IL-12 and IL-23) or interferon- $\gamma$ -specific antibodies antagonize the development of spontaneous IBD in the IL-10-deficient mouse, but only neutralization of IL-12p40 ameliorated the disease. The spontaneous development of IBD in IL-10-deficient mice is prevented by a cross with IL-23p19 (also known as IL23a)-deficient mice, also suggesting an essential role for IL-23 in the induction of colitis<sup>48,87–89</sup>. Future studies will need to determine if IL-17-deficiency alters onset of murine colitis in these models.

In addition to its ability to support the development of  $T_H17$  cells, IL-23 induces the secretion of IL-17 by non-T-cells in an inflammatory environment, and both T cells and monocytes serve as sources of increased expression in the mucosa of IBD patients. Recent data suggest that IL-17 induces antimicrobial peptides and may regulate tight junction barrier formation<sup>90</sup>. Taken together, data suggest that IL-23–IL-23R signalling may be subject to compartment-specific regulation at multiple levels and seems to function as a key conductor of innate and adaptive inflammatory responses in the intestinal mucosa.

Compelling evidence in human as well as murine models also suggest a role for  $T_{reg}$  cells in maintaining intestinal homeostasis<sup>91</sup>. In addition to thymic-derived  $T_{reg}$  cells, induced  $T_{reg}$  cells may be generated in the periphery from activated effector memory CD4<sup>+</sup> CD25<sup>+</sup> cells<sup>92</sup>. As outlined in (Fig. 4d), in the absence of inflammatory mediators, TGF- $\beta$  promotes the development of Foxp3<sup>+</sup>  $T_{reg}$  cells associated with suppression of the inflammatory response<sup>93</sup>. In contrast, in the presence of proinflammatory cytokines such as IL-6, TGF- $\beta$  induces the differentiation of  $T_H17$  cells. The complex interactions between pleiotropic factors such as IL-17 and

TGF- $\beta$  influence intestinal homeostasis and may affect initiation, persistence and relapses in human IBD.

In the lamina propria,  $T_{reg}$  cells may have evolved to suppress immune responses to resident commensal microbes.  $T_{reg}$  cells could have a critical role in modulating the clinical spectrum of the disease.  $T_{reg}$  cells are expanded in both inflamed and non-inflamed ulcerative colitis<sup>94</sup>. Additional regulatory cells within the CD8 compartment (CD8<sup>+</sup> CD28<sup>−</sup>) have been described in IBD<sup>95</sup>. These cells are reduced or absent in lamina propria of patients with IBD. In addition to T cells, B cells termed  $B_{reg}$  also have a regulatory role in intestinal inflammation, on the basis of observations in a number of murine models<sup>96</sup>. Unlike  $T_{reg}$  cells, these cells are seen only in states of inflammation and suppress progression rather than initiation of murine colitis. Additional evidence points to a key role for CD1d-restricted natural killer T (NKT) cells in the induction and amplification of  $T_H2$ -cytokine-driven intestinal inflammation in ulcerative colitis<sup>97</sup>. Future studies will need to identify additional phenotypic markers for these cells in the lamina propria and address the role of these location-specific regulatory cells in the prevention and the resolution of intestinal inflammation in human IBD.

### Future perspectives

The number of potential IBD genes continues to increase<sup>9,12,14,73</sup>. Additional novel loci map to chromosome 16q24.1, *TNFSF15*, *NKX2-3* and an intergenic region on chromosome 10q21.1. Future biological studies will be required to identify the functional or gene regulatory implications of these non-coding variants in human IBD, and how qualitative and quantitative differences in expression contribute to disease pathogenesis. Modelling the available data predicts that the IBD-prone genotype results from multiple genetic variants that each exert a small effect on overall risk. Genetic variants may permit improved definition of disease phenotype, help monitor clinical progression and more importantly provide insight for the development of targeted preventive therapies. Furthermore alternative splicing of messenger RNA precursors, such as those that occur within *NOD2* and *ATG16L1*, is a common mechanism of gene control and future studies will need to address the functional implications of splicing within genetic variants that contribute to immunity.

An important conceptual development in the understanding of IBD pathogenesis has been the more focused appreciation of the nature of the microbial–innate-immune-response interaction during the transition from physiological to pathological intestinal inflammation. As highlighted above, achieving a thorough understanding may depend as much on more rigorous analysis of the complex dynamics of luminal microbial communities as on understanding of the host mucosal defence and response mechanisms.

Explaining the geographic restriction of inflammation to the intestine is a major cognitive challenge when disease-associated gene variants are usually expressed broadly. This paradox might be explained by the combined effect of a relatively subtle alteration of gene function and an exceptional challenge provided by the dense microbial flora unique to the gut. When innate immune function is only slightly attenuated, a phenotype may be manifest only where there is a very dense bacterial antigenic challenge, resulting in gut-restricted disease. Host defence defects in ulcerative colitis patients may be sufficiently subtle that inflammation occurs only in the context of the intense stimulus of the colonic flora. This supposition may explain why inflammation frequently occurs in the pouch created from the terminal ileum in ulcerative colitis patients undergoing colectomy when the 'ileal flora' becomes more colonic-like, despite the absence of ileal inflammation in ulcerative colitis patients before surgery.

Recent studies indicate that the outcome of microbe–host-cell interaction may depend on the competence of the host response rather than the intrinsic invasiveness of the bacteria *per se*. If the mechanisms for intracellular inhibition and killing are diminished, persistent survival may stimulate progressive inflammation. A

better definition of disease, coupled with host gene expression profiles, metabolomic profiling of microbes and metagenomic approaches may help narrow the microbial factors central to disease pathogenesis<sup>98</sup>.

Finally, functional dissection of genetic variants in IBD susceptibility is still in its infancy. Searching for more complete genotype–phenotype correlations and for independent evidence of the functional consequences of sequence alteration will be an important step in placing disease variants in functional biology. Systematic pathway analysis will help guide future in-depth functional studies and provide a common framework for understanding how these genetic variants influence biological pathways in ways that lead to IBD.

- Podolsky, D. K. Inflammatory bowel disease. *N. Engl. J. Med.* **347**, 417–429 (2002).
- Orholm, M. *et al.* Familial occurrence of inflammatory bowel disease. *N. Engl. J. Med.* **324**, 84–88 (1991).
- Tysk, C., Lindberg, E., Jarnerot, G. & Floderus-Myrhed, B. Ulcerative colitis and Crohn's disease in an unselected population of monozygotic and dizygotic twins. A study of heritability and the influence of smoking. *Gut* **29**, 990–996 (1988).
- Hugot, J. P. *et al.* Association of NOD2 leucine-rich repeat variants with susceptibility to Crohn's disease. *Nature* **411**, 599–603 (2001).
- Ogura, Y. *et al.* A frameshift mutation in NOD2 associated with susceptibility to Crohn's disease. *Nature* **411**, 603–606 (2001).
- Duerr, R. H. *et al.* A genome-wide association study identifies IL23R as an inflammatory bowel disease gene. *Science* **314**, 1461–1463 (2006).
- Goyette, P., Labbe, C., Trinh, T. T., Xavier, R. J. & Rioux, J. D. Molecular pathogenesis of inflammatory bowel disease: genotypes, phenotypes and personalized medicine. *Ann. Med.* **39**, 177–199 (2007).
- Hampe, J. *et al.* A genome-wide association scan of nonsynonymous SNPs identifies a susceptibility variant for Crohn disease in ATG16L1. *Nature Genet.* **39**, 207–211 (2007).
- Libioulle, C. *et al.* Novel crohn disease locus identified by genome-wide association maps to a gene desert on 5p13.1 and modulates expression of PTGER4. *PLoS Genet.* **3**, e58 (2007).
- Peltokova, V. D. *et al.* Functional variants of OCTN cation transporter genes are associated with Crohn disease. *Nature Genet.* **36**, 471–475 (2004).
- Rioux, J. D. *et al.* Genetic variation in the 5q31 cytokine gene cluster confers susceptibility to Crohn disease. *Nature Genet.* **29**, 223–228 (2001).
- Rioux, J. D. *et al.* Genome-wide association study identifies new susceptibility loci for Crohn disease and implicates autophagy in disease pathogenesis. *Nature Genet.* **39**, 596–604 (2007).
- Silverberg, M. S. *et al.* Refined genomic localization and ethnic differences observed for the IBD5 association with Crohn's disease. *Eur. J. Hum. Genet.* **15**, 328–335 (2007).
- Yamazaki, K. *et al.* Single nucleotide polymorphisms in *TNFSF15* confer susceptibility to Crohn's disease. *Hum. Mol. Genet.* **14**, 3499–3506 (2005).
- Gionchetti, P. *et al.* Prophylaxis of pouchitis onset with probiotic therapy: a double-blind, placebo-controlled trial. *Gastroenterology* **124**, 1202–1209 (2003).
- Sutherland, L. *et al.* Double blind, placebo controlled trial of metronidazole in Crohn's disease. *Gut* **32**, 1071–1075 (1991).
- Barnich, N. *et al.* CEACAM6 acts as a receptor for adherent-invasive *E. coli*, supporting ileal mucosa colonization in Crohn disease. *J. Clin. Invest.* **117**, 1566–1574 (2007).
- Darfeuille-Michaud, A. *et al.* Presence of adherent *Escherichia coli* strains in ileal mucosa of patients with Crohn's disease. *Gastroenterology* **115**, 1405–1413 (1998).
- Elson, C. O. *et al.* Experimental models of inflammatory bowel disease reveal innate, adaptive, and regulatory mechanisms of host dialogue with the microbiota. *Immunol. Rev.* **206**, 260–276 (2005).
- Onderdonk, A. B., Hermos, J. A. & Bartlett, J. G. The role of the intestinal microflora in experimental colitis. *Am. J. Clin. Nutr.* **30**, 1819–1825 (1977).
- Sellon, R. K. *et al.* Resident enteric bacteria are necessary for development of spontaneous colitis and immune system activation in interleukin-10-deficient mice. *Infect. Immun.* **66**, 5224–5231 (1998).
- Gill, S. R. *et al.* Metagenomic analysis of the human distal gut microbiome. *Science* **312**, 1355–1359 (2006).
- Buhner, S. *et al.* Genetic basis for increased intestinal permeability in families with Crohn's disease: role of *CARD15* 3020insC mutation? *Gut* **55**, 342–347 (2006).
- Irvine, E. J. & Marshall, J. K. Increased intestinal permeability precedes the onset of Crohn's disease in a subject with familial risk. *Gastroenterology* **119**, 1740–1744 (2000).
- May, G. R., Sutherland, L. R. & Meddings, J. B. Is small intestinal permeability really increased in relatives of patients with Crohn's disease? *Gastroenterology* **104**, 1627–1632 (1993).
- Soderholm, J. D. *et al.* Augmented increase in tight junction permeability by luminal stimuli in the non-inflamed ileum of Crohn's disease. *Gut* **50**, 307–313 (2002).
- Gassler, N. *et al.* Inflammatory bowel disease is associated with changes of enterocytic junctions. *Am. J. Physiol. Gastrointest. Liver Physiol.* **281**, G216–G228 (2001).
- Kabashima, K. *et al.* The prostaglandin receptor EP4 suppresses colitis, mucosal damage and CD4 cell activation in the gut. *J. Clin. Invest.* **109**, 883–893 (2002).
- Cario, E. *et al.* Lipopolysaccharide activates distinct signaling pathways in intestinal epithelial cell lines expressing Toll-like receptors. *J. Immunol.* **164**, 966–972 (2000).
- Hisamatsu, T. *et al.* CARD15/NOD2 functions as an antibacterial factor in human intestinal epithelial cells. *Gastroenterology* **124**, 993–1000 (2003).
- Yoshida, M. *et al.* Neonatal Fc receptor for IgG regulates mucosal immune responses to luminal bacteria. *J. Clin. Invest.* **116**, 2142–2151 (2006).
- Neish, A. S. *et al.* Prokaryotic regulation of epithelial responses by inhibition of I $\kappa$ B- $\alpha$  ubiquitination. *Science* **289**, 1560–1563 (2000).
- Kelly, D. *et al.* Commensal anaerobic gut bacteria attenuate inflammation by regulating nuclear–cytoplasmic shuttling of PPAR- $\gamma$  and RelA. *Nature Immunol.* **5**, 104–112 (2004).
- Nenci, A. *et al.* Epithelial NEMO links innate immunity to chronic intestinal inflammation. *Nature* **446**, 557–561 (2007).
- Zaph, C. *et al.* Epithelial cell-intrinsic IKK- $\beta$  expression regulates intestinal immune homeostasis. *Nature* **446**, 552–556 (2007).
- Wehkamp, J. *et al.* NOD2 (CARD15) mutations in Crohn's disease are associated with diminished mucosal alpha-defensin expression. *Gut* **53**, 1658–1664 (2004).
- Wehkamp, J. *et al.* Reduced Paneth cell  $\alpha$ -defensins in ileal Crohn's disease. *Proc. Natl Acad. Sci. USA* **102**, 18129–18134 (2005).
- Mashimo, H., Wu, D. C., Podolsky, D. K. & Fishman, M. C. Impaired defense of intestinal mucosa in mice lacking intestinal trefoil factor. *Science* **274**, 262–265 (1996).
- McVay, L. D. *et al.* Absence of bacterially induced RELM $\beta$  reduces injury in the dextran sodium sulfate model of colitis. *J. Clin. Invest.* **116**, 2914–2923 (2006).
- Van der Sluis, M. *et al.* Muc2-deficient mice spontaneously develop colitis, indicating that MUC2 is critical for colonic protection. *Gastroenterology* **131**, 117–129 (2006).
- An, G. *et al.* Increased susceptibility to colitis and colorectal tumors in mice lacking core 3-derived O-glycans. *J. Exp. Med.* **204**, 1417–1429 (2007).
- Itoh, H., Beck, P. L., Inoue, N., Xavier, R. & Podolsky, D. K. A paradoxical reduction in susceptibility to colonic injury upon targeted transgenic ablation of goblet cells. *J. Clin. Invest.* **104**, 1539–1547 (1999).
- Salzman, N. H., Underwood, M. A. & Bevins, C. L. Paneth cells, defensins, and the commensal microbiota: A hypothesis on intimate interplay at the intestinal mucosa. *Semin. Immunol.* **19**, 70–83 (2007).
- Coomes, J. L. & Maloy, K. J. Control of intestinal homeostasis by regulatory T cells and dendritic cells. *Semin. Immunol.* **19**, 116–126 (2007).
- Chieppa, M., Rescigno, M., Huang, A. Y. & Germain, R. N. Dynamic imaging of dendritic cell extension into the small bowel lumen in response to epithelial cell TLR engagement. *J. Exp. Med.* **203**, 2841–2852 (2006).
- Niess, J. H. *et al.* CX3CR1-mediated dendritic cell access to the intestinal lumen and bacterial clearance. *Science* **307**, 254–258 (2005).
- Becker, C. *et al.* Constitutive p40 promoter activation and IL-23 production in the terminal ileum mediated by dendritic cells. *J. Clin. Invest.* **112**, 693–706 (2003).
- Hue, S. *et al.* Interleukin-23 drives innate and T cell-mediated intestinal inflammation. *J. Exp. Med.* **203**, 2473–2483 (2006).
- Mizoguchi, A. *et al.* Dependence of intestinal granuloma formation on unique myeloid DC-like cells. *J. Clin. Invest.* **117**, 605–615 (2007).
- Smith, P. D., Ochsenbauer-Jambor, C. & Smythies, L. E. Intestinal macrophages: unique effector cells of the innate immune system. *Immunol. Rev.* **206**, 149–159 (2005).
- Takeda, K. *et al.* Enhanced Th1 activity and development of chronic enterocolitis in mice devoid of Stat3 in macrophages and neutrophils. *Immunity* **10**, 39–49 (1999).
- Kamada, N. *et al.* Abnormally differentiated subsets of intestinal macrophage play a key role in Th1-dominant chronic colitis through excess production of IL-12 and IL-23 in response to bacteria. *J. Immunol.* **175**, 6900–6908 (2005).
- Fort, M. M., Leach, M. W. & Rennick, D. M. A role for NK cells as regulators of CD4<sup>+</sup> T cells in a transfer model of colitis. *J. Immunol.* **161**, 3256–3261 (1998).
- Watanabe, T. *et al.* Nucleotide binding oligomerization domain 2 deficiency leads to dysregulated TLR2 signaling and induction of antigen-specific colitis. *Immunity* **25**, 473–485 (2006).
- Franchimont, D. *et al.* Deficient host-bacteria interactions in inflammatory bowel disease? The toll-like receptor (TLR)-4 Asp299gly polymorphism is associated with Crohn's disease and ulcerative colitis. *Gut* **53**, 987–992 (2004).
- Pierik, M. *et al.* Toll-like receptor-1, -2, and -6 polymorphisms influence disease extension in inflammatory bowel diseases. *Inflamm. Bowel Dis.* **12**, 1–8 (2006).
- Torok, H. P. *et al.* Crohn's disease is associated with a toll-like receptor-9 polymorphism. *Gastroenterology* **127**, 365–366 (2004).
- Inohara, N., Chamailard, M., McDonald, C. & Nunez, G. NOD-LRR proteins: role in host-microbial interactions and inflammatory disease. *Annu. Rev. Biochem.* **74**, 355–383 (2005).
- Kobayashi, K. *et al.* RICK/Rip2/CARDIAK mediates signalling for receptors of the innate and adaptive immune systems. *Nature* **416**, 194–199 (2002).
- Barnich, N. *et al.* GRIM-19 interacts with nucleotide oligomerization domain 2 and serves as downstream effector of anti-bacterial function in intestinal epithelial cells. *J. Biol. Chem.* **280**, 19021–19026 (2005).



61. Chen, C. M., Gong, Y., Zhang, M. & Chen, J. J. Reciprocal cross-talk between Nod2 and TAK1 signaling pathways. *J. Biol. Chem.* **279**, 25876–25882 (2004).
62. Mayor, A., Martinon, F., De Smedt, T., Petrilli, V. & Tschopp, J. A crucial function of SGT1 and HSP90 in inflammasome activity links mammalian and plant innate immune responses. *Nature Immunol.* **8**, 497–503 (2007).
63. McDonald, C. *et al.* A role for Erbin in the regulation of Nod2-dependent NF- $\kappa$ B signaling. *J. Biol. Chem.* **280**, 40301–40309 (2005).
64. Pan, Q. *et al.* NF- $\kappa$ B-inducing kinase regulates selected gene expression in the Nod2 signaling pathway. *Infect. Immun.* **74**, 2121–2127 (2006).
65. da Silva Correia, J., Miranda, Y., Leonard, N. & Ulevitch, R. SGT1 is essential for Nod1 activation. *Proc. Natl Acad. Sci. USA* **104**, 6764–6769 (2007).
66. Bruey, J. M. *et al.* Bcl-2 and Bcl-XL regulate proinflammatory caspase-1 activation by interaction with NALP1. *Cell* **129**, 45–56 (2007).
67. Kobayashi, K. S. *et al.* Nod2-dependent regulation of innate and adaptive immunity in the intestinal tract. *Science* **307**, 731–734 (2005).
68. Li, J. *et al.* Regulation of IL-8 and IL-1 $\beta$  expression in Crohn's disease associated NOD2/CARD15 mutations. *Hum. Mol. Genet.* **13**, 1715–1725 (2004).
69. Maeda, S. *et al.* Nod2 mutation in Crohn's disease potentiates NF- $\kappa$ B activity and IL-1 $\beta$  processing. *Science* **307**, 734–738 (2005).
70. Gutierrez, M. G. *et al.* Protective role of autophagy against *Vibrio cholerae* cytotoxin, a pore-forming toxin from *V. cholerae*. *Proc. Natl Acad. Sci. USA* **104**, 1829–1834 (2007).
71. Mizushima, N. & Klionsky, D. J. Protein Turnover Via Autophagy: Implications for Metabolism. *Annu. Rev. Nutr.* **27**, doi:10.1146/annurev.nutr.27.061406.093749 (2007).
72. Ogawa, M. *et al.* Escape of intracellular Shigella from autophagy. *Science* **307**, 727–731 (2005).
73. Parkes, M. *et al.* Sequence variants in the autophagy gene *IRGM* and multiple other replicating loci contribute to Crohn's disease susceptibility. *Nature Genet.* **39**, 830–832 (2007).
74. Singh, S. B., Davis, A. S., Taylor, G. A. & Deretic, V. Human IRGM induces autophagy to eliminate intracellular mycobacteria. *Science* **313**, 1438–1441 (2006).
75. Taylor, G. A. IRG proteins: key mediators of interferon-regulated host resistance to intracellular pathogens. *Cell. Microbiol.* **9**, 1099–1107 (2007).
76. Ellson, C. D. *et al.* Neutrophils from p40<sup>phox</sup><sup>-/-</sup> mice exhibit severe defects in NADPH oxidase regulation and oxidant-dependent bacterial killing. *J. Exp. Med.* **203**, 1927–1937 (2006).
77. Matute, J. D., Arias, A. A., Dinuer, M. C. & Patino, P. J. p40<sup>phox</sup>: the last NADPH oxidase subunit. *Blood Cells Mol. Dis.* **35**, 291–302 (2005).
78. Stuart, L. M. & Ezekowitz, R. A. Phagocytosis: elegant complexity. *Immunity* **22**, 539–550 (2005).
79. Mosmann, T. R., Cherwinski, H., Bond, M. W., Giedlin, M. A. & Coffman, R. L. Two types of murine helper T cell clone. I. Definition according to profiles of lymphokine activities and secreted proteins. *J. Immunol.* **136**, 2348–2357 (1986).
80. Murphy, K. M. Fate vs choice: the immune system reloaded. *Immunol. Res.* **32**, 193–200 (2005).
81. Weaver, C. T., Hatton, R. D., Mangan, P. R. & Harrington, L. E. IL-17 family cytokines and the expanding diversity of effector T cell lineages. *Annu. Rev. Immunol.* **25**, 851–852 (2007).
82. Kastelein, R. A., Hunter, C. A. & Cua, D. J. Discovery and biology of IL-23 and IL-27: related but functionally distinct regulators of inflammation. *Annu. Rev. Immunol.* **25**, 221–242 (2007).
83. Bettelli, E., Oukka, M. & Kuchroo, V. K. T<sub>H</sub>-17 cells in the circle of immunity and autoimmunity. *Nature Immunol.* **8**, 345–350 (2007).
84. Laurence, A. *et al.* Interleukin-2 signaling via STAT5 constrains T helper 17 cell generation. *Immunity* **26**, 371–381 (2007).
85. Ivanov, I. I. *et al.* The orphan nuclear receptor ROR $\gamma$ t directs the differentiation program of proinflammatory IL-17<sup>+</sup> T helper cells. *Cell* **126**, 1121–1133 (2006).
86. Schnurr, M. *et al.* Extracellular nucleotide signaling by P2 receptors inhibits IL-12 and enhances IL-23 expression in human dendritic cells: a novel role for the cAMP pathway. *Blood* **105**, 1582–1589 (2005).
87. Kullberg, M. C. *et al.* IL-23 plays a key role in *Helicobacter hepaticus*-induced T cell-dependent colitis. *J. Exp. Med.* **203**, 2485–2494 (2006).
88. Uhlig, H. H. *et al.* Differential activity of IL-12 and IL-23 in mucosal and systemic innate immune pathology. *Immunity* **25**, 309–318 (2006).
89. Yen, D. *et al.* IL-23 is essential for T cell-mediated colitis and promotes inflammation via IL-17 and IL-6. *J. Clin. Invest.* **116**, 1310–1316 (2006).
90. Kinugasa, T., Sakaguchi, T., Gu, X. & Reinecker, H. C. Claudins regulate the intestinal barrier in response to immune mediators. *Gastroenterology* **118**, 1001–1011 (2000).
91. Izcue, A., Coombes, J. L. & Powrie, F. Regulatory T cells suppress systemic and mucosal immune activation to control intestinal inflammation. *Immunol. Rev.* **212**, 256–271 (2006).
92. Akbar, A. N., Vukmanovic-Stejic, M., Taams, L. S. & Macallan, D. C. The dynamic co-evolution of memory and regulatory CD4<sup>+</sup> T cells in the periphery. *Nature Rev. Immunol.* **7**, 231–237 (2007).
93. Kim, J. M. & Rudensky, A. The role of the transcription factor Foxp3 in the development of regulatory T cells. *Immunol. Rev.* **212**, 86–98 (2006).
94. Yu, Q. T. *et al.* Expression and functional characterization of FOXP3<sup>+</sup> CD4<sup>+</sup> regulatory T cells in ulcerative colitis. *Inflamm. Bowel Dis.* **16**, 1898–1909 (2006).
95. Allez, M., Brimnes, J., Dotan, I. & Mayer, L. Expansion of CD8<sup>+</sup> T cells with regulatory function after interaction with intestinal epithelial cells. *Gastroenterology* **123**, 1516–1526 (2002).
96. Mizoguchi, A. & Bhan, A. K. A case for regulatory B cells. *J. Immunol.* **176**, 705–710 (2006).
97. Fuss, I. J. *et al.* Nonclassical CD1d-restricted NK T cells that produce IL-13 characterize an atypical Th2 response in ulcerative colitis. *J. Clin. Invest.* **113**, 1490–1497 (2004).
98. Ley, R. E., Peterson, D. A. & Gordon, J. I. Ecological and evolutionary forces shaping microbial diversity in the human intestine. *Cell* **124**, 837–848 (2006).

**Acknowledgements** This work is supported by grants from the NIH (to R.J.X. and D.K.P.).

**Author Information** Reprints and permissions information is available at [www.nature.com/reprints](http://www.nature.com/reprints). The authors declare no competing financial interests. Correspondence should be addressed to D.K.P. ([dpodolsky@partners.org](mailto:dpodolsky@partners.org)).

## HYPOTHESIS

# A lipid-based model for the creation of an escape hatch from the endoplasmic reticulum

Hidde L. Ploegh<sup>1</sup>

**Lipids are not encoded by a DNA template and therefore cannot be mutated, knocked out or knocked down. This by no means renders them impotent from a cell biological perspective. Here I propose a model for the involvement of lipid rearrangements in the execution of crucial steps in (glyco)protein quality control.**

Lipids allow life forms to exist by separating, but not insulating, the extracellular environment from the cytoplasm. For eukaryotes, their delimiting membranes define the identity of intracellular compartments. Import and export of macromolecules across these membranes require specialized machinery, including transport proteins of various stripe and colour. Nowhere is this more evident than in the endoplasmic reticulum (ER), where nascent secretory and membrane proteins rely on the Sec61 complex (translocon) to acquire a topology equivalent to extracellular exposure, a co-translational process. The translocon accommodates the nascent chain in an extended conformation, and folding starts only when the polypeptide emerges on the luminal side<sup>1</sup>.

## Elimination of misfolded proteins from the ER

Endoplasmic reticulum (ER)-inserted proteins that fail to attain their proper conformation are destroyed by extraction from the ER, followed by proteolysis in the cytosol<sup>2–4</sup>. Eukaryotes use several pathways for elimination of ER proteins that have exhausted their folding options<sup>3,5</sup>. Key steps involve (1) an assessment of folding status; (2) relegation to a conduit through which the unwanted polypeptide leaves the ER; and (3) proteolysis on the cytoplasmic side of the ER. We know the identity of several of the components in the ER that assess protein folding status (step 1)<sup>3,5</sup>. Furthermore, proteolysis revolves around ubiquitin-dependent, proteasomal destruction (step 3)<sup>3,6,7</sup>. The unsolved question concerns the identity of the channel through which extraction from the ER occurs (step 2). Notwithstanding several plausible suggestions<sup>3,8–11</sup>, no protein complex has been identified that convincingly accounts for all steps of the topological reversal that precedes cytoplasmic destruction. Moreover, certain non-enveloped viruses such as polyoma virus and simian virus 40 (SV40) escape from the ER as largely intact particles, and do so by using proteins drawn from the same set as those involved in extraction of misfolded glycoproteins<sup>12–14</sup>. This raises the question of the identity of the channel through which misfolded proteins or viruses such as polyoma virus escape from the ER, and the exact role of proteins therein. A substantial body of evidence points to Der1 in yeast and its homologues in other eukaryotes, the Derlins, as proteins around which a dislocation channel could be organized<sup>3,4,8,10,11</sup>. I here propose an alternative model that invokes a role for lipids—and exploits the mechanism by which lipid droplets form—both as an escape hatch for viruses like polyoma virus, and in the removal of misfolded proteins from the ER. The proposed exit model by no means excludes purely protein-based alternatives and

may even require proteins for assistance, but it does account for a number of observations not readily reconciled with our current knowledge of existing protein-based channels.

## Lipid droplets: biogenesis and composition

Lipid droplets are present in all eukaryotic cells. Their biogenesis involves local delamination of the ER through insertion of a 'lens' composed of neutral lipids (triglycerides, cholesterol esters), followed by budding from the ER of the nascent lipid droplet, now surrounded by a single layer of phospholipids<sup>15,16</sup> (Fig. 1a–e). Lipid droplets also have a distinctive protein composition: some proteins (adipophilins) are unique constituents of lipid droplets<sup>17</sup>, others (caveolin) are found associated with the plasma membrane and with lipid droplets<sup>18</sup>, but ER constituents, notably calnexin and the immunoglobulin heavy chain binding protein BiP, are consistently found as well<sup>19–21</sup>. This is surprising: calnexin is a type I membrane protein, the amino-terminal domain of which is lumenally exposed. BiP, too, resides in the ER lumen. The possibility that an isolation artefact accounts for the presence of BiP and calnexin in lipid droplets cannot be dismissed out of hand, especially in view of the propensity of the ER to enwrap lipid droplets<sup>16</sup>, but their presence is no less remarkable than the absence of other, abundant ER-resident proteins. Because of the presence of calnexin and BiP, we consider an alternative means of releasing a lipid droplet from the ER. It involves the (transient) formation of bicellar structures, created by fusion of the luminal and cytoplasmic leaflets of the ER membrane (Fig. 1h, k). A lipid droplet would thus be surrounded by a phospholipid monolayer<sup>15</sup>, with at least a portion taken from the ER-luminal leaflet, together with its inserted proteins. To accommodate membrane proteins in these structures, not all bilayer characteristics need to be lost in the course of lipid droplet formation (Fig. 1k). A 'wrinkled' surface would create ridges with local bilayer properties to which membrane proteins could be anchored in the conventional way by means of their transmembrane segment(s). Misfolded secretory proteins targeted for destruction could then piggy-back onto chaperones such as calnexin or BiP. Localized curvature of lipid vesicles and lateral separation of lipids of different composition are known to occur, at least in model membranes, with spectacular structural consequences and sharp demarcations between lipid domains of unique composition<sup>22</sup>.

Excess lipid is present opposite the site where a lipid droplet forms, because the bulk of the lipids necessary for formation of the droplet is

<sup>1</sup>Whitehead Institute, MIT Department of Biology, Cambridge, Massachusetts 02142, USA.



'borrowed' from the cytoplasmic leaflet only. Both lipid composition and membrane curvature may prepare these droplet intermediates for excision from the ER by bicelle formation between the luminal and cytoplasmic phospholipid leaflets, rather than by simple scission. Bicellar structures favour the presence of lysophospholipids and glycolipids with bulky headgroups<sup>23</sup>. Viruses such as polyoma virus and SV40 bind to just such glycolipid receptors at the cell surface and are delivered to the ER by means of caveosomes<sup>24</sup>. En route from the surface to the ER, the virus particles presumably remain tethered to their glycolipid receptors. Once in the ER, they may prefer areas based on local membrane curvature and/or lipid composition and thus seek out areas where lipid droplets form. This scenario would

position the virus particle at the right site to leave the ER in the slipstream of a departing lipid droplet (Fig. 1m, n). Upon release of a lipid droplet and exit of the virus from the ER, the resulting pore then closes by progressive constriction and, finally, coalescence of the luminal and the cytoplasmic leaflets (Fig. 1o). Not all lipid droplets must necessarily arise by the same mechanism, or yield structures of identical composition: some may serve a lipid storage function (Fig. 1a–f); others may carry out functions related to ensuring ER homeostasis and protein quality control. The integrity of the ER is important to maintain its unique ionic composition<sup>25</sup>. The existence of channels of a size sufficient to allow passage of virions or folded protein domains would require gating mechanisms that ensure

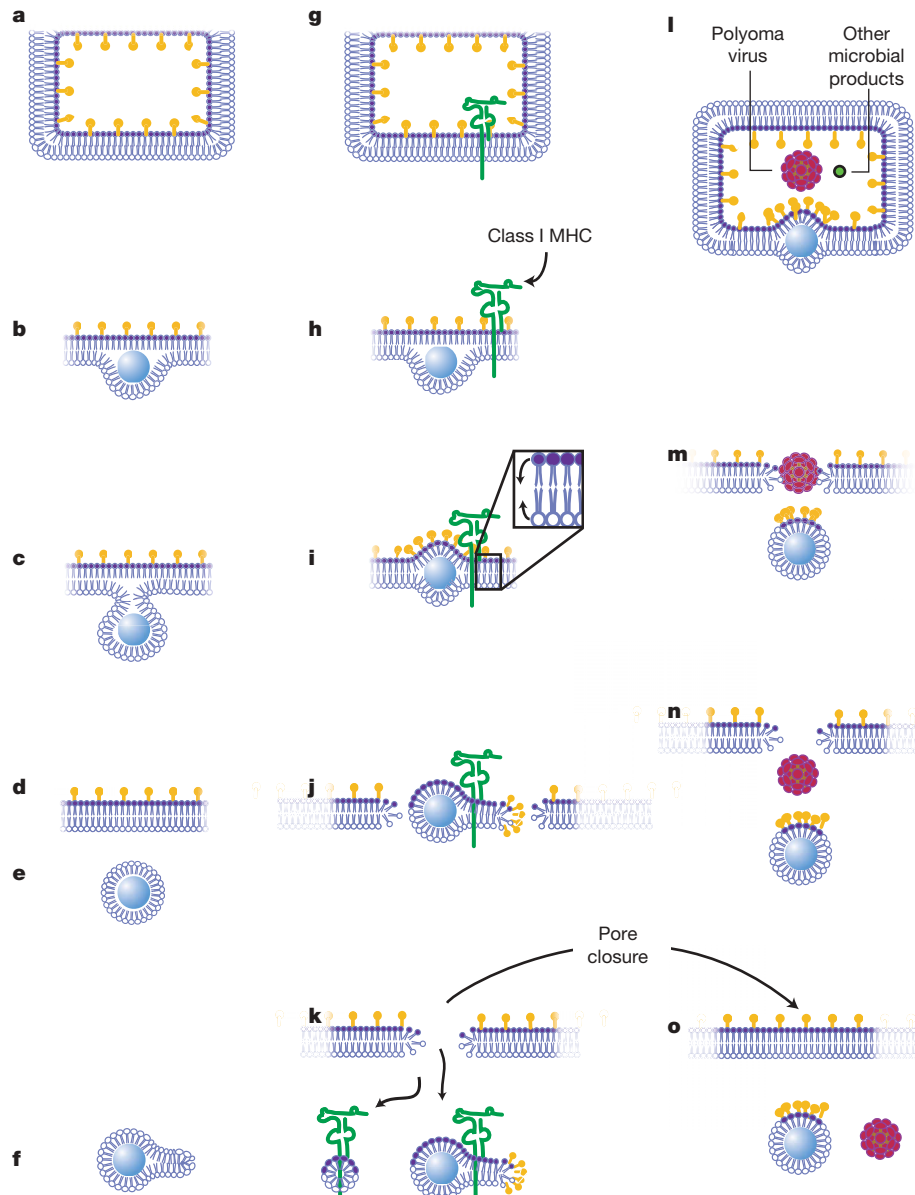


**Figure 1 | Biogenesis of lipid droplets and a model for their involvement in escape of macromolecules and viruses from the ER.** **a–f**, Lipid droplet formation. Phospholipids on the luminal face of the ER lipid bilayer are depicted with purple headgroups; phospholipids on the cytoplasmic face are depicted with white headgroups. The yellow lollipops represent lysophospholipids and/or glucosylceramides. **b**, Lipid droplet formation starts with the formation of a neutral lipid 'lens' in between the two sheets of phospholipids. **e**, A lipid droplet consists of a neutral lipid core surrounded by a monolayer of phospholipids, derived by scission from the cytoplasmic face of the ER membrane. **f**, 'Wrinkles' on the surface of a lipid droplet impart local phospholipid bilayer character. **g–k**, Resolution of lipid droplet

intermediates by bicelle formation. The route taken by the class I MHC molecule (green) is representative of the fate proposed for a type I membrane protein about to be discharged from the ER, either as part of a lipid droplet (**k**, right) or as a structure composed solely of the class I MHC molecule and phospholipid (**k**, left). **l–o**, Polyoma virus leaves the ER in the slipstream of a lipid droplet, through a bicelle-stabilized hole created by the departure of the lipid droplet. Other microbial products (perhaps muramyl dipeptide) might use the same route to access the cytosol. **n**, **o**, The hole created transiently (**n**) closes by coalescence of the luminal and cytoplasmic phospholipid leaflets, leaving polyoma virus in the cytoplasm (**o**).

maintenance of these ionic gradients<sup>26,27</sup>. A transient breach of ER integrity, through modification of pathways via which the ER handles lipids, may be more readily controlled than the (still no less hypothetical) proteinaceous dislocon. The surface to volume ratio of the ER might well tolerate the formation of short-lived holes, with the locally dissipated ion gradients quickly restored.

### Lipid rearrangements and protein extraction from the ER

The formation of a lipid droplet need not go to completion, yet still allow the formation of bicellar structures. Arrangements topologically equivalent to lipid droplets may have a role in removal of unwanted membrane proteins from the ER. Dislocation of class I major histocompatibility complex (MHC) molecules (type I membrane glycoproteins) in cells expressing the viral immunoevasins US2 or US11 yields a cytosolic intermediate that consists of the complete class I MHC heavy chain, with its transmembrane segment intact<sup>9,28</sup>. Although the single N-linked glycan is removed from the class I MHC heavy chain by cytosolic N-glycanase, such removal is dispensable for dislocation: the continued presence of this glycan does not prevent delivery of the class I MHC heavy chain to the cytosol<sup>29,30</sup>. The size alone of the attached high-mannose glycan<sup>31</sup> again raises questions about the identity of the conduit through which dislocation of the glycosylated class I MHC heavy chains occurs. The radius of gyration of the single N-linked glycan attached to a glycoprotein, as predicted by molecular dynamics calculations and based on the structure of the N-linked glycan as determined by nuclear magnetic resonance<sup>32</sup>, would yield an almost protein-sized impediment to dislocation. Even attachment of compactly folded dihydrofolate reductase or green fluorescent protein to the luminal portion of the class I MHC heavy chain does not impede dislocation and results in delivery of the intact fusion protein to the cytoplasm<sup>33,34</sup>. I propose that the action of US2 and US11 creates a local environment favourable to the generation of bicellar structures, through recruitment of proteins or protein complexes that facilitate lipid rearrangements. Perhaps in the case of US2- or US11-dependent dislocation, the lipid droplet equivalent consists of only the class I MHC molecule itself, its transmembrane region shielded by lipids (Fig. 1k). The transmembrane segment of the class I MHC heavy chain would thus be the equivalent of the neutral lipids that otherwise make up lipid droplet content. Why can properly folded class I MHC molecules, devoid of all lysine residues in their cytoplasmic tails, still be detected in ubiquitin-conjugated form<sup>35</sup>, presumably involving lysine residues in the luminal domain for ubiquitin attachment? The intermediates depicted in Fig. 1k immediately suggest the solution. Isolation and chemical analysis of these and other dislocation intermediates should allow a test of this part of the model. Of note, in cells that actively degrade apolipoprotein B (ApoB), the protein is found in association with a subset of lipid droplets, is ubiquitin-modified and recruits proteasomes to the lipid droplets that contain ubiquitin-modified ApoB<sup>36,37</sup>.

Immune recognition makes use of diverse proteolytic pathways to generate peptide fragments that are presented to antigen-specific T lymphocytes, which may then initiate an immune response<sup>38–40</sup>. At least one such pathway, referred to as cross-presentation, involves the transfer into the cytoplasm of materials that originate from endosomal or phagosomal compartments<sup>41–43</sup>, the lumina of which are equivalent to extracellular space. Perhaps not surprisingly, involvement of similar machinery has been invoked to explain both degradation of misfolded proteins that originate in the ER, and cross-presentation<sup>44,45</sup>. However, as argued here, it may not be necessary to postulate the involvement of a proteinaceous protein-conducting channel to accomplish this feat.

- Osborne, A. R., Rapoport, T. A. & van den Berg, B. Protein translocation by the Sec61/SecY channel. *Annu. Rev. Cell Dev. Biol.* **21**, 529–550 (2005).
- Meusser, B., Hirsch, C., Jarosch, E. & Sommer, T. ERAD: the long road to destruction. *Nature Cell Biol.* **7**, 766–772 (2005).
- Romisch, K. Endoplasmic reticulum-associated degradation. *Annu. Rev. Cell Dev. Biol.* **21**, 435–456 (2005).
- Tsai, B., Ye, Y. & Rapoport, T. A. Retro-translocation of proteins from the endoplasmic reticulum into the cytosol. *Nature Rev. Mol. Cell Biol.* **3**, 246–255 (2002).
- Ellgaard, L. & Helenius, A. Quality control in the endoplasmic reticulum. *Nature Rev. Mol. Cell Biol.* **4**, 181–191 (2003).
- Goldberg, A. L. Protein degradation and protection against misfolded or damaged proteins. *Nature* **426**, 895–899 (2003).
- Varshavsky, A. Regulated protein degradation. *Trends Biochem. Sci.* **30**, 283–286 (2005).
- Schekman, R. Cell biology: a channel for protein waste. *Nature* **429**, 817–818 (2004).
- Wiertz, E. J. et al. Sec61-mediated transfer of a membrane protein from the endoplasmic reticulum to the proteasome for destruction. *Nature* **384**, 432–438 (1996).
- Ye, Y., Shibata, Y., Yun, C., Ron, D. & Rapoport, T. A. A membrane protein complex mediates retro-translocation from the ER lumen into the cytosol. *Nature* **429**, 841–847 (2004).
- Lilley, B. N. & Ploegh, H. L. A membrane protein required for dislocation of misfolded proteins from the ER. *Nature* **429**, 834–840 (2004).
- Pelkmans, L., Puntener, D. & Helenius, A. Local actin polymerization and dynamin recruitment in SV40-induced internalization of caveolae. *Science* **296**, 535–539 (2002).
- Lilley, B. N., Gilbert, J. M., Ploegh, H. L. & Benjamin, T. L. Murine polyomavirus requires the endoplasmic reticulum protein Derlin-2 to initiate infection. *J. Virol.* **80**, 8739–8744 (2006).
- Gilbert, J., Ou, W., Silver, J. & Benjamin, T. Downregulation of protein disulfide isomerase inhibits infection by the mouse polyomavirus. *J. Virol.* **80**, 10868–10870 (2006).
- Tsuchi-Sato, K., Ozeki, S., Houjou, T., Taguchi, R. & Fujimoto, T. The surface of lipid droplets is a phospholipid monolayer with a unique Fatty Acid composition. *J. Biol. Chem.* **277**, 44507–44512 (2002).
- Martin, S. & Parton, R. G. Lipid droplets: a unified view of a dynamic organelle. *Nature Rev. Mol. Cell Biol.* **7**, 373–378 (2006).
- McManaman, J. L., Zabaronick, W., Schaack, J. & Orlicky, D. J. Lipid droplet targeting domains of adipophilin. *J. Lipid Res.* **44**, 668–673 (2003).
- Ostermeyer, A. G. et al. Accumulation of caveolin in the endoplasmic reticulum redirects the protein to lipid storage droplets. *J. Cell Biol.* **152**, 1071–1078 (2001).
- Umlauf, E. et al. Association of stomatin with lipid bodies. *J. Biol. Chem.* **279**, 23699–23709 (2004).
- Liu, P. et al. Chinese hamster ovary K2 cell lipid droplets appear to be metabolic organelles involved in membrane traffic. *J. Biol. Chem.* **279**, 3787–3792 (2004).
- Brasaemle, D. L., Dolios, G., Shapiro, L. & Wang, R. Proteomic analysis of proteins associated with lipid droplets of basal and lipolytically stimulated 3T3-L1 adipocytes. *J. Biol. Chem.* **279**, 46835–46842 (2004).
- Baumgart, T., Hess, S. T. & Webb, W. W. Imaging coexisting fluid domains in biomembrane models coupling curvature and line tension. *Nature* **425**, 821–824 (2003).
- van Meer, G. & Sprong, H. Membrane lipids and vesicular traffic. *Curr. Opin. Cell Biol.* **16**, 373–378 (2004).
- Pelkmans, L., Kartenbeck, J. & Helenius, A. Caveolar endocytosis of simian virus 40 reveals a new two-step vesicular-transport pathway to the ER. *Nature Cell Biol.* **3**, 473–483 (2001).
- Liao, S., Lin, J., Do, H. & Johnson, A. E. Both luminal and cytosolic gating of the aqueous ER translocon pore are regulated from inside the ribosome during membrane protein integration. *Cell* **90**, 31–41 (1997).
- de Jong, A. S. et al. The coxsackievirus 2B protein increases efflux of ions from the endoplasmic reticulum and Golgi, thereby inhibiting protein trafficking through the Golgi. *J. Biol. Chem.* **281**, 14144–14150 (2006).
- van Kuppeveld, F. J. et al. Coxsackievirus protein 2B modifies endoplasmic reticulum membrane and plasma membrane permeability and facilitates virus release. *EMBO J.* **16**, 3519–3532 (1997).
- Wiertz, E. J. et al. The human cytomegalovirus US11 gene product dislocates MHC class I heavy chains from the endoplasmic reticulum to the cytosol. *Cell* **84**, 769–779 (1996).
- Blom, D., Hirsch, C., Stern, P., Tortorella, D. & Ploegh, H. L. A glycosylated type I membrane protein becomes cytosolic when peptide: N-glycanase is compromised. *EMBO J.* **23**, 650–658 (2004).
- Misaghi, S., Pacold, M. E., Blom, D., Ploegh, H. L. & Korbel, G. A. Using a small molecule inhibitor of peptide: N-glycanase to probe its role in glycoprotein turnover. *Chem. Biol.* **11**, 1677–1687 (2004).
- Daniels, R., Svedine, S. & Hebert, D. N. N-linked carbohydrates act as luminal maturation and quality control protein tags. *Cell Biochem. Biophys.* **41**, 113–138 (2004).
- Rudd, P. M. et al. The effects of variable glycosylation on the functional activities of ribonuclease, plasminogen and tissue plasminogen activator. *Biochim. Biophys. Acta* **1248**, 1–10 (1995).
- Tirosh, B., Furman, M. H., Tortorella, D. & Ploegh, H. L. Protein unfolding is not a prerequisite for endoplasmic reticulum-to-cytosol dislocation. *J. Biol. Chem.* **278**, 6664–6672 (2003).



34. Fiebigler, E., Story, C., Ploegh, H. L. & Tortorella, D. Visualization of the ER-to-cytosol dislocation reaction of a type I membrane protein. *EMBO J.* **21**, 1041–1053 (2002).
  35. Furman, M. H., Loureiro, J., Ploegh, H. L. & Tortorella, D. Ubiquitinylation of the cytosolic domain of a type I membrane protein is not required to initiate its dislocation from the endoplasmic reticulum. *J. Biol. Chem.* **278**, 34804–34811 (2003).
  36. Ohsaki, Y., Cheng, J., Fujita, A., Tokumoto, T. & Fujimoto, T. Cytoplasmic lipid droplets are sites of convergence of proteasomal and autophagic degradation of apolipoprotein B. *Mol. Biol. Cell* **17**, 2674–2683 (2006).
  37. Fujimoto, T. & Ohsaki, Y. Proteasomal and autophagic pathways converge on lipid droplets. *Autophagy* **2**, 299–301 (2006).
  38. Loureiro, J. & Ploegh, H. L. Antigen presentation and the ubiquitin-proteasome system in host-pathogen interactions. *Adv. Immunol.* **92**, 225–305 (2006).
  39. Heemels, M. T. & Ploegh, H. Generation, translocation, and presentation of MHC class I-restricted peptides. *Annu. Rev. Biochem.* **64**, 463–491 (1995).
  40. Cresswell, P. Assembly, transport, and function of MHC class II molecules. *Annu. Rev. Immunol.* **12**, 259–293 (1994).
  41. Cresswell, P., Ackerman, A. L., Giodini, A., Peaper, D. R. & Wearsch, P. A. Mechanisms of MHC class I-restricted antigen processing and cross-presentation. *Immunol. Rev.* **207**, 145–157 (2005).
  42. Ackerman, A. L. & Cresswell, P. Cellular mechanisms governing cross-presentation of exogenous antigens. *Nature Immunol.* **5**, 678–684 (2004).
  43. Guermonprez, P. *et al.* ER-phagosome fusion defines an MHC class I cross-presentation compartment in dendritic cells. *Nature* **425**, 397–402 (2003).
  44. Imai, J., Hasegawa, H., Maruya, M., Koyasu, S. & Yahara, I. Exogenous antigens are processed through the endoplasmic reticulum-associated degradation (ERAD) in cross-presentation by dendritic cells. *Int. Immunol.* **17**, 45–53 (2005).
  45. Ackerman, A. L., Giodini, A. & Cresswell, P. A role for the endoplasmic reticulum protein retrotranslocation machinery during crosspresentation by dendritic cells. *Immunity* **25**, 607–617 (2006).
- Acknowledgements** I thank E. Klemm, J. Loureiro and B. Mueller, as well as D. Hoekstra and G. van Meer, for discussions. I thank T. Di Cesare for the artwork.
- Author Information** Reprints and permissions information is available at [www.nature.com/reprints](http://www.nature.com/reprints). The author declares no competing financial interests. Correspondence should be addressed to H.L.P. ([ploegh@wi.mit.edu](mailto:ploegh@wi.mit.edu)).

# A transforming mutation in the pleckstrin homology domain of AKT1 in cancer

John D. Carpten<sup>1</sup>, Andrew L. Faber<sup>2</sup>, Candice Horn<sup>2</sup>, Gregory P. Donoho<sup>2</sup>, Stephen L. Briggs<sup>3</sup>, Christiane M. Robbins<sup>1</sup>, Galen Hostetter<sup>1</sup>, Sophie Boguslawski<sup>2</sup>, Tracy Y. Moses<sup>1</sup>, Stephanie Savage<sup>1</sup>, Mark Uhlik<sup>2</sup>, Aimin Lin<sup>4</sup>, Jian Du<sup>2</sup>, Yue-Wei Qian<sup>4</sup>, Douglas J. Zeckner<sup>2</sup>, Greg Tucker-Kellogg<sup>5</sup>, Jeffrey Touchman<sup>1</sup>, Ketan Patel<sup>5</sup>, Spyro Mousses<sup>6</sup>, Michael Bittner<sup>1</sup>, Richard Schevitz<sup>3</sup>, Mei-Huei T. Lai<sup>2</sup>, Kerry L. Blanchard<sup>2</sup> & James E. Thomas<sup>2</sup>

Although AKT1 (v-akt murine thymoma viral oncogene homologue 1) kinase is a central member of possibly the most frequently activated proliferation and survival pathway in cancer, mutation of *AKT1* has not been widely reported. Here we report the identification of a somatic mutation in human breast, colorectal and ovarian cancers that results in a glutamic acid to lysine substitution at amino acid 17 (E17K) in the lipid-binding pocket of AKT1. Lys 17 alters the electrostatic interactions of the pocket and forms new hydrogen bonds with a phosphoinositide ligand. This mutation activates AKT1 by means of pathological localization to the plasma membrane, stimulates downstream signalling, transforms cells and induces leukaemia in mice. This mechanism indicates a direct role of AKT1 in human cancer, and adds to the known genetic alterations that promote oncogenesis through the phosphatidylinositol-3-OH kinase/AKT pathway. Furthermore, the E17K substitution decreases the sensitivity to an allosteric kinase inhibitor, so this mutation may have important clinical utility for AKT drug development.

AKT activation is driven by membrane localization initiated by binding of the pleckstrin homology domain (PHD) to phosphatidylinositol-3,4,5-trisphosphate (PtdIns(3,4,5)P<sub>3</sub>) or phosphatidylinositol-3,4-bisphosphate (PtdIns(3,4)P<sub>2</sub>), followed by phosphorylation of the regulatory amino acids serine 473 (Ser 473) and threonine 308 (Thr 308) (ref. 1). The pathological association of AKT with the plasma membrane is a common thread that connects AKT to cancer. The oncogenic behaviour of the Gag-AKT fusion protein from the murine leukaemia retrovirus AKT8 requires a membrane-targeting myristoylation signal—the first presumptive evidence that pathological membrane localization of AKT1 kinase activity could be transforming in mice<sup>2</sup>. The importance of AKT in human cancer is largely inferred from common recurring mutations in enzymes that produce or degrade short-lived second messenger phospholipids (for example, PtdIns(3,4,5)P<sub>3</sub> or its metabolite, PtdIns(3,4)P<sub>2</sub>) and consequently indirectly activate AKT through membrane recruitment. Tumours from patients with breast and colorectal cancer frequently harbour activating somatic mutations in PIK3CA, the catalytic subunit of phosphatidylinositol-3-OH kinase (PI(3)K)—an enzyme that catalyses the production of D3-phosphorylated phosphoinositides<sup>3–8</sup>. In addition, the loss of phosphatase and tensin homologue (*PTEN*) lipid phosphatase activity in glioblastoma, prostate and endometrial cancers by means of somatic mutations<sup>9</sup>, or in breast cancer by means of epigenetic silencing<sup>10</sup>, represents an alternative indirect mechanism for activating AKT by inhibiting the breakdown of PtdIns(3,4,5)P<sub>3</sub> and PtdIns(3,4)P<sub>2</sub>. Finally, Cowden's disease, an inherited cancer syndrome, results from germline mutations in the gene for *PTEN*<sup>9</sup>. Hence, AKT1 mainly seems to have a passive role in oncogenesis as an indirect intermediary between mutated upstream regulatory proteins and downstream signalling molecules<sup>11</sup>.

The PHD has a critical regulatory role in AKT function, and disruption of PHD function seems to be important in biology and disease. In *Drosophila*, cellular survival in the presence of high levels of PtdIns(3,4,5)P<sub>3</sub> was only possible if the *Drosophila* AKT PHD was inactivated<sup>12</sup>. Naturally occurring mutations in the PHD of Bruton's tyrosine kinase interfere with phosphoinositide binding and result in X-linked agammaglobulinaemia in humans and X-linked immunodeficiency in mice<sup>13</sup>. Introduction of a homologous mutation into the PHD of AKT1—an arginine to cysteine substitution at amino acid 25 (AKT1(R25C))—results in a kinase that does not efficiently bind phosphoinositides, fails to localize to the membrane, and is not activated<sup>14</sup>. AKT1 does not efficiently transform cells in culture<sup>15</sup>, unless, like its retroviral homologue, it is targeted to the membrane by a myristoylation signal<sup>16–18</sup>. Given the importance of AKT activation in cancer, we initiated a study to determine whether mutations in AKT might exist in human cancer. We have identified a previously unknown mechanism for AKT1-mediated transformation driven by a recurring mutation in the PHD of AKT1 that leads to pathological association of AKT1 with the plasma membrane and constitutive activation.

## Identification of a mutation in the PHD of AKT1

We evaluated the complete coding regions of AKT family members for mutations in genomic DNA from clinical tumour specimens representing breast ( $n = 61$ ), colorectal ( $n = 51$ ) and ovarian ( $n = 50$ ) cancers. No genetic alterations were found in the catalytic domain of *AKT1*, *AKT2* or *AKT3* in breast, colorectal or ovarian clinical cancer specimens; however, further analysis of these samples revealed a unique mutation in the PHD of *AKT1*. A G > A point mutation at nucleotide 49 that results in a lysine substitution for glutamic acid at amino acid 17 (AKT(E17K)) was identified in 5 of

<sup>1</sup>Division of Integrated Cancer Genomics, Translational Genomics Research Institute, 445 N. Fifth Street, Phoenix, Arizona 85004, USA. <sup>2</sup>Cancer Discovery Research, <sup>3</sup>Global Structural Biology, <sup>4</sup>Integrative Biology, Lilly Research Laboratories, Eli Lilly & Company, Indianapolis, Indiana 46285, USA. <sup>5</sup>Lilly Singapore Centre for Drug Discovery, 1 Science Park Road 04-01, The Capricorn, Singapore Science Park II, 117528 Singapore. <sup>6</sup>Pharmaceutical Genomics, Translational Genomics Research Institute, TGen Suite 110, 13208 E. Shea Boulevard, Scottsdale, Arizona 85259, USA.



61 (8%) breast, 3 of 51 (6%) colorectal and 1 of 50 (2%) ovarian cancers (Supplementary Table 1 and Supplementary Fig. 1). DNA from normal adjacent tissue or white blood cells was sequenced to verify that the mutation is somatic (data not shown). The AKT1 mutation is mutually exclusive with respect to mutations in PIK3CA and complete loss of PTEN protein expression (Supplementary Table 1 and Supplementary Fig. 2). Although the sample size was insufficient to document statistical significance, the lack of coincidence of these mutations indicates that the AKT1 mutation is sufficient for pathological activation of the PI(3)K/AKT pathway. This mutation is not present in the Catalogue of Somatic Mutations in Cancer (COSMIC; <http://www.sanger.ac.uk/genetics/CGP/cosmic/>) and was not revealed in a recent report of large-scale sequencing of approximately 13,000 genes in breast and colorectal cancers<sup>19</sup>.

### E17K alters AKT1-PHD conformation

The binding of phosphoinositides to the PHD activates AKT1. In the *apo* conformation, Glu 17 occupies the phosphoinositide-binding pocket and forms a network of hydrogen bonds<sup>20</sup>. Entry of the PtdIns(3,4,5)P<sub>3</sub> and PtdIns(3,4)P<sub>2</sub> inositol head groups disrupts this conformation, thus Glu 17 has a pivotal role in AKT1 activation<sup>20,21</sup>. We have solved the crystal structure of wild-type and E17K PHDs from human AKT1 to 1.1 Å and 1.9 Å resolution, respectively, as well as the E17K PHD–Ins(1,3,4,5)P<sub>4</sub> complex to 2.6 Å resolution. In the *apo* conformation, acidic Glu 17 forms an ionic interaction with basic Lys 14 in the pocket<sup>20</sup> (Fig. 1a, the line represents the interaction); however, in the case of the Lys 17 substitution in E17K PHD, the positively charged Lys 17 cannot interact with Lys 14 (Fig. 1b). Moreover, the Lys 17 substitution results in a shift in the surface charge around the pocket from negative with Glu 17 to effectively neutral in the mutant (Supplementary Fig. 3). To accommodate the inositol head group in the wild-type PHD, Glu 17 swings down and away (4.7 Å) from the pocket, as does Tyr 18 (Protein Data Bank code: 1UNQ). In the E17K PHD, Tyr 18 moves 7.5 Å out of the pocket and forms a hydrogen bond with Lys 17. Additional hydrogen bonds form between Lys 17, a conserved water molecule and the 5-phosphate and 6-hydroxyl of Ins(1,3,4,5)P<sub>4</sub> (Fig. 1c). Lys 17 could enhance the affinity or decrease the off-rate of D5-phosphorylated phosphoinositides for AKT1, or both. Notably, the PHD of phosphoinositide-dependent protein kinase 1 (PDK1; also called PDKP1) contains a lysine at the position homologous to Glu 17 in AKT1 (ref. 22), and PDK1, unlike AKT1, shows higher affinity for PtdIns(3,4,5)P<sub>3</sub> than for PtdIns(3,4)P<sub>2</sub> (refs 23–25).

### Activation of AKT1 by the E17K mutation

To assess the effects of the E17K mutation on AKT1 regulation, we expressed Flag-tag-fused AKT1(WT), AKT1(E17K) or AKT1(R25C) in NIH 3T3 cells. Unlike the R25C PHD, the E17K substitution

resulted in an increased level of AKT phosphorylation on Thr 308 and Ser 473 compared to wild-type (Fig. 2a, c, lower panel). After immunoprecipitation with a Flag antibody, AKT1(E17K) kinase activity was approximately fourfold higher than that of AKT1(WT), and AKT1(R25C) kinase activity was significantly lower than that of AKT1(WT) (Fig. 2b). In whole-cell lysates the expression levels of AKT1(WT), AKT1(E17K) and AKT1(R25C) were similar (Fig. 2c, lower panel), whereas the amount of AKT1(E17K) and AKT1(R25C) immunoprecipitated by the Flag antibody was slightly less than AKT1(WT) (Fig. 2c, upper panel). Nevertheless, the level of AKT1(E17K) *in vitro* kinase activity was significantly higher than that of AKT1(WT) or AKT1(R25C), indicating that the E17K substitution alters AKT1 regulation and enhances cellular activity. An increase in phosphorylation on the AKT substrate FKHR1 was observed in AKT1(E17K)-transfected cells compared to either vector-transfected or AKT1(WT)-transfected cells under serum-starved conditions (Fig. 2d, lanes 4–6) or in confluent cultures (data not shown), but was not apparent in subconfluent cultures grown in 10% serum (Fig. 2d, lanes 1–3). These results indicate that AKT1(E17K) upregulates survival signalling under adverse conditions.

The kinetic properties of purified AKT1(WT) and AKT1(E17K) were assessed in an *in vitro* kinase assay using a synthetic peptide substrate, 'Crosstide'. Neither AKT1(WT) nor AKT1(E17K) had measurable *in vitro* kinase activity before activation by phosphorylation (data not shown). After *in vitro* activation, the Michaelis constants (*K<sub>m</sub>*) for both ATP and Crosstide (Supplementary Fig. 4a, b) were similar for AKT1(WT) and AKT1(E17K), indicating that the increased activity of AKT1(E17K) observed in cells is not because the mutation changes the biochemical properties of the kinase, but probably reflects the increased phosphorylation of AKT1 induced by the E17K mutation in the PHD. We next examined the sensitivity of activated AKT1(E17K) to AKT1/2 inhibitor VIII—an inhibitor that does not compete with ATP or peptide, but does require the PHD<sup>26</sup>. The half-maximal inhibitory concentrations (IC<sub>50</sub> values) for AKT1/2 inhibitor VIII for AKT1(E17K) and AKT1(WT) were 0.53 μM and 0.11 μM, respectively (Supplementary Fig. 4c), whereas the IC<sub>50</sub> values for ATP-competitive inhibitors were nearly identical (data not shown). Hence, the E17K PHD mutation may result in structural changes in the PHD that alter its interaction with AKT1/2 inhibitor VIII.

### E17K alters the subcellular location of AKT1

Translocation of a green fluorescent protein (GFP)–AKT1 PHD fusion protein from the cytoplasm to the plasma membrane is dependent on growth-factor-stimulation of serum-starved cells<sup>27</sup>. To determine whether the E17K mutation alters protein localization, we tracked the position of GFP-tagged wild-type PHD (GFP-PH(WT)) or GFP-tagged E17K PHD (GFP-PH(E17K)) chimaeric

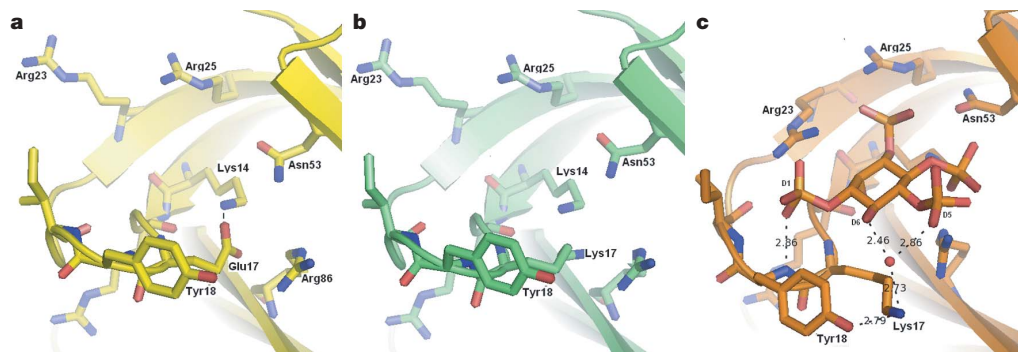


**Figure 1 | Lys 17 alters the *apo* and Ins(1,3,4,5)P<sub>4</sub>-complexed AKT1 PHD structure.** **a**, In *apo* wild-type PHD, an ionic interaction between Glu 17 and Lys 14 (line) fills the binding pocket. **b**, E17K PHD *apo* with Lys 17 turned away from Lys 14. **c**, E17K PHD with Lys 17 involved in new hydrogen bonds (dashed lines) with a water molecule (orange sphere), interposed with the

D6-hydroxyl group, and the D5-phosphate of Ins(1,3,4,5)P<sub>4</sub> (orange). Lys 17 also forms a new hydrogen bond with the hydroxyl of Tyr 18. The D1-phosphate forms a hydrogen bond with the amide of Tyr 18, similar to the wild-type PHD. Distances shown are in angstroms.

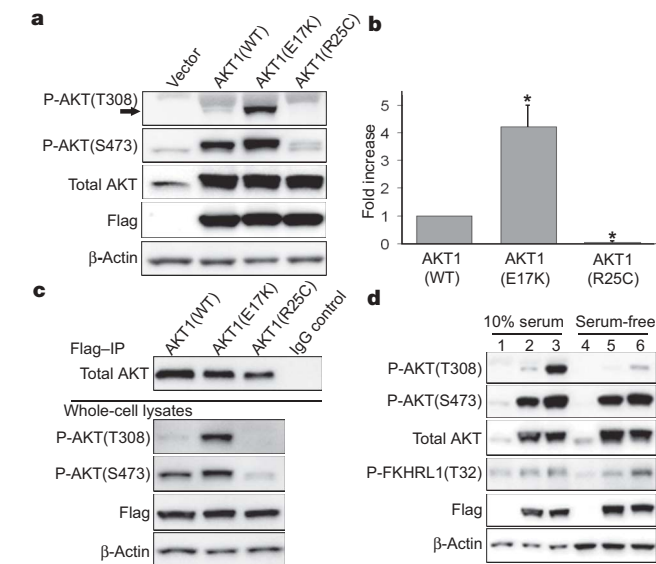


**Figure 2 | The E17K mutation increases AKT1 activation in NIH 3T3 cells.** **a**, Immunoblots from cells transfected with vector, Flag-tagged AKT1(WT), Flag-tagged AKT1(E17K) or Flag-tagged AKT1(R25C). The arrow represents the position of AKT. **b**, Kinase activity of AKT1(WT), AKT1(E17K) or AKT1(R25C) immunoprecipitated with Flag antibody. Values were normalized against an IgG control and fold activity is expressed relative to AKT1(WT). Error bars, s.e.m. ( $n = 4$ , asterisk,  $P < 0.002$  Tukey's HSD). **c**, Immunoprecipitated Flag-tagged protein (Flag-IP) was immunoblotted with total AKT antibody (upper panel). Whole-cell lysates of AKT1(WT), AKT1(E17K) and AKT1(R25C) were immunoblotted for P-AKT (S473 or T308), Flag or β-actin (lower panel). **d**, Immunoblots of P-AKT and phosphorylated FKHRL1 (P-FKHRL1) in cells transfected with vector (lanes 1 and 4), AKT1(WT) (lanes 2 and 5) or AKT1(E17K) (lanes 3 and 6). Cells were grown in 10% serum-supplemented media (lanes 1–3) or shifted into serum-free media for 24 h, 48 h after transfection (lanes 4–6).

proteins by immunofluorescence. Under serum-starved conditions, GFP-PH(WT) was found in the cytoplasm and nucleus, but rapidly translocated to the plasma membrane on platelet-derived growth factor (PDGF) stimulation (Fig. 3a, and Supplementary Movie 1). In contrast, GFP-PH(E17K) was localized to the plasma membrane in the absence of serum stimulation and was only slightly stimulated by PDGF (Fig. 3a, and Supplementary Movie 2). A GFP-tagged R25C PHD (GFP-PH(R25C)) was found throughout the cell, including the membrane and cytoplasm, and did not translocate to the plasma membrane on PDGF stimulation (Supplementary Movie 3). The PI(3)K inhibitor LY294002 inhibited PDGF-stimulated translocation of GFP-PH(WT) to the plasma membrane; however, this inhibitor had minimal effect on the localization of GFP-PH(E17K) either in the absence or in the presence of PDGF stimulation (Fig. 3a, and Supplementary Movies 4 and 5). The E17K mutation seems to abrogate the requirement of the AKT1 PHD for D3-phosphorylated phosphoinositides for inducing membrane association, as GFP-PH(E17K) is still detected at the plasma membrane when membrane levels of PtdIns(3,4,5)P<sub>3</sub> or PtdIns(3,4)P<sub>2</sub> are low<sup>27</sup>.

We next assessed the localization and activation of full-length AKT1(E17K) by biochemical fractionation of NIH 3T3 cells that transiently express Flag-tagged AKT1(E17K). Western blot analysis revealed that both AKT1(WT) and AKT1(E17K) were found at the plasma membrane under serum-starved conditions, although the highest fraction of both proteins was in the cytoplasm (Fig. 3b). Under serum-starved conditions, the level of membrane-associated AKT phosphorylated at Thr 308 and Ser 473 (P-AKT) was more than 4.5-fold higher in the AKT1(E17K)-transfected cells than that in the AKT1(WT)-transfected cells (Fig. 3b, and Supplementary Fig. 5). The increased level of P-AKT Thr 308 or Ser 473 in AKT1(E17K) compared to AKT1(WT) in the membrane fractions

of the serum-starved cells is not entirely caused by the nominal increase in the level of Flag tag detected in these lysates. Thus, the E17K mutation not only facilitates membrane localization but also results in increased phosphorylation of AKT in the absence of serum. PDGF stimulation of both AKT1(WT)-transfected and AKT1(E17K)-transfected cells activates AKT phosphorylation at Thr 308 and Ser 473 to nearly the same extent, which indicates that the mutation does not alter the normal physiological response to growth factors. Moreover, the results are consistent with the concept that AKT1 activation is linked to positional information<sup>25,28</sup>, and indicate that the increased kinase activity associated with AKT1(E17K) may be owing to an increased presence at the plasma membrane.

### AKT1(E17K) transforms cells in culture

To assess whether the E17K mutation is sufficient to transform, we infected Rat1 cells with retroviral constructs that encode Myr-AKT1, AKT1(WT) or AKT1(E17K). Foci developed on the AKT1(E17K) and Myr-AKT1 infected cells 15 d after cells were confluent (Fig. 4a, and Supplementary Fig. 6), and soft agar colonies were observed 25 d after initial infections (Fig. 4b). No foci were observed either on the control vector or on the control AKT1(WT) plates, nor were soft agar colonies detected on the control vector plates. Only five colonies were apparent on the AKT1(WT) plates. In contrast, the introduction of AKT1(E17K) and Myr-AKT1 resulted in generation of 43 and 61 colonies, respectively. These constructs contain a GFP reporter gene, and the soft agar colonies that were observed in these assays expressed GFP (Fig. 4c). We found increased levels of P-AKT Ser 473 and Thr 308 in

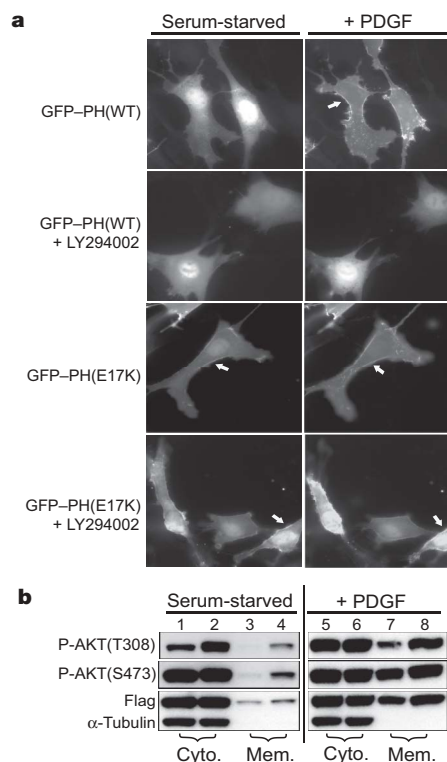


**Figure 3 | The E17K mutation alters AKT1 cellular localization.** **a**, Still images from Supplementary Movies demonstrating the localization of GFP-PH in serum-starved GFP-PH(WT)-expressing and GFP-PH(E17K)-expressing NIH 3T3 cells stimulated with PDGF. Cells were serum-starved before being stimulated with PDGF or treated with LY294002 (20 μM). Cells were imaged at ×63 magnification; the arrows highlight membrane localization. **b**, Immunoblot analysis of AKT1 localization by biochemical cell fractionation of NIH 3T3 cells transfected with AKT1(WT) (lanes 1, 3, 5 and 7) or AKT1(E17K) (lanes 2, 4, 6 and 8). Eight or twenty-five micrograms of isolated cytoplasmic (cyto.) or membrane (mem.) proteins were loaded per lane, respectively. This result is representative of three identical experiments.



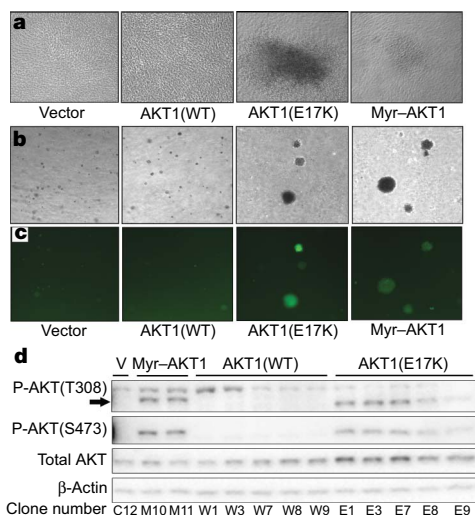


**Figure 4 | Transformation of Rat1 fibroblasts by AKT1(E17K).** **a**, Monolayer background of Rat1 cells transduced with vector alone or AKT1(WT), and representative foci transduced by AKT1(E17K) or Myr-AKT1 retrovirus. Colonies were imaged ( $\times 4$  magnification) approximately 15 d after becoming confluent. **b**, Representative images from parallel soft agar colony growth experiment with transduced cells from **a**. Colonies were imaged 29 d after initial infection. **c**, Detection of GFP expression in soft agar colonies ( $\times 4$  magnification). **d**, Immunoblot analysis of isolated clones from foci formation plates (T308, arrow).

several AKT1(E17K)-expressing or Myr-AKT1-expressing clones compared to control vector- or AKT1(WT)-infected cells (Fig. 4d), and sequence analysis confirmed the expression of each transgene, Myr-AKT1, AKT1(WT) or AKT1(E17K), as expected for each clone (data not shown). The E17K mutation transforms cells in culture, consistent with our initial hypothesis that this mutation is oncogenic in human cancers.

#### AKT1(E17K) induces leukaemia in mice

Adoptive transfer of embryonic liver haematopoietic stem cells from the  $E_{\mu}$ -Myc transgenic mouse (TgN(IgH-Myc)22Bri) (ref. 29) modified to express the murine anti-apoptotic protein Bcl2, the eukaryotic initiation factor 4E (eIF4E) or Myr-AKT1 rapidly induce B-cell lymphomas<sup>30</sup>. We have used a similar system to generate cancers that require the presence of the Myc transgene as well as a second oncogene. In our investigation, expression of human Myr-AKT1, Bcl2 or eIF4E led to leukaemia rather than lymphomas (data not shown). The difference in cancer phenotype could be due to genetic variation in mouse colonies carrying the  $E_{\mu}$ -Myc transgene<sup>31</sup>, or to our use of the human rather than the murine oncogenes.

We investigated whether expression of the human AKT1(E17K) allele could induce leukaemia similar to Myr-AKT1. Cells from pooled embryonic  $E_{\mu}$ -Myc livers were mock-transduced, or transduced with a retroviral vector that expresses AKT1(WT), Myr-AKT1 or AKT1(E17K), in addition to a GFP reporter gene. Flow cytometry of nucleated peripheral blood cells showed increasing P-AKT Ser 473 and/or GFP fluorescence signals over time in Myr-AKT1 and AKT1(E17K) animals; however, neither AKT1(WT) nor mock transduction animals showed any P-AKT Ser 473 or GFP above background levels in C57BL/6J mice (Fig. 5a, b). All of the Myr-AKT1-transduced mice developed leukaemia, whereas six out of ten of the AKT1(E17K) mice and none of the AKT1(WT) mice developed leukaemia. The fraction of mice that developed leukaemia (E17K versus wild-type) was statistically significant in both Wilcoxon and log-rank analysis (both  $P = 0.0041$  and  $P = 0.047$ , respectively). The leukaemic cells from AKT1(E17K) mice were 20–30  $\mu$ m in diameter, had basophilic cytoplasm, and had nuclei with an irregular folded-to-cleaved morphology and generally inconspicuous nucleoli:

cytological characteristics of lymphoblasts (Fig. 5c). The E17K leukaemic blasts are slightly B220<sup>+</sup>, CD11b<sup>+</sup> and CD3<sup>−</sup>, consistent with a pre-pro-B-cell leukaemia, and express GFP and P-AKT Ser 473. In contrast, the Myr-AKT blasts are B220<sup>+</sup>, but CD11b<sup>−</sup> and CD3<sup>−</sup>, consistent with a more mature B-cell leukaemia. Expression of AKT1(E17K) and Myr-AKT was confirmed by sequence analysis of RNA from lysed nucleated cells (data not shown).

#### Clinical implications

AKT gene family members have been associated with cancer in humans by analysing gene copy number; especially prominent is the genetic amplification of AKT2 (refs 32, 33). AKT1 gene amplification was detected in a single gastric carcinoma out of a screen of more than 225 diverse human malignancies<sup>34</sup>, and in 1 gliosarcoma out of 103 malignant glial cancers<sup>35</sup>. Another study found that AKT1 kinase

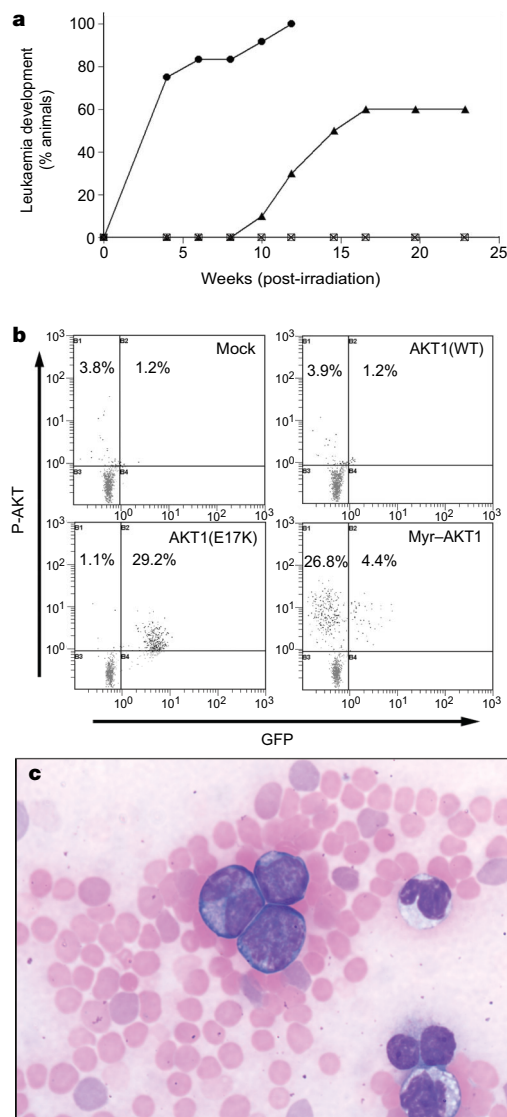


**Figure 5 | Timing and signature of AKT1(E17K)-driven leukaemia.**

**a**, Timing of leukaemia onset as determined by the appearance of discernible P-AKT(Ser 473)-GFP cells in blood of rescued lethally irradiated host animals. Myr-AKT1 ( $n = 12$ , solid circles), AKT1(E17K) ( $n = 10$ , filled triangles), AKT1(WT) ( $n = 10$ , open squares) and mock transduction ( $n = 3$ , X) is shown. **b**, Representative flow cytometry results from leukaemic mice (AKT1(E17K) and Myr-AKT1) and non-leukaemic mice (Mock and AKT1(WT)) after staining for P-AKT(Ser 473). **c**, Stained blood smear from a representative AKT1(E17K) animal showing leukaemic blasts ( $\times 100$  magnification).

activity was frequently elevated in several high-grade, late-stage cancers; however, several of these cancers had corresponding elevations in PI(3)K or loss of PTEN expression, hence the mechanism for AKT1 activation is unclear<sup>18</sup>. A comprehensive screen of human cancers for genetic mutations in the catalytic domains of 340 serine/threonine kinases did not reveal any AKT1 mutations<sup>33</sup>, nor did a specific screen of the kinase domains of AKT1, AKT2 or AKT3 (ref. 36). In ref. 33, 2 mutations were found in AKT2 out of 204 colorectal cancer samples; however, the physiological role of these mutations was not reported. Here we provide direct evidence for the involvement of AKT1 in human cancer by means of structural, biochemical and biological studies.

We have demonstrated the oncogenic potential of the E17K mutation, and have revealed detailed aspects of the molecular and cellular mechanisms of activation. This recurring mutation in a regulatory domain of AKT1 leads to structural alteration of the ligand-binding site, pathological membrane association, constitutive activation of the kinase, *in vitro* transformation, soft agar colony formation and leukaemia in mice. Whether this mutation provides prognostic significance in cancer, or is predictive of response to a particular therapy, is not known. One could surmise that how the PI(3)K/AKT pathway is activated may define whether a patient will respond to a particular therapy. Indeed, our studies show that the E17K mutation does not alter the sensitivity of AKT1 to ATP competitive inhibitors, yet does alter the sensitivity to an allosteric kinase inhibitor.

## METHODS SUMMARY

Samples were obtained under approved human subjects institutional review and contained >60% cancer. Exons were amplified from genomic DNA, sequenced using BigDye terminator chemistry and separated on ABI DNA analysers. Centre d'Etude du Polymorphisme Humain (CEPH) 1347-02 was the normal reference. Immunohistochemistry was performed using a BondMax autostainer. AKT1 (E17K) and AKT1(R25C) were generated by site-directed mutagenesis. pMSCV6-PGK/GFP and pMSCV6-Myr-AKT1-PGK/GFP were derived from pMSCVneo<sup>37</sup>. Ecotropic retrovirus was generated in HEK293T. Flag-tagged AKT1 was purified on anti-Flag M2 agarose, confirmed by matrix-assisted laser desorption/ionization, and activated with mitogen-activated protein kinase-activated protein kinase 2 (MAPKAP K2) and PDK1. Kinase activity was determined using K-LISA AKT activity kit. In the immunoprecipitation studies, NIH3T3 cells were treated with lysis buffer, and lysates were mixed with anti-Flag antibody and protein G-sepharose. Phosphorylated AKT substrate was detected using anti-pPRAS40 (proline-rich AKT substrate) (Thr 246). Cell fractionation was performed as described<sup>28</sup> with minor modifications. Live-cell imaging was performed at  $\times 63$  magnification on a Leica DMI6000B inverted microscope. For foci formation or anchorage-independent growth studies, Rat1 cells were transduced with retrovirus. In the leukaemia induction studies, liver cells from C57BL/6J  $\times$  C57BL/6Jtg(IgH-Myc)22Bri/J embryos were transduced with retrovirus and injected into lethally irradiated C57BL/6J hosts. Co-crystals of apo AKT1(WT) PHD and AKT1(E17K) PHD, or AKT1(E17K) and Ins (1,3,4,5)P<sub>4</sub>, were grown from hanging drops in 0.1 M HEPES (pH 7.5) and 1.4 M sodium citrate, or in 0.1 M sodium acetate (pH 4.6), 0.2 M ammonium acetate and 15–30% poly(ethylene glycol) 3350, respectively. Data were collected at the Argonne National Laboratory, Industrial Macromolecular Crystallography Association, beam line 17-ID. Antibodies were: anti-Flag (M2) and  $\beta$ -actin (AC-15); total AKT and P-AKT (Ser 473); P-AKT (Thr 308) and P-FKHRL1 (Thr 32); and  $\alpha$ -tubulin (TU-02).

**Full Methods** and any associated references are available in the online version of the paper at [www.nature.com/nature](http://www.nature.com/nature).

Received 8 March; accepted 11 May 2007.

Published online 4 July 2007.

- Vivanco, I. & Sawyers, C. L. The phosphatidylinositol 3-kinase AKT pathway in human cancer. *Nature Rev. Cancer* **2**, 489–501 (2002).
- Ahmed, N. N. *et al.* The proteins encoded by *c-akt* and *v-akt* differ in post-translational modification, subcellular localization and oncogenic potential. *Oncogene* **8**, 1957–1963 (1993).
- Bachman, K. E. *et al.* The *PIK3CA* gene is mutated with high frequency in human breast cancers. *Cancer Biol. Ther.* **3**, 772–775 (2004).
- Campbell, I. G. *et al.* Mutation of the *PIK3CA* gene in ovarian and breast cancer. *Cancer Res.* **64**, 7678–7681 (2004).
- Lee, J. W. *et al.* *PIK3CA* gene is frequently mutated in breast carcinomas and hepatocellular carcinomas. *Oncogene* **24**, 1477–1480 (2005).
- Levine, D. A. *et al.* Frequent mutation of the *PIK3CA* gene in ovarian and breast cancers. *Clin. Cancer Res.* **11**, 2875–2878 (2005).
- Saai, L. H. *et al.* *PIK3CA* mutations correlate with hormone receptors, node metastasis, and ERBB2, and are mutually exclusive with PTEN loss in human breast carcinoma. *Cancer Res.* **65**, 2554–2559 (2005).
- Samuels, Y. *et al.* High frequency of mutations of the *PIK3CA* gene in human cancers. *Science* **304**, 554 (2004).
- Cantley, L. C. & Neel, B. G. New insights into tumor suppression: PTEN suppresses tumor formation by restraining the phosphoinositide 3-kinase/AKT pathway. *Proc. Natl Acad. Sci. USA* **96**, 4240–4245 (1999).
- Khan, S. *et al.* PTEN promoter is methylated in a proportion of invasive breast cancers. *Int. J. Cancer* **112**, 407–410 (2004).
- Cantley, L. C. The phosphoinositide 3-kinase pathway. *Science* **296**, 1655–1657 (2002).
- Stocker, H. *et al.* Living with lethal PIP3 levels: viability of flies lacking PTEN restored by a PH domain mutation in Akt/PKB. *Science* **295**, 2088–2091 (2002).
- Fukuda, M., Kojima, T., Kabayama, H. & Mikoshiba, K. Mutation of the pleckstrin homology domain of Bruton's tyrosine kinase in immunodeficiency impaired inositol 1,3,4,5-tetrakisphosphate binding capacity. *J. Biol. Chem.* **271**, 30303–30306 (1996).
- Franke, T. F. *et al.* The protein kinase encoded by the Akt proto-oncogene is a target of the PDGF-activated phosphatidylinositol 3-kinase. *Cell* **81**, 727–736 (1995).
- Li, W., Zhu, T. & Guan, K. L. Transformation potential of Ras isoforms correlates with activation of phosphatidylinositol 3-kinase but not ERK. *J. Biol. Chem.* **279**, 37398–37406 (2004).
- Andjelkovic, M. *et al.* Role of translocation in the activation and function of protein kinase B. *J. Biol. Chem.* **272**, 31515–31524 (1997).
- Mirza, A. M., Kohn, A. D., Roth, R. A. & McMahon, M. Oncogenic transformation of cells by a conditionally active form of the protein kinase Akt/PKB. *Cell Growth Differ.* **11**, 279–292 (2000).
- Sun, M. *et al.* AKT1/PKB $\alpha$  kinase is frequently elevated in human cancers and its constitutive activation is required for oncogenic transformation in NIH3T3 cells. *Am. J. Pathol.* **159**, 431–437 (2001).
- Sjoberg, T. *et al.* The consensus coding sequences of human breast and colorectal cancers. *Science* **314**, 268–274 (2006).
- Milburn, C. C. *et al.* Binding of phosphatidylinositol 3,4,5-trisphosphate to the pleckstrin homology domain of protein kinase B induces a conformational change. *Biochem. J.* **375**, 531–538 (2003).
- Thomas, C. C., Deak, M., Alessi, D. R. & van Aalten, D. M. High-resolution structure of the pleckstrin homology domain of protein kinase B/Akt bound to phosphatidylinositol (3,4,5)-trisphosphate. *Curr. Biol.* **12**, 1256–1262 (2002).
- Komander, D. *et al.* Structural insights into the regulation of PDK1 by phosphoinositides and inositol phosphates. *EMBO J.* **23**, 3918–3928 (2004).
- Franke, T. F., Kaplan, D. R., Cantley, L. C. & Tokier, A. Direct regulation of the Akt proto-oncogene product by phosphatidylinositol-3,4-bisphosphate. *Science* **275**, 665–668 (1997).
- Klippel, A., Kavanaugh, W. M., Pot, D. & Williams, L. T. A specific product of phosphatidylinositol 3-kinase directly activates the protein kinase Akt through its pleckstrin homology domain. *Mol. Cell. Biol.* **17**, 338–344 (1997).
- Stephens, L. *et al.* Protein kinase B kinases that mediate phosphatidylinositol 3,4,5-trisphosphate-dependent activation of protein kinase B. *Science* **279**, 710–714 (1998).
- Barnett, S. F. *et al.* Identification and characterization of pleckstrin-homology-domain-dependent and isoenzyme-specific Akt inhibitors. *Biochem. J.* **385**, 399–408 (2005).
- Watton, S. J. & Downward, J. Akt/PKB localisation and 3' phosphoinositide generation at sites of epithelial cell-matrix and cell-cell interaction. *Curr. Biol.* **9**, 433–436 (1999).
- Scheid, M. P., Marignani, P. A. & Woodgett, J. R. Multiple phosphoinositide 3-kinase-dependent steps in activation of protein kinase B. *Mol. Cell. Biol.* **22**, 6247–6260 (2002).
- Adams, J. M. *et al.* The *c-myc* oncogene driven by immunoglobulin enhancers induces lymphoid malignancy in transgenic mice. *Nature* **318**, 533–538 (1985).
- Wendel, H. G. *et al.* Survival signalling by Akt and eIF4E in oncogenesis and cancer therapy. *Nature* **428**, 332–337 (2004).
- Adams, J. M. & Cory, S. Transgenic models for haemopoietic malignancies. *Biochim. Biophys. Acta* **1072**, 9–31 (1991).
- Altomare, D. A. & Testa, J. R. Perturbations of the AKT signaling pathway in human cancer. *Oncogene* **24**, 7455–7464 (2005).
- Parsons, D. W. *et al.* Colorectal cancer: mutations in a signalling pathway. *Nature* **436**, 792 (2005).
- Staal, S. P. Molecular cloning of the akt oncogene and its human homologues AKT1 and AKT2: amplification of AKT1 in a primary human gastric adenocarcinoma. *Proc. Natl Acad. Sci. USA* **84**, 5034–5037 (1987).
- Knobbe, C. B. & Reifemberger, G. Genetic alterations and aberrant expression of genes related to the phosphatidylinositol-3'-kinase/protein kinase B (Akt) signal transduction pathway in glioblastomas. *Brain Pathol.* **13**, 507–518 (2003).
- Soung, Y. H. *et al.* Mutational analysis of AKT1, AKT2 and AKT3 genes in common human carcinomas. *Oncology* **70**, 285–289 (2006).



37. Hawley, R. G. *et al.* Versatile vectors for potential use in gene therapy. *Gene Ther.* 1, 136–138 (1994).

**Supplementary Information** is linked to the online version of the paper at [www.nature.com/nature](http://www.nature.com/nature).

**Acknowledgements** We thank the Economic Development Board of Singapore for their support of this project through a RISC grant conferred to Lilly Research Laboratories. We also thank R. Gaynor for his comments, and W. Roeder for managing this project. We would like to thank the TGen DNA Sequencing Core, and are grateful to J. Tarrant for performing pathology examination of mouse blood smears, K. Neote and M. Swearingen for immunophenotyping, and P. Iversen for statistical analysis.

**Author Contributions** A.L.F. and C.H. contributed equally to this work. S.L.B. and R.S. crystallized the PHDs of AKT1. G.P.D. and D.J.Z performed the adoptive transfer studies. All authors discussed the results and commented on the manuscript.

**Author Information** X-ray crystallographic coordinates and structure factor files have been deposited in the Protein Data Bank (see Supplementary Table 2). E17K\_APO has been assigned the code 2UZR for the coordinate entry. E17K\_P4-inositol has been assigned the code 2UZS for the coordinate entry. Reprints and permissions information is available at [www.nature.com/reprints](http://www.nature.com/reprints). The authors declare no competing financial interests. Correspondence and requests for materials should be addressed to K.L.B. ([kblanc@lilly.com](mailto:kblanc@lilly.com)) or J.E.T. ([thomas\\_james\\_e@lilly.com](mailto:thomas_james_e@lilly.com)).

## METHODS

**Clinical cancer specimens.** Cancer specimens were obtained from ProteoGenex and the Indiana University School of Medicine, under appropriate and approved human subjects institutional review. Samples were quality controlled for sufficient mass and cancer content (>100 mg and >60% cancer); normal adjacent tissue or blood cells were analysed to verify somatic alterations.

**Genomic DNA mutational analysis.** *AKT1* (NM\_005163) exons and adjacent splice sites were amplified from genomic DNA. Primer sequences and annealing temperatures are available on request. PCR amplicons were purified using AMPURE (Agencourt), sequenced using BigDye Terminator chemistry (Applied Biosystems) and separated on DNA analysers (ABI). Raw sequencing data were imported into Sequencher 4.2 (GeneCodes) for analysis. For each exon, normal CEPH sample 1347-02 germline DNA was sequenced and used as a reference along with the publicly available sequence.

**Immunohistochemical analysis of tumours.** A tumour-specific tissue microarray was constructed from paraffin blocks of breast cancers. Immunohistochemistry with PTEN antibody clone 6H2.1 at 1:100 dilution (Cascade Biosciences) was performed on tumour-specific tissue microarray sections, with deparaffinization and antigen retrieval performed on-line using the BondMax autostainer (Vision Biosystems). Antibody staining was detected by Bond Polymer Refine Kit. Sections were visualized with 3,3'-diaminobenzidine, enhanced with copper sulphate and counterstained with haematoxylin.

**Plasmids and retrovirus production.** Human full-length *AKT1* was subcloned into pcDNA3.1 (Invitrogen) or modified pJB02 with the amino-terminal Flag tag. *AKT1*(E17K) and *AKT1*(R25C) were generated by site-directed mutagenesis. *AKT1* PHD (amino acids 1–123) was subcloned into pEGFP-C1 (Clontech) in which a six-residue N-terminal glycine linker had been inserted<sup>27</sup>. pMSCV6-PGK/GFP, pMSCV6-*AKT1*-PGK/GFP, pMSCV6-*AKT1*(E17K)-PGK/GFP, and pMSCV6-myr-*AKT1*-PGK/GFP were derived from pMSCVneo<sup>37</sup> (Clontech), with PGKegFP replacing PGKneo. Murine *Lck* myristoylation sequence was fused to the N terminus of *AKT1* to generate Myr-*AKT1*. Ecotropic retrovirus was generated by co-transfecting pVPack-GP (Stratagene), pVPack-Eco (Stratagene) and pMSCV6-*AKT1*-PGK/GFP or pMSCV6-myr-*AKT1*-PGK/GFP into HEK293T cells using FuGENE 6 (Roche).

**Cells, transfections and antibodies.** NIH 3T3 cells (ATCC) and Rat1 cells (M. Marshall, Eli Lilly) were cultured in DMEM plus 10% calf serum or 10% fetal bovine serum (FBS), respectively, in 10% CO<sub>2</sub>. Lysates from transiently transfected cells (Lipofectamine, Invitrogen) were prepared in lysis buffer consisting of 20 mM Tris buffer, 137 mM NaCl, 1 mM EGTA, 1% Triton-X100, 10% glycerol, 1.5 mM MgCl<sub>2</sub>, 1 mM sodium vanadate, 1 mM Pefabloc (Roche), 1 mM dithiothreitol, 10 µg ml<sup>-1</sup> leupeptin and 10 µg ml<sup>-1</sup> aprotinin. Antibodies used as probes in western blots were: anti-Flag (M2) and β-actin (AC-15) from Sigma; total AKT and P-AKT (Ser 473) from Cell Signaling; P-AKT (Thr 308) and anti-FKHRL1 (pThr 32) from Upstate Biosource International (UBI); and anti-α-tubulin (TU-02) from Santa Cruz Biotechnology. Quantification and statistical analysis were with Total Lab software (Nonlinear Dynamics) and JMP 5.1 software (SAS Institute, Inc), respectively.

**Kinetic constants and enzyme activity.** Flag-tagged *AKT1* constructs were expressed in HEK293E cells and protein purified by anti-Flag M2 agarose column (Sigma). Purified fractions were pooled, and *AKT1* confirmed by matrix-assisted laser desorption/ionization. Flag-tagged *AKT1* was activated with MAPKAP kinase 2 and PDK1 kinase (UBI). Kinetic constants and kinase activity in the presence of *AKT1*/2 inhibitor VIII (Calbiochem) were determined using the K-LISA AKT activity kit (Calbiochem).

**Immunoprecipitation and kinase assay.** Transfected NIH 3T3 cell lysates were mixed with anti-Flag antibody and protein G-sepharose. The beads were washed with lysis buffer and then divided for western blot analysis and AKT activity assays. For the activity assay, the beads were washed in K-LISA reaction buffer before re-suspending in 20 µl of 5 × K-LISA kinase buffer, 20 µl enzyme dilution buffer, 0.2 µg AKT substrate PRAS40 (Biomol) and 20 µl ATP/MgCl<sub>2</sub> mix (final concentration, 200 µM ATP and 15 mM MgCl<sub>2</sub>). Reactions were carried out at 30 °C for 30 min. Phosphorylated PRAS40 was detected with the PRAS40 ELISA kit (Calbiochem) using anti-pPRAS40 (Thr 246) (UBI).

**Cell fractionation.** Transfected NIH 3T3 cells were serum-starved before stimulation with 30 ng ml<sup>-1</sup> PDGF for 10 min. Cell fractionation was performed as described previously with the following modifications<sup>28</sup>: cells were washed with PBS supplemented with 200 nM sodium vanadate, membrane pellets were washed once with hypotonic buffer, and membrane pellets were solubilized in lysis buffer. Purity of the membrane fraction was assessed by western blot analysis with α-tubulin.

**Live-cell imaging.** NIH 3T3 cells were plated on cover glasses, transfected and serum-starved. Cells were pre-treated with LY294002 (Calbiochem) at 37 °C for 10 min and/or stimulated with 37 °C equilibrated PDGF (30 ng ml<sup>-1</sup>) media. Cells were imaged every 30 s using a Leica DMI6000B inverted microscope and analysed with FW4000 image acquisition software (Leica).

**Transformation studies.** Rat1 cells were transduced with titred viral supernatant plus 8 µg ml<sup>-1</sup> diethylaminoethyl dextran hydrochloride (Fluka). Seventy-two hours after transduction, cells were split into 100-mm dishes for foci formation or for anchorage-independent growth by seeding 5 × 10<sup>4</sup> cells per 60-mm Petri dish in 0.33% Bacto agar, 6.7% Bacto tryptose phosphate broth (Becton–Dickinson), 10% FBS and DMEM. Brightfield and fluorescent images were taken on an inverted Nikon microscope fitted with a Spot camera.

**Mouse leukaemia model.** Single-cell suspensions were derived from livers of embryonic day (E)16.5–E18.5 embryos from C57BL/6J × C57BL/6J(Tg(IgH–Myc)22Bri/J matings. Freshly isolated cells were placed in haematopoietic stem cell media (Iscove's modified Dulbecco's media with l-glutamine, 25 mM HEPES, 55 µM 2-mercaptoethanol, penicillin/streptomycin, 20% FBS, and the following recombinant murine proteins: 2 ng ml<sup>-1</sup> interleukin-6, 100 ng ml<sup>-1</sup> stem cell factor, 100 ng ml<sup>-1</sup> thrombopoietin and 100 ng ml<sup>-1</sup> fms-like tyrosine kinase-3 ligand) and transduced with fresh or frozen retroviral supernatants of various constructs in the presence of 8 µg ml<sup>-1</sup> diethylaminoethyl dextran hydrochloride for 4 h. Approximately 3 × 10<sup>6</sup> cells were injected into lethally irradiated C57BL/6J hosts (700 rad followed at 3 h by 400 rad).

For the P-AKT–GFP assay, nucleated cells from the blood of rescued animals were fixed, permeabilized and stained with anti-P-AKT Ser 473 antibody (Cell Signaling) according to the manufacturer's recommended protocol. Flow cytometry was performed on cells following a secondary stain with R-phycoerythrin-conjugated anti-rabbit Ig antibody (BioSource).

**Crystallography studies.** Crystals of *AKT1*(WT) PHD *apo* and *AKT1*(E17K) PHD *apo* were grown in 0.1 M HEPES pH 7.5 and 1.4 M sodium citrate for one week (80 × 80 × 100 µm). Co-crystals of *AKT1*(E17K) and Ins(1,3,4,5)P<sub>4</sub> were grown in 0.1 M sodium acetate (pH 4.6), 0.2 M ammonium acetate and 25 ± 5% poly(ethylene glycol) 3350 for one week (80 × 80 × 100 µm). Crystals were grown from hanging drops and frozen in liquid nitrogen with the cryo-protectant 25% glycerol. Data were collected at the Argonne National Laboratory, Industrial Macromolecular Crystallography Association, beam line 17-ID at 1 λ and 100 K. Ramachandran statistics for E17K\_APO and E17K\_P<sub>4</sub>-inositol are as follows: residues in favoured regions, 93.9, 87.6; additionally allowed regions, 4.0, 10.5; generously allowed regions, 1.0, 1.0; and disallowed regions, 1.0, 1.0, respectively. Crystallography figures were generated using the program PyMol (<http://www.pymol.org>).



# Non-transcriptional control of DNA replication by c-Myc

David Dominguez-Sola<sup>1\*</sup>, Carol Y. Ying<sup>1\*</sup>, Carla Grandori<sup>2†</sup>, Luca Ruggiero<sup>1</sup>, Brenden Chen<sup>1</sup>, Muyang Li<sup>1</sup>, Denise A. Galloway<sup>2</sup>, Wei Gu<sup>1</sup>, Jean Gautier<sup>1\*</sup> & Riccardo Dalla-Favera<sup>1\*</sup>

**The *c-Myc* proto-oncogene encodes a transcription factor that is essential for cell growth and proliferation and is broadly implicated in tumorigenesis. However, the biological functions required by c-Myc to induce oncogenesis remain elusive. Here we show that c-Myc has a direct role in the control of DNA replication. c-Myc interacts with the pre-replicative complex and localizes to early sites of DNA synthesis. Depletion of c-Myc from mammalian (human and mouse) cells as well as from *Xenopus* cell-free extracts, which are devoid of RNA transcription, demonstrates a non-transcriptional role for c-Myc in the initiation of DNA replication. Overexpression of c-Myc causes increased replication origin activity with subsequent DNA damage and checkpoint activation. These findings identify a critical function of c-Myc in DNA replication and suggest a novel mechanism for its normal and oncogenic functions.**

Since its identification as the cellular homologue of the avian myelocytomatosis virus oncogene (*v-Myc*)<sup>1,2</sup>, the *c-Myc* proto-oncogene has emerged as a critical regulator of cell growth and one of the genes most frequently altered in cancer<sup>3</sup>. *c-Myc* encodes a DNA-binding factor (hereafter called Myc) that can activate and repress RNA transcription. Via this mechanism, Myc regulates the expression of an unusually large number of target genes involved in the control of key cellular functions including cell growth and cell cycle progression<sup>3–5</sup>.

Multiple transcriptional and post-transcriptional control mechanisms ensure tight control of Myc protein levels in cycling cells. Deregulated Myc expression, as a result of different types of genetic alterations, leads to its constitutive activity in a variety of cancers<sup>6–9</sup> and promotes oncogenesis, as demonstrated in different cell types and in transgenic mice<sup>10</sup>. However, the biological functions critical for Myc-induced oncogenesis have not been identified. Myc may contribute to tumorigenesis by overstimulating cell growth and metabolism, and/or by causing genomic instability<sup>11</sup>. The latter effect has been attributed to the ability of Myc to induce DNA damage, promote gross chromosomal rearrangements, induce inappropriate cell cycle progression and impair DNA repair. However, the mechanistic basis of these effects is only partially characterized<sup>12</sup>.

Our results suggest an alternative mechanism by which Myc can regulate proliferation in normal cells and cause genomic instability in tumours, by controlling DNA replication. Initiation of DNA replication requires coordination between the stepwise assembly of the pre-replicative complex at replication origins during late mitosis and early G1, the regulated activation of these origins at the G1/S transition<sup>13</sup>, and epigenetic events such as chromatin remodelling<sup>14</sup>. Alterations of this space- and time-controlled process can lead to unscheduled DNA synthesis, checkpoint activation, genomic instability and/or cell death<sup>13</sup>. A role for Myc in DNA replication has been proposed<sup>15</sup>, but it was thought to depend on its capacity to regulate the transcription of cell-cycle-related genes<sup>16</sup>. We now show that Myc controls DNA replication origin activity through a non-transcriptional mechanism. When deregulated, Myc generates DNA replication stress and DNA damage.

## Myc interacts with the pre-replicative complex

Myc-containing protein complexes were isolated by affinity purification from a human tumour cell line that stably expresses a double-tagged (haemagglutinin (HA) and Flag) form of Myc (Supplementary Fig. 1a). Peptide microsequencing by mass spectrometry identified MCM5 and MCM7, among other proteins, as candidate Myc-associated proteins (Fig. 1a, arrowhead, and Supplementary Table 1).

Minichromosome maintenance (MCM) proteins are part of the pre-replicative complex, a multiprotein complex essential for the assembly and activity of DNA replication origins<sup>13</sup>. Indeed, all MCM2–MCM7 subunits, ORC2, Cdc6 and Cdt1, were present in the affinity-purified Myc complex (Fig. 1b), consistent with a recent report on the interaction of Myc with MCM2 and MCM7 (ref. 17). In contrast, proteins involved in DNA replication elongation (MCM10, RPA and PCNA; Fig. 1b) were absent. The physiological nature of these interactions was validated in various native cell lines (Fig. 1c, 1d and data not shown). The interaction with pre-replicative complex components was also observed with N-Myc (Supplementary Fig. 1b). Other proteins forming complexes with Myc, such as TRRAP<sup>18</sup>, were not found in this Myc and pre-replicative-complex-associated complex, whereas small, non-stoichiometrical amounts of Max (Myc-associated factor X) were detectable.

Myc and pre-replicative complex proteins co-sedimented in high molecular mass fractions (~1.7 MDa) after glycerol density gradient sedimentation and size-exclusion chromatography of Myc-bound protein complexes (Fig. 1e, fractions 4–8, and Supplementary Fig. 1c). Notably, Myc was also present in a distinct set of fractions that contained the majority of Max protein that co-purified with this complex (Fig. 1e, fractions 20–22). These fractions also contained MCM5, which might be involved in other transcriptional complexes<sup>19</sup>. Overall, these results identify a novel Myc-associated complex in mammalian cells that contains pre-replicative complex components and thus suggests a direct role of Myc in DNA replication.

<sup>1</sup>Institute for Cancer Genetics, Department of Genetics and Development and Herbert Irving Comprehensive Cancer Center, Columbia University Medical Center, New York, New York 10032, USA. <sup>2</sup>Division of Human Biology, Fred Hutchinson Cancer Research Center, Seattle, Washington 98109, USA. <sup>†</sup>Present address: Rosetta Inpharmatics, Merck, Seattle, Washington 98109, USA.

\*These authors contributed equally to this work.

## Myc binds a DNA replication origin

To investigate the role of Myc in DNA replication, we first compared the distribution of Myc and sites of DNA synthesis in mammalian cells. Primary human foreskin fibroblasts (HFFs) were synchronized in S phase and pulse-labelled with 5-bromodeoxyuridine (BrdU) to visualize DNA synthesis foci (Fig. 2a). Immunofluorescence analysis

using an anti-Myc antibody (Supplementary Fig. 2a) demonstrated a significant degree (40%) of co-localization between BrdU foci and Myc in early S phase (Fig. 2a, Supplementary Fig. 2b and Supplementary Movies). The degree of overlap between Max and BrdU foci, although lower, was also significant (Fig. 2a). In contrast, c-Jun, which has a punctate nuclear distribution, did not co-localize with BrdU (Fig. 2a and Supplementary Fig. 9b).

Because Myc and BrdU co-localization was limited to early S phase (Supplementary Fig. 2b), we proposed that Myc might be present at or near replication origins. We used chromatin immunoprecipitation (ChIP) experiments in human primary and tumour cell lines to validate this hypothesis (Fig. 2b and Supplementary Fig. 3). We selected an origin that is not a direct target of Myc-mediated transcriptional activation (*c-Myc* itself)<sup>20,21</sup> and an origin that has been finely mapped (lamin B2)<sup>22</sup> and for which no evidence of transcriptional responsiveness to Myc has been documented. Myc and Max were detected at both the 5' P0–P1 promoter regions in the *c-Myc* gene<sup>23</sup> (Fig. 2b), and the lamin B2 origin (Supplementary Fig. 3b, c). ORC2 binding was also detected at the same sites (Supplementary Fig. 3a), further suggesting that Myc binding might occur at or in close proximity to these origins, although the extent of this correlation remains unclear due to the small number of testable origins.

## Non-transcriptional control of DNA replication by Myc

Conditional inactivation of Myc precludes the G1/S transition and causes subsequent entry in G0 (ref. 24); transient RNA interference (RNAi)-based depletion of Myc in cell lines caused inhibition of DNA replication, followed by G1 arrest (Supplementary Fig. 4). These results might reflect a lack of transcriptional induction of S-phase-promoting factors by Myc, or the absence of Myc association with the replication apparatus, as suggested by our results. To discriminate between these possibilities, we used an experimental strategy (Fig. 3c and Supplementary Fig. 5a) based on the observation that G1 cells initiate DNA synthesis when fused to S-phase-synchronized cells<sup>25</sup> that provide S-phase-promoting factors required for the G1/S transition, including cyclin–cdk complexes. The presence of cycloheximide before and during this procedure ensured that the outcome relied solely on the activity of proteins present in the cells before fusion. Fusion of S-phase donor HeLa cells to 3T9 mouse fibroblasts containing a conditionally excisable allele of Myc (*v-src*<sup>+</sup>, *c-myc*<sup>+/–</sup>)<sup>24</sup>

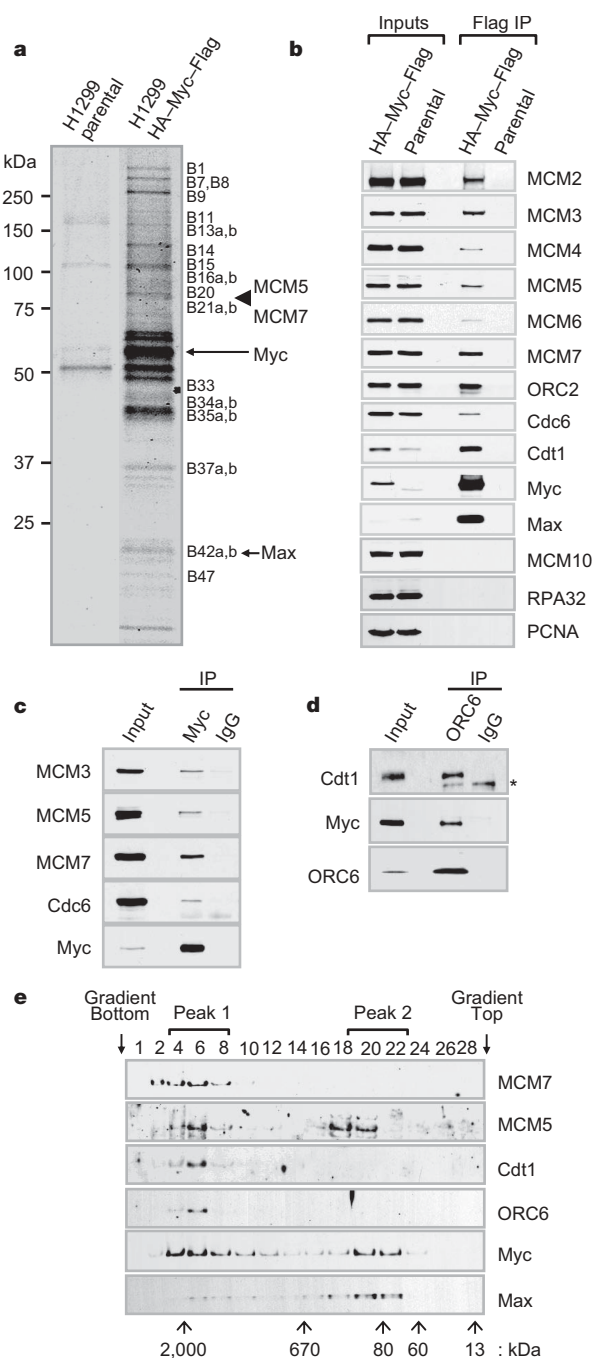


**Figure 1 | Myc interacts with the pre-replicative complex in mammalian cells.** **a**, Coomassie-stained SDS-PAGE gel of an HA-Myc-Flag complex purified from H1299 cells. Arrows indicate Myc and Max. The arrowhead shows the region where MCM5 and MCM7 were isolated. Labels on the right side correspond to the polypeptides listed in Supplementary Table 1. **b**, Western blot of the complex shown in **a**, probed with the indicated antibodies. **c**, **d**, Co-immunoprecipitation from native H1299 cells using anti-Myc or control antibodies (**c**) or anti-ORC6 or control antibodies (**d**). The asterisk indicates a nonspecific band. **e**, HA-Myc-Flag-associated complex (**a**) resolved in a 25–75% glycerol gradient and analysed by western blot. We estimate that ~2% of the pre-replicative complex proteins are associated with Myc in this complex.

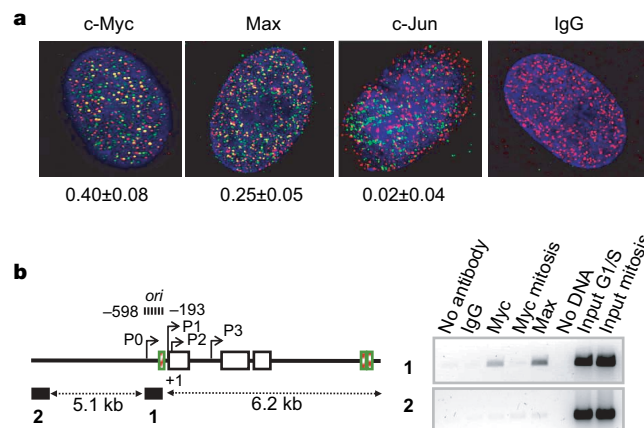


**Figure 2 | Myc co-localizes with early DNA synthesis foci and binds the Myc gene replication origin.** **a**, HFFs were synchronized in G0, re-plated at low density and fixed 14–16 h after a short BrdU pulse (early S phase). Co-localization between Myc, Max, c-Jun (all fluorescein isothiocyanate (FITC), green) and BrdU (TRITC, red) foci was determined by deconvolution microscopy. 'IgG' denotes the FITC-conjugated secondary antibody. Pearson's correlation indexes between FITC/TRITC signals (10 cells, 100 foci) are indicated below. **b**, Chromatin immunoprecipitation (H1299 cells) and at the human *c-Myc* gene. Left panel: map depicting the location of relevant regions and PCR probes. Coloured boxes, non-canonical E-boxes. Right panel: ethidium bromide staining of PCR products.



allowed us to examine whether DNA replication can occur in an S-phase environment in the absence of Myc (Fig. 3 and Supplementary Fig. 5). Upon recombination-induced *c-myc* gene deletion, these 3T9 cells arrest in early G1 and DNA synthesis is inhibited<sup>24</sup>. Cell fusion in the absence of new protein synthesis allowed the S-phase-promoting factors of HeLa cells to shuttle within each heterokaryon, as shown for human cyclin E (Fig. 3a). This promoted DNA replication in the early G1 mouse *c-myc*<sup>+/-</sup> nuclei, but was not sufficient to trigger replication in G1 *c-myc*<sup>-/-</sup> nuclei (Fig. 3d, e). Early G1 *c-myc*<sup>+/-</sup> and *c-myc*<sup>-/-</sup> cells lacked expression of S-phase proteins and expressed comparable levels of pre-replicative complex components (Fig. 3b and Supplementary Fig. 5e). These observations suggest that Myc controls DNA replication initiation in mammalian cells at least in part through a non-transcriptional mechanism operating in G1.

To obtain definitive evidence for a non-transcriptional role of Myc in DNA replication, we took advantage of *Xenopus* cell-free extracts, which support cell-cycle-regulated, semi-conservative chromosomal DNA replication in the absence of transcription and new protein synthesis<sup>26</sup>. Particularly, a *Xenopus* soluble, nuclear-free system (HSS/NPE)<sup>27</sup> allows for independent evaluation of events preceding and subsequent to the initiation of DNA synthesis. In this system, DNA synthesis of templates assembled in cytosolic high-speed supernatant (HSS) is triggered by the addition of nucleoplasmic extracts (NPE) containing the S-phase-promoting factors required to promote DNA replication. Using antibodies raised against both *Xenopus* c-Myc homologues (Myc I and Myc II, hereafter called XMyC;

Supplementary Fig. 6), immunodepletion of XMyC from HSS (Fig. 3f) resulted in an 80% decrease in nucleotide incorporation into genomic DNA (Fig. 3g, lanes 1 and 2). This replication defect was fully rescued by addition of recombinant XMyC protein to XMyC-depleted HSS before NPE addition (Fig. 3g, lane 3). In contrast, no rescue was attained by the addition of truncated forms of XMyC lacking either the amino-terminal 140 residues (XMyC $\Delta$ TAD), or the DNA binding and dimerization domains (residues 337–420) (XMyC $\Delta$ CT) (Fig. 3g, lanes 4 and 5). Notably, when recombinant XMyC was supplemented at the time of NPE addition, rescue of replication was not achieved (Fig. 3g, lane 6 versus lane 3). Overall, these results demonstrate that Myc has a non-transcriptional role in the control of normal DNA replication initiation, and suggest that Myc executes its role before the action of S-phase-promoting factors in both *Xenopus* and mammalian systems.

### Myc modulates DNA replication origin activity

Initiation of DNA replication is the final outcome of a poorly understood process, by which a fraction of all the potential replication origins is selected and subsequently activated to fire in each cell cycle<sup>14</sup>. Analysis of chromosomal replication kinetics in *Xenopus* cell-free extracts showed that XMyC depletion caused a major delay in the completion of full genome replication (Fig. 4a and Supplementary Fig. 7). To examine whether this result reflects a defect in replication origin activity (number of origins generating replication forks), or defects in the processivity of DNA synthesis (slow

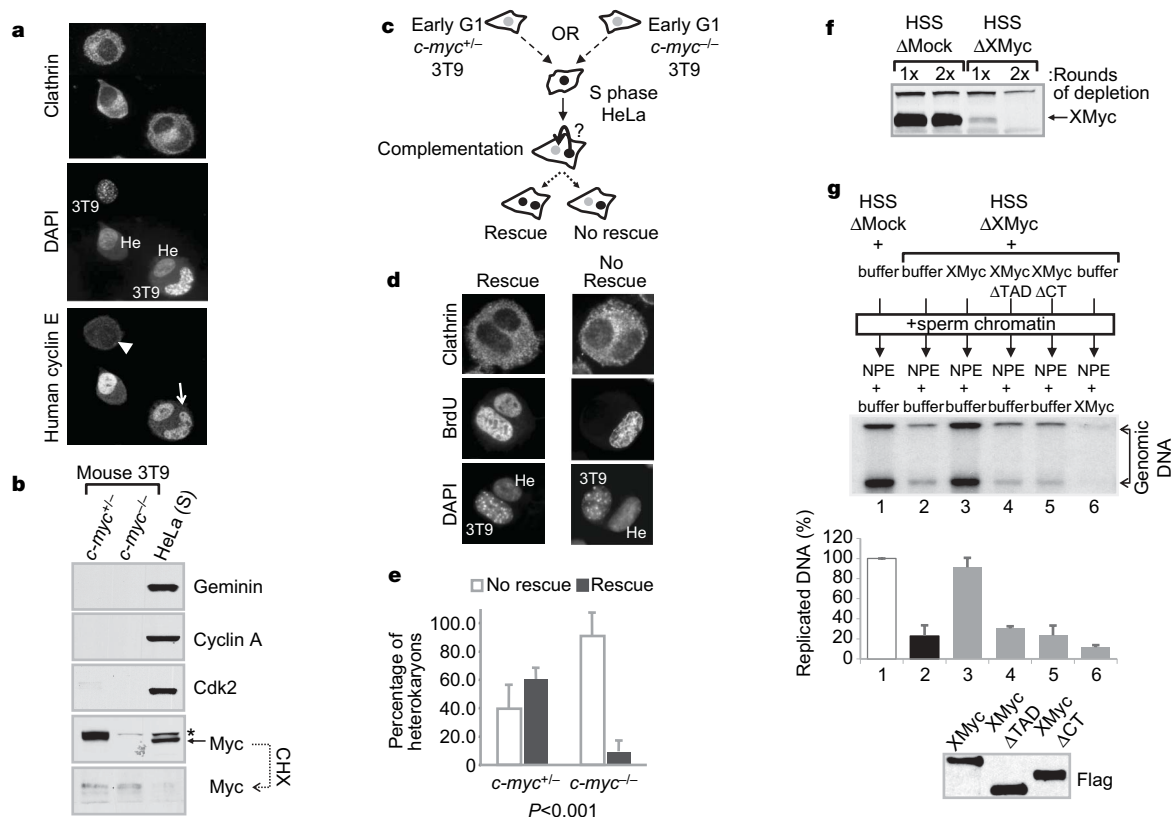


**Figure 3 | Myc is required for efficient DNA replication and proper origin specification in the absence of transcription.** **a**, Cyclin/Cdk shuttles within human/mouse heterokaryons. Isolated heterokaryons were stained with a human-specific antibody against cyclin E. Arrow, 3T9 mouse nuclei within the heterokaryons uptaking cyclin E; arrowhead, isolated 3T9 cells, devoid of cyclin E. Mouse (3T9) and human (He) nuclei exhibit distinct 4,6-diamidino-2-phenylindole (DAPI) staining patterns. **b**, Western blot analysis of selected proteins in whole-cell lysates from the indicated cells before cell fusion. CHX, cycloheximide; asterisk, nonspecific band in HeLa cells. **c**, Experimental scheme for the cell fusion experiments (see also Supplementary Information). **d**, Representative images of heterokaryons

identified in the screen for replication rescue, summarized in **e**. **e**, Average of cell fusion experiments. More than 70 heterokaryons were counted and classified according to the patterns shown in **d**. The *P* value ( $\chi^2$  analysis) is shown below. Error bars indicate s.d. **f**, Western blot analysis of mock- or XMyC-depleted *Xenopus* cell-free extracts. **g**, Replication assay in the *Xenopus* HSS/NPE system. Genomic DNA was extracted at 90 min and incorporated <sup>32</sup>P was quantified by PhosphorImager. Recombinant XMyC proteins (50 nM) were added to XMyC-depleted HSS extracts (lanes 3–5) or to NPE (lane 6) as indicated. A representative autoradiograph is shown. An average of three experiments is shown in the graph below. Error bars indicate s.d. Bottom panel: western blot analysis of recombinant XMyC protein levels.

progression of these replication forks), we monitored the progression of replication forks in *Xenopus* extracts by analysing nascent replication products formed after release from synchronization (Fig. 4b). Depletion of XMyc caused a significant decrease in the number of active replicons (Fig. 4b, upper panel), consistent with the decrease in overall replication described above (Figs 3g and 4a). However, replication fork progression was not affected, as demonstrated by similar elongation rates in both mock- and XMyc-depleted extracts (Fig. 4b, bottom panel). This observation establishes that the slow replication kinetics observed upon XMyc depletion probably reflect defective replication origin activity, and suggests that the absence of Myc before DNA replication initiation prevents activation of replication origins. In both *Xenopus* and mammalian systems, active origins are selected among all assembled pre-replicative complexes before the initiation of DNA synthesis<sup>13</sup>. Because XMyc immunodepletion from *Xenopus* extracts, as well as RNAi-mediated Myc depletion in mammalian cells, did not prevent the loading of pre-replicative complex components to chromatin, nor their localization to the lamin B2 replication origin (Supplementary Fig. 8), we propose that Myc may affect origin activity by influencing a step subsequent to pre-replicative complex assembly, possibly during origin selection.

To strengthen these observations, we examined the effect of Myc protein overexpression on origin activity. Expression of exogenous Myc in primary fibroblasts caused a significant increase in the number of DNA synthesis foci in early S phase as detected by BrdU labelling, consistent with an increase in the number of active replicons (Fig. 4e and Supplementary Fig. 9a). BrdU foci co-localized with exogenous Myc protein (Supplementary Fig. 9b), and were not affected by  $\alpha$ -amanitin, a specific inhibitor of RNA-polymerase-II-mediated RNA synthesis<sup>28</sup> (Fig. 4e, f), indicating that this effect did not require transcriptional activity. Precocious onset of DNA synthesis was also observed in *Xenopus* extracts on addition of recombinant XMyc, with a dose-dependent increase of replicated DNA at early time points (Figs 4c, d and 5c). Notably, this replicative burst was accompanied by an >8-fold increase in the amount of chromatin-bound Cdc45 (Fig. 4d), a direct indication of the number of active origins<sup>29</sup>. This effect was also observed in mammalian cells on transient Myc overexpression (Fig. 4g, h). Thus, Myc deregulation leads to an aberrant increase in the number of active replicons owing to unscheduled origin activation by means of a non-transcriptional mechanism. Together with the results obtained through Myc depletion, these observations demonstrate that Myc regulates DNA replication origin activity.

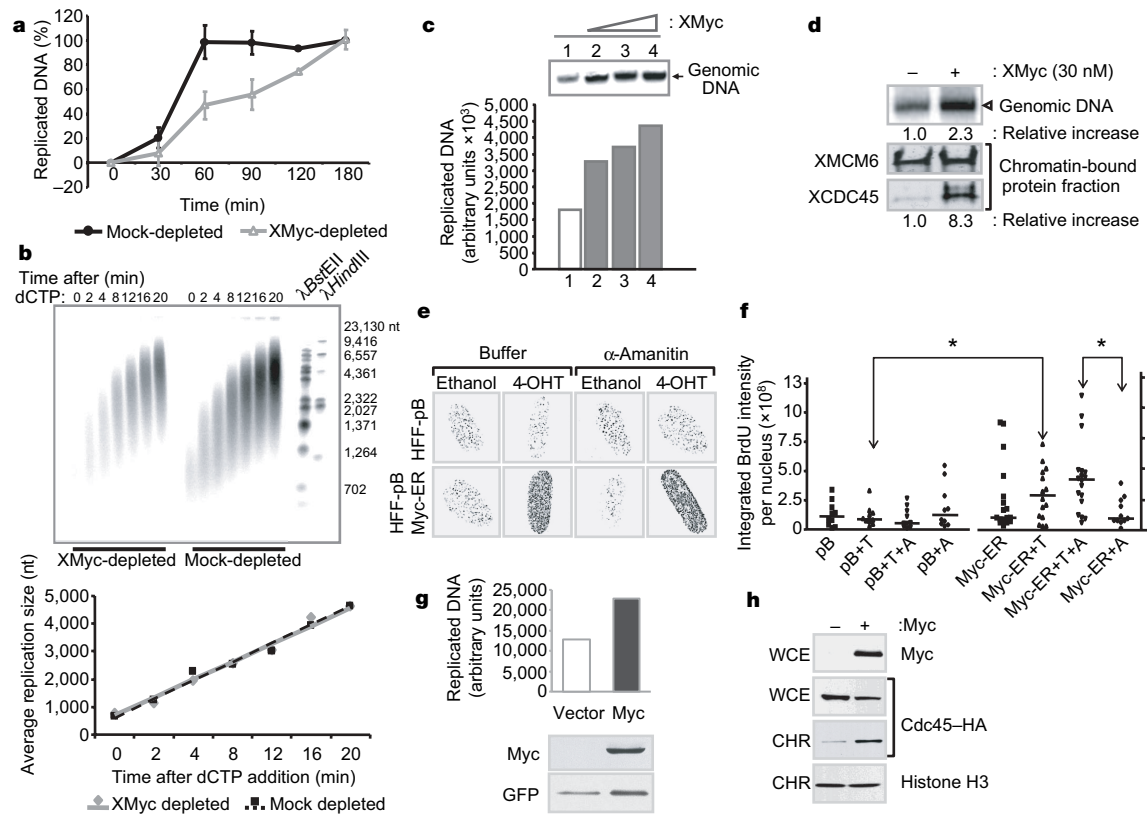


**Figure 4 | Relationship between Myc protein levels and the number of active DNA replication origins.** **a**, Replication reactions in mock- and XMyc-depleted *Xenopus* cell-free extracts were stopped at the indicated time points and quantified. An average of three experiments is shown ( $\pm$ s.d.). **b**, Electrophoretic analysis of nascent replication products on Ara-C-induced synchronization of depleted *Xenopus* extracts (top panel). Bottom panel: average size of replication products plotted over time to indicate elongation rates (best-fit curves). dCTP, deoxy-cytidine triphosphate. **c**, Replication reactions in *Xenopus* extracts, supplemented with increasing amounts of XMyc, were stopped at 60 min and analysed. **d**, Top panel: replication reactions in *Xenopus* extracts assembled in the presence or absence of XMyc and analysed after 40 min. Bottom panel: western blot analysis of corresponding chromatin fractions. Chromatin-bound *Xenopus* Cdc45 was quantified using Scion software and normalized to *Xenopus* MCM6. **e**, Analysis of BrdU foci unclear distribution in synchronized W138

fibroblasts (Myc-ER or empty vector).  $\alpha$ -Amanitin ( $2 \mu\text{g ml}^{-1}$ ) or buffer was added 30 min before tamoxifen (4-OHT) exposure and BrdU labelling (see scheme in Supplementary Fig. 10). **f**, Quantification of the experiment shown in **e**. Nuclear BrdU intensity is the sum of all BrdU spots. The threshold is set above 3 s.d. from background. Asterisk,  $P < 0.05$ , based on a two-sided Student's  $t$ -test. Each dot is the sum intensity of one cell. pB, empty vector; T, tamoxifen; A,  $\alpha$ -amanitin. **g**, Transiently transfected H1299 cells (GFP with or without c-Myc cDNA), synchronized in G1/S and released to S phase in the presence of  $^{32}\text{P}$  orthophosphate. After 3 h, DNA was isolated and incorporated nucleotides quantified by scintillation counting. Bottom panel: western blot analysis of whole-cell lysates from the same cells. **h**, H1299 cells were co-transfected with an HA-tagged Cdc45 cDNA and empty vector or c-Myc cDNA. On synchronization, cells were collected in S phase and chromatin fractions (CHR) or whole-cell extracts (WCE) resolved by SDS-PAGE and analysed by western blot.



### Myc causes DNA damage by inducing replication stress

Unscheduled origin firing is a source of replication stress, which in turn may generate DNA damage. Addition of recombinant XMyc to replicating *Xenopus* extracts caused a fivefold increase in histone H2A.X Ser 139 phosphorylation ( $\gamma$ -H2A.X) in chromatin fractions, an indicator of aberrant DNA structures and damage<sup>30,31</sup> (Fig. 5a, lanes 1 and 2).  $\gamma$ -H2A.X levels were maximal when genome replication was close to completion, suggesting that it might accumulate during replication (Supplementary Fig. 11a). This effect was specifically prevented by geminin (Fig. 5a, lanes 3 and 4), which blocks MCM loading and DNA synthesis<sup>32</sup>, indicating that XMyc-induced DNA damage requires active DNA replication. These results show that deregulation of XMyc can generate replication-dependent DNA damage in the absence of transcription. Depletion of DNA polymerase  $\alpha$  (Fig. 5b, top panel), which is not involved in DNA repair processes<sup>33</sup>, abrogated the XMyc-dependent increase in nucleotide incorporation (Fig. 5b, lower panel), suggesting its association with replication rather than DNA repair.

Kinetic analysis in *Xenopus* extracts showed that after the initial replicative burst, XMyc, but not replication-incompetent XMyc

truncated proteins, led to a precocious arrest in DNA synthesis (Fig. 5c, 90–180 min; see also Fig. 5d). The replication arrest was abrogated by the addition of caffeine, an ATM/ATR inhibitor (Fig. 5d, lanes 6, 7), and partially reverted by a specific ATM inhibitor or a selective Chk1 inhibitor, but not by a DNA-PK inhibitor (Supplementary Fig. 11b, c). Caffeine addition also abrogated the appearance of  $\gamma$ -H2A.X (data not shown). Deregulation of XMyc triggered phosphorylation of *Xenopus* ATM at Ser 1981 before stalling of DNA synthesis (Fig. 5e). Thus, overexpression of XMyc activates an ATM/ATR–Chk1-dependent checkpoint, coincident with the appearance of replication-dependent DNA damage. Given that ATM and ATR signalling pathways monitor and negatively regulate origin activity to control origin density<sup>34</sup>, these observations indicate the existence of crosstalk between Myc and ATM/ATR in the control of origin activity, which might provide an explanation for the nature of Myc-dependent ‘oncogenic stress’.

Consistent with these observations, transient Myc deregulation caused an increase in  $\gamma$ -H2A.X primarily during S phase in synchronized mammalian cells (Fig. 5f). This effect was abrogated when S-phase entry was blocked by the addition of aphidicolin (Fig. 5g,

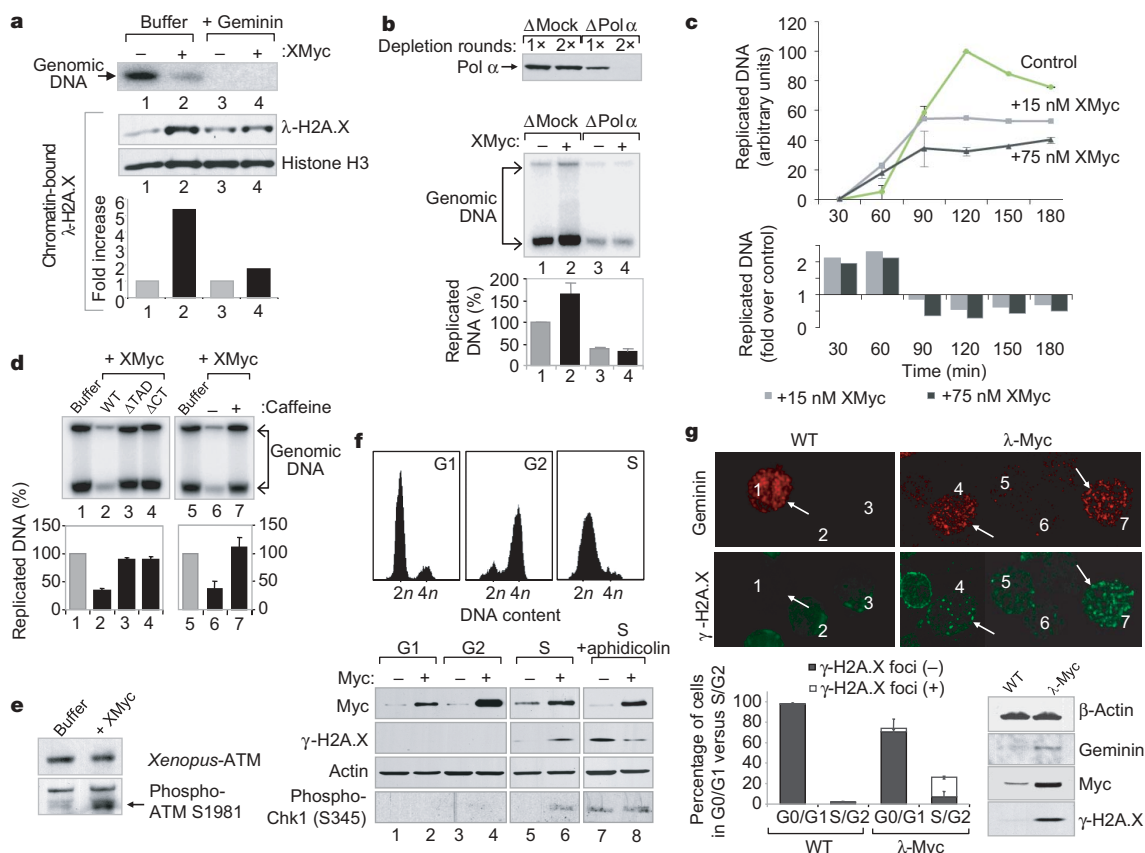


**Figure 5 | Myc deregulation induces replication-dependent DNA damage.**

**a**, Replication reactions in *Xenopus* extracts, assembled in the presence or absence of XMyc (75 nM) and geminin, were stopped at 120 min (top panel). Middle panel: western blot analysis of chromatin fractions. Chromatin-bound  $\gamma$ -H2A.X was quantified by Scion software and normalized to histone H3 (graph). **b**, Immunodepletion of DNA polymerase  $\alpha$  (Pol  $\alpha$ ) from *Xenopus* extracts (top panel). Replication reactions were then assembled with buffer or XMyc (30 nM) (middle panel) and quantified. The graph shows an average of three experiments ( $\pm$ s.d.). **c**, Replication reactions assembled in *Xenopus* extracts in the presence or absence of XMyc. Samples taken at indicated time points were quantified (average of two experiments,  $\pm$ s.d.; top graph). The bottom graph shows fold change between control (set at 1) and XMyc-treated extracts. **d**, Replication reactions in *Xenopus* extracts performed in the presence or absence of XMyc (wild type (WT) and mutants, 75 nM, lanes 1–4), or 5 mM caffeine (lanes 5–7). Reactions were analysed after 120 min. The graph shows the average of three experiments ( $\pm$ s.d.).

**e**, Western blot analysis of cytosolic fractions from replication reactions performed in the presence or absence of XMyc for 20 min, and probed with phospho-specific anti-ATM antibodies. **f**, Mammalian U2OS cells transfected with Myc and synchronized by nocodazole (G1, G2) or thymidine (S) blocks. Where indicated, aphidicolin (2.5  $\mu$ M) was added to prevent S-phase entry. FACS profiles depict cell cycle status at collection. Bottom panel: western blot analysis of whole-cell lysates. **g**, Analysis of  $\gamma$ -H2A.X distribution in splenic B cells from  $\lambda$ -Myc mice and wild-type littermates. Top panel: immunofluorescence analysis for geminin and  $\gamma$ -H2A.X distribution. Numbers identify cells within the images; arrows indicate cells with nuclear geminin (S/G2). The graph shows cell cycle distribution (based on geminin staining) and quantification of cells with nuclear  $\gamma$ -H2A.X foci within these subpopulations (average of two experiments ( $\pm$ s.d.),  $n > 1,000$ ). A western blot analysis on whole-cell lysates from both B-cell populations is shown (bottom right panel).

lanes 7, 8) or thymidine (data not shown). Most notably, phosphorylation of Chk1 at Ser 345 was only observed on Myc deregulation in S phase (Fig. 5f, lane 6), suggesting that, as in *Xenopus*, Myc-induced damage in mammalian cells is S-phase-dependent.

To validate these observations in a physiological context, we monitored the appearance of  $\gamma$ -H2A.X in murine splenic B cells isolated from a transgenic mouse carrying a deregulated Myc allele ( $\lambda$ -Myc)<sup>35</sup>. We found that Myc deregulation was associated with the appearance of  $\gamma$ -H2A.X (Fig. 5g, bottom right panel) and other DNA markers of the DNA damage response pathway (phospho-ATM and phospho-Chk1, data not shown), as well as with geminin expression, an indicator of the S and G2 phases of the cell cycle<sup>32</sup>. Notably, immunofluorescence analysis showed that  $\gamma$ -H2A.X foci preferentially occur in geminin-positive cells in  $\lambda$ -Myc mouse B cells (that is, S/G2), whereas no geminin-positive cells showed evidence for  $\gamma$ -H2A.X foci in cells from wild-type mice (Fig. 5g). Taken together, our observations suggest that Myc-induced DNA damage requires S-phase progression in both the *Xenopus* and mammalian systems, and occurs, at least in part, as a consequence of deregulated Myc activity on DNA replication.

## Discussion

It was previously proposed that Myc promotes G1/S transition and DNA replication through the transcription of factors promoting S-phase entry and/or cell growth<sup>3,5</sup>. Our results indicate that Myc control of DNA replication is not dependent on its transcriptional activity in both *Xenopus* extracts and mammalian cells. Nonetheless, transcriptional regulation of critical target genes may also be an important component of the overall role of Myc in regulating DNA replication initiation. Notably, the transactivation domain of Myc is required to control both DNA replication initiation and transcriptional activity, suggesting that Myc may use a common molecular mechanism to facilitate both DNA transactions. This mechanism might involve Myc-dependent chromatin modifications<sup>36</sup> such as histone acetylation, which might also be implicated in the selection of replication origins<sup>37</sup>.

Our results indicate that Myc deregulation generates DNA damage and may promote genomic instability by inducing DNA replication stress, strengthening previous observations<sup>38–41</sup>. This notion is also supported by the dependence on Werner RecQ helicase for Myc-driven proliferation<sup>42</sup>, and by the requirement for RecQ helicases during replication stress<sup>43</sup>. These observations can explain the occurrence of genomic alterations, such as gene amplification and illegitimate replication of some loci<sup>41</sup>, that are consistently associated with Myc deregulation during tumorigenesis. However, in contrast with other oncogenes that may cause DNA re-replication when deregulated<sup>44</sup>, overexpression of Myc increases the number of active replication origins in the absence of detectable re-replication (data not shown).

Our results also suggest that the p53-dependent G2/M checkpoint and subsequent apoptosis observed in mammalian cells carrying deregulated Myc alleles<sup>45</sup> may be due to DNA damage generated predominantly during S phase. Frequent p53 inactivation in tumours carrying deregulated Myc genes<sup>46</sup> may then reflect selection for tumoural cells with disabled checkpoint responses. Thus, our results suggest that Myc may exert its oncogenic function, at least in part, by promoting origin activity, thereby inducing replication stress and genomic instability.

## METHODS SUMMARY

The Methods and Supplementary Information provide detailed information regarding all experimental procedures: (1) lists of cell lines, antibodies and a detailed description of constructs and transfection procedures; (2) preparation of fractionated cell extracts, co-immunoprecipitation procedures (including Myc complex isolation) and *in vitro* pull-down assays; (3) chromatin immunoprecipitation primer sequences; (4) details on replication reactions in the *Xenopus* system, nascent replication product (nascent strand) analysis and

chromatin isolation procedures; (5) radioactive labelling of newly synthesized DNA in mammalian cells; (6) purification and characterization of antibodies generated against XMyc; (7) preparation of baculovirus-based recombinant XMyc proteins and *in vitro* pull-down assays; and (8) cell synchronization and BrdU labelling protocols.

**Full Methods** and any associated references are available in the online version of the paper at [www.nature.com/nature](http://www.nature.com/nature).

Received 9 August 2006; accepted 18 May 2007.

Published online 27 June 2007.

- Dalla-Favera, R. *et al.* Cloning and characterization of different human sequences related to the onc gene (v-myc) of avian myelocytomatosis virus (MC29). *Proc. Natl Acad. Sci. USA* **79**, 6497–6501 (1982).
- Vennstrom, B., Sheiness, D., Zabielski, J. & Bishop, J. M. Isolation and characterization of c-myc, a cellular homolog of the oncogene (v-myc) of avian myelocytomatosis virus strain 29. *J. Virol.* **42**, 773–779 (1982).
- Grandori, C., Cowley, S. M., James, L. P. & Eisenman, R. N. The Myc/Max/Mad network and the transcriptional control of cell behavior. *Annu. Rev. Cell Dev. Biol.* **16**, 653–699 (2000).
- Fernandez, P. C. *et al.* Genomic targets of the human c-Myc protein. *Genes Dev.* **17**, 1115–1129 (2003).
- Patel, J. H., Loboda, A. P., Showe, M. K., Showe, L. C. & McMahon, S. B. Analysis of genomic targets reveals complex functions of MYC. *Nature Rev. Cancer* **4**, 562–568 (2004).
- Dalla-Favera, R. *et al.* Human c-myc onc gene is located on the region of chromosome 8 that is translocated in Burkitt lymphoma cells. *Proc. Natl Acad. Sci. USA* **79**, 7824–7827 (1982).
- Dalla-Favera, R., Wong-Staal, F. & Gallo, R. C. Onc gene amplification in promyelocytic leukaemia cell line HL-60 and primary leukaemic cells of the same patient. *Nature* **299**, 61–63 (1982).
- Pasqualucci, L. *et al.* Hypermutation of multiple proto-oncogenes in B-cell diffuse large-cell lymphomas. *Nature* **412**, 341–346 (2001).
- Collins, S. & Groudine, M. Amplification of endogenous myc-related DNA sequences in a human myeloid leukaemia cell line. *Nature* **298**, 679–681 (1982).
- Adams, J. M. *et al.* The c-myc oncogene driven by immunoglobulin enhancers induces lymphoid malignancy in transgenic mice. *Nature* **318**, 533–538 (1985).
- Pelengaris, S., Khan, M. & Evan, G. c-MYC: more than just a matter of life and death. *Nature Rev. Cancer* **2**, 764–776 (2002).
- Wade, M. & Wahl, G. M. c-Myc, genome instability, and tumorigenesis: the devil is in the details. *Curr. Top. Microbiol. Immunol.* **302**, 169–203 (2006).
- Machida, Y. J., Hamlin, J. L. & Dutta, A. Right place, right time, and only once: replication initiation in metazoans. *Cell* **123**, 13–24 (2005).
- Gilbert, D. M. In search of the holy replicator. *Nature Rev. Mol. Cell Biol.* **5**, 848–855 (2004).
- Iguchi-Arigo, S. M., Itani, T., Kiji, Y. & Ariga, H. Possible function of the c-myc product: promotion of cellular DNA replication. *EMBO J.* **6**, 2365–2371 (1987).
- Obaya, A. J., Mateyak, M. K. & Sedivy, J. M. Mysterious liaisons: the relationship between c-Myc and the cell cycle. *Oncogene* **18**, 2934–2941 (1999).
- Koch, H. B. *et al.* Large-scale identification of c-MYC-associated proteins using a combined TAP/MudPIT approach. *Cell Cycle* **6**, 205–217 (2007).
- McMahon, S. B., Van Buskirk, H. A., Dugan, K. A., Copeland, T. D. & Cole, M. D. The novel ATM-related protein TRRAP is an essential cofactor for the c-Myc and E2F oncoproteins. *Cell* **94**, 363–374 (1998).
- Zhang, J. J. *et al.* Ser727-dependent recruitment of MCM5 by Stat1 $\alpha$  in IFN- $\gamma$ -induced transcriptional activation. *EMBO J.* **17**, 6963–6971 (1998).
- Facchini, L. M., Chen, S., Marhin, W. W., Lear, J. N. & Penn, L. Z. The Myc negative autoregulation mechanism requires Myc-Max association and involves the c-myc P2 minimal promoter. *Mol. Cell Biol.* **17**, 100–114 (1997).
- Grignani, F. *et al.* Negative autoregulation of c-myc gene expression is inactivated in transformed cells. *EMBO J.* **9**, 3913–3922 (1990).
- Abdurashidova, G. *et al.* Start sites of bidirectional DNA synthesis at the human lamin B2 origin. *Science* **287**, 2023–2026 (2000).
- Tao, L., Dong, Z., Leffak, M., Zannis-Hadjopoulos, M. & Price, G. Major DNA replication initiation sites in the c-myc locus in human cells. *J. Cell. Biochem.* **78**, 442–457 (2000).
- Prathapam, T., Tegen, S., Oskarsson, T., Trumpp, A. & Martin, G. S. Activated Src abrogates the Myc requirement for the G0/G1 transition but not for the G1/S transition. *Proc. Natl Acad. Sci. USA* **103**, 2695–2700 (2006).
- Rao, P. N. & Johnson, R. T. Mammalian cell fusion: studies on the regulation of DNA synthesis and mitosis. *Nature* **225**, 159–164 (1970).
- Blow, J. J. & Laskey, R. A. Initiation of DNA replication in nuclei and purified DNA by a cell-free extract of *Xenopus* eggs. *Cell* **47**, 577–587 (1986).
- Walter, J., Sun, L. & Newport, J. Regulated chromosomal DNA replication in the absence of a nucleus. *Mol. Cell* **1**, 519–529 (1998).
- Grandori, C. *et al.* c-Myc binds to human ribosomal DNA and stimulates transcription of rRNA genes by RNA polymerase I. *Nature Cell Biol.* **7**, 311–318 (2005).
- Woodward, A. M. *et al.* Excess Mcm2–7 license dormant origins of replication that can be used under conditions of replicative stress. *J. Cell Biol.* **173**, 673–683 (2006).

30. Rogakou, E. P., Pilch, D. R., Orr, A. H., Ivanova, V. S. & Bonner, W. M. DNA double-stranded breaks induce histone H2AX phosphorylation on serine 139. *J. Biol. Chem.* **273**, 5858–5868 (1998).
31. Costanzo, V. *et al.* Mre11 protein complex prevents double-strand break accumulation during chromosomal DNA replication. *Mol. Cell* **8**, 137–147 (2001).
32. McGarry, T. J. & Kirschner, M. W. Geminin, an inhibitor of DNA replication, is degraded during mitosis. *Cell* **93**, 1043–1053 (1998).
33. Wang, X. *et al.* Role of DNA replication proteins in double-strand break-induced recombination in *Saccharomyces cerevisiae*. *Mol. Cell. Biol.* **24**, 6891–6899 (2004).
34. Shechter, D., Costanzo, V. & Gautier, J. ATR and ATM regulate the timing of DNA replication origin firing. *Nature Cell Biol.* **6**, 648–655 (2004).
35. Kovalchuk, A. L. *et al.* Burkitt lymphoma in the mouse. *J. Exp. Med.* **192**, 1183–1190 (2000).
36. Knoepfler, P. S. *et al.* Myc influences global chromatin structure. *EMBO J.* **25**, 2723–2734 (2006).
37. Norio, P. DNA replication: the unbearable lightness of origins. *EMBO Rep.* **7**, 779–781 (2006).
38. Bartkova, J. *et al.* DNA damage response as a candidate anti-cancer barrier in early human tumorigenesis. *Nature* **434**, 864–870 (2005).
39. Gorgoulis, V. G. *et al.* Activation of the DNA damage checkpoint and genomic instability in human precancerous lesions. *Nature* **434**, 907–913 (2005).
40. Felsher, D. W. & Bishop, J. M. Transient excess of MYC activity can elicit genomic instability and tumorigenesis. *Proc. Natl Acad. Sci. USA* **96**, 3940–3944 (1999).
41. Mai, S. & Mushinski, J. F. c-Myc-induced genomic instability. *J. Environ. Pathol. Toxicol. Oncol.* **22**, 179–199 (2003).
42. Grandori, C. *et al.* Werner syndrome protein limits MYC-induced cellular senescence. *Genes Dev.* **17**, 1569–1574 (2003).
43. Cobb, J. A. *et al.* Replisome instability, fork collapse, and gross chromosomal rearrangements arise synergistically from Mec1 kinase and RecQ helicase mutations. *Genes Dev.* **19**, 3055–3069 (2005).
44. Di Micco, R. *et al.* Oncogene-induced senescence is a DNA damage response triggered by DNA hyper-replication. *Nature* **444**, 638–642 (2006).
45. Felsher, D. W., Zetterberg, A., Zhu, J., Tlsty, T. & Bishop, J. M. Overexpression of MYC causes p53-dependent G2 arrest of normal fibroblasts. *Proc. Natl Acad. Sci. USA* **97**, 10544–10548 (2000).
46. McCormack, S. J. *et al.* Myc/p53 interactions in transgenic mouse mammary development, tumorigenesis and chromosomal instability. *Oncogene* **16**, 2755–2766 (1998).

**Supplementary Information** is linked to the online version of the paper at [www.nature.com/nature](http://www.nature.com/nature).

**Acknowledgements** We thank R. Baer for critical reading of the manuscript; J. Walter and H. Nishitani for *Xenopus* Cdc45 and human Cdt1 antibodies; W. M. Michael for DNA polymerase  $\alpha$  antibodies; D. Shechter for NPE and technical suggestions; A. Lasorella and A. Iavarone for N-Myc plasmids; G. S. Martin and T. Prathapam for 3T9 *c-myc*<sup>+/−</sup> cells; W. Zhang for mass spectrometry analysis; P. Liccardo for generating the Myc H1299 cell line; G. Cattoreti, P. Smith and J. Kosek for technical advice with the immunofluorescence; H. Morse for providing the  $\lambda$ -Myc mouse strain; U. Klein and L. Pasqualucci for advice on mouse B-cell isolation; C. Li for Myc siRNA sequences; M. Lia for GAPDH primers; C. Franci for advice on peptide selection for XMyC antibody; and K. Robinson for technical help with ChIP, quantitative PCR and deconvolution microscopy analysis. This work was supported by grants from the National Institutes of Health (to R.D.-F. and J.G.) and the American Cancer Society (to J.G.). D.D.-S. was a recipient of a postdoctoral grant from Fundacio “la Caixa” (Spain).

**Author Contributions** R.D.-F. and J.G. supervised the entire project and contributed equally as co-senior authors; D.D.-S. designed and conducted the experiments in mammalian cells; D.D.-S. and C.Y.Y. designed the experiments in *Xenopus*, which were conducted by C.Y.Y.; D.D.-S. and C.Y.Y. wrote the manuscript under the supervision of R.D.-F. and J.G. and comments from all co-authors; C.G. designed and conducted immunofluorescence and ChIP experiments in human primary cells; B.C. and M.L. conducted the initial purification and chromatography of the Myc complex, designed and supervised by W.G.; and L.R. contributed to the biochemical characterization of the complex.

**Author Information** Reprints and permissions information is available at [www.nature.com/reprints](http://www.nature.com/reprints). The authors declare no competing financial interests. Correspondence and requests for materials should be addressed to R.D.-F. ([rd10@columbia.edu](mailto:rd10@columbia.edu)) or J.G. ([jg130@columbia.edu](mailto:jg130@columbia.edu)).



## METHODS

**Cell lines and transfections.** All the cell lines, transfection procedures and technical details regarding the manipulation of the 3T9 mouse cell line with a conditionally excisable Myc allele are described in the Supplementary Information.

**RNAi experiments (duplex sequences and procedure).** *c-Myc* siRNA duplexes were designed against the 3' UTR and coding sequence of the *c-Myc* cDNA (NCBI number NM\_002467). All duplexes were purchased from Invitrogen (Stealth<sup>®</sup> siRNA duplexes, 25 MER). siRNA duplexes for human *c-Myc* were: siRNA Myc1, 5'-GCAGUACACAGAAUUUCAUCCUA-3' (3' UTR); siRNA Myc2, 5'-AGCCATAATGTAACTGCCTCAAAT-3' (3' UTR); siRNA Myc3, 5'-CCCA-GCGAGGAUAUCUGGAAGAAU-3' (coding). siRNA control duplex targets eGFP or the luciferase gene in different experiments. Sequences: siRNA Luc+, 5'-UAGUCUUGCAAGCUGCGCAAGAAUA-3'; siRNA GFP, 5'-GCUACCUG-UUCCAUGGCCA.dT.dT-3' (Dharmacon). All siRNA transient transfections were performed using 10-nM duplexes and Lipofectamine RNAiMAX reagent (Invitrogen) following the manufacturer's instructions. Under these conditions, acceptable knockdown levels (>75%) could be achieved in less than 12 h after transfection. For most of the experiments, RNAi-mediated transient Myc knockdown was performed by 1–2 rounds of siRNA transfection within 48 h.

**Myc-associated protein complex isolation.** The protocol is based on a previously published procedure<sup>47</sup>, with minor modifications. Approximately  $3.0 \times 10^8$  cells (control and Myc stable cell line) were harvested upon treatment with MG132 (50 mM, Sigma) for 3–4 h, to increase Myc intracellular levels. Modifications to the previously published protocol, as well as the procedures regarding the purification and characterization (that is, composition, size) of this complex, are detailed in the Supplementary Information.

**Chromatin immunoprecipitation.** ChIP assays were performed as described<sup>48</sup>, with slight modifications. For the analysis of Myc binding to DNA replication origins shown in Fig. 2, cells were crosslinked for 10–15 min at room temperature in 1% formaldehyde, and crosslink reactions stopped by adding 0.125 M glycine for 5 min. Cells were then extracted in a 0.5% Triton X-100 buffer (20 mM HEPES, 340 mM sucrose, 1 mM EDTA) for 10 min in ice, nuclei collected by brief centrifugation and further extracted in 1% SDS containing buffer and sonicated. For the experiment shown in Supplementary Fig. 8 using lower amounts of cells (siRNA and mitosis exit), the procedure was similar except for the use of a 0.1% SDS lysis buffer (instead of 1%) for the extraction and sonication steps to increase the final chromatin yield. Sonication generated 500-bp fragments on average (300–700 bp) (not shown). Pre-clearing and immunocomplex purification steps were performed using Protein-G-agarose beads (Upstate). DNA was purified by phenol-chloroform extraction and ethanol precipitation.

For quantitative PCR analysis of Myc-bound targets, the immunoprecipitated DNA was resuspended in 25–50 µl of TE. Input DNA was used to build a standard curve as reference to which arbitrary units were given for convenience. A value of 1 in the graphs indicates a recovery of ~0.0024% of the input DNA for Raji and 0.0012% for HFFs. This is the range obtained with nonspecific rabbit immunoglobulin. Maximal enrichments with anti-Myc on the lamin B2 gene in HFFs and Raji was ~75-fold (corresponding to ~0.091% and 0.18% respectively of the input) and for Max was in general higher, ~100-fold (corresponding to ~0.24% of the input DNA). These values are comparable to what has been reported for other high-affinity transcriptional targets of Myc and Max.

Primers for PCR, quantitative PCR analyses are provided in the Supplementary Information.

**Anti-XMyc antibody purification and characterization.** Antibodies against a synthetic peptide encompassing residues 5–18 in the N terminus of the *Xenopus* c-Myc homologues were raised in New Zealand rabbits by Evoquest Services (Invitrogen-Zymed) using a standard 10-week protocol. All experiments were performed using antibodies obtained from two different rabbits, and gave similar results and performance. Further details on the purification of these antibodies are provided in the Supplementary Information.

**Immunodepletions and replication assays in *Xenopus* cell-free extracts.** Cell-free extracts (LSS<sup>49</sup>; HSS and NPE<sup>50</sup>) were prepared from unfertilized *Xenopus* eggs as described. Chromosomal templates were prepared from demembrated *Xenopus* sperm nuclei. Immunodepletions were performed by incubating extracts with anti-XMyc antibodies (2 × 90 min at 4 °C, 50 ml of extracts per 100 mg of purified antibody); anti-*Xenopus* DNA polymerase  $\alpha$  antibodies<sup>51</sup> coupled to Protein A-Sepharose (2 × 60 min at 4 °C) or Rabbit IgG (Sigma) as a control. Other technical details regarding the preparation of *in vitro* replication reactions using this system are provided in the Supplementary Information. Where indicated, caffeine (Sigma, 5 mM), geminin (50 ng ml<sup>-1</sup>), Ku5933 (ATM inhibitor, KuDOS)<sup>52</sup>, NU7026 (DNA-PK<sub>CS</sub> inhibitor, Sigma) or SB-218078 (2.5 mM, Calbiochem)<sup>53</sup> were added when assembling the reactions.

**Immunofluorescence protocols, and confocal and deconvolution microscopy.** After blocking for 1 h in 3% BSA, 0.3% Triton X-100, PBS, cells were incubated with primary antibodies for 2 h at room temperature, or 4 °C overnight (for BrdU, clathrin and cyclin E). For BrdU detection, cells were either treated with DNase (Sigma, 25 µg ml<sup>-1</sup>) during the antibody incubation, or fixed for 20 min in 10% buffered formalin after incubation with anti-Myc or anti-Max antibodies, and the DNA depurinated by incubating for 30 min in 2 N HCl at 37 °C, and further neutralized in 0.1 M sodium borate (pH 8.5) for 10 min. Secondary anti-rabbit-Cy3 or TRITC antibodies (Jackson) were used to detect Myc, Max, or c-Jun, or anti-goat-Cy3 antibodies (Jackson) for clathrin in the cell-fusion experiments. Further details of the protocol for BrdU and Myc co-localization in primary cells are available upon request.

For confocal microscopy analysis, images were captured using a Zeiss LSM510-Meta confocal microscope. For deconvolution analysis, pictures were taken with a ×100 objective (Olympus IX70 inverted microscope) by wide-field epi-fluorescence deconvolution microscopy (Delta Vision). Images were taken at each 0.2-µm section through the nucleus (20–25 sections per field). Deconvolution was performed using SoftWoRx 2.5 software (Applied Precision). Exposure times were kept constant for each fluorescence channel within each experiment and antibody used.

**Cell fusion experiments and heterokaryon-mediated rescue.** After DAPI staining, mouse and HeLa nuclei display specific chromatin patterns (mouse, speckled; HeLa, homogenous) that can be readily distinguished upon close inspection (see Fig. 3). This allowed us to identify and score the rescue events in each heterokaryon.

3T9 *v-src*<sup>+</sup>, *c-myc*<sup>-/-</sup> cells are arrested in a G1-like state, as defined by the G1 DNA content and the levels of MCM proteins and Ki67 (Supplementary Fig. 5). Cells were selected after 4 days upon Cre-ER induction, a time when Myc expression was absent in ≥90% of cells (western blot and RT-PCR analysis). As a control, we selected *c-myc*<sup>+/+</sup> populations collected at an early G1 point, 3 h after mitosis, that constitute an accurate control population based on the above described parameters (FACS analysis and western blot, Supplementary Fig. 5d, e).

Metaphase arrested 3T9 *c-myc*<sup>+/+</sup> cells (mitotic shake-off after nocodazole block), *c-myc*<sup>-/-</sup> 3T9 cells (4 day knockdown) and G1/S arrested HeLa cells (double thymidine block), were plated at a 1:3 ratio (3T9/HeLa) in the presence of 2 mM thymidine. Three hours later, medium was replaced (no thymidine) and cycloheximide (50 µg ml<sup>-1</sup>) was added. At this time, 3T9 cells had completed mitosis and were in G1. After 1 h, cells were washed once in warm PBS, and 52% warm polyethyleneglycol (PEG 8000, Sigma) in PBS was added for 3 min. PEG was then discarded and cells were washed several times with PBS (plus cycloheximide), and fresh complete medium containing cycloheximide and 20 µM BrdU was added for 3 h. Cells/heterokaryons were then trypsinized, cytopspins obtained and fixed in formalin for 20 min. Cytopspins were further analysed by immunofluorescence plus DAPI counterstaining to locate and score the resulting heterokaryons.

**Mouse B-cell isolation and immunofluorescence.** Mouse B cells were isolated from spleens of non-immunized (40–45 days old)  $\lambda$ -Myc mice<sup>54</sup> or age-matched littermates. No tumour burden was observed at the time of isolation under macroscopic inspection. Isolation was achieved by using magnetic cell separation through an 'untouched isolation' procedure (MACS affinity 'B-cell isolation kit', Miltenyi Biotech, catalogue number 130-090-862) following the manufacturer's instructions. Isolated cells were resuspended in cold PBS plus 0.5% BSA and kept in ice. Purity of B-cell pools was assessed by FACS analysis upon anti-B220 FITC staining (BD Pharmingen) (>90% in all samples, not shown). Isolated B cells were processed for immunofluorescence (upon cytopspin) and western blot analysis.

Wild-type and  $\lambda$ -Myc B cells were cytopspun on two independent spots on the same slide to minimize variability. After formalin fixation and a 10 min methanol post-fixation, slides were blocked-extracted in PBS, 0.3% Triton X-100, 3% BSA for 30 min. Anti- $\gamma$ -H2A.X (mouse, Upstate) and anti-geminin (Rabbit, Santa Cruz) antibodies were used for immunostaining (overnight, 4 °C). An anti-mouse biotin secondary antibody (horse, Vector) was used to enhance H2A.X detection (60 min), followed by a short incubation with avidin-FITC (Molecular Probes/Invitrogen) (15 min).

47. Nikolaev, A. Y., Li, M., Puskas, N., Qin, J. & Gu, W. Parc: a cytoplasmic anchor for p53. *Cell* 112, 29–40 (2003).
48. Grandori, C. *et al.* c-Myc binds to human ribosomal DNA and stimulates transcription of rRNA genes by RNA polymerase I. *Nature Cell Biol.* 7, 311–318 (2005).
49. Smythe, C. & Newport, J. W. Systems for the study of nuclear assembly, DNA replication, and nuclear breakdown in *Xenopus laevis* egg extracts. *Methods Cell Biol.* 35, 449–468 (1991).

50. Walter, J. Sun, L. & Newport, J. Regulated chromosomal DNA replication in the absence of a nucleus. *Mol Cell* **1**, 519–529 (1998).
51. Michael, W. M. Ott, R. Fanning, E. & Newport, J. Activation of the DNA replication checkpoint through RNA synthesis by primase. *Science* **289**, 2133–2137 (2000).
52. Hickson, I, *et al.* Identification and characterization of a novel and specific inhibitor of the ataxia-telangiectasia mutated kinase ATM. *Cancer Res* **64**, 9152–9159 (2004).
53. Jackson, J. R, *et al.* An indolocarbazole inhibitor of human checkpoint kinase (Chk1) abrogates cell cycle arrest caused by DNA damage. *Cancer Res* **60**, 566–572 (2000).
54. Kovalchuk, A. L, *et al.* Burkitt lymphoma in the mouse. *J. Exp. Med.* **192**, 1183–1190 (2000).

## LETTERS

# Controlled exchange interaction between pairs of neutral atoms in an optical lattice

Marco Anderlini<sup>1</sup>†, Patricia J. Lee<sup>1</sup>, Benjamin L. Brown<sup>1</sup>, Jennifer Sebby-Strabley<sup>1</sup>†, William D. Phillips<sup>1</sup> & J. V. Porto<sup>1</sup>

Ultracold atoms trapped by light offer robust quantum coherence and controllability, providing an attractive system for quantum information processing and for the simulation of complex problems in condensed matter physics. Many quantum information processing schemes require the manipulation and deterministic entanglement of individual qubits; this would typically be accomplished using controlled, state-dependent, coherent interactions among qubits. Recent experiments have made progress towards this goal by demonstrating entanglement among an ensemble of atoms<sup>1</sup> confined in an optical lattice. Until now, however, there has been no demonstration of a key operation: controlled entanglement between atoms in isolated pairs. Here we use an optical lattice of double-well potentials<sup>2,3</sup> to isolate and manipulate arrays of paired <sup>87</sup>Rb atoms, inducing controlled entangling interactions within each pair. Our experiment realizes proposals to use controlled exchange coupling<sup>4</sup> in a system of neutral atoms<sup>5</sup>. Although <sup>87</sup>Rb atoms have nearly state-independent interactions, when we force two atoms into the same physical location, the wavefunction exchange symmetry of these identical bosons leads to state-dependent dynamics. We observe repeated interchange of spin between atoms occupying different vibrational levels, with a coherence time of more than ten milliseconds. This observation demonstrates the essential component of a neutral atom quantum SWAP gate (which interchanges the state of two qubits). Its ‘half-implementation’, the  $\sqrt{\text{SWAP}}$  gate, is entangling, and together with single-qubit rotations it forms a set of universal gates for quantum computation<sup>4</sup>.

Particle exchange symmetry plays a crucial role in much of condensed matter physics, for example allowing spin-independent, purely electrostatic interactions between electrons to give rise to magnetism by correlating their spins. While such effects have been extensively discussed in the context of fermions, similar exchange effects also apply to bosons, such as <sup>87</sup>Rb, except that here the particle wavefunctions are symmetrized rather than anti-symmetrized. Exchange interactions leading to SWAP operations (interchanging the state of two qubits) have been proposed for entangling qubits in condensed matter implementations of quantum computing<sup>4,6</sup>, and as a mechanism for single-qubit control in coded qubit spaces<sup>7</sup>. More recently, exchange-induced entanglement has been proposed for ultracold neutral atoms<sup>5,8</sup>. Other schemes<sup>9–11</sup> that do not involve exchange have relied on mechanisms that directly depend on the internal (qubit) state, requiring state-dependent motion, interaction or excitation of the atoms. Exchange interactions have the advantage that they require none of these. Ordinary state-dependent mechanisms often suffer from decoherence because of state-dependent coupling with the environment. Exchange mechanisms can be relatively free of such decoherence. For example, one could choose magnetic-field-insensitive states as the

qubit basis even if those states had no direct spin-dependent interactions.

To illustrate the working scheme of the two-qubit  $\sqrt{\text{SWAP}}$  gate with bosons, consider a pair of atoms, each occupying the single-particle vibrational ground state of two adjacent potential wells, left (L) and right (R), with spatial wavefunctions  $\phi_L(\mathbf{x})$  and  $\phi_R(\mathbf{x})$  (see Fig. 1a). The full, single-atom wavefunction is  $|q_v\rangle = \phi_v(\mathbf{x})|q\rangle$ , where each qubit (specified by its location  $v = \{L, R\}$ ) can be encoded in two internal spin states of an atom as  $|q\rangle = a|0\rangle + b|1\rangle$ , for amplitudes  $a$  and  $b$  associated with the qubit states  $|0\rangle$  and  $|1\rangle$ . For our demonstration,  $|0\rangle$  and  $|1\rangle$  are Zeeman states of <sup>87</sup>Rb atoms, which are in adjacent sites of a double-well potential<sup>2</sup>. Neutral atoms have short range ‘contact’ interactions, and in <sup>87</sup>Rb are nearly spin-independent. To initiate the interaction, we merge the L and R sites into a single site so that the atoms’ spatial probability distributions overlap<sup>12</sup>. During this merger, the trapping potential is carefully adjusted so that the atoms in L and R are adiabatically transferred to the excited (e) and ground (g) vibrational states of the single well<sup>3</sup>, respectively:  $\phi_L(\mathbf{x}) \rightarrow \phi_e(\mathbf{x})$  and  $\phi_R(\mathbf{x}) \rightarrow \phi_g(\mathbf{x})$  (see Fig. 1a). The two qubits are encoded in identical bosons, so the full two-particle wavefunction must be symmetric under particle exchange, for example,  $|q_L, p_R\rangle = \phi_L(\mathbf{x}_1)\phi_R(\mathbf{x}_2)|q\rangle_1|p\rangle_2 + \phi_R(\mathbf{x}_1)\phi_L(\mathbf{x}_2)|p\rangle_1|q\rangle_2$ , where the two atoms are labelled 1 and 2. (In the merged trap, the subscripts L and R are replaced by e and g, respectively.) The symmetrized states  $|0_L, 0_R\rangle$ ,  $|0_L, 1_R\rangle$ ,  $|1_L, 0_R\rangle$ ,  $|1_L, 1_R\rangle$  represent a convenient computational basis because the identification of the qubit is straightforward:  $|q\rangle$  is always associated with  $\phi_L(\mathbf{x})$  (or  $\phi_e(\mathbf{x})$  when merged), while  $|p\rangle$  is always associated with  $\phi_R(\mathbf{x})$  (or  $\phi_g(\mathbf{x})$ ). When the atoms interact in the merged trap, the symmetrized energy eigenstates are no longer the computational basis. The eigenstates are separable into spin and spatial components (S and T indicate singlet and triplet):

$$|\psi_S\rangle = \phi_S(\mathbf{x}_1, \mathbf{x}_2)|S\rangle = (|1_e, 0_g\rangle - |0_e, 1_g\rangle) / \sqrt{2}$$

$$|\psi_T^0\rangle = \phi_T(\mathbf{x}_1, \mathbf{x}_2)|T^0\rangle = (|1_e, 0_g\rangle + |0_e, 1_g\rangle) / \sqrt{2}$$

$$|\psi_T^-\rangle = \phi_T(\mathbf{x}_1, \mathbf{x}_2)|T^-\rangle = |0_e, 0_g\rangle$$

$$|\psi_T^+\rangle = \phi_T(\mathbf{x}_1, \mathbf{x}_2)|T^+\rangle = |1_e, 1_g\rangle$$

where  $\phi_S(\mathbf{x}_1, \mathbf{x}_2) = \phi_e(\mathbf{x}_1)\phi_g(\mathbf{x}_2) - \phi_g(\mathbf{x}_1)\phi_e(\mathbf{x}_2)$  and  $\phi_T(\mathbf{x}_1, \mathbf{x}_2) = \phi_e(\mathbf{x}_1)\phi_g(\mathbf{x}_2) + \phi_g(\mathbf{x}_1)\phi_e(\mathbf{x}_2)$ ;  $|S\rangle = (|1\rangle_1|0\rangle_2 - |0\rangle_1|1\rangle_2) / \sqrt{2}$ ,  $|T^0\rangle = (|1\rangle_1|0\rangle_2 + |0\rangle_1|1\rangle_2) / \sqrt{2}$ ,  $|T^-\rangle = |0\rangle_1|0\rangle_2$ , and  $|T^+\rangle = |1\rangle_1|1\rangle_2$ . The spatial component of the singlet state  $|\psi_S\rangle$  is antisymmetric under exchange of particles; there is no density overlap between the two particles, giving essentially zero interaction energy for the short-range contact interactions between the atoms. On the other hand, the triplet states have an interaction energy

<sup>1</sup>Joint Quantum Institute, National Institute of Standards and Technology and University of Maryland, Gaithersburg, Maryland 20899, USA. †Present addresses: INFN sezione di Firenze, Via Sansone 1, I-50019 Sesto Fiorentino, Florence, Italy (M.A.); Honeywell Aerospace, 12001 State Highway 55, Plymouth, Minnesota 55441, USA (J.S.-S.).



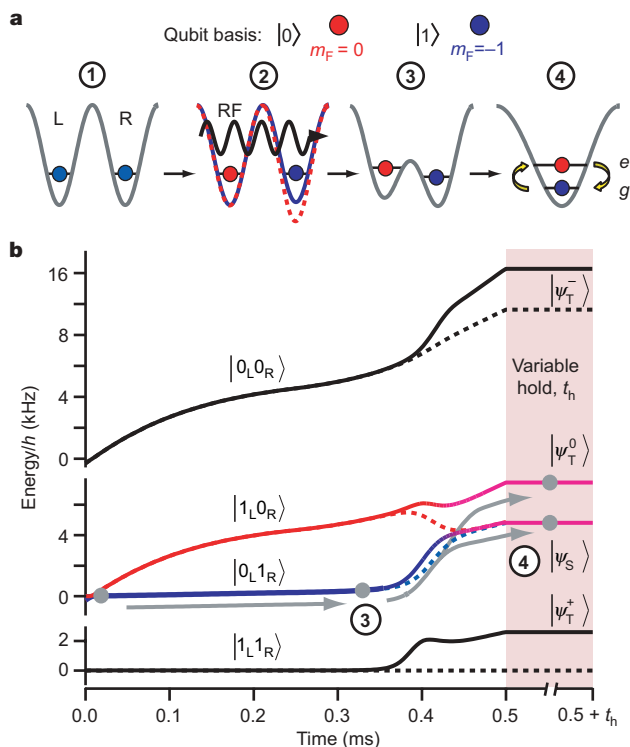


**Figure 1 | Experimental sequence.** **a**, Preparation and interaction of two qubits. Step 1: the system is initialized as qubit state  $|1_L, 1_R\rangle$ . Step 2: the two neighbouring atoms in a double well are prepared in the qubit state  $|0_L, 1_R\rangle$  using site-selective radio-frequency addressing based on the spin-state dependence of the potential (indicated by the differing blue and red potentials). Step 3: the potential barrier between the two sites is then lowered. Step 4: the two sites merge, allowing the atoms to interact. Careful control of the potentials during this merger forces the atom in the left site into the first excited state and the atom from the right site into the ground state of the final single-well configuration. **b**, Plot of the interacting (solid lines) and non-interacting (dashed lines) two-particle energies during the gate sequence (steps 2 to 4 in **a**). For visual clarity the energies are relative to the non-interacting  $|1_L, 1_R\rangle$  eigenenergy, and the 34 MHz Zeeman shifts are not included. The grey arrows indicate the evolution of the state  $|0_L, 1_R\rangle$  from step 2 to step 4. The colour transition from red ( $|1_L, 0_R\rangle$ ) and blue ( $|0_L, 1_R\rangle$ ) to purple ( $|\psi_T^0\rangle$  and  $|\psi_S^0\rangle$ ) indicates the mixing of the two logical qubit states. The evolution from the initial state  $|0_L, 1_R\rangle$  is non-adiabatic with respect to interactions, and the projection onto the final singlet/triplet eigenstates results in spin exchange oscillations.

$U_{\text{eg}} = (8\pi\hbar^2 a_s/m) \int |\phi_e(\mathbf{x})|^2 |\phi_g(\mathbf{x})|^2 d^3x$ , where  $a_s$  is the s-wave scattering length and  $m$  is the mass of  $^{87}\text{Rb}^{13}$ . This energy difference between the ‘singlet’ and the ‘triplet’ states can be viewed as arising from an effective magnetic interaction  $\propto \sigma_e \sigma_g$  between atoms in the ground and excited states, where  $\sigma_v$  is the Pauli spin operator acting on the qubit basis, for the atom in the vibrational state  $v = \{e, g\}$ . This interaction can give rise to a spin exchange oscillation between the qubit states  $|0_e, 1_g\rangle$  and  $|1_e, 0_g\rangle$ . If atoms in any of the four states of the computational basis are combined into a single site adiabatically with respect to the lattice vibrational level spacing, but diabatically with respect to  $U_{\text{eg}}$  (thus projecting onto the interacting eigenstates), they evolve in time as shown in Table 1. At time  $T_{\text{SWAP}} \equiv \pi\hbar/U_{\text{eg}}$ , the

internal states associated with  $\phi_e(\mathbf{x})$  and  $\phi_g(\mathbf{x})$  are swapped. If the interaction is stopped at  $T_{\text{SWAP}}/2$  (for example, by separating the atoms into the L and R sites), then the result is an entangling  $\sqrt{\text{SWAP}}$ .

We realized this exchange-mediated SWAP operation using arrays of pairs of  $^{87}\text{Rb}$  atoms in a three-dimensional optical lattice. The lattice consists of a dynamically adjustable two-dimensional lattice of double-wells in the horizontal plane<sup>2,3</sup>, and an independent one-dimensional lattice along the vertical direction. By controlling the laser polarization, the unit cell of the two-dimensional lattice can be continuously changed between the single-well ( $\lambda$ -lattice) or double-well (the half-wavelength  $\lambda/2$ -lattice) configurations (see Fig. 1a), where  $\lambda = 816\text{ nm}$ . We start with a magnetically trapped Bose-Einstein condensate of  $\sim 6.0 \times 10^4$  atoms of  $^{87}\text{Rb}$  in the  $5S_{1/2}$   $|F=1, m_F=-1\rangle$  magnetic state, and slowly (in 140 ms) turn on the  $\lambda/2$ -lattice and vertical lattice, reaching depths of  $40 \pm 2 E_R$  and  $54 \pm 3 E_R$ , respectively. ( $E_R = \hbar^2 k_R^2 / 2m = 3.45 h \text{ kHz}$  is the photon recoil energy and  $k_R = 2\pi/\lambda$  is the photon recoil momentum.) Ideally, the ensemble crosses the Mott insulator transition<sup>14</sup>, creating a central core of atoms with unit filling factor<sup>15</sup> in the ground state of the  $\lambda/2$ -lattice. The magnetic confining fields are then turned off, leaving a homogeneous field  $B_0 \approx 4.85\text{ mT}$ , which defines the quantization axis. It also provides a quadratic Zeeman shift large enough that we can selectively radio-frequency couple only the  $|F=1, m_F=-1\rangle$  and  $|F=1, m_F=0\rangle$  states<sup>12</sup>, designated as our qubit states  $|1\rangle$  and  $|0\rangle$ , respectively. Following this loading procedure, isolated pairs of qubits are in the state  $|1_L, 1_R\rangle$  inside separate unit cells of the lattice (see Fig. 1a, step 1).

We can prepare every pair of atoms in any non-entangled two-qubit state by selectively addressing the atoms in the L and R sites. We exploit the spin-dependence of the potential, which can be manipulated through the same polarization control used to adjust the lattice topology<sup>2,12</sup>. We first induce a state-dependence in the optical potential that produces an effective magnetic field gradient between the two adjacent sites of the double well. This introduces a differential shift  $\Delta\nu_{\text{RF}}$  in the spin-resonant frequencies between the two sites. The L or R qubits are then selectively addressed by applying a radio-frequency pulse resonant only with those qubits. In our experiment,  $\Delta\nu_{\text{RF}} \approx 20$  kHz and we can prepare the state  $|0_{\text{L}}, 1_{\text{R}}\rangle$  with 95% fidelity.

To measure the qubit state after the double well is transformed into a single well, we map the quasi-momentum of atoms occupying different vibrational bands of the optical potential onto real momenta lying within different Brillouin zones<sup>16,17</sup>. This is achieved by switching off the  $\lambda$ -lattice and the vertical lattice in 500  $\mu\text{s}$ ; after a 13 ms time-of-flight, atoms occupying different vibrational levels become spatially separated and can be absorption imaged. Moreover, applying a magnetic field gradient during time-of-flight separates atoms in different spin states along another axis. The populations of atoms in  $|0\rangle$ ,  $|1\rangle$  and  $\phi_e(\mathbf{x})$ ,  $\phi_g(\mathbf{x})$  can thus be differentiated in a single image (see Fig. 2). By measuring the population in the different Brillouin zones resulting from the samples loaded either only in the left or only in the right sites of the double wells, we found that more than 80% (or 85%) of the atoms starting in the L (or R) sites end in the first excited (or ground) state of the single-well potential.

As a demonstration of an exchange-induced SWAP, we initially prepare the atoms in the state  $|0_L, 1_R\rangle$ . We then merge each double well into a single well, transferring the atoms from the L and R sites into the first excited and ground states, respectively, of the single-well

**Table 1 | Truth table for SWAP and  $\sqrt{\text{SWAP}}$  gates**

Initial	State after time $t$	$\sqrt{\text{SWAP}}\ t = \pi\hbar/2U_{eg} = T_{\text{SWAP}}/2$	SWAP $t = \pi\hbar/U_{eg} \equiv T_{\text{SWAP}}$
$ 0_e, 0_g\rangle$	$e^{-iU_{eg}t/2\hbar} 0_e, 0_g\rangle$	$e^{-i\pi/4} 0_e, 0_g\rangle$	$ 0_e, 0_g\rangle$
$ 0_e, 1_g\rangle$	$\cos(U_{eg}t/2\hbar) 0_e, 1_g\rangle - i\sin(U_{eg}t/2\hbar) 1_e, 0_g\rangle$	$( 0_e, 1_g\rangle - i 1_e, 0_g\rangle)/\sqrt{2}$	$ 1_e, 0_g\rangle$
$ 1_e, 0_g\rangle$	$-i\sin(U_{eg}t/2\hbar) 0_e, 1_g\rangle + \cos(U_{eg}t/2\hbar) 1_e, 0_g\rangle$	$(-i 0_e, 1_g\rangle +  1_e, 0_g\rangle)/\sqrt{2}$	$ 0_e, 1_g\rangle$
$ 1_e, 1_g\rangle$	$e^{-iU_{eg}t/2\hbar} 1_e, 1_g\rangle$	$e^{-i\pi/4} 1_e, 1_g\rangle$	$ 1_e, 1_g\rangle$

The table ignores a global phase factor  $e^{-iU_{\text{eg}}t/2\hbar}$

potential. The lattice parameters are adjusted throughout the transformation so that the vibrational frequencies along all three spatial directions remain non-degenerate to avoid unwanted energy level crossings; the lowest vibrational frequency is always along the direction of the double wells. This transformation takes 500  $\mu\text{s}$ , a time-scale chosen to be adiabatic with respect to vibration. The basis change due to interactions occurs during a small fraction of the total merge time (as indicated by the colour transition at  $\sim 0.45$  ms in Fig. 1b), so this transformation is nearly diabatic with respect to interactions. This projects the atoms onto a superposition of the two eigenstates  $|\psi_S\rangle$  and  $|\psi_T\rangle$  (see Fig. 1b), which oscillates between the states  $|0_e, 1_g\rangle$  and  $|1_e, 0_g\rangle$ . We calculate that, assuming vibrational adiabaticity, the failure to be completely diabatic would result in approximately 92% population oscillation. (We estimate that it would take longer than 4 ms to be fully adiabatic with respect to interactions.) The state evolves in this single-well configuration for a hold time  $t_h$  before measurement. As shown in Fig. 3, the population in each spin component oscillates between the ground and the first excited states. Fitting an exponentially damped sinusoid to the time-dependent populations in  $|0\rangle$  and  $|1\rangle$  in the excited state gives a period  $2T_{\text{SWAP}} = 285 \pm 1 \mu\text{s}$ , an amplitude of  $27 \pm 2\%$ , and a  $1/e$  decay time longer than 10 ms.

The  $>10$  ms decay of the swap oscillations in Fig. 3 is much longer than the single-spin phase coherence time<sup>12</sup> of  $\sim 150 \mu\text{s}$ . This long decay time results from the Zeeman-degeneracy of the  $|0_e, 1_g\rangle$  and  $|1_e, 0_g\rangle$  states, because superpositions of these two-atom states are insensitive to spatial and temporal magnetic field noise, and they form a decoherence-free subspace<sup>18</sup>. This is similar to fermionic double quantum dot systems<sup>19</sup>, but there the underlying noise arises from the inherent fluctuating background of nuclear spins. In contrast, here the inhomogeneous broadening arises from technical sources such as background magnetic field gradients and shot-to-shot field fluctuations. One could choose to encode a single qubit in this two-atom decoherence-free subspace, for which spin exchange would act as a single qubit operation<sup>7</sup>. Here, however, we have sufficient coherence and individual control of the two spins to use the two qubits separately; in this case spin exchange acts to entangle the two qubits.

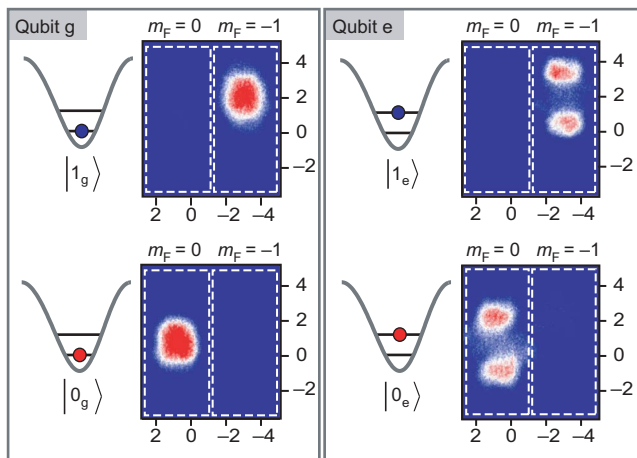


**Figure 2 | Qubit state analysis.** Time-of-flight images mapping the atoms' internal and vibrational states: the images were produced by preparing single atoms in one of the two single-qubit basis states (internal spin states) in either the L or R qubit and performing the full sequence (steps 2 to 4 in Fig. 1a), followed by Brillouin zone mapping (see text) and time-of-flight absorption imaging. Different vibrational states are thus mapped to different momentum regions. In addition, a magnetic field gradient (diagonal in the image plane) applied during time-of-flight spatially separates atoms in different spin states, indicated by the white dashed-line boxes. Each of the input states maps to a distinct region of the image, allowing us to measure the populations in the spin state  $|0\rangle$  or  $|1\rangle$  separately for each qubit. All axes are momentum in units of  $\hbar k_R/\sqrt{2}$ .

To investigate spin coherence during the exchange interaction within the full two-qubit Hilbert space, we place both qubits in a superposition of  $|0\rangle$  and  $|1\rangle$  and allow them to evolve under exchange (see Fig. 4a). Starting with atoms in  $|0_e, 1_g\rangle$ , we apply a radio-frequency  $\pi/2$  pulse to both qubits, producing a superposition of all four two-qubit logical states. The atoms evolve for 165  $\mu\text{s}$ , longer than is required for a full swap, and a second  $\pi/2$  pulse is applied to read out the coherence. (A  $\pi$ -pulse inserted between the  $\pi/2$  pulses creates a spin echo to cancel the effects of the magnetic field inhomogeneity<sup>12</sup>.) The subsequent swap oscillations (Fig. 4c) have the expected phase and  $80 \pm 2\%$  of the amplitude compared to the case

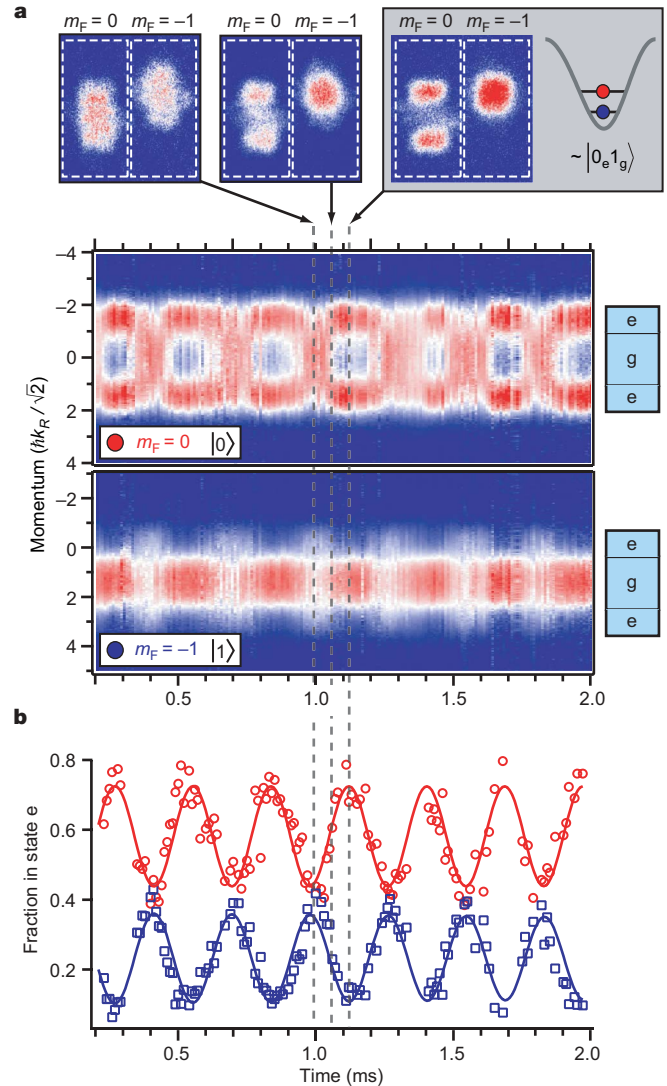


**Figure 3 | Collisional swap dynamics.** **a**, Concatenated slices of absorption images as a function of hold time  $t_h$  in the single-well configuration (Fig. 1a, step 4). For technical reasons, the hold time can be no less than 200  $\mu\text{s}$ . Atoms in each vibrational level oscillate between spin states  $|0\rangle$  and  $|1\rangle$ . **b**, Fraction of atom populations in the excited state for atoms in  $|0\rangle$  (red) and  $|1\rangle$  (blue). Each point is extracted from the data in **a** by fitting the time-of-flight image slices and extracting the relative amount of population in each Brillouin zone. The solid lines are sinusoidal fits to the data, with a common period of  $285 \pm 1 \mu\text{s}$  and a common amplitude of  $0.27 \pm 0.02$ . The amplitude of the oscillation is smaller than the initial excited  $|0\rangle$  (or ground  $|1\rangle$ ) fraction, which gives rise to the difference in the bottom two panels of **a** and the offset of the  $|0\rangle$  and  $|1\rangle$  fractions in **b**. The phase of the oscillations is affected by interaction during the merging and during the process of switching off the lattice. After more than six full periods of oscillation, corresponding to  $24 \sqrt{\text{SWAP}}$  cycles, the amplitude of the oscillations shows negligible decay. If the qubits are prepared initially in  $|1_e, 1_g\rangle$  or  $|0_e, 0_g\rangle$ , we observe no evolution of the spin populations.

without the additional radio-frequency pulses (Fig. 4b), a degradation approximately consistent with the measured single-qubit decoherence. This shows that the coherence time of the system is longer than the time needed for both a swap operation and single-qubit operations using radio-frequency addressing, which together constitute a set of universal quantum logic operations.

Although the exchange oscillations show almost no decay over many cycles, the initial amplitude is only 27% of the ideal case. Assuming, pessimistically, that the remaining 73% of the atoms do not SWAP, and so project onto the target state after  $\sqrt{\text{SWAP}}$  with 50% probability, we find a minimum fidelity of 0.64. The true fidelity is probably higher and can be improved: we believe the major reduction in oscillation amplitude is due to imperfect loading of the initial  $\lambda/2$ -lattice Mott insulator state. Previous experiments in this apparatus<sup>20</sup> indicate that in the  $\lambda/2$ -lattice there are relatively few doubly occupied sites, but there may be a significant fraction of empty sites. An empty site merged with an occupied site produces a site where no SWAPPING can occur, reducing the oscillation amplitude. From our previous measurements, we estimate that approximately 50% of the  $\lambda$ -sites (33% of the atoms) are unpaired. However, this initialization infidelity is distinct from gate fidelity and can be improved<sup>21</sup>.

Imperfection in vibrational adiabaticity of the transfer from L and R to e and g results in unwanted excitations of atoms to other vibrational states, which are visible in the Brillouin zone mapping of Fig. 2. Such motional problems are likely to be among the limiting factors for the fidelity and speed of any collision-based gate, and will be a topic of future study. Possible improvements include using deeper lattices and coherent control techniques<sup>22</sup>. Imperfections in the radio-frequency spin-flip state preparation, the vibrational adiabaticity of the transfer from L and R to e and g, and the diabaticity with respect to interactions during the merge account for an amplitude reduction to approximately 59%. Other effects, including the state-dependence of the  $\lambda$ -lattice and of the interaction energies are relatively small. Finally, the coherence of the individual qubits can be significantly improved by actively stabilizing the magnetic field and improving its spatial homogeneity. With the freedom to choose the qubit spin states, we can improve the coherence even further by storing the qubit information in field-insensitive hyperfine 'clock-states'. In this configuration, site-selective addressing could still be

achieved using two-photon transitions<sup>23</sup> through an intermediate site-dependent Zeeman state.

This demonstration of a controlled two-atom exchange operation is the first realization of the key component of an exchange gate in neutral atoms. As with all ensemble qubit measurements<sup>1</sup>, we do not directly show non-classical correlations, but our observed spin SWAPPING oscillations clearly indicate that during every SWAP cycle the system undergoes the entangling/disentangling dynamics associated with a  $\sqrt{\text{SWAP}}$  operation. Our results show that the double-well optical lattice can be used as a testbed for exploring the two-atom dynamics that underlie some of the key challenges in neutral-atom-based quantum computing. Scaling to a large number of individually controlled qubits requires individual and pairwise addressing, which could be accomplished with state-dependent focused laser beams<sup>24</sup>. The direct observation of exchange interactions is also relevant for proposals to engineer quantum spin systems<sup>8,25</sup> in which tunnelling and exchange give rise to an effective magnetic interaction between ground vibrational state atoms on neighbouring sites  $i$  and  $i+1$ , which is  $\propto \sigma_i \sigma_{i+1}$ . The direct on-site exchange interaction observed here,  $\propto \sigma_e \sigma_g$ , could be used to provide effective magnetic interactions between atoms in different vibrational bands<sup>26,27</sup>, or to 'stroboscopically' generate magnetic interactions between nearest neighbours<sup>28,29</sup>.

Received 3 April; accepted 7 June 2007.

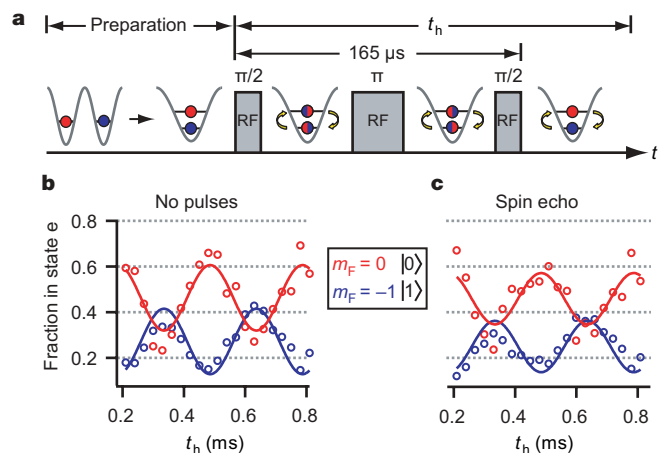


**Figure 4 | Spin-phase coherence during the SWAP operation.** **a**, The temporal sequence of the experiment. Each pair of atoms in a double well is initially prepared in the state  $|0_L, 1_R\rangle$ , and transferred into the single-well configuration. The measured fraction of atom population in the excited state for atoms in  $|0\rangle$  (red) and  $|1\rangle$  (blue) versus  $t_h$  is plotted for **b**, a control case identical to the conditions in Fig. 3, where no additional radio-frequency pulses are applied, and **c**, the spin echo case. Between the two  $\pi/2$  pulses of the spin echo sequence the atoms were in a superposition of all possible spin states while undergoing a full swap. The exchange oscillations following the spin-echo sequence shown in **c** indicate that spin coherence is preserved during the swap.

- Mandel, O. *et al.* Controlled collisions for multi-particle entanglement of optically trapped atoms. *Nature* **425**, 937–940 (2003).
- Sebby-Strabley, J., Anderlini, M., Jessen, P. S. & Porto, J. V. Lattice of double wells for manipulating pairs of cold atoms. *Phys. Rev. A* **73**, 033605 (2006).
- Anderlini, M., Sebby-Strabley, J., Kruse, J., Porto, J. V. & Phillips, W. D. Controlled atom dynamics in a double-well optical lattice. *J. Phys. B* **39**, S199–S210 (2006).
- Loss, D. & DiVincenzo, D. P. Quantum computation with quantum dots. *Phys. Rev. A* **57**, 120–126 (1998).
- Hayes, D., Julienne, P. S. & Deutsch, I. H. Quantum logic via the exchange blockade in ultracold collisions. *Phys. Rev. Lett.* **98**, 070501 (2007).
- Kane, B. E. A silicon-based nuclear spin quantum computer. *Nature* **393**, 133–137 (1998).
- DiVincenzo, D. P., Bacon, D., Kempe, J., Burkard, G. & Whaley, K. B. Universal quantum computation with the exchange interaction. *Nature* **408**, 339–342 (2000).
- Duan, L. M., Demler, E. & Lukin, M. D. Controlling spin exchange interactions of ultracold atoms in optical lattices. *Phys. Rev. Lett.* **91**, 090402 (2003).
- Brennen, G. K., Caves, C. M., Jessen, F. S. & Deutsch, I. H. Quantum logic gates in optical lattices. *Phys. Rev. Lett.* **82**, 1060–1063 (1999).
- Jaksch, D., Briegel, H. J., Cirac, J. I., Gardiner, C. W. & Zoller, P. Entanglement of atoms via cold controlled collisions. *Phys. Rev. Lett.* **82**, 1975–1978 (1999).
- Jaksch, D. *et al.* Fast quantum gates for neutral atoms. *Phys. Rev. Lett.* **85**, 2208–2211 (2000).
- Lee, P. J. *et al.* Sublattice addressing and spin-dependent motion of atoms in a double-well lattice. *Phys. Rev. Lett.* (in the press); preprint at <<http://arxiv.org/quant-ph/0702039>>.
- Pethick, C. J. & Smith, H. *Bose-Einstein Condensation in Dilute Gases* Ch. 5 (Cambridge Univ. Press, Cambridge, UK, 2002).
- Greiner, M., Mandel, O., Esslinger, T., Hansch, T. W. & Bloch, I. Quantum phase transition from a superfluid to a Mott insulator in a gas of ultracold atoms. *Nature* **415**, 39–44 (2002).
- Batrouni, G. G. *et al.* Mott domains of bosons confined on optical lattices. *Phys. Rev. Lett.* **89**, 117203 (2002).
- Kastberg, A., Phillips, W. D., Rolston, S. L., Spreew, R. J. C. & Jessen, P. S. Adiabatic cooling of cesium to 700-nK in an optical lattice. *Phys. Rev. Lett.* **74**, 1542–1545 (1995).
- Greiner, M., Bloch, I., Mandel, O., Hansch, T. W. & Esslinger, T. Exploring phase coherence in a 2D lattice of Bose-Einstein condensates. *Phys. Rev. Lett.* **87**, 160405 (2001).
- Lidar, D. A., Chuang, I. L. & Whaley, K. B. Decoherence-free subspaces for quantum computation. *Phys. Rev. Lett.* **81**, 2594–2597 (1998).
- Petta, J. R. *et al.* Coherent manipulation of coupled electron spins in semiconductor quantum dots. *Science* **309**, 2180–2184 (2005).
- Sebby-Strabley, J. *et al.* Preparing and probing atomic number states with an atom interferometer. *Phys. Rev. Lett.* **98**, 200405 (2007).
- Widera, A. *et al.* Coherent collisional spin dynamics in optical lattices. *Phys. Rev. Lett.* **95**, 190405 (2005).
- Calarco, T., Dorner, U., Julienne, P. S., Williams, C. J. & Zoller, P. Quantum computations with atoms in optical lattices: Marker qubits and molecular interactions. *Phys. Rev. A* **70**, 012306 (2004).
- Matthews, M. R. *et al.* Dynamical response of a Bose-Einstein condensate to a discontinuous change in internal state. *Phys. Rev. Lett.* **81**, 243–247 (1998).



24. Zhang, C. W., Rolston, S. L. & Das Sarma, S. Manipulation of single neutral atoms in optical lattices. *Phys. Rev. A*, **74**, 042316 (2006).
25. Altman, E., Hofstetter, W., Demler, E. & Lukin, M. D. Phase diagram of two-component bosons on an optical lattice. *N. J. Phys.* **5**, 113–(1–19) (2003).
26. Scarola, V. W. & Das Sarma, S. Quantum phases of the extended Bose-Hubbard hamiltonian: Possibility of a supersolid state of cold atoms in optical lattices. *Phys. Rev. Lett.* **95**, 033003 (2005).
27. Isacsson, A. & Girvin, S. M. Multiflavor bosonic Hubbard models in the first excited Bloch band of an optical lattice. *Phys. Rev. A*, **72**, 053604 (2005).
28. Jané, E., Vidal, G., Dür, W., Zoller, P. & Cirac, J. I. Simulation of quantum dynamics with quantum optical systems. *Quantum Inf. Comput.* **3**, 15–37 (2003).
29. Sørensen, A. & Mølmer, K. Spin-spin interaction and spin squeezing in an optical lattice. *Phys. Rev. Lett.* **83**, 2274–2277 (1999).

**Acknowledgements** We thank I. Spielman and S. Rolston for contributions to the project, and I. Deutsch for discussions. P.J.L., B.L.B. and J.S.-S. acknowledge support from the National Research Council Postdoctoral Research Associateship Program. This work was supported by DTO, ONR and NASA.

**Author Information** Reprints and permissions information is available at [www.nature.com/reprints](http://www.nature.com/reprints). The authors declare no competing financial interests. Correspondence and requests for materials should be addressed to J.V.P. (trey@nist.gov).

# Preparation and characterization of graphene oxide paper

Dmitriy A. Dikin<sup>1</sup>, Sasha Stankovich<sup>1</sup>, Eric J. Zimney<sup>1</sup>, Richard D. Piner<sup>1</sup>, Geoffrey H. B. Dommett<sup>1</sup>, Guennadi Evmenenko<sup>2</sup>, SonBinh T. Nguyen<sup>3</sup> & Rodney S. Ruoff<sup>1</sup>

Free-standing paper-like or foil-like materials are an integral part of our technological society. Their uses include protective layers, chemical filters, components of electrical batteries or supercapacitors, adhesive layers, electronic or optoelectronic components, and molecular storage<sup>1</sup>. Inorganic ‘paper-like’ materials based on nanoscale components such as exfoliated vermiculite or mica platelets have been intensively studied<sup>2,3</sup> and commercialized as protective coatings, high-temperature binders, dielectric barriers and gas-impermeable membranes<sup>4,5</sup>. Carbon-based flexible graphite foils<sup>6–8</sup> composed of stacked platelets of expanded graphite have long been used<sup>9,10</sup> in packing and gasketing applications because of their chemical resistivity against most media, superior sealability over a wide temperature range, and impermeability to fluids. The discovery of carbon nanotubes brought about bucky paper<sup>11</sup>, which displays excellent mechanical and electrical properties that make it potentially suitable for fuel cell and structural composite applications<sup>12–15</sup>. Here we report the preparation and characterization of graphene oxide paper, a free-standing carbon-based membrane material made by flow-directed assembly of individual graphene oxide sheets. This new material outperforms many other paper-like materials in stiffness and strength. Its combination of macroscopic flexibility and stiffness is a result of a unique interlocking-tile arrangement of the nanoscale graphene oxide sheets.

Graphite oxide is a layered material consisting of hydrophilic oxygenated graphene sheets (graphene oxide sheets) bearing oxygen functional groups on their basal planes and edges. Graphite-oxide-based thin films have been fabricated via solvent-casting methods<sup>16</sup> but it is not clear whether the graphite oxide dispersions used were completely exfoliated into individual sheets. In addition, the morphology and mechanical properties of the resulting thin-film materials have not been elucidated in detail.

Recently, we have shown that under suitable conditions<sup>17–19</sup> graphite oxide can undergo complete exfoliation in water, yielding colloidal suspensions of almost entirely individual graphene oxide sheets<sup>17–19</sup> with a mean lateral dimension of approximately 1  $\mu\text{m}$ . Such sheets can be chemically functionalized, dispersed in polymer matrices, and deoxygenated to yield novel composites<sup>18</sup>. We thus sought a method for assembling these graphene oxide sheets into well-ordered macroscopic structures. We found that, similar to carbon nanotubes<sup>11</sup>, graphene oxide sheets could indeed be assembled into a paper-like material under a directional flow. Vacuum filtration of colloidal dispersions of graphene oxide sheets through an Anodisc membrane filter yielded, after drying, free-standing graphene oxide paper with thicknesses ranging from 1 to 30  $\mu\text{m}$  (Supplementary Information 1). This material is uniform and dark brown under transmitted white light and almost black in reflection when thicker

than 5  $\mu\text{m}$  (Fig. 1a–c). The fracture edges of a graphene oxide paper sample when imaged via scanning electron microscopy (SEM) revealed well-packed layers through almost the entire cross-section of the paper samples, sandwiched between less densely packed ‘wavy’ skin layers that were about 100–200 nm thick (Fig. 1e–g).

The layering in our graphene oxide paper is evident from its X-ray diffraction pattern (Fig. 1h). The peak in the X-ray spectrum of a typical graphene oxide paper specimen corresponds to the layer-to-layer distance ( $d$ -spacing) of about 0.83 nm. From studies on the dependence of  $d$ -spacing in graphite oxide on the water content<sup>20</sup>, the measured distance can be attributed to an approximately one-molecule-thick layer of water that is presumably hydrogen-bonded between the graphene oxide sheets<sup>21</sup>. The mean dimension of an ordered stack of graphene oxide sheets in the paper material that are oriented perpendicularly to the diffracting plane was calculated from the width of the X-ray diffraction peak using the Debye–Scherrer equation<sup>22</sup>, and was found to be  $5.2 \pm 0.2$  nm. This size corresponds to about 6 to 7 stacked graphene oxide sheets.

In a typical stress–strain curve three regimes of deformation can be observed for samples of graphene oxide paper: straightening, almost linear (‘elastic’), and plastic (Fig. 2a). This behaviour is similar to that of most paper-like or foil-like materials; however, graphene oxide paper is very stiff. Although there are different levels of wrinkling and ‘waviness’ in the graphene oxide paper at different length scales, the initial straightening during the tensile loading is quite small. The rupture of graphene oxide paper samples loaded beyond the ‘elastic’ regime is not accompanied by any pull-out of its lamellae, and produces almost straight and flat fracture surfaces (Fig. 1e–g). This is in contrast to the rupture of bucky paper, and suggests good material homogeneity and strong interlayer binding. The ultimate tensile strain for graphene oxide paper (0.6%) was the highest recorded number for samples that did not exhibit slip–stick behaviour, see below) is comparable to that of flexible graphite foils (0.5% along the rolling direction), and much lower than that of vermiculite (2.5%) and bucky paper (3–5.6%) prepared by similar filtration strategies. However, the work of extension to fracture for graphene oxide paper is as high as  $350 \text{ kJ m}^{-3}$  ( $\sim 190 \text{ J kg}^{-1}$ , at the material density of  $\sim 1.8 \text{ g cm}^{-3}$ , Supplementary Information 7). These values are more than ten times higher than the corresponding values for flexible graphite foils<sup>6,7</sup>, and of similar magnitude to the values for ‘pristine’ bucky paper<sup>15,23</sup>.

Tensile test measurements of our graphene oxide paper revealed very high values of tensile modulus and fracture strength (Fig. 2). The average modulus of graphene oxide paper was determined to be 32 GPa (average from 31 tested samples, Supplementary Information 2) with the highest being  $42 \pm 2$  GPa. These values are much higher than those reported for bucky paper<sup>23</sup>, paper-like materials

<sup>1</sup>Department of Mechanical Engineering, <sup>2</sup>Department of Physics and Astronomy, <sup>3</sup>Department of Chemistry, Northwestern University, 2145 Sheridan Road, Evanston, Illinois 60208-3111, USA.

based on vermiculite<sup>2</sup> (prepared by either filtration or casting strategies), and flexible graphite foil<sup>6</sup> (Fig. 3). The tensile strength of our graphene oxide paper is also considerably higher than values obtained for flexible graphite foil and bucky paper, and is only slightly lower than the highest value reported for vermiculite-based paper materials<sup>2</sup> (Fig. 3).

Cyclic loading experiments revealed that permanent deformations were introduced in the samples even when they were loaded within the limits of the 'elastic' regime (Fig. 2c). Both the load and unload portions of each subsequent cycle displayed an increase in modulus of elasticity with a total increase of about 20% after five cycles. Such self-reinforcing behaviour is well known for aligned polymer chains and other fibrous materials<sup>24</sup>, where tensile loading can lead to a macromolecular/fibril alignment along the load direction and a mechanically stiffer sample. Similarly, stretching graphene oxide paper should lead to a better alignment of the two-dimensional lamellae and thus also the individual graphene oxide sheets, increase their contact and interactions, and result in a stiffer material. This behaviour of graphene oxide paper is in stark contrast to that of flexible graphite foil for which the elasticity modulus decreases upon stress cycling<sup>6</sup>.

Interestingly, the stress-strain curves for graphene oxide paper samples often displayed 'washboard' patterns and sometimes even sharp upturns (Supplementary Information 3), manifested as a sequence of the peaks in the derivative ( $\delta\sigma/\delta\varepsilon$ ) of the stress-strain curve (Fig. 2d). Similar local-reinforcing behaviour was observed during basal plane shear in single-crystal graphite<sup>25</sup> and in the

material produced by layer-by-layer assembly of montmorillonite clay platelets and polyelectrolytes<sup>26</sup>. However, if the sample was loaded into the plastic regime (Fig. 2b) and failed, then the stiffness of the reloaded segments at low strain was similar to that of the original sample just before its failure. These results indicate that the loss of material stiffness is not a local effect, but rather a homogeneous softening of the paper upon loading in this manner. In

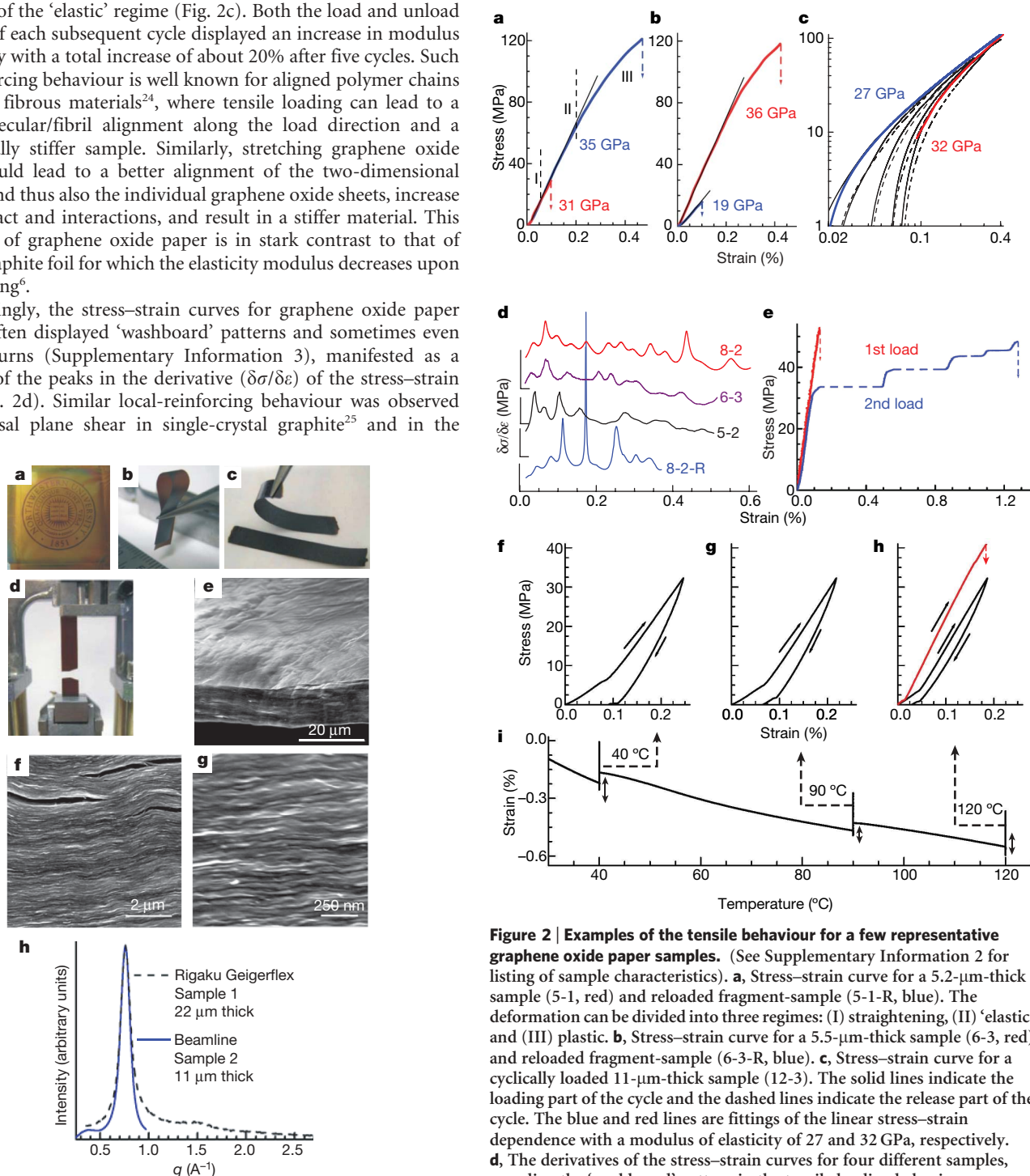


**Figure 1 | Morphology and structure of graphene oxide paper.** **a–d**, Digital camera images of graphene oxide paper. **a**, ~1-μm-thick (the Northwestern University logo is beneath the paper); **b**, folded ~5-μm-thick semi-transparent film; **c**, folded ~25-μm-thick strip; **d**, strip after fracture from tensile loading. **e–g**, Low-, middle- and high-resolution SEM side-view images of ~10-μm-thick sample. **h**, X-ray diffraction pattern of two graphene oxide paper samples obtained with two different instruments (see Methods).

**Figure 2 | Examples of the tensile behaviour for a few representative graphene oxide paper samples.** (See Supplementary Information 2 for listing of sample characteristics). **a**, Stress-strain curve for a 5.2-μm-thick sample (5-1, red) and reloaded fragment-sample (5-1-R, blue). The deformation can be divided into three regimes: (I) straightening, (II) 'elastic' and (III) plastic. **b**, Stress-strain curve for a 5.5-μm-thick sample (6-3, red) and reloaded fragment-sample (6-3-R, blue). **c**, Stress-strain curve for a cyclically loaded 11-μm-thick sample (12-3). The solid lines indicate the loading part of the cycle and the dashed lines indicate the release part of the cycle. The blue and red lines are fittings of the linear stress-strain dependence with a modulus of elasticity of 27 and 32 GPa, respectively. **d**, The derivatives of the stress-strain curves for four different samples, revealing the 'washboard' pattern in the tensile loading behaviour. **e**, Stress-strain curve for a 5.5-μm-thick sample (6-4) and a reloaded fragment (6-4-R) showing slip-stick behaviour. **f–h**, Stress-strain cyclic measurements for an 11-μm-thick sample (12-4) at 40 °C, 90 °C and 120 °C, respectively. **i**, Linear thermal contraction of the same 11-μm-thick sample recorded between tensile tests (coefficient for linear negative thermal expansion, about  $-50 \times 10^{-6} \text{ K}^{-1}$ ). The red curve in **h** indicates the final sample pulling step before fracture.



exceptional situations, the stress–strain response had several consecutive steps each with a large change in elongation (Fig. 2e), suggesting a slide-and-lock mechanism whereby the individual ‘nanoplates’ that make up the macroscopic sample slide and then ‘click’ into place when progressively stressed.

Given that water molecules are present between graphene oxide sheets (see above) one would expect the mechanical properties of graphene oxide paper to depend strongly on its water content. Indeed, as the moisture content of graphene oxide paper decreases with increasing temperature (see thermogravimetric analysis curve, Supplementary Information 6), the modulus increases (from 17 to 25 GPa for the same sample shown in Fig. 2f–h). As expected, the loss of water is also accompanied by slow contraction of the graphene oxide paper (Fig. 2i). Simultaneously, the magnitude of permanent deformation decreases for each loading cycle conducted at 40, 90 and 120 °C, respectively (Fig. 2g, h). This water-related behaviour is similar in cellulose-based paper: a wet sheet has lower strength and stiffness than does a dry one<sup>27</sup>.

In addition to tensile tests, we performed bending experiments (see Supplementary Information 5) for several samples of graphene oxide paper with varying thicknesses  $t$ . A strip of a graphene oxide paper was bent so that a simple curve was formed (Fig. 4b), and then compressed between two parallel plates until a kink (or more than one) was formed (Fig. 4b, c). We measured the radius of curvature  $R$  for such a strip just before the loss of structural stability (that is, kink formation). According to the solution for pure uniform bending of a bar comprised of an isotropically homogeneous material<sup>28</sup>, the positive (or negative) normal strain  $\epsilon_x$  at the outer (or inner) bar surface is  $|\epsilon_x| = 0.5t/R$ . The linear fitting of experimental points (red line in Fig. 4a) gives the average normal strain value  $\epsilon_x \approx 1.1 \pm 0.1\%$ . As the ultimate tensile strain of graphene oxide paper is only 0.6% (see above), it can sustain more deformation during bending than during uniaxial tension.

The mechanics of deformation at tension and bending are schematically shown in Fig. 4e. The uniaxial tension leads to an equal (across the sample) distribution of stresses, which are transferred mostly through the shear deformation of the interlamellar adhesive (hydrogen-bonded water molecules), whereas the material bending introduces very localized stresses at the paper surfaces. The stress at the outer surface is transferred between the layers by the combination of shear and pull-out of the water adhesive and results in delamination of layers, particularly along the defects in the stacked structure (Fig. 4e and d). At the inner surface, this stress is compressive, which leads to local shear and buckling of the layers (Fig. 4c and d). In contrast to the case for the critical uniaxial tension stress in which the fracture propagates almost straight across the sample without significant pull-out (Fig. 1e), under a bending load delamination occurs primarily along the microdefects (voids between some neighbouring layers) (Fig. 1f). The experimental results thus suggest that

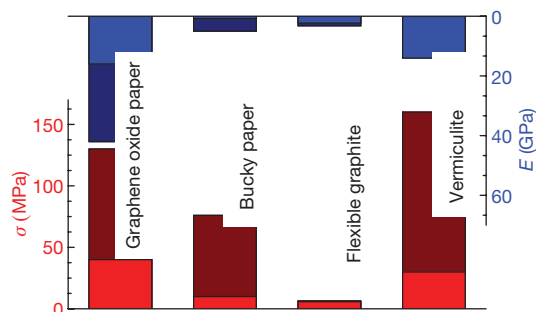


**Figure 3 | Comparison of tensile strength  $\sigma$  and modulus  $E$  for a set of thin paper-like materials.** The data presented are from ref. 22 for bucky paper and ref. 2 for vermiculite prepared by a similar filtration strategy. Flexible graphite foil was prepared by rolling of expanded graphite<sup>6</sup>. Note that high and low values are shown by the two colours. See also Supplementary Information 4.

graphene oxide paper is a pliable macroscopic material composed of stiff (in-plane) but compliant (out-of-plane) graphene oxide layers that are relatively tightly interlocked.

In conclusion, our directed-flow assembly method has yielded a novel graphene oxide paper-like material possessing a unique layered structure in which individual compliant graphene oxide sheets are interlocked/tiled together in a near-parallel fashion. The large interaction surfaces between these sheets, their corrugation at the atomic scale, and their wrinkled morphology at the submicrometre scale all allow for a highly effective load distribution across the entire macroscopic sample, and thus make this material more resilient than traditional carbon- and clay-based papers. An inexpensive starting material such as graphite oxide should facilitate the fabrication of large-area paper-like sheets for use in membranes with controlled permeability, anisotropic ionic conductors, supercapacitors, and materials for molecular storage, among many other uses. Graphene oxide paper can also be infused or serve as a carrier substance for producing hybrid materials containing polymers, ceramics and metals. Additionally, the numerous chemical functionalities on the

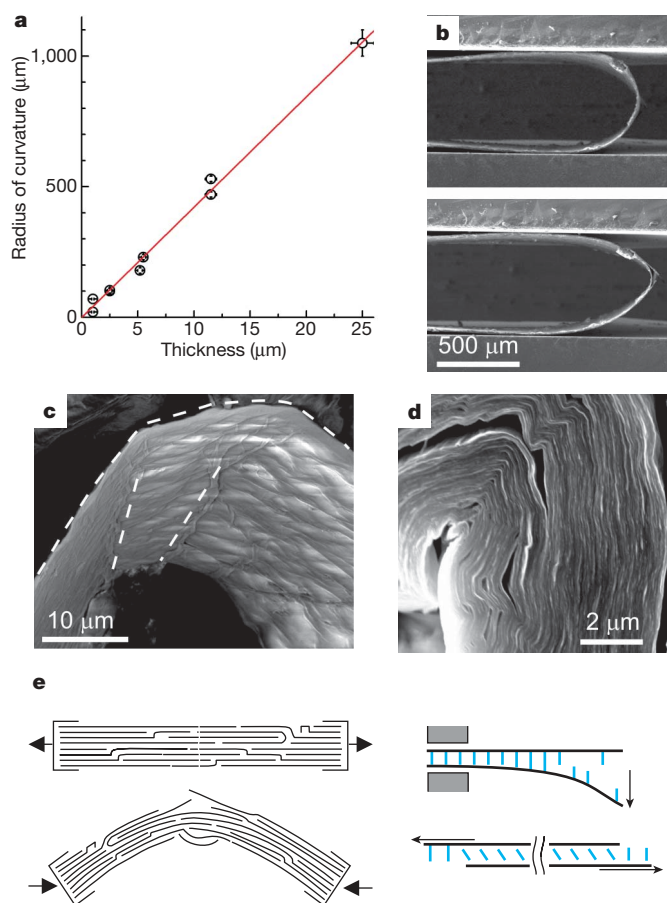


**Figure 4 | The results of bending experiments for samples of graphene oxide paper with different thicknesses  $t$ .** a, The radius of curvature at which the strip of paper loses mechanical stability (buckles) during bending, where the red line is a linear fit of experimental points. Error bars ( $\pm$  s.d.) are displayed at each data point. b, Two low-magnification SEM images of a strip cut from membrane 5 (5.2- $\mu$ m-thick) as it was compressed between two parallel plates. The upper image was taken immediately before, and the lower one after, the sample buckled. c, An SEM image of a  $\sim$ 1- $\mu$ m-thick curved graphene oxide paper strip having a  $\sim$ 20- $\mu$ m radius of curvature and showing two major creases (dotted white lines) as a consequence of the buckling. d, A high-resolution SEM image of an 11- $\mu$ m-thick buckled strip. e, Schematic drawings of the uniaxial in-plane load-to-fracture and a bending-to-buckling test. The additional schematics are meant to represent the interlamellar water molecules (blue) holding neighbouring graphene oxide sheets together. These interactions are broken upon bending of the stack or when in tension, leading to fracture with no pull-out.

surface of the layered graphene oxide sheets should readily lend themselves to further chemical functionalization. This latter strategy can then be used to crosslink the adjacent layers and improve the mechanical interaction between the individual sheets and to tailor the physical properties of the material. This combination of excellent mechanical properties and chemical tunability should make graphene oxide paper an exciting material.

## METHODS

Graphite oxide was synthesized from purified natural graphite (SP-1, Bay Carbon) by the Hummers method<sup>29</sup>. Colloidal dispersions of individual graphene oxide sheets in water at the concentration of 3 mg ml<sup>-1</sup> were prepared<sup>17</sup> with the aid of ultrasound (Fisher Scientific FS60 ultrasonic cleaning bath) in 20 ml batches. Graphene oxide paper was made by filtration of the resulting colloid through an Anodisc membrane filter (47 mm in diameter, 0.2 µm pore size; Whatman), followed by air drying and peeling from the filter. The thickness of each graphene oxide paper sample was controlled by adjusting the volume of the colloidal suspension. Samples of graphene oxide paper prepared in this manner were cut by a razor blade into rectangular strips of approximately 5 mm × 30 mm for testing without further modification.

Light microscopy (Axioskop, Zeiss) and scanning electron microscopy (Nova NanoSEM, FEI) were used. The material density was measured using the Archimedes method in water (33360 kit with the PB303-S DeltaRange Mettler-Toledo balance).

X-ray diffraction experiments were performed at room temperature using specular reflection mode. Measurements were carried out in-house with a Geigerflex (Rigaku) diffractometer (Cu K $\alpha$  radiation, X-ray wavelength  $\lambda$  = 1.5406 Å, operating at 40 keV, cathode current of 20 mA) under normal laboratory conditions; and at beamline X23B of the National Synchrotron Light Source (Brookhaven National Laboratory, New York) with a four-circle diffractometer operating at 10 keV ( $\lambda$  = 1.2398 Å, beam size 0.4 × 1.0 mm<sup>2</sup>). During the beamline measurements, the samples were kept under a slight overpressure of helium to reduce the background scattering from the ambient gas and radiation damage. The inherent and instrumental broadenings of the diffraction peak were higher for the in-house measurements.

The thermal stability of graphene oxide paper was characterized by thermogravimetric analysis (TGA-SDT 2960, TA Instruments). All measurements were conducted under dynamic nitrogen flow (industrial grade, flow rate 100 ml min<sup>-1</sup>) over a temperature range of 35–800 °C with a slow ramp rate of 1 °C min<sup>-1</sup> to prevent sample loss. Results are presented in Supplementary Information 6.

Static mechanical uniaxial in-plane tensile tests were conducted with a dynamic mechanical analyser (2980 DMA, TA Instruments). The samples were gripped using film tension clamps with a clamp compliance of about 0.2 µm N<sup>-1</sup>. All tensile tests were conducted in controlled force mode with a preload of 0.01 N and a force ramp rate of 0.02 N min<sup>-1</sup>. The sample width was measured using standard calipers (Mitutoyo). The length between the clamps was measured by the DMA instrument, and the sample thickness was obtained from SEM imaging of the fracture edge.

Received 2 January; accepted 12 June 2007.

1. Pitkethly, M. J. Nanomaterials—the driving force. *Nanotoday* **7**, 20–29 (2004).
2. Ballard, D. G. H. & Rideal, G. R. Flexible inorganic films and coatings. *J. Mater. Sci.* **18**, 545–561 (1983).
3. Kellar, J. J. (ed.) *Functional Fillers and Nanoscale Minerals: New Markets/ New Horizons* (Society for Mining, Metallurgy and Exploration, Littleton, Colorado, 2006).
4. US. *Samica* ([www.ussamica.com](http://www.ussamica.com)) (Isovolta Inc./US Samica, Rutland, Vermont, 2007).
5. Dowell, M. B. & Howard, R. A. Tensile and compressive properties of flexible graphite foils. *Carbon* **24**, 311–323 (1986).

7. Leng, Y., Gu, J., Cao, W. & Zhang, T. Y. Influences of density and flake size on the mechanical properties of flexible graphite. *Carbon* **36**, 875–881 (1998).
8. Reynolds, R. A. & Greinke, R. A. Influence of expansion volume of intercalated graphite on tensile properties of flexible graphite. *Carbon* **39** (3), 479–481 (2001).
9. Grafoil. ([www.graftech.com/Home/Brands/GRAFOIL.aspx](http://www.graftech.com/Home/Brands/GRAFOIL.aspx)) (GrafTech International Inc., Lakewood, Ohio, copyright, 2005).
10. Sigraflex. ([http://www.sglcarbon.com/sglT/expanded/markets/energy/power\\_plants.html](http://www.sglcarbon.com/sglT/expanded/markets/energy/power_plants.html)) (SGL Carbon AG, Wiesbaden, Germany, copyright 2000–, 2007).
11. Liu, J. et al. Fullerene pipes. *Science* **280**, 1253–1256 (1998).
12. Baughman, R. H. et al. Carbon nanotube actuators. *Science* **284**, 1340–1344 (1999).
13. Hennrich, F. et al. Preparation, characterization and applications of free-standing single walled carbon nanotube thin films. *Phys. Chem. Chem. Phys.* **4**, 2273–2277 (2002).
14. Coleman, J. N. et al. Improving the mechanical properties of single-walled carbon nanotube sheets by intercalation of polymeric adhesives. *Appl. Phys. Lett.* **82**, 1682–1684 (2003).
15. Berhan, L. et al. Mechanical properties of nanotube sheets: Alterations in joint morphology and achievable moduli in manufacturable materials. *J. Appl. Phys.* **95**, 4335–4345 (2004).
16. Titelman, G. I. et al. Characteristics and microstructure of aqueous colloidal dispersions of graphite oxide. *Carbon* **43**, 641–649 (2005).
17. Stankovich, S. et al. Stable aqueous dispersions of graphitic nanoplatelets via the reduction of exfoliated graphite oxide in the presence of poly(sodium 4-styrenesulfonate). *J. Mater. Chem.* **16**, 155–158 (2006).
18. Stankovich, S. et al. Graphene-based composite materials. *Nature* **442**, 282–286 (2006).
19. Stankovich, S. et al. Synthesis of graphene-based nanosheets via chemical reduction of exfoliated graphite oxide. *Carbon* **45**, 1558–1564 (2007).
20. Scholz, W. & Boehm, H. P. Untersuchungen am graphitoxid. VI. Betrachtungen zur struktur des graphitoxids. *Z. Anorg. Allg. Chem.* **369**, 327–340 (1969).
21. Lerf, A. et al. Hydration behavior and dynamics of water molecules in graphite oxide. *J. Phys. Chem. Solids* **67**, 1106–1110 (2006).
22. Bartram, S. F. in *Handbook of X-rays* (ed. Kaelble, E. F.) 17.1–17 (McGraw-Hill, New York, 1967).
23. Zhang, X. F., Sreekumar, T. V., Liu, T. & Kumar, S. Properties and structure of nitric acid oxidized single wall carbon nanotube films. *J. Phys. Chem. B* **108**, 16435–16440 (2004).
24. Ward, I. M. *Mechanical Properties of Solid Polymers* Ch. 11 329–398 (Wiley, Chichester/New York, 1983).
25. Soule, D. E. & Nezbeda, C. W. Direct basal-plane shear in single-crystal graphite. *J. Appl. Phys.* **39**, 5122–5139 (1968).
26. Tang, Z., Kotov, N., Magonov, S. & Ozturk, B. Nanostructured artificial nacre. *Nature Mater.* **2**, 413–418 (2003).
27. Alava, M. & Niskanen, K. The physics of paper. *Rep. Prog. Phys.* **69**, 669–723 (2006).
28. Timoshenko, S. P. & Goodier, J. N. *Theory of Elasticity* (McGraw-Hill, New York, 1970).
29. Hummers, W. S. & Offeman, R. E. Preparation of graphite oxide. *J. Am. Chem. Soc.* **80**, 1339 (1958).

Supplementary Information is linked to the online version of the paper at [www.nature.com/nature](http://www.nature.com/nature).

**Acknowledgements** We appreciate support from NASA through the University Research, Engineering and Technology Institute (URETI) on Bio-inspired Materials (BiMat), and from the NSF. This work made use of X-ray facilities supported by the MRSEC programme of the National Science Foundation at the Materials Research Center of Northwestern University, and the X23B beamline of the National Synchrotron Light Source supported by the US Department of Energy. We thank I. M. Daniel for the use of his mechanical testing instruments, and A. L. Ruoff for commenting on an earlier version of this manuscript.

**Author Information** Reprints and permissions information is available at [www.nature.com/reprints](http://www.nature.com/reprints). The authors declare no competing financial interests. Correspondence and requests for materials should be addressed to R.S.R. ([r-ruoff@northwestern.edu](mailto:r-ruoff@northwestern.edu)).

# Detection of human influence on twentieth-century precipitation trends

Xuebin Zhang<sup>1</sup>, Francis W. Zwiers<sup>1</sup>, Gabriele C. Hegerl<sup>2</sup>, F. Hugo Lambert<sup>3</sup>, Nathan P. Gillett<sup>4</sup>, Susan Solomon<sup>5</sup>, Peter A. Stott<sup>6</sup> & Toru Nozawa<sup>7</sup>

Human influence on climate has been detected in surface air temperature<sup>1–5</sup>, sea level pressure<sup>6</sup>, free atmospheric temperature<sup>7</sup>, tropopause height<sup>8</sup> and ocean heat content<sup>9</sup>. Human-induced changes have not, however, previously been detected in precipitation at the global scale<sup>10–12</sup>, partly because changes in precipitation in different regions cancel each other out and thereby reduce the strength of the global average signal<sup>13–19</sup>. Models suggest that anthropogenic forcing should have caused a small increase in global mean precipitation and a latitudinal redistribution of precipitation, increasing precipitation at high latitudes, decreasing precipitation at sub-tropical latitudes<sup>15,18,19</sup>, and possibly changing the distribution of precipitation within the tropics by shifting the position of the Intertropical Convergence Zone<sup>20</sup>. Here we compare observed changes in land precipitation during the twentieth century averaged over latitudinal bands with changes simulated by fourteen climate models. We show that anthropogenic forcing has had a detectable influence on observed changes in average precipitation within latitudinal bands, and that these changes cannot be explained by internal climate variability or natural forcing. We estimate that anthropogenic forcing contributed significantly to observed increases in precipitation in the Northern Hemisphere mid-latitudes, drying in the Northern Hemisphere subtropics and tropics, and moistening in the Southern Hemisphere subtropics and deep tropics. The observed changes, which are larger than estimated from model simulations, may have already had significant effects on ecosystems, agriculture and human health in regions that are sensitive to changes in precipitation, such as the Sahel.

We used monthly precipitation observations over global land areas from the most recent version of the Global Historical Climatology Network (GHCN)<sup>21</sup> to analyse precipitation trends in two twentieth-century periods (1925–1999 and 1950–1999), during which observational data are considered to be sufficient to describe global-scale land precipitation change. This data set has been carefully quality controlled. Previous studies of external influence on global precipitation changes<sup>10–12</sup> used a gridded data set<sup>22</sup> based on an earlier version of the GHCN that was less complete during the last few years of the twentieth century; we obtained similar results when using this original data set. We focused on the region 40°S–70°N because observational coverage elsewhere is limited.

We compared observed trends to those simulated by a large number of climate models to determine whether observed changes over the two twentieth-century periods have been caused by external influences on the climate system. The climate simulations were obtained from the multi-model data archive at PCMDI ([http://www.pcmdi.llnl.gov/ipcc/about\\_ipcc.php](http://www.pcmdi.llnl.gov/ipcc/about_ipcc.php)) and from modelling

centres directly. We considered three groups of twentieth-century simulations. One group (ANT) includes 27 simulations conducted with 8 models forced with estimates of historical anthropogenic forcing only, including greenhouse gases and sulphate aerosols. A second group (ALL) includes 50 simulations conducted with 10 models forced with estimates of both historical anthropogenic and natural external forcing, including volcanic aerosols and solar irradiance change. A third group (NAT4) includes 15 simulations conducted with 4 models forced with natural external forcing only. Slightly different configurations of historical forcing were used by different modelling centres<sup>12</sup>. The make-up of each group and the number of simulations used from each model is summarized in Supplementary Table 1. Four models (ECHO-G, HadCM3, MIROC, PCM) contributed simulations to all three groups; the subsets of ANT and ALL simulations from these models are referred to as ANT4 and ALL4 respectively.

We analysed trends in annual zonal mean precipitation anomalies expressed relative to 1961–90. Trends in observed and simulated precipitation were computed and compared quantitatively using the ‘optimal fingerprint’ method<sup>23,24</sup>, a regression procedure that has been used in many previous detection studies<sup>1</sup>.

Linear precipitation trends from observations and the average of multiple model simulations for 1925–1999 (Figs 1 and 2) exhibit important areas of consistency in the spatial distribution of precipitation change. Both observations and models show that precipitation increased in the Southern Hemisphere deep tropics and subtropics, decreased in the Northern Hemisphere tropics and subtropics, and increased in the Northern Hemisphere poleward of 50°N. We note an important difference, however: observations suggest a slight upward trend in zonal precipitation between about 20–40°N, while the mean ALL simulation shows a slight downward trend (Fig. 1a). Also we note that uncertainty in model-simulated trends is high: the range of trends from available simulations includes zero for all latitudinal bands, indicating that the simulated change in individual latitude bands could be explained by internal variability. However, the pattern of precipitation change across different latitudes may still allow detection. The observed latitudinal pattern of precipitation trends correlates well with the all-forcings multi-model simulated pattern (correlation 0.83 for the 75-year trend, Fig. 1a, compared to 0.69 for the ANT simulations, Fig. 1b, and 0.02 for the NAT4 simulations, Fig. 1c). We obtained similar results from the 50-year trends (Fig. 1d–f). Differences in zonal precipitation trends between different models are greater than those between individual ensemble members from the same model, although robust physical characteristics of rainfall changes can be found in the ALL and ANT multi-model means<sup>15</sup>.

<sup>1</sup>Climate Research Division, Environment Canada, Toronto, Ontario M3H 5T4, Canada. <sup>2</sup>Nicholas School for the Environment and Earth Sciences, Box 90227, Duke University, Durham, North Carolina 27708, USA. <sup>3</sup>Department of Geography, 507 McCone Hall, University of California, Berkeley, California 94720, USA. <sup>4</sup>Climatic Research Unit, School of Environmental Sciences, University of East Anglia, Norwich NR4 7TJ, UK. <sup>5</sup>NOAA Earth System Research Laboratory, 325 Broadway, Boulder, Colorado 80305, USA. <sup>6</sup>Met Office Hadley Centre (Reading Unit), Meteorology Building, University of Reading, Reading RG6 6BB, UK. <sup>7</sup>National Institute for Environmental Studies, Tsukuba, Ibaraki 305-8506, Japan.



We estimated the combined effect of anthropogenic and natural external forcing on observed precipitation trends by regressing the observed trends onto the trends simulated in ALL simulations. Estimates of the individual influences of anthropogenic and natural forcing were similarly obtained by using the ANT and NAT4 simulation trend patterns respectively. The regression scaling factors that best match ALL and ANT simulation trends to the observed trends are shown in Fig. 3. The response to ALL, or to ANT alone, was detected in the observed trends in both periods; the response to natural forcing alone was not detected.

To separate the contributions from natural and anthropogenic forcing to observed trends, two-signal attribution analyses must be used<sup>2,3</sup>. Using combinations of two signal patterns from the ALL, ANT and NAT4 simulations in two-way regressions, we also found that the response to anthropogenic forcing is separable from the response to natural forcing and internal variability. The ANT and NAT responses were detected in the observed 50-year trends when ALL and ANT mean responses were used to estimate the contributions of ANT and NAT to trends (Fig. 3, right hand panel; see also Supplementary Fig. 7). The response to anthropogenic and natural forcings were also detected using the ALL4 and ANT4 ensembles

(Supplementary Fig. 7), indicating that the response to anthropogenic forcing can be reliably separated from the effects of natural forcing and internal variability, although the residual consistency test<sup>25</sup> failed in the latter case, indicating that internal variability might be underestimated, or that uncaptured aspects of the forced response have increased residual variability. This is consistent with an earlier study detecting volcanic influence on globally averaged land precipitation<sup>10</sup>. The estimated contribution of natural forcing to observed zonal precipitation trends is small in relation to the estimated contribution from anthropogenic forcing. From this and the separate detection of anthropogenic influence in a two-way analysis we conclude that the detected changes in observed land rainfall are largely in response to anthropogenic forcing.

A series of considerations show that the detection of an anthropogenic influence on precipitation is robust. While uncertainty in the magnitude of the observationally based estimate of precipitation change is considerable, there is little uncertainty in the sign of trend (see Supplementary Information). Thus sampling uncertainty is unlikely to have altered the observed pattern of latitudinal moistening and drying and is thus unlikely to nullify our detection results, which are based on the agreement in the observed and simulated

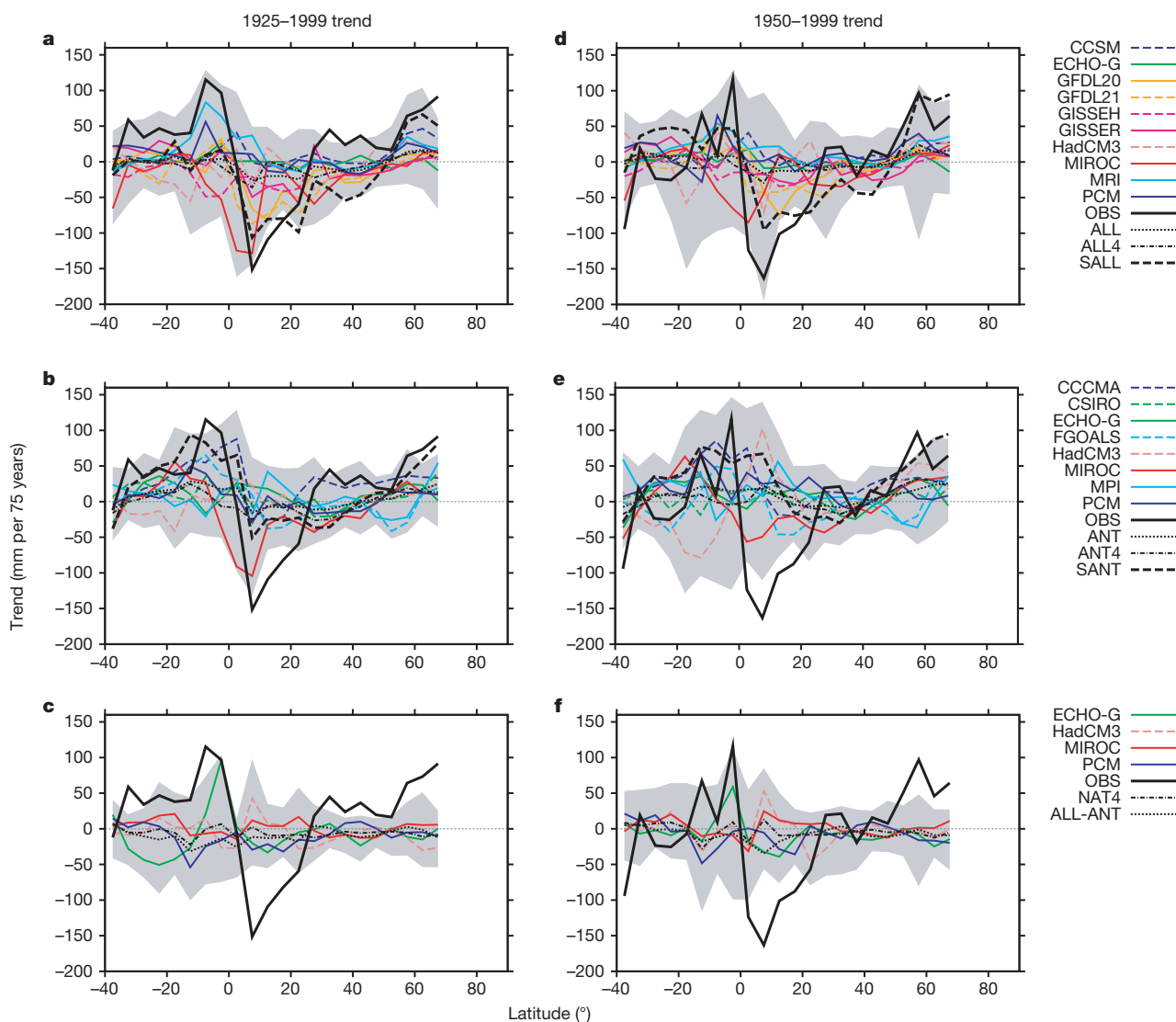


**Figure 1 | Comparison between observed (solid black) and simulated zonal mean land precipitation trends for 1925–1999 (left) and 1950–1999 (right).** Black dotted lines indicate the multi-model means from all available models (ALL in **a** and **d**, ANT in **b** and **e**, and NAT as represented by ALL-ANT in **c** and **f**), and black dashed-dotted lines those from the subset of

four models that simulated the response to each of the forcing scenarios (ALL4, ANT4 and NAT4). The model-simulated range of trends is shaded. Black dashed lines indicate ensemble means of ALL and ANT simulations that have been scaled (SALL and SANT) to best fit the observations based on a one-signal analysis. Coloured lines indicate individual model mean trends.

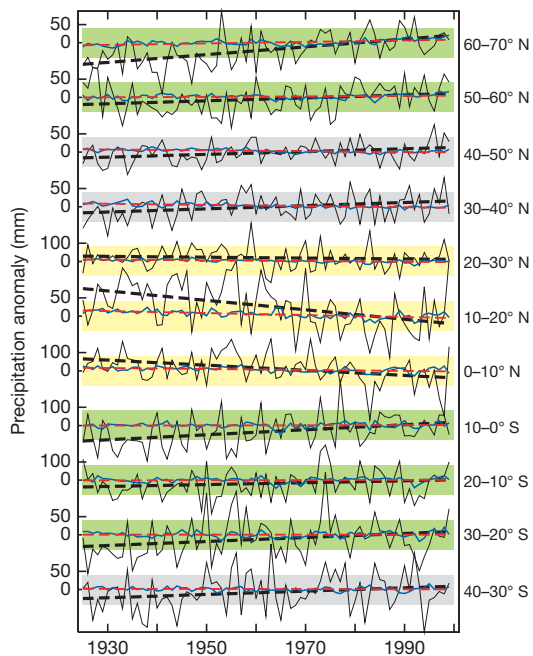


**Figure 2 | 1925–1999 changes in observed and simulated precipitation anomalies.** Time series (left panel) of observed annual zonal mean precipitation anomalies in  $10^\circ$  latitude bands (thin black trace) together with ensemble mean annual zonal mean precipitation anomalies in the 50 available ALL simulations (thin blue trace). Straight dashed black and red lines indicate the trends. Green (or yellow) shading identifies latitude bands

patterns of trends. Furthermore, our results are robust to the use of a data set that is based on less-complete observations and is gridded differently<sup>22</sup>. Our results are also robust to the use of signal patterns estimated from subsets of models, although, as expected, the robustness of detection deteriorates with decreasing number of models being used (not shown). Multi-model estimates of the pattern of external forcing response in precipitation are probably less susceptible to model error than are single model estimates<sup>26</sup>. The structure of the multi-model simulated fingerprint is consistent with our understanding of the mechanisms of precipitation response to anthropogenic forcing. It is expected that wet tropical regions would

become wetter and dry regions drier if there were an increase in tropospheric temperature from anthropogenic forcing but no change in lower-tropospheric relative humidity or flow<sup>15</sup>. The apparent shift in the Intertropical Convergence Zone is also consistent with hemispheric asymmetry in indirect aerosol forcing<sup>20</sup>, although indirect aerosol forcing is not needed in all models to produce subtropical drying over land<sup>15</sup>.

Because the observed record is relatively short and may be affected by the response to external forcing, we used climate models to estimate the variations in zonal rainfall trends expected from internal climate variability. This model-based internal variability estimate is

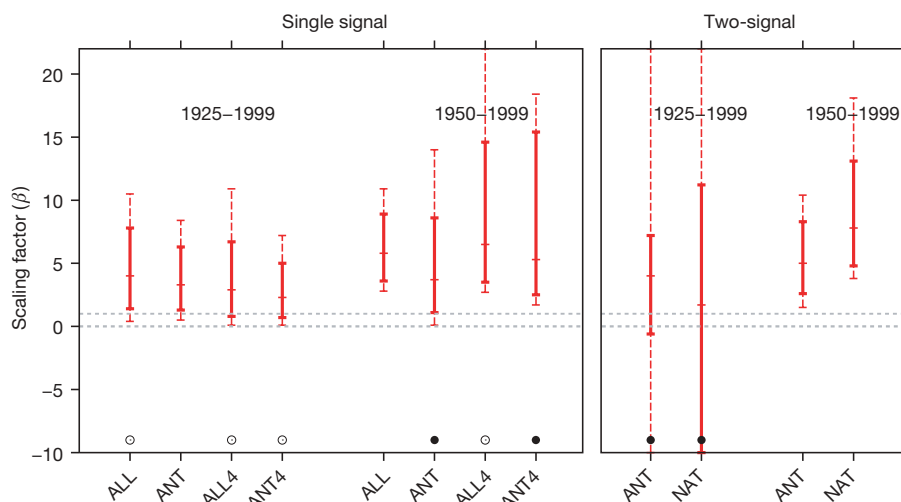


**Figure 3 | Results from detection and attribution analysis of zonal precipitation anomalies.** Scaling factors and their 5–95% uncertainty ranges are given from one-signal fingerprint detection analyses for ALL, ANT and NAT4 forced signals as well as subsets of four models, ALL4 and ANT4 (left panel) and from two-signal fingerprint detection analyses (right panel) for ANT and NAT forced signals based on the ALL and ANT ensembles (see

Fig. 1) The residual consistency test<sup>25</sup> passes except where indicated by open circles (test passes after doubling the estimate of internal variability) or closed circles (indicating that the test does not pass even after doubling). Dashed error bars correspond to 5–95% uncertainty ranges when the model simulated variance is doubled.

smaller than the observationally based estimate, particularly in the tropics, but a substantial part of the discrepancy may be the result of scale mismatch in the observational data (see Supplementary Information). Our finding of a detectable external influence on zonal precipitation trend holds when doubling the model-derived internal variance estimate, indicating that our finding is robust to possible moderate under-simulation of rainfall variability.

While the detection and attribution of an anthropogenic influence on zonal precipitation changes is robust, there are discrepancies in the magnitude of the changes. The multi-model mean significantly underestimates observed trends (Figs 1 and 3; see also ref. 27), consistent with the finding that the multi-model response to volcanic eruptions in global mean land rainfall is undersimulated<sup>10</sup>. The tropical mean precipitation responses simulated by atmospheric models to tropical ocean warming during El Niño events are also weaker than observed, despite correct simulation of the observed change in atmospheric column integrated water vapour<sup>28,29</sup>. A similar mechanism may be affecting tropical and subtropical zonal land rainfall changes here. Observational uncertainty might also have contributed to the discrepancy between observed and simulated trends. Furthermore, the statistical significance of the mismatch might be overestimated if the internal variability of precipitation is underestimated (Fig. 3). If the finding that observed changes are larger than simulated is robust, then projections may also underestimate future precipitation changes. However, some models in the ANT and ALL ensembles do show response features, particularly in the tropics, that are as large as those observed (see Fig. 1), but these are situated somewhat differently latitudinally, impeding detection and damping the amplitude of the multi-model pattern of response. Furthermore, different models contribute to different aspects of the multi-model mean response. Some models show little tropical response but increasing high-latitude precipitation, while others show a more realistic tropical and subtropical response but fail to increase high-latitude precipitation (see Fig. 1).

Overall, we find that anthropogenic forcing has had a detectable and attributable influence on the latitudinal pattern of large-scale precipitation change over the part of the twentieth century that we were able to analyse. Our best estimate of the response to anthropogenic forcing suggests (Fig. 1b) that anthropogenic forcing has contributed approximately 50–85% (5–95% uncertainty) of the observed 1925–1999 trend in annual total land precipitation between 40° N and 70° N (62 mm per century), 20–40% of the observed drying trend in the northern subtropics and tropics (0° to 30° N; a decrease of 98 mm per century) and most (75–120%) of the moistening trend in the southern tropics and subtropics (0° to 30° S; 82 mm per century).

## METHODS SUMMARY

**Data processing.** Observed annual land precipitation anomalies were obtained by subtracting the 1961–90 climatology from station monthly precipitation amounts<sup>21</sup> and summing monthly values if the year had at least 7 months with data. All other years were treated as missing. Annual values were gridded by averaging station values within 5° × 5° latitude–longitude grid boxes. Zonal mean precipitation anomalies were obtained by averaging available annual anomalies within each latitudinal band.

Model data were first transferred to the same 5° × 5° latitude–longitude grid as were the observations and subsequently processed in the same way as were the observations, including ‘masking’ missing values so that model values are available at the same times and places as the gridded observations.

**Detection and attribution.** The ‘optimal fingerprint’ method assumes that the observed trends  $\mathbf{y}$  (organized as a vector with one entry per latitude band) may be represented as the sum  $\mathbf{y} = \mathbf{X}\boldsymbol{\beta} + \mathbf{u}$  of scaled simulated responses to external forcing, or signals  $\mathbf{X}$  (a matrix with one column for each signal considered) and natural internal variability  $\mathbf{u}$ . To account for uncertainty in the modelled response patterns, we used generalized total-least-squares<sup>23</sup> to estimate the scaling factors  $\boldsymbol{\beta}$ . Signals were estimated by averaging trends in all available model runs in the same forcing group. Two independent estimates of internal variability covariance,  $\hat{\mathbf{C}}_{N1}$  and  $\hat{\mathbf{C}}_{N2}$ , which were needed for optimization and scaling factor estimation<sup>2</sup>, were estimated from model simulations as in other studies<sup>1–12</sup>.

We computed trends in 10° latitude bands to reduce the effects of internal variability. Our detection analysis is conducted in a subspace spanned by the first five leading empirical orthogonal functions of the estimated model covariance. The joint influences of ANT and NAT signals in observations were inferred from two-way regressions using combinations of two signal patterns from the multi-model ALL, ANT and NAT4 ensembles.

**Full Methods** and any associated references are available in the online version of the paper at [www.nature.com/nature](http://www.nature.com/nature).

**Received 21 February; accepted 14 June 2007.**

**Published online 23 July 2007.**

1. IDAG (International ad hoc Detection and Attribution Group). Detecting and attributing external influences on the climate system: A review of recent advances. *J. Clim.* **18**, 1291–1314 (2005).
2. Hegerl, G. C. *et al.* Multi-fingerprint detection and attribution of greenhouse-gas and aerosol-forced climate change. *Clim. Dyn.* **13**, 613–634 (1997).
3. Tett, S. F. B., Stott, P. A., Allen, M. R., Ingram, W. & Mitchell, J. Causes of twentieth-century temperature change near the Earth’s surface. *Nature* **339**, 569–572 (1999).
4. Zhang, X., Zwiers, F. W. & Stott, P. A. Multi-model multi-signal climate change detection at regional scale. *J. Clim.* **19**, 4294–4307 (2006).
5. Stott, P. A. Attribution of regional-scale temperature changes to anthropogenic and natural causes. *Geophys. Res. Lett.* **30**, 1724, doi:10.1029/2003GL017324 (2003).
6. Gillett, N. P., Zwiers, F. W., Weaver, A. J. & Stott, P. A. Detection of human influence on sea level pressure. *Nature* **422**, 292–294 (2003).
7. Jones, G. S., Tett, S. F. B. & Stott, P. A. Causes of atmospheric temperature change 1960–2000: A combined attribution analysis. *Geophys. Res. Lett.* **30**, 1228, doi:10.1029/2002GL016377 (2003).
8. Santer, B. D. *et al.* Contributions of anthropogenic and natural forcing to recent tropopause height changes. *Science* **301**, 479–483 (2003).
9. Barnett, T. P. & Pierce, D. AchutaRao, K., Santer, B. & Gleick, P. Penetration of human-induced warming into the world’s oceans. *Science* **309**, 284–287 (2005).
10. Gillett, N. P., Weaver, A. J., Zwiers, F. W. & Wehner, M. F. Detection of volcanic influence on global precipitation. *Geophys. Res. Lett.* **31**, L12217, doi:10.1029/2004GL020044 (2004).
11. Lambert, F. H., Stott, P. A., Allen, M. R. & Palmer, M. A. Detection and attribution of changes in 20th century land precipitation. *Geophys. Res. Lett.* **31**, L10203, doi:10.1029/2004GL019545 (2004).
12. Lambert, F. H., Gillett, N. P., Stone, D. A. & Huntingford, C. Attribution studies of observed land precipitation changes with nine coupled models. *Geophys. Res. Lett.* **32**, L18704, doi:10.1029/2005GL023654 (2005).
13. Hulme, M., Osborne, T. J. & Johns, T. C. Precipitation sensitivity to global warming: comparison of observations with HadCM2 simulations. *Geophys. Res. Lett.* **25**, 3379–3382 (1998).
14. Dai, A., Fung, I. Y. & Del Genio, A. D. Surface observed global land precipitation variation during 1900–88. *J. Clim.* **10**, 2943–2962 (1997).
15. Held, I. M. & Soden, B. J. Robust responses of the hydrological cycle to global warming. *J. Clim.* **19**, 5686–5699 (2006).
16. Hegerl, G. C., Zwiers, F. W., Kharin, V. V. & Stott, P. A. Detectability of anthropogenic changes in temperature and precipitation extremes. *J. Clim.* **17**, 3683–3700 (2004).
17. Allen, M. R. & Ingram, W. J. Constraints on future changes in climate and the hydrologic cycle. *Nature* **429**, 224–232 (2002).
18. Cubasch, U. *et al.* in *Climate Change 2001: The Scientific Basis* (ed. Houghton, J. T. *et al.*) 525–582 (Cambridge Univ. Press, New York, 2001).
19. Emori, S. & Brown, S. J. Dynamic and thermodynamic changes in mean and extreme precipitation under changed climate. *Geophys. Res. Lett.* **32**, L17706, doi:10.1029/2005GL023272 (2005).
20. Rotstayn, L. D. & Lohmann, U. Tropical rainfall trends and the indirect aerosol effect. *J. Clim.* **15**, 2103–2116 (2002).
21. Vose, R. S. *et al.* *The Global Historical Climatology Network: Long-Term Monthly Temperature, Precipitation, Sea Level Pressure, and Station Pressure Data*. Report ORNL/CDIAC-53, NDP-041 (Carbon Dioxide Information Analysis Center, Oak Ridge National Laboratory, Oak Ridge, Tennessee, 1992); (<http://cdiac.esd.ornl.gov/ftp/ndp041/ndp041.pdf>).
22. Hulme, M. A. 1951–80 global land precipitation climatology for the evaluation of general circulation models. *Clim. Dyn.* **7**, 57–72 (1992).
23. Allen, M. R. & Stott, P. A. Estimating signal amplitudes in optimal fingerprinting. Part I: Theory. *Clim. Dyn.* **21**, 477–491 (2003).
24. Hasselmann, K. Multi-pattern fingerprint method for detection and attribution of climate change. *Clim. Dyn.* **13**, 601–612 (1997).
25. Allen, M. R. & Tett, S. F. B. Checking for model consistency in optimal fingerprinting. *Clim. Dyn.* **15**, 419–434 (1999).
26. Gillett, N. P. *et al.* Detecting anthropogenic influence with a multi-model ensemble. *Geophys. Res. Lett.* **29**, doi:10.1029/2002GL015836 (2002).
27. Wentz, F. J., Ricciardulli, L., Hilburn, K. & Mears, C. How much more rain will global warming bring? *Science* doi:10.1126/science.1140746 (2007); published online 31 May 2007.



28. Soden, B. J. The sensitivity of the tropical hydrological cycle to ENSO. *J. Clim.* **13**, 538–549 (2000).
29. Soden, B. J., Jackson, D. L., Ramaswamy, V., Schwarzkopf, M. D. & Huang, X. The radiative signature of upper tropospheric moistening. *Science* **310**, doi:10.1126/science.1115602 (2005).
30. Held, I. M., Delworth, T. D., Lu, J., Findell, K. L. & Knutson, T. R. Simulation of Sahel drought in the 20th and 21st centuries. *Proc. Natl Acad. Sci. USA* **102**, 17891–17896 (2005).

**Supplementary Information** is linked to the online version of the paper at [www.nature.com/nature](http://www.nature.com/nature).

**Acknowledgements** We thank R. Vose (National Climatic Data Centre, NOAA) for the observed precipitation data, S.-K. Min for the provision of ECHO-G data, J. Wang (supported by the Canadian Foundation for Climate and Atmospheric Sciences) for processing model data and Y. Feng for computational assistance. We

acknowledge the international modeling groups who contributed to the multi-model data archive at PCMDI (the Program for Climate Model Diagnostics and Intercomparison), which is supported by the Office of Science, US Department of Energy. Part of this work was supported by NOAA's Office of Global Programs (G.C.H. and S.S.) and the DOE's Office of Biological and Environmental Research (G.C.H.). G.C.H. was also supported by the NSF and by Duke University. N.P.G., F.H.L. and T.N. were supported by the Leverhulme Trust, the Comer Science and Education Foundation, and the MEXT (Ministry of Education, Culture, Sports, Science and Technology), respectively. P.A.S. was supported by the UK Department for Environment, Food and Rural Affairs.

**Author Information** Reprints and permissions information is available at [www.nature.com/reprints](http://www.nature.com/reprints). The authors declare no competing financial interests. Correspondence and requests for materials should be addressed to F.W.Z. ([francis.zwiers@ec.gc.ca](mailto:francis.zwiers@ec.gc.ca)).

## METHODS

**Detection and attribution.** Signals were obtained by averaging results from multi-model ensembles. This has been found to improve estimates of surface temperature response to anthropogenic forcing<sup>4,26</sup>, suggesting that the bias in the multi-model mean is smaller than individual model biases<sup>31</sup>.

The observed precipitation record is too short to provide estimates of  $\hat{C}_{N1}$  and  $\hat{C}_{N2}$  and may be affected by the response to external forcing. Internal climate variability is therefore estimated, as outlined below, from model simulations as in other studies<sup>1–12</sup>. More details are given in the Supplementary Information.

The covariance matrices were estimated from independent parts of a 1,700-year control simulation (which was divided into 17 non-overlapping 100-year samples) performed with model HadCM3, for which there is no year-to-year change in external forcing, and from variability between members in ensembles of forced simulations. The latter consist of a total of 9,200 years of climate simulation with ALL, ANT or NAT forcing in ensembles of three to nine 100-year simulations (Supplementary Table 1).

For the 75-year detection analysis, trends were estimated from the last 75 years of the 100-year samples of model output that were masked to mimic the availability of gridded observations during 1925–99. For the 50-year detection analysis, we split each of the 100-year chunks of data into two 50-year periods, and computed trends in each 50-year data segment that was masked to mimic the 1950–1999 availability of gridded observations. We then partitioned the control and forced simulations in such a way that every model is represented in the covariance matrix estimates  $\hat{C}_{N1}$  and  $\hat{C}_{N2}$ . In the case of ensembles with an odd number of members  $k$ , we assigned  $(k + 1)/2$  members randomly to either sample N1 or N2, and the remaining members were allocated to the other sample; the allocation of the larger number of members was alternated between models to ensure that N1 and N2 contain the same number of members in total. In the case of ensembles with an even number of members, half of the members were randomly allocated to each sample. Overall mean trend patterns were removed separately from the control, ALL, ANT and NAT simulations in each sample N1 and N2, and the residual trends were used to estimate  $C_{N1}$  and  $C_{N2}$ . The covariance estimates were appropriately adjusted to reflect the fact that ensemble mean trend patterns were removed from individual ensembles.

Because model data for estimating the covariance matrix were limited, and because optimal detection involves inversion of the estimated covariance matrix<sup>23,24</sup>, we had to conduct our detection analysis in a reduced dimension space. This was accomplished by first calculating trends in 10° latitude bands to

reduce the effects of internal variability. The spatial pattern of trends at this coarser resolution preserves most of the structure seen in 5° bands. Dimensionality was further reduced by retaining only the first five leading empirical orthogonal functions of the estimated model covariance. Model-based and observation-based estimates of precipitation variability are more often consistent with each other in this reduced dimension space according to a standard test<sup>25</sup>, indicating that this space retains only the more robustly simulated aspects of rainfall change, and that the covariance matrix is robustly estimated. This truncation preserves the spatial pattern of trends, including key physical aspects, and retains more than 76% of signal variance (see Supplementary Information). It is of concern that model simulated precipitation variability is generally lower than observationally based estimates. However, the latter are probably biased high owing to sampling noise in the observations (see Supplementary Information).

The optimal detection method described previously was used to determine whether the responses to ALL, ANT and NAT signals are individually detectable in observed trends in zonal mean precipitation. However, two-signal attribution analyses must be used to separate the contribution from natural and anthropogenic forcing to observed trends. Thus the joint influence of ANT and NAT signals in observations was inferred from two-way regressions using combinations of two signal patterns from the multi-model ALL, ANT and NAT4 ensembles. Relatively few NAT only simulations were available for our analysis, so the most robust two-signal analysis results were obtained using the ALL and ANT ensembles; the contribution from ANT and NAT separately could be derived from a linear combination of the scaling factors of ALL and ANT<sup>2</sup>. Scaling factors estimated jointly in two-signal detection analysis were generally correlated (see Supplementary Information).

The methods used to make inferences about the scaling factors  $\beta$  and the residual consistency assume that the natural internal variability  $u$  is gaussian-distributed. While daily precipitation is far from gaussian, the Central Limit Theorem indicates that the large-area averages of annual mean precipitation anomalies that are used in our analysis should nevertheless be approximately gaussian. Repeating our analyses using transformed annual anomalies assuming a gamma distribution for the annual anomalies produced very similar detection and attribution results.

31. Kharin, V. V., Zwiers, F. W. & Zhang, X. Intercomparison of near-surface temperature and precipitation extremes in AMIP2 simulations, reanalyses, and observations. *J. Clim.* **18**, 5201–5223 (2005).

## LETTERS

# Variation in styles of rifting in the Gulf of California

Daniel Lizarralde<sup>1</sup>, Gary J. Axen<sup>2</sup>, Hillary E. Brown<sup>3</sup>, John M. Fletcher<sup>4</sup>, Antonio González-Fernández<sup>4</sup>, Alistair J. Harding<sup>5</sup>, W. Steven Holbrook<sup>3</sup>, Graham M. Kent<sup>5</sup>, Pedro Paramo<sup>3,7</sup>, Fiona Sutherland<sup>5,7</sup> & Paul J. Umhoefer<sup>6</sup>

Constraints on the structure of rifted continental margins and the magmatism resulting from such rifting can help refine our understanding of the strength of the lithosphere, the state of the underlying mantle and the transition from rifting to seafloor spreading. An important structural classification of rifts is by width<sup>1</sup>, with narrow rifts thought to form as necking instabilities<sup>2</sup> (where extension rates outpace thermal diffusion<sup>3</sup>) and wide rifts thought to require a mechanism to inhibit localization, such as lower-crustal flow in high heat-flow settings<sup>1,4</sup>. Observations of the magmatism that results from rifting range from volcanic margins with two to three times the magmatism predicted from melting models<sup>5</sup> to non-volcanic margins with almost no rift or post-rift magmatism. Such variations in magmatic activity are commonly attributed to variations in mantle temperature. Here we describe results from the PESCADOR seismic experiment in the southern Gulf of California and present crustal-scale images across three rift segments. Over short lateral distances, we observe large differences in rifting style and magmatism—from wide rifting with minor synchronous magmatism to narrow rifting in magmatically robust segments. But many of the factors believed to control structural evolution and magmatism during rifting (extension rate, mantle potential temperature and heat flow) tend to vary over larger length scales. We conclude instead that mantle depletion, rather than low mantle temperature, accounts for the observed wide, magma-poor margins, and that mantle fertility and possibly sedimentary insulation, rather than high mantle temperature, account for the observed robust rift and post-rift magmatism.

The Gulf of California is an oblique rift system with short spreading segments connected by long transform faults (Fig. 1)<sup>6</sup>. Rifting in the gulf began ~12–15 million years (Myr) ago when subduction ended west of the Baja California peninsula. As the East Pacific Rise (EPR) approached the palaeo-trench, the subducting Farallón plate broke into a number of microplates; as subduction stalled, those microplates and the Baja California peninsula coupled to the Pacific plate, resulting in the onset of rifting and eventually the modern plate boundary within the Gulf of California in the vicinity of the former arc<sup>7–10</sup>. The peninsula now moves nearly completely with the Pacific plate, with ~48 mm yr<sup>-1</sup> of spreading across the Gulf of California representing ~92% of Pacific–North America relative motion<sup>11,12</sup>. No shear zones cut across the peninsula south of the Agua Blanca fault (Fig. 1 inset), and the Pacific–North American Euler pole is sufficiently distant that the rift segments of the southern gulf have all experienced the same net extension rate since rifting began.

Previously, little was known about the variation in rifted-margin crustal structure along the gulf, with constraints limited to geologic observations, seafloor bathymetry, gravity transects, sparse seismic

refraction measurements<sup>13</sup>, and the CORTES-P96 (ref. 14) crustal-scale seismic transect in the northern gulf (Fig. 1). The seafloor expression of rift structure is masked by sediments in much of the gulf, and the considerable variation in sediment thickness, from thick sediments in the north to little sediment input in the south, gives the impression that rift structure varies from narrow in the south to wide in the north. This impression is enhanced by the obscuring effect of sediment on the development of seafloor-spreading magnetic lineations<sup>6</sup>, such that diagnostic magnetic lineations are only observed across the southernmost segments of the gulf. Our results indicate that a simple north-to-south variation does not exist in the southern gulf, south of Tiburon Island (Fig. 1). Instead, distinct styles of rifting and rift magmatism occur within the southern gulf, and this variation appears to be related to pre-rift magmatic history.

We acquired wide-angle and multi-channel seismic data across the northern Guaymas, Alarcón, and the San José del Cabo to Puerto Vallarta (Cabo–PV) segments of the southern Gulf of California as part of the PESCADOR experiment. Each of these transects was instrumented with ocean-bottom seismometers spaced 10–15 km apart and similarly spaced seismometers on land recording the offshore shots to ~100 km inland. Excellent-quality data from this dense source and receiver coverage enable imaging of detailed crustal structure across these rift segments<sup>15–17</sup> (Fig. 2 and Supplementary Information). Each transect reveals a rifting style that is distinct in terms of structure and magmatism.

The Guaymas basin is a narrow rift<sup>1</sup> segment (a total conjugate-margin width less than 200 km) that has been robustly magmatic since continental break-up. We estimate the location of the continent–ocean transition here from the well-constrained rapid shallowing of the Moho and coincident lateral increase in seismic velocity to ~6.8 km s<sup>-1</sup>, a value typical of gabbroic composition rock. We interpret the crust seaward of the continent–ocean transitions to be new igneous crust formed at an oceanic spreading centre that accommodated the majority of extension in this segment since lithospheric rupture. The spreading centre has been robustly magmatic, forming new intrusive igneous crust 6–8 km thick, with an additional unknown volume of igneous material intruded into the overlying sediments. The ~280 km width of new igneous crust and spreading rates of ~48 mm yr<sup>-1</sup> imply that lithospheric rupture occurred ~6 Myr ago. Lithospheric rupture followed at least 70 km of continental extension, the amount estimated across the thinned continental-margin crust of the velocity model. It is likely that the low-lying crust of the coastal plain beyond our transect to the south-east was also extended.

The Alarcón segment is a wide rift. This segment experienced ~350 km of continental extension before the onset of seafloor

<sup>1</sup>Department of Geology and Geophysics, Woods Hole Oceanographic Institution, Woods Hole, Massachusetts 02543, USA. <sup>2</sup>Department of Earth and Environmental Sciences, New Mexico Institute of Mining and Technology, Socorro, New Mexico 87801, USA. <sup>3</sup>Department of Geology and Geophysics, University of Wyoming, Laramie, Wyoming 82071, USA. <sup>4</sup>Department of Geology, Centro de Invest. Científica y de Educación Superior de Ensenada, Ensenada C.P. 22860, Mexico. <sup>5</sup>Institute of Geophysics and Planetary Physics, Scripps Institution of Oceanography, La Jolla, California 92037, USA. <sup>6</sup>Department of Geology, Northern Arizona University, Flagstaff, Arizona 86011, USA. <sup>7</sup>BP Exploration Operating Company Ltd, Sunbury-on-Thames TW16 7LN, UK.



spreading 2–3 Myr ago, which has produced ~135 km of oceanic crust ~6 km thick<sup>15</sup>. The continent–ocean boundary is marked by a sharp transition from a shallowing to a flat Moho below normal-thickness oceanic crust with clearly identifiable magnetic anomalies (Supplementary Fig. 1). In this segment, the transition to seafloor spreading appears to be coincident with the northward propagation of the EPR<sup>6,18</sup>. Earlier, extension localized beneath the Tamayo trough thinned the continental crust there to ~7 km, but left little evidence there or elsewhere within the segment for syn-rift magmatism apart from a layer 250–500 m thick with seismic velocities of 2.5–2.8 km s<sup>-1</sup>, which overlies basement along much of the transect and may represent volcanic or volcanoclastic strata<sup>15</sup>. The Alarcón segment was thus magma-poor during rifting, suggesting that the underlying ‘continental’ asthenospheric mantle did not readily melt upon decompression. We speculate that as the EPR propagated northward, dykes sourced from the presumably more fertile EPR asthenospheric mantle ultimately enabled rupturing of the continental lithosphere<sup>19</sup>.

The Cabo–PV segment is a narrow rift. The continent–ocean boundary at the western margin is similar to that in Alarcón, juxtaposing EPR-sourced oceanic crust against extended continental crust. In this segment, however, seafloor spreading initiated ~1 Myr before the propagation of the EPR into the gulf ~3.5 Myr ago. The initial spreading centre is preserved in the southeast as the María Magdalena rise<sup>6,20</sup>. The crust produced at the María Magdalena

rise was presumably derived from ‘continental’ asthenosphere and is ~1 km thicker than the crust formed at the EPR. The EPR propagated into the segment along the western continent–ocean boundary, and it is believed that a brief period of coincident spreading at the two spreading centres resulted in convergence along the eastern margin<sup>6</sup>. Estimating pre-rift extension in this segment is thus complicated, but the steep western margin indicates that this is a narrow rift segment (Supplementary Fig. 5). There is little direct evidence of syn-rift magmatism in this segment, but the rapid transition to magmatic seafloor spreading suggests that this segment is neither magma-poor nor magma-rich and that the underlying continental asthenosphere produced melt as would be expected during rifting.

The crustal structure of the Alarcón segment challenges the common notion of how wide<sup>1</sup> rifts (conjugate-margin width >200 km) form. A mechanism of wide-rift formation in which buoyancy-driven lower-crustal flow inhibits localization<sup>1,4</sup> does not apply to this segment, because substantial Moho topography persists to the present. The localized extension beneath the Tamayo trough indicates that the lithosphere resisted rupture even after substantial thinning, suggesting that the lithospheric mantle was strong and that the asthenosphere did not produce sufficient melt to rupture the lithosphere via dyking<sup>19</sup> before the arrival of the presumably more fertile EPR mantle. The adjacent Pescadero and Farallón segments north of Alarcón have rifted-margin morphologies that are similar to Alarcón (Supplementary Fig. 5). These segments differ from Alarcón in that

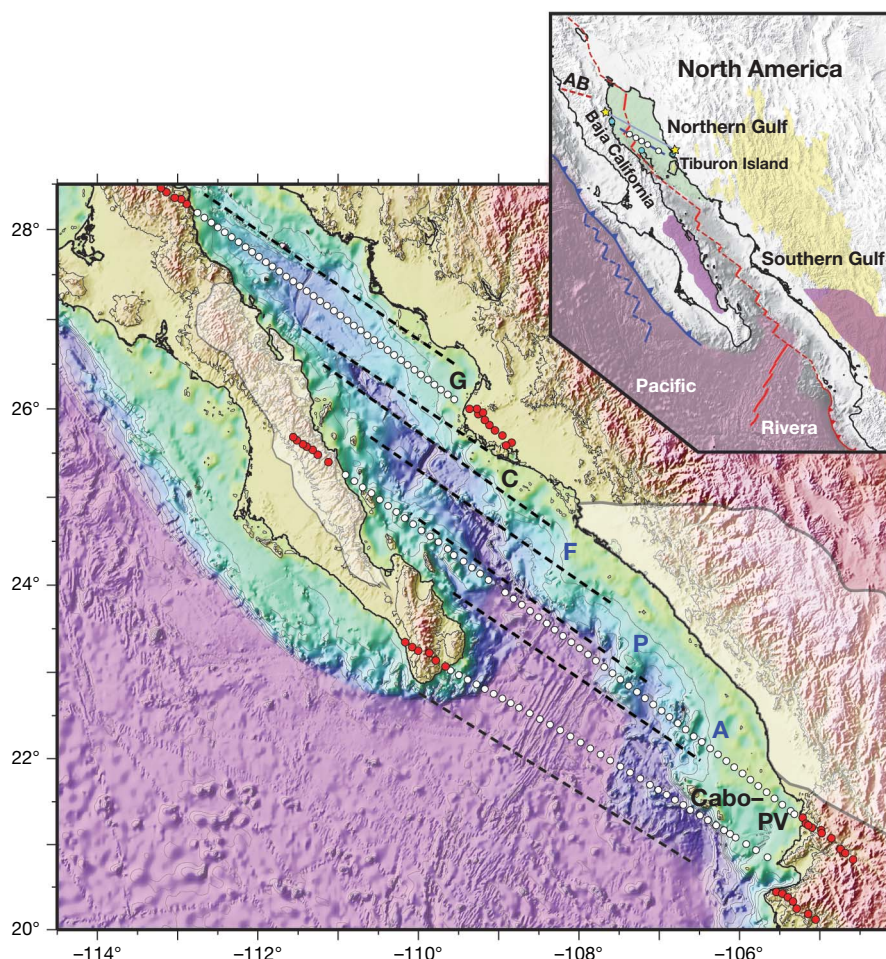


**Figure 1 | Map of the PESCADOR experiment in southern Gulf of California.** The Guaymas (G), Carmen (C), Farallón (F), Pescadero (P), Alarcón (A) and the San José del Cabo to Puerto Vallarta (Cabo–PV) segments are separated by dashed lines. Blue labels indicate south-central segments, white and red dots are the instrument locations of the three seismic transects, and white shading indicates the extent of early Miocene ignimbrite volcanism<sup>21</sup>. In the

inset, green shading denotes the northern gulf and pink shading EPR-sourced crust, and extinct and modern plate boundaries are shown in blue and red. AB, Agua Blanca; white and blue dots, CORTES-P96 (ref. 14) instruments. The geologic constraints on northern gulf spreading<sup>27</sup> is indicated by yellow stars; yellow shading shows the mapped extent<sup>21</sup> of the Oligocene and purple shading indicates early Miocene ignimbrite events.

their spreading centres are defined by narrow bathymetric deeps that indicate only nascent seafloor spreading or none (Supplementary Figs 4–6). This suggests that the EPR mantle has not propagated into them and that these are also magma-poor segments underlain by continental mantle that does not readily melt. We call these wide-rift segments collectively the south-central domain.

The south-central segments rifted over the locus of voluminous early-Miocene ignimbrite volcanism<sup>21</sup> (Fig. 1). This early Miocene event, which followed a more extensive early Oligocene event, deposited 1–2 km of ignimbrite and lava over a wide area and may have left the residual mantle both depleted and dry, reducing its ability to melt and deform<sup>22</sup>. Magmatic depletion of the mantle may thus be a primary factor controlling the evolution of rifting in the south-central domain. The relatively abrupt transition in rift style between the south-central domain and the surrounding segments may be related to the focused magmatism characteristic of volcanic arcs and indicated by their long-lived volcanic centres, which may be manifested in part in the mantle. Alternatively, the triggering mechanism of ignimbrite magmatism, perhaps slab foundering<sup>21</sup>, may have been laterally discontinuous. Either situation could enable voluminous arc volcanism to impart depleted mantle signatures that vary over small spatial scales, thus explaining the relatively abrupt variation in rifting style between the south-central domain and the segments to the north and south.

Magmatism within the Guaymas basin is anomalous with respect to the south-central segments and with respect to globally averaged mid-ocean ridge crustal production<sup>23</sup> (~6 km). The average thickness of the plutonic component of new igneous crust (average  $V_p = 6.8 \text{ km s}^{-1}$ ) in the northern Guaymas segment is greater than 7 km, and velocities of  $4.0\text{--}5.5 \text{ km s}^{-1}$  in the overlying 2–3-km-thick layer of sediments and igneous rocks<sup>24</sup> suggest an additional 1 km or

more equivalent igneous thickness. It is likely that the southern Guaymas segment, which hosts a basaltic shield volcano<sup>25</sup>, is similarly magmatic. It is possible that the underlying mantle here is more fertile and/or hotter than that beneath the south-central domain and the average MORB-source mantle. The mantle may be 'charged'<sup>26</sup> in a similar fashion to how the mantle beneath the south-central domain was charged before the early Miocene ignimbrite event. That ignimbrite event did not extend northward beneath the Guaymas basin, however, and so the inherited fertility/hydration beneath the Guaymas basin has been expressed as ongoing robust magmatism since continental break-up, with this magmatism probably contributing to lithospheric rupture after only moderate extension.

A second factor possibly contributing to the anomalous magmatism in the Guaymas basin may also explain crustal structure within the northern gulf and has implications for sedimented spreading centres and mantle melt extraction generally. The crustal structure of the Delfín–Tiburón segment in the northern gulf<sup>4</sup> is similar to the northern Guaymas segment, with a thick layer (>5 km) of intruded sediments overlying a thick igneous layer with mafic ( $6.5\text{--}6.8 \text{ km s}^{-1}$ ) seismic velocities. Geologic evidence suggests that ~275 km of extension has occurred across the Delfín–Tiburón segment between points separated by 300 km (ref. 27; Fig. 1), and so it is likely that most of this extension was accommodated by the creation of new igneous crust. A common feature shared by the Guaymas and Delfín–Tiburón segments, and not shared by the Cabo–PV segment, is a thick sedimentary layer, and we speculate that this sediment blanket may enhance mantle melt extraction. It is unlikely that melt extraction beneath mid-ocean ridges is 100% efficient, and so the global average oceanic crustal thickness probably underestimates the available melt. The thermal structure near mid-ocean ridges may place controls on melt

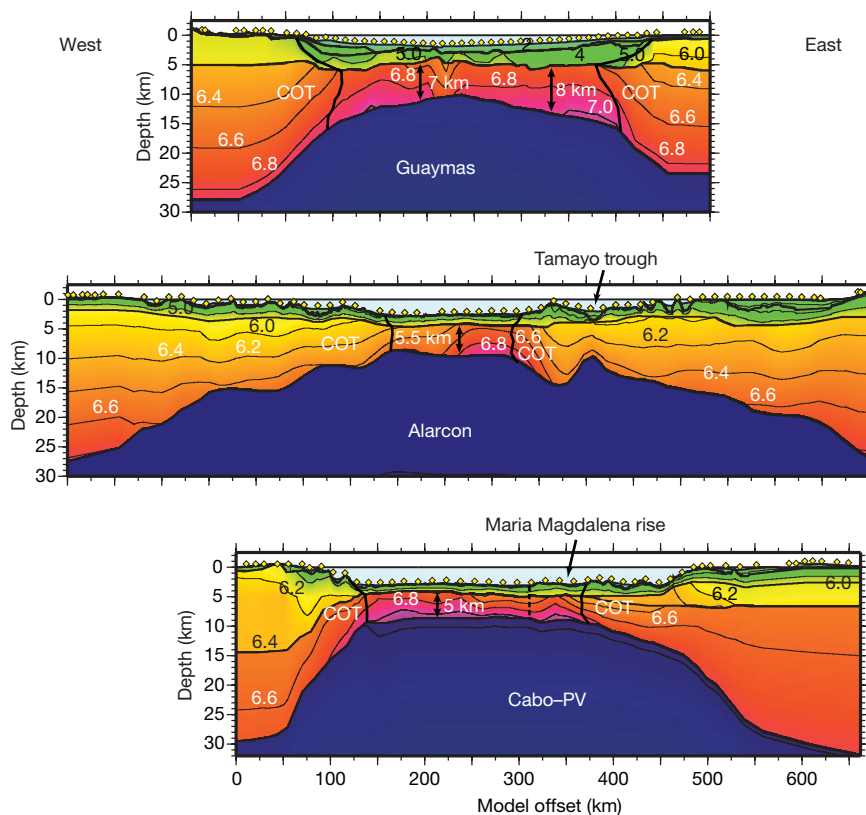


**Figure 2 | Models of seismic velocity structure along the Guaymas, Alarcón and the San José del Cabo to Puerto Vallarta transects of the PESCADOR experiment.** Velocity contours are colour-coded and labelled in units of  $\text{km s}^{-1}$ . Yellow diamonds are the instrument locations. COT indicates the interpreted continent/ocean transition. The dashed line in the Cabo–PV

model indicates the interpreted boundary between oceanic crust formed at the María Magdalena Rise and the EPR. Models were determined using a combined forward/inverse travel-time modelling approach<sup>30</sup>. Examples of data are presented in the Supplementary Information.

extraction<sup>28</sup>, and hydrothermal circulation is a robust mechanism for enhancing heat flux<sup>29</sup>. It might thus be expected that a thick blanket of sediment, by inhibiting hydrothermal circulation, would enhance melt extraction, resulting in new igneous crust thicker than that at unsegmented mid-ocean ridges.

The results presented here highlight the importance of inherited mantle fertility/hydration and possibly of sediments as controlling parameters of the rifting process. Our primary observations are variations in rift width and magmatism over small spatial scales, with wide, magma-poor rift segments formed over mantle that sourced voluminous pre-rift arc magmatism, and magma-rich segments associated with thick sediments. Many rifts initiate or localize at formerly convergent boundaries in response to ridge subduction, in back-arc settings, or along suture zones following continent-continent collision. Substantial along-strike variations in the expression of rifting, with these variations controlled by pre-rift tectonics and magmatism of the formerly convergent margin, may thus be common along many rifted margins. Similarly, substantial along-strike variability in syn-rift sedimentation is likely in many rifts, depending on topography, climate and regional drainage patterns.

Received 1 February; accepted 18 June 2007.

- Hopper, J. R. & Buck, W. R. The effect of lower crustal flow on continental extension and passive margin formation. *J. Geophys. Res.* **101**, 21175–20194 (1996).
- Braun, J. & Beaumont, C. Styles of continental rifting from dynamical models of lithospheric extension. *Mem. Can. Soc. Petrol. Geol.* **12**, 241–258 (1987).
- England, P. C. Constraints on extension of continental lithosphere. *J. Geophys. Res.* **88**, 1145–1152 (1983).
- Buck, W. R., Lavier, L. L. & Poliakov, A. N. B. How to make a rift wide. *Phil. Trans. R. Soc. Lond.* **357**, 671–693 (1999).
- McKenzie, D. & Bickle, M. J. The volume and composition of melt generated by extension of the lithosphere. *J. Petrol.* **29**, 625–679 (1988).
- Lonsdale, P. Geology and tectonic history of the Gulf of California. In *The Eastern Pacific Ocean and Hawaii* (eds Winterer, E. L., Hussong, D. M. & Decker, R. W.) 499–521, Vol. N of *The Geology of North America* (Geological Society of America, Boulder, Colorado, 1989).
- Atwater, T. M. Implications of plate tectonics for the Cenozoic evolution of western North America. *Geol. Soc. Am. Bull.* **81**, 3513–3536 (1970).
- Menard, H. W. Fragmentation of the Farallon plate by pivoting subduction. *J. Geol.* **86**, 99–110 (1978).
- Stock, J. M. & Lee, J. Do microplates in subduction zones leave a geological record? *Tectonics* **13**, 1472–1487 (1994).
- Michaud, F. et al. Oceanic-ridge subduction vs. slab break off: Plate tectonic evolution along the Baja California Sur continental margin since 15 Ma. *Geology* **34**, 13–16 (2006).
- DeMets, C. & Dixon, T. H. New kinematic models for Pacific-North America motion from 3 Ma to present. I. Evidence for steady motion and biases in the NUVEL-1A model. *Geophys. Res. Lett.* **26**, 1921–1924 (1999).
- Dixon, T. H., Farina, F., DeMets, C., Suarez-Vidal, F., Fletcher, J., Marquez-Azua, B., Miller, M., Sanchez, O. & Umhoefer, P. J. New kinematic models for Pacific-North America motion from 3 Ma to present. II. Evidence for a “Baja California shear zone”. *Geophys. Res. Lett.* **26**, 1921–1924 (2000).
- Phillips, R. P. Seismic refraction studies in Gulf of California. In *Marine Geology of the Gulf of California* (eds van Andel, T. & Shor, G. G.) AAPG Mem. **3**, 90–125 (1964).
- González-Fernández, A. et al. Mode of extension and rifting history of upper Tiburón and upper Delfin basins, northern Gulf of California. *J. Geophys. Res.* **110**, doi:10.1029/2003JB002941 (2005).
- Sutherland, F. H. *Continental Rifting Across the Southern Gulf of California*. PhD thesis, Univ. of California, San Diego (2006).
- Paramo, P. *Seismic Studies of Continental Rupture and Ocean Finestructure in the Gulf of California*. PhD thesis, Univ. of Wyoming (2006).
- Brown, H. E. et al. Crustal structure of the southern Gulf of California and subducting Rivera plate. *Eos* **87** (Fall Meet. Suppl.), T41D–1607 (2006).
- Castillo, P. R. et al. Petrology of Alarcón Rise lavas, Gulf of California: Nascent intracontinental ocean crust. *J. Geophys. Res.* **107**, doi:10.1029/2001JB000666 (2002).
- Buck, W. R. The role of magma in development of the Afro-Arabian rift system. In *The Afar Volcanic Province Within the East African Rift System* (eds Yirgu, G., Ebinger, C. J. & Maguire, P. K. H.) *Geol. Soc. Spec. Publ.* **259**, 43–54 (2006).
- Larsen, R. L. Bathymetry, magnetic anomalies, and plate tectonic history of the mouth of the Gulf of California. *Geol. Soc. Am. Bull.* **83**, 3345–3360 (1972).
- Ferrari, L., Valencia-Moreno, M. & Bryan, S. Magmatismo y tectónica en la Sierra Madre Occidental y su relación con la evolución de la margen occidental de Norteamérica. *Bull. Geol. Soc. Mexico* **57**, 343–378 (2005).
- Hirth, G. & Kohlstedt, D. L. Water in the oceanic upper mantle: Implications for rheology, melt extraction, and the evolution of the lithosphere. *Earth Planet. Sci. Lett.* **144**, 93–108 (1996).
- White, R. S., McKenzie, D. & O’Nions, R. K. Oceanic crustal thickness from seismic measurements and rare earth element inversions. *J. Geophys. Res.* **97**, 19,683–19,715 (1992).
- Einsele, G. et al. Intrusion of basaltic sills into highly porous sediments, and resulting hydrothermal activity. *Nature* **283**, 441–445 (1980).
- Batiza, R. Geology, petrology, and geochemistry of Isla Tortuga, a recently formed tholeiitic island in the Gulf of California. *Geol. Soc. Am. Bull.* **89**, 1309–1324 (1978).
- Humphreys, E. et al. How Laramide-age hydration of North American lithosphere by the Farallon slab controlled subsequent activity in the western United States. *Int. Geol. Rev.* **45**, 575–595 (2003).
- Oskin, M., Stock, J. M. & Martin-Barajas, A. Rapid localization of Pacific-North America plate motion in the Gulf of California. *Geology* **29**, 459–462 (2001).
- Brown, J. W. & White, R. S. Effect of finite extension rate on melt generation at rifted continental margins. *J. Geophys. Res.* **100**, 18,011–18,029 (1995).
- Johnson, H. P. & Pruis, M. J. Fluxes of fluid and heat from the oceanic crustal reservoir. *Earth. Planet. Sci. Lett.* **216**, 565–574 (2003).
- Zelt, C. A. & Smith, R. B. Seismic traveltime inversion for 2-D crustal velocity structure. *Geophys. J. Int.* **108**, 16–34 (1992).

**Supplementary Information** is linked to the online version of the paper at [www.nature.com/nature](http://www.nature.com/nature).

**Acknowledgements** We thank the captains and crew of the RV *Maurice Ewing* and RV *New Horizon*, the OBSIP teams, J. Urban, and A. Gorman for his efforts as Chief Scientist on the RV *New Horizon*. The Lamont Earth Observatory Marine Office and CICESE provided support before and during the experiment. This work was funded by a grant from the US NSF-MARGINS programme.

**Author Contributions** D.L., P.J.U., G.M.K., W.S.H., A.J.H., A.G.-F., J.M.F. and G.J.A. were the principal investigators on this project and each contributed substantially to this work. F.S., P.P. and H.E.B. analysed data from the Alarcón and Cabo-PV segments as portions of their PhD theses. D.L. analysed data from Guaymas and wrote the paper. All authors discussed the results and commented on the manuscript.

**Author Information** Reprints and permissions information is available at [www.nature.com/reprints](http://www.nature.com/reprints). The authors declare no competing financial interests. Correspondence and requests for materials should be addressed to D.L. (danl@whoi.edu).



## LETTERS

# Genetic variants regulating *ORMDL3* expression contribute to the risk of childhood asthma

Miriam F. Moffatt<sup>1\*</sup>, Michael Kabesch<sup>2\*</sup>, Liming Liang<sup>3\*</sup>, Anna L. Dixon<sup>4</sup>, David Strachan<sup>5</sup>, Simon Heath<sup>6</sup>, Martin Depner<sup>2</sup>, Andrea von Berg<sup>7</sup>, Albrecht Bufe<sup>8</sup>, Ernst Rietschel<sup>9</sup>, Andrea Heinzmann<sup>10</sup>, Burkard Simma<sup>11</sup>, Thomas Frischer<sup>12</sup>, Saffron A. G. Willis-Owen<sup>1</sup>, Kenny C. C. Wong<sup>1</sup>, Thomas Illig<sup>13</sup>, Christian Vogelberg<sup>14</sup>, Stephan K. Weiland<sup>15</sup>, Erika von Mutius<sup>2</sup>, Gonçalo R. Abecasis<sup>3</sup>, Martin Farrall<sup>4</sup>, Ivo G. Gut<sup>6</sup>, G. Mark Lathrop<sup>6</sup> & William O. C. Cookson<sup>1</sup>

Asthma is caused by a combination of poorly understood genetic and environmental factors<sup>1,2</sup>. We have systematically mapped the effects of single nucleotide polymorphisms (SNPs) on the presence of childhood onset asthma by genome-wide association. We characterized more than 317,000 SNPs in DNA from 994 patients with childhood onset asthma and 1,243 non-asthmatics, using family and case-referent panels. Here we show multiple markers on chromosome 17q21 to be strongly and reproducibly associated with childhood onset asthma in family and case-referent panels with a combined *P* value of  $P < 10^{-12}$ . In independent replication studies the 17q21 locus showed strong association with diagnosis of childhood asthma in 2,320 subjects from a cohort of German children ( $P = 0.0003$ ) and in 3,301 subjects from the British 1958 Birth Cohort ( $P = 0.0005$ ). We systematically evaluated the relationships between markers of the 17q21 locus and transcript levels of genes in Epstein–Barr virus (EBV)-transformed lymphoblastoid cell lines from children in the asthma family panel used in our association study. The SNPs associated with childhood asthma were consistently and strongly associated ( $P < 10^{-22}$ ) in *cis* with transcript levels of *ORMDL3*, a member of a gene family that encodes transmembrane proteins anchored in the endoplasmic reticulum<sup>3</sup>. The results indicate that genetic variants regulating *ORMDL3* expression are determinants of susceptibility to childhood asthma.

Our study design aimed to provide internal replication of potentially positive results with family and case-referent panels of subjects with childhood asthma (Fig. 1). This structure also allowed comparison for consistency between case-control and family-based tests of association. To systematically investigate the effects of polymorphisms on the transcription of positional candidate genes, we further measured global gene expression in B-cell-derived EBV-transformed lymphoblastoid cell lines (EBVL) in probands and siblings of the family panel.

The study subjects included a panel of 207 predominantly (99%) nuclear families (MRC-A). These were recruited through a proband with severe (Step 3) childhood onset asthma and contained 295 sib pairs, 11 half-sib pairs and 3 singletons (counting all possible sibs). Four-hundred and thirty-seven non-asthmatic Caucasian UK

controls (UK-C) were studied by the same protocols. We also genotyped 728 children of German origin recruited in the Multicentre Asthma Genetics in Childhood Study (MAGICS) study with physician-diagnosed asthma for comparison with 694 reference children recruited in the cross sectional International Study of Asthma and Allergies in Childhood (ISAAC) study<sup>4</sup>.

We genotyped all children in the primary association study with the Illumina Sentrix HumanHap300 BeadChip. After quality control and elimination of markers with low minor-allele frequencies ( $<0.5\%$ ), extreme Hardy–Weinberg equilibrium statistics ( $\chi^2 > 25$ ) or low genotyping call rates ( $<95\%$ ), we retained 307,328 SNPs and 684 million genotypes (99.4% call rate) for analysis. Amongst the 2,236,212 common (minimum allele frequency  $> 0.05$ ) SNPs in the HapMap panel, 79% were tagged with correlation  $R^2 > 0.8$  and 90.9% with  $R^2 > 0.5$  with our successfully typed markers.

We also typed the parents and children in the MRC-A panel with the Illumina Sentrix Human-1 Genotyping BeadChip (concentrated on genes and surrounding sequences) (Fig. 1), producing an

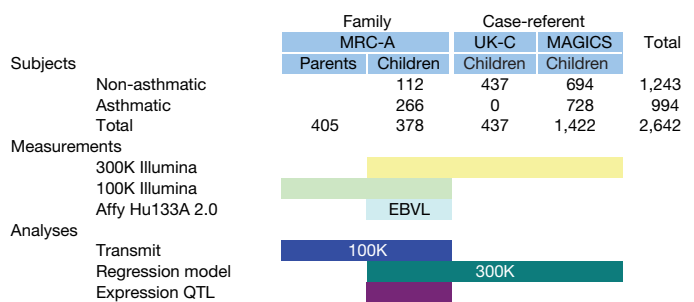


**Figure 1 | Study design.** The subjects were recruited from family (MRC-A) and case-control panels (MAGICS and UK-C). All children were genotyped with the Illumina Sentrix HumanHap300 BeadChip. The children and parents in the MRC-A panel were in addition genotyped with the Illumina Sentrix Human-1 Genotyping BeadChip. Gene expression in lymphoblastoid cell lines (EBVL) was measured in the affected and unaffected children of the MRC-A panel. Replication of positive results was sought in two independent panels of subjects from the ISAAC Phase II and 1958 British Birth Cohort studies.

<sup>1</sup>National Heart and Lung Institute, Imperial College, London SW3 6LY, UK. <sup>2</sup>University Children's Hospital, Ludwig Maximilians University, D80337 Munich, Germany. <sup>3</sup>Center for Statistical Genetics, Department of Biostatistics, SPH II, Ann Arbor, Michigan 48109-2029, USA. <sup>4</sup>Wellcome Trust Centre for Human Genetics, University of Oxford, Oxford OX3 7BN, UK. <sup>5</sup>Division of Community Health Science, St George's, University of London, London SW17 0RE, UK. <sup>6</sup>Centre National de Génotypage, Institut Génomique, Commissariat à l'Énergie Atomique, 91057 Evry, France. <sup>7</sup>Research Institute for the Prevention of Allergic Diseases, Children's Department, Marien-Hospital, D46483 Wesel, Germany. <sup>8</sup>Department of Experimental Pneumology, Ruhr-University, D44789 Bochum, Germany. <sup>9</sup>University Children's Hospital, University of Cologne, D50924 Cologne, Germany. <sup>10</sup>University Children's Hospital, Albert Ludwigs University, D79106 Freiburg, Germany. <sup>11</sup>Children's Department, Feldkirch Hospital, A6800 Feldkirch, Austria. <sup>12</sup>University Children's Hospital Vienna, A1090 Vienna, Austria. <sup>13</sup>Institute of Epidemiology, GSF-Research Centre for Environment and Health, D85764 Neuherberg, Germany. <sup>14</sup>University Children's Hospital, Technical University Dresden, D01307 Dresden, Germany. <sup>15</sup>Institute of Epidemiology, Ulm University, D89081 Germany.

\*These authors contributed equally to this work.

additional 91,293 SNPs with 36.0% average heterozygosity and 89,815,992 genotypes (99.0% call rate). We found only 0.412 mendelian errors per SNP; these were excluded from subsequent analyses.

We tested for association of the 300K panel to childhood onset asthma in the combined primary data set of 994 asthmatics and 1,243 non-asthmatics (Fig. 2). We calculated the 1% false-discovery rate (FDR) threshold<sup>5</sup> to be  $P \leq 6.8 \times 10^{-7}$  and the 5% FDR to be  $P \leq 5.0 \times 10^{-6}$ . We tested for population stratification in the combined data set, finding a genomic control parameter of 1.07. This minor degree of background stratification reflected small differences in allele frequencies within and between the two nationally defined European populations that contributed to the study.

We further tested the effects of stratification on our top results by analysing the 34 SNPs that surpassed the 5% FDR threshold with 102 randomly selected SNPs as covariates in a backward stepwise logistic regression procedure<sup>6</sup>. The results of the stepwise logistic regression analysis showed only modest reduction of the support for association for 31 of the SNPs. Of 34 SNPs, 16 continued to surpass the 5% FDR and 12 of 20 SNPs remained above the 1% FDR threshold (Supplementary Table 1).

Strikingly, 7 of the 12 markers still below the 1% FDR threshold mapped to a 112 kb interval on chromosome 17q21. Several other markers in this interval also showed strong evidence of association (Supplementary Table 2, Fig. 2 and Fig. 3a). The SNP with the strongest evidence of association within the interval was *rs7216389* (uncorrected  $P = 9 \times 10^{-11}$ ). With the exception of the 17q21 locus, none of the markers below the 5% FDR, after controlling for stratification, were within 1 Mb of each other (Supplementary Table 1).

The patterns of association for the chromosome 17q21 markers were similar and significant in both the UK family panel and the German case-referent panel (Table 1 and Supplementary Table 2). There was no evidence of heterogeneity of the association, or of significant allele frequency differences in cases or controls from the UK and Germany.

We selected 27 markers from the NCBI database of genetic variation (dbSNP) that were within or adjacent to the strongly associated interval for genotyping. These exhibited similar patterns and strengths of association as the genome-wide association (GWA) markers (Supplementary Table 2).

SNPs from the region that we had typed in whole families in the MRC-A panel showed significant associations in a family-based association test (Supplementary Table 3). The most strongly associated marker was *rs8067378* (248 informative transmissions,  $P = 3 \times 10^{-6}$ ; odds ratio, 1.84; 95% confidence interval, 1.43–2.42). The pattern of alleles transmitted in excess to affected offspring was consistent with the case-referent association results, further indicating that the association was robust to population stratification.

The trait-associated markers (with  $P < 10^{-6}$  in the combined data set) from chromosome 17q21 fall within a 206.5 kb core containing

three consecutive haplotype blocks (linkage disequilibrium coefficient ( $D'$ )  $> 0.94$  for adjacent markers,  $D' < 0.82$  between blocks), as well as one 'isolated' marker in moderate ( $D' = 0.7$ ) linkage disequilibrium with an adjacent marker (Supplementary Fig. 1). Low linkage disequilibrium between markers that showed strong association with the disease trait indicated that multiple variants may independently confer disease susceptibility. We evaluated this hypothesis statistically in a forward stepwise regression potentially incorporating all the genotyped markers between 34.5 and 36.0 Mb on chromosome 17. This identified three SNPs (*rs7216389*, *rs11650680* and *rs3859192*), which jointly showed strong association to childhood asthma ( $P < 10^{-12}$ ) and contributed statistically independent significant effects (Supplementary Table 4). This result is consistent with the possibility that more than one functional SNP underlies the locus or (less likely given the SNP density across this region) the presence of a single functional SNP in incomplete linkage disequilibrium with the typed markers. Further fine-mapping studies will be required to resolve these alternatives.

We further examined the impact of the chromosome 17q21 locus on childhood asthma with the aid of 200 asthmatic cases and 2,120 non-asthmatic controls from within the cross-sectional study population of ISAAC Phase II, recruited in Dresden and Munich. The corresponding DNAs were genotyped for a series of nine markers from across the locus that had shown evidence of association in the GWA (Table 1). These showed the same trends as observed in the GWA samples (odds ratios ranging from 1.52 to 1.11), and most were significantly associated with disease with  $P < 0.001$  (4 out of 9 markers) or  $P < 0.01$  (5 out of 9 markers).

One chromosome 17q21 SNP associated with childhood asthma in the GWA analysis (*rs3894194*, Table 1) had been previously examined in 3,301 subjects from the UK 1958 birth cohort. The genotype data for this marker were deposited for public use in the database maintained by the investigators responsible for the cohort study (<http://www.b58cgene.sgul.ac.uk/>). Although data were not available for the other disease-associated chromosome 17q21 markers, we were able to confirm association to childhood asthma with *rs3894194*, which is in linkage disequilibrium with the other markers at the locus (linkage disequilibrium block 3 in Supplementary Fig. 1). Restricting analyses to cohort members of Caucasian ethnicity, we found that the 398 cases recalling 'asthma ever' at age 42, showed a significant association (odds ratio, 1.21, 95% confidence interval, 1.04–1.40,  $P = 0.012$ ). Ninety-three individuals were reported to have 'asthma attacks' in the first seven years of life (that is during 1958 to 1965), and these were strongly associated to *rs3894194* (odds ratio = 1.68, 95% confidence interval, 1.25–2.26,  $P = 0.0005$ ).

The disease-associated chromosome 17q21 markers had consistent odds ratios and directions of association effects in the GWA panels and the two replication cohorts ( $P = 0.19$  for heterogeneity)

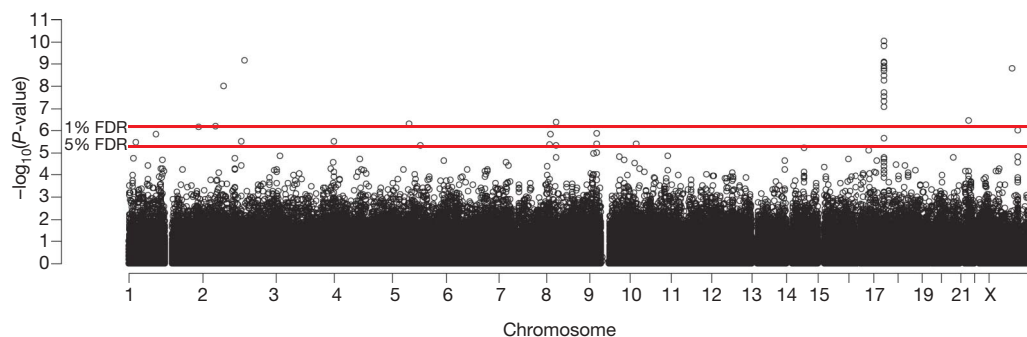


**Figure 2 | Genome-wide association of 317,447 SNPs and asthma in 994 asthmatic children and 1,243 non-asthmatic children.** Position in the genome, divided by chromosome, is depicted along the x axis. Strength of association is shown on the y axis. The result for each individual marker is

depicted as a black circle. The genome-wide thresholds for 1% and 5% false discovery rates (FDR) are shown as horizontal red lines. Numerous markers on chromosome 17q21 show association to asthma above the 1% FDR threshold in the region of maximum association.

(Table 1), suggesting that we have identified a robust risk factor for childhood asthma.

Variation in gene transcription is an important mechanism in mediating susceptibility to asthma and other diseases, and the transcript abundances of genes may be directly modified by polymorphisms in regulatory elements<sup>7,8</sup>. We therefore measured global gene expression in EBVL from children in the MRC-A panel (Fig. 1). These same subjects had been typed with the Illumina Sentrix HumanHap300 and Sentrix Human-1 Genotyping BeadChips (Fig. 1). EBVLs represent the B-cell lineage, and are consequently of direct relevance to asthma. Cells were harvested at log-phase in the first growth after EBV transformation. Global transcript abundance was measured with Affymetrix HG-U133 Plus 2.0 chips. We used quantile normalization after Robust Multi-Array Average (RMA) to enforce normality and reduce outlier leverage. A complete description of the global results will be presented in another paper.

Expression data were available for 14 of 19 annotated genes in the region from 35.0 to 35.5 Mb on chromosome 17 (that is, within or near the 206 kb region of association on 17q21.1) (Fig. 3d). We found that transcripts in one gene, *ORMDL3*, were strongly ( $P < 10^{-22}$  for *rs7216389*) and consistently positively associated to exactly the same SNPs from the Illumina Sentrix HumanHap300 BeadChip as childhood asthma (Fig. 3c). The disease-associated markers accounted for 29.5% of the variance of expression. No other markers were significantly correlated to *ORMDL3* expression after adjustment for genome-wide multiple testing. After accounting for the effects of the disease-associated markers, the residual heritability of the *ORMDL3* expression was not significant ( $P = 0.29$  compared to  $P = 0.0009$  before adjustment).

These findings suggested that the 17q21 disease-associated locus is the principal genetic determinant of *ORMDL3* expression. None of the other transcripts from the region or elsewhere in the genome showed a significant relationship to the disease-associated markers

in our data set. Despite the strength of these effects, the presence of several SNPs independently associated to asthma nevertheless makes it possible that *ORMDL3* may not be the exclusive determinant of the disease susceptibility at this locus.

In the subset of individuals for whom expression data are available, the T nucleotide allele at *rs7216389* (the marker most strongly associated with disease in the combined GWA analysis) has a frequency of 62% amongst asthmatics compared to 52% in non-asthmatics ( $P = 0.005$  in this sample). The additive effect of this allele corresponds to a change of 0.78 standard deviation units in *ORMDL3* expression ( $P < 10^{-22}$ ). We saw the expected increase of  $\sim 0.064$  standard deviation units in *ORMDL3* expression among asthmatics, but this was not significant given the sample size. Patterns of *ORMDL3* expression by genotype in asthmatics and non-asthmatics are shown in Supplementary Fig. 2.

*ORMDL3* is the third member of a novel class of genes of unknown function that encode transmembrane proteins anchored in the endoplasmic reticulum (ER)<sup>3</sup>. We examined multiple tissue complementary (MTC) DNA panels by PCR with reverse transcription (RT-PCR), and found *ORMDL3* to be expressed in many tissues, particularly liver and peripheral blood lymphocytes (Fig. 3g). The SNPs showing the strongest association to asthma and *ORMDL3* transcript abundances are contained within an island of linkage disequilibrium between 35.2 and 35.4 Mb on chromosome 17q21 (Fig. 3b and 3c). The one-locus support unit for SNPs showing maximum association to *ORMDL3* levels lies within the first intron of the neighbouring *GSDML* gene. This non-coding sequence shows significant homology between species (Fig. 3e and 3f), and contains an element with high homology to the pro-inflammatory transcription factor C/EBPb (transcription factor score, 86.8; <http://www.cbrc.jp/research/db/TFSEARCH.html>).

Genomic regions other than the 17q21 locus did not contain multiple markers with significant evidence of association at the 1%

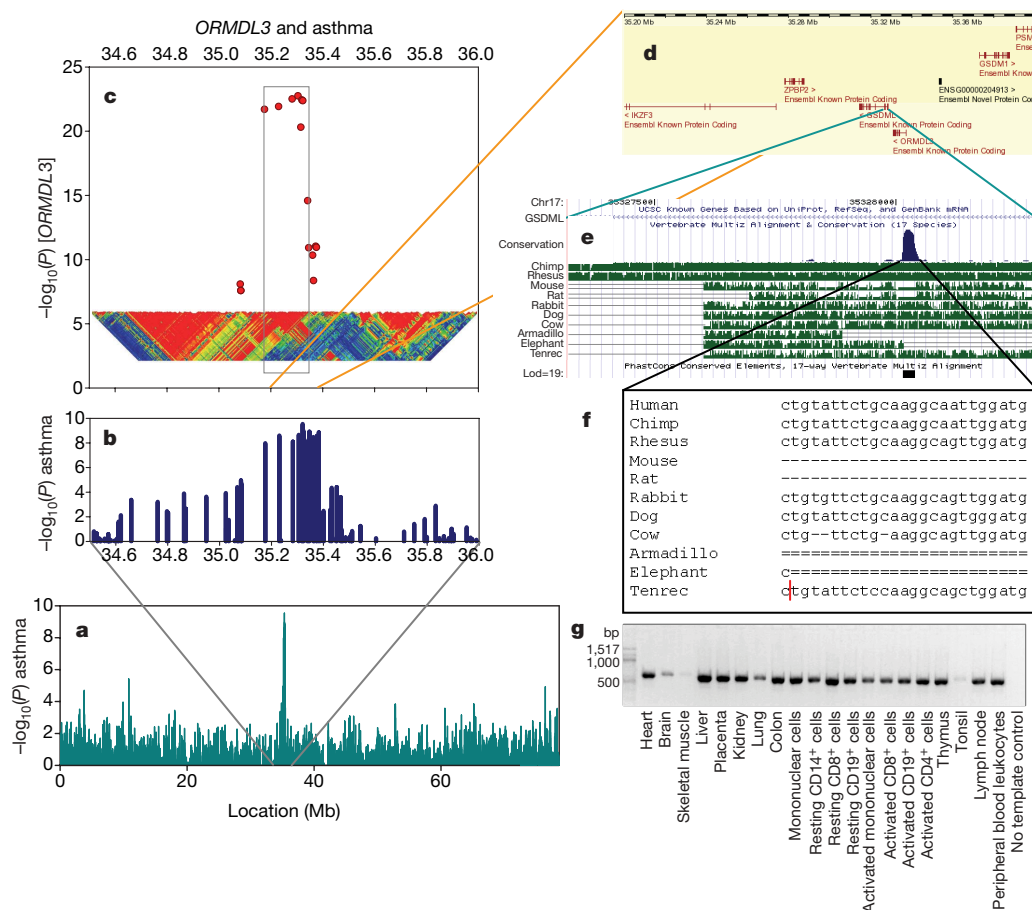


**Figure 3 | Association to asthma and transcript abundances of *ORMDL3* on chromosome 17q21.**

**a**, Mapping of association to asthma on chromosome 17. **b**, Detail of association to SNPs on chromosome 17q21. **c**, Association to *ORMDL3* transcript abundance with the same markers. A GOLD plot<sup>22</sup> of linkage disequilibrium between markers is also shown, with red indicating high linkage disequilibrium and blue denoting low. The central island of linkage disequilibrium, which contains maximum association to *ORMDL3* and asthma, is contained within the grey rectangle. **d**, Genes contained within the associated interval. **e**, Homology plot from the region of maximum association. **f**, Sequence homology from intron I of *GSDML*. **g**, RT-PCR (34 cycles) of *ORMDL3* cDNA from representative tissues (Clontech).



**Table 1 | Association of asthma and *ORMDL3* to chromosome 17q21 in combined and replication panels**

Marker	Location (Mb)	Primary GWA study -log <sub>10</sub> (P) asthma			eQTL -log <sub>10</sub> (P) [ <i>ORMDL3</i> ] MRC-A	Ref. allele	Alt. allele	ISAAC II replication cohort			-log <sub>10</sub> (P) asthma
		MRC-A	MAGICS	Combined				Odds ratio	Lower 95% CI	Upper 95% CI	
rs9303277	35.230	4.4	5.0	8.8	21.9	C	T	1.41	1.14	1.76	2.8
rs11557467	35.282	4.6	5.2	9.1	22.5	G	T	1.45	1.16	1.82	3.1
rs8067378	35.305	4.3	5.3	9.0	22.7						
rs2290400	35.320	4.0	6.4	9.8	22.4	A	G	1.47	1.18	1.82	3.2
rs7216389	35.323	4.3	6.4	10.0	22.4	T	C	1.45	1.17	1.81	3.1
rs4795405	35.342	4.1	5.3	8.7	14.6	C	T	1.52	1.20	1.89	3.6
rs8079416	35.346	2.4	6.5	8.2	10.9	C	T	1.30	1.05	1.61	1.9
rs4795408	35.361	2.1	6.1	7.5	10.3	A	G	1.25	1.01	1.54	1.4
rs3894194	35.376	1.9	6.6	7.7	11.0	T	C	1.22	0.98	1.51	1.2
rs3859192	35.382	2.0	6.0	7.3	3.5	T	C	1.11	0.89	1.37	0.4

SNPs are from the Illumina 300K panel. Results were calculated with logistic regression models. Association to *ORMDL3* transcript abundance is shown for comparison and is based on the family panel only. Replication results are shown for the ISAAC II population. CI, confidence interval; Ref., reference; Alt., alternative; eQTL, expression quantitative trait locus.

FDR threshold in either of the individual collections or the combined samples. Several other loci (Supplementary Table 1) passed a less stringent 5% FDR threshold after adjustment for population stratification, indicating that other susceptibility loci for childhood asthma could be present, perhaps having smaller effects than those found on chromosome 17q21. These results will be explored in large scale replication studies in multiple centres and population samples (the GABRIEL project: <http://www.gabriel-fp6.org/project>).

## METHODS SUMMARY

Children and their parents from the UK panels were administered a standard questionnaire<sup>9</sup> by a nurse or doctor. Asthma was defined as a positive response to the question "Has your doctor ever told you that you have asthma?" Probands had Step 3 asthma or worse according to British Thoracic Society guidelines<sup>10</sup>. Siblings were included regardless of asthma status<sup>11</sup>. Asthma cases from the MAGICS were diagnosed by a paediatric pulmonologist or allergologist on the basis of clinical examination, history and objective tests of lung function. The transformation of peripheral blood lymphocytes in all children in the MRC-A panel was carried out by the ECACC (<http://www.ecacc.org.uk>). Microarray hybridization of EBVL RNA to the U133 Plus 2.0 GeneChips (Affymetrix) was under standard conditions. Whole-genome genotyping was carried out using Illumina Sentrix Human-1 Genotyping BeadChip<sup>12</sup> and Sentrix HumanHap300 Genotyping BeadChips<sup>13</sup> (Illumina, San Diego). Genotyping of additional markers was performed on an ABI7900HT Sequence Detection System using TaqMan probes (Applied Biosystems, Foster City, California). German replication samples were genotyped using matrix-assisted laser desorption/ionization-time of flight (<http://www.sequenom.com>)<sup>14</sup>. Logistic regression models with robust sandwich estimation of the variance<sup>15</sup> implemented in the Stata *logit* function were used to detect association to asthma in the combined panels. The TRANSMIT program<sup>16</sup> was used to analyse nuclear family data (including parental genotypes). The false-discovery rate (FDR) method<sup>5</sup> was used to assess the overall statistical significance of the genome-wide association results, and FDR thresholds were calculated by applying the QVALUE (<http://faculty.washington.edu/~jstorey/qvalue/>) package<sup>17</sup>. Gene expression data were normalized with the RMA package<sup>18,19</sup> to remove any technical or spurious background variation. An inverse normalization transformation step was also applied to each trait to avoid any outliers. Association analysis was applied with Merlin (FASTASSOC option)<sup>20</sup>, after probabilistically inferring missing genotypes<sup>21</sup>.

**Full Methods** and any associated references are available in the online version of the paper at [www.nature.com/nature](http://www.nature.com/nature).

**Received 24 April; accepted 14 June 2007.**

**Published online 4 July 2007.**

1. Cookson, W. The immunogenetics of asthma and eczema: a new focus on the epithelium. *Nature Rev. Immunol.* **4**, 978–988 (2004).
2. Ober, C. & Hoffman, S. Asthma genetics 2006: the long and winding road to gene discovery. *Genes Immun.* **7**, 95–100 (2006).
3. Hjelmqvist, L. *et al.* *ORMDL* proteins are a conserved new family of endoplasmic reticulum membrane proteins. *Genome Biol.* **3**, RESEARCH0027 (2002).
4. Weiland, S. K. *et al.* Phase II of the International Study of Asthma and Allergies in Childhood (ISAAC II): rationale and methods. *Eur. Respir. J.* **24**, 406–412 (2004).
5. Benjamini, Y. & Hochberg, Y. Controlling the false discovery rate: a practical and powerful approach to multiple testing. *J. R. Statist. Soc. B* **57**, 289–300 (1995).

6. Setakis, E., Stirnadel, H. & Balding, D. J. Logistic regression protects against population structure in genetic association studies. *Genome Res.* **16**, 290–296 (2006).
7. Schadt, E. E. *et al.* Genetics of gene expression surveyed in maize, mouse and man. *Nature* **422**, 297–302 (2003).
8. Morley, M. *et al.* Genetic analysis of genome-wide variation in human gene expression. *Nature* **430**, 743–747 (2004).
9. Standards for the diagnosis and care of patients with chronic obstructive pulmonary disease (COPD) and asthma. This official statement of the American Thoracic Society was adopted by the ATS Board of Directors, November 1986. *Am. Rev. Respir. Dis.* **136**, 225–244 (1987).
10. British guideline on the management of asthma. *Thorax* **58** (Suppl 1), ii–i94 (2003).
11. Abecasis, G., Cardon, L. & Cookson, W. Selection strategies for disequilibrium mapping of quantitative traits in nuclear families. *Am. J. Hum. Genet.* **65**, A245 (1999).
12. Gunderson, K. L., Steemers, F. J., Lee, G., Mendoza, L. G. & Chee, M. S. A genome-wide scalable SNP genotyping assay using microarray technology. *Nature Genet.* **37**, 549–554 (2005).
13. Steemers, F. J. *et al.* Whole-genome genotyping with the single-base extension assay. *Nature Methods* **3**, 31–33 (2006).
14. Buetow, K. H. *et al.* High-throughput development and characterization of a genomewide collection of gene-based single nucleotide polymorphism markers by chip-based matrix-assisted laser desorption/ionization time-of-flight mass spectrometry. *Proc. Natl Acad. Sci. USA* **98**, 581–584 (2001).
15. Williams, R. L. A note on robust variance estimation for cluster-correlated data. *Biometrics* **56**, 645–646 (2000).
16. Clayton, D. A generalization of the transmission/disequilibrium test for uncertain-haplotype transmission. *Am. J. Hum. Genet.* **65**, 1170–1177 (1999).
17. Storey, J. D. & Tibshirani, R. Statistical significance for genomewide studies. *Proc. Natl Acad. Sci. USA* **100**, 9440–9445 (2003).
18. Irizarry, R. A. *et al.* Exploration, normalization, and summaries of high density oligonucleotide array probe level data. *Biostatistics* **4**, 249–264 (2003).
19. Bolstad, B. M., Irizarry, R. A., Astrand, M. & Speed, T. P. A comparison of normalization methods for high density oligonucleotide array data based on variance and bias. *Bioinformatics* **19**, 185–193 (2003).
20. Abecasis, G. R., Cherny, S. S., Cookson, W. O. & Cardon, L. R. Merlin—rapid analysis of dense genetic maps using sparse gene flow trees. *Nature Genet.* **30**, 97–101 (2002).
21. Burdick, J. T., Chen, W. M., Abecasis, G. R. & Cheung, V. G. *In silico* method for inferring genotypes in pedigrees. *Nature Genet.* **38**, 1002–1004 (2006).
22. Abecasis, G. R. & Cookson, W. O. GOLD—graphical overview of linkage disequilibrium. *Bioinformatics* **16**, 182–183 (2000).

**Supplementary Information** is linked to the online version of the paper at [www.nature.com/nature](http://www.nature.com/nature).

**Acknowledgements** The study was funded by the Wellcome Trust, the Medical Research Council, the French Ministry of Higher Education and Research, the German Ministry of education and research (BMBF), the national genome research network (NGFN), the National Institutes of Health (NHGRI and NHLBI; G.R.A.), and the European Commission as part of GABRIEL (a multidisciplinary study to identify the genetic and environmental causes of asthma in the European Community). We acknowledge use of genotype data from the British 1958 Birth Cohort DNA collection, funded by the Medical Research Council and the Wellcome Trust. We thank J. Todd for genotyping rs3894194 in the 1958 British Birth cohort.

**Author Information** Microarray and chromosome 17 genotyping data have been deposited in the GEO database, with accession number GSE8052. Reprints and permissions information is available at [www.nature.com/reprints](http://www.nature.com/reprints). The authors declare no competing financial interests. Correspondence and requests for materials should be addressed to W.O.C.C. ([w.cookson@imperial.ac.uk](mailto:w.cookson@imperial.ac.uk)).

## METHODS

**Subjects.** Children and their parents from the UK panels were recruited as part of the MRC UK National family collection and were administered a standard questionnaire (based on the American Thoracic Society and International Study of Asthma and Allergies in Childhood (ISAAC) questionnaires<sup>9</sup>) by a nurse practitioner or a doctor. Asthma was defined as a positive response to the question “Has your doctor ever told you that you have asthma?” Proband had Step 3 asthma or worse according to the British Thoracic Society guidelines (high-dose inhaled steroids, or low-dose inhaled steroids and a long-acting  $\beta$ -agonist)<sup>10</sup>. Siblings were included regardless of asthma status<sup>11</sup>. Asthma cases from the Multicentre Asthma Genetics in Childhood Study (MAGICS) were diagnosed by a paediatric pulmonologist or allergologist on the basis of clinical examination, case history and objective tests of lung function. Asthmatics (mean age 10.95 yr) were recruited from 7 centres located in Germany and Austria (Wesel, Bochum Cologne, Freiberg, Munich, Feldkirch and Vienna), and as a reference, 800 German children (mean age 9.62 yr) from Dresden ( $n = 400$ ) and Munich ( $n = 400$ ) were randomly drawn from all German children with DNA available in the cross sectional ISAAC Phase II study<sup>4</sup>. Further cases and controls for replication were drawn from the German ISAAC population in which asthma was diagnosed using standardized questionnaires and validated by lung function and bronchial hyper-responsiveness testing<sup>4</sup>. All study methods were approved by the appropriate ethics committees.

**EBV.** The transformation of the Peripheral Blood Lymphocytes (PBL) in all children in the MRC-A panel was carried out by the ECACC (<http://www.ecacc.org.uk>). Previously transformed cryo-preserved EBV cell lines were grown as 500 ml roller cultures. Once log phase had been obtained, cells were pelleted, media discarded and a mixture of RLT buffer and  $\beta$ -mercaptoethanol added. Pellets were vortexed to ensure thorough re-suspension, after which they were frozen at  $-70^{\circ}\text{C}$  and stored at  $-80^{\circ}\text{C}$ . RNA was extracted in batches after cell homogenization using RNeasy Maxi Kits (Quiagen), and quality and quantity assessed.

**Microarray hybridization.** RNA (10  $\mu\text{g}$ ) was used to synthesize double-stranded cDNA using the One-cycle cDNA synthesis kit (Affymetrix). Using the cDNA as a template, *in vitro* transcription of cRNA was carried out using the IVT kit (Affymetrix), following the manufacturer's protocol. A hybridization cocktail was made according to protocol, using 15  $\mu\text{g}$  of labelled, fragmented cRNA, and hybridized to U133 Plus 2.0 GeneChips (Affymetrix) for 16 h at  $45^{\circ}\text{C}$  in a rotating oven. GeneChips were washed and stained according to manufacturer's protocols and scanned on a high-resolution scanner (Affymetrix).

**Genotyping.** Whole-genome genotyping (WGGT) was carried out using Illumina Sentrix Human-1 Genotyping BeadChip<sup>12</sup> and Sentrix HumanHap300 Genotyping BeadChips<sup>13</sup> (Illumina, San Diego), according to the manufacturer's instructions in a BeadLab with full automation at the Centre National de Genotypage. All DNA samples were subjected to rigorous quality control to check for fragmentation and amplification. Twenty microlitres of DNA at a concentration of 50 ng  $\mu\text{l}^{-1}$  was used for each array. DNA samples were tracked using a

Laboratory Information Management System. The HumanHap300 Genotyping BeadChip was used with an Illumina LIMS, whereas the Sentrix Human-1 Genotyping BeadChip was tracked through the Illumina process by hand. Groups of 24 samples were batched. Five percent of the samples were selected from different batches, re-genotyped and the results compared to the original data. No sample discrepancies were detected. Raw data were analysed using GTS Image and extracted for statistical analysis. Genotyping of additional markers on chromosome 17q21 was performed on an ABI7900HT Sequence Detection System using TaqMan probes (Applied Biosystems, Foster City, California). German replication samples were genotyped using matrix-assisted laser desorption/ionization time-of flight (MALDI-TOF) mass spectrometry (<http://www.sequenom.com>)<sup>14</sup>. Primer extension products were analysed by a MassARRAY mass spectrometer (<http://www.bdal.de>) and resulting mass spectra were analysed using the SpectroTYPER RT 2.0 software.

**Association testing.** Tests of Hardy–Weinberg equilibrium were performed in cases and controls using the genhw procedure (<http://www.biostat-resources.com/stata/>) and Stata version 9.2, and SNPs showing Hardy–Weinberg disequilibrium in controls ( $\chi^2 > 25$ ) were excluded. As the data comprised a mixture of unrelated and related cases and controls, we used logistic regression models with robust sandwich estimation of the variance<sup>15</sup> as implemented in the Stata logit function to model clustering of siblings' genotypes. Simulations using the MRC-A family structures (data available on request) confirmed that this method appropriately controls the Type I error. Heterogeneity of association between the two main strata (UK and Germany) was assessed by a weighted linear combination test using the results of an additive-effects-only regression analysis within each stratum. X-linked markers were analysed by fitting an additive-effects-only logit model that equates the risks of male hemizygotes with female homozygotes. The TRANSMIT program<sup>16</sup> was used to analyse nuclear family data (including parental genotypes), using the sandwich variance estimation option to robustly incorporate information from multiple affected siblings; confidence intervals for odds ratio estimates were computed as described. The false-discovery rate (FDR) method<sup>5</sup> was used to assess the overall statistical significance of the genome-wide association results, taking into account the multiple hypothesis testing implications inherent in the analysis of more than 300K SNPs. The FDR thresholds were calculated by applying the QVALUE (<http://faculty.washington.edu/~jstorey/qvalue/>) software package<sup>17</sup>.

**Association to transcript abundances.** Data from the gene expression experiment were normalized together using the RMA package<sup>18,19</sup> to remove any technical or spurious background variation. An inverse normalization transformation step was also applied to each trait to avoid any outliers. Association analysis was applied with Merlin (FASTASSOC option)<sup>20</sup>. We estimated an additive effect for each SNP and tested its significance using a score test that adjusts for familiarity and takes into account uncertainty in the inference of missing genotypes. In the absence of a positive genomic control test, we did not adjust for stratification. We probabilistically inferred missing genotypes<sup>21</sup> and adjusted for familiarity, but not for linkage signal.

## LETTERS

# Protective and therapeutic role for $\alpha$ B-crystallin in autoimmune demyelination

Shalina S. Ousman<sup>1</sup>, Beren H. Tomooka<sup>2,3</sup>, Johannes M. van Noort<sup>4</sup>, Eric F. Wawrousek<sup>5</sup>, Kevin C. O'Connor<sup>6</sup>, David A. Hafler<sup>6</sup>, Raymond A. Sobel<sup>7</sup>, William H. Robinson<sup>2,3</sup> & Lawrence Steinman<sup>1</sup>

$\alpha$ B-crystallin (CRYAB) is the most abundant gene transcript present in early active multiple sclerosis lesions, whereas such transcripts are absent in normal brain tissue<sup>1</sup>. This crystallin has anti-apoptotic<sup>2–7</sup> and neuroprotective<sup>8</sup> functions. CRYAB is the major target of CD4<sup>+</sup> T-cell immunity to the myelin sheath from multiple sclerosis brain<sup>9,10</sup>. The pathophysiological implications of this immune response were investigated here. We demonstrate that CRYAB is a potent negative regulator acting as a brake on several inflammatory pathways in both the immune system and central nervous system (CNS). *Cryab*<sup>−/−</sup> mice showed worse experimental autoimmune encephalomyelitis (EAE) at the acute and progressive phases, with higher Th1 and Th17 cytokine secretion from T cells and macrophages, and more intense CNS inflammation, compared with their wild-type counterparts. Furthermore, *Cryab*<sup>−/−</sup> astrocytes showed more cleaved caspase-3 and more TUNEL staining, indicating an anti-apoptotic function of Cryab. Antibody to CRYAB was detected in cerebrospinal fluid from multiple sclerosis patients and in sera from mice with EAE. Administration of recombinant CRYAB ameliorated EAE. Thus, the immune response against a negative regulator of inflammation, CRYAB, in multiple sclerosis, would exacerbate inflammation and demyelination. This can be countered by giving CRYAB itself for therapy of ongoing disease.

Responses to injury often are accompanied by protective mechanisms that antagonize the damaging events or mediate repair. This is relevant in autoimmune demyelinating diseases such as multiple sclerosis, where the current and experimental treatment strategies aim to decrease the pathological immune activity in the CNS. We investigated whether CRYAB, a member of the small heat shock family of proteins, and a dominant target of the T cells in multiple sclerosis<sup>9,10</sup>, with pro-survival<sup>2–7</sup> and anti-neurotoxic<sup>8</sup> properties, was protective in demyelinating disease.

EAE was examined in *Cryab*<sup>−/−</sup> mice immunized with myelin oligodendrocyte glycoprotein (MOG). These mice showed more severe clinical EAE, particularly at the peak and chronic phases of disease compared to 129S6 wild-type animals (Fig. 1a and Supplementary Table 1). This difference was associated with more severe inflammation and demyelination in the brain and spinal cord of *Cryab*<sup>−/−</sup> animals both in the acute (day 14) and progressive (day 42) phases of disease (Table 1 and Supplementary Fig. 1). To determine whether there was more cell death, which may have contributed to the worsened disease in *Cryab*<sup>−/−</sup> animals, we analysed brains and spinal cords from wild-type and *Cryab*<sup>−/−</sup> EAE mice for cleaved and uncleaved caspase-3. Cryab protects cells from apoptosis by down-regulating caspase-3 expression during stress<sup>7,11</sup>. Compared to wild-type animals, mice lacking *Cryab* expression had more staining for

uncleaved caspase-3 in inflammatory lesions in the CNS, particularly in spinal cord at both the acute (day 14) (Supplementary Fig. 2) and later (day 42) stages (Fig. 1g, h) of EAE. Cleaved caspase-3 expression was only observed at day 42 in both wild-type and *Cryab*<sup>−/−</sup> mice with EAE (Fig. 1d–f and Supplementary Fig. 2). The *Cryab*<sup>−/−</sup> mice showed more staining of cells with large nuclei and abundant cytoplasm, which were morphologically consistent with glia in the white matter, whereas few smaller immune cells were positive (Fig. 1f). To correlate the cleaved caspase-3 expression with apoptosis, we performed TUNEL staining on CNS tissues of mice with late-stage EAE. Most TUNEL-positive cells in wild-type animals with EAE showed typical dense nuclear staining (Fig. 1i), whereas TUNEL-positive cells in the *Cryab*<sup>−/−</sup> mice were more numerous, and a greater proportion of positive cells had more abundant, diffuse cytoplasm staining and processes, suggesting that they were glia (Fig. 1j). We quantified the numbers of TUNEL-positive presumed immune cells (parenchymal nuclei) from apoptotic glial cells (Table 1). Null animals had more TUNEL-positive parenchymal and glial staining at both the acute (day 14) and progressive (day 42) EAE stages (Table 1). These results indicate that *Cryab* may have a role in preventing apoptosis of glial cells in the CNS during EAE.

EAE is driven by pathogenic immune responses against myelin proteins and lipids. *Cryab* may have an anti-inflammatory role<sup>8</sup>. To determine whether the immune response to constitutively expressed myelin proteins was also affected in *Cryab*<sup>−/−</sup> mice with EAE, we compared the proliferative ability and cytokine secretion of lymphoid cells from the spleen and lymph nodes from *Cryab*<sup>−/−</sup> and wild-type animals. Splenocytes and lymph node cells from *Cryab*<sup>−/−</sup> MOG-immunized mice showed significantly higher proliferation and secretion of the Th1 cytokines IL-2, IFN- $\gamma$ , TNF, IL-12 p40 and Th17 cytokine IL-17 compared to wild-type animals (Fig. 1b, c). No Th2 cytokines (IL-4 and IL-10) were detectable in these cell types from either *Cryab*<sup>−/−</sup> or wild-type animals (not shown).

To determine the specific immune cells that were hyper-responsive during EAE in *Cryab*<sup>−/−</sup> mice, we assessed the proliferation capabilities and cytokine production of T cells and antigen-presenting cells such as macrophages and dendritic cells. CD3<sup>+</sup> T cells from *Cryab*<sup>−/−</sup> MOG-immunized mice stimulated with MOG proliferated more and secreted higher concentrations of IL-2, IFN- $\gamma$  and IL-17 compared with their wild-type counterparts (Fig. 2a). Naive CD3<sup>+</sup> T cells from null animals also showed a similar hyper-responsiveness when stimulated in culture with anti-CD3 and anti-CD28 (not shown).

To assess whether antigen-presenting cell function was also affected, macrophages and dendritic cells from wild-type and *Cryab*<sup>−/−</sup> mice were stimulated with lipopolysaccharide (LPS).

<sup>1</sup>Department of Neurology and Neurological Sciences, Stanford University, <sup>2</sup>Division of Immunology and Rheumatology, Stanford University School of Medicine, Stanford, California 94305, USA. <sup>3</sup>GRECC and <sup>4</sup>Laboratory Service, Veterans Affairs Palo Alto Health Care System, Palo Alto, California 94304, USA. <sup>5</sup>Department of Biosciences, TNO Quality of Life, 2301 CE Leiden, The Netherlands. <sup>6</sup>National Eye Institute, National Institutes of Health, Bethesda, Maryland 20892, USA. <sup>7</sup>Center for Neurologic Disease, Harvard Medical School, Brigham and Women's Hospital, 77 Avenue Louis Pasteur, Boston, Massachusetts 02115, USA.



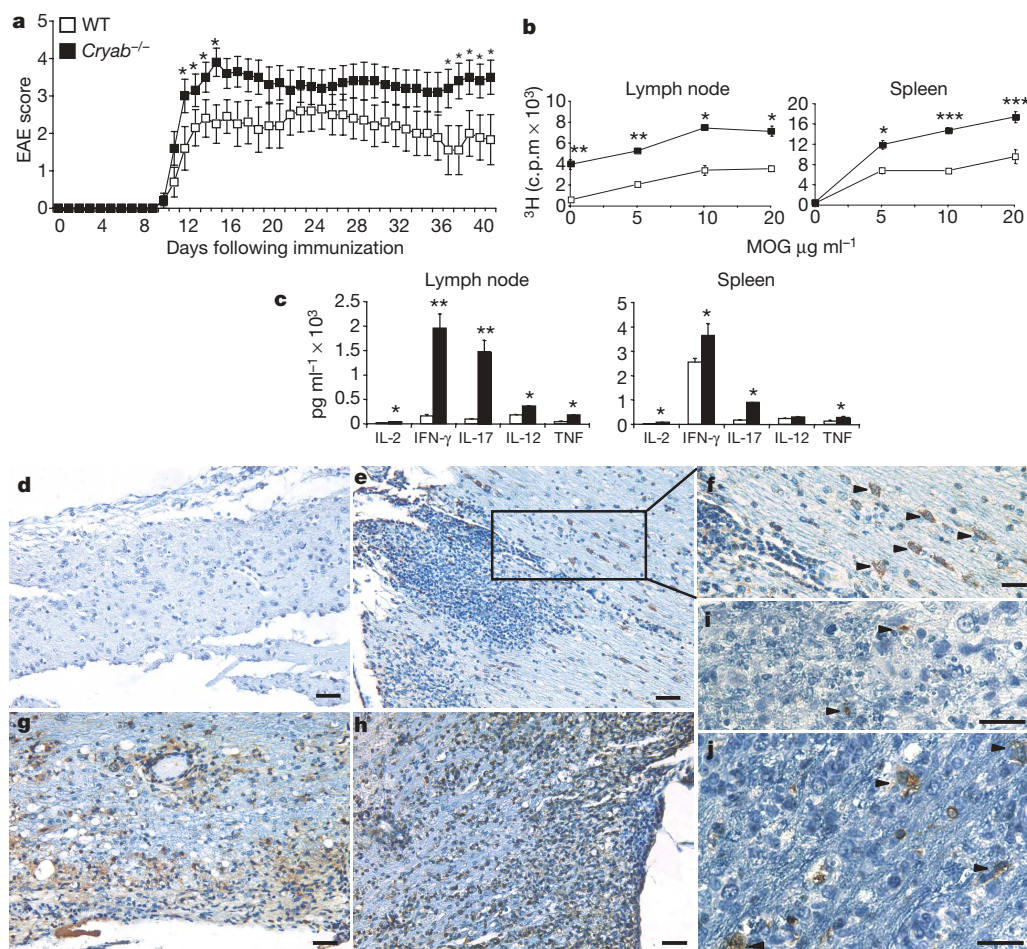


**Figure 1 | Worse EAE, increased immune activation and glial apoptosis in *Cryab*<sup>-/-</sup> mice.** Representatives from four EAE experiments show mean  $\pm$  s.e.m. clinical scores of wild-type (WT) and *Cryab*<sup>-/-</sup> mice (a) (\* $P$  < 0.05 Mann–Whitney;  $P$  = 0.0008 linear regression days 9–15;  $n$  = 10 mice per group); and proliferation rate (b) and cytokine production

(c) from wild-type and *Cryab*<sup>-/-</sup> (mean  $\pm$  s.e.m.; \* $P$  < 0.05, \*\* $P$  < 0.02, \*\*\* $P$  < 0.005, Student's  $t$ -test). d–j, Day 42 spinal cord from wild-type (d, g, i) and *Cryab*<sup>-/-</sup> (e, f, h, j) immuno-stained for cleaved (d–f) and uncleaved caspase-3 (g, h) and TUNEL (i, j). Arrows indicate glia. Scale bar, 200  $\mu\text{m}$  (d, e, g, h) or 100  $\mu\text{m}$  (f, i, j).

Null macrophages showed increased capacities to secrete inflammatory cytokines, releasing more IL-12 p40, IL-6 and IL-1 $\beta$  (Fig. 3a). These cells also secreted more IL-10, whereas there was no difference in TNF production. Similar to *Cryab*-deficient macrophages, LPS-stimulated *Cryab*<sup>-/-</sup> dendritic cells produced more IL-6, IL-12 p40 and TNF compared with wild-type cells (Supplementary Fig. 4). Wild-type dendritic cells on the other hand secreted more IL-1 $\beta$ .

To determine whether hyper-responsive immune cells from *Cryab*<sup>-/-</sup> mice contributed to either the inductive or the chronic phase of worsened EAE in *Cryab*-null animals, adoptive transfer experiments were performed. MOG-reactive splenocytes from wild-type and *Cryab*<sup>-/-</sup> immunized mice were injected into *Rag2*<sup>-/-</sup> mice. Significantly worse disease was observed in *Rag2*<sup>-/-</sup>

recipients with *Cryab*<sup>-/-</sup> cells, but only in the acute phase of disease (Supplementary Fig. 5).

Because the MAP kinase signal transduction pathways are involved in *Cryab* function<sup>12–14</sup>, we determined whether the JNK (c-Jun NH<sub>2</sub>-terminal kinase), ERK (extracellular signal-regulated kinase) or p38 MAPK (p38 mitogen-activated protein kinase) pathways played a part in the immune cell hyper-responsiveness seen in *Cryab*<sup>-/-</sup> mice with EAE. We found that total and phosphorylated p38 expression was upregulated in stimulated *Cryab*<sup>-/-</sup> CD3<sup>+</sup> T cells (Fig. 2b and Supplementary Table 2) and macrophages (Fig. 3b and Supplementary Table 3). There was no difference in expression of the JNK and ERK pathway molecules between wild-type and *Cryab*<sup>-/-</sup> T cells and macrophages (not shown). These results demonstrated that the inflammatory response was hyperactive in *Cryab*<sup>-/-</sup> animals and

**Table 1 | Quantification of inflammatory foci and TUNEL-positive (TUNEL<sup>+</sup>) cells in brain and spinal cord samples of wild-type and *Cryab*<sup>-/-</sup> mice with EAE**

	Meninges	Parenchyma	Total	TUNEL <sup>+</sup> parenchymal nuclei	TUNEL <sup>+</sup> glia
Day 14					
Wild-type	59 $\pm$ 17.6	49.5 $\pm$ 12.3	108.5 $\pm$ 29.1	145.7 $\pm$ 46.8	108.3 $\pm$ 38.7
<i>Cryab</i> <sup>-/-</sup>	127.6 $\pm$ 17.7***	116.4 $\pm$ 7.2**	234 $\pm$ 17.7**	321.7 $\pm$ 56.1****	153.3 $\pm$ 40.9
Day 42					
Wild-type	20 $\pm$ 10.1	21 $\pm$ 11.1	41 $\pm$ 11.1	41 $\pm$ 13	3.5 $\pm$ 1.5
<i>Cryab</i> <sup>-/-</sup>	135 $\pm$ 25.1*	151 $\pm$ 49.1****	286 $\pm$ 24.1*	275 $\pm$ 35.1*	142.5 $\pm$ 7.5*

Values are means  $\pm$  s.e.m.; \* $P$  < 0.05, \*\* $P$  < 0.01, \*\*\* $P$  < 0.001, \*\*\*\* $P$  = 0.06; Student's  $t$ -test,  $n$  = 4 mice per group.

indicate that Cryab may have a dampening role on immune cell populations during EAE, though the dampening effect may be insufficient by itself to completely abrogate the disease.

Astrocytes use the canonical NF- $\kappa$ B pathway to modulate inflammation in EAE<sup>15,16</sup>, and they upregulate expression of Cryab during EAE and multiple sclerosis<sup>2</sup>. We assessed whether the function of astrocytes is altered in *Cryab*<sup>-/-</sup> mice. Primary astrocytes isolated from *Cryab*<sup>-/-</sup> pups produced more IL-6 compared with wild-type astrocytes, 48 h following either TNF or staurosporine stimulation (Fig. 4a). Because Cryab is anti-apoptotic, we assessed whether *Cryab*<sup>-/-</sup> astrocytes underwent cell death at a different rate compared to wild-type astrocytes. Naive astrocytes from both wild-type and *Cryab*<sup>-/-</sup> mice expressed caspase-3 after four weeks in culture. However, naive and TNF-stimulated astrocytes from *Cryab*<sup>-/-</sup> mice showed differential levels of cleaved caspase-3 compared with wild-type cells, in which this apoptotic factor remained uncleaved even after stimulation with TNF (Fig. 4b). Furthermore, compared with wild-type cells a greater percentage of *Cryab*<sup>-/-</sup> astrocytes had more TUNEL staining with and without TNF stimulation (Fig. 4c), suggesting that Cryab protects astrocytes against normal cell death and during stress injury.

To determine the underlying signalling mechanism(s) mediating the increased cell death in the *Cryab*<sup>-/-</sup> astrocytes, we assessed the expression of the MAP kinase signal transduction pathways involved with Cryab function. Astrocytes from wild-type animals showed increased expression of Cryab 72h following TNF stimulation. These cells also showed a small increase in p-Cryab (Ser 59) levels but p-Cryab (Ser 45) decreased slightly (Fig. 4b). In terms of MAP kinase signalling, we found that ERK and p-ERK were upregulated in *Cryab*<sup>-/-</sup> astrocytes 72 h after TNF stimulation compared to wild-type astrocytes (Fig. 4b and Supplementary Table 4). p38 was also upregulated in null astrocytes after TNF stimulation, but the phosphorylated form of this protein was not detected. The levels of

protein in TNF-stimulated astrocytes compared with media control also demonstrated an increase in p-ERK, ERK and p38 in *Cryab*<sup>-/-</sup> astrocytes. No changes in JNK and p-JNK expression were seen in wild-type and *Cryab*<sup>-/-</sup> astrocytes (not shown).

We then assessed whether the NF- $\kappa$ B pathway was modulated by Cryab. Astrocytes null for *Cryab* upregulated expression of the active subunits NF- $\kappa$ B p65 and NF- $\kappa$ B p105/p50 while down-regulating their negative regulator I $\kappa$ B- $\alpha$ , following TNF stimulation (Fig. 4b and Supplementary Table 4). Wild-type astrocytes on the other hand showed an increase in the I $\kappa$ B- $\alpha$  inhibitor and low NF- $\kappa$ B p50 was evident in total protein extracts in this genotype even after TNF stimulation (Fig. 4b). An assay for NF- $\kappa$ B DNA binding using nuclear extracts confirmed an enhancement in NF- $\kappa$ B p50 and NF- $\kappa$ B p65 DNA binding activity in null glia compared with wild-type cells (Fig. 4d). A small increase in NF- $\kappa$ B p50 DNA binding was seen in wild-type glia following TNF stimulation, but this level was much less than in activated *Cryab*<sup>-/-</sup> astrocytes (Fig. 4d). Therefore, Cryab probably prevents cell death of astrocytes by inhibiting caspase-3 activation, and suppresses the inflammatory role of NF- $\kappa$ B in astrocytes during demyelinating disease.

We have constructed large scale arrays to detect auto-antibodies to various myelin antigens, including full length CRYAB, and a number of its peptide epitopes<sup>17</sup>. In EAE, antibody to peptide regions, known as epitopes, p16–35, p26–45 and p116–135 on CRYAB appears within 17 days in the sera after immunization with PLPp139–151 (ref. 17). We applied these arrays to analyse antibody to CRYAB in the cerebrospinal fluid (CSF) of patients with relapsing remitting multiple sclerosis (RRMS). Antibodies to native CRYAB and to p21–40 and p116–135 of CRYAB were prominently detected compared to other neurological control (OND) patients (Fig. 5). We also detected free CRYAB in the serum and CSF of multiple sclerosis patients (Supplementary Fig. 7).

Our results indicated that CRYAB has both a suppressive effect on immunity and an anti-apoptotic role in glia. To show that antibody to CRYAB from the CSF of multiple sclerosis patients worsened EAE would be complicated by the fact that in EAE there are already antibodies to CRYAB that arise from epitope spreading<sup>18</sup>, as we and others have shown earlier<sup>17,19</sup>. We therefore assessed whether recombinant CRYAB itself could resolve ongoing EAE. To test this, we

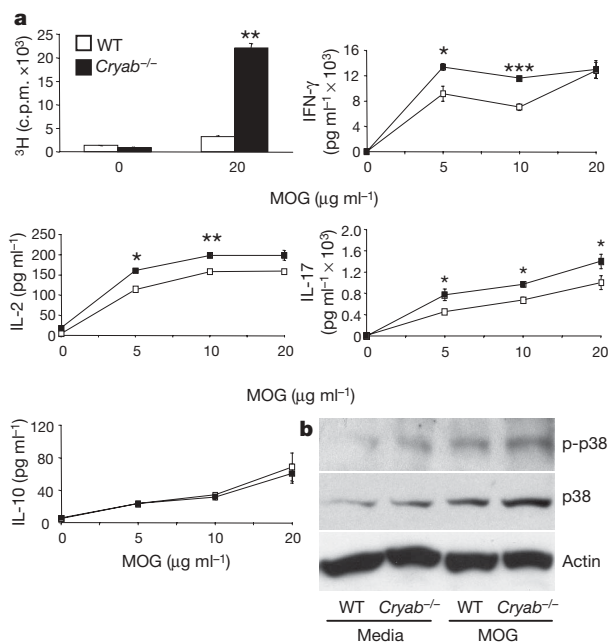


**Figure 2 | T cells from *Cryab*<sup>-/-</sup> EAE mice are hyper-responsive.**

**a**, Representative graphs from three experiments showing proliferation rate (c.p.m.) and secretion of Th1 (IFN- $\gamma$ , IL-2), Th17 (IL-17) and Th2 (IL-10) cytokines (pg ml<sup>-1</sup>) from CD3<sup>+</sup> T cells isolated from wild-type and *Cryab*<sup>-/-</sup> EAE mice and stimulated with syngeneic irradiated splenocytes and MOG 35–55; mean  $\pm$  s.e.m.; \* $P$  < 0.05, \*\* $P$  < 0.02, \*\*\* $P$  < 0.001, Student's *t*-test. **b**, Representative western blots from two separate experiments showing p38 and phospho-p38 (p-p38) expression in CD3<sup>+</sup> T cells from wild-type and *Cryab*<sup>-/-</sup> EAE mice stimulated with syngeneic irradiated splenocytes and MOG 35–55 peptide for 1 h.

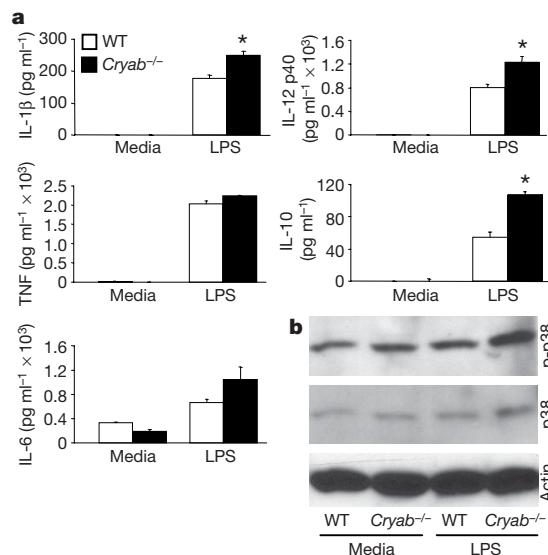


**Figure 3 | Macrophages deficient in *Cryab* are hyperactive.**

**a**, Representative graphs from three experiments showing production of cytokines (IL-1 $\beta$ , TNF, IL-6, IL-12 p40, IL-10) by wild-type and *Cryab*<sup>-/-</sup> macrophages stimulated *in vitro* with LPS; mean  $\pm$  s.e.m.; \* $P$  < 0.05 Student's *t*-test. **b**, Representative western blot from two separate experiments showing p38 and phospho-p38 (p-p38) expression in wild-type and *Cryab*-null macrophages 72 h after stimulation with LPS.

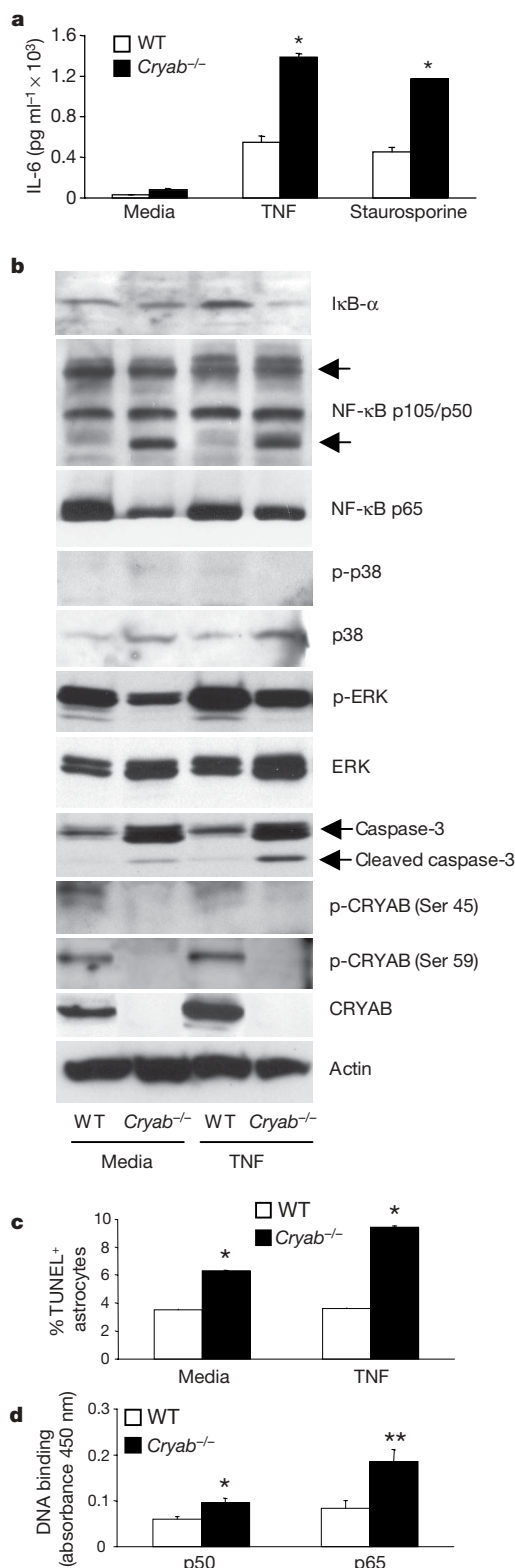


**Figure 4** | *Cryab*<sup>-/-</sup> astrocytes are more susceptible to cell death and augment ERK and NF-κB signalling. **a**, IL-6 production by wild-type and *Cryab*<sup>-/-</sup> astrocytes 48 h post-TNF stimulation; \**P* < 0.03, mean ± s.e.m. **b**, Representative blots from two experiments showing *Cryab*, phospho-*Cryab*, cleaved and uncleaved caspase-3, p38, phospho-p38, ERK, phospho-ERK, NF-κB p105/p50, p65 and IκB-α levels in wild-type and *Cryab*<sup>-/-</sup> astrocytes 72 h post-TNF stimulation. **c**, Mean ± s.e.m. of percentages of TUNEL<sup>+</sup> astrocytes after 72 h with TNF; \**P* < 0.005. **d**, Mean ± s.e.m. of DNA binding of NF-κB p50 and p65 in wild-type and *Cryab*<sup>-/-</sup> astrocytes 72 h post-TNF stimulation; \**P* = 0.067, \*\**P* = 0.017, all *P* values by Student's *t*-test.

treated wild-type 129S6 mice with EAE with recombinant human CRYAB, administered intravenously. Mice treated with CRYAB showed significantly lower clinical disease scores compared with animals injected with PBS or an inert protein control, recombinant human myoglobin (Fig. 6a, b). PBS and myoglobin were similar in their inability to influence clinical EAE. *Cryab*<sup>-/-</sup> and SJL/J mice with EAE were also successfully treated with recombinant CRYAB (Supplementary Fig. 6a, b). The amelioration of disease by CRYAB in 129S6 mice was in part due to decreased infiltration of immune cells into the brain and spinal cord (Table 2) and suppression of immune cell function (Fig. 6b). We observed decreased proliferation and diminished production of IL-2, IL-12 p40, TNF, IFN-γ and IL-17 cytokines by splenocytes taken from mice treated with recombinant CRYAB (Fig. 6b). Interestingly, increased production of the immune suppressive cytokine, IL-10, was observed at high concentrations of MOG stimulation (Fig. 6b). A decrease in immune cell function was similarly observed in CD3<sup>+</sup> T cells stimulated *in vitro* with anti-CD3/anti-CD28 and treated with recombinant CRYAB (not shown).

To assess whether recombinant CRYAB treatment affected cell death in the CNS we performed TUNEL-staining on brain and spinal cord sections from PBS and CRYAB-treated EAE mice. Less TUNEL staining was observed in CNS parenchyma in mice treated with CRYAB compared to PBS-injected animals (Table 2; Supplementary Fig. 3). In addition, fewer TUNEL-positive cells with diffuse cytoplasmic staining suggestive of dying glial cells were seen in the CNS of crystallin-treated animals, suggesting a protective effect on glia by exogenously administered recombinant CRYAB.

Other mechanisms of CRYAB therapy are being investigated, such as whether recombinant CRYAB could bind to or traverse across plasma membranes<sup>20</sup> or neutralize CRYAB antibodies akin to strategies in Alzheimer's disease<sup>21,22</sup>.

One of the main adaptive immunological responses in multiple sclerosis and its animal model, EAE, is thus directed to an inducible stress protein, CRYAB. Such an immune response targeting a negative regulator of brain inflammation thus disrupting its function<sup>23,24</sup>, is comparable to damaging the braking system of a vehicle that is already careening into danger. Remarkably, addition of that very same stress protein, akin to restoring the brakes that were failing,

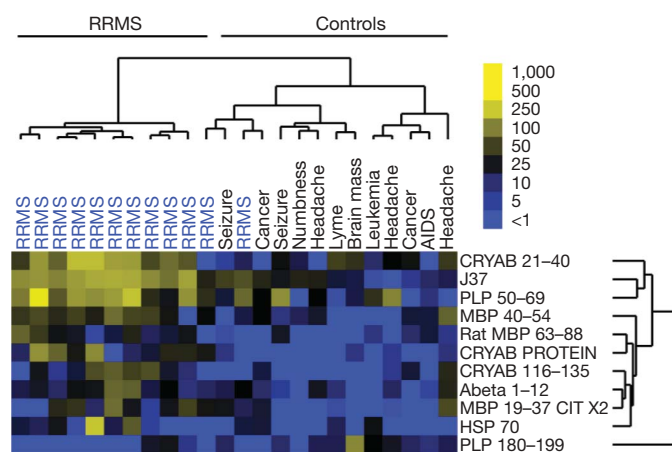


**Figure 5** | Myelin antigen array analysis demonstrates antibody targeting of CRYAB in RRMS patients. Analysis was performed on CSF from RRMS and OND patients. Statistical analysis of microarrays (SAM) identified significant differences in antibodies in RRMS compared with OND. Samples are arranged with hierarchical clustering, and displayed as a heat map. RRMS patients demonstrated significantly increased auto-antibodies against various myelin epitopes including CRYAB protein and peptides (J37, Golli-myelin basic protein isoform J37); PLP, proteolipid protein; MBP, myelin basic protein; HSP, heat shock protein; Abeta, amyloid beta). A false discovery rate threshold of 1.9% and numerator threshold of 2.0 were used. Prediction analysis of microarrays (PAM) yielded a classification model with 21 markers, with cross-validated sensitivity of 10/12 = 83% and specificity of 11/12 = 92%.



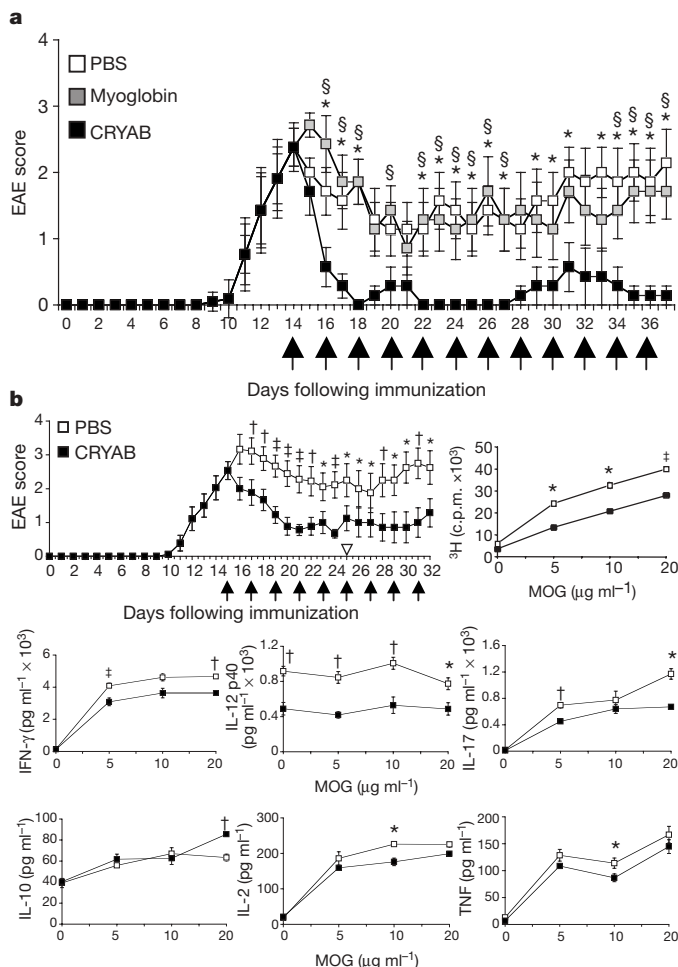


**Figure 6 | CRYAB suppresses disease and inflammation in EAE.**

**a**, Representative graph from three experiments showing mean  $\pm$  s.e.m. scores of 129S6 EAE mice treated with CRYAB, PBS or myoglobin. Treatment indicated with arrows.  $^{\dagger}P < 0.05$  Mann–Whitney,  $^{\ddagger}P < 0.05$  CRYAB versus myoglobin,  $^{\ast}P < 0.05$  CRYAB versus PBS; linear regression (CRYAB versus PBS,  $P = 0.0011$ ; CRYAB versus myoglobin,  $P = 0.038$ ), days 13–22;  $n = 10$  mice per group. **b**, Proliferation rate (c.p.m.) and cytokine production ( $\text{pg ml}^{-1}$ ) of splenocytes at day 25 (white arrow head) of EAE during CRYAB or PBS treatment. EAE:  $^{\ast}P < 0.05$ ,  $^{\dagger}P < 0.01$  Mann–Whitney;  $P = 0.0258$  linear regression ( $n = 10$  mice per group); proliferation and cytokine:  $^{\ast}P < 0.05$ ,  $^{\dagger}P < 0.01$ ,  $^{\ddagger}P < 0.005$ , Student's  $t$ -test.

returns control. CRYAB, a negative regulator of inflammation in EAE and multiple sclerosis brain, and a potent modulator of glial apoptosis, is apparently located at a critical tipping point in the pathophysiology of multiple sclerosis.

## METHODS

**EAE.** EAE was induced in *Cryab*-null (*Cryab* $^{-/-}$ ) and wild-type 129S6/SvEvTac mice with myelin oligodendrocyte glycoprotein (MOG p35–55) and *Bordetella pertussis* toxin. Clinical disease was scored as followed: 0, no disease; 1, limp tail; 2, hindlimb weakness; 3, complete hindlimb paralysis; 4, hindlimb paralysis plus forelimb paralysis; and 5, moribund or dead. For recombinant CRYAB treatment, EAE mice were injected intravenously every second day with saline, 10  $\mu\text{g}$  recombinant human CRYAB or 10  $\mu\text{g}$  recombinant human myoglobin. Paraffin-embedded brain and spinal cords were processed for histological analysis and apoptosis detection.

**Cell activation.** Splenocytes, lymph node cells, CD3 $^{+}$  T cells, primary macrophages, dendritic cells or astrocytes were stimulated with MOG, LPS or TNF. Proliferation rates were determined by [ $^3\text{H}$ ]-thymidine incorporation and cytokine secretion assessed by enzyme-linked immunosorbent assay (ELISA).

**Western blot.** CD3 $^{+}$  T cells, macrophages and astrocytes protein lysates were subjected to SDS–PAGE electrophoresis. Proteins were transferred to PVDF membranes and immunoblotted with various CRYAB, caspase-3, MAP

**Table 2 | Quantification of inflammatory foci and TUNEL-positive (TUNEL $^{+}$ ) cells in brain and spinal cord samples of wild-type mice with EAE treated with PBS or recombinant human CRYAB**

	Meninges	Parenchyma	Total	TUNEL $^{+}$
PBS	115.3 $\pm$ 31.8	107.7 $\pm$ 28.3	223 $\pm$ 60.1	487.1 $\pm$ 104.1
Recombinant CRYAB	48.7 $\pm$ 19.8 $^{\ast}$	52 $\pm$ 38.5 $^{\ast}$	100.7 $\pm$ 55.8 $^{\ast\ast}$	152.7 $\pm$ 74 $^{\ast}$

Values are means  $\pm$  s.e.m.;  $^{\ast}P < 0.03$ ,  $^{\ast\ast}P < 0.005$ ; Student's  $t$ -test,  $n = 3$  mice per group.

kinase and NF- $\kappa\text{B}$  antibodies. Bound antibodies were visualized by enhanced chemiluminescence.

**Myelin arrays.** Proteins and peptides representing candidate myelin auto-antigens were printed in ordered arrays on the surface of SuperEpoxy microscope slides. Myelin arrays were probed with 1:20 dilutions of cerebrospinal fluid derived from relapsing remitting multiple sclerosis or other neurologic disease control patients, followed by Cy-3-conjugated anti-human IgG/M secondary antibody. Arrays were scanned, and fluorescence quantified as a measure of auto-antibody binding $^{17}$ .

**Statistical analysis.** Data are presented as means  $\pm$  s.e.m. EAE results were analysed by Mann–Whitney statistics and linear regression, whereas proliferation rate, cytokine production, histological analysis and densitometry were assessed by Student's  $t$ -test. Myelin array results were analysed using Significance Analysis of Microarrays (SAM) $^{25}$  and Prediction Analysis of Microarrays (PAM).

A detailed description of the materials and methods is described in Methods.

**Full Methods** and any associated references are available in the online version of the paper at [www.nature.com/nature](http://www.nature.com/nature).

Received 6 March; accepted 17 May 2007.

Published online 13 June; corrected 26 July 2007 (see online for details).

- Chabas, D. *et al.* The influence of the proinflammatory cytokine, osteopontin, on autoimmune demyelinating disease. *Science* **294**, 1731–1735 (2001).
- Aoyama, A., Frohli, E., Schafer, R. & Klemenz, R.  $\alpha\text{B}$ -crystallin expression in mouse NIH 3T3 fibroblasts: glucocorticoid responsiveness and involvement in thermal protection. *Mol. Cell. Biol.* **13**, 1824–1835 (1993).
- Mao, Y. W. *et al.* Human *bcl-2* gene attenuates the ability of rabbit lens epithelial cells against  $\text{H}_2\text{O}_2$ -induced apoptosis through down-regulation of the alpha B-crystallin gene. *J. Biol. Chem.* **276**, 43435–43445 (2001).
- Dasgupta, S., Hohman, T. C. & Carper, D. Hypertonic stress induces alpha B-crystallin expression. *Exp. Eye Res.* **54**, 461–470 (1992).
- Mehlen, P., Kretz-Remy, C., Preville, X. & Arrigo, A. P. Human hsp27, *Drosophila* hsp27 and human alphaB-crystallin expression-mediated increase in glutathione is essential for the protective activity of these proteins against TNFalpha-induced cell death. *EMBO J.* **15**, 2695–2706 (1996).
- Andley, U. P., Song, Z., Wawrousek, E. F., Fleming, T. P. & Bassnett, S. Differential protective activity of alpha A- and alphaB-crystallin in lens epithelial cells. *J. Biol. Chem.* **275**, 36823–36831 (2000).
- Li, D. W. *et al.* Caspase-3 is actively involved in okadaic acid-induced lens epithelial cell apoptosis. *Exp. Cell Res.* **266**, 279–291 (2001).
- Masilamoni, J. G. *et al.* Molecular chaperone alpha-crystallin prevents detrimental effects of neuroinflammation. *Biochim. Biophys. Acta* **1762**, 284–293 (2006).
- van Noort, J. M. *et al.* The small heat-shock protein  $\alpha\text{B}$ -crystallin as candidate autoantigen in multiple sclerosis. *Nature* **375**, 798–801 (1995).
- Bajramovic, J. J. *et al.* Presentation of alpha B-crystallin to T cells in active multiple sclerosis lesions: an early event following inflammatory demyelination. *J. Immunol.* **164**, 4359–4366 (2000).
- Kamradt, M. C., Chen, F., Sam, S. & Cryns, V. L. The small heat shock protein alpha B-crystallin negatively regulates apoptosis during myogenic differentiation by inhibiting caspase-3 activation. *J. Biol. Chem.* **277**, 38731–38736 (2002).
- Morrison, L. E., Hoover, H. E., Thuerauf, D. J. & Glembofski, C. C. Mimicking phosphorylation of alphaB-crystallin on serine-59 is necessary and sufficient to provide maximal protection of cardiac myocytes from apoptosis. *Circ. Res.* **92**, 203–211 (2003).
- Webster, K. A. Serine phosphorylation and suppression of apoptosis by the small heat shock protein alphaB-crystallin. *Circ. Res.* **92**, 130–132 (2003).
- Liu, J. P. *et al.* Human alphaA- and alphaB-crystallins prevent UVA-induced apoptosis through regulation of PKCalpha, RAF/MEK/ERK and AKT signaling pathways. *Exp. Eye Res.* **79**, 393–403 (2004).
- van Loo, G. *et al.* Inhibition of transcription factor NF- $\kappa\text{B}$  in the central nervous system ameliorates autoimmune encephalomyelitis in mice. *Nature Immunol.* **7**, 954–961 (2006).
- Youssef, S. & Steinman, L. At once harmful and beneficial: the dual properties of NF- $\kappa\text{B}$ . *Nature Immunol.* **7**, 901–902 (2006).
- Robinson, W. H. *et al.* Protein microarrays guide tolerizing DNA vaccine treatment of autoimmune encephalomyelitis. *Nature Biotechnol.* **21**, 1033–1039 (2003).
- Ellmerich, S. *et al.* Disease-related epitope spread in a humanized T cell receptor transgenic model of multiple sclerosis. *Eur. J. Immunol.* **34**, 1839–1848 (2004).

19. van Noort, J. M., Verbeek, R., Meilof, J. F., Polman, C. H. & Amor, S. Autoantibodies against alpha B-crystallin, a candidate autoantigen in multiple sclerosis, are part of a normal human immune repertoire. *Mult. Scler.* **12**, 287–293 (2006).
20. Cobb, B. A. & Petrash, J. M. Characterization of alpha-crystallin-plasma membrane binding. *J. Biol. Chem.* **275**, 6664–6672 (2000).
21. Matsuoka, Y. *et al.* Novel therapeutic approach for the treatment of Alzheimer's disease by peripheral administration of agents with an affinity to  $\beta$ -amyloid. *J. Neurosci.* **23**, 29–33 (2003).
22. Bard, F. *et al.* Peripherally administered antibodies against amyloid  $\beta$ -peptide enter the central nervous system and reduce pathology in a mouse model of Alzheimer disease. *Nature Med.* **6**, 916–919 (2000).
23. Korlimbinis, A., Hains, P. G., Truscott, R. J. & Aquilina, J. A. 3-Hydroxykynurenine oxidizes alpha-crystallin: potential role in cataractogenesis. *Biochemistry* **45**, 1852–1860 (2006).
24. Finley, E. L., Dillon, J., Crouch, R. K. & Schey, K. L. Identification of tryptophan oxidation products in bovine alpha-crystallin. *Protein Sci.* **7**, 2391–2397 (1998).
25. Tusher, V. G., Tibshirani, R. & Chu, G. Significance analysis of microarrays applied to the ionizing radiation response. *Proc. Natl Acad. Sci. USA* **98**, 5116–5121 (2001).

**Supplementary Information** is linked to the online version of the paper at [www.nature.com/nature](http://www.nature.com/nature).

**Acknowledgements** This research was supported by NIH and National Multiple Sclerosis Society (NMSS) grants to L.S. and fellowships to S.S.O. from the NMSS and Multiple Sclerosis Society of Canada (MSSC). We thank R. Tibshirani for his advice on statistical analysis.

**Author Contributions** S.S.O. and L.S. formulated the hypothesis and aims and designed all experiments. W.H.R. and B.H.T. did the myelin array experiment. D.A.H. and K.C.O'C. provided multiple sclerosis CSF for the myelin array. R.A.S. analysed and quantified the EAE and astrocyte histology. J.M.V.N. provided the CRYAB human protein construct for the myelin array and performed the western blot for CRYAB in multiple sclerosis sera and CSF. E.F.W. developed and provided the *Cryab*<sup>-/-</sup> mice.

**Author Information** Reprints and permissions information is available at [www.nature.com/reprints](http://www.nature.com/reprints). The authors declare no competing financial interests. Correspondence and requests for materials should be addressed to L.S. ([steinman@stanford.edu](mailto:steinman@stanford.edu)).

## METHODS

**Mice.** *Cryab*-null mice (*Cryab*<sup>-/-</sup>) were developed at the NIH National Eye Institute<sup>26</sup>. These mice were generated from embryonic stem cells with a 129S4/SvJae background and maintained in 129S6/SvEvTac × 129S4/SvJae background. *Cryab*<sup>-/-</sup> mice are viable and fertile, with no obvious prenatal defects and normal lens transparency. Older mice show postural defects and progressive myopathy that are apparent at approximately 40 weeks of age<sup>26</sup>. We studied these mice between 8–12 weeks thus removing the possible effects of myopathy on our clinical evaluation. The *Cryab*<sup>-/-</sup> mice also have a deletion of the related gene, *Hspb2*. It is unlikely that deletion of the *Hspb2* gene would have any effects on the immunological or neurobiological processes involved in this study, primarily because it is not normally expressed in brain and in any lymphoid cell<sup>27</sup>. Also, *Hspb2* is not heat-shock-inducible, unlike *Cryab*, and is thus unlikely to act as a general 'chaperone'<sup>27,28</sup>. We therefore attribute the effects observed to *Cryab* deficiency only, and not to *Hspb2* deficiency. 129S6/SvEvTac (Taconic Farms) mice were used as controls. Colonies of wild-type and *Cryab*<sup>-/-</sup> mice were maintained in our animal colony and bred according to Stanford University Comparative Medicine guidelines. SJL/J mice were purchased from Jackson Laboratories, Bar Harbor, Maine.

**EAE induction.** EAE was induced in 8–12-week-old female mice via subcutaneous immunization with 100 µg myelin oligodendrocyte glycoprotein (MOG p35–55) (*Cryab*<sup>-/-</sup> and wild-type 129S6/SvEvTac animals) or proteolipid protein (PLP 139–151) (SJL/J) peptide in an emulsion mixed (volume ratio 1:1) with Complete Freund's Adjuvant (CFA) (containing 4 mg ml<sup>-1</sup> of heat-killed *Mycobacterium tuberculosis* H37Ra, Difco Laboratories). MOG-immunized *Cryab*<sup>-/-</sup> and wild-type 129S6/SvEvTac animals were additionally injected intravenously with 50 ng of *Bordetella pertussis* toxin (Difco Laboratories) in PBS at the time of, and two days following immunization. MOG p35–55 and PLP 139–151 peptides were synthesized by the Stanford Pan Facility and purified by high performance liquid chromatography (HPLC). Mice (*n* = 8–10 per group) were examined daily for clinical signs of EAE and were scored. All animal protocols were approved by the Division of Comparative Medicine at Stanford University and animals were maintained in accordance with the guidelines of the National Institutes of Health.

**Adoptive transfer.** Female, 8–12-week-old *Cryab*<sup>-/-</sup> and wild-type 129S6/SvEvTac animals were immunized with 100 µg myelin oligodendrocyte glycoprotein (MOG p35–55) peptide in CFA (containing 4 mg ml<sup>-1</sup> of heat-killed *Mycobacterium tuberculosis* H37Ra, Difco Laboratories) along with 50 ng of *Bordetella pertussis* toxin (Difco Laboratories) in PBS administered intravenously at days 0 and 2 following immunization. Splenocytes were isolated at day 10 following immunization and cultured in the presence of 20 µg ml<sup>-1</sup> MOG 35–55 and 20 ng ml<sup>-1</sup> murine rIL-12 (R&D Systems). Cells were collected and washed in PBS after 4 days in culture. Living ( $2 \times 10^7$ ) wild-type and *Cryab*<sup>-/-</sup> cells were intravenously injected into female *Rag2*<sup>-/-</sup> mice (Taconic Farms). Animals were also injected intravenously with 50 ng *pertussis* toxin on the day of, and 48 h after cell transfer<sup>29</sup>.

**Histopathology.** Brains and spinal cords were dissected from mice, fixed in 10% formalin in PBS and embedded in paraffin. Seven-micron-thick sections were stained with haematoxylin and eosin to detect inflammatory infiltrates and luxol fast blue for demyelination. Inflammatory foci (greater than 10 inflammatory cells per focus) were counted in meninges and parenchyma of sections containing brain, thoracic and lumbar spinal cord from each mouse by an examiner masked to the treatment status of the animal.

**Astrocyte culture.** Astrocytes were derived from the brains of 2-day-old *Cryab*<sup>-/-</sup> and wild-type pups. Briefly, the cerebral cortices from three pups of each genotype were dissected and placed in modified Dulbecco's modified Eagle's medium (DMEM, Invitrogen) containing penicillin-streptomycin-L-glutamine (Invitrogen). The meninges were removed and the cortices placed in 1 ml of complete DMEM containing 10% fetal bovine serum, 2 mM L-glutamine, 1 mM sodium pyruvate, 0.1 mM non-essential amino acids, 100 U ml<sup>-1</sup> penicillin and 0.1 mg ml<sup>-1</sup> streptomycin (Invitrogen). The cortices were minced, vortexed at high speed for 1 min, and passed through an 18.5-gauge needle. The ensuing mixture was filtered successively through sterile 80-µm and 11-µm nylon filters (Millipore) using a 25-mm Swinnex syringe filter holder (Millipore). The filtered cells were then diluted up to 1 ml with complete DMEM, plated into three 75-cm<sup>2</sup> tissue culture flasks containing 10 ml of complete DMEM, and placed in a 5% aerated CO<sub>2</sub> incubator kept at 37 °C. After 10–12 days in culture flasks, cells were shaken at 250 r.p.m. for two hours at 37 °C to remove microglia, fibroblasts or endothelial cells. Confluent astrocytes were stimulated with 200 ng ml<sup>-1</sup> recombinant TNF (BioSource) or 100 nM staurosporine (Sigma) and the cells and supernatants harvested for ELISA and western blot analysis following stimulation. Astrocytes were also grown on glass coverslips, stimulated with 200 ng ml<sup>-1</sup> recombinant TNF and stained for apoptosing cells using the TUNEL technique (described below).

**Immune cell activation assays and cytokine analysis.** Splenocytes and lymph node cells ( $5 \times 10^5$  cells/well) or CD3<sup>+</sup> T cells ( $5 \times 10^4$  cells per well; purified by negative selection, R&D Systems) were cultured in flat-bottomed, 96-well plates in media (RPMI 1640 supplemented with 2 mM L-glutamine, 1 mM sodium pyruvate, 0.1 mM non-essential amino acids, 100 U ml<sup>-1</sup> penicillin, 0.1 mg ml<sup>-1</sup> streptomycin, 0.5 µM 2-mercaptoethanol and 10% fetal calf serum) with MOG p35–55 peptide (5–20 µg ml<sup>-1</sup>). To determine *in vivo* T-cell function CD3<sup>+</sup> T cells were purified from the spleens and lymph nodes of day 9 MOG-immunized mice and cultured 1:5 with irradiated syngeneic splenocytes and MOG p35–55 peptide (5–20 µg ml<sup>-1</sup>).

Primary macrophages were isolated from the peritoneal cavity of *Cryab*<sup>-/-</sup> and wild-type mice 3 days after intraperitoneal injection with 3 ml of 3% (w/v) thioglycollate (BD Diagnostics Systems) and cultured ( $1 \times 10^6$  cells ml<sup>-1</sup>) with media alone (DMEM supplemented with 10% FCS, 1 mM sodium pyruvate, 100 U ml<sup>-1</sup> penicillin, and 0.1 mg ml<sup>-1</sup> streptomycin) in 24-well plates for 72 h and then activated with 100 ng ml<sup>-1</sup> of LPS.

Primary dendritic cells were isolated from the spleens of naive *Cryab*<sup>-/-</sup> and wild-type animals by magnetic cell sorting according to the manufacturer's directions for the CD11c MACS dendritic cell kit (Miltenyi Biotec). Dendritic cells ( $1 \times 10^6$  cells ml<sup>-1</sup>) were cultured in DMEM containing 10% FCS, 100 U ml<sup>-1</sup> penicillin, and 0.1 mg ml<sup>-1</sup> streptomycin in 24-well plates and pulsed with 100 ng ml<sup>-1</sup> LPS for 1 h, 24 h, 48 h and 72 h.

To assess proliferation rate, cultures were pulsed with [<sup>3</sup>H]-thymidine (1 µCi per well) after 72 h of culture and harvested 18 h later onto filter paper. The counts per minute (c.p.m.) of incorporated [<sup>3</sup>H]-thymidine were read using a beta counter. Cytokines were measured in the supernatants of cultured cells using anti-mouse OPTEIA ELISA kits (BD Pharmingen). Supernatants were taken at the time of peak production for each cytokine (48 h: IL-2, IL-12 p40, IL-6, IL-1β; 72 h: IFN-γ, TNF; 96 h: IL-17; 120 h: IL-4, IL-10). For all activation assays, cells were pooled from three animals per group and triplicate wells plated.

**Recombinant CRYAB treatment.** 129S6, *Cryab*<sup>-/-</sup>, and SJL/J mice were induced with EAE using 100 µg MOG p35–55 (for 129S6 and *Cryab*<sup>-/-</sup>) or 100 µg PLP 139–151 (for SJL/J) peptide emulsified in CFA. 129S6 and *Cryab*<sup>-/-</sup> mice were also injected intravenously with 50 ng of *Bordetella pertussis* toxin (Difco Laboratories) in PBS at the time of, and two days following immunization. When mice had hindlimb paralysis animals were divided into three groups balanced for mean clinical disease scores, and then injected intravenously every second day with saline pH 7.0, 10 µg recombinant human CRYAB (US Biological) or 10 µg recombinant human myoglobin (US Biological) diluted in saline. To determine the effect of CRYAB treatment on immune cell function during EAE splenocytes from 129S6 mice were isolated during the remission phase, and stimulated *in vitro* with MOG 35–55 (5–20 µg ml<sup>-1</sup>). Proliferation rate was determined by [<sup>3</sup>H]-thymidine (1 µCi per well) incorporation after 72 h of culture, whereas cytokines were measured in the supernatants at the time of their peak production (48 h: IL-2, IL-12 p40, IL-6, IL-1β; 72 h: IFN-γ, TNF; 96 h: IL-17; 120 h: IL-4, IL-10). Brains and spinal cords were harvested at the end of the experiment, embedded in paraffin and sections processed for histological analysis and TUNEL staining.

**Western blot analysis.** CD3<sup>+</sup> T cells, macrophages and astrocytes were lysed in 50 mM Tris-HCl buffer, pH 7.4, containing 1% NP-40, 10% glycerol, 1 mM EDTA, 1 mM Na<sub>3</sub>VO<sub>4</sub>, 1 mM NaF, 1 mM DTT, 4.5 mM Na pyrophosphate, 10 mM β-glycerophosphate, and a protease inhibitor cocktail tablet (Roche Diagnostics). The supernatants were collected after centrifugation at 13,000 r.p.m. at 4 °C for 30 min, and protein content determined with a spectrophotometer using absorption at 280 nm. Protein lysates (30–50 µg) were suspended in two volumes of double-strength sodium dodecyl sulphate (SDS) Sample Buffer (Bio-Rad Laboratories) and subjected to SDS-polyacrylamide gel electrophoresis using 10 or 15% Tris-HCl Ready Gels (Bio-Rad Laboratories). Proteins were transferred to PVDF membranes and blocked with 5% non-fat dried milk in 20 mM Tris-HCl-buffered saline (TBS), pH 7.4, containing 0.05% Tween-20. Membranes were immunoblotted 1:500 with the following antibodies overnight at 4 °C: p-CRYAB (Ser 45), p-CRYAB (Ser 59), CRYAB (StressGen BioReagents); actin (Sigma); p-p38, p38, p-ERK, ERK, p-SAPK/JNK, SAPK/JNK, caspase-3, NFκB p105/p50, NF-κB p65, IκB-α (Cell Signalling Technology). Membranes were washed three times for 15 min with TBS buffer containing 0.1% Tween-20. Bound antibodies were visualized using peroxidase-conjugated secondary antibody (Amersham) followed by detection using an ECL kit (Pierce). For reblotting, the membrane was first stripped in buffer (62.5 mM Tris-HCl, pH 6.8, with 2% SDS and 100 mM β-mercaptoethanol) for 1 h at 50 °C.

**Immunohistochemistry.** Paraffin-embedded sagittal sections (7 µm) were hydrated and treated for antigen retrieval using 10 mM sodium citrate. Sections were incubated in 1% hydrogen peroxide to quench endogenous peroxidase, blocked in 1% BSA in PBS for 1 h at room temperature, and incubated



overnight at 4 °C with caspase-3 (1:50) or cleaved caspase-3 (1:400) (Cell Signaling). Bound antibody was detected using Vectastain ABC anti-rabbit kits (Vector Laboratories) and 3,5-diaminobenzidine (DAB)/H<sub>2</sub>O<sub>2</sub> reagent as substrate. Before mounting, sections were counterstained with Mayer's haematoxylin and dehydrated in graded ethanols. To detect for apoptosis using the TUNEL method, we used the ApopTag peroxidase *in situ* apoptosis detection kit according to the manufacturer's directions for paraffin-embedded sections (Chemicon). TUNEL-positive small, round parenchymal cells and larger glia were counted in CNS tissue from representative mice. For astrocyte cultures, proportions of TUNEL-positive cells in fifty randomly selected fields per slide were quantified.

**NF- $\kappa$ B binding assay.** Wild-type and *Cryab*<sup>-/-</sup> astrocytes were stimulated with 200 ng ml<sup>-1</sup> TNF (BioSource) for 72 h and nuclear protein extracts isolated using Clontech Laboratories' Transfactor Extraction kit. NF- $\kappa$ B p50 and NF- $\kappa$ B DNA binding was detected with 15  $\mu$ g of nuclear protein using Clontech Transfactor Family Colorimetric kit-NF- $\kappa$ B.

**Myelin arrays.** Myelin antigen arrays were printed and probed as previously described<sup>17</sup>. Briefly, proteins and peptides representing candidate myelin auto-antigens were printed in ordered arrays on the surface of SuperEpoxy microscope slides (TeleChem). Myelin arrays were probed with 1:20 dilutions of cerebrospinal fluid (CSF) derived from relapsing remitting multiple sclerosis (RRMS) or other neurologic disease (OND) control patients, followed by Cy-3-conjugated anti-human IgG/M secondary antibody (Jackson Immuno-research). Arrays were scanned, and fluorescence quantified as a measure of auto-antibody binding.

**Measurement of free CRYAB in sera and CSF.** Paired post-mortem samples of CSF (0.5 mL) and serum (1.0 mL) of clinically definite, and neuropathologically confirmed multiple sclerosis patients were subjected to denaturation by 1:10 dilution in 8 M urea and 2% (vol/vol) acetic acid and left at room temperature for 1 h to disrupt all possible immune complexes. Samples were next applied onto a reversed-phase HPLC column (C4 matrix, 5 micron particle size, 250 Å pores) and washed with 0.1% (vol/vol) trifluoroacetic acid (TFA) in water, containing 25% acetonitrile. In a final step, any CRYAB in the samples was eluted from the column with 45% acetonitrile in 0.1% TFA (CRYAB elutes at 37% acetonitrile under these conditions) and the eluate was lyophilized. Dried proteins were redissolved in 120 ml (CSF) and 500 ml (serum) and 20 ml of these

samples were subjected to SDS-PAGE and western blotting using a monoclonal antibody to CRYAB. Thus, CSF samples were concentrated about 4 times, and serum 2 times. Human recombinant CRYAB (0.4 mg) was used as a reference.

**Western blot densitometric quantification.** Western blot bands were quantified using NIH Image Analysis 1.63 software. Briefly, arbitrary pixel units were obtained for an area around each band and the optical density (OD) within that area. A ratio of OD:area was derived for each band. The OD:area values for a protein of interest were then normalized to the corresponding actin OD:area values.

**Statistical analysis.** Data are presented as means  $\pm$  s.e.m. When data were parametric a *t*-test (*n* = 2 groups) was used to detect between-group differences. When data were non-parametric, Mann-Whitney U statistics were used for *n* = 2 groups. Clinical results when measured on a daily basis were compared with linear regression analysis in a pairwise comparison with either PBS or myoglobin or both controls. Myelin array results were analysed using Significance Analysis of Microarrays (SAM)<sup>25</sup> to identify antigen features with significant differences in antibody reactivity. These antigen 'hits' and the patient samples were then ordered using a hierarchical clustering algorithm and the results displayed as a heat map using TreeView software<sup>30</sup>.

26. Brady, J. P. *et al.*  $\alpha$ B-crystallin in lens development and muscle integrity: a gene knockout approach. *Invest. Ophthalmol. Vis. Sci.* **42**, 2924–2934 (2001).
27. Suzuki, A. *et al.* MKBP, a novel member of the small heat shock protein family, binds and activates the myotonic dystrophy protein kinase. *J. Cell Biol.* **140**, 1113–1124 (1998).
28. Doerwald, L. *et al.* Sequence and functional conservation of the intergenic region between the head-to-head genes encoding the small heat shock proteins  $\alpha$ B-crystallin and HspB2 in the mammalian lineage. *J. Mol. Evol.* **59**, 674–686 (2004).
29. Huang, D. R., Wang, J., Kivisakk, P., Rollins, B. J. & Ransohoff, R. M. Absence of monocyte chemoattractant protein 1 in mice leads to decreased local macrophage recruitment and antigen-specific T helper cell type 1 immune response in experimental autoimmune encephalomyelitis. *J. Exp. Med.* **193**, 713–726 (2001).
30. Eisen, M. B., Spellman, P. T., Brown, P. O. & Botstein, D. Cluster analysis and display of genome-wide expression patterns. *Proc. Natl Acad. Sci. USA* **95**, 14863–14868 (1998).

## LETTERS

# Essential autocrine regulation by IL-21 in the generation of inflammatory T cells

Roza Nurieva<sup>1</sup>, Xuexian O. Yang<sup>1</sup>, Gustavo Martinez<sup>1</sup>, Yongliang Zhang<sup>1</sup>, Athanasia D. Panopoulos<sup>1</sup>, Li Ma<sup>2</sup>, Kimberly Schluns<sup>1</sup>, Qiang Tian<sup>2</sup>, Stephanie S. Watowich<sup>1</sup>, Anton M. Jetten<sup>3</sup> & Chen Dong<sup>1</sup>

After activation, CD4<sup>+</sup> helper T (T<sub>H</sub>) cells differentiate into distinct effector subsets that are characterized by their unique cytokine expression and immunoregulatory function<sup>1,2</sup>. During this differentiation, T<sub>H</sub>1 and T<sub>H</sub>2 cells produce interferon- $\gamma$  and interleukin (IL)-4, respectively, as autocrine factors necessary for selective lineage commitment. A distinct T<sub>H</sub> subset, termed T<sub>H</sub>IL-17, T<sub>H</sub>17 or inflammatory T<sub>H</sub> (T<sub>H</sub>i), has been recently identified as a distinct T<sub>H</sub> lineage mediating tissue inflammation<sup>3,4</sup>. T<sub>H</sub>17 differentiation is initiated by transforming growth factor- $\beta$  and IL-6 (refs 5–7) and reinforced by IL-23 (ref. 8), in which signal transduction and activators of transcription (STAT)3 and retinoic acid receptor-related orphan receptor (ROR)- $\gamma$  mediate the lineage specification<sup>8–10</sup>. T<sub>H</sub>17 cells produce IL-17, IL-17F and IL-22, all of which regulate inflammatory responses by tissue cells but have no importance in T<sub>H</sub>17 differentiation<sup>11–14</sup>. Here we show that IL-21 is another cytokine highly expressed by mouse T<sub>H</sub>17 cells. IL-21 is induced by IL-6 in activated T cells, a process that is dependent on STAT3 but not ROR- $\gamma$ . IL-21 potently induces T<sub>H</sub>17 differentiation and suppresses Foxp3 expression, which requires STAT3 and ROR- $\gamma$ , which is encoded by *Rorc*. IL-21 deficiency impairs the generation of T<sub>H</sub>17 cells and results in protection against experimental autoimmune encephalomyelitis. IL-21 is therefore an autocrine cytokine that is sufficient and necessary for T<sub>H</sub>17 differentiation, and serves as a target for treating inflammatory diseases.

In a gene expression analysis of T<sub>H</sub>1, T<sub>H</sub>2 and T<sub>H</sub>17 cells differentiated *in vitro*, we found that the expression of IL-21 increased in T<sub>H</sub>17 cells in comparison with that of T<sub>H</sub>1 or T<sub>H</sub>2 cells (data not shown). IL-21, belonging to the common  $\gamma$ -chain family, regulates T, B, natural killer and dendritic cells<sup>15</sup>. IL-21 is expressed mainly by CD4<sup>+</sup> T cells, at higher levels by T<sub>H</sub>2 than by T<sub>H</sub>1 cells<sup>16</sup>. The addition of IL-21 during T<sub>H</sub>1 differentiation decreased interferon (IFN)- $\gamma$  production through repressing the expression of Eomes<sup>17</sup>. However, IL-21 expression by T<sub>H</sub>17 cells has not been reported. In OT-II cells activated under neutral (T<sub>H</sub>0), T<sub>H</sub>1 (IL-12 plus anti-IL-4), T<sub>H</sub>2 (IL-4 plus anti-IFN- $\gamma$ ) and T<sub>H</sub>17 (IL-6, transforming growth factor (TGF)- $\beta$ , IL-23, anti-IFN- $\gamma$  and anti-IL-4) conditions, we found IL-17 and IL-21 messenger RNA expression to be significantly higher in T<sub>H</sub>17 cells than other effector cells (Fig. 1a). Consistently, although IL-21 was also produced by T<sub>H</sub>2 cells, IL-21 secretion was significantly increased in T<sub>H</sub>17 cells after re-stimulation with anti-CD3 (Supplementary Fig. S1a). These data indicate that IL-21 is another cytokine highly produced by T<sub>H</sub>17 cells.

To assess the regulation of IL-21 expression during T<sub>H</sub>17 differentiation, naive CD4<sup>+</sup>CD25<sup>−</sup>CD62L<sup>hi</sup>CD44<sup>lo</sup> T<sub>H</sub> cells from C57BL/6 (B6) mice were sorted by fluorescence-activated cell sorting and activated with plate-bound anti-CD3 and anti-CD28 in the presence

of various cytokine stimuli. Analysed on days 2 and 5 after activation, mRNA encoding IL-21 was upregulated by IL-6 but not by TGF- $\beta$  or IL-23 (Fig. 1b). No synergistic effect of TGF- $\beta$  and IL-6 was observed, distinct from the regulation of IL-17 and IL-17F, with which TGF- $\beta$  and IL-6 exhibited a remarkable synergy<sup>7</sup>, possibly by means of chromatin remodelling at the chromosomal locus containing these two

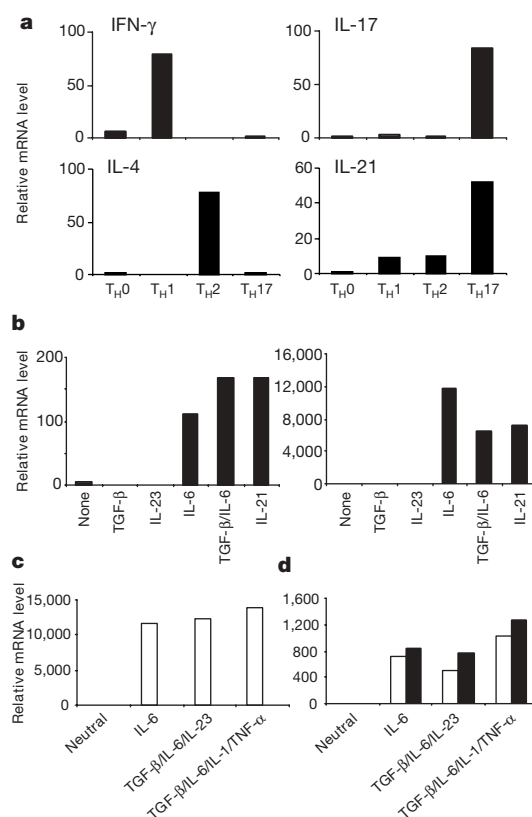


**Figure 1 | IL-21 is highly expressed by T<sub>H</sub>17 cells.** **a**, OT-II T cells differentiated under various conditions were re-stimulated with anti-CD3 for 4 h for real-time RT-PCR analysis. **b**, Naive B6 T cells were activated with anti-CD3, anti-CD28 and IL-2 with indicated cytokines for 2 days (left) or 5 days (right). After re-stimulation with anti-CD3, cytokine mRNA expression was analysed by RT-PCR. **c**, **d**, Naive T cells from wild-type (open columns) and STAT3-deficient (**c**, filled columns) or ROR- $\gamma$ -deficient (**d**, filled columns) mice were activated as indicated. T cells were re-stimulated for IL-21 mRNA expression. The RT-PCR data shown were normalized to  $\beta$ -actin levels, and expression in neutral conditions was set as 1.0. The results shown are representative of at least two independent experiments.

<sup>1</sup>Department of Immunology, M. D. Anderson Cancer Center, Houston, Texas 77030, USA. <sup>2</sup>Institute for Systems Biology, Seattle, Washington 98103, USA. <sup>3</sup>Cell Biology Section, LRB, National Institutes of Health, NIEHS, Research Triangle Park, North Carolina 27709, USA.

highly homologous genes<sup>18</sup>. IL-21 also increased its own mRNA expression (Fig. 1b), indicating an autocrine regulation.

To examine the requirement for IL-6 in IL-21 expression *in vivo*, we immunized B6 and IL-6 knockout (KO) mice with keyhole limpet haemocyanin (KLH) in complete Freund's adjuvant (CFA). One week later, spleen cells from immunized mice were re-stimulated with KLH *ex vivo*. Enhanced production of IL-4 and reduced IFN- $\gamma$  was observed in the supernatants of IL-6-deficient cells when compared with wild-type cells (Supplementary Fig. S1b), which is consistent with previous studies<sup>19,20</sup>. IL-6-deficient cells did not produce IL-17 or IL-21. These data indicate that IL-6 is sufficient and necessary for inducing IL-21 production by T<sub>H</sub> cells.

STAT3 and the ROR- $\gamma$ t isoform of ROR- $\gamma$  are key transcription factors in T<sub>H</sub>17 differentiation<sup>8–10</sup>. To determine their regulation in IL-21 expression, naive T<sub>H</sub> cells from STAT3-deficient<sup>8</sup> or ROR- $\gamma$ -deficient<sup>21</sup> mice and their controls were activated as above. STAT3-deficient T<sub>H</sub> cells activated under all conditions failed to produce IL-21 mRNA or protein (Fig. 1c, and Supplementary Fig. S1c), as well as IL-17, IL-17F and IL-22 (Supplementary Fig. S2a). In contrast, although *Rorc*<sup>-/-</sup> T<sub>H</sub> cells showed a severe deficiency in IL-17, IL-17F and IL-22 expression (Supplementary Fig. S2b), IL-21 mRNA and protein expression were normal in these cells compared with those from wild-type mice (Fig. 1d, and Supplementary Fig. S1d). All these data indicate that whereas both STAT3 and ROR- $\gamma$  are required for IL-17 expression, IL-21 expression is regulated by STAT3 but not ROR- $\gamma$ .

T<sub>H</sub> cell differentiation is regulated by distinct autocrine cytokines. IFN- $\gamma$  regulates T<sub>H</sub>1 differentiation through STAT1 to upregulate T-bet expression<sup>22</sup>, whereas IL-4 regulates T<sub>H</sub>2 differentiation through STAT6 (ref. 2). To test the possible function of IL-21 in T<sub>H</sub> differentiation, we activated naive T<sub>H</sub> cells from B6 mice in the presence or absence of IL-21. In a similar way to IL-6, IL-21 alone inhibited IFN- $\gamma$  expression but only induced a small percentage of IL-17-producing cells (Fig. 2a). Addition of IL-21 or IL-6 together with TGF- $\beta$  strongly inhibited Foxp3 expression and greatly enhanced IL-17 production (Fig. 2a). IL-23 synergizes with TGF- $\beta$  and IL-6 in T<sub>H</sub>17 differentiation<sup>8</sup>; similarly, it also enhanced the generation of T<sub>H</sub>17 cells by TGF- $\beta$  and IL-21 (Fig. 2a). To assess the role of IL-21 further, expression of lineage-specific genes was examined by reverse-transcriptase-mediated polymerase chain reaction (RT-PCR). IL-21 or IL-6, alone or in combination with TGF- $\beta$ , resulted in upregulation of IL-23 receptor (IL-23R), ROR- $\gamma$  and the T<sub>H</sub>17 cytokines IL-17, IL-17F and IL-22, and inhibition of Foxp3 and T-bet mRNA expression (Fig. 2b). These data indicate that IL-21, in a similar way to IL-6, selectively regulates the differentiation of T<sub>H</sub>17 cells. Moreover, activation of wild-type and *Il6*<sup>-/-</sup> T<sub>H</sub> cells in the presence of TGF- $\beta$  plus IL-21 resulted in similar numbers of T<sub>H</sub>17 cells (Supplementary Fig. S3). Thus, IL-21 functions independently of IL-6 in driving T<sub>H</sub>17 differentiation. We observed no synergistic effect of IL-21 and IL-6 (data not shown), which supports the hierarchy of these two cytokines in T<sub>H</sub> differentiation.

IL-21 activates STAT3 and STAT1 and, to a smaller degree, STAT5 (ref. 15), of which only STAT3 regulates T<sub>H</sub>17 differentiation<sup>8</sup>. When naive T cells from STAT3-deficient mice and control mice were differentiated in the presence of IL-21 plus TGF- $\beta$ , the expression of IL-17 by STAT3-deficient T cells was greatly reduced and Foxp3 expression was enhanced (Fig. 2c, and Supplementary Fig. S4a). In addition, deficient mRNA expression of IL-23R, ROR- $\gamma$ , IL-17, IL-17F, IL-22 and IL-21 was observed (Fig. 2c). These data indicate an essential role of STAT3 in IL-21-mediated T<sub>H</sub>17 differentiation.

We next examined whether IL-21-mediated T<sub>H</sub>17 differentiation is also dependent on ROR- $\gamma$ . Naive T<sub>H</sub> cells from wild-type and ROR- $\gamma$ -deficient mice were differentiated as above. ROR- $\gamma$ -deficient T cells were found to produce markedly decreased levels of IL-17, whereas Foxp3 expression was moderately enhanced (Fig. 2d, and Supplementary Fig. S4b). Real-time PCR analysis also indicated decreased expression of IL-23R, IL-17, IL-17F and IL-22 mRNA in

ROR- $\gamma$ -deficient T<sub>H</sub> cells compared with the wild type, whereas IL-21 production in wild-type and *Rorc*<sup>-/-</sup> T<sub>H</sub> cells remained the same (Fig. 2d). IL-21 therefore induces T<sub>H</sub>17 differentiation and suppresses Foxp3 upregulation, in which STAT3 and ROR- $\gamma$  are required.

We then examined whether IL-21 is necessary for T<sub>H</sub>17 differentiation by using an IL-21 KO mouse. T<sub>H</sub>17 cells generated from these

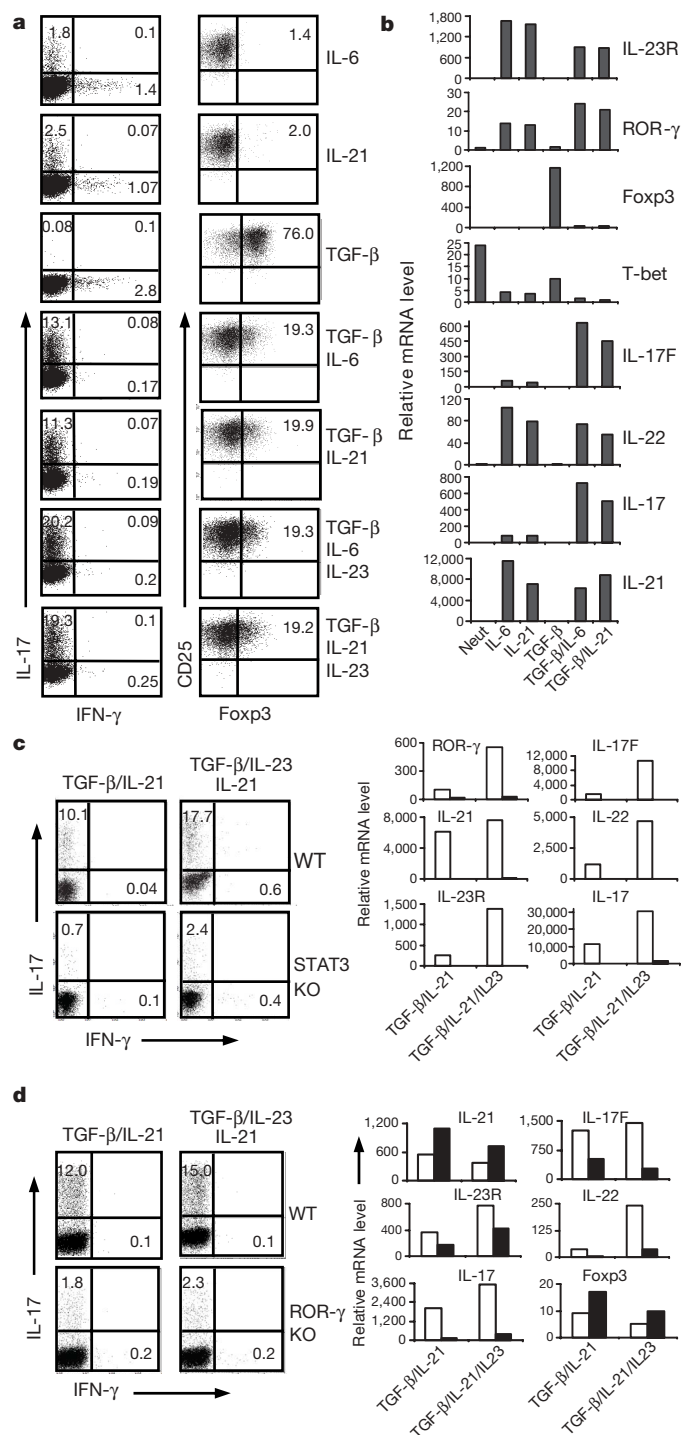


**Figure 2 | IL-21 promotes T<sub>H</sub>17 differentiation *in vitro*.** **a, b**, Naive B6 T cells activated as indicated were subsequently analysed by intracellular staining (**a**). mRNA expression of indicated genes was analysed by real-time RT-PCR (**b**). **c, d**, Naive T cells from STAT3 (**c**) or ROR- $\gamma$  (**d**) KO mice (filled columns) and their appropriate controls (open columns) were activated and analysed as above. Numbers in dot-plot quadrants show percentages. The data represent at least two independent experiments with consistent results. WT, wild type.



mice failed to express IL-21 (data not shown). In a similar way to IL-21R-deficient mice<sup>15,23</sup>, IL-21 KO mice exhibit normal T-cell development (Supplementary Fig. S5). Naive wild-type and *Il21*<sup>-/-</sup> T<sub>H</sub> cells were subjected to T<sub>H</sub>17 differentiation in the presence of IL-6. IL-21-deficient T<sub>H</sub> cells showed a deficiency in the generation of IL-17-producing cells (Fig. 3a), associated with a significantly increased number of Foxp3<sup>+</sup> cells compared with wild-type cells (Fig. 3b). They were consistently defective in the expression of IL-23R, IL-17, IL-17F, IL-22 and ROR-γ mRNA, with increased Foxp3 expression (Fig. 3c). Similarly, anti-IL-21 or an IL-21 receptor antagonist also decreased T<sub>H</sub>17 differentiation (data not shown). Addition of exogenous IL-21 to IL-21-deficient T cells partly restored IL-17 expression and greatly decreased Foxp3 expression (Supplementary Fig. S6a, b).

To determine whether IL-21 is essential in the generation of T<sub>H</sub>17 cells *in vivo*, we first analysed lamina propria and splenic T cells from IL-21-deficient mice. In IL-21-deficient mice, lamina propria and splenic TCRγδ<sup>+</sup> T cells showed an at least tenfold decrease in IL-17-expressing cells compared with those from wild-type mice (Supplementary Fig. S7a). IL-17<sup>+</sup>CD4<sup>+</sup> cells in lamina propria and spleen were completely absent from *Il21*<sup>-/-</sup> mice (Supplementary Fig. S7a).

IL-17-producing T<sub>H</sub> cells have been shown to have an important pathogenic function in an experimental autoimmune encephalomyelitis (EAE)<sup>12,24</sup>. Although IL-21 is important for humoral immunity<sup>15</sup>, its function in inflammatory disease is unclear. It has previously been shown that B cells are not important in an EAE model<sup>25</sup>. On day 5 after second immunization with myelin oligodendrocyte glycoprotein (MOG) peptide, wild-type and *Il21*<sup>+/-</sup> mice started to develop disease and by day 11 reached a score of 2.5–3.0 (Fig. 4a). In contrast, IL-21-deficient mice first showed signs of disease on day 8 after the second immunization; on day 11, only very mild disease was found in these mice (Fig. 4a). Lack of IL-21 thus results in an amelioration of EAE. To understand the underlying cause, we further analysed the production of cytokines by CD4<sup>+</sup> cells infiltrating into the central nervous system (CNS) and by splenocytes. CNS-infiltrating and splenic CD4<sup>+</sup> T cells from wild-type

and *Il21*<sup>+/-</sup> mice produced similar levels of IL-17; those from *Il21*<sup>+/-</sup> mice expressed more IFN-γ (Fig. 4b). In contrast, CD4<sup>+</sup> cells from IL-21 KO mice predominantly expressed IFN-γ, but not IL-17 (Fig. 4b).

To confirm further the role of IL-21 in the differentiation of IL-17-producing T<sub>H</sub>17 cells *in vivo*, we immunized wild-type and IL-21-deficient mice with MOG peptide in CFA. One week later, spleen cells from immunized mice were re-stimulated with 12-*O*-tetradecanoylphorbol-13-acetate (TPA) plus ionomycin or MOG peptide *ex vivo*. Although CD4<sup>+</sup> T cells from *Il21*<sup>-/-</sup> mice showed normal IFN-γ expression, IL-17-producing cells were almost completely absent (Supplementary Fig. S7b). Taken together, these results show that the lack of IL-21 resulted in impaired T<sub>H</sub>17 differentiation *in vivo* and in protection against EAE.

Thus, IL-21 is induced in T cells by IL-6 by means of STAT3 and is sufficient and necessary for the generation of T<sub>H</sub>17 cells, through the STAT3-dependent upregulation of ROR-γ. IL-21 therefore acts in an autocrine fashion as IFN-γ does for T<sub>H</sub>1 and IL-4 for T<sub>H</sub>2. Considering the IL-25-mediated potentiation of T<sub>H</sub>2 differentiation and inhibition of T<sub>H</sub>17-mediated autoimmunity<sup>26,27</sup>, we suggest a revised model of T<sub>H</sub> differentiation regulated by the innate system and a T-cell-intrinsic mechanism (Supplementary Fig. S8). Specifically, given that IL-21-deficient mice were protected against EAE, IL-21 may be targeted in treating inflammatory diseases. Moreover, because IL-21 has broad regulatory functions in immune responses,

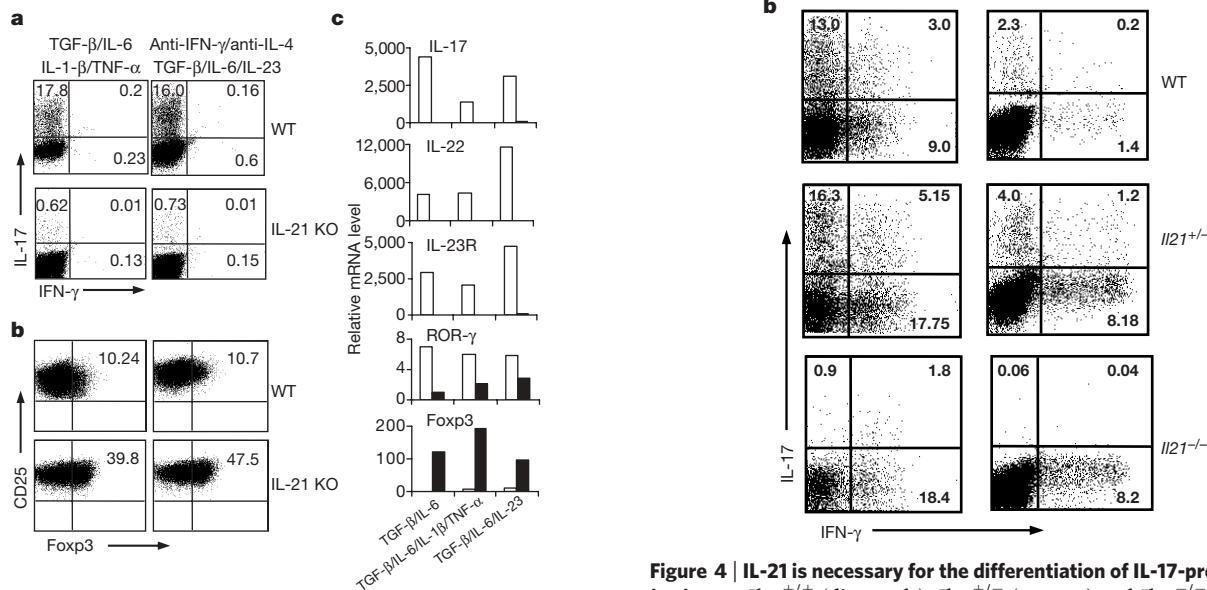


**Figure 4 | IL-21 is necessary for the differentiation of IL-17-producing cells *in vivo*.** **a**, *Il21*<sup>+/-</sup> (diamonds), *Il21*<sup>+/-</sup> (squares) and *Il21*<sup>-/-</sup> (triangles) mice were immunized with MOG peptide to induce EAE. Disease scores (means ± s.e.m.) combining three independent experiments (wild type (WT), *n* = 6 mice; *Il21*<sup>+/-</sup>, *n* = 17 mice; *Il21*<sup>-/-</sup>, *n* = 9 mice) are shown. *P* values were calculated with the Mann–Whitney *U*-test by comparing the disease score of WT and *Il21*<sup>-/-</sup> mice and are indicated as followed: asterisk, *P* < 0.05; two asterisks, *P* < 0.005; three asterisks, *P* < 0.001. **b**, Mononuclear cells isolated from spinal cords and brains (left) were stimulated for 5 h with TPA and ionomycin, and splenocytes (right) were re-stimulated with MOG peptide for 24 h, followed by intracellular staining of IL-17 and IFN-γ and analysis in a CD4<sup>+</sup> gate.

**Figure 3 | IL-21 deficiency impairs the generation of T<sub>H</sub>17 cells *in vitro*.** Naive T<sub>H</sub> cells from IL-21 KO mice and their littermate control mice were activated with the indicated cytokines and neutralizing antibodies. Five days later, cells were assessed for IFN-γ and IL-17 production (**a**) or Foxp3 expression (**b**) by using intracellular staining. Numbers in quadrants are percentages. mRNA expression of various genes was analysed by real-time RT-PCR (**c**). The data shown are normalized to the expression of a reference gene, that encoding β-actin. Open columns, wild type; filled columns, IL-21 KO. The experiments were repeated three times with consistent results. WT, wild type.

IL-17-expressing T cells, which produce large amounts of IL-21, may have an additional immune function that remains to be understood.

## METHODS SUMMARY

**Mice.** IL-6-deficient mice were purchased from Jackson Laboratories, and IL-21 KO mice came from NIH Mutant Mouse Regional Resource Centers. *Rorc* KO mice were backcrossed six generations into C57BL/6 mice. *Stat3* fl and *Tie2-Cre* mice were bred to yield *fl/Δ Cre<sup>+</sup>* and *Cre<sup>-</sup>* littermates as described<sup>8</sup>. The animal experiments were performed with protocols approved by the Institutional Animal Care and Use Committee.

**T-cell isolation and differentiation.** Naive CD4<sup>+</sup>CD25<sup>-</sup>CD62L<sup>hi</sup>CD44<sup>lo</sup> T cells were activated with plate-bound 2 μg ml<sup>-1</sup> anti-CD3 and 2 μg ml<sup>-1</sup> anti-CD28 and 50 U ml<sup>-1</sup> IL-2 in the presence of 30 ng ml<sup>-1</sup> IL-6 (Peprotech), 80 ng ml<sup>-1</sup> IL-21, 50 ng ml<sup>-1</sup> IL-23 (R&D Systems), 2.5 ng ml<sup>-1</sup> TGF-β (Peprotech), 10 μg ml<sup>-1</sup> anti-IL-4 (11B11), 10 μg ml<sup>-1</sup> anti-IFN-γ (XMG 1.2), 10 ng ml<sup>-1</sup> tumour necrosis factor-α or 10 ng ml<sup>-1</sup> IL-1β, or a combination of these stimuli.

**Induction of EAE.** For the induction of EAE, mice were immunized with MOG peptide emulsified in CFA. Mice were immunized subcutaneously at the dorsal flanks with 150 μg of MOG peptide in CFA on days 0 and 7. Pertussis toxin was given intraperitoneally on days 1 and 8 with the dose of 500 ng per mouse. Signs of EAE were assigned scores on a scale of 1–5 as follows: 0, none; 1, limp tail or waddling gait with tail tonic; 2, wobbly gait; 3, hindlimb paralysis; 4, hindlimb and forelimb paralysis; 5, death.

**Full Methods** and any associated references are available in the online version of the paper at [www.nature.com/nature](http://www.nature.com/nature).

**Received 7 March; accepted 4 June 2007.**

**Published online 20 June 2007.**

- Dong, C. & Flavell, R. A. Cell fate decision: T-helper 1 and 2 subsets in immune responses. *Arthritis Res.* **2**, 179–188 (2000).
- Glimcher, L. H. & Murphy, K. M. Lineage commitment in the immune system: the T helper lymphocyte grows up. *Genes Dev.* **14**, 1693–1711 (2000).
- Dong, C. Diversification of T-helper-cell lineages: finding the family root of IL-17-producing cells. *Nature Rev. Immunol.* **6**, 329–334 (2006).
- Weaver, C. T., Harrington, L. E., Mangan, P. R., Gavrieli, M. & Murphy, K. M. Th17: an effector CD4 T cell lineage with regulatory T cell ties. *Immunity* **24**, 677–688 (2006).
- Bettelli, E. *et al.* Reciprocal developmental pathways for the generation of pathogenic effector T<sub>H</sub>17 and regulatory T cells. *Nature* **441**, 235–238 (2006).
- Mangan, P. R. *et al.* Transforming growth factor-β induces development of the T<sub>H</sub>17 lineage. *Nature* **441**, 231–234 (2006).
- Veldhoen, M., Hocking, R. J., Atkins, C. J., Locksley, R. M. & Stockinger, B. TGFβ in the context of an inflammatory cytokine milieu supports *de novo* differentiation of IL-17-producing T cells. *Immunity* **24**, 179–189 (2006).
- Yang, X. O. *et al.* STAT3 regulates cytokine-mediated generation of inflammatory helper T cells. *J. Biol. Chem.* **282**, 9358–9363 (2007).
- Chen, Z. *et al.* Selective regulatory function of Socs3 in the formation of IL-17-secreting T cells. *Proc. Natl Acad. Sci. USA* **103**, 8137–8142 (2006).
- Ivanov, I. I. *et al.* The orphan nuclear receptor RORγt directs the differentiation program of proinflammatory IL-17<sup>+</sup> T helper cells. *Cell* **126**, 1121–1133 (2006).
- Chung, Y. *et al.* Expression and regulation of IL-22 in the IL-17-producing CD4<sup>+</sup> T lymphocytes. *Cell Res.* **16**, 902–907 (2006).
- Langrish, C. L. *et al.* IL-23 drives a pathogenic T cell population that induces autoimmune inflammation. *J. Exp. Med.* **201**, 233–240 (2005).
- Liang, S. C. *et al.* Interleukin (IL)-22 and IL-17 are coexpressed by Th17 cells and cooperatively enhance expression of antimicrobial peptides. *J. Exp. Med.* **203**, 2271–2279 (2006).
- Zheng, Y. *et al.* Interleukin-22, a T<sub>H</sub>17 cytokine, mediates IL-23-induced dermal inflammation and acanthosis. *Nature* **445**, 648–651 (2007).
- Leonard, W. J. & Spolski, R. Interleukin-21: a modulator of lymphoid proliferation, apoptosis and differentiation. *Nature Rev. Immunol.* **5**, 688–698 (2005).
- Wurster, A. L. *et al.* Interleukin 21 is a T helper (Th) cell 2 cytokine that specifically inhibits the differentiation of naive Th cells into interferon γ-producing Th1 cells. *J. Exp. Med.* **196**, 969–977 (2002).
- Suto, A., Wurster, A. L., Reiner, S. L. & Grusby, M. J. IL-21 inhibits IFN-γ production in developing Th1 cells through the repression of Eomesodermin expression. *J. Immunol.* **177**, 3721–3727 (2006).
- Akimzhanov, A. M., Yang, X. O. & Dong, C. Chromatin remodeling of interleukin-17 (IL-17)–IL-17F cytokine gene locus during inflammatory helper T cell differentiation. *J. Biol. Chem.* **282**, 5969–5972 (2007).
- Okuda, Y. *et al.* IL-6 plays a crucial role in the induction phase of myelin oligodendrocyte glycoprotein 35–55 induced experimental autoimmune encephalomyelitis. *J. Neuroimmunol.* **101**, 188–196 (1999).
- Okuda, Y., Sakoda, S., Saeki, Y., Kishimoto, T. & Yanagihara, T. Enhancement of Th2 response in IL-6-deficient mice immunized with myelin oligodendrocyte glycoprotein. *J. Neuroimmunol.* **105**, 120–123 (2000).
- Kurebayashi, S. *et al.* Retinoid-related orphan receptor γ (RORγ) is essential for lymphoid organogenesis and controls apoptosis during thymopoiesis. *Proc. Natl Acad. Sci. USA* **97**, 10132–10137 (2000).
- Afkarian, M. *et al.* T-bet is a STAT1-induced regulator of IL-12R expression in naive CD4<sup>+</sup> T cells. *Nature Immunol.* **3**, 549–557 (2002).
- Ozaki, K. *et al.* A critical role for IL-21 in regulating immunoglobulin production. *Science* **298**, 1630–1634 (2002).
- Park, H. *et al.* A distinct lineage of CD4 T cells regulates tissue inflammation by producing interleukin 17. *Nature Immunol.* **6**, 1133–1141 (2005).
- Hjelmstrom, P., Juedes, A. E., Fjell, J. & Ruddle, N. H. B-cell-deficient mice develop experimental allergic encephalomyelitis with demyelination after myelin oligodendrocyte glycoprotein sensitization. *J. Immunol.* **161**, 4480–4483 (1998).
- Angkasekwinai, P. *et al.* IL-25 promotes the initiation of pro-allergic type 2 responses. *J. Exp. Med.* (in the press).
- Kleinschek, M. A. *et al.* IL-25 regulates Th17 function in autoimmune inflammation. *J. Exp. Med.* **204**, 161–170 (2007).
- Laky, K., Lefrancois, L. & Puddington, L. Age-dependent intestinal lymphoproliferative disorder due to stem cell factor receptor deficiency: parameters in small and large intestine. *J. Immunol.* **158**, 1417–1427 (1997).

**Supplementary Information** is linked to the online version of the paper at [www.nature.com/nature](http://www.nature.com/nature).

**Acknowledgements** We thank the Dong laboratory members for their help. The work is supported by research grants from NIH (to C.D.), an Intramural Research Program of the NIEHS, NIH (to A.M.J.), and the M. D. Anderson Cancer Center (to S.S.W.). R.N. received a postdoctoral fellowship from the Arthritis Foundation and is a recipient of a Scientist Development Grant from the American Heart Association. K.S. and C.D. are M. D. Anderson Cancer Center Trust Fellows, and C.D. is a Cancer Research Institute Investigator and American Lung Association Career Investigator.

**Author Contributions** C.D. and R.N. designed the research and analysed the data. R.N., X.O.Y., G.M., Y.Z., A.D.P., L.M. and K.S. performed the experiments, and R.N., Q.T., S.S.W., A.M.J. and C.D. prepared the manuscript.

**Author Information** Reprints and permissions information is available at [www.nature.com/reprints](http://www.nature.com/reprints). The authors declare no competing financial interests. Correspondence and requests for materials should be addressed to C.D. ([cdong@mdanderson.org](mailto:cdong@mdanderson.org)) or R.N. ([rnurieva@mdanderson.org](mailto:rnurieva@mdanderson.org)).

## METHODS

**Mice.** IL-6-deficient mice on a C57BL/6 background were purchased from Jackson Laboratories, and C57BL/6 mice were used as controls. ROR- $\gamma$  KO mice previously reported<sup>21</sup> were backcrossed for six or seven generations onto a C57BL/6 background, and splenocytes from these and their littermate control mice were used for differentiation *in vitro*. *Stat3 fl* and *Tie2-Cre* mice were bred on a 129  $\times$  C57BL/6 mixed background to yield *fl*/ $\Delta$  *Cre*<sup>+</sup> and *Cre*<sup>-</sup> littermates as described<sup>8</sup>, and their spleen and lymph node cells were used for differentiation *in vitro*. IL-21 KO mice on a 129  $\times$  C57BL/6 F<sub>1</sub> mixed background were obtained from NIH Mutant Mouse Regional Resource Centers. *Il21*<sup>+/-</sup> mice were intercrossed to generate *Il21*<sup>+/+</sup>, *Il21*<sup>+/-</sup> and *Il21*<sup>-/-</sup> mice for the experiments including EAE. Mice (except the ROR- $\gamma$  KO mice) were housed in the SPF animal facility at the M. D. Anderson Cancer Center and the animal experiments were performed at the age of 6–10 weeks with the use of protocols approved by the Institutional Animal Care and Use Committee.

**Immunizations.** IL-6 KO and C57BL/6 mice (6–8 weeks old; three per group) were immunized with KLH (0.5 mg ml<sup>-1</sup>) emulsified in CFA (0.5 mg ml<sup>-1</sup>) at the base of the tail (100  $\mu$ l for each mouse). Seven days later, spleen cells from KLH-immunized mice were stimulated with or without KLH for three days, and effector cytokines (IFN- $\gamma$ , IL-4, IL-17 and IL-21) were measured by enzyme-linked immunosorbent assay (ELISA) (Pharmingen). IL-21 KO mice and their littermate controls (three per group) were immunized with MOG peptide (amino acids 35–55; MEVGWYRSPFSROVHLYRNGK) in CFA. Seven days later, spleen cells from immunized mice were re-stimulated with 50 ng ml<sup>-1</sup> TPA and 500 ng ml<sup>-1</sup> ionomycin (Sigma-Aldrich) for 5 h, or with 25  $\mu$ g of MOG peptide for 24 h. In the final 5 h, Golgi-stop (BD Bioscience) was added, and IL-17- and IFN- $\gamma$ -producing cells were analysed with a BD CytoFix/CytoPerm intracellular staining kit (BD Bioscience). In the same experiment, spleen cells were re-stimulated with or without MOG peptide for 3 days, and cytokine production was measured by ELISA.

**T-cell differentiation.** Differentiation of OT-II cells in Fig. 1a was performed as described previously<sup>11</sup>. For naive T-cell differentiation in other experiments, CD4<sup>+</sup>CD25<sup>-</sup>CD62L<sup>hi</sup>CD44<sup>lo</sup> cells were sorted by FACS as described<sup>8</sup>. Naive CD4<sup>+</sup> T cells were activated with plate-bound 2  $\mu$ g ml<sup>-1</sup> anti-CD3 and 2  $\mu$ g ml<sup>-1</sup>

anti-CD28 and 50 U ml<sup>-1</sup> IL-2 in the presence of 30 ng ml<sup>-1</sup> IL-6 (Peprotech), 80 ng ml<sup>-1</sup> IL-21, 50 ng ml<sup>-1</sup> IL-23 (R&D Systems), 2.5 ng ml<sup>-1</sup> TGF- $\beta$  (Peprotech), 10  $\mu$ g ml<sup>-1</sup> anti-IL-4 (11B11), 10  $\mu$ g ml<sup>-1</sup> anti-IFN- $\gamma$  (XMG 1.2), 10 ng ml<sup>-1</sup> tumour necrosis factor- $\alpha$  or 10 ng ml<sup>-1</sup> IL-1 $\beta$ , or a combination of these stimuli. Four to five days after activation, cells were washed and re-stimulated with TPA and ionomycin in the presence of Golgi-stop for 5 h, after which IL-17- and IFN- $\gamma$ -producing cells were analysed by intracellular staining. Intracellular staining for Foxp3 was performed by using a Foxp3 staining kit (eBioscience). Lymphocytes were isolated from small intestine lamina propria as described previously<sup>28</sup> and re-stimulated with TPA and ionomycin in the presence of Golgi-stop for 5 h, after which IL-17-producing cells were analysed by intracellular staining.

**Quantitative real-time PCR.** Total RNA was prepared from T cells with the use of TriZol reagent (Invitrogen). cDNAs were synthesized with Superscript reverse transcriptase and oligo(dT) primers (Invitrogen) and gene expression was examined with a Bio-Rad iCycler Optical System using a iQ SYBR green real-time PCR kit (Bio-Rad). The data were normalized to a  $\beta$ -actin reference. The following primer pair for IL-21 was used: forward, 5'-TCATCATTGACCTCGTGGCCC-3', reverse, 5'-ATCGTACTTCTCCACTTGCAATCCC-3'. The primers for genes encoding IL-17, IL-17F, IL-23R, ROR- $\gamma$ , IL-22, T-bet, Foxp3 and  $\beta$ -actin were as described previously<sup>8</sup>.

**Induction of EAE.** For the induction of EAE, female mice were immunized with the MOG peptide emulsified in CFA. Mice were immunized subcutaneously at the dorsal flanks with 150  $\mu$ g of MOG peptide in CFA on days 0 and 7. Pertussis toxin was given intraperitoneally on days 1 and 8 with a dose of 500 ng per mouse. Signs of EAE were assigned scores on a scale of 1–5 as follows: 0, none; 1, limp tail or waddling gait with tail tonic; 2, wobbly gait; 3, hindlimb paralysis; 4, hindlimb and forelimb paralysis; 5, death. Disease scores from three independent experiments (WT,  $n$  = 6 mice; *Il21*<sup>+/-</sup>,  $n$  = 17 mice; *Il21*<sup>-/-</sup>,  $n$  = 9 mice) were combined.  $P$  values were calculated with the Mann–Whitney  $U$ -test by comparing the disease scores of WT and *Il21*<sup>-/-</sup> mice and *Il21*<sup>+/-</sup> and *Il21*<sup>-/-</sup> mice. To analyse central nervous system infiltrates, both brain and spinal cord were collected from perfused mice and mononuclear cells were prepared with a Percoll gradient.



## LETTERS

# IL-21 initiates an alternative pathway to induce proinflammatory T<sub>H</sub>17 cells

Thomas Korn<sup>1\*</sup>, Estelle Bettelli<sup>1\*</sup>, Wenda Gao<sup>2\*</sup>, Amit Awasthi<sup>3</sup>, Anneli Jäger<sup>1</sup>, Terry B. Strom<sup>2</sup>, Mohamed Oukka<sup>3</sup> & Vijay K. Kuchroo<sup>1</sup>

On activation, naive T cells differentiate into effector T-cell subsets with specific cytokine phenotypes and specialized effector functions<sup>1</sup>. Recently a subset of T cells, distinct from T helper (T<sub>H</sub>)1 and T<sub>H</sub>2 cells, producing interleukin (IL)-17 (T<sub>H</sub>17) was defined and seems to have a crucial role in mediating autoimmunity and inducing tissue inflammation<sup>2–5</sup>. We and others have shown that transforming growth factor (TGF)- $\beta$  and IL-6 together induce the differentiation of T<sub>H</sub>17 cells, in which IL-6 has a pivotal function in dictating whether T cells differentiate into Foxp3<sup>+</sup> regulatory T cells (T<sub>reg</sub> cells) or T<sub>H</sub>17 cells<sup>6–9</sup>. Whereas TGF- $\beta$  induces Foxp3 and generates T<sub>reg</sub> cells, IL-6 inhibits the generation of T<sub>reg</sub> cells and induces the production of IL-17, suggesting a reciprocal developmental pathway for T<sub>H</sub>17 and T<sub>reg</sub> cells. Here we show that IL-6-deficient (*Il6*<sup>-/-</sup>) mice do not develop a T<sub>H</sub>17 response and their peripheral repertoire is dominated by Foxp3<sup>+</sup> T<sub>reg</sub> cells. However, deletion of T<sub>reg</sub> cells leads to the reappearance of T<sub>H</sub>17 cells in *Il6*<sup>-/-</sup> mice, suggesting an additional pathway by which T<sub>H</sub>17 cells might be generated *in vivo*. We show that an IL-2 cytokine family member, IL-21, cooperates with TGF- $\beta$  to induce T<sub>H</sub>17 cells in naive *Il6*<sup>-/-</sup> T cells and that IL-21-receptor-deficient T cells are defective in generating a T<sub>H</sub>17 response.

We previously proposed a reciprocal relationship between T<sub>H</sub>17 and T<sub>reg</sub> cells and suggested that IL-6 is pivotal in determining whether an immune response is dominated by T<sub>H</sub>17 or T<sub>reg</sub> cells<sup>9,10</sup>. We predicted that *Il6*<sup>-/-</sup> mice would not develop a T<sub>H</sub>17 response and should have high numbers of CD4<sup>+</sup>CD25<sup>+</sup>Foxp3<sup>+</sup> T<sub>reg</sub> cells in the peripheral repertoire. Thus, we crossed *Il6*<sup>-/-</sup> mice with *Foxp3gfp* 'knock-in' (*Foxp3gfp.KI*) mice<sup>9,11</sup> and analysed the presence of T<sub>reg</sub> versus T<sub>H</sub>17 cells in *Il6*<sup>-/-</sup>  $\times$  *Foxp3gfp.KI* mice after immunization with the encephalitogenic myelin oligodendrocyte glycoprotein 35–55 (MOG<sub>35–55</sub>) peptide emulsified in complete Freund's adjuvant (CFA). We and others have shown previously that *Il6*<sup>-/-</sup> mice are resistant to the development of experimental autoimmune encephalomyelitis (EAE)<sup>9,12–15</sup>. However, the cellular or molecular basis for this resistance was unclear although some studies suggested that *Il6*<sup>-/-</sup> mice might have a defect in T-cell priming<sup>12,13,16</sup>. On immunization, *Il6*<sup>-/-</sup>  $\times$  *Foxp3gfp.KI* mice mounted an attenuated T-cell response with a defect in the generation of T<sub>H</sub>17 cells (Fig. 1a). We found that *Il6*<sup>-/-</sup>  $\times$  *Foxp3gfp.KI* mice had a significantly elevated fraction of Foxp3<sup>+</sup> T<sub>reg</sub> cells in the draining lymph nodes (Fig. 1b). Thus, the 'impaired priming' of antigen-specific T-cell responses reported in *Il6*<sup>-/-</sup> mice could simply be due to the expansion of T<sub>reg</sub> cells at the expense of effector T cells in an environment that is devoid of IL-6. We therefore used MOG<sub>35–55</sub>/IA<sup>b</sup> (MHC class II) tetramers to analyse the frequency of antigen-specific (tetramer<sup>+</sup>) effector T cells (Foxp3/GFP<sup>-</sup>) and T<sub>reg</sub> cells (Foxp3/GFP<sup>+</sup>). In

contrast with wild-type mice, *Il6*<sup>-/-</sup> mice had more MOG-specific T<sub>reg</sub> cells than effector T cells and the ratio of antigen-specific T<sub>reg</sub> to effector T cells was reversed (Fig. 1c, d). Thus, the lack of IL-6 favoured the generation or expansion of antigen-specific T<sub>reg</sub> cells and inhibited the development of effector T-cell responses. These data are consistent with our hypothesis that IL-6 is crucial in dictating the balance between effector T cells and T<sub>reg</sub> cells.

The deletion of T<sub>reg</sub> cells from the peripheral repertoire of *Il6*<sup>-/-</sup> mice should therefore result in T-cell priming and induction of autoimmunity dominated by interferon (IFN)- $\gamma$ -producing T<sub>H</sub>1 cells but

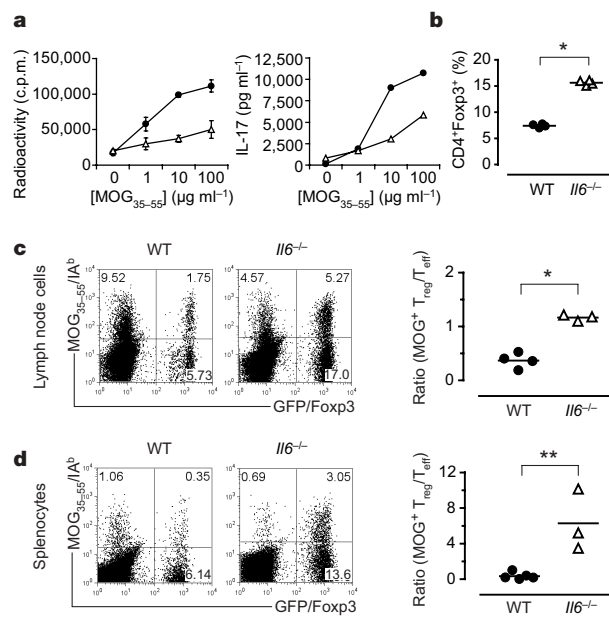


**Figure 1 | In the absence of IL-6, antigen-specific Foxp3<sup>+</sup> T<sub>reg</sub> cells expand at the expense of effector T cells (T<sub>eff</sub> cells) *in vivo*.** *Foxp3gfp.KI* (filled circles) or *Il6*<sup>-/-</sup>  $\times$  *Foxp3gfp.KI* (*Il6*<sup>-/-</sup>; open triangles) mice were immunized with MOG<sub>35–55</sub>/CFA. **a**, Draining lymph-node cells were tested for MOG-specific proliferation and IL-17 production (means  $\pm$  s.d. for triplicate determinations). **b**, The fraction of Foxp3/GFP<sup>+</sup> T cells was determined *ex vivo* by flow cytometry (asterisk,  $P < 6 \times 10^{-2}$ ; *t*-test). WT, wild type. **c**, **d**, Lymph-node cells (**c**) and splenocytes (**d**) from MOG<sub>35–55</sub>/CFA-immunized WT and *Il6*<sup>-/-</sup> mice were cultured for four days in the presence of MOG<sub>35–55</sub> and stained with a MOG<sub>35–55</sub>/IA<sup>b</sup> tetramer. The ratios of antigen-specific T<sub>reg</sub> cells (MOG tetramer<sup>+</sup>CD4<sup>+</sup>Foxp3<sup>+</sup>) to T<sub>eff</sub> (MOG tetramer<sup>+</sup>CD4<sup>+</sup>Foxp3<sup>-</sup>) cells are presented (asterisk,  $P < 0.0003$ ; two asterisks,  $P < 0.05$ ; *t*-test).

<sup>1</sup>Center for Neurologic Diseases, Brigham and Women's Hospital, Harvard Medical School, Boston, Massachusetts 02115, USA. <sup>2</sup>Transplant Research Center, Beth Israel Deaconess Medical Center, Harvard Medical School, Boston, Massachusetts 02115, USA. <sup>3</sup>Center for Neurologic Diseases, Brigham and Women's Hospital, Harvard Medical School, 65 Landsdowne Street, Cambridge, Massachusetts 02139, USA.

\*These authors contributed equally to this work.

not  $T_H17$  cells. We depleted  $T_{reg}$  cells in  $Il6^{-/-}$  mice by using a monoclonal antibody against CD25 (which led to more than 50% depletion of  $Foxp3^{+}$   $T_{reg}$  cells; Supplementary Fig. 1) and then immunized with MOG<sub>35–55</sub>/CFA. As predicted and in contrast with untreated  $Il6^{-/-}$  mice,  $T_{reg}$ -depleted  $Il6^{-/-}$  mice became susceptible to EAE (Fig. 2a, b and Table 1). However, cytokine analysis by enzyme-linked immunosorbent assay (ELISA) and intracellular cytokine staining of  $CD4^{+}$  T cells from  $T_{reg}$ -depleted  $Il6^{-/-}$  mice yielded a reappearance of  $T_H17$

cells (Fig. 2c, d). IL-17 production in  $T_{reg}$ -depleted  $Il6^{-/-}$  mice reached almost wild-type levels, suggesting that  $T_H17$  cells can be generated *in vivo* in the absence of IL-6. After confirming that  $Il6^{-/-}$  mice did not produce residual amounts of IL-6 (Supplementary Fig. 2), we reasoned that there might be an alternative pathway that induces  $T_H17$  cells in the absence of IL-6.

Our previous studies suggested a reciprocal relationship between  $T_{reg}$  and  $T_H17$  cells<sup>9</sup>. Using this logic, we screened several cytokines to identify possible candidates that could substitute for IL-6. We first tested those cytokines that were able to suppress the TGF- $\beta$ -mediated induction of Foxp3 in sorted naive Foxp3/GFP<sup>+</sup> T cells derived from *Foxp3gfp*.K1 mice. As well as IL-6, the IL-12 family member IL-27 and the IL-2 family member IL-21 were most efficient in inhibiting TGF- $\beta$ -driven Foxp3 induction (Fig. 3a, b, and Supplementary Fig. 3). Our analysis confirmed previous results<sup>17,18</sup> showing that IL-27 did not induce the differentiation of  $T_H17$  cells when combined with TGF- $\beta$ . In contrast, IL-21 in combination with TGF- $\beta$  not only suppressed Foxp3 expression but also induced IL-17 production from naive T cells, although not as strongly as TGF- $\beta$  plus IL-6 (Fig. 3b, c). Retinoic acid receptor-related orphan receptor (ROR)- $\gamma$ t has been shown to be a transcription factor involved in the differentiation of  $T_H17$  cells<sup>19</sup>, and TGF- $\beta$  plus IL-21 also induced ROR- $\gamma$ t expression in differentiating  $T_H17$  cells (Fig. 3d). Thus, IL-21 could substitute for IL-6 in the induction of ROR- $\gamma$ t and IL-17, indicating that in addition to IL-6, IL-21 might cooperate with TGF- $\beta$  to drive the differentiation of  $T_H17$  cells.

To test whether IL-21 was responsible for the induction of IL-17 from naive T cells that do not produce IL-6, we compared the differentiation of naive wild-type and  $Il6^{-/-}$  T cells *in vitro* in the presence of TGF- $\beta$  plus IL-21 or TGF- $\beta$  plus IL-6. TGF- $\beta$  plus IL-21 was sufficient to drive  $Il6^{-/-}$  T cells into the  $T_H17$  pathway, although less efficiently than for wild-type T cells (Fig. 4a). Thus, in an IL-6-deficient environment, TGF- $\beta$  plus IL-21 could act independently of IL-6 to induce  $T_H17$  cells. However, the frequency of  $T_H17$  cells induced by TGF- $\beta$  plus IL-21 was consistently lower than that of the induction of  $T_H17$  cells driven by TGF- $\beta$  plus IL-6.

Next we evaluated whether IL-21 was involved in the induction of  $T_H17$  differentiation under 'standard' differentiation conditions of IL-6 plus TGF- $\beta$  and whether the two cytokines (IL-6 and IL-21) cooperated to induce  $T_H17$  cells. T cells activated in the presence of IL-6 alone or in combination with TGF- $\beta$  expressed IL-21 (Fig. 4b). Furthermore, of all  $CD4^{+}$  T-cell subsets,  $T_H17$  cells were the highest producers of IL-21 (Fig. 4b). This suggested that there might be an amplification loop in which IL-21 produced by  $T_H17$  cells participates in enhancing further differentiation of  $T_H17$  cells. We therefore compared the induction of  $T_H17$  cells by TGF- $\beta$  plus IL-6 in wild-type and  $Il21r^{-/-}$  T cells<sup>20</sup>. When IL-6 and TGF- $\beta$  were used to drive the differentiation of  $T_H17$  cells, the frequency of  $T_H17$  cells induced in  $Il21r^{-/-}$   $CD4^{+}$  T cells was half that of wild-type T cells (Fig. 4c), suggesting that IL-21 might normally contribute to  $T_H17$  differentiation mediated by TGF- $\beta$  plus IL-6. If these *in vitro* data were accurate, the  $T_H17$  response in  $Il21r^{-/-}$  mice should be deficient. We found that the fraction of  $CD4^{+}$   $CD44^{hi}$  IL-17<sup>+</sup> T cells was significantly reduced in  $Il21r^{-/-}$  mice in comparison with wild-type controls (data not shown), and this difference was also observed when  $CD44^{hi}$  T cells were activated *in vitro* (Fig. 4d, e). Notably, the addition of recombinant IL-23 could not compensate

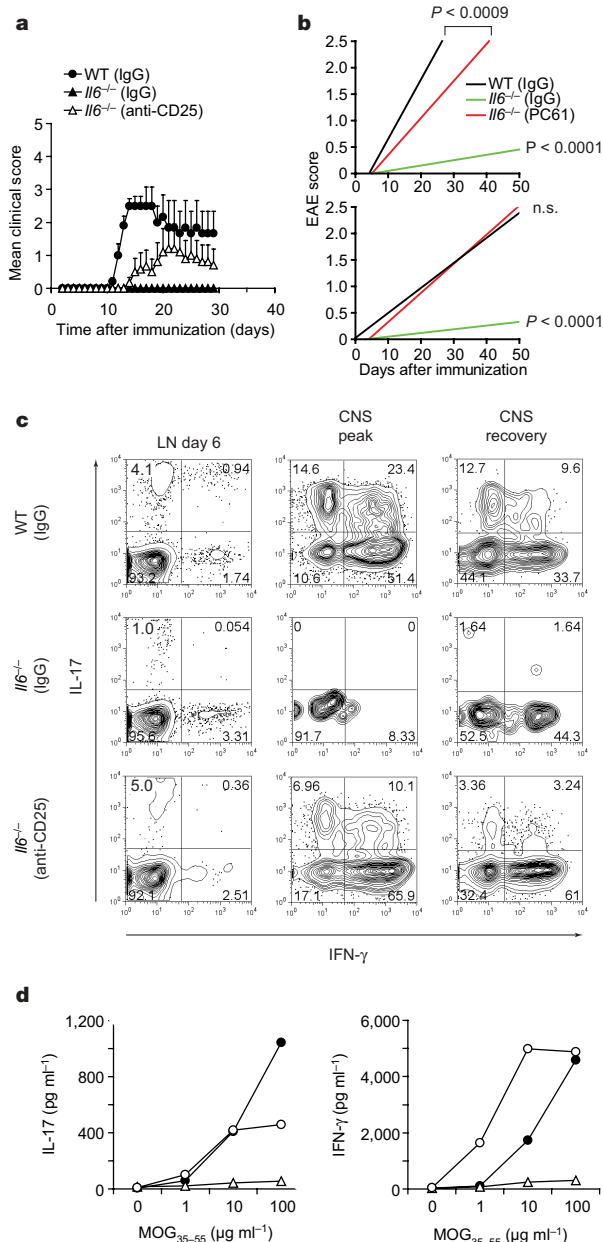


**Figure 2 | Depletion of  $T_{reg}$  cells in  $Il6^{-/-}$  mice restores the development of  $T_H17$  cells and susceptibility to EAE.**  $Il6^{-/-} \times Foxp3gfp$ .K1 mice were treated with antibody against CD25 to deplete  $T_{reg}$  cells or with a control immunoglobulin (rat IgG1) and then immunized with MOG<sub>35–55</sub>/CFA. **a**, **b**, Clinical EAE scores (means and s.e.m.) (**a**) and linear regression analysis in acute (**b**, top) and chronic (**b**, bottom) stages of the disease for wild-type (WT), control  $Il6^{-/-}$  and  $T_{reg}$ -depleted  $Il6^{-/-}$  mice (n.s., not significant). **c**, Lymph-node (LN) cells and mononuclear cells from the central nervous system (CNS) were recovered on days 6, 14–17 (peak disease) and 29 (recovery) and stained for CD4 and intracellular IL-17 and IFN- $\gamma$ . The numbers in the quadrants show percentages. **d**, Splenocytes (day 10) were stimulated with MOG<sub>35–55</sub> *in vitro*. Culture supernatants were collected after 48 h, and IL-17 and IFN- $\gamma$  concentrations were determined. Filled circles, WT (IgG); open triangles,  $Il6^{-/-}$  (IgG); open circles,  $Il6^{-/-}$  (anti-CD25).

**Table 1 | EAE in wild-type and  $Il6^{-/-}$  mice**

Group	Incidence	Mean day of onset (mean $\pm$ s.d.)	Mean maximum score (mean $\pm$ s.d.)
Wild type (IgG)	11 of 13 (85%)	12.4 $\pm$ 1.0*	2.5 $\pm$ 0.7‡
$Il6^{-/-}$ (IgG)	2 of 7 (29%)	16.5 $\pm$ 3.5†	1.0 $\pm$ 0§
$Il6^{-/-}$ (anti-CD25)	6 of 11 (55%)	14.5 $\pm$ 1.9*†	2.9 $\pm$ 0.5‡§

Mice treated with rat IgG1 (control) or monoclonal antibody against CD25 (PC61) were immunized with MOG<sub>35–55</sub> peptide emulsified in complete Freund's adjuvant. The animals were monitored for EAE development. Statistical analysis was performed by comparing groups using one-way analysis of variance. \* $P < 0.008$ . †Not significant. ‡Not significant (mean maximum score of wild-type (IgG) versus  $Il6^{-/-}$  (anti-CD25)). § $P < 0.002$  (mean maximum score of  $Il6^{-/-}$  (IgG) versus  $Il6^{-/-}$  (anti-CD25)).

for the defective  $T_H17$  response observed in  $CD44^+ Il21r^{-/-}$  T cells (Fig. 4d, e). On immunization,  $Il21r^{-/-}$  mice showed no appreciable defect in T-cell proliferation but a marked decrease in their ability to generate a  $T_H17$  response, whereas the production of IFN- $\gamma$  seemed to be increased (Fig. 4f). These data suggest that IL-21 produced by differentiated  $T_H17$  cells must have a function in amplifying  $T_H17$  differentiation such that in the absence of IL-21 signalling, the  $T_H17$  response is compromised. Whereas IL-6 is predominantly produced by cells of the innate immune system, IL-21 is produced mainly by the adaptive immune system, and activated T cells are the main source of IL-21 (Supplementary Fig. 4). We therefore speculate that TGF- $\beta$  and IL-6 together initiate the differentiation of  $T_H17$  cells, which in turn can produce IL-21 and thus further amplify the  $T_H17$  differentiation process. However, in the absence of IL-6, TGF- $\beta$  together with IL-21 can drive  $T_H17$  differentiation on their own. IL-6 and IL-21 cooperate in  $T_H17$  differentiation, which is further supported by the observation that *in vivo* neutralization of IL-21 in  $T_{reg}$ -depleted  $Il6^{-/-}$  mice essentially abrogated the generation of  $T_H17$  cells (Supplementary Fig. 5). This suggests that IL-6 and IL-21 independently and together must cooperate with TGF- $\beta$  to induce  $T_H17$  differentiation.

In summary, together with TGF- $\beta$ , IL-21 constitutes an additional pathway for the generation of pathogenic  $T_H17$  cells. The induction of IL-17 in naive T cells by a combination of TGF- $\beta$  and IL-21 also

suppresses Foxp3 expression, suggesting that similarly to IL-6, IL-21 is able to regulate the reciprocal developmental pathway of generation of  $T_{reg}$  and  $T_H17$  cells. The importance of the *Idd3* genetic locus, which controls susceptibility to both EAE and type 1 diabetes and regulates the function of  $T_{reg}$  cells<sup>21</sup>, might in part be due to the presence of *Il21* in addition to *Il2* in the *Idd3* interval. IL-21 binds to the IL-21 receptor, which consists of a unique IL-21 receptor

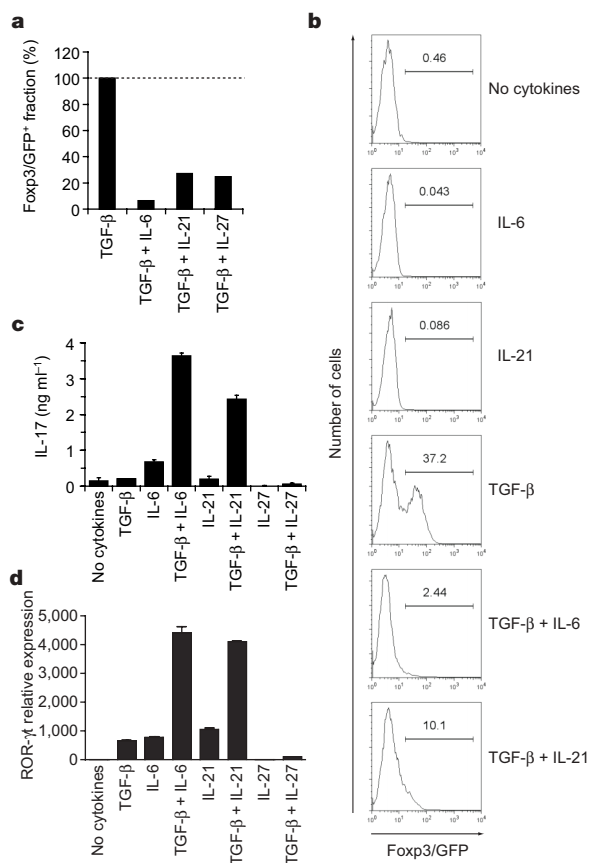


**Figure 3 | Inhibition of induction of  $T_{reg}$  cells and generation of  $T_H17$  cells by IL-21.**  $CD4^+CD62L^{hi}$ Foxp3/GFP<sup>+</sup> T cells from *Foxp3<sup>gfp</sup>*.KI mice were stimulated with anti-CD3 and anti-CD28 for three days in the presence of the indicated cytokines. **a**, The expression of Foxp3/GFP was measured and the fraction of Foxp3<sup>+</sup> cells induced by TGF- $\beta$  was normalized to 100%. **b**, Individual histograms showing Foxp3/GFP expression. The numbers above the histogram regions (horizontal lines) represent the percentages of Foxp3/GFP<sup>+</sup> cells. **c**, IL-17 production in these cultures after 48 h as measured by ELISA. **d**, ROR- $\gamma$ t expression as determined by quantitative RT-PCR in naive 2D2 (ref. 30) T cells activated for 48 h with anti-CD3 in the presence of irradiated syngeneic antigen-presenting cells and the indicated cytokines. ROR- $\gamma$ t expression is shown as mean and s.e.m. for duplicate determinations, relative to  $\beta$ -actin.

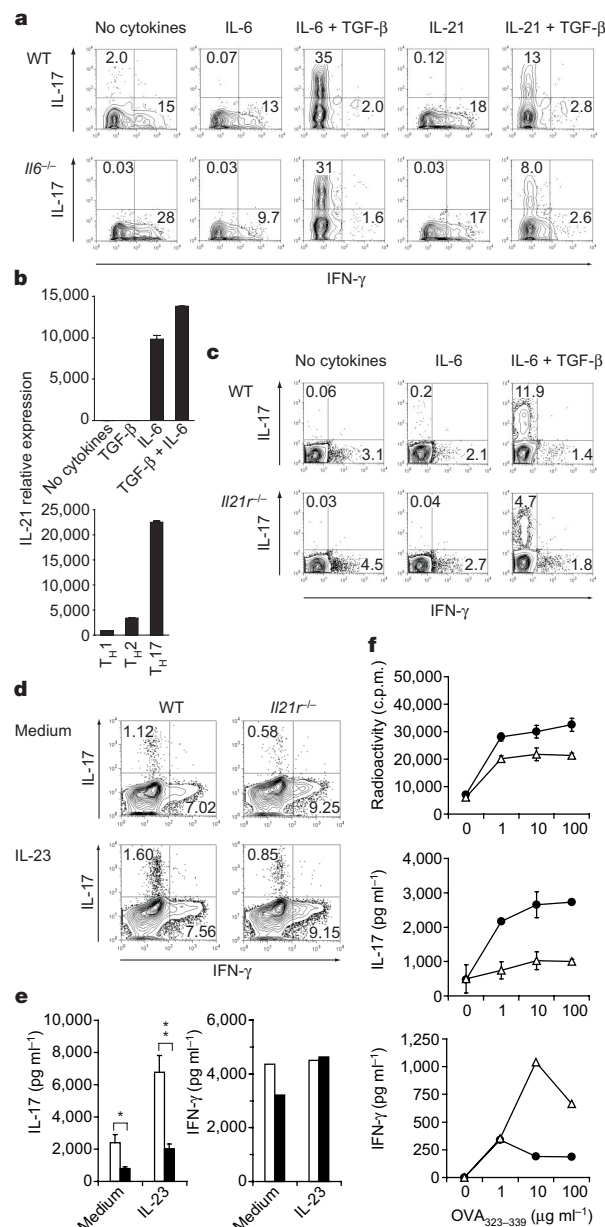


**Figure 4 | IL-21-driven  $T_H17$  differentiation is independent of IL-6.** Naive (a, b), total (c) or  $CD44^+CD4^+$  T cells (d, e) were cultured with anti-CD3 plus corresponding irradiated antigen-presenting cells (a, c) or anti-CD3 plus anti-CD28 (b, d, e) and the indicated cytokines. **a**, **c**, Percentages of IL-17<sup>+</sup> and IFN- $\gamma$ <sup>+</sup> cells in T cells from wild-type (WT) or *Il6*<sup>-/-</sup> mice (a) and WT or *Il21r*<sup>-/-</sup> mice (c) after four days of culture. **b**, IL-21 mRNA was determined by quantitative RT-PCR (means and s.e.m. for duplicate determinations). **d**, **e**,  $CD4^+CD44^+$  T cells from WT or *Il21r*<sup>-/-</sup> mice were stimulated with or without recombinant IL-23 for 48 h. IL-17 and IFN- $\gamma$  production were determined by intracellular cytokine staining (d) and ELISA (e; open columns, WT; filled columns, *Il21r*<sup>-/-</sup>) (asterisk,  $P < 0.0005$ ; two asterisks,  $P < 0.003$ ;  $t$ -test). **f**, WT (filled circles) and *Il21r*<sup>-/-</sup> (open triangles) mice were immunized with ovalbumin 323–339 peptide (OVA<sub>323-339</sub>)/CFA. Draining lymph-node cells were assayed for antigen-specific proliferation and cytokine production (means and s.d. for triplicate cultures).



subunit and the common cytokine receptor  $\gamma$ -chain shared by other cytokine receptors including the receptors for IL-2, IL-4, IL-7, IL-9 and IL-15 (ref. 22). In contrast to these cytokines, binding of IL-21 to its receptor preferentially activates the downstream signalling molecules STAT1 and STAT3 (ref. 23). Because STAT3 is an important signalling molecule in  $T_H17$  differentiation<sup>24</sup>, it is likely that IL-21-induced activation of STAT3, like IL-6-induced activation of STAT3, cooperates with TGF- $\beta$  signalling to induce the transcription factor ROR- $\gamma$ t and drive  $T_H17$  differentiation.

Because differentiated  $T_H17$  cells may be the most robust producers of IL-21, we propose that the ability of  $T_H17$  cells to produce IL-21 further amplifies the  $T_H17$  response. This reverberating pathway is similar to the mechanism in which IL-4 produced by  $T_H2$  cells promotes  $T_H2$  differentiation<sup>25,26</sup>. However,  $T_H17$  responses also seem to be tightly counter-regulated in that IL-27, an IL-12 family member produced by cells of the innate immune system, and IL-25, an IL-17 family member produced by the innate immune system and activated T cells, can dampen and eventually shut off  $T_H17$  responses<sup>17,18,27</sup>. We suggest that enhanced autoimmunity observed in mice injected with exogenous IL-21 (ref. 28) might be partly due to increased differentiation of  $T_H17$  cells and suppression of  $T_{reg}$  generation *in vivo*. Targeting IL-21 in autoimmune diseases may therefore readjust the balance between pathogenic  $T_H17$  and Foxp3<sup>+</sup>  $T_{reg}$  cells, which is believed to be defective in human autoimmune diseases.

## METHODS SUMMARY

**Mice and reagents.** *Foxp3gfp*.KI mice have been described<sup>9</sup>. *Il21r*<sup>-/-</sup> mice on the Balb/c background<sup>20</sup> were obtained from M. Grusby. IL-6-deficient mice and wild-type C57BL/6 and Balb/c mice were obtained from Jackson Laboratories. EAE induction and analysis, isolation of mononuclear cells from the central nervous system as well as the generation of MOG<sub>35–55</sub>/IA<sup>b</sup> tetramers and IL-21R-Ig are described in Methods.

***In vitro* T-cell proliferation and measurement of cytokines.** Proliferation was determined by incorporation of [<sup>3</sup>H]thymidine. Cytokines were measured by ELISA, cytometric bead array (BD Biosciences) or fluorescent bead assay (Luminex). Intracellular cytokine staining and isolation of mRNA for determination of cytokine expression by real-time polymerase chain reaction (PCR) were performed after stimulation with 12-*O*-tetradecanoylphorbol-13-acetate/ionomycin (see Methods).

**T-cell differentiation *in vitro*.** Naive CD4<sup>+</sup> T cells (CD4<sup>+</sup>CD62L<sup>hi</sup> or CD4<sup>+</sup>CD62L<sup>hi</sup>Foxp3/GFP<sup>-</sup>) were purified by fluorescence-activated cell sorting and stimulated for three days with plate-bound antibody against CD3 (145-2C11, 4  $\mu$ g ml<sup>-1</sup>) plus soluble antibody against CD28 (PV-1, 2  $\mu$ g ml<sup>-1</sup>) or by soluble anti-CD3 (2  $\mu$ g ml<sup>-1</sup>) plus irradiated syngeneic splenocytes as antigen-presenting cells and recombinant cytokines: human TGF- $\beta$ 1 (3 ng ml<sup>-1</sup>), mouse IL-6 (30 ng ml<sup>-1</sup>), mouse IL-21 (100 ng ml<sup>-1</sup>) or mouse IL-27 (25 ng ml<sup>-1</sup>; all from R&D Systems). Blocking of IL-21 activity *in vitro* was performed by the addition of a goat anti-mouse IL-21 antibody (25  $\mu$ g ml<sup>-1</sup>; R&D Systems) or by IL-21R-Ig (100  $\mu$ g ml<sup>-1</sup>). Polarization of T cells into  $T_H1$ ,  $T_H2$  or  $T_H17$  cells was performed by solid-phase anti-CD3 (4  $\mu$ g ml<sup>-1</sup>) and soluble anti-CD28 (2  $\mu$ g ml<sup>-1</sup>) in the presence of recombinant mouse IL-12 (10 ng ml<sup>-1</sup>; R&D Systems) plus anti-IL-4 (11B.11; 10  $\mu$ g ml<sup>-1</sup>) for  $T_H1$ , mouse IL-4 (10 ng ml<sup>-1</sup>; R&D Systems) plus anti-IL-12 (C17.8; 10  $\mu$ g ml<sup>-1</sup>) for  $T_H2$ , and TGF- $\beta$  plus IL-6 for  $T_H17$ . Monoclonal antibodies against mouse CD3, mouse CD28, mouse IL-4 and mouse IL-12 were purified from the supernatants of hybridomas obtained from the American Type Culture Collection (ATCC).

**Full Methods** and any associated references are available in the online version of the paper at [www.nature.com/nature](http://www.nature.com/nature).

Received 26 March; accepted 4 June 2007.

Published online 20 June 2007.

- Abbas, A. K., Murphy, K. M. & Sher, A. Functional diversity of helper T lymphocytes. *Nature* **383**, 787–793 (1996).
- Cua, D. J. *et al.* Interleukin-23 rather than interleukin-12 is the critical cytokine for autoimmune inflammation of the brain. *Nature* **421**, 744–748 (2003).
- Langrish, C. L. *et al.* IL-23 drives a pathogenic T cell population that induces autoimmune inflammation. *J. Exp. Med.* **201**, 233–240 (2005).
- Weaver, C. T., Hatton, R. D., Mangan, P. R. & Harrington, L. E. IL-17 family cytokines and the expanding diversity of effector T cell lineages. *Annu. Rev. Immunol.* **25**, 821–852 (2007).

- Steinman, L. A brief history of  $T_H17$ , the first major revision in the  $T_H1/T_H2$  hypothesis of T cell-mediated tissue damage. *Nature Med.* **13**, 139–145 (2007).
- Veldhoen, M., Hocking, R. J., Atkins, C. J., Locksley, R. M. & Stockinger, B. TGF $\beta$  in the context of an inflammatory cytokine milieu supports *de novo* differentiation of IL-17-producing T cells. *Immunity* **24**, 179–189 (2006).
- Veldhoen, M., Hocking, R. J., Flavell, R. A. & Stockinger, B. Signals mediated by transforming growth factor- $\beta$  initiate autoimmune encephalomyelitis, but chronic inflammation is needed to sustain disease. *Nature Immunol.* **7**, 1151–1156 (2006).
- Mangan, P. R. *et al.* Transforming growth factor- $\beta$  induces development of the  $T_H17$  lineage. *Nature* **441**, 231–234 (2006).
- Bettelli, E. *et al.* Reciprocal developmental pathways for the generation of pathogenic effector  $T_H17$  and regulatory T cells. *Nature* **441**, 235–238 (2006).
- Bettelli, E., Oukka, M. & Kuchroo, V. K.  $T_H17$  cells in the circle of immunity and autoimmunity. *Nature Immunol.* **8**, 345–350 (2007).
- Korn, T. *et al.* Myelin-specific regulatory T cells accumulate in the CNS but fail to control autoimmune inflammation. *Nature Med.* **13**, 423–431 (2007).
- Samoilova, E. B., Horton, J. L., Hilliard, B., Liu, T. S. & Chen, Y. IL-6-deficient mice are resistant to experimental autoimmune encephalomyelitis: roles of IL-6 in the activation and differentiation of autoreactive T cells. *J. Immunol.* **161**, 6480–6486 (1998).
- Okuda, Y. *et al.* IL-6-deficient mice are resistant to the induction of experimental autoimmune encephalomyelitis provoked by myelin oligodendrocyte glycoprotein. *Int. Immunol.* **10**, 703–708 (1998).
- Mendel, I., Katz, A., Kozak, N., Ben-Nun, A. & Revel, M. Interleukin-6 functions in autoimmune encephalomyelitis: a study in gene-targeted mice. *Eur. J. Immunol.* **28**, 1727–1737 (1998).
- Eugster, H. P., Frei, K., Kopf, M., Lassmann, H. & Fontana, A. IL-6-deficient mice resist myelin oligodendrocyte glycoprotein-induced autoimmune encephalomyelitis. *Eur. J. Immunol.* **28**, 2178–2187 (1998).
- Okuda, Y. *et al.* IL-6 plays a crucial role in the induction phase of myelin oligodendrocyte glycoprotein 35–55 induced experimental autoimmune encephalomyelitis. *J. Neuroimmunol.* **101**, 188–196 (1999).
- Batten, M. *et al.* Interleukin 27 limits autoimmune encephalomyelitis by suppressing the development of interleukin 17-producing T cells. *Nature Immunol.* **7**, 929–936 (2006).
- Stumhofer, J. S. *et al.* Interleukin 27 negatively regulates the development of interleukin 17-producing T helper cells during chronic inflammation of the central nervous system. *Nature Immunol.* **7**, 937–945 (2006).
- Ivanov, I. I. *et al.* The orphan nuclear receptor ROR $\gamma$ t directs the differentiation program of proinflammatory IL-17<sup>+</sup> T helper cells. *Cell* **126**, 1121–1133 (2006).
- Kasaian, M. T. *et al.* IL-21 limits NK cell responses and promotes antigen-specific T cell activation: a mediator of the transition from innate to adaptive immunity. *Immunity* **16**, 559–569 (2002).
- Yamanouchi, J. *et al.* Interleukin-2 gene variation impairs regulatory T cell function and causes autoimmunity. *Nature Genet.* **39**, 329–337 (2007).
- Leonard, W. J. & Spolski, R. Interleukin-21: a modulator of lymphoid proliferation, apoptosis and differentiation. *Nature Rev. Immunol.* **5**, 688–698 (2005).
- Zeng, R. *et al.* The molecular basis of IL-21-mediated proliferation. *Blood* **109**, 4135–4142 (2007).
- Yang, X. O. *et al.* STAT3 regulates cytokine-mediated generation of inflammatory helper T cells. *J. Biol. Chem.* **282**, 9358–9363 (2007).
- Murphy, E. *et al.* Reversibility of T helper 1 and 2 populations is lost after long-term stimulation. *J. Exp. Med.* **183**, 901–913 (1996).
- Nakamura, T., Kamogawa, Y., Bottomly, K. & Flavell, R. A. Polarization of IL-4- and IFN- $\gamma$ -producing CD4<sup>+</sup> T cells following activation of naive CD4<sup>+</sup> T cells. *J. Immunol.* **158**, 1085–1094 (1997).
- Kleinschek, M. A. *et al.* IL-25 regulates Th17 function in autoimmune inflammation. *J. Exp. Med.* **204**, 161–170 (2007).
- Vollmer, T. L. *et al.* Differential effects of IL-21 during initiation and progression of autoimmunity against neuroantigen. *J. Immunol.* **174**, 2696–2701 (2005).
- Reddy, J. *et al.* Detection of autoreactive myelin proteolipid protein 139–151-specific T cells by using MHC II (IAs) tetramers. *J. Immunol.* **170**, 870–877 (2003).
- Bettelli, E. *et al.* Myelin oligodendrocyte glycoprotein-specific T cell receptor transgenic mice develop spontaneous autoimmune optic neuritis. *J. Exp. Med.* **197**, 1073–1081 (2003).

**Supplementary Information** is linked to the online version of the paper at [www.nature.com/nature](http://www.nature.com/nature).

**Acknowledgements** We thank M. Collins for providing *Il21r*<sup>-/-</sup> mice, and D. Kozoriz, S. Tente, R. Chandwaskar and D. Lee for cell sorting and technical assistance. This work was supported by grants from the National Multiple Sclerosis Society, the National Institutes of Health, the Juvenile Diabetes Research Foundation Center for Immunological Tolerance at Harvard, and the Deutsche Forschungsgemeinschaft. V.K.K. is the recipient of the Javits Neuroscience Investigator Award from the National Institutes of Health.

**Author Information** Reprints and permissions information is available at [www.nature.com/reprints](http://www.nature.com/reprints). The authors declare no competing financial interests. Correspondence and requests for materials should be addressed to M.O. (moukka@rics.bwh.harvard.edu) or V.K.K. (vkuchroo@rics.bwh.harvard.edu).

## METHODS

**Induction of EAE.** EAE was induced by subcutaneous immunization of mice with 100  $\mu$ l of an emulsion containing 100  $\mu$ g of MOG<sub>35–55</sub> peptide (MEVGWYRSPFSRVVHLYRNGK) and 250  $\mu$ g of *M. tuberculosis* H37 Ra (Difco) in incomplete Freund's adjuvant oil plus an intraperitoneal injection of 200 ng of pertussis toxin (List Biological Laboratories) on days 0 and 2. For T<sub>reg</sub> depletion, animals were injected intraperitoneally with 500  $\mu$ g of monoclonal antibody against CD25 (PC61) on days –5 and –3 before immunization. Clinical signs of EAE were assessed as reported<sup>11</sup>. Linear regression analysis of individual EAE scores was performed for the acute disease phase (until the mean maximum score was reached in each group) and the chronic disease phase (over the complete disease course). Animals were kept in a conventional, pathogen-free facility at the Harvard Institutes of Medicine, and all experiments were performed in accordance with the guidelines prescribed by the standing committee of animals at Harvard Medical School, Boston, Massachusetts.

**Generation of IL-21 receptor-Ig (IL-21R-Ig).** The complementary DNA fragment encoding the extracellular domain (amino acids 20–236) of mouse IL-21R (GenBank accession number NM\_021887) was amplified by PCR from a mouse splenocyte cDNA library. A second cDNA fragment encoding the Fc portion of human IgG4 was cloned by PCR from a human cDNA library from peripheral blood mononuclear cells. The two cDNA fragments were joined in frame by overlapping PCR and subsequently cloned into the mammalian expression vector pSecTag/FRT/V5-His-TOPO (Invitrogen). The ligated construct (1.0  $\mu$ g) was co-transfected with pOG44 (10.0  $\mu$ g; Invitrogen) into the Flp-In CHO cell line (Invitrogen), using GeneJammer transfection reagent (Stratagene), in accordance with the manufacturer's instructions. Transfectants were selected in 800  $\mu$ g ml<sup>–1</sup> hygromycin B, and maintained in UltraCHO (BioWhittaker). IL-21R-Ig was purified from the culture supernatant by passage through a Protein G–Sepharose column. Bound protein was eluted with 100 mM glycine-HCl pH 3.0 and immediately neutralized with 1.25 M Tris-HCl pH 8.8. The eluted protein was concentrated with an UltraFree-4 centrifugal device (Millipore), and the concentration was determined spectrophotometrically. The reagent was tested *in vitro* for its ability to neutralize the activity of IL-21-mediated T<sub>H</sub>17 differentiation.

**Preparation of mononuclear cells from the central nervous system.** After perfusion through the left cardiac ventricle with cold PBS, forebrain and cerebellum were dissected and spinal cords were flushed out with PBS by hydrostatic pressure followed by digestion with collagenase D (2.5 mg ml<sup>–1</sup>; Roche Diagnostics) and DNase I (1 mg ml<sup>–1</sup>; Sigma) at 37 °C for 45 min. Mononuclear cells were isolated by passing the tissue through a cell strainer (70  $\mu$ m mesh) and

Percoll gradient (70%–37%) centrifugation. Mononuclear cells were removed from the interphase, washed and resuspended in culture medium for further analysis.

**In vitro T-cell proliferation.** Draining lymph-node cells or splenocytes were cultured in DMEM/10% FCS supplemented with 50  $\mu$ M 2-mercaptoethanol, 1 mM sodium pyruvate, non-essential amino acids, L-glutamine and 100 U ml<sup>–1</sup> penicillin/100  $\mu$ g ml<sup>–1</sup> streptomycin. For antigen-specific recall cultures, 2.5  $\times$  10<sup>6</sup> lymph-node cells or 5  $\times$  10<sup>6</sup> ml<sup>–1</sup> splenocytes were cultured for three days in the presence of MOG<sub>35–55</sub> or OVA<sub>323–339</sub>. During the last 16 h, cells were pulsed with 1  $\mu$ Ci of [<sup>3</sup>H]thymidine (PerkinElmer). [<sup>3</sup>H]Thymidine incorporation in triplicate wells was measured with a  $\beta$ -counter (1450 MicroBeta Trilux; PerkinElmer).

**Measurement of cytokines.** Cell culture supernatants were collected after 48 h and the secreted cytokines were determined by ELISA (antibodies for IL-17 from BD Biosciences), by cytometric bead array (BD Biosciences) or by fluorescent bead assay (Luminex) for the indicated cytokines, in accordance with the manufacturers' instructions. For quantitative PCR, RNA was extracted from FACS-sorted cells by using RNeasy columns (Qiagen) after 48 h of stimulation *in vitro*. cDNA was transcribed as recommended (Applied Biosystems) and used as a template for quantitative PCR. Primer/probe mixtures for mouse ROR- $\gamma$ t and mouse IL-21 were obtained from Applied Biosystems. The Taqman analysis was performed on the AB 7500 Fast System (Applied Biosystems). Gene expression was normalized to the expression of  $\beta$ -actin.

**Staining with MOG<sub>35–55</sub>/IA<sup>b</sup> tetramers and intracellular cytokine staining.** MOG<sub>35–55</sub>/IA<sup>b</sup> tetramers were generated as reported<sup>11</sup>. The procedure for staining *ex vivo* with MOG<sub>35–55</sub>/IA<sup>b</sup> tetramers has been described in detail previously<sup>29</sup>. In brief, single-cell suspensions were incubated at a density of 10<sup>7</sup> cells ml<sup>–1</sup> with the IA<sup>b</sup> multimers (30  $\mu$ g ml<sup>–1</sup>) in DMEM supplemented with 5  $\mu$ M IL-2 and 2% FCS (pH 8.0) at room temperature for 2.5 h. After being washed, cells were stained with 7-AAD (Molecular Probes) and CD4 (RM4-5; BD Biosciences). The percentage of tetramer<sup>+</sup> cells was determined in the CD4<sup>+</sup> gate of live (7-AAD<sup>–</sup>) cells. To control for non-specific binding, IA<sup>s</sup> control tetramers were used<sup>29</sup>. For intracellular cytokine staining, cells were stimulated for 4 h in culture medium containing 12-O-tetradecanoylphorbol-13-acetate (50 ng ml<sup>–1</sup>; Sigma), ionomycin (1  $\mu$ g ml<sup>–1</sup>; Sigma), and monensin (GolgiStop, 1  $\mu$ l ml<sup>–1</sup>; BD Biosciences) at 37 °C under 10% CO<sub>2</sub>. After staining of surface markers, cells were fixed and permeabilized (Cytofix/Cytoperm and Perm/Wash buffer, BD Biosciences) followed by staining with monoclonal antibodies against mouse IL-17 and IFN- $\gamma$  (BD Biosciences) and fluorocytometric analysis (FACSCalibur).

## LETTERS

# Functional diversification of closely related ARF-GEFs in protein secretion and recycling

Sandra Richter<sup>1</sup>, Niko Geldner<sup>1†</sup>, Jarmo Schrader<sup>1</sup>, Hanno Wolters<sup>1</sup>, York-Dieter Stierhof<sup>2</sup>, Gabino Rios<sup>3†</sup>, Csaba Koncz<sup>3</sup>, David G. Robinson<sup>4</sup> & Gerd Jürgens<sup>1</sup>

Guanine-nucleotide exchange factors on ADP-ribosylation factor GTPases (ARF-GEFs) regulate vesicle formation in time and space by activating ARF substrates on distinct donor membranes<sup>1</sup>. Mammalian GBF1 (ref. 2) and yeast Gea1/2 (ref. 3) ARF-GEFs act at Golgi membranes, regulating COPI-coated vesicle formation. In contrast, their *Arabidopsis thaliana* homologue GNOM (GN) is required for endosomal recycling, playing an important part in development<sup>4</sup>. This difference indicates an evolutionary divergence of trafficking pathways between animals and plants, and raised the question of how endoplasmic reticulum–Golgi transport is regulated in plants. Here we demonstrate that the closest homologue of GNOM in *Arabidopsis*, GNOM-LIKE1 (GNL1; NM\_123312; At5g39500), performs this ancestral function. GNL1 localizes to and acts primarily at Golgi stacks, regulating COPI-coated vesicle formation. Surprisingly, GNOM can functionally substitute for GNL1, but not vice versa. Our results suggest that large ARF-GEFs of the GBF1 class perform a conserved role in endoplasmic reticulum–Golgi trafficking and secretion, which is done by GNL1 and GNOM in *Arabidopsis*, whereas GNOM has evolved to perform an additional plant-specific function of recycling from endosomes to the plasma membrane. Duplication and diversification of ARF-GEFs in plants contrasts with the evolution of entirely new classes of ARF-GEFs<sup>5</sup> for endosomal trafficking in animals, which illustrates the independent evolution of complex endosomal pathways in the two kingdoms.

Large ARF-GEFs are represented by two subfamilies conserved among eukaryotes: the GBF1 clade, including mammalian GBF1, yeast Gea1/2 and *Arabidopsis* GNOM; and the BIG clade, including mammalian BIG1/2, yeast Sec7 and *Arabidopsis* BIG1–5 (refs 5, 6) (Fig. 1a). Whereas GBF1 and Gea1/2 have been localized to the Golgi<sup>2,3,7</sup>, and a double knockout for Gea1/2 is cell-lethal<sup>3,7</sup>, GNOM performs a plant-specific endosomal recycling function important for development but not essential for cell viability<sup>4,8,9</sup>. Large ARF-GEFs are the molecular targets for brefeldin A (BFA), which causes reversible inhibition of vesicle trafficking<sup>4</sup>. BFA traps sensitive ARF-GEFs on the membrane by blocking the guanine-nucleotide exchange reaction<sup>10</sup>. BFA sensitivity or resistance can be engineered by site-directed mutagenesis, without affecting protein function<sup>11</sup>, providing a unique tool to selectively inhibit specific ARF-GEFs to probe their function *in vivo*. This approach revealed that GNOM is involved in endosomal recycling of PIN1, a polarly localized component of auxin efflux carriers<sup>4</sup>. We now extend this approach to identify the ARF-GEF responsible for endoplasmic reticulum (ER)–Golgi trafficking. BFA was shown to cause the release of COPI coats from membranes in mammalian cells<sup>12,13</sup>. In *Arabidopsis*, however, BFA treatment has no effect on Golgi structure

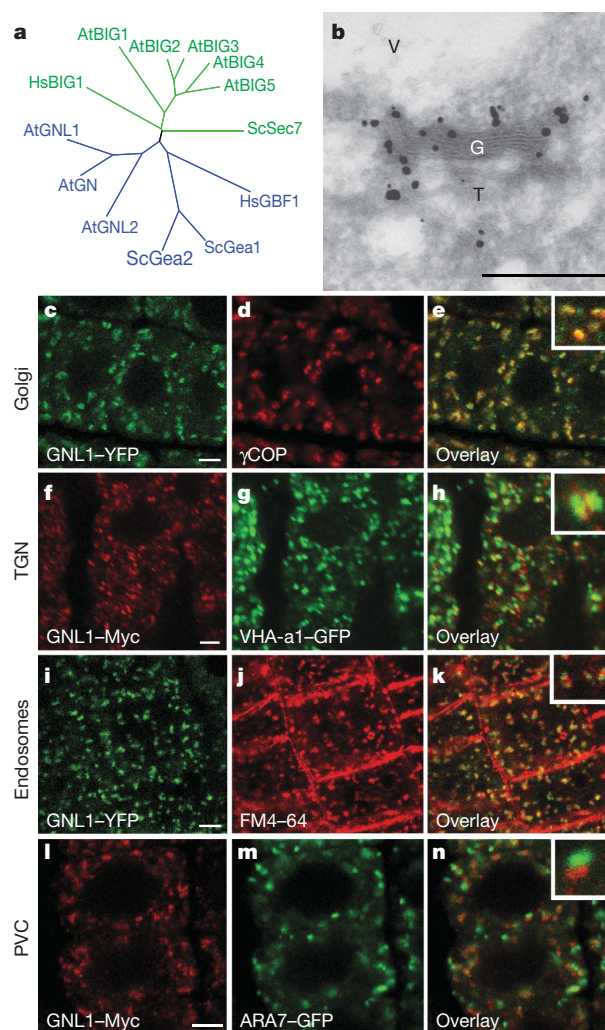


**Figure 1 | Identification of the GNL1 compartment.** **a**, Unrooted phylogenetic tree of large ARF-GEFs from *Arabidopsis* (At), human (Hs) and yeast (Sc). **b**, Immunogold localization of GNL1–YFP on an ultrathin cryosection. G, Golgi; T, TGN; V, vacuole. Scale bar, 500 nm. **c–n**, Immunofluorescence localization of GNL1 and endomembrane markers. Scale bars, 4  $\mu$ m. **c–e**, GNL1–YFP partially colocalizes with Golgi marker  $\gamma$ COP. No colocalization was observed for GNL1–Myc and TGN marker VHA–a1–GFP (**f–h**), GNL1–YFP and endocytic tracer FM4–64 (**i–k**) or GNL1–Myc and prevacuolar compartment marker ARA7–GFP (**l–n**).

<sup>1</sup>ZMBP, Entwicklungsgenetik, and <sup>2</sup>ZMBP, Mikroskopie, Universität Tübingen, Auf der Morgenstelle 3, D-72076 Tübingen, Germany. <sup>3</sup>Max-Planck-Institut für Pflanzengzüchtung, Carl-von-Linné-Weg 10, D-50829 Köln, Germany. <sup>4</sup>Department of Cell Biology, Heidelberg Institute for Plant Sciences, University of Heidelberg, D-69120 Heidelberg, Germany. <sup>†</sup>Present addresses: Salk Institute for Biological Studies, La Jolla, California 92037, USA (N.G.); Departamento Bioquímica y Biología Molecular, Facultad Biología, Universidad de Valencia, E-46100 Burjassot, Spain (G.R.).



or membrane association of the COPI subunit  $\gamma$ COP<sup>4,14</sup>, suggesting that a BFA-resistant ARF-GEF mediates this process. Evident candidates are the two closest homologues of GNOM. We decided to focus on ubiquitously expressed GNOM-LIKE1 (GNL1) because GNL2 seems to be pollen-specific<sup>15</sup> (Supplementary Fig. 2).

To identify the endomembrane compartment at which GNL1 acts, we generated plants expressing functional GNL1-Myc or GNL1-YFP (yellow fluorescent protein). GNL1 was localized relative to compartment-specific markers (Fig. 1; Supplementary Table 1). GNL1 partially co-localized with the Golgi marker  $\gamma$ COP<sup>16</sup> but did not, or only marginally so, with the *trans*-Golgi network (TGN) marker VHA-a1-GFP<sup>17</sup>, which was consistent with the immunogold-localization of GNL1 (Fig. 1b–h; Supplementary Fig. 3f). In contrast, GNL1 did not co-localize with ARA7-GFP labelling endosomes/pre-vacuolar compartments<sup>18,19</sup> nor the endocytic tracer FM4-64 (ref. 4) (Fig. 1i–n). These results suggest a role for GNL1 in Golgi-related trafficking.

BFA treatment of *Arabidopsis* seedlings causes aggregation of endosomal membrane vesicles (so-called BFA compartments), to which GNOM has been localized<sup>4,14</sup>. Predominantly at the periphery of BFA compartments, GNL1 partially co-localized with the Golgi markers  $\gamma$ COP and N-ST-YFP<sup>20</sup>, and also overlapped with VHA-a1-GFP and FM4-64 (Fig. 2a–d; Supplementary Fig. 4). To conditionally inactivate GNL1 by BFA treatment, we introduced an engineered BFA-sensitive GNL1 into a *gnl1* knockout background. This switch to BFA-sensitivity of GNL1 caused a dramatic change in BFA effects. We now observed a release of  $\gamma$ COP into the cytosol and a block in ER–Golgi traffic, as highlighted by the accumulation of the Golgi marker N-ST-YFP in the ER as well as the fusion of Golgi stacks with the ER (Figs 2g, h and 3c, d; Supplementary Fig. 3). Consistently, BFA-sensitive GNL1 localized to the ER but also co-localized with FM4-64 in BFA compartments (Fig. 2f; Supplementary Fig. 5; see Supplementary Fig. 3g and h for immunogold localization of GNL1-YFP). This indicates that GNL1 activity is required for the integrity of Golgi stacks and for COPI-coated vesicle formation. To analyse whether GNL1 might also have another role in trafficking, we studied the membrane association of another major vesicle coat protein, clathrin (Supplementary Fig. 6). In contrast to  $\gamma$ COP, however, clathrin was not released into the cytosol by BFA treatment of BFA-sensitive GNL1, which is consistent with the localization of GNL1 and clathrin to adjacent but distinct compartments (Supplementary Fig. 6a–c, g–i). As a consequence of blocking anterograde traffic of newly synthesized proteins from the ER to the Golgi, the TGN marker VHA-a1-GFP also accumulated at the ER (Fig. 2i). Thus, GNL1 is a major regulator of ER–Golgi trafficking and protein secretion.

If GNL1 has such an important role in membrane traffic one would expect inactivation of the *GNL1* gene to be lethal. We identified a T-DNA insertion knockout line for *GNL1* (Supplementary Fig. 7a). Surprisingly, the *gnl1* mutant plants were viable and fertile—although short and bushy—and pollen competitiveness was reduced to 76% (Fig. 3i). Another strong allele, *gnl1-2*, isolated as a secretion mutant, showed a very similar phenotype (ref. 21; our unpublished

observations). These results indicate that GNL1 is not essential. Consistently, *gnl1* mutant cells displayed slightly abnormal Golgi stacks with cisternae laterally expanded by approximately 35% (Fig. 3a, b; Supplementary Fig. 3i). However, BFA treatment of *gnl1* mutant cells caused fusion of the Golgi with the ER, suggesting

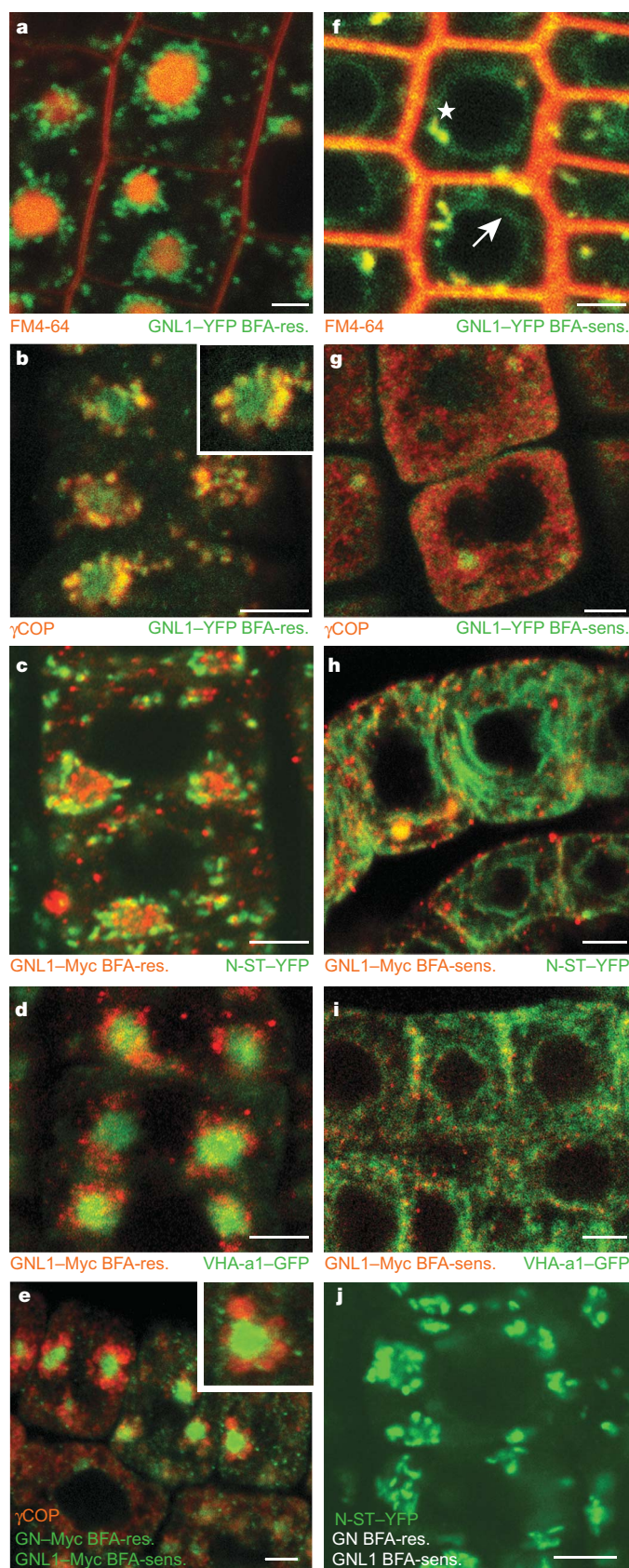


**Figure 2 | Localization of BFA-resistant and BFA-sensitive GNL1 after BFA treatment.** BFA-resistant (a–d) or BFA-sensitive (f–i) GNL1 in *gnl1* mutant background localized relative to compartment markers after BFA-treatment. **a, f**, Endocytic tracer FM4-64 (red) in BFA compartments colocalizes partially with GNL1-YFP and is surrounded by GNL1-YFP aggregates (a), whereas BFA-sensitive GNL1-YFP localizes to ER (arrow) and colocalizes with FM4-64 in small BFA compartments (f, asterisk). **b, g**, Golgi marker  $\gamma$ COP (red) partially overlaps with GNL1-YFP (b) but is released into the cytosol when GNL1-YFP is BFA-sensitive (g). **c, h**, Golgi marker N-ST-YFP (green) colocalizes partially with GNL1-Myc (c) but relocates to the ER when GNL1-Myc is BFA-sensitive (h). **d, i**, TGN marker VHA-a1-GFP (green) accumulates in BFA compartments (d) but is trapped in the ER when GNL1-Myc is BFA-sensitive (i). **e, j**, Golgi localization of  $\gamma$ COP (e, red) and N-ST-YFP (j, green) restored by BFA-resistant GN in BFA-sensitive GNL1, *gnl1* mutant background. All scale bars, 4  $\mu$ m.



that another, BFA-sensitive ARF-GEF is also involved in ER–Golgi trafficking (Fig. 3c, d; Supplementary Fig. 3e). One candidate would be GNOM, although GNOM is involved in endosomal recycling<sup>4</sup>. In addition, *gnom* mutant embryo cells did not display major Golgi abnormalities (Supplementary Fig. 3c) and GNOM did not co-localize with GNL1 (Fig. 3e). However, when both ARF-GEFs were

rendered either BFA-resistant or BFA-sensitive they co-localized partially or completely, respectively, after BFA treatment (Fig. 3f, g). In addition, the BFA-resistant form of both ARF-GEFs also co-localized partially with  $\gamma$ COP, suggesting the additional presence of GNOM protein at Golgi stacks (Figs 3h and 2b). To determine whether GNOM can substitute for GNL1 function, we analysed the localization of  $\gamma$ COP and N-ST-YFP in BFA-treated BFA-sensitive GNL1, *gnl1* mutant plants expressing engineered BFA-resistant GNOM (Fig. 2e, j). Surprisingly, the wild-type localization of the two markers was restored, although the BFA sensitivity of the two ARF-GEFs was reversed, indicating that BFA-resistant GNOM could compensate for the inactivation of BFA-sensitive GNL1 (Fig. 2e, j, compare with Fig. 2b, g and 2c, h, respectively). Thus, although GNOM might play only a minor part in ER–Golgi trafficking, it can take over the Golgi function of GNL1.

We also tested whether GNL1 can replace GNOM in the PIN1 endosomal recycling required for polar localization of PIN1 at the plasma membrane<sup>4</sup> (Fig. 4a–d). Polar targeting of PIN1 to the plasma membrane was only observed in BFA-treated seedlings when GNOM was BFA-resistant, regardless of BFA resistance or sensitivity of GNL1 (Fig. 4b, d). Thus, GNL1 has no obvious role in endosomal recycling. Interestingly, the BFA compartments were very small when both GNL1 and GNOM were BFA-sensitive, but attained their normal size when one or the other ARF-GEF was BFA-resistant. This suggests that BFA compartments are formed from both GNL1-dependent secretory and endocytic membrane material, although we cannot rule out a minor contribution of GNL1 to PIN1 recycling (compare Fig. 4c with 4a, d).

The capacity of GNOM to replace GNL1 cellular function could account for the observed, weak *gnl1* mutant phenotypes (Fig. 3i). Indeed, *gnl1 gnom* double mutants lacking both ARF-GEF activities were gametophytic lethal (Supplementary Table 2). This indicates that both ARF-GEFs are functionally redundant and that their double knockout affects some fundamental cellular function that leads to lethality even before fertilisation. Interestingly, other allele combinations with reduced ARF-GEF activity were also lethal, suggesting that the combined level of activity is critical (Supplementary Table 2). To determine their requirements in diploid somatic cells, both *GNL1* and *GNOM* were simultaneously downregulated by RNA interference (RNAi) expression (Supplementary Fig. 7b, c). The RNAi(*GNL1*, *GN*) expressing seedlings eventually died after 10–12 days of growth (Fig. 3j). Their ultrastructural analysis revealed abnormalities of the Golgi stacks, supporting our notion that ER–Golgi trafficking requires ARF-GEF function provided by both GNL1 and GNOM (Supplementary Fig. 3b).

To examine whether there are additional non-overlapping functions of GNL1 and GNOM, we performed promoter swaps and analysed the chimaeric genes for their ability to replace the two mutated genes. Surprisingly, *GNL1*–*GNOM* was able to rescue both *gnom* and *gnl1* mutants, whereas *GNOM*–*GNL1* only rescued *gnl1* but not *gnom* mutants (Fig. 4e; Supplementary Fig. 8a–c). Thus, GNOM and GNL1

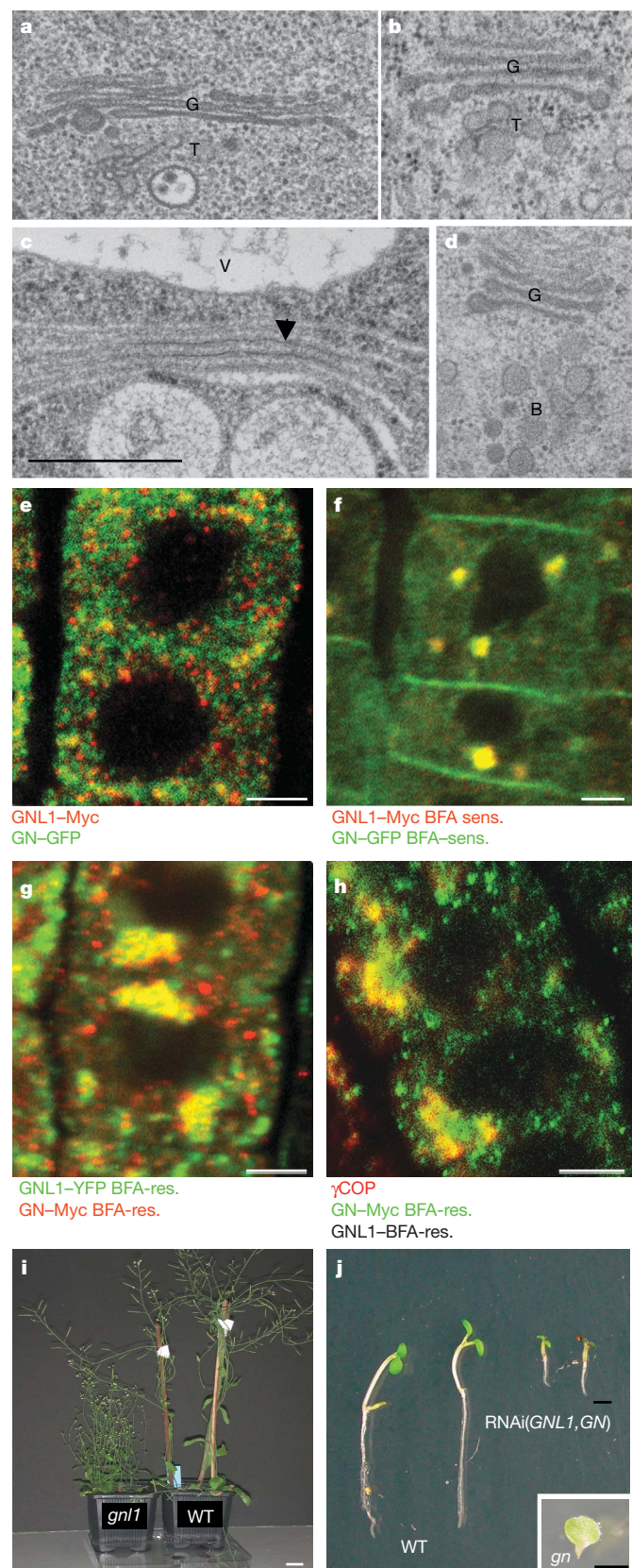
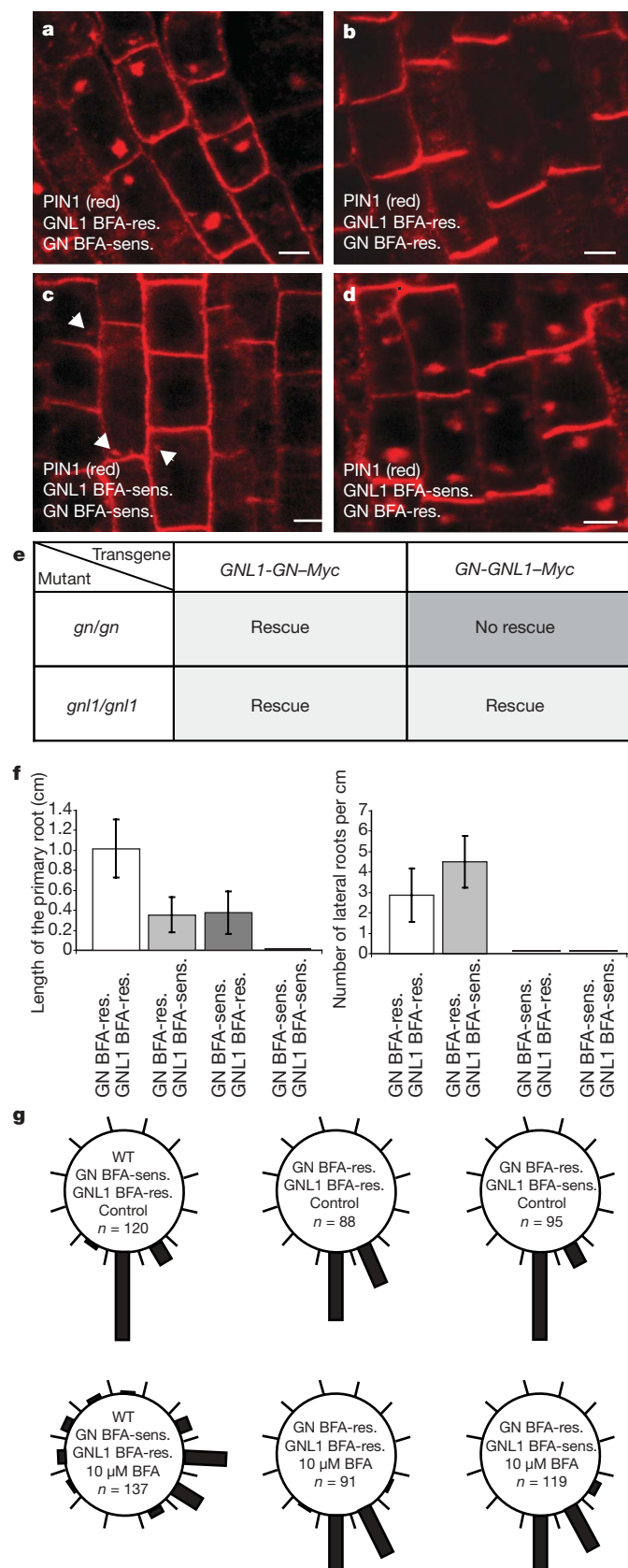


**Figure 3 | Phenotype of *gnl1* mutants and relationship of GNL1 to GN.**

**a–d**, Golgi morphology of *gnl1* mutant (**a**, **c**) in comparison to wild-type (**b**, **d**) after BFA treatment (**c**, **d**). **a**, **b**, Golgi of *gnl1* mutant (**a**) laterally expanded compared to wild-type in untreated controls. **c**, **d**, After 50  $\mu$ M BFA for 1 h, Golgi fuses with ER (arrowhead) in *gnl1* mutant (**c**), whereas Golgi morphology is retained in wild type (**d**). **B**, BFA compartment; **G**, Golgi; **T**, TGN; **V**, vacuole. Scale bar for **a–d**, 500 nm. **e–g**, Subcellular localization of GNL1 and GN. **e**, No colocalization of GNL1–Myc (red) with GN–GFP (green) in untreated cells. Nearly complete colocalization of BFA-sensitive versions in *gnl1* mutant (**f**) and partial colocalization of BFA-resistant versions (**g**) after BFA treatment. **h**, Partial colocalization of BFA-resistant GN with Golgi marker  $\gamma$ COP. Scale bars for **e–h**, 4  $\mu$ m. **i**, **j**, Phenotype of *gnl1* mutant plants and RNAi(*GNL1*, *GN*) seedlings. **i**, *gnl1* mutant plant (*gnl1*; left), wild type (WT; right). Scale bar, 2 cm. **j**, Seedling phenotypes of *RPS5A*-RNAi(*GNL1*, *GN*) (right) compared with wild type (left), 6 days after germination. Inset, *gn* mutant. Scale bar, 2 mm.





share one common, essential function in ER–Golgi trafficking, whereas only GNOM has another, unique essential function in endosomal recycling.

We then used BFA to determine the relative contributions of GNL1 and GNOM in different BFA-sensitive developmental processes such as seed germination, primary root growth, lateral root

**Figure 4 | Functional relationship between GN and GNL1.** **a–d**, PIN1 localization after BFA treatment. **a**, GN BFA-sensitive, GNL1 BFA-resistant (wild type): PIN1 is localized in BFA compartments and symmetrically at the plasma membrane. **b, d**, Polar localization of PIN1 at the plasma membrane and variable accumulation of PIN1 in BFA compartments when only GN (**b**) or both GN and GNL1 (**d**) are BFA-resistant. **c**, GN and GNL1 BFA-sensitive in *gnl1* mutant background: PIN1 is localized in very small BFA compartments (arrowheads) and symmetrically at the plasma membrane (similar to wild type, Fig. 4a). Scale bars for **a–d**, 4  $\mu$ m. **e**, Promoter swaps between GN and GNL1 suggest asymmetric functional redundancy. **f, g**, Seedlings expressing different combinations of BFA-resistant (res.) versus BFA-sensitive (sens.) GNL1 and GNOM (GN) in *gnl1* mutant background (except for wild-type) were treated with BFA. **f**, Left panel, additive effects of GNL1 and GN in primary root growth. Right panel, lateral root formation is mainly dependent on GN but not on GNL1. Error bars indicate standard deviation;  $n = 46$  (GN BFA-res., GNL1 BFA-res.), 46 (GN BFA-res., GNL1 BFA-sens.), 22 (GN BFA-sens., GNL1 BFA-res.), which corresponds to wild type, 25 (GN BFA-sens., GNL1 BFA-sens.). **g**, Root gravitropism is a GN-dependent process (upper panel, control; lower panel, BFA treatment).

initiation and root gravitropism. The two ARF-GEFs acted interchangeably in seed germination (Supplementary Fig. 9). Unexpectedly, expression of either BFA-resistant ARF-GEF, GNL1 or GNOM, was sufficient to sustain root growth at half the rate of roots expressing both BFA-resistant ARF-GEFs, indicating that primary root growth requires both GNL1 and GNOM function (Fig. 4f, left). In contrast, both lateral root initiation and root gravitropism were dependent on BFA-resistant GNOM, whereas BFA sensitivity or resistance of GNL1 had no effect of its own (Fig. 4f, right; 4g). This requirement for GNOM-specific ARF-GEF function is related to its role in endosomal recycling of PIN1 (ref. 4, 22).

Our results offer a surprising explanation for why ARF-GEFs of the GBF1 clade act in different trafficking pathways in plants than in mammals or yeast. There are two closely related ARF-GEFs, GNL1 and GNOM, that share the ancestral Golgi-associated function of GBF1-type ARF-GEFs in *Arabidopsis* and probably in other flowering plants as well (Supplementary Fig. 1). This was not noticed before because, unlike in mammals, there was no BFA effect on the localization of  $\gamma$ COP in wild-type *Arabidopsis*, although GNOM is BFA-sensitive<sup>4,14</sup>. In contrast, a rapid effect of BFA on the Golgi morphology and the localization of  $\gamma$ COP was described for tobacco BY-2 cells<sup>23</sup>, suggesting that the tobacco GNL1 orthologue is BFA-sensitive. Indeed, we found a BFA-sensitive signature for the rice putative orthologue of GNL1 (Supplementary Fig. 10). Our data imply that the Golgi-localized ARF-GEF function is ancestral and conserved among eukaryotes, although the plant lineage has apparently undergone gene duplication such that two closely related ARF-GEFs perform the GBF1-equivalent function. GNOM acquired an additional specific function in endosomal recycling of plasma membrane proteins that is not shared by GNL1. Unlike plants, animals have evolved new classes of small or medium-sized ARF-GEFs named cytohesin, EFA and BRAG, which are involved in endosomal trafficking<sup>5</sup>. In addition, a member of the BIG class of large ARF-GEFs named BIG2 acts not only at the TGN, like its close relative BIG1, but also at recycling endosomes<sup>24</sup>. Thus, the elaboration of post-Golgi trafficking seems to have evolved independently in the two major multicellular lineages, whereas the regulation by ARF-GEF of ER–Golgi traffic was already in place in unicellular eukaryotes.

## METHODS SUMMARY

**Molecular biology.** For expression of tagged GNL1, a complementing genomic fragment was transformed into *gnl1* mutants, and BFA sensitivity was engineered by replacing methionine with leucine in the SEC7 domain. For RNAi(GN, GNL1) analysis, fragments of GNL1 and GN coding sequence in tandem in sense and antisense direction were introduced into a two-component vector for expression by *RPSSA-GAL4* activator<sup>25</sup>. Transcript levels were analysed by RT–PCR. Promoter swaps involved 2-kb promoter fragments and were introduced into *gnl1* and *emb30-1* (ref. 8) heterozygous plants.



**Expression analysis.** Protein blots<sup>26</sup>, immunofluorescence localization<sup>4,26,27</sup>, FM4-64 staining<sup>4</sup>, BFA treatment<sup>4</sup>, immunolocalization on cryosections<sup>28</sup>, electron microscopy<sup>28</sup> and physiological tests<sup>4</sup> were performed as described.

**Bioinformatics.** An unrooted phylogenetic tree of SEC7 domains from different ARF-GEFs was derived from sequence alignment using ClustalW ([www.ebi.ac.uk/clustalw](http://www.ebi.ac.uk/clustalw)).

**Full Methods** and any associated references are available in the online version of the paper at [www.nature.com/nature](http://www.nature.com/nature).

**Received 18 February; accepted 30 May 2007.**

- Shin, H. W. & Nakayama, K. Guanine nucleotide-exchange factors for arf GTPases: their diverse functions in membrane traffic. *J. Biochem.* **136**, 761–767 (2004).
- Zhao, X. et al. GBF1, a cis-Golgi and VTCs-localized ARF-GEF, is implicated in ER-to-Golgi protein traffic. *J. Cell Sci.* **119**, 3743–3753 (2006).
- Peyroche, A., Courbeyrette, R., Rambourg, A. & Jackson, C. L. The ARF exchange factors Gea1p and Gea2p regulate Golgi structure and function in yeast. *J. Cell Sci.* **114**, 2241–2253 (2001).
- Geldner, N. et al. The *Arabidopsis* GNOM ARF-GEF mediates endosomal recycling, auxin transport, and auxin-dependent plant growth. *Cell* **112**, 219–230 (2003).
- Cox, R., Mason-Gamer, R. J., Jackson, C. L. & Segev, N. Phylogenetic analysis of Sec7-domain-containing Arf nucleotide exchangers. *Mol. Biol. Cell* **15**, 1487–1505 (2004).
- Mouratou, B. et al. The domain architecture of large guanine nucleotide exchange factors for the small GTP-binding protein Arf. *BMC Genom.* **6**, 20 (2005).
- Spang, A., Herrmann, J. M., Hamamoto, S. & Schekman, R. The ADP ribosylation factor-nucleotide exchange factors Gea1p and Gea2p have overlapping, but not redundant functions in retrograde transport from the Golgi to the endoplasmic reticulum. *Mol. Biol. Cell* **12**, 1035–1045 (2001).
- Mayer, U., Büttner, G. & Jürgens, G. Apical-basal pattern formation in the *Arabidopsis* embryo: studies on the role of the *gnom* gene. *Development* **117**, 149–162 (1993).
- Steinmann, T. et al. Coordinated polar localization of auxin efflux carrier PIN1 by GNOM ARF GEF. *Science* **286**, 316–318 (1999).
- Cherfils, J. & Melançon, P. On the action of Brefeldin A on Sec7-stimulated membrane-recruitment and GDP/GTP exchange of Arf proteins. *Biochem. Soc. Trans.* **33**, 635–638 (2005).
- Peyroche, A. et al. Brefeldin A acts to stabilize an abortive ARF–GDP–Sec7 domain protein complex: involvement of specific residues of the Sec7 domain. *Mol. Cell* **3**, 275–285 (1999).
- Barzilay, E., Ben-Califa, N., Hirschberg, K. & Neumann, D. Uncoupling of brefeldin A-mediated coatomer protein complex-I dissociation from Golgi redistribution. *Traffic* **6**, 794–802 (2005).
- Niu, T. K., Pfeifer, A. C., Lippincott-Schwartz, J. & Jackson, C. L. Dynamics of GBF1, a Brefeldin A-sensitive Arf1 exchange factor at the Golgi. *Mol. Biol. Cell* **16**, 1213–1222 (2005).
- Geldner, N., Friml, J., Stierhof, Y.-D., Jürgens, G. & Palme, K. Auxin transport inhibitors block PIN1 cycling and vesicle trafficking. *Nature* **413**, 425–428 (2001).
- Schmid, M. et al. A gene expression map of *Arabidopsis thaliana* development. *Nature Genet.* **37**, 501–506 (2005).
- Pimpl, P. et al. *In situ* localization and *in vitro* induction of plant COPI-coated vesicles. *Plant Cell* **12**, 2219–2236 (2000).
- Dettmer, J., Hong-Hermesdorf, A., Stierhof, Y.-D. & Schumacher, K. Vacuolar H<sup>+</sup>-ATPase activity is required for endocytic and secretory trafficking in *Arabidopsis*. *Plant Cell* **18**, 715–730 (2006).
- Ueda, T., Uemura, T., Sato, M. H. & Nakano, A. Functional differentiation of endosomes in *Arabidopsis* cells. *Plant J.* **40**, 783–789 (2004).
- Lee, G. J., Sohn, E. J., Lee, M. H. & Hwang, I. The *Arabidopsis* rab5 homologs Rha1 and Ara7 localize to the prevacuolar compartment. *Plant Cell Physiol.* **45**, 1211–1220 (2004).
- Grebe, M. et al. *Arabidopsis* sterol endocytosis involves actin-mediated trafficking via ARA6-positive early endosomes. *Curr. Biol.* **13**, 1378–1387 (2003).
- Teh, O. & Moore, I. An ARF-GEF acting at the Golgi and in selective endocytosis in polarized plant cells. *Nature* doi:10.1038/nature06023 (this issue).
- Geldner, N. et al. Partial loss-of-function alleles reveal a role for GNOM in auxin transport-related, post-embryonic development of *Arabidopsis*. *Development* **131**, 389–400 (2004).
- Ritzenthaler, C. et al. Reevaluation of the effects of brefeldin A on plant cells using tobacco Bright Yellow 2 cells expressing Golgi-targeted green fluorescent protein and COPI antisera. *Plant Cell* **14**, 237–261 (2002).
- Shin, H. W., Morinaga, N., Noda, M. & Nakayama, K. BIG2, a guanine nucleotide exchange factor for ADP-ribosylation factors: its localization to recycling endosomes and implication in the endosome integrity. *Mol. Biol. Cell* **15**, 5283–5294 (2004).
- Weijers, D., Van Hamburg, J. P., Van Rijn, E., Hooykaas, P. J. & Offringa, R. Diphtheria toxin-mediated cell ablation reveals interregional communication during *Arabidopsis* seed development. *Plant Physiol.* **133**, 1882–1892 (2003).
- Lauber, M. H. et al. The *Arabidopsis* KNOLLE protein is a cytokinesis-specific syntaxin. *J. Cell Biol.* **139**, 1485–1493 (1997).
- Müller, A. et al. AtPIN2 defines a locus of *Arabidopsis* for root gravitropism control. *EMBO J.* **17**, 6903–6911 (1998).
- Völker, A., Stierhof, Y.-D. & Jürgens, G. Cell cycle-independent expression of the *Arabidopsis* cytokinesis-specific syntaxin KNOLLE results in mistargeting to the plasma membrane and is not sufficient for cytokinesis. *J. Cell Sci.* **114**, 3001–3012 (2001).
- Rios, G. et al. Rapid identification of *Arabidopsis* insertion mutants by non-radioactive detection of T-DNA tagged genes. *Plant J.* **32**, 243–253 (2002).
- Vieten, A. et al. Functional redundancy of PIN proteins is accompanied by auxin-dependent cross-regulation of PIN expression. *Development* **132**, 4521–4531 (2005).
- Song, J., Lee, M. H., Lee, G. J., Yoo, C. M. & Hwang, I. *Arabidopsis* EPSIN1 plays an important role in vacuolar trafficking of soluble cargo proteins in plant cells via interactions with clathrin, AP-1, VT11, and VSR1. *Plant Cell* **18**, 2258–2274 (2006).

**Supplementary Information** is linked to the online version of the paper at [www.nature.com/nature](http://www.nature.com/nature).

**Acknowledgements** We thank N. Takada and L. Müller for technical assistance, A. Vieten, J. Friml, F. El-Kasmi, G. Strompen and K. Steinborn for screening the Cologne T-DNA insertion lines, K. Schumacher, I. Hwang, M. Grebe, A. Schlereth and D. Weijers for providing materials, O. Teh and I. Moore for sharing unpublished material and results, and N. Anders, U. Mayer, K. Schumacher and D. Weigel for critically reading the manuscript and suggestions. We especially thank N. Anders for advice and discussions. This work was supported by an EMBO long-term Fellowship to J.S. and by grants from the Human Frontier in Science Program Organization and the SFB 446 of the Deutsche Forschungsgemeinschaft to G.J.

**Author Contributions** S.R. carried out most of the experiments, N.G. initiated the project, J.S. generated the RNAi and promoter-swap lines, H.W. generated the ARA7–GFP marker line, Y.-D.S. performed the electron microscopy analysis and immunogold localization experiments, G.R. and C.K. provided the T-DNA collection, D.G.R. generated antisera against markers, and G.J. and S.R. designed the experiments, discussed the results and wrote the manuscript.

**Author Information** Reprints and permissions information is available at [www.nature.com/reprints](http://www.nature.com/reprints). The authors declare no competing financial interests. Correspondence and requests for materials should be addressed to G.J. (gerd.juergens@zmbp.uni-tuebingen.de).

## METHODS

**Plant material and growth conditions.** *Arabidopsis* wild-type (ecotype Col-0) and mutant lines carrying *gnom* alleles *R5* (ref. 22) or *emb30-1* (ref. 8) have been described. Plant growth conditions were as described<sup>22</sup>. Seedlings (Col-0 ecotype) were grown from surface-sterilized seeds on vertical agar plates at 24 °C for 5 days under long day conditions<sup>22</sup>.

***gnl1* mutant.** The *gnl1-1* T-DNA insertion line (ecotype Col-0) was isolated as described<sup>29</sup>. The T-DNA insertion is located in the first exon at 102 base pairs downstream of the ATG and confers hygromycin resistance. The plants were selected on plates containing 15 µg ml<sup>-1</sup> hygromycin (Gibco). The genotype was characterized by two PCRs: one to detect the T-DNA insertion (sense primer, 5'-GATTGAGCCAAGAAGTTGGGGCGAG-3'; antisense primer, 5'-CTGGGAATGGCGAAATCAAGGCAT-3'), another to amplify the wild-type gene sequence spanning the T-DNA insertion site (sense primer, 5'-ACCAAAAGGGTA-GAGTTGAAAAGGG-3'; antisense primer: 5'-TACATTTCTCCTCATCACA-GCCAAA-3').

**Generating transgenic plants.** An 8.8-kb genomic *GNL1* fragment containing 2-kb of 5' UTR and 1-kb of 3' UTR from BAC clone MUL8 complemented the *gnl1* mutant phenotype. Primer-extension PCR was used to insert 3 × Myc or YFP tag at the C-terminus as well as to introduce the leucine 696 (TTG) to methionine 696 (ATG) mutation in the SEC7 domain. All constructs were transformed into *gnl1/GNL1* heterozygous plants, and at least five *gnl1* mutant lines each were established for BFA-resistant and BFA-sensitive *GNL1* transgenes and shown to complement the bushy plant phenotype of *gnl1* mutants.

For RNAi (*GN*, *GNL1*) analysis, 172 bp of *GNL1* and 162 bp of *GNOM* coding sequence were cloned in tandem in sense and antisense orientation, introduced into the UAS vector of the *GAL4* >> *UAS* two-component expression system and transformed into Col-0 plants. T<sub>2</sub> plants were crossed with *RPS5A-GAL4* plants<sup>25</sup>, and the F<sub>1</sub> seedling progeny with abnormal phenotypes were analysed.

A 2-kb promoter fragment of *GNL1* and a 2.1-kb promoter fragment of *GN* were fused to genomic fragments for promoter swapping. These constructs were introduced into *gnl1/GNL1* as well as *emb30-1/GN* heterozygous plants<sup>8</sup>.

All T<sub>1</sub> plants were selected by spraying seedlings on soil with BASTA (1:1,000; AgrEvo) or by adding kanamycin (50 µg ml<sup>-1</sup>; Sigma) to plates.

**Immunofluorescence localization.** Five-day-old seedlings were incubated in 1 ml of liquid growth medium (×0.5 MS medium, 1% sucrose, pH 5.8) containing 50 µM BFA (Invitrogen, Molecular Probes) for 1 h (or, 100 µM for 2 h in double labelling for GN and GNL1) at room temperature in 24-well cell-culture plates. Incubation was stopped by fixation with 4% paraformaldehyde in MTSB. Immunofluorescence staining was performed as described<sup>26</sup> or with an InsituPro machine (Intavis)<sup>27</sup>.

Antibodies used were: mouse anti-c-Myc mAb 9E10 (Santa Cruz Biotechnologies) diluted 1:600; mouse anti-GFP (Roche) 1:600; rabbit anti-GFP (Invitrogen, Molecular Probes) 1:600; rabbit anti-PIN1 (ref. 30) 1:1,000; rabbit anti-AtγCOP (ref. 16) 1:1,000; and anti-clathrin<sup>31</sup> 1:500. FITC or Cy3-conjugated secondary antibodies (Dianova) were diluted 1:600.

Epitope-tagged or GFP-fusion markers were transformed or crossed into tagged *GNL1* lines: *RPS5A-GFP-ARA7* (ref. 18) (GFP-ARA7; cloned into pGrIIK *RPS5a-tNOS*; ref. 25), *VHA-a1-GFP*<sup>17</sup>, *N-ST-YFP*<sup>20</sup>, *GN-3 × Myc*<sup>4</sup> (BFA-sensitive and resistant) and BFA-sensitive *GN-GFP*<sup>4</sup>.

Fluorescence signals of GFP- or YFP-tagged proteins were enhanced by staining with anti-GFP antibody in fixed cells. Live cell imaging was performed with 2 µM FM4-64 (Invitrogen, Molecular Probes).

**Acquisition and processing of fluorescence images.** Fluorescence images were acquired at 512 × 512 pixels with the confocal laser scanning microscope TCS-SP2 from Leica, using the ×63 water-immersion objective and Leica software. All images were processed with Adobe Photoshop CS2 only for adjustment of contrast and brightness.

**Immunolocalization on cryosections, and electron microscopy.** Ultrastructural analysis of high-pressure frozen, freeze-substituted and resin-embedded root tips and embryos, and immunogold labeling using silver-enhanced Nanogold (Nanoprobes, USA) of ultrathin cryosections were carried out as described<sup>17</sup>.

**Physiological tests.** To investigate primary root growth and lateral root formation, 5-day-old seedlings were transferred to plates with 20 µM BFA and analysed after 7 additional days.

For measurement of gravitropic responses, 4-day-old seedlings were transferred to plates containing 10 µM BFA. After 1 day, the plates were turned by 135°. Pictures were taken 12 h later and deviation from the gravity vector was measured.

For the germination assay, surface-sterilized seeds were plated on agar plates (×0.5 MS medium, 1% sucrose, pH 5.8) containing 20 µM BFA. After two days of stratification, the plates were incubated at 23 °C for 4 days before seed germination rates were determined.

**Analysis of transcript levels in *gnl1* mutants and RNAi (*GN*, *GNL1*) lines.** RNA isolation was performed using Plant RNAeasy Kit from Qiagen. RT-PCR was done with Revert Aid H Minus First Strand cDNA Synthesis Kit (Fermentas). PCR on *gnl1* cDNA from plants was performed with sense primer 5'-CTGGGAATGGCGAAATCAAGGCAT-3' and antisense primer 5'-CTTTTCTCTCCAGAATTCGG-3'. PCR on cDNA from RNAi seedlings was done with sense primer 5'-GTGCAGTTTGGCTGTGATG-3' and antisense primer 5'-CTTTTCTCTCCAGAATTCGG-3' to investigate *GNL1* transcript level. For *GN*, sense primer 5'-TACACTTGTCACAGAGCTGGTAGC-3' and antisense primer 5'-TCTGTCATTATATGCAAATCATATGGAGAAGCCG-3' were used.

**Western blot analysis.** Five-day-old seedlings were used for protein extraction<sup>26</sup>. Protein extracts were loaded onto a 12% polyacrylamide gel and transferred onto a PVDF membrane. Rabbit anti-GNOM(SEC7) antiserum diluted 1:2,000 and anti-rabbit horseradish peroxidase (POD)-conjugated secondary antibody (Roche) 1:5,000 were used to detect endogenous GNOM protein. Detection was performed with BM chemiluminescence blotting substrate (Roche).

**Phylogenetic tree.** SEC7 domain sequences of ARF-GEFs from different species, corresponding to the GN SEC7 domain, were aligned by ClustalW (www.ebi.ac.uk/clustalw) and the phylogenetic tree was drawn with TreeViewer.

# An ARF-GEF acting at the Golgi and in selective endocytosis in polarized plant cells

Ooi-kock Teh<sup>1</sup> & Ian Moore<sup>1</sup>

Circumstantial evidence suggests that intracellular membrane trafficking pathways diversified independently in the plant kingdom<sup>1–10</sup>, but documented examples are rare<sup>6,11,12</sup>. ARF-GEFs (guanine-nucleotide exchange factors for ADP-ribosylation factor GTPases) are essential for vesicular trafficking in all eukaryotic kingdoms, but of the eight ARF-GEF families, only the ancestral BIG and GBF types are found in plants<sup>1,2</sup>. Whereas fungal and animal GBF proteins perform conserved functions at the Golgi, the *Arabidopsis thaliana* GBF protein GNOM is thought to act in only the process of recycling from endosomes<sup>3–5</sup>. We now show that the related *Arabidopsis* GBF protein GNOM-LIKE1 (GNL1) has an ancestral function at the Golgi but is also required for selective internalization from the plasma membrane in the presence of brefeldin A (BFA). We identified *gnl1* mutants that accumulated biosynthetic and recycling endoplasmic reticulum markers in enlarged internal compartments. Notably, in the absence of functional GNL1, Golgi stacks were rendered sensitive to the selective ARF-GEF inhibitor BFA, which caused them to fuse with the endoplasmic reticulum. Furthermore, in BFA-treated *gnl1* roots, the internalization of a polar plasma-membrane marker, the auxin efflux carrier PIN2, was selectively inhibited. Thus, GNL1 is a BFA-resistant GBF protein that functions with a BFA-sensitive ARF-GEF both at the Golgi and in selective endocytosis, but not in recycling from endosomes. We propose that the evolution of endocytic trafficking in plants was accompanied by neofunctionalization within the GBF family, whereas in other kingdoms it occurred independently by elaboration of additional ARF-GEF families.

Plant membrane trafficking exhibits several unusual features with respect to vacuole and Golgi organization, endocytic cycling, cell polarity and cytokinesis<sup>6,7</sup>. Because gene families that are essential for membrane identity and vesicular traffic have diversified independently in the plant kingdom<sup>2,8–10</sup>, it has been suggested that trafficking pathways have been elaborated independently in plant cells<sup>2,8–10</sup>. Few examples have been provided, however, and plant trafficking processes remain poorly described in molecular terms.

To further our understanding of plant-specific trafficking processes, we isolated *Arabidopsis* mutants defective in biosynthetic membrane traffic to the plasma membrane by screening mutagenized seedlings for intracellular accumulation of a secreted green fluorescent protein (secGFP)<sup>13,14</sup>. Mutant 44 and mutant 54 carried allelic mutations that caused the accumulation of secGFP in spheroid bodies, the diameters and heterogeneity of which increased (from diameter 0.5  $\mu$ m to 3  $\mu$ m) with the age of root epidermal cells (Fig. 1a, b, and Supplementary Fig. 2). Mutant 44 exhibited more pronounced secGFP accumulation and various developmental abnormalities that were absent in mutant 54 (Fig. 1c, and Supplementary Figs 3 and 4). In wild-type roots, secGFP existed predominantly in its truncated apoplastic form<sup>13</sup>, whereas in mutant 44 its full-length intracellular

form accumulated (Fig. 1d, e, arrowhead). Positional cloning and sequencing identified stop codons in the *GNL1* locus (At5g39500) in mutant 44 and mutant 54, which were named *gnl1-2* and *gnl1-3*, respectively (Fig. 1f and Supplementary Fig. 5). A T-DNA allele (*gnl1-1*) showed allelism to and similar developmental phenotypes as *gnl1-2*, which could be complemented by a GNL1–YFP (yellow fluorescent protein) fusion (Supplementary Fig. 5). *gnl1-1* also accumulated secGFP in the spheroid bodies, which were termed *gnl1*-bodies. Thus, the trafficking defects exhibited by all three mutants were attributed to loss of GNL1 function.

GNL1 is a putative ARF-GEF: these are nucleotide exchange factors for ARF GTPases, which have diverse functions in vesicle coat formation and vesicle–cytoskeleton interactions<sup>15,16</sup>. In animals and fungi there are eight ARF-GEF families, but only the apparently ancestral GBF and BIG families are known in plants<sup>1,2</sup>. GNL1 is one of three GBF proteins encoded by the *Arabidopsis* genome and is the closest relative of GNOM, the only *Arabidopsis* ARF-GEF characterized so far (Supplementary Fig. 1). Whereas mammalian and yeast GBF1-family ARF-GEFs function at the *cis*-Golgi, GNOM is essential for recycling from endosomes to the plasma membrane<sup>3,4,12</sup> but is not thought to act in the secretory pathway<sup>12</sup>. In contrast, the intracellular accumulation of secGFP in *gnl1* mutants suggested that this close relative of GNOM does function on a biosynthetic trafficking pathway. Consistent with this, the fluorescent dye FM4-64—which labels a variety of endosomal and vacuolar compartments<sup>7,12,16–18</sup>—was excluded from *gnl1*-bodies, even after treatment with brefeldin A (BFA), which causes the aggregation of endosomal and *trans*-Golgi compartments<sup>12,16,17</sup> (Fig. 1g). Furthermore, *gnl1*-bodies co-accumulated fluorescent protein markers<sup>14,18,19</sup> of secretory and vacuolar traffic (Fig. 1h, i, and Supplementary Fig. 6) as well as a luminal endoplasmic reticulum (ER) marker that recycles from the Golgi by virtue of an ER retrieval signal (Supplementary Fig. 6; all markers used in this study are described in Methods). Therefore *gnl1* mutants seemed to be defective in biosynthetic traffic at a point before the divergence of secretory and vacuolar pathways at the *trans*-Golgi.

The Golgi membrane marker ST–RFP (sialyltransferase–red fluorescent protein) was excluded from the *gnl1*-bodies (Fig. 1j). Although Golgi stacks maintained their characteristic flattened-ring morphology, their apparent diameter in confocal microscopy was increased by 50% in *gnl1*, from  $1.2 \pm 0.07 \mu$ m to  $1.8 \pm 0.25 \mu$ m ( $n = 275$  and  $287$ , respectively) (Supplementary Fig. 7). GNL1 therefore has a role in maintaining Golgi organization. Consistent with this, YFP-tagged GNL1 (a gift of S. Richter and G. Jürgens) colocalized with a Golgi marker (Supplementary Fig. 8a–i). However, the subtlety of the Golgi defect in *gnl1* and the viability of *gnl1-1* and *gnl1-2* plants suggested either that GNL1 acts in a non-essential process or that its function overlaps with another ARF-GEF. To distinguish these possibilities we used the selective ARF-GEF inhibitor brefeldin A (BFA). Sensitivity

<sup>1</sup>Department of Plant Sciences, University of Oxford, South Parks Road, Oxford OX1 3RB, UK.



of ARF-GEFs to BFA is determined by the identity of five residues in the Sec7 domain<sup>1,2</sup>. Of the three *Arabidopsis* GBF-family ARF-GEFs, only GNL1 is predicted to be BFA-resistant<sup>1,12</sup>. Therefore if GNL1

shares a function with either of the other two GBF-family ARF-GEFs, this function should be rendered BFA-sensitive in *gnl1* mutants. Consistent with this prediction, growth of *gnl1* seedlings or of *gnl1* seedlings complemented with a BFA-sensitive GNL1 mutant was severely inhibited by BFA concentrations that did not affect wild-type plants (Fig. 2a, b, and Supplementary Fig. 9). Therefore GNL1 is BFA-resistant *in vivo* and acts redundantly with a BFA-sensitive ARF-GEF in a function essential for growth.

In BFA-treated *Arabidopsis* roots, Golgi stacks do not fuse with the ER as they do in several other species<sup>12,20–25</sup> but remain apparently intact and functional<sup>25</sup>, often clustering around the drug-induced BFA-bodies. These are derived from endosomal membranes and accumulate endocytosed markers, but apparently exclude biosynthetic cargo<sup>12,20–25</sup> (Fig. 1g). To determine whether GNL1 is the BFA-resistant ARF-GEF responsible for maintaining *Arabidopsis* root Golgi organization in the presence of BFA, we examined the localization of two integral Golgi membrane markers and two peripherally associated Rab GTPase markers. Strikingly, although the Golgi remained intact in BFA-treated wild-type plants, in *gnl1* mutants the integral Golgi markers were rapidly transferred to the ER and the peripheral markers redistributed to the cytoplasm (Fig. 2c–j, and Supplementary Fig. 10a–l). Furthermore, the ER-resident glycoprotein calreticulin accumulated in an endoglycosidase-H-resistant form, indicating processing by Golgi-resident enzymes (Fig. 2k, and Supplementary Fig. 10m, n). We conclude that BFA treatment of *gnl1* induces fusion of ER and Golgi membranes, indicating that GNL1 acting together with one or more BFA-sensitive ARF-GEFs performs an essential function in maintaining Golgi integrity. Moreover, GNL1 activity can explain the BFA-resistance of *Arabidopsis* root Golgi. These observations also show that GBF proteins can be naturally BFA resistant and imply that the effect of

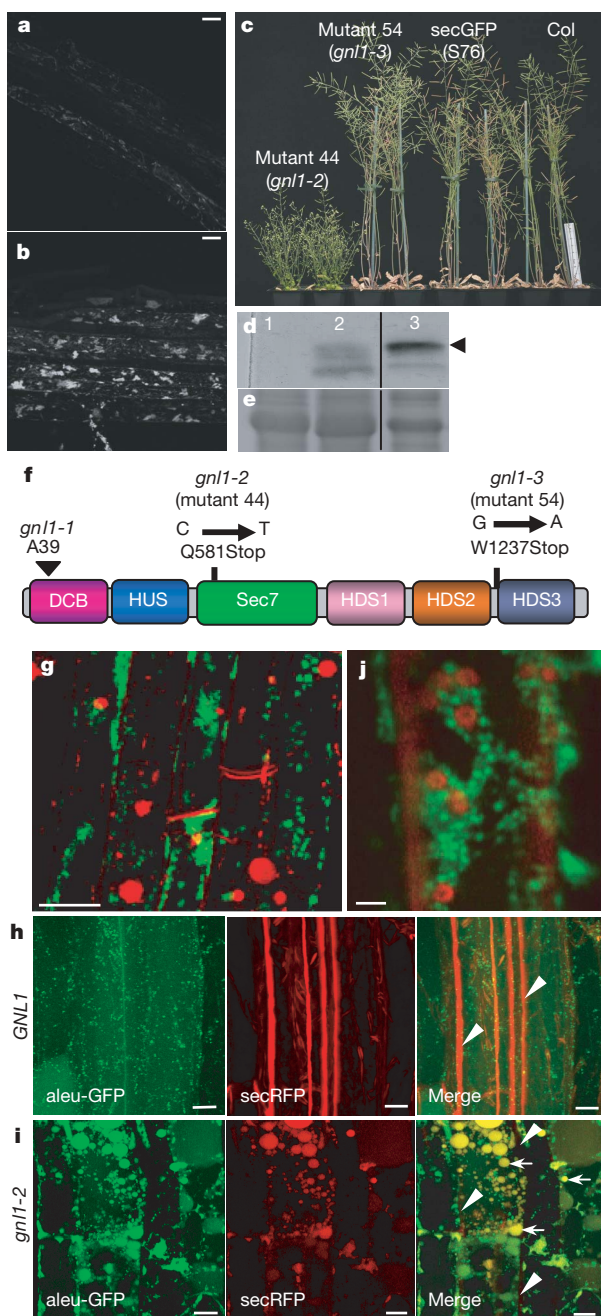


**Figure 1 | Phenotypes of *gnl1* plants.** **a, b**, secGFP fluorescence in mature root epidermal cells of wild type (**a**) and mutant 44 (**b**) imaged under identical conditions; scale bars, 20  $\mu$ m. **c**, Growth phenotypes of mutants 44 and 54, secGFP reporter line (S76) and untransformed control (Col). **d, e**, Anti-GFP immunoblot (**d**) and coomassie stained gel (**e**) of untransformed plants (lane 1), secGFP (S76) (lane 2) and mutant 44 (lane 3). **f**, Schematic diagram of GNL1 showing the conserved domain structure<sup>2</sup> and location of mutations in *gnl1* alleles; the signature for ARF-GEFs is the catalytic Sec7 domain. DCB, dimerization/cyclophilin binding; HUS, homology upstream of Sec7; HDS, homology downstream of Sec7. **g**, Root epidermis of *gnl1-2* expressing secGFP (green) incubated with FM4-64 (red) and treated with 100  $\mu$ M of BFA for 90 min; scale bar, 10  $\mu$ m. **h, i**, Vacuolar marker aleu-GFP<sup>18,19</sup> (green) and the secreted marker secRFP<sup>14,18</sup> (red) in roots of the indicated genotypes; scale bar, 5  $\mu$ m; accumulation of apoplastic secRFP (arrowheads) and vacuolar aleu-GFP is reduced in *gnl1-2*; arrows, *gnl1*-bodies. **j**, Golgi marker ST-RFP (red) and secGFP (green) in mature root epidermal cells of *gnl1-2*; scale bar, 2  $\mu$ m.

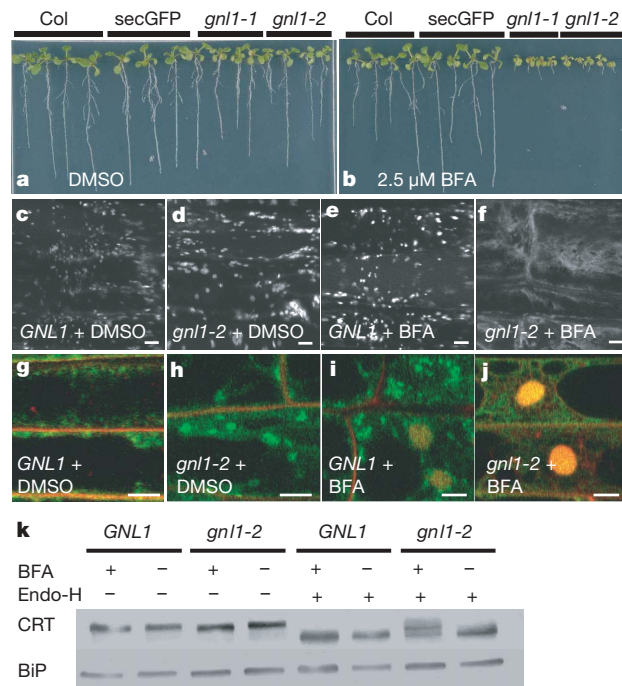


**Figure 2 | Golgi stacks in *gnl1* are hypersensitive to BFA.** **a, b**, *gnl1* and GNL1 seedlings grown with 2.5  $\mu$ M BFA or solvent (DMSO). **c–j**, Integral Golgi membrane marker ST-RFP (**c–f**) and peripheral Rab GTPase marker YFP-AtRAB-E1<sup>d</sup> (green) and FM4-64 (red) (**g–j**) in mature root cells of the indicated genotypes after treatment for 1 h with 25  $\mu$ M BFA (BFA) or solvent only (DMSO); scale bar, 5  $\mu$ m. **k**, Immunoblot of the reticuloplasmic calreticulin (CRT) and BiP in wild-type and *gnl1-2* root tissue treated with BFA (+) or solvent (–) before protein extraction, and treated with (+) or without (–) endoglycosidase-H (Endo-H); endo-H resistant forms of calreticulin accumulate in BFA-treated roots of *gnl1-2*.

BFA in other plant species will depend on the presence or absence of largely neutral amino acid substitutions in their GBF proteins. For example, the three GBF proteins of rice are all predicted to be BFA sensitive<sup>16</sup>.

In BFA-treated *Arabidopsis* root tips, endocytosed proteins accumulate in BFA-bodies because recycling from endosomes to the plasma membrane is inhibited but traffic from the plasma membrane to endosomes is not (Supplementary Fig. 1)<sup>7,12,16</sup>. Traffic to the endosomes is therefore either independent of ARF-GEF activity or uses BFA-resistant ARF-GEFs such as GNL1 (refs 12, 25, 26). To establish whether GNL1 normally contributes to BFA-insensitive endocytosis we asked whether plasma membrane markers were trafficked to BFA-bodies in *gnl1* mutants.

The plasma-membrane marker PMA4-GFP and the lipophilic endocytic dye FM4-64 accumulated in the BFA-bodies of BFA-treated wild-type and *gnl1-2* roots with similar efficiency (Fig. 3a, b), indicating that endocytosis can occur in the absence of GNL1 function. In epidermal and cortical cells, the auxin efflux carrier PIN2 adopts distinct polar distributions that are determined by largely unknown trafficking mechanisms<sup>27–29</sup>. Strikingly, PIN2 exhibited substantially reduced accumulation in BFA-compartments of *gnl1-1* and *gnl1-2* (Fig. 3c–i, and Supplementary Fig. 11) and in *gnl1* complemented with BFA-sensitive GNL1 (data not shown), even though BFA-bodies were clearly detectable in these cell types using other markers (Fig. 3b). Thus trafficking of PIN2 from the plasma membrane to endosomes is selectively promoted by GNL1, which is the only BFA-resistant ARF-GEF that acts in this step. We also investigated the internalization of PIN1 in the stele. In BFA-treated wild-type roots, PIN1 was almost completely internalized into BFA compartments after 1 h. This was greatly reduced in

*gnl1-2*, in which PIN1-labelled BFA-bodies were less distinct and more PIN1 was retained at the plasma membrane where its polar distribution was lost (Supplementary Fig. 12). Because PIN proteins in *gnl1* were polar before BFA treatment, GNL1 function in endocytic trafficking apparently overlaps with one or more BFA-sensitive ARF-GEFs, as it does at the Golgi (Supplementary Fig. 1). Support for independent functions of GNL1 at the Golgi and in endocytosis was provided by the observation that a BFA-sensitive GNL1 derivative, GNL1(L696M)-YFP, accumulated prominently at the cell periphery in BFA-treated meristematic cells of *gnl1* seedlings (Supplementary Fig. 8j–n). This may have resulted either from stabilization<sup>1–5,12</sup> of BFA-sensitive GNL1 at a peripheral site of action, or from perturbation of GNL1 trafficking at this location.

Our results indicate that GNL1 has an ancestral function at the Golgi but is also required for selective endocytosis in the presence of BFA. The simplest interpretation is that GNL1 promotes selective internalization at the plasma membrane, but we cannot rule out either a role in subsequent traffic to an endosome or an indirect selective effect on cycling. ARF-GEFs of the EFA6 family have been implicated in endocytosis in mammalian cells<sup>15,30</sup> but are absent in plants. Whereas other eukaryotic kingdoms have elaborated several families of small ARF-GEFs that function in endosomal trafficking and post-Golgi sorting, plants rely solely on the ancestral large ARF-GEFs of the GBF and BIG families<sup>1,2</sup>. Within the GBF family, the distinct phenotypes of *gnom* (ref. 12) and *gnl1* plants and the BFA-sensitivity of the GNOM-mediated endocytic recycling pathway<sup>12</sup> show that GNOM and GNL1 have distinct functions. We propose that during land plant evolution the endocytic cycling pathways that underpin cell polarity have arisen in part by duplication of GBF genes whose products have acquired distinct novel functions independently of ARF-GEF evolution in other kingdoms.

## METHODS SUMMARY

*Arabidopsis thaliana* seedlings of the Col ecotype were grown and transformed as described in ref. 14. Sequence alignments and phylograms were produced using ClustalW with default parameters ([www.ebi.ac.uk/clustalw/](http://www.ebi.ac.uk/clustalw/)). *GNOMLIKE1* is At5g39500; TAIR accession, Locus:2175728; GenBank, NM\_123312.

**Genetic screen and confocal microscopy.** M<sub>2</sub> seedlings expressing secGFP (S76) were screened for increased fluorescence intensities using a Leica MZ FLIII fluorescence stereomicroscope. Mutants identified were backcrossed twice before being used for phenotypic characterization and positional cloning. An LSM 510 META confocal laser-scanning microscope (Carl Zeiss) was used for confocal analysis as described in refs 13, 14, and Zeiss AIM software was used for image processing and analysis as described in Methods.

**Staining and inhibitor treatment.** FM4-64 (Invitrogen-Molecular Probes) was prepared from a 5 mM stock in water. Brefeldin and cycloheximide (Sigma-Aldrich) were prepared as 200 mM and 355 mM stocks in dimethylsulphoxide (DMSO), respectively. Four-to-six-day-old seedlings were treated in 5 ml water, with equal amount of solvents as the controls.

**Immunoblot analysis and immunolocalization on intact root tissues.** Proteins from roots of 8-day-old seedlings were extracted and analysed by immunoblot as described<sup>14</sup>. Immunolocalization was performed by indirect immunofluorescence on 4-day-old seedlings as described in Methods.

**Full Methods** and any associated references are available in the online version of the paper at [www.nature.com/nature](http://www.nature.com/nature).

Received 27 February; accepted 11 June 2007.

- Cox, R., Mason-Gamer, R. J., Jackson, C. L. & Segev, N. Phylogenetic analysis of Sec7-domain-containing Arf nucleotide exchangers. *Mol. Biol. Cell* 15, 1487–1505 (2004).
- Mouratou, B. *et al.* The domain architecture of large guanine nucleotide exchange factors for the small GTP-binding protein Arf. *BMC Genomics* 6, 20 (2005).
- Garcia-Mata, R., Szul, T., Alvarez, C. & Sztul, E. ADP-ribosylation factor/COPI-dependent events at the endoplasmic reticulum–Golgi interface are regulated by the guanine nucleotide exchange factor GBF1. *Mol. Biol. Cell* 14, 2250–2261 (2003).
- Niu, T. K., Pfeifer, A. C., Lippincott-Schwartz, J. & Jackson, C. L. Dynamics of GBF1, a Brefeldin A-sensitive Arf1 exchange factor at the Golgi. *Mol. Biol. Cell* 16, 1213–1222 (2005).
- Jackson, C. L. & Casanova, J. E. Turning on ARF: the Sec7 family of guanine-nucleotide-exchange factors. *Trends Cell Biol.* 10, 60–67 (2000).

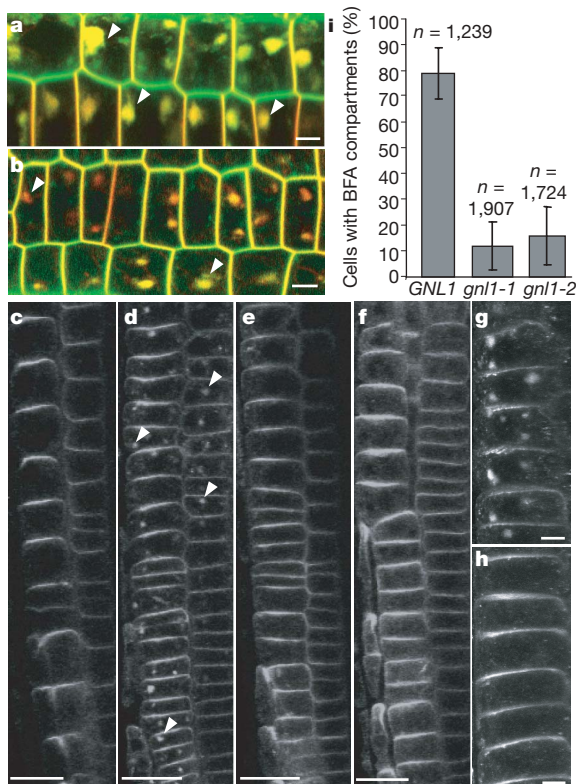


**Figure 3 | GNL1 is required for PIN2 accumulation in BFA bodies.** **a, b**, PMA4-GFP (green) and FM4-64 (red) in *GNL1* (**a**) and *gnl1-2* (**b**) roots treated with 25  $\mu$ M of BFA for 1 h; scale bar, 5  $\mu$ m. **c–h**, Immunolocalization of PIN2 in root epidermis and cortex; *GNL1* (**c, d**) and *gnl1-2* (**e, f**) treated with DMSO (**c–e**) or 25  $\mu$ M of BFA (**d–f**) for 1 h; scale bar, 20  $\mu$ m. **g, h**, Higher magnification of (**d**) and (**f**), respectively; scale bar, 5  $\mu$ m. **i**, Percentage of epidermal and cortical cells with PIN2-labelled BFA-bodies; error bars indicate s.d. **a, b, d**, Arrowheads indicate BFA-bodies.



6. Jürgens, G. Membrane trafficking in plants. *Annu. Rev. Cell Dev. Biol.* **20**, 481–504 (2004).
7. Murphy, A. S., Bandyopadhyay, A., Holstein, S. E. & Peer, W. A. Endocytotic cycling of PM proteins. *Annu. Rev. Plant Biol.* **56**, 221–251 (2005).
8. Rutherford, S. & Moore, I. The *Arabidopsis* Rab GTPase family: another enigma variation. *Curr. Opin. Plant Biol.* **5**, 518–528 (2002).
9. Sanderfoot, A. A., Assaad, F. F. & Raikhel, N. V. The *Arabidopsis* genome. An abundance of soluble *N*-ethylmaleimide-sensitive factor adaptor protein receptors. *Plant Physiol.* **124**, 1558–1569 (2000).
10. Vernoud, V., Horton, A. C., Yang, Z. & Nielsen, E. Analysis of the small GTPase gene superfamily of *Arabidopsis*. *Plant Physiol.* **131**, 1191–1208 (2003).
11. Lauber, M. H. *et al.* The *Arabidopsis* KNOLLE protein is a cytokinesis-specific syntaxin. *J. Cell Biol.* **139**, 1485–1493 (1997).
12. Geldner, N. *et al.* The *Arabidopsis* GNOM ARF-GEF mediates endosomal recycling, auxin transport, and auxin-dependent plant growth. *Cell* **112**, 219–230 (2003).
13. Zheng, H., Kunst, L., Hawes, C. & Moore, I. A GFP-based assay reveals a role for RHD3 in transport between the endoplasmic reticulum and Golgi apparatus. *Plant J.* **37**, 398–414 (2004).
14. Samalova, M., Fricker, M. & Moore, I. Ratiometric fluorescence-imaging assays of plant membrane traffic using polyproteins. *Traffic* **7**, 1701–1723 (2006).
15. D'Souza-Schorey, C. & Chavrier, P. ARF proteins: roles in membrane traffic and beyond. *Nature Rev. Mol. Cell Biol.* **7**, 347–358 (2006).
16. Geldner, N. The plant endosomal system—its structure and role in signal transduction and plant development. *Planta* **219**, 547–560 (2004).
17. Dettmer, J., Hong-Hermesdorf, A., Stierhof, Y. D. & Schumacher, K. Vacuolar H<sup>+</sup>-ATPase activity is required for endocytic and secretory trafficking in *Arabidopsis*. *Plant Cell* **18**, 715–730 (2006).
18. Zheng, H. *et al.* A Rab-E GTPase mutant acts downstream of the Rab-D subclass in biosynthetic membrane traffic to the plasma membrane in tobacco leaf epidermis. *Plant Cell* **17**, 2020–2036 (2005).
19. Kotzer, A. M. *et al.* AtRabF2b (Ara7) acts on the vacuolar trafficking pathway in tobacco leaf epidermal cells. *J. Cell Sci.* **117**, 6377–6389 (2004).
20. Ritzenthaler, C. *et al.* Reevaluation of the effects of brefeldin A on plant cells using tobacco Bright Yellow 2 cells expressing Golgi-targeted green fluorescent protein and COPI antisera. *Plant Cell* **14**, 237–261 (2002).
21. Satiat-Jeunemaitre, B., Cole, L., Bourett, T., Howard, R. & Hawes, C. Brefeldin A effects in plant and fungal cells: something new about vesicle trafficking? *J. Microsc.* **181**, 162–177 (1996).
22. Saint-Jore, C. M. *et al.* Redistribution of membrane proteins between the Golgi apparatus and endoplasmic reticulum in plants is reversible and not dependent on cytoskeletal networks. *Plant J.* **29**, 661–678 (2002).
23. Hawes, C. Cell biology of the plant Golgi apparatus. *New Phytol.* **165**, 29–44 (2005).
24. Lippincott-Schwartz, J. *et al.* Microtubule-dependent retrograde transport of proteins into the ER in the presence of brefeldin A suggests an ER recycling pathway. *Cell* **60**, 821–836 (1990).
25. Grebe, M. *et al.* *Arabidopsis* sterol endocytosis involves actin-mediated trafficking via ARA6-positive early endosomes. *Curr. Biol.* **13**, 1378–1387 (2003).
26. Xu, J. & Scheres, B. Dissection of *Arabidopsis* ADP-RIBOSYLATION FACTOR 1 function in epidermal cell polarity. *Plant Cell* **17**, 525–536 (2005).
27. Li, G. & Xue, H. W. *Arabidopsis* PLD $\zeta$ 2 regulates vesicle trafficking and is required for auxin response. *Plant Cell* **19**, 281–295 (2007).
28. Abas, L. *et al.* Intracellular trafficking and proteolysis of the *Arabidopsis* auxin-efflux facilitator PIN2 are involved in root gravitropism. *Nature Cell Biol.* **8**, 249–256 (2006).
29. Jaillais, Y., Fobis-Loisy, I., Miede, C., Rollin, C. & Gaude, T. AtSNX1 defines an endosome for auxin-carrier trafficking in *Arabidopsis*. *Nature* **443**, 106–109 (2006).
30. Macia, E. *et al.* The GDP-bound form of Arf6 is located at the plasma membrane. *J. Cell Sci.* **117**, 2389–2398 (2004).

**Supplementary Information** is linked to the online version of the paper at [www.nature.com/nature](http://www.nature.com/nature). A summary figure is also included.

**Acknowledgements** We are indebted to S. Richter, Y.-D. Stierhof and G. Jürgens for generously providing plasmids and seeds with YFP-tagged GNL1, seeds of *gnl1-1*, antibodies, for sharing data before publication, and for discussions; A. Murphy for PIN2 antisera, advice on immunolocalization, and discussions; H. Zheng, who generated mutagenized secGFP(S76) seed; J. Denecke for anti-calreticulin/BiP antibody; and M. Bennett, M. Fricker, J. Pérez-Gómez, M. Grebe and J. Langdale for comments and discussions. We thank J. Baker and C. O'Brien for photographs and technical assistance. This work was supported by a studentship from the Malaysian Palm Oil Board (O.T.) and a grant from the BBSRC (I.M.).

**Author Contributions** O.T. isolated and characterized *gnl1-2* and *gnl1-3*. I.M. assisted with imaging, wrote the paper and participated in discussions.

**Author Information** Reprints and permissions information is available at [www.nature.com/reprints](http://www.nature.com/reprints). The authors declare no competing financial interests. Correspondence and requests for materials should be addressed to I.M. ([ian.moore@plants.ox.ac.uk](mailto:ian.moore@plants.ox.ac.uk)).



## METHODS

**Miscellaneous.** Transient expression was performed in leaves of 2-week-old greenhouse-grown *Arabidopsis* seedlings, as described in ref. 14 but with 300 mM MgCl<sub>2</sub> in place of the infiltration buffer. Expressed proteins were imaged 3 or 4 days after infiltration.

**Fluorescent marker constructs.** aleu-GFP has a sequence-specific vacuolar sorting signal from petunia aleurain and traffics to the central vacuole via the ER, Golgi and a punctate prevacuolar compartment<sup>18,19</sup>. secRFP<sup>14,18</sup> is a secreted version of mRFP1 carrying the same signal peptide as secGFP. N-YFP-HDEL is a YFP-based spectral variant of N-GFP-HDEL<sup>22</sup>, which carries the ER-retrieval signal His-Asp-Glu-Leu at its carboxy terminus and a signal peptide followed by an engineered N-glycosylation site at its amino terminus. ST-RFP<sup>31</sup> is an mRFP1 derivative carrying the amino terminus and transmembrane domain of rat N- $\alpha$ -2,6-sialyltransferase, which targets proteins to the plant Golgi apparatus<sup>13,22,23,25</sup>, preferentially to *trans*-cisternae<sup>17</sup>. YFP-RAB-E1<sup>d</sup> is YFP fused to an *Arabidopsis* paralogue of Rab8 and Ypt2 of mammals and yeasts<sup>8,18</sup>. YFP-AtRAB-B1<sup>b</sup> is a YFP fusion to an *Arabidopsis* paralogue of animal Rab2 (ref. 8) that localizes to the Golgi (ref. 32; and C. Chow and I.M., unpublished results). YFP-AtRAB-H1<sup>b</sup>, a YFP fusion to a paralogue of Ypt6 and Rab6 in yeast and mammals, respectively<sup>8</sup>, that localizes to the plant Golgi (C. Chow and I. Moore, unpublished results). N-ST-RFP-2A-GFP-HDEL<sup>14</sup>, which produces a Golgi-localized RFP (red) and an ER-localized GFP (green) in stoichiometric quantities from a single polyprotein that is cleaved by the FMDV 2A peptide<sup>14</sup>. Targeting signals are the same as those of ST-RFP and N-YFP-HDEL (see above). N-secRFP-2A-GFP-HDEL<sup>14</sup> produces stoichiometric quantities of an ER-localized GFP and an RFP that is targeted to the vacuole via the ER and Golgi by virtue of the FMDV 2A-peptide sequence at its carboxy terminus (see ref. 14 for further details). Nag-EGFP is an *Arabidopsis* N-acetylglucosaminyl transferase I fusion to EGFP. PMA4-GFP is a GFP fusion to a *Nicotiana plumbaginifolia* plasma membrane H<sup>+</sup>-ATPase<sup>33</sup>.

**Confocal microscopy and image analysis.** An LSM 510 META laser-scanning microscope (Carl Zeiss) with 25mW Argon and 2mW HeNe lasers was used for confocal analysis. The instrument was configured as described in refs 13 and 14 except for imaging of: GNL1-YFP and GNL1(L696M)-YFP fusions, which were detected using 488 nm excitation and a 505–550 nm bandpass filter; Alexa Fluor 488, which was excited using a 405/488/543 primary dichroic mirror and the 488 nm argon line and detected with a 490–510 nm bandpass filter; and FM4-64 and MitoTracker Orange, which were each excited using a 458/543 nm primary dichroic and 543 nm excitation from a HeNe laser and were detected with 585–615 nm band pass or 585 nm long-pass filter (FM4-64) or 565–615 nm bandpass filter (MitoTracker). When GFP was imaged together with other fluorescent molecules, GFP was excited by the 458 nm line of the argon laser in a multi-track configuration with line sequential scanning. Projections are maximum projections in z. Measurements of apparent Golgi sizes were performed on z-stack images acquired using a C-Apochromat  $\times 40/1.2$  numerical aperture water-immersion coverslip-corrected objective at scan zoom 4. The 'Measure' mode of the Zeiss LSM Image Browser was used to measure the diameter of ST-RFP-labelled Golgi stacks in face view with sub-saturating fluorescence, as revealed by a look-up table in the image palette. The presence or absence of PIN2-labelled BFA bodies was determined in z-stack images acquired using a C-Apochromat  $\times 40/1.2$  water immersion coverslip-corrected objective at scan zoom 1.1. To score cells with PIN2-labelled BFA compartments the percentage of cells with BFA compartments from each seedling, gathered from two experiments using two independent anti-PIN2 antisera, were used to compute the average values and standard deviations.

For live cell imaging seedlings were mounted whole in water with dyes or drugs added at the appropriate concentration. For analysis of transient expression, infiltrated leaves were excised and mounted in water immediately before imaging. Material was mounted under a coverslip raised by two strips of insulating tape and retained by Whatmann 3M micropore tape.

All images are presented in 8-bit linear greyscale or linear RGB and were imported into Microsoft Powerpoint for assembly of figures. Brightness and contrast were sometimes adjusted equally for sets of images in Microsoft Powerpoint. In Supplementary Information, an Excel file named Image Parameters lists the imaging parameters and processing for each individual image of Figs 1–3.

**Staining and inhibitor treatment.** FM4-64 (Molecular Probes) was prepared from a 5 mM stock in water. MitoTracker Orange (Molecular Probes) was used at 0.5  $\mu$ M. Brefeldin and cycloheximide (Sigma) were prepared as 200 mM and 355 mM stocks in DMSO, respectively. Four-to-six-day-old seedlings were treated in 5 ml of water, with equal amounts of solvents as the controls.

**Genetic screen.** M<sub>2</sub> seedlings expressing secGFP (S76) were screened for increased fluorescence intensities using a Leica MZ FLIII fluorescence stereomicroscope. In total, 141,000 M<sub>2</sub> seedlings from 28,000 M<sub>1</sub> plants were sown in Petri dishes and after 4 days growth were screened for enhanced GFP fluorescence using a dissecting microscope equipped for epifluorescence. To identify potential temperature-sensitive (*ts*) mutants, plates were then transferred to 31 °C and rescreened daily for 3 days. Eleven mutants exhibited a non-*ts* enhancement of fluorescence and transmitted the phenotype to the M<sub>3</sub> and the F<sub>2</sub> of a backcross to Col-0. These mutants were analysed by confocal laser scanning microscopy to confirm that they accumulated increased quantities of secGFP in intracellular compartments. Two mutants, numbered 44 and 54, exhibited a similar pattern of secGFP accumulation, which they inherited as a monogenic recessive mendelian trait. Both mutants identified were backcrossed twice before being used for phenotypic characterization and positional cloning.

**Immunoblot analysis, and immunolocalization on intact root tissues.** Proteins from roots of 8-day-old seedlings grown on agar plates were extracted and analysed by immunoblot as described<sup>14</sup>. Endoglycosidase-H treatments were performed as described<sup>34</sup>. Rabbit anti-GFP (Molecular Probes) and anti-calreticulin (gift from J. Denecke) were diluted at 1:1,000 and 1:10,000, respectively. Four-day-old seedlings were used for immunolocalization of PIN1 and PIN2 as previously described in refs 12 and 35, respectively, with either Cys3- or Alexa Fluor 488-conjugated secondary antibody (Molecular Probes) diluted 1:600 and 1:500, respectively. Rabbit anti-PIN1 and PIN2 (refs 28, 30) were diluted at 1:200 and 1:250, respectively.

31. Renna, L. *et al.* Identification and characterization of AtCASP, a plant transmembrane Golgi matrix protein. *Plant Mol. Biol.* **58**, 109–122 (2005).
32. Cheung, A. Y. *et al.* Rab2 GTPase regulates vesicle trafficking between the endoplasmic reticulum and the Golgi bodies and is important for pollen tube growth. *Plant Cell* **14**, 945–962 (2002).
33. Lefebvre, B., Batoko, H., Duby, G. & Boutry, M. Targeting of a *Nicotiana plumbaginifolia* H<sup>+</sup>-ATPase to the plasma membrane is not by default and requires cytosolic structural determinants. *Plant Cell* **16**, 1772–1789 (2004).
34. Batoko, H., Zheng, H.-Q., Hawes, C. & Moore, I. A. Rab1 GTPase is required for transport between the endoplasmic reticulum and Golgi apparatus and for normal Golgi movement in plants. *Plant Cell* **12**, 2201–2217 (2000).
35. Peer, W. A. *et al.* Variation in expression and protein localization of the PIN family of auxin efflux facilitator proteins in flavonoid mutants with altered auxin transport in *Arabidopsis thaliana*. *Plant Cell* **16**, 1898–1911 (2004).

# A flagellin-induced complex of the receptor FLS2 and BAK1 initiates plant defence

Delphine Chinchilla<sup>1</sup>, Cyril Zipfel<sup>1,2</sup>, Silke Robatzek<sup>1,3</sup>, Birgit Kemmerling<sup>4</sup>, Thorsten Nürnberger<sup>4</sup>, Jonathan D. G. Jones<sup>2</sup>, Georg Felix<sup>1,4</sup> & Thomas Boller<sup>1</sup>

Plants sense potential microbial invaders by using pattern-recognition receptors to recognize pathogen-associated molecular patterns (PAMPs)<sup>1</sup>. In *Arabidopsis thaliana*, the leucine-rich repeat receptor kinases flagellin-sensitive 2 (FLS2) (ref. 2) and elongation factor Tu receptor (EFR) (ref. 3) act as pattern-recognition receptors for the bacterial PAMPs flagellin<sup>4</sup> and elongation factor Tu (EF-Tu) (ref. 5) and contribute to resistance against bacterial pathogens. Little is known about the molecular mechanisms that link receptor activation to intracellular signal transduction. Here we show that BAK1 (BRI1-associated receptor kinase 1), a leucine-rich repeat receptor-like kinase that has been reported to regulate the brassinosteroid receptor BRI1 (refs 6,7), is involved in signalling by FLS2 and EFR. Plants carrying *bak1* mutations show normal flagellin binding but abnormal early and late flagellin-triggered responses, indicating that BAK1 acts as a positive regulator in signalling. The *bak1*-mutant plants also show a reduction in early, but not late, EF-Tu-triggered responses. The decrease in responses to PAMPs is not due to reduced sensitivity to brassinosteroids. We provide evidence that FLS2 and BAK1 form a complex *in vivo*, in a specific ligand-dependent manner, within the first minutes of stimulation with flagellin. Thus, BAK1 is not only associated with developmental regulation through the plant hormone receptor BRI1 (refs 6,7), but also has a functional role in PRR-dependent signalling, which initiates innate immunity.

PAMPs have key roles as activators of the innate immune response in animals<sup>8</sup> and, analogously, as 'general elicitors' of defence responses in plants<sup>1–5,9–11</sup>. We have previously characterized FLS2 and EFR as the pattern-recognition receptors (PRRs) for flagellin (represented by a 22-amino-acid peptide, flg22) and for EF-Tu (represented by the peptides elf18 and elf26, which correspond to its amino terminus), respectively<sup>2–5,10</sup>. Flagellin and EF-Tu rapidly induce a common set of *Arabidopsis* genes for leucine-rich repeat receptor-like kinases (LRR-RLKs), including *FLS2* and *EFR* themselves<sup>3,11</sup>. This led to the assumption that some of these PAMP-induced LRR-RLKs might encode additional components of PAMP perception or signalling. Using a reverse genetic approach, we tested a collection of insertional mutants in these LRR-RLKs (previously used for identification of the *EFR* gene<sup>3</sup>) for responsiveness to flg22 and found that two mutants with insertions in the LRR-RLK gene *At4g33430* have reduced sensitivity to flg22 in seedling growth assays (Fig. 1a,b). In more than 10 repetitions of seedling growth assays with these mutants, we always observed a clear reduction (but never a complete loss) of sensitivity to flg22 and flg22-related peptides. By contrast, the mutants seemed to be as sensitive as the wild type to treatment with elf18 in more than five seedling growth assays (Fig. 1b and data not shown).

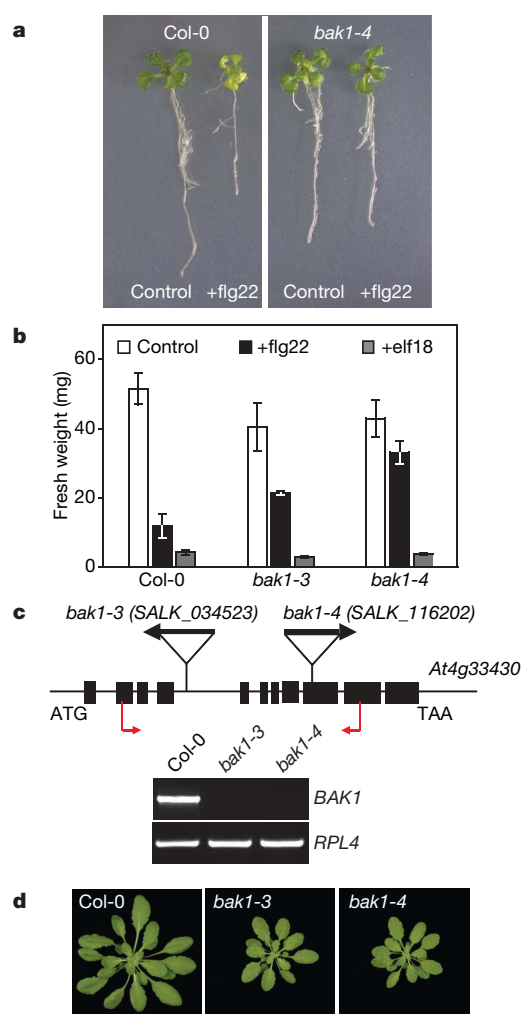


**Figure 1 | *bak1* mutants show reduced sensitivity to flagellin in growth assays.** **a**, Wild-type (Col-0) and *bak1-4* seedlings grown for 9 days in the presence of 10 nM flg22. **b**, Seedling growth of Col-0, *bak1-3* and *bak1-4* after treatment with 10 nM flg22 or 10 nM elf18. Results shown are means  $\pm$  s.d. ( $n = 6$ ). **c**, T-DNA insertion sites in *bak1-3* and *bak1-4* with exons shown as black boxes (top). RT-PCR analysis of *BAK1* and *RPL4* (control) transcripts in Col-0, *bak1-3* and *bak1-4* seedlings (bottom). Primers indicated by red arrows were used to test for the presence of a full-length *BAK1* transcript. **d**, Col-0, *bak1-3* and *bak1-4* plants, photographed 4 weeks after germination.

<sup>1</sup>Zurich-Basel Plant Science Center, Botanical Institute, University of Basel, Hebelstrasse 1, 4056 Basel, Switzerland. <sup>2</sup>The Sainsbury Laboratory, Colney Lane, Norwich, Norfolk NR4 7UH, UK. <sup>3</sup>Max-Planck-Institute for Plant Breeding Research, Carl-von-Linné Weg 10, 50829 Cologne, Germany. <sup>4</sup>Institute of Plant Biochemistry, ZMBP, University of Tuebingen, 72076 Tuebingen, Germany.

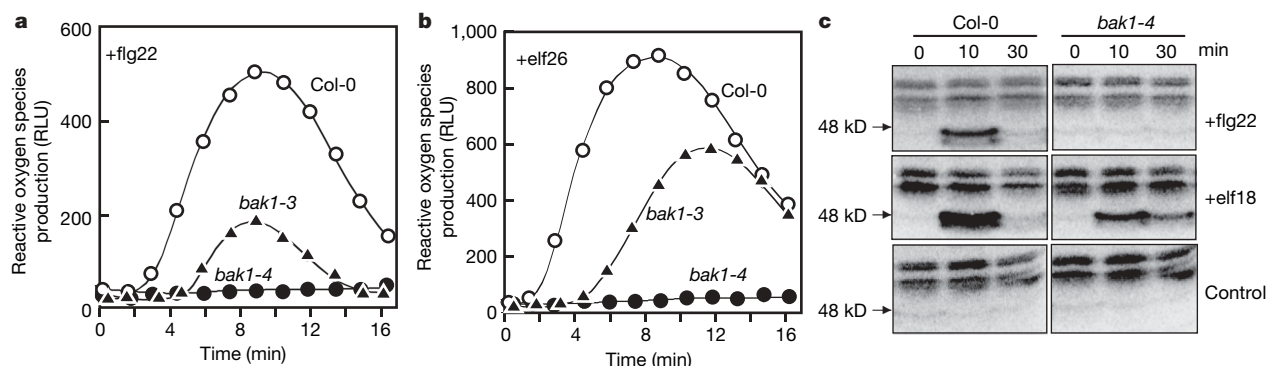


**Figure 2 | *bak1* mutants are impaired in responsiveness to flagellin and EF-Tu.** **a**, Oxidative burst induced by 10 nM flg22, measured in relative light units (RLU) in leaves of wild-type (Col-0), *bak1-3* and *bak1-4* plants. Results shown are means of six replicates. **b**, Oxidative burst induced by 10 nM elf26. Results shown are means of six replicates. **c**, MBP kinase activity in Col-0

plants and *bak1-4* mutants after mock treatment (control) or treatment with 1  $\mu$ M flg22<sup>Xac</sup> or 1  $\mu$ M elf18. Gels were loaded with equal amounts of protein; no radiolabelled bands were observed in the parts of the gel omitted from the figure.

The LRR-RLK that is encoded by *At4g33430* has been shown to interact with the brassinosteroid receptor BRI1 and was therefore named BRI1-associated receptor kinase 1 (BAK1)<sup>6,7</sup>. We consequently renamed the allelic lines *SALK\_034523* and *SALK\_116202* as *bak1-3* and *bak1-4*, respectively (Fig. 1c). Both T-DNA insertion lines lacked the signal for BAK1 mRNA that is seen in wild-type plants when tested with appropriate primers by PCR with reverse transcription (RT-PCR; Fig. 1c) or by northern blot analysis (Supplementary Fig. 1). Complementation of *bak1* mutants with wild-type BAK1 restored their responsiveness to flg22 (data not shown).

Brassinolide and other brassinosteroids are structurally related to the animal steroid hormones and control many aspects of plant growth and development<sup>12</sup>. The two *bak1* mutants that have been previously characterized show a semi-dwarf phenotype and reduced sensitivity to brassinolide<sup>6,7</sup>. Similarly, the *bak1-3* and *bak1-4* mutant lines showed reduced size when grown in soil (Fig. 1d). In our standard growth assays to measure long-term flg22 and elf18 responses<sup>2,3</sup>, exogenous brassinolide applied at 10 nM had a marginal growth-promoting effect in wild-type but not in *bak1* mutant seedlings (Supplementary Fig. 2a). Treatments with 100 nM and 1  $\mu$ M brassinolide stimulated the growth of *bak1* and wild-type seedlings to the same degree, showing that any *bak1*-mediated defect was overcome by brassinolide at 100 nM or more. In the presence of 100 nM brassinolide, flg22 still inhibited the growth of wild-type much more than *bak1-4* seedlings (Supplementary Fig. 2b), indicating that the growth inhibition that is induced by flg22 is independent of brassinosteroid signalling. Corroborating this conclusion, *cabbage 1* (*cbb1*) mutant plants, which are defective in brassinosteroid synthesis<sup>13</sup>, were as sensitive to flg22 as were wild-type plants (Supplementary Fig. 2c,d).

To test whether BAK1 has a direct role in flagellin signalling, we studied some of the early responses that are triggered by PAMPs in plants. Wild-type plants responded rapidly to flg22 with the induction of an oxidative burst (Fig. 2a). This response was clearly reduced and delayed in *bak1-3* plants and almost abolished in *bak1-4* mutants. Interestingly, the oxidative burst triggered by elf26 was also impaired in *bak1-3* and *bak1-4* mutants (Fig. 2b), providing evidence that mutations in *bak1* also affect EF-Tu responses. Signalling in response to flagellin and EF-Tu involves the rapid activation of MAP kinases (MAPK)<sup>3</sup>. In-gel assays with myelin basic protein (MBP) as a substrate showed that activation of MAPK was delayed and reduced or even absent after stimulation with EF-Tu or flagellin in the *bak1-4* mutant, when compared to the wild type (Fig. 2c). These results show that signalling and early responses to flg22 and EF-Tu are affected in *bak1* mutants. Therefore, we propose that BAK1 is a positive regulator of PAMP signalling in *Arabidopsis*.

The reduced sensitivity of *bak1* mutants to flagellin might be due to a reduction in the expression or function of the flagellin receptor FLS2. However, western blotting detected similar amounts of FLS2 protein in wild-type and *bak1* mutant plants (Fig. 3a). In addition, the amount and affinity of functional receptor binding sites were similar in wild-type and *bak1* plants (Fig. 3b,c). Similarly, *bak1* mutants have been reported to show normal binding of brassinolide to BRI1 (ref. 14). Thus, BAK1 seems to regulate the function of both receptors, BRI1 and FLS2, at a step after ligand binding. There is evidence that BAK1 is involved in BRI1 endocytosis<sup>15</sup>, and we recently found that FLS2 undergoes ligand-induced endocytosis<sup>16</sup>. Compared to wild-type plants, *bak1-3* mutants showed markedly reduced endocytosis of FLS2 (Supplementary Fig. 3).

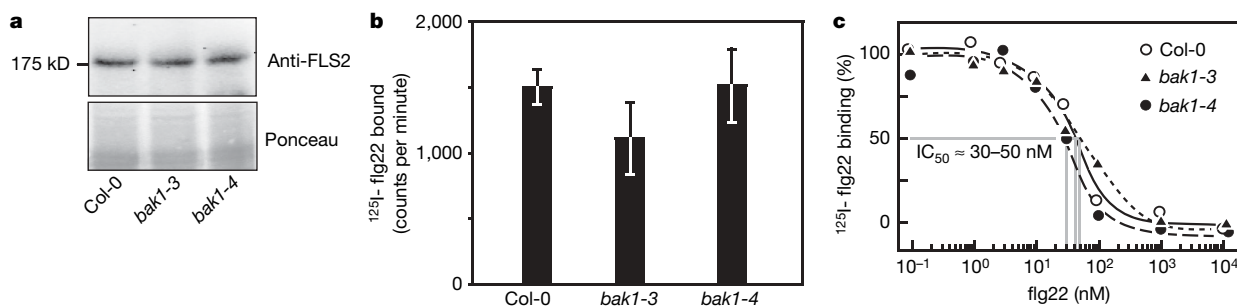


**Figure 3 | Flg22 binding sites are unaffected in *bak1* mutants.** **a**, Western blot analysis of extracts from wild-type (Col-0), *bak1-3* and *bak1-4* seedlings with anti-FLS2 antibodies (top). Ponceau stain of the blot shows equal loading (bottom). **b**, Abundance of flagellin receptor binding sites in Col-0, *bak1-3* and *bak1-4* plants, estimated by specific binding of <sup>125</sup>I-flg22. Results

shown are means  $\pm$  s.d. ( $n = 3$ ). **c**, Competitive binding assays in *bak1-3*, *bak1-4* and Col-0. Binding of <sup>125</sup>I-flg22 was tested in the presence of different concentrations of unlabelled flg22. The concentration of flg22 required to reduce binding by 50% (IC<sub>50</sub>) is indicated by the vertical grey lines.



To test whether BAK1 interacts with FLS2, we used transgenic plants expressing Myc-tagged BAK1 in co-immunoprecipitation experiments (Fig. 4). Immunoprecipitates with anti-FLS2 antibodies revealed very little BAK1–Myc in untreated controls (Fig. 4). By contrast, the immunoprecipitates from plants stimulated with flg22 contained much more BAK1–Myc, indicating that FLS2 interacts with BAK1 in a stimulus-dependent manner (Fig. 4). BAK1–Myc could not be detected in immunoprecipitates with control antibodies (Fig. 4a), or in anti-FLS2 immunoprecipitates from non-transgenic plants (Fig. 4d). The reciprocal immunoprecipitation using anti-Myc antibodies confirmed the flg22-dependent heteromerization of BAK1 and FLS2 (Fig. 4b). We used immunoprecipitates such as those presented in Fig. 4a,b to study flg22 binding (Fig. 4c). Immunoprecipitates obtained with anti-FLS2 antibodies contained similar, large amounts of FLS2-binding sites, regardless of flg22 treatment. Thus, FLS2 binds flg22 independently of its association with BAK1. Immunoprecipitates obtained with anti-Myc antibodies prepared from untreated plants did not contain FLS2 (Fig. 4b) and had negligible flg22 binding (Fig. 4c), showing that BAK1 by itself does not bind flg22. By contrast, anti-Myc immunoprecipitates from flg22-treated cells contained FLS2 (Fig. 4b) and were able to bind flg22 (Fig. 4c). Fewer binding sites were detectable in this precipitate than in the immunoprecipitates generated with anti-FLS2 antibodies, indicating that only a fraction of the FLS2 present in the solubilised was pulled down in association with BAK1. Ligand-induced formation of the FLS2–BAK1 complex was specific for flg22 and did not occur after stimulation of the plants with elf26 (Fig. 4d) or treatment with brassinolide (Fig. 4e). Moreover, the antagonist peptide flg22- $\Delta$ 2, which binds FLS2 without activating a response<sup>10</sup>, failed to induce complex formation (Fig. 4e). Pre-treatment with the protein kinase inhibitor K-252a, which inhibits elicitor responses<sup>4,17</sup>, reduced the flg22-induced formation of the complex between the two serine/threonine kinases<sup>6,7,18</sup> BAK1 and FLS2 (Fig. 4f). We could not trigger an association of FLS2 and BAK1 *in vitro* by adding flg22 to extracts of untreated plants (data not shown). *In vivo*, however, complex

formation occurred rapidly—within 2 min of treatment with flg22 (Fig. 4g). These kinetics are consistent with the idea that the FLS2–BAK1 complex is involved in receptor activation, as the earliest flg22-triggered responses can be measured after about 2 min of lag phase<sup>4</sup>.

Ligand-induced dimerization is important for the activation of receptor kinases in animals<sup>19,20</sup>. Interestingly, classifying receptor kinases according to the occurrence of an arginine–aspartic acid (RD) motif in the catalytic site, FLS2 belongs to the non-RD class and BAK1 to the RD class<sup>21</sup>. This extends the similarity of signalling by PRRs in plants and animals highlighted in a recent review<sup>21</sup>: PAMP recognition in animals through Toll-like receptors initially involves interaction with interleukin-1 receptor-associated kinase 1 (IRAK1), a non-RD kinase, and subsequently with IRAK4, an RD kinase.

BAK1 also associates with BRI1 (refs 22,23), an RD kinase<sup>21</sup>. However, the physiological responses that are triggered by BRI1 and FLS2 are very different. Therefore, BAK1 probably does not determine the specificity of the signal output; rather, it is likely to have a common role as an adaptor or co-receptor for the regulation of various receptors. Recent findings also show that *bak1* mutants have altered susceptibility to microbial pathogens such as oomycetes and true fungi<sup>24</sup>, indicating that BAK1 might regulate PRRs other than FLS2 and EFR.

Clearly, *bak1* mutants retain partial sensitivity to flagellin and EF-Tu. One possible explanation for this is that closely related proteins might substitute for BAK1: BAK1 is also named SERK3 because it belongs to the SERK (somatic embryogenesis receptor-like kinase) family, which comprises five closely related LRR-RLKs<sup>25</sup>. The different SERKs might be partially functionally redundant, as reported for SERK1 and SERK2 (refs 26,27). BRI1 was recently found in complex with SERK1 (ref. 28), indicating that BAK1 might be substituted by other SERKs. In contrast to the *serk3* (*bak1*) mutants described in this report, however, the other single mutants *serk1*, *serk2*, *serk4* and *serk5* showed no defect in flg22 and elf18 responses (data not shown). In ongoing work we are trying to establish mutants in multiple *SERK*

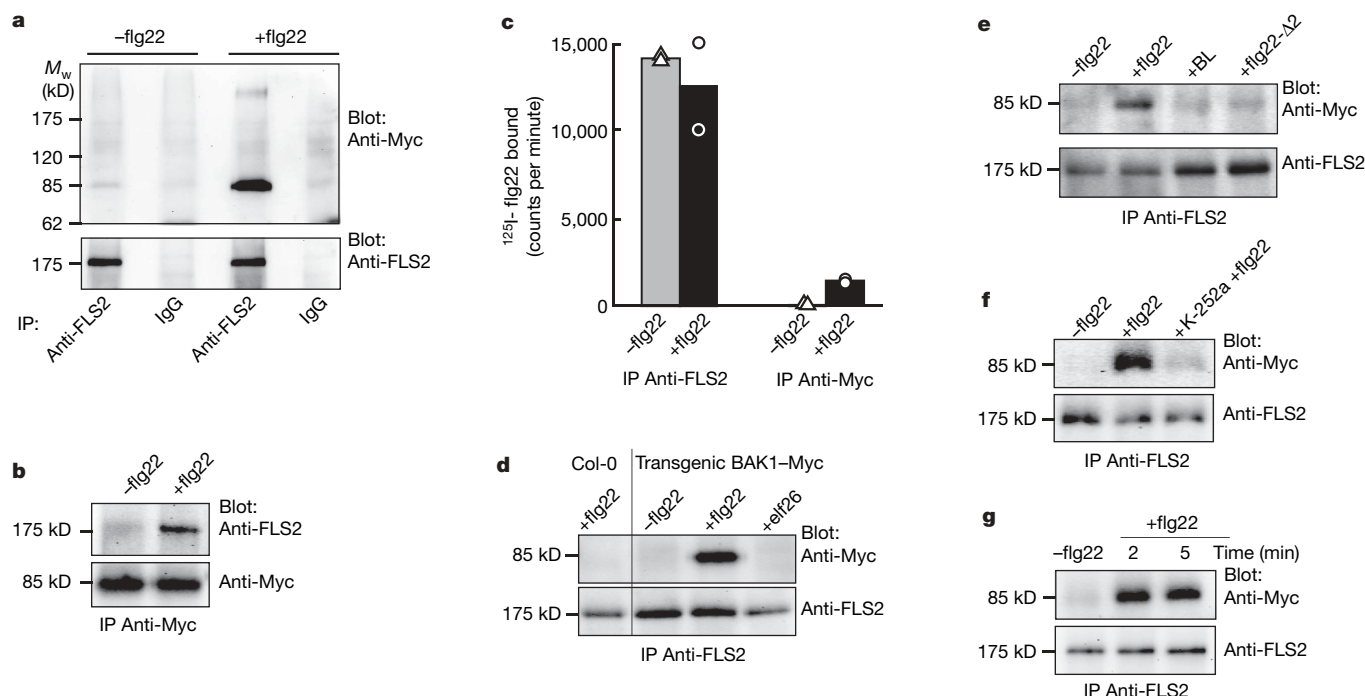


**Figure 4 | FLS2 rapidly interacts with BAK1 in a ligand-dependent manner.** **a**, Seedlings expressing BAK1–Myc were treated (or not) with flg22 for 5 min. Solubilized membrane proteins were immunoprecipitated (IP) with anti-FLS2 or control antibodies (IgG). Top: western blot with anti-Myc antibodies. Bottom: re-analysis of the blot with anti-FLS2 antibodies. **b**, Reciprocal co-immunoprecipitation with anti-Myc antibodies. **c**, Specific

<sup>125</sup>I-flg22 binding in anti-FLS2 and anti-Myc IPs from plants treated (or not) with 1  $\mu$ M flg22. Results are means of two samples. **d**, Formation of FLS2–BAK1 complex is specific for induction by flg22. **e**, Complex formation does not occur after treatment with the antagonist flg22- $\Delta$ 2 or brassinolide (BL). **f**, Pre-treatment with the protein kinase inhibitor K-252a reduces complex formation. **g**, Time course of complex formation.

genes. However, as found for the *serk3 serk4* double mutants, which die within 2 weeks of germination (data not shown, and J. Li, personal communication), this straightforward genetic approach might be impeded by essential functions carried out by the SERK proteins.

In conclusion, receptor activation of FLS2 by its ligand flagellin involves rapid complex formation with BAK1. Our results widen the scope for BAK1 function in a way reminiscent of the TOLL receptor in *Drosophila*, which controls embryo development as well as innate immunity<sup>29</sup>: BAK1 has at least two roles in plants, being a positive regulator of PAMP receptors (thus influencing innate immunity) and of the plant hormone receptor BRI1 (thus influencing development).

## METHODS SUMMARY

The *Arabidopsis* plants used in this study were grown as one plant per pot at 20–21 °C with an 8 h photoperiod, or on plates containing MS salts medium (Duchefa), 1% sucrose, and 0.8% agar under continuous light. The BAK1 T-DNA insertion lines SALK\_034523 (*bak1-3*) and SALK\_116202 (*bak1-4*) were generated by SIGnAL<sup>30</sup> and obtained from the Nottingham *Arabidopsis* Stock Centre (Nottingham, UK). BAK1- and T-DNA-specific primers were used to select plants homozygous for the inserts. *cbi1* (*cabbage 1*) mutant seeds<sup>13</sup> were obtained from the NASC collection. The flagellin peptide flg22, flg22-Δ2 and the EF-Tu peptides elf18 and elf26 used in this study have been described<sup>4,5,11</sup>. The peptide flg22<sup>Xac</sup> (QRLSSGLRINSKDDAAGLAIS), which is equivalent in its action to flg22, was synthesized according to the sequence of the flg22-domain in *Xanthomonas axonopodis* pv. *citri*.

Assays for seedling growth inhibition, oxidative burst, in-gel MBP protein kinase activity, flg22-binding assays and western blot analysis with anti-FLS2 antibodies were performed as described<sup>4,5,10,11</sup>.

For co-immunoprecipitation experiments, seedlings transformed with a pBAK1-BAK1-Myc construct were extracted and immunoprecipitated with anti-FLS2 antibodies, anti-Myc polyclonal antibodies (Upstate), or anti-GFP rabbit serum (Molecular Probes). Immunoprecipitates were analysed by western blot with anti-Myc polyclonal antibodies or FLS2 antibodies.

**Full Methods** and any associated references are available in the online version of the paper at [www.nature.com/nature](http://www.nature.com/nature).

Received 27 April; accepted 7 June 2007.

Published online 11 July 2007.

- Nürnberg, T., Brunner, F., Kemmerling, B. & Piater, L. Innate immunity in plants and animals: striking similarities and obvious differences. *Immunol. Rev.* **198**, 249–266 (2004).
- Gómez-Gómez, L. & Boller, T. FLS2: an LRR receptor-like kinase involved in the perception of the bacterial elicitor flagellin in *Arabidopsis*. *Mol. Cell* **5**, 1003–1011 (2000).
- Zipfel, C. *et al.* Perception of the bacterial PAMP EF-Tu by the receptor EFR restricts agrobacterium-mediated transformation. *Cell* **125**, 749–760 (2006).
- Felix, G., Duran, J. D., Volko, S. & Boller, T. Plants have a sensitive perception system for the most conserved domain of bacterial flagellin. *Plant J.* **18**, 265–276 (1999).
- Kunze, G. *et al.* The N terminus of bacterial elongation factor Tu elicits innate immunity in *Arabidopsis* plants. *Plant Cell* **16**, 3496–3507 (2004).
- Li, J. *et al.* BAK1, an *Arabidopsis* LRR receptor-like protein kinase, interacts with BRI1 and modulates brassinosteroid signalling. *Cell* **110**, 213–222 (2002).
- Nam, K. H. & Li, J. BRI1/BAK1, a receptor kinase pair mediating brassinosteroid signalling. *Cell* **110**, 203–212 (2002).
- Janeway, C. A. Jr & Medzhitov, R. Innate immune recognition. *Annu. Rev. Immunol.* **20**, 197–216 (2002).
- Zeidler, D. *et al.* Innate immunity in *Arabidopsis thaliana*: lipopolysaccharides activate nitric oxide synthase (NOS) and induce defense genes. *Proc. Natl Acad. Sci. USA* **101**, 15811–15816 (2004).

- Chinchilla, D., Bauer, Z., Regenass, M., Boller, T. & Felix, G. The *Arabidopsis* receptor kinase FLS2 binds flg22 and determines the specificity of flagellin perception. *Plant Cell* **18**, 465–476 (2006).
- Zipfel, C. *et al.* Bacterial disease resistance in *Arabidopsis* through flagellin perception. *Nature* **428**, 764–767 (2004).
- Vert, G., Nemhauser, J. L., Geldner, N., Hong, F. & Chory, J. Molecular mechanisms of steroid hormone signalling in plants. *Annu. Rev. Cell Dev. Biol.* **21**, 177–201 (2005).
- Kauschmann, A. *et al.* Genetic evidence for an essential role of brassinosteroids in plant development. *Plant J.* **9**, 701–713 (1996).
- Kinoshita, T. *et al.* Binding of brassinosteroids to the extracellular domain of plant receptor kinase BRI1. *Nature* **433**, 167–171 (2005).
- Rusinova, E. *et al.* Heterodimerization and endocytosis of *Arabidopsis* brassinosteroid receptors BRI1 and AtSERK3 (BAK1). *Plant Cell* **16**, 3216–3229 (2004).
- Robatzek, S., Chinchilla, D. & Boller, T. Ligand-induced endocytosis of the pattern recognition receptor FLS2 in *Arabidopsis*. *Genes Dev.* **20**, 537–542 (2006).
- Felix, G., Grosskopf, D. G., Regenass, M. & Boller, T. Rapid changes of protein phosphorylation are involved in transduction of the elicitor signal in plant cells. *Proc. Natl Acad. Sci. USA* **88**, 8831–8834 (1991).
- Gómez-Gómez, L., Bauer, Z. & Boller, T. Both the extracellular leucine-rich repeat domain and the kinase activity of FLS2 are required for flagellin binding and signalling in *Arabidopsis*. *Plant Cell* **13**, 1155–1163 (2001).
- Massague, J. TGF-β signal transduction. *Annu. Rev. Biochem.* **67**, 753–791 (1998).
- Schlessinger, J. Ligand-induced, receptor-mediated dimerization and activation of EGF receptor. *Cell* **110**, 669–672 (2002).
- Dardick, C. & Ronald, P. Plant and animal pathogen recognition receptors signal through non-RD kinases. *PLoS Pathogens* **2**, e2 (2006).
- Li, J. & Jin, H. Regulation of brassinosteroid signalling. *Trends Plant Sci.* **12**, 37–41 (2007).
- Wang, X. *et al.* Identification and functional analysis of *in vivo* phosphorylation sites of the *Arabidopsis* BRASSINOSTEROID-INSENSITIVE1 receptor kinase. *Plant Cell* **17**, 1685–1703 (2005).
- Kemmerling, B. *et al.* The BRI1-associated kinase 1, BAK1, has a brassinolide-independent role in plant cell-death control. *Curr. Biol.* doi:10.1016/j.cub.2007.05.046 (published online 21 June 2007).
- Hecht, V. *et al.* The *Arabidopsis* SOMATIC EMBRYOGENESIS RECEPTOR KINASE 1 gene is expressed in developing ovules and embryos and enhances embryogenic competence in culture. *Plant Physiol.* **127**, 803–816 (2001).
- Colcombet, J., Boisson-Dernier, A., Ros-Palau, R., Vera, C. E. & Schroeder, J. I. *Arabidopsis* SOMATIC EMBRYOGENESIS RECEPTOR KINASES1 and 2 are essential for tapetum development and microspore maturation. *Plant Cell* **17**, 3350–3361 (2005).
- Albrecht, C., Rusinova, E., Hecht, V., Baaijens, E. & de Vries, S. The *Arabidopsis thaliana* SOMATIC EMBRYOGENESIS RECEPTOR-LIKE KINASES1 and 2 control male sporogenesis. *Plant Cell* **17**, 3337–3349 (2005).
- Karlov, R. *et al.* The *Arabidopsis* SOMATIC EMBRYOGENESIS RECEPTOR-LIKE KINASE1 protein complex includes BRASSINOSTEROID-INSENSITIVE1. *Plant Cell* **18**, 626–638 (2006).
- Lemaître, B., Nicolas, E., Michaut, L., Reichhart, J. M. & Hoffmann, J. A. The dorsoventral regulatory gene cassette spatzle/Toll/cactus controls the potent antifungal response in *Drosophila* adults. *Cell* **86**, 973–983 (1996).
- Alonso, J. M. *et al.* Genome-wide insertional mutagenesis of *Arabidopsis thaliana*. *Science* **301**, 653–657 (2003).

**Supplementary Information** is linked to the online version of the paper at [www.nature.com/nature](http://www.nature.com/nature).

**Acknowledgements** We thank A. Bent and V. Lipka for critically reading the manuscript; S. Salomon and A. Caniard for technical help; and the Salk Institute Genomic Analysis Laboratory (SIGnAL) and the NASC stock center for the T-DNA insertion lines and *cbi1* seeds. This work was supported by the Swiss National Foundation and the European Molecular Biology Organization.

**Author Information** Reprints and permissions information is available at [www.nature.com/reprints](http://www.nature.com/reprints). The authors declare no competing financial interests. Correspondence and requests for materials should be addressed to D.C. ([delphine.chinchilla@unibas.ch](mailto:delphine.chinchilla@unibas.ch)) or T.B. ([thomas.boller@unibas.ch](mailto:thomas.boller@unibas.ch)).

## METHODS

**Plant material and growth conditions.** *Arabidopsis* plants used in this study were grown as one plant per pot at 20–21 °C with an 8-h photoperiod, or on plates containing MS salts medium (Duchefa), 1% sucrose, and 0.8% agar under continuous light. The *BAK1* T-DNA insertion lines *SALK\_034523* (*bak1-3*) and *SALK\_116202* (*bak1-4*) were generated by SIGnAL<sup>30</sup> and obtained from the Nottingham *Arabidopsis* Stock Centre (Nottingham, UK). *BAK1*- and T-DNA-specific primers were used to select plants homozygous for the inserts. *cbi1* (*cabbage 1*) mutant seeds<sup>13</sup> were obtained from the NASC collection.

**Materials.** The flagellin peptide flg22, flg22-Δ2 and the EF-Tu peptides elf18 and elf26 used in this study have been described<sup>4,5,11</sup>. The peptide flg22<sup>Xac</sup> (QRLSSGLRINSAKDD AAGLAIS), which is equivalent in its action to flg22, was synthesized according to the sequence of the flg22-domain in *Xanthomonas axonopodis* pv. *citri*. Brassinolide (Sigma) and K-252a (Alexis) were prepared as stock solutions of 10 mM in formamide and 2 mM in DMSO, respectively.

**Bioassays.** Assays for seedling growth inhibition, oxidative burst and in-gel MBP protein kinase activity were performed as described<sup>4,5,11</sup>.

**RT-PCR analysis.** One microgram of DNase-treated RNA was reverse-transcribed using Superscript II reverse transcriptase (Invitrogen), and one microlitre of the reaction mix was used for PCR amplification with 30 cycles and the *BAK1* primers that span the T-DNA insertion locations (5'-GGTG-CTTCAAAGTTGGGATG-3' and 5'-GGCTTCAAACCTT CATCCAACAAA-3') or for the constitutively expressed control gene *RPL4* (*At1g07320* (5'-TGATAGGTCAGGTCAGGGAACAAC-3' and 5'-CCACCACCACGAA CTC-ACCGCG AGTC-3')).

**Binding assays.** Binding assays with plant extracts were done as described<sup>10</sup>. Briefly, 100 mg of leaves ground in liquid nitrogen were resuspended in 500 µl of binding buffer (25 mM MES/KOH pH 6.0, 3 mM MgCl<sub>2</sub>, 10 mM NaCl). Aliquots of 80 µl of extract were incubated in binding buffer in a total volume of 100 µl with <sup>125</sup>I-flg22 (60 fmol per standard assay, >2,000 Ci mmol<sup>-1</sup>) for 25 min either alone (total binding) or with an excess of 10 µM unlabelled flg22 (non-specific binding). After incubation for 25 min at 4 °C, unbound ligand was removed by filtration and radioactivity retained on the filters was determined by

γ-counting. To determine the specific binding, non-specific binding was subtracted from total binding.

**Generation of transgenic plants.** A 1-kb fragment of the *BAK1* promoter was amplified from genomic DNA (wild-type Col-0) and introduced into the *XbaI* and *BamHI* sites of binary vector pGREENII/ T-0229 (ref. 31). The *BAK1* gene was amplified by PCR from genomic DNA and cloned into the *BamHI* and *XhoI* sites of pGREENII; the 3xMyc tag was PCR amplified and cloned in *XhoI* of this construct. The final construct *BAK1p-BAK1-3xMyc* was verified by sequencing, electroporated into *Agrobacterium* EHA101 containing the helper plasmid pSOUP<sup>31</sup> and used to transform *bak1-4* mutant plants. Plants of the T2 generation were chosen for the co-immunoprecipitation experiments.

**Immunoprecipitation experiments.** Seedlings (1 g fresh weight), grown for 2 weeks in liquid MS medium, were frozen in liquid nitrogen, extracted by grinding with mortar and pestle, and taken up in 2.5 ml of cold extraction buffer (50 mM Tris-HCl pH 8, 150 mM NaCl, 10% glycerol, 1% (w/v) Nonidet P-40, 0.5% (w/v) sodium deoxycholate and protease inhibitor cocktail (Sigma)). After incubation for 2 h at 4 °C with gentle shaking, this preparation was filtered through Miracloth and centrifuged at 40,000 r.p.m. for 30 min. The supernatant was incubated overnight at 4 °C with proteinA-sepharose beads (Amersham Biosciences) and polyclonal anti-FLS2 antibodies, anti-Myc (Upstate), or anti-GFP rabbit serum (Molecular Probes) used as control. The beads were collected and washed three times with ice-cold extraction buffer and once with 50 mM Tris-HCl pH 7.5. Proteins that were retained on the beads were separated by SDS-PAGE 7% (w/v) and analysed by western blot with antibodies against Myc or FLS2 as described<sup>10</sup>. Unless indicated otherwise, seedlings were treated for 5 min with 10 µM of peptides (flg22 or elf26 as indicated), with 1 µM of flg22-Δ2, with 1 µM of brassinolide or 1 µM of K-252a. Controls were run in parallel with application of the solvents alone (DMF for brassinolide and DMSO for K-252a, respectively).

31. Hellens, R. P., Edwards, E. A., Leyland, N. R., Bean, S. & Mullineaux, P. M. pGreen: a versatile and flexible binary Ti vector for *Agrobacterium*-mediated plant transformation. *Plant Mol. Biol.* **42**, 819–832 (2000).



# DAI (DLM-1/ZBP1) is a cytosolic DNA sensor and an activator of innate immune response

Akinori Takaoka<sup>1,3\*</sup>, ZhiChao Wang<sup>1\*</sup>, Myoung Kwon Choi<sup>1\*</sup>, Hideyuki Yanai<sup>1</sup>, Hideo Negishi<sup>1</sup>, Tatsuma Ban<sup>1</sup>, Yan Lu<sup>1</sup>, Makoto Miyagishi<sup>2</sup>, Tatsuhiko Kodama<sup>5</sup>, Kenya Honda<sup>1</sup>, Yusuke Ohba<sup>4</sup> & Tadatsugu Taniguchi<sup>1</sup>

Central to innate immunity is the sensing of pathogen-associated molecular patterns by cytosolic and membrane-associated receptors<sup>1–4</sup>. In particular, DNA is a potent activator of immune responses during infection or tissue damage<sup>5–7</sup>, and evidence indicates that, in addition to the membrane-associated Toll-like receptor 9, an unidentified cytosolic DNA sensor(s) can activate type I interferon (IFN) and other immune responses<sup>8–10</sup>. Here we report on a candidate DNA sensor, previously named DLM-1 (also called Z-DNA binding protein 1 (ZBP1))<sup>11</sup>, for which biological function had remained unknown; we now propose the alternative name DAI (DNA-dependent activator of IFN-regulatory factors<sup>12</sup>). The artificial expression of otherwise IFN-inducible DAI (DLM-1/ZBP1) in mouse fibroblasts selectively enhances the DNA-mediated induction of type I IFN and other genes involved in innate immunity. On the other hand, RNA interference of messenger RNA for DAI (DLM-1/ZBP1) in cells inhibits this gene induction programme

upon stimulation by DNA from various sources. Moreover, DAI (DLM-1/ZBP1) binds to double-stranded DNA and, by doing so, enhances its association with the IRF3 transcription factor and the TBK1 serine/threonine kinase. These observations underscore an integral role of DAI (DLM-1/ZBP1) in the DNA-mediated activation of innate immune responses, and may offer new insight into the signalling mechanisms underlying DNA-associated antimicrobial immunity and autoimmune disorders.

Nucleic acids, exposed in a cell by infection or by incomplete clearance during cell damage, can evoke immune responses<sup>6,13,14</sup>. In addition to RNA-sensing mechanisms<sup>4,15–19</sup>, recent attention has focused on characterizing DNA-sensing systems as they also evoke protective and pathological immune responses. Evidence indicates the presence of a cytosolic DNA sensor(s) that can initiate innate immune responses, including the induction of type I IFN genes<sup>8,9,20</sup>, independently of Toll-like receptor 9 (TLR9), the membrane

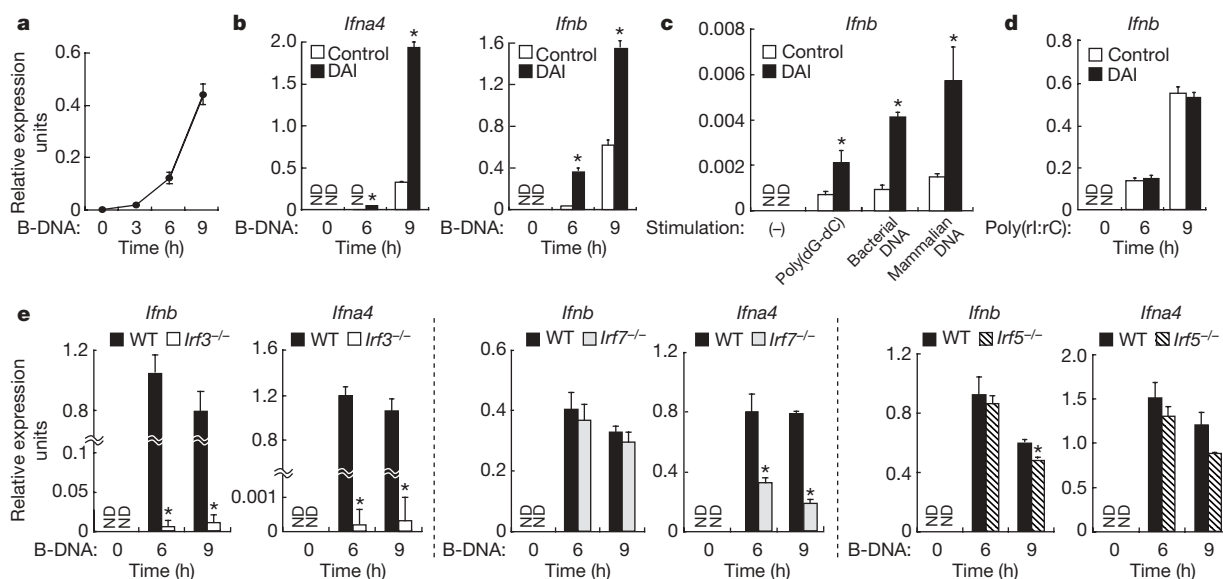


**Figure 1 | DAI (DLM-1/ZBP1) is a positive regulator for type I IFN induction by cytosolic DNA.** **a**, Induction of DAI (*DLM-1/Zbp1*) mRNA by poly(dA-dT)•poly(dT-dA) (B-DNA) in MEFs was analysed by quantitative RT-PCR. Error bars in all panels indicate s.d. ( $n = 3$ ). **b–d**, L929 fibroblasts retrovirally expressing mock (control) or DAI (DLM-1/ZBP1) were treated with B-DNA (**b**), poly(dG-dC)•poly(dC-dG) and bacterial (*Escherichia coli*) or mammalian (calf thymus) genomic DNAs (**c**), or poly(rI:rC) (**d**), and then

assayed for IFN- $\alpha/\beta$  mRNAs by quantitative RT-PCR. Similarly, an enhanced effect by DAI (DLM-1/ZBP1) expression was observed in MEFs (Supplementary Fig. 1g). Asterisk,  $P < 0.01$ , DAI (DLM-1/ZBP1) versus control. ND, not detected. **e**, Wild-type (WT) and littermate *Irf3*<sup>-/-</sup>, *Irf7*<sup>-/-</sup> and *Irf5*<sup>-/-</sup> MEFs were treated with B-DNA, and then assessed for the expression of IFN- $\alpha/\beta$  mRNAs by quantitative RT-PCR. Asterisk,  $P < 0.01$  as compared with wild-type MEFs.

<sup>1</sup>Department of Immunology, and <sup>2</sup>Department of 21st Century Center of Excellence Program, Graduate School of Medicine and Faculty of Medicine, University of Tokyo, Hongo 7-3-1, Bunkyo-ku, Tokyo 113-0033, Japan. <sup>3</sup>Division of Signaling in Cancer and Immunology, Institute for Genetic Medicine, Hokkaido University, and <sup>4</sup>Department of Laboratory Medicine, Hokkaido University Graduate School of Medicine, N15, W7, Kita-ku, Sapporo 060-0815, Japan. <sup>5</sup>Department of Molecular Biology and Medicine, Research Center for Advanced Science and Technology, University of Tokyo, Komaba 4-6-1, Meguro-ku, Tokyo 153-8904, Japan.

\*These authors contributed equally to this work.

receptor activated by hypomethylated DNA<sup>5,20</sup>. We came across an IFN-inducible gene that piqued our interest for its potential role in DNA sensing (Supplementary Fig. 1a–c)—this gene was first identified in tumour stromal tissue and named *DLM-1* (ref. 11), and was later reported to contain two binding domains for left-handed Z-form DNA (Z-DNA) and hence was also termed *Zbp1* (refs 21, 22). Nevertheless, neither a rigorous assessment of its biological function nor its ability to interact with other DNA was performed.

As shown in Fig. 1a and Supplementary Fig. 1d, mRNA expression for *DLM-1/Zbp1* is strongly upregulated in mouse embryonic fibroblasts (MEFs) and L929 cells when stimulated with a synthetic DNA, poly(dA-dT)•poly(dT-dA), which may take on a B-form configuration in solution and strongly evoke innate immune responses<sup>9</sup> (hereafter referred to as B-DNA for convenience; see Methods). This gene induction is dependent on type I IFN signalling (Supplementary Fig. 1e; see also ref. 9). Many genes involved in stimulating IFN responses, including those for cytosolic RNA sensors<sup>15,16</sup>, are themselves IFN-inducible; this positive feedback regulation thereby ensures a robust innate immune response. Thus, we hypothesized

that *DLM-1/ZBP1* may function in the DNA-mediated activation of innate immunity. In light of its newly revealed function demonstrated below, we propose the alternative name of DAI (DNA-dependent activator of IFN-regulatory factors), although we use DAI (*DLM-1/ZBP1*) throughout for continuity and to acknowledge previous publications.

To assess the contribution of DAI (*DLM-1/ZBP1*) to a DNA-mediated immune response, we artificially expressed DAI (*DLM-1/ZBP1*) cDNA in L929 cells (Supplementary Fig. 1f), stimulated the cells with B-DNA, and then examined type I IFN gene induction. As shown in Fig. 1b, B-DNA-induced expression of IFN- $\alpha$  ( $\alpha 4$ ) and IFN- $\beta$  mRNAs (*Ifna4* and *Ifnb*, respectively) occurred much earlier and reached a higher level in DAI (*DLM-1/ZBP1*)-expressing L929 cells than in control cells. This DAI (*DLM-1/ZBP1*)-mediated response was dose dependent (Supplementary Fig. 2a, b) and probably TLR9-independent (refs 9, 10; see also Supplementary Fig. 3a, b). Notably, enhancement of *Ifnb* mRNA induction in DAI (*DLM-1/ZBP1*)-expressing L929 cells was also observed upon treatment with bacteria- and calf-thymus-derived DNA as well as with a synthetic poly(dG-dC)•poly(dC-dG) DNA that may take on a Z-form

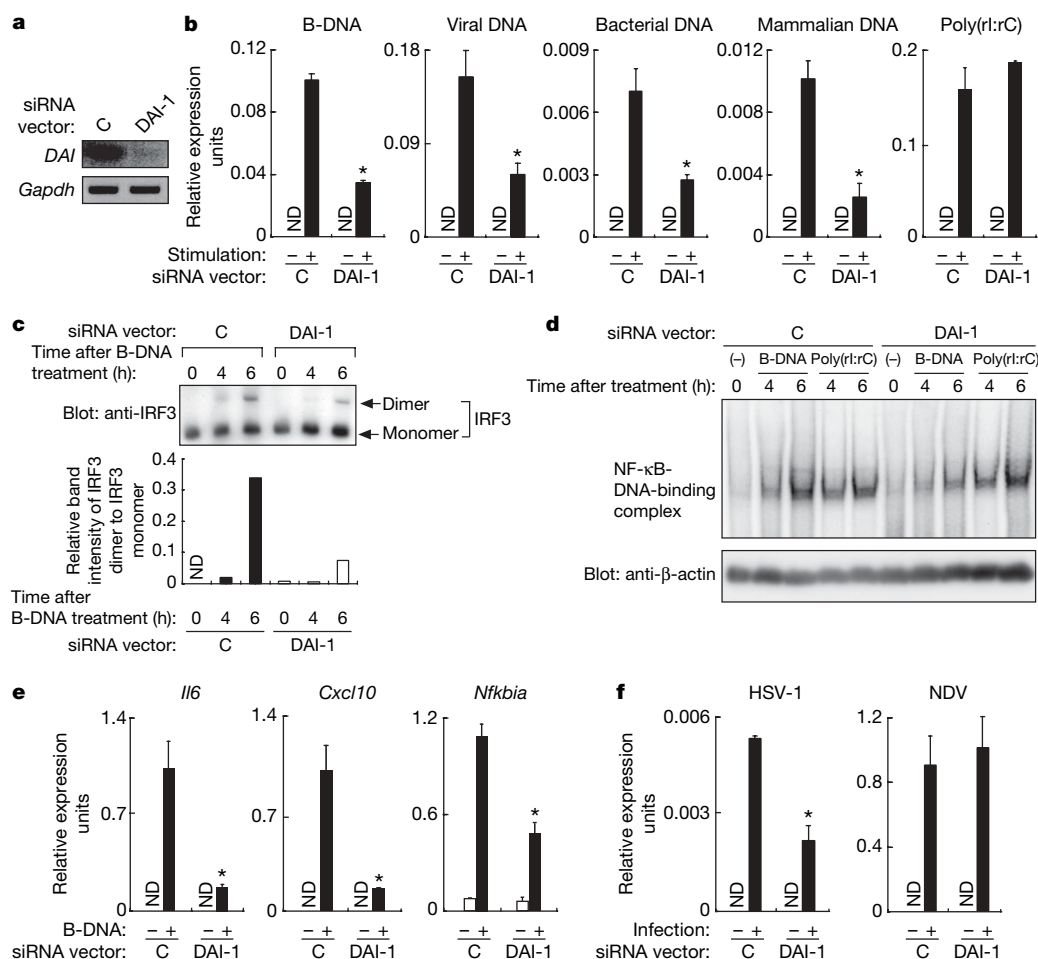


**Figure 2 | DAI (*DLM-1/ZBP1*) is critical for B-DNA-mediated IRF3 activation and *Ifnb* mRNA expression.** **a**, L929 cells were transfected with a plasmid vector encoding a control siRNA (C) or DAI (*DLM-1/Zbp1*)-targeting siRNA (DAI-1), and subjected to RT-PCR analysis to evaluate the expression of *DAI* (*DLM-1/Zbp1*) and *Gapdh* mRNA. **b**, The induction of *Ifnb* mRNA in siRNA-expressing L929 cells was measured by quantitative RT-PCR upon treatment with B-DNA, viral (vaccinia virus), bacterial (*E. coli*) or mammalian (calf thymus) genomic DNAs, or poly(rI:rC). Data are mean  $\pm$  s.d. ( $n = 3$ ). Asterisk,  $P < 0.01$ , siRNA-DAI-1 versus siRNA-C. ND, not detected. The protein levels of IFN- $\beta$  were also evaluated by ELISA (Supplementary Fig. 7e). **c**, B-DNA-induced dimerization of IRF3 in siRNA-expressing L929 cells. The relative band intensities of IRF3 dimer quantified

by a densitometer were normalized to those of IRF3 monomer, and depicted in graphs (bottom). **d**, B-DNA- or poly(rI:rC)-induced activation of NF- $\kappa$ B in siRNA-expressing L929 cells was analysed by EMSA. Immunoblots with anti- $\beta$ -actin from a parallel set of identical samples is also shown as a loading control (bottom panel). **e**, B-DNA-induced expression of *Il6*, *Cxcl10* and *Nfkb* mRNAs in siRNA-expressing L929 cells was assessed by quantitative RT-PCR. Data are mean  $\pm$  s.d. ( $n = 3$ ). Asterisk,  $P < 0.01$ , siRNA-DAI-1 versus siRNA-C. The protein levels of these cytokines were also evaluated by ELISA (Supplementary Fig. 7e). **f**, The induction of *Ifnb* mRNA by HSV-1 (left panel) or NDV (right) was examined in siRNA-expressing L929 cells by quantitative RT-PCR. Data are mean  $\pm$  s.d. ( $n = 3$ ). Asterisk,  $P < 0.01$ , siRNA-DAI-1 versus siRNA-C.

configuration<sup>23</sup> (Fig. 1c). On the other hand, such an enhancement was not made when these cells were stimulated with poly(rI:rC), a synthetic double-stranded RNA that activates the RIG-I/MDA5 cytosolic pathway (Fig. 1d and Supplementary Fig. 2a; see also refs 15, 16). Consistent with these findings, in MEFs deficient for IFN- $\alpha/\beta$  receptor subunit 1 (*Ifnar1*)—in which impaired *Ifnb* mRNA induction by B-DNA stimulation (Supplementary Fig. 4a) is presumably due, in part, to the failure to induce DAI (DLM-1/ZBP1)—exogenous DAI (DLM-1/ZBP1) expression resulted in the rescue of *Ifnb* mRNA induction in response to DNA, but not to RNA (Supplementary Fig. 4b, c). The B-DNA-mediated induction of mRNAs for other DNA-inducible genes<sup>9,10</sup> involved in innate immunity was also up-regulated in DAI (DLM-1/ZBP1)-expressing L929 cells (Supplementary Fig. 5a, b).

Whereas IFN-regulatory factor 3 (IRF3) is critical to the cytosolic DNA-mediated induction of IFN genes, the contribution of other IRFs has not been examined. Therefore, we next examined the induction of IFN genes upon B-DNA stimulation in MEFs derived from mice deficient in one of three IRFs (*Irf3*<sup>-/-</sup>, *Irf7*<sup>-/-</sup> or *Irf5*<sup>-/-</sup> MEFs; refs 24–26). As shown in Fig. 1e, B-DNA-mediated *Ifnb* mRNA induction was abolished in *Irf3*<sup>-/-</sup> MEFs, but was similar to wild-type levels in *Irf7*<sup>-/-</sup> and *Irf5*<sup>-/-</sup> MEFs. On the other hand, the induction of *Ifna4* mRNA was impaired in *Irf7*<sup>-/-</sup> MEFs, suggesting that IRF7 cooperates with IRF3 in the activation of this (and possibly other) IFN- $\alpha$  gene subtype (Fig. 1e). Because the effect of DAI (DLM-1/ZBP1) was observed in wild-type MEFs (Supplementary Fig. 1g) but not in *Irf3*<sup>-/-</sup> or *Irf7*<sup>-/-</sup> MEFs (Supplementary Fig. 6), we presume that these transcription factors function downstream of DAI (DLM-1/ZBP1).

We next used a small interfering RNA (siRNA) to knockdown DAI (*DLM-1/Zbp1*) mRNA levels and then examined the activation of IFN and other genes involved in innate immune responses. The siRNA-DAI-1 construct strongly knocked down endogenous DAI (*DLM-1/Zbp1*) mRNA (Fig. 2a) and its protein (Z.W., unpublished

data) in L929 cells and effectively suppressed the levels of an artificially expressed DAI (DLM-1/ZBP1) protein in HEK293T cells (Supplementary Fig. 7a). Notably, the induction of *Ifnb* and *Ifna4* mRNAs by B-DNA as well as by viral, bacterial or mammalian DNA was strongly inhibited in cells expressing siRNA-DAI-1, but not in cells expressing a control siRNA vector (siRNA-C) (Fig. 2b and data not shown). Induction of *Ifnb* mRNA upon poly(rI:rC) stimulation, however, was not affected by siRNA-DAI-1 expression (Fig. 2b and Supplementary Fig. 7b). Similar observations were made in the macrophage cell line RAW264.7 when transfected with the same siRNA vectors (Supplementary Fig. 7c) and in L929 cells transfected with siRNA-DAI-2, an siRNA vector targeted to a different region of DAI (*DLM-1/Zbp1*) mRNA (Supplementary Fig. 7d). Consistent with these data, B-DNA-induced dimerization of IRF3 was inhibited by approximately fourfold in siRNA-DAI-1-expressing L929 cells (Fig. 2c). Notably, the DNA-mediated activation of NF- $\kappa$ B was also inhibited in siRNA-DAI-1-expressing cells (Fig. 2d), as was the induction of NF- $\kappa$ B-dependent genes and their products (Fig. 2e and Supplementary Fig. 7e). Therefore, DAI (DLM-1/ZBP1) may also be involved in the DNA-mediated activation of the NF- $\kappa$ B pathway, although we cannot exclude the possibility that a DNA sensor(s) other than DAI (DLM-1/ZBP1) is also involved.

Consistent with the notion that DAI (DLM-1/ZBP1) is involved in DNA-mediated antiviral responses through type I IFN induction, siRNA-DAI-1-expressing cells were found to be more sensitive to virus infection than siRNA-C-expressing cells after B-DNA stimulation (Supplementary Fig. 8). To address this issue further, we next measured the effect of siRNA-DAI-1 expression on the induction of *Ifnb* mRNA in response to infection by a DNA virus, herpes simplex virus-1 (HSV-1), or an RNA virus, Newcastle disease virus (NDV). As shown in Fig. 2f, induction of *Ifnb* mRNA was inhibited, albeit not completely, when siRNA-DAI-1-expressing L929 cells were infected by HSV-1, but not by NDV. Furthermore, the HSV-1 yield was notably higher (between five- and sixfold) in

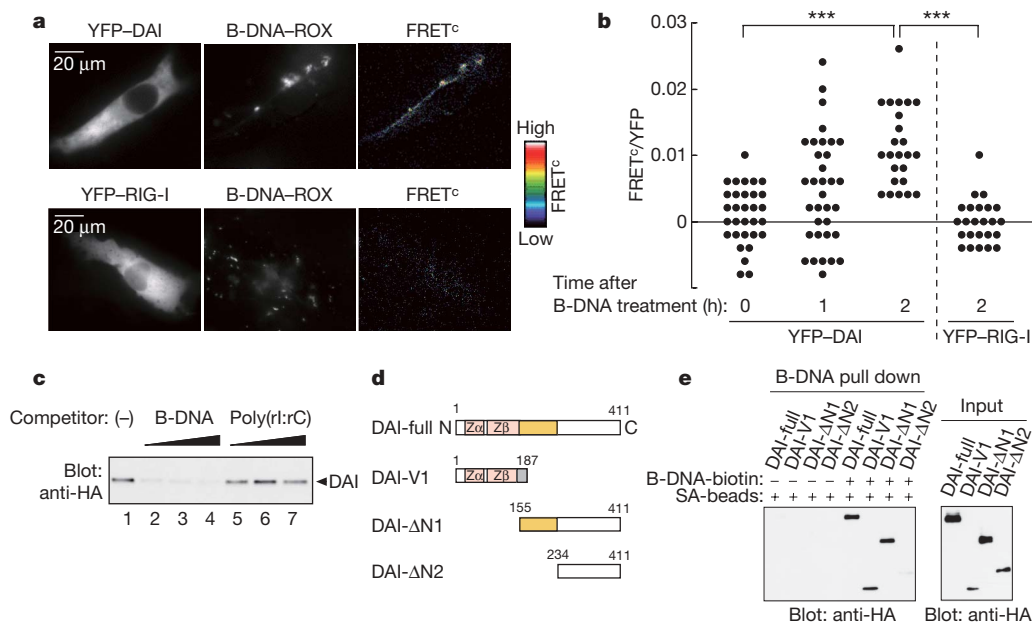


**Figure 3 | Interaction of DAI (DLM-1/ZBP1) with B-DNA in the cytoplasm.** **a, b**, Intermolecular FRET analysis for the interaction between DAI (DLM-1/ZBP1) and B-DNA. HeLa cells expressing YFP-tagged DAI (DLM-1/ZBP1) (top row) or YFP-tagged RIG-I (bottom row) were stimulated for 2 h with rhodamine (ROX)-conjugated B-DNA and then analysed by fluorescence microscopy. Representative fluorescence images of YFP, ROX and FRET<sup>c</sup> (corrected FRET; displayed in pseudo-colour mode) are shown from left to right (**a**). FRET<sup>c</sup>/YFP values were calculated and plotted as a histogram (**b**). Triple asterisk,  $P < 0.0001$ . **c**, Pull-down assays were performed with whole-cell lysates from HA-DAI (DLM-1/ZBP1)-expressing HEK293T cells

in the absence ((-); lane 1) of or after pre-incubation with unconjugated B-DNA (lanes 2–4) or poly(rI:rC) (lanes 5–7; 5.0, 10, 20 μg ml<sup>-1</sup>; wedges). Bound proteins were analysed by immunoblotting with anti-HA antibody. **d, e**, A pull-down assay was performed for the HA-tagged full length of DAI (DLM-1/ZBP1) (DAI-full) and three deletion mutant proteins (illustrated in **d**; numbers denote the residue numbers), as described in **c**. The domain in yellow corresponds to the D3 region (see text for details). Input protein levels for this assay are shown. Quantitative analysis of the levels of pulled-down proteins is shown in Supplementary Fig. 11. Zα and Zβ indicate the N-terminal Z-DNA binding domains. SA, streptavidin.



siRNA-DAI-1-expressing cells as compared to control cells 12 h after viral infection (Supplementary Fig. 9a), whereas there was no such increase upon NDV infection (Supplementary Fig. 9b), further supporting the view that DAI (DLM-1/ZBP1) selectively contributes to HSV-1-mediated type I IFN gene induction and antiviral immune response. The mechanisms for sensing DNA viruses are, nevertheless, likely to involve additional molecules and complexities.

To examine the interaction between DNA and DAI (DLM-1/ZBP1), we next performed fluorescence resonance energy transfer (FRET) analysis in HeLa cells using B-DNA labelled with rhodamine (ROX), and DAI (DLM-1/ZBP1) or RIG-I each tagged with yellow fluorescent protein (YFP). As shown in Fig. 3a, b, a FRET signal was observed only between B-DNA and DAI (DLM-1/ZBP1), demonstrating that DNA is in selective and direct contact with DAI (DLM-1/ZBP1). DAI (DLM-1/ZBP1) mainly resides in the cytosol with a diffuse but partially granular-like pattern in HeLa cells and L929 cells (Fig. 3a and Supplementary Fig. 10a; see also refs 27, 28). We next studied the interaction of DAI (DLM-1/ZBP1) with B-DNA by co-precipitation assay. Protein lysates from HEK293T cells transiently expressing haemagglutinin (HA)-tagged DAI (DLM-1/ZBP1) or the transcription factor Stat1, used as a control, were subjected to a 'pull-down assay' with biotin-labelled B-DNA and streptavidin-conjugated magnetic beads. As shown in Fig. 3c and Supplementary Fig. 10b, DAI (DLM-1/ZBP1), but not Stat1, precipitated with the DNA. This precipitation was inhibited by an excess amount of non-conjugated B-DNA, but not poly(rI:rC). Thus, DAI (DLM-1/ZBP1) may selectively and directly interact with B-DNA, although it cannot be excluded that other intermediate protein(s) may also participate in this intermolecular interaction.

To determine the region(s) of DAI (DLM-1/ZBP1) involved in this interaction, we constructed a series of complementary DNA expression vectors each encoding a deletion mutant of DAI (DLM-1/ZBP1) (Fig. 3d), expressed them in HEK293T cells, and then performed the co-precipitation assay. As shown in Fig. 3e, the DAI-V1 and DAI-ΔN1 mutants precipitated with the conjugated B-DNA, whereas DAI-ΔN2 failed to do so. Thus, in addition to the previously determined DNA-binding domains<sup>22</sup>, another region tentatively denoted as the D3 region (Fig. 3d, yellow) may also participate in the interaction with DNA. A more detailed analysis, however, will be required to determine whether this interaction is direct or indirect and which of the DNA-binding regions are critical for the activation of DAI (DLM-1/ZBP1) in response to a given DNA stimulus. It is intriguing that a variety of DNA, be it synthetic DNA or DNA of bacterial, viral or mammalian origin, activate DAI (DLM-1/ZBP1), albeit with different efficiencies (Figs 1c and 2b). Thus, we infer that DAI (DLM-1/ZBP1) activation by and discrimination between B- and Z-form and host- and pathogen-derived DNA may not be absolutely stringent. Rather, DAI (DLM-1/ZBP1) activation is also likely to be a function of the quantitative amount and the length of the DNA in the cytosol.

Because TBK1 is essential for the DNA-induced activation of IRF3 (ref. 9), we further analysed the molecular association of DAI (DLM-1/ZBP1) with TBK1 and IRF3 by assaying for the co-immunoprecipitation of HA-tagged DAI (DLM-1/ZBP1) with Flag-tagged TBK1 or IRF3 in L929 cells. As shown in Fig. 4a, DAI (DLM-1/ZBP1) co-precipitated with both TBK1 and IRF3, maximally, 2 h after B-DNA stimulation, suggesting that DAI (DLM-1/ZBP1) associates, either directly or indirectly, with TBK1 and IRF3 and that this association is enhanced upon cytosolic DNA stimulation of cells. We therefore postulate that when TBK1 and IRF3 are recruited to the DNA-DAI (DLM-1/ZBP1) complex, IRF3 is activated and undergoes nuclear translocation and, in the absence of IRF3, TBK1 dissociates from the complex. Although further work will be required, this notion is consistent with our preliminary observations that indicate the nuclear translocation of IRF3 after its dissociation from DNA-DAI (DLM-1/ZBP1) (data not shown). To determine which region of DAI (DLM-1/ZBP1) is necessary for its interaction with TBK1 and IRF3, HA-tagged deletion mutants of DAI

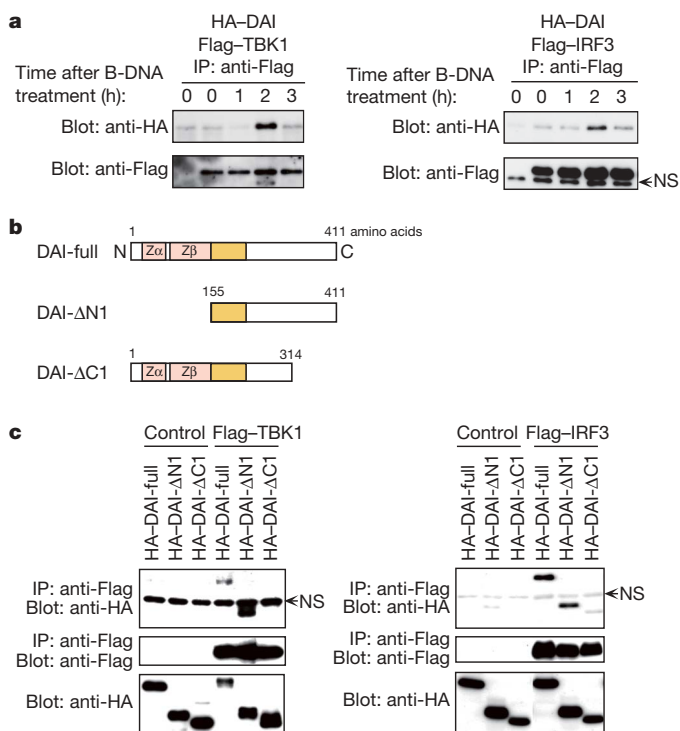


**Figure 4 | Interaction of DAI (DLM-1/ZBP1) with IRF3 and TBK1.** **a**, L929 cells transiently expressing HA-DAI (DLM-1/ZBP1) together with Flag-TBK1 (left panel) or Flag-IRF3 (right panel) were stimulated with B-DNA and analysed by immunoprecipitation with anti-Flag antibody, followed by immunoblotting with anti-HA (top panel) and anti-Flag (bottom panel) antibodies. The first lane of each panel shows the results of cells expressing HA-DAI (DLM-1/ZBP1) alone. NS, nonspecific bands. **b, c**, Full-length DAI (DLM-1/ZBP1) or two deletion mutants (illustrated in **b**) were transiently expressed in HEK293T cells alone (control) or along with either Flag-TBK1 (left panel) or Flag-IRF3 (right panel). Cell lysates were analysed as described in **a**. DAI (DLM-1/ZBP1) can be readily co-immunoprecipitated by these proteins even without DNA stimulation, presumably because of its high level of protein expression in HEK293T cells.

(DLM-1/ZBP1) were co-expressed with Flag-tagged TBK1 or IRF3 in HEK293T cells (Fig. 4b). As shown in Fig. 4c, interaction of DAI-ΔN1 but not DAI-ΔC1 with TBK1 and IRF3 was observed, suggesting that the ~100 carboxy-terminal amino acids of DAI (DLM-1/ZBP1) are critical for its intermolecular associations.

Our present study reveals that DAI (DLM-1/ZBP1) is a cytoplasmic recognition receptor that senses and is activated by DNA from a variety of sources, leading to type I IFN gene induction through the activation of IRF3 and, probably, IRF7. Notably, this sensor may itself recruit IRF3 and TBK1 in a DNA-dependent manner, although additional experiments will be required to confirm the formation of this signalling complex. Thus, unlike the RNA sensor RIG-I, which becomes constitutively active in the absence of its RNA interaction region (ref. 15), DAI (DLM-1/ZBP1) may require both its amino-terminal DNA-binding region and carboxy-terminal TBK1/IRF binding region for its activity. Therefore, DNA is not only critical to initiate but also to sustain the active signalling complex. Consistent with this notion, neither DAI-ΔN2 lacking the DNA-binding region nor DAI-ΔC1 lacking the TBK1/IRF recruiting region can mediate DNA-stimulated *Ifnb* mRNA induction (Supplementary Fig. 12).

The rigorous examination to determine the extent to which DAI (DLM-1/ZBP1) contributes to the cytosolic DNA-mediated and/or virus-mediated activation of innate immune responses must await the generation of mice deficient in the corresponding gene. The mutant mice will permit the study of DAI (DLM-1/ZBP1)'s function in distinct cell types *in vitro* and *in vivo* in the context of protective and pathological immune responses.

## METHODS SUMMARY

**Mice, cells and reagents.** The generation of *Irf3*<sup>-/-</sup>, *Irf5*<sup>-/-</sup> and *Irf7*<sup>-/-</sup> mice has been described previously<sup>24,26</sup>. MEFs were prepared and murine L929 fibroblasts were cultured as described previously<sup>24</sup>. Details of nucleic acid ligands and other reagents are described in the Methods.

**Viral infection.** Cells were infected for 12 h with 1.0 multiplicity of infection (M.O.I.) of HSV-1 (KOS strain; VR-1493; ATCC) or 25 haemagglutinin units (HAU) of NDV, as described previously<sup>24</sup>.

**Plasmids and gene transfer.** Details of plasmid construction are described in the Methods. Retroviral gene transfer or transfection by electroporation was carried out as described previously<sup>24,26</sup>. Briefly, two days after infection with retrovirus, cells were selected with puromycin (3.0 µg ml<sup>-1</sup>) for 2 days, and used for further experiments.

**RNA analysis.** RNA extraction and RT-PCR were performed as described previously<sup>26</sup>. The primers used in quantitative RT-PCR analysis are described in the Methods. Details of RNA interference are described in the Methods.

**Electrophoretic mobility shift assay (EMSA).** EMSA was performed as described previously<sup>26</sup>, and the protocol is briefly described in the Methods.

**Fluorescence microscopy.** These analyses including FRET were carried out as described previously<sup>26</sup>, and are briefly mentioned in the Methods.

**Pull-down assay.** This assay was performed with a synthetic, biotin-conjugated poly(dA-dT)•poly(dT-dA) and streptavidin-conjugated magnetic beads (Dynal Biotech). The details are described in the Methods.

**Immunoprecipitation and immunoblotting.** Cell lysis, co-immunoprecipitation and immunoblotting were carried out as described previously<sup>26</sup>. IRF3 dimer was assessed by native PAGE, followed by immunoblotting with anti-mouse IRF3 antibody, as described previously<sup>15</sup>. The quantification of IRF3 dimer was performed by the NIH Image application. Similar results were obtained in three independent transfection experiments.

**Full Methods** and any associated references are available in the online version of the paper at [www.nature.com/nature](http://www.nature.com/nature).

Received 13 March; accepted 13 June 2007.

Published online 8 July 2007.

- Janeway, C. A. Jr & Medzhitov, R. Innate immune recognition. *Annu. Rev. Immunol.* **20**, 197–216 (2002).
- Takeda, K., Kaisho, T. & Akira, S. Toll-like receptors. *Annu. Rev. Immunol.* **21**, 335–376 (2003).
- Meylan, E., Tschopp, J. & Karin, M. Intracellular pattern recognition receptors in the host response. *Nature* **442**, 39–44 (2006).
- Creagh, E. M. & O'Neill, L. A. TLRs, NLRs and RLRs: a trinity of pathogen sensors that co-operate in innate immunity. *Trends Immunol.* **27**, 352–357 (2006).
- Krieg, A. M. *et al.* CpG motifs in bacterial DNA trigger direct B-cell activation. *Nature* **374**, 546–549 (1995).
- Tokunaga, T., Yamamoto, T. & Yamamoto, S. How BCG led to the discovery of immunostimulatory DNA. *Jpn. J. Infect. Dis.* **52**, 1–11 (1999).
- Ishii, K. J. & Akira, S. Innate immune recognition of, and regulation by, DNA. *Trends Immunol.* **27**, 525–532 (2006).
- Hochrein, H. *et al.* Herpes simplex virus type-1 induces IFN-α production via Toll-like receptor 9-dependent and -independent pathways. *Proc. Natl Acad. Sci. USA* **101**, 11416–11421 (2004).
- Ishii, K. J. *et al.* A Toll-like receptor-independent antiviral response induced by double-stranded B-form DNA. *Nature Immunol.* **7**, 40–48 (2006).
- Stetson, D. B. & Medzhitov, R. Recognition of cytosolic DNA activates an IRF3-dependent innate immune response. *Immunity* **24**, 93–103 (2006).
- Fu, Y. *et al.* Cloning of DLM-1, a novel gene that is up-regulated in activated macrophages, using RNA differential display. *Gene* **240**, 157–163 (1999).
- Honda, K. & Taniguchi, T. IRFs: master regulators of signalling by Toll-like receptors and cytosolic pattern-recognition receptors. *Nature Rev. Immunol.* **6**, 644–658 (2006).
- Napirei, M. *et al.* Features of systemic lupus erythematosus in Dnase1-deficient mice. *Nature Genet.* **25**, 177–181 (2000).
- Yoshida, H., Okabe, Y., Kawane, K., Fukuyama, H. & Nagata, S. Lethal anemia caused by interferon-β produced in mouse embryos carrying undigested DNA. *Nature Immunol.* **6**, 49–56 (2005).
- Yoneyama, M. *et al.* The RNA helicase RIG-I has an essential function in double-stranded RNA-induced innate antiviral responses. *Nature Immunol.* **5**, 730–737 (2004).
- Kato, H. *et al.* Differential roles of MDA5 and RIG-I helicases in the recognition of RNA viruses. *Nature* **441**, 101–105 (2006).
- Alexopoulou, L., Holt, A. C., Medzhitov, R. & Flavell, R. A. Recognition of double-stranded RNA and activation of NF-κB by Toll-like receptor 3. *Nature* **413**, 732–738 (2001).
- Hornung, V. *et al.* 5'-Triphosphate RNA is the ligand for RIG-I. *Science* **314**, 994–997 (2006).
- Pichlmair, A. *et al.* RIG-I-mediated antiviral responses to single-stranded RNA bearing 5'-phosphates. *Science* **314**, 997–1001 (2006).
- Verthelyi, D. & Zeuner, R. A. Differential signaling by CpG DNA in DCs and B cells: not just TLR9. *Trends Immunol.* **24**, 519–522 (2003).
- Ha, S. C. *et al.* Biochemical characterization and preliminary X-ray crystallographic study of the domains of human ZBP1 bound to left-handed Z-DNA. *Biochim. Biophys. Acta* **1764**, 320–323 (2006).
- Schwartz, T., Behlke, J., Lowenhaupt, K., Heinemann, U. & Rich, A. Structure of the DLM-1–Z-DNA complex reveals a conserved family of Z-DNA-binding proteins. *Nature Struct. Biol.* **8**, 761–765 (2001).
- Rich, A. & Zhang, S. Timeline: Z-DNA: the long road to biological function. *Nature Rev. Genet.* **4**, 566–572 (2003).
- Sato, M. *et al.* Distinct and essential roles of transcription factors IRF-3 and IRF-7 in response to viruses for IFN-α/β gene induction. *Immunity* **13**, 539–548 (2000).
- Honda, K. *et al.* IRF-7 is the master regulator of type-I interferon-dependent immune responses. *Nature* **434**, 772–777 (2005).
- Takaoka, A. *et al.* Integral role of IRF-5 in the gene induction programme activated by Toll-like receptors. *Nature* **434**, 243–249 (2005).
- Deigendesch, N., Koch-Nolte, F. & Rothenburg, S. ZBP1 subcellular localization and association with stress granules is controlled by its Z-DNA binding domains. *Nucleic Acids Res.* **34**, 5007–5020 (2006).
- Pham, H. T., Park, M. Y., Kim, K. K., Kim, Y. G. & Ahn, J. H. Intracellular localization of human ZBP1: Differential regulation by the Z-DNA binding domain, Zα, in splice variants. *Biochem. Biophys. Res. Commun.* **348**, 145–152 (2006).

**Supplementary Information** is linked to the online version of the paper at [www.nature.com/nature](http://www.nature.com/nature).

**Acknowledgements** We thank A. Katoh and M. Kidokoro for the vaccinia virus (MO) genome for ligand stimulation; T. Fujita and M. Yoneyama for RIG-I cDNA; J. Miyazaki for pCAGGS; A. Miyawaki for Venus; R. Kuroda for her support for CD spectrometry; Toray Industries for murine IFN-β; J. V. Ravetch for advice; Y. Fujita, R. Takeda and M. Shishido for technical assistance; and D. Savitsky for critical reading of the manuscript. This work was supported in part by a grant for Advanced Research on Cancer and a Grant-In-Aid for Scientific Research on Priority Areas, and for Scientific Research, from the Ministry of Education, Culture, Sports, Science, and Technology of Japan. Z.W. and H.N. are research fellows of the Japan Society for the Promotion of Science. M.K.C. is a research fellow of the Korea Science and Engineering Foundation.

**Author Contributions** A.T., Z.W., M.K.C., H.Y., H.N., T.B., Y.L. and T.T. conceived the research, planned experiments and analyses, and largely conducted experiments. K.H. and M.M. helped to design RNAi experimental protocols. T.K. performed microarray experiments and data analysis. Fluorescence microscopy and FRET analysis were conducted by Y.O. T.T. oversaw the entire project.

**Author Information** Reprints and permissions information is available at [www.nature.com/reprints](http://www.nature.com/reprints). The authors declare no competing financial interests. Correspondence and requests for materials should be addressed to T.T. (tada@m.u-tokyo.ac.jp).

## METHODS

**Mice, cells and reagents.** All mice used for this study were backcrossed to the C57BL/6 background. Poly(dA-dT)•poly(dT-dA), poly(dG-dC)•poly(dC-dG) and calf thymus genomic DNA were purchased from Sigma. There is an abundance of literature showing that poly(dA-dT)•poly(dT-dA) can adopt non-B-DNA conformations including left-handed Z-DNA<sup>29</sup>. We confirmed by circular dichroism (CD) analysis that poly(dA-dT)•poly(dT-dA) adopts a B-conformation in solution, and that the transfection reagent Lipofectamine2000 does not induce Z-conformation of the DNA (data not shown), as previously described<sup>9,30</sup>. Therefore, we expediently used the term B-DNA for poly(dA-dT)•poly(dT-dA) for convenience as a ligand for stimulation, although it currently remains unclear whether the poly(dA-dT)•poly(dT-dA) used in our study is indeed in a B-conformation during its interaction with DAI (DLM-1/ZBP1). Rhodamine (ROX)- and biotin-conjugated poly(dA-dT)•poly(dT-dA) were purchased from Hokkaido System Science. Purified vaccinia virus (MO) DNA was provided by A. Kato and M. Kidokoro. *Escherichia coli* DNA and poly(rI:rC) were purchased from InvivoGen and Amersham Biosciences, respectively. B-DNA or poly(rI:rC) was used at a concentration of 6.0 µg ml<sup>-1</sup> or 5.0 µg ml<sup>-1</sup>, respectively, unless otherwise mentioned. Other nucleic acid ligands were used at 10.0 µg ml<sup>-1</sup> following complex formation with Lipofectamine2000 (Invitrogen) at a ratio of 1.0 µl lipofectamine to 1.0 µg DNA in OptiMEM (Invitrogen). Antibodies against the following proteins were purchased from the vendors indicated: IRF3 (ZM3; Zymed), β-actin (AC-15; Sigma-Aldrich), HA (3F10; Roche), Flag (M2; Sigma), NFκB p65 (C20; Santa Cruz Biotechnology).

**Plasmid constructions.** HA-IRF3 expression vector has been described previously<sup>26</sup>. Mouse DAI (*DLM-1/Zbp1*) cDNA was obtained by polymerase chain reaction with reverse transcription (RT-PCR) on total RNA from splenocytes, and then cloned into the pT7Blue vector (Novagen). To generate YFP-, Flag- and HA-tagged DAI (*DLM-1/ZBP1*) expression vectors, the DAI (*DLM-1/Zbp1*) cDNA was cloned into the *XhoI* and *NotI* sites of the pCAGGS-YFP, pCXN2-Flag and pCAGGS-HA vectors. Flag-IRF3 and Flag-TBK1 expression vectors were generated by subcloning the respective cDNAs into the same sites of pCXN2-Flag. The pCAGGS vector and Venus, which we refer to as YFP, were provided by J. Miyazaki and A. Miyawaki, respectively. To generate the DAI (*DLM-1/ZBP1*) retroviral expression vector, DAI (*DLM-1/Zbp1*) cDNA was excised from pCAGGS-HA-DAI (*DLM-1/ZBP1*) and cloned into the *SalI* and *NotI* sites of the MSCVpac-Flag. A splicing variant DAI-V1 (1–187 amino acids) and other deletion mutants (DAI-ΔN1 (155–411), DAI-ΔN2 (234–411) and DAI-ΔC1 (1–314)) were isolated by PCR and inserted into the *XhoI* and *NotI* sites of pCAGGS-HA. Each cDNA of DAI-ΔN2 or DAI-ΔC1 was excised from pCAGGS-HA-DAI and cloned into the *SalI* and *NotI* sites of MSCVpac-Flag. As shown in Fig. 3d, DAI-V1 is a naturally occurring splice variant that encodes a truncated protein containing 36 unique amino acids at its carboxy terminus (grey; Ensembl Gene ID ENSMUSESTT00003754309). DAI-ΔN1 is lacking both of the N-terminal Z-DNA binding domains (Zα and Zβ), whereas DAI-ΔN2 is missing the D3 region as well as both of the Z-DNA binding domains. RIG-I cDNA was provided by T. Fujita and M. Yoneyama. YFP-tagged RIG-I was generated by subcloning RIG-I cDNA into the *XhoI* and *NotI* sites of the pCAGGS-YFP expression vector.

**Quantitative RT-PCR analysis.** This analysis was performed with a Lightcycler480 and SYBR Green system (Roche Molecular Biochemicals). All data were presented as relative expression units after normalization to *Gapdh*.

Primer sequences for murine DAI (*DLM-1/Zbp1*), *Ccl5* and *Cxcl10* are as follows: DAI sense 5'-GACGACAGCCAAAGAAGTGA-3'; DAI antisense 5'-GAGCTATGTCTTGGCCTTCC-3'; *Ccl5* sense 5'-ACGTCAAGGAGTATTTCTACAC-3'; *Ccl5* antisense 5'-GATGTATTCTTGAACCCACT-3'; *Cxcl10* sense 5'-ACTGCATCCATATCGATGAC-3'; *Cxcl10* antisense 5'-TTCATCGTGGCAATGATCTC-3'; *Il6* sense 5'-GTAGCTATGGTACTCCAGAAGAC-3'; *Il6* antisense 5'-ACGATGATGCACCTGCAGAA-3'. Primer sequences for *Gapdh*, *Nfkb1a*, *Ifna4* and *Ifnb* are the same as those previously published<sup>24,26</sup>.

**RNA interference.** Small interfering (si) RNA vectors were constructed by inserting oligonucleotides into *BspMI* sites of the pcPUR-U6i expression vector. The siRNA targeting sequences for murine DAI (*DLM-1/Zbp1*) (DAI-1 and DAI-2) and *Renilla* luciferase (control) are 5'-GGTCAAAGGGTGAAGTCAT-3' (DAI-1), 5'-GATGAAAGAATATTAAGAT-3' (DAI-2) and 5'-GTAGCGCGGTGTATTATACA-3' (control), respectively. L929 cells (1 × 10<sup>6</sup>) were transfected with 2.0 µg of siRNA vector in 6.0 µl Lipofectamine2000 transfection reagent (Invitrogen). The cells were then used for subsequent assays after incubation for 48 h in the presence of puromycin (4.0 µg ml<sup>-1</sup>; Sigma).

**EMSA.** Equal amounts, 40 µg, of whole-cell protein extract were analysed by EMSA with a <sup>32</sup>P-radiolabelled oligonucleotide probe containing a consensus NF-κB binding sequence. The presence of p65 in the NF-κB-DNA binding complex was also confirmed by detection of a supershifted band with an anti-p65 antibody (data not shown).

**Fluorescence microscopy.** Cell culture, image acquisition and processing for the sensitized FRET were performed as described previously<sup>25,26</sup>. We used the following filters in this study: XF1068 and XF3079 excitation/emission filters (Omega Optical Inc.) for the YFP images; BP520-550 and BA580IF (Olympus) for rhodamine; and XF1068 and BA580IF for FRET. As a dichroic mirror, a U-MREF glass reflector (Olympus) was used. Corrected FRET (FRET<sup>C</sup>) was calculated using the equation: FRET<sup>C</sup> = FRET - 0.108 × YFP - 0.194 × ROX, where FRET, YFP and ROX represents background-subtracted images acquired through the FRET, YFP and rhodamine channels, respectively. Under our experimental condition, the fractions of the bleed-through of YFP and ROX fluorescence through the FRET channel and the bleed-through of YFP through the ROX channel were 0.176, 0.194 and 0.348, respectively.

**Pull-down assay.** Cell lysates were extracted from HEK293T cells transiently transfected with pCAGGS-HA-DAI and were first incubated for 15 min at room temperature with streptavidin-conjugated magnetic beads, and after centrifugation, the supernatants were then mixed for 20 min at 4 °C with poly(dA-dT)•poly(dT-dA), the 5'-terminal of which is unilaterally conjugated with biotin, following its pre-incubation with streptavidin-conjugated magnetic beads. The mixture was washed extensively with lysis buffer, separated by SDS-PAGE, and immunoblotted with anti-HA antibody. For the competition assay, unconjugated poly(dA-dT)•poly(dT-dA) or poly(rI:rC) was added to the binding reaction at the concentrations specified in the figure legend.

**Statistical analysis.** Differences between control and experimental groups were evaluated using the Student's *t*-test.

29. Suggs, J. W. & Wagner, R. W. Nuclease recognition of an alternating structure in a d(AT)<sub>14</sub> plasmid insert. *Nucleic Acids Res.* 14, 3703–3716 (1986).

30. Braun, C. S. *et al.* The structure of DNA within cationic lipid/DNA complexes. *Biophys. J.* 84, 1114–1123 (2003).



# naturejobs

**JOBS OF  
THE WEEK**

**H**aving trouble finishing graduate school? You're not alone. Many students, especially in the United States, drag out their postgraduate education for up to ten years. Arguably, these extended stays waste not only the time and energy of students, but also the resources of universities and funding bodies.

This week the Council of Graduate Schools (CGS), based in Washington DC, released data for attrition and completion rates in 316 doctoral programmes at 29 colleges and universities in the United States. The results, part of an ongoing multi-year project, tell an interesting tale. Completion rates aren't as bad as some had feared: 57% of PhD students get their degree by their tenth year. Many had assumed that this number would be about 50% on the basis of older studies. And in the social sciences and humanities, unlike science and engineering, the proportion actually rises from years 7 to 10. This has implications for how universities run their programmes. "Draconian policies that say 'finish by year 7 or you're out' are probably not a wise move," says CGS president Debra Stewart.

In a separate CGS survey of 1,358 students who had completed their PhD, 80% said that financial support was an important factor in helping them to finish their degree and 63% said mentoring or advising. And most respondents said that the best advice they received from their mentors was related to their research rather than career guidance or teaching. Stewart says that some of the PhD programmes participating in the multi-year project are already attempting to reduce the long stays in graduate school. They have introduced measures such as selecting students who are more likely to finish, offering stipends without teaching obligations after a student's first few years and finding better ways to cater for women who are balancing work and family.

But finding the right intervention will be a difficult, case-by-case endeavour based mostly on anecdotal evidence. Colleges and universities will need to use the data as a guide to find specific courses of action that benefit both them and their students.

**Gene Russo, acting editor of *Naturejobs***

## CONTACTS

**Acting Editor:** Gene Russo

### European Head Office, London

The Macmillan Building,  
4 Crinan Street,  
London N1 9XW, UK  
Tel: +44 (0) 20 7843 4961  
Fax: +44 (0) 20 7843 4996  
e-mail: [naturejobs@nature.com](mailto:naturejobs@nature.com)

### European Sales Manager:

Andy Douglas (4975)  
e-mail: [a.douglas@nature.com](mailto:a.douglas@nature.com)  
**Business Development  
Manager:**  
Amelie Pequignot (4974)  
e-mail: [a.pequignot@nature.com](mailto:a.pequignot@nature.com)

### Natureevents:

Claudia Paulsen Young  
(+44 (0) 20 7014 4015)  
e-mail: [c.paulsenyoung@nature.com](mailto:c.paulsenyoung@nature.com)

### France/Switzerland/Belgium:

Muriel Lestringuez (4994)

### Southwest UK/RoW:

Nils Moeller (4953)

### Scandinavia/Spain/Portugal/Italy:

Evelina Rubio-Hakansson (4973)

### Northeast UK/Ireland:

Matthew Ward (+44 (0) 20 7014 4059)

### North Germany/The Netherlands:

Reya Silao (4970)

### South Germany/Austria:

Hildi Rowland (+44 (0) 20 7014 4084)

### Advertising Production Manager:

Stephen Russell  
To send materials use London  
address above.

Tel: +44 (0) 20 7843 4816

Fax: +44 (0) 20 7843 4996

e-mail: [naturejobs@nature.com](mailto:naturejobs@nature.com)

### Naturejobs web development:

Tom Hancock

### Naturejobs online production:

Jasmine Myer

### US Head Office, New York

75 Varick Street, 9th Floor,  
New York, NY 10013-1917  
Tel: +1 800 989 7718  
Fax: +1 800 989 7103  
e-mail: [naturejobs@natureny.com](mailto:naturejobs@natureny.com)

### US Sales Manager: Peter Bless

### Japan Head Office, Tokyo

Chiyoda Building,  
2-37 Ichigayatamachi,  
Shinjuku-ku, Tokyo 162-0843  
Tel: +81 3 3267 8751  
Fax: +81 3 3267 8746

### Asia-Pacific Sales Manager:

Ayako Watanabe  
Tel: +81-3-3267-8765  
e-mail: [a.watanabe@natureasia.com](mailto:a.watanabe@natureasia.com)

# MOVERS

**Gerd Kempermann, professor, Center for Regenerative Therapies, Dresden, Germany**



**2000–07:** Group leader, Max Delbrück Center for Molecular Medicine, Berlin, Germany

**1998–2000:** Resident and senior scientist, Department of Neurology, University of Regensburg, Germany

Gerd Kempermann took up science for the thrill of discovery and found success by tackling biology's complexity head-on rather than trying to circumvent it.

Kempermann trained as a medical doctor at the University Medical Center Freiburg in his native Germany and, fascinated with the brain, he pursued graduate work in neuropathology. His decision to do a postdoc with Fred Gage at the Salk Institute in San Diego, California, proved pivotal. Gage had developed a method to manipulate neurons in disease models. But Kempermann's proposed grant work based on this methodology seemed passé; signs of adult stem-cell formation, or neurogenesis, were more tantalizing. So Kempermann sought direct proof. Working with Gage, he stumbled on a way to study how physical activity, as well as genetics, affects neurogenesis. "I came to the right lab with the wrong proposal," he says.

Together with Robert Williams at the University of Tennessee Health Science Center, he investigated the natural variation seen in adult neurogenesis.

"Gerd launched into a massive undertaking," says Williams. The four-year, 50-strain panel screening for the genetic basis of variation in neurogenesis could have been a career-killer, he adds. "Most scientists, particularly postdocs, like to find a unique phenotype in one strain of engineered mouse and get a top paper quickly." Although they didn't identify the genes responsible for neurogenesis variation, they found evidence for the complex structure of genetic networks controlling the process.

Back in Germany, Kempermann continued describing how exercise and the environment direct neurogenesis, first at Regensburg University, then at Max Delbrück Center for Molecular Medicine. This month, he will take up a professorship studying the genomics of regeneration at the Center for Regenerative Therapies in Dresden — a collaborative collective of local research groups. "The opportunity to enter a pioneering situation, building a new institute, is one that you rarely get," he says.

Kempermann is pragmatic about the ethical problems connected to human embryonic stem cells. An adviser on stem-cell policy to the German government, Kempermann tempers the current focus on engineering stem cells by advocating research that will help unravel the complex biological puzzles of tissue development. "Gerd is able to navigate the dangerous hype-infested waters of this research area — he's a sceptical optimist," says Williams. ■

Virginia Gewin

## NETWORKS & SUPPORT

### Order of merit

Authorship order is of increasing importance for scientific careers and the success of collaborations. This is especially true in biological sciences, where the first author typically makes the greatest contribution and the last has a leadership role. The process of choosing the order needs to foster understanding and accountability, while recognizing each author's contribution. This can be difficult. So how does a group get it right? We have devised a model for finding the best order, avoiding conflict and promoting long-term collaborations. First step: you need to discuss authorship before starting the project, and again while you prepare the manuscript and make revisions.

Using a multi-criterion decision making (MCDM) approach, a group of potential co-authors decides on a set of items — such as figures, tables, text and ideas — that comprise a manuscript. They score each person's contribution to each item as a percentage. Types of contribution vary across publications, but a group of co-authors is well placed to make judgements. As they may not always agree exactly, a range can be assigned that they can 'agree to disagree' on.

The group should then assess the relative importance of each item and put them in categories, in order of importance to the manuscript. For

example, category A (the most important) might constitute a 15% weighting, category B 10% and category C 5%. This way, each item is given a weighting that represents its importance to the whole work. Finally, each author's relative contribution to each item is calculated.

It's important to work out authors' contributions to each item first, as this is likely to be simpler than assessing categories and weighting. A culture of understanding and agreement about the relative importance of different activities will help the process to run smoothly. In our system, co-authors are encouraged to appreciate different perspectives and negotiate on criteria. This process should enhance scientific best practice and increase researcher accountability.

The MCDM approach enables a rational, project-specific account of all factors that led to the publication. It's of particular use for multidisciplinary work and for teams with different experiences and at different stages of their careers. Focusing on items one at a time helps to resolve potential conflict, encourages authors to value other perspectives and helps to clarify any ambiguity over contributions. ■

**Christine Beveridge and Suzanne Morris are plant scientists at the University of Queensland in Brisbane, Australia.**

#### POSTDOC JOURNAL

### Isolation

I had mixed feelings about maternity leave last time I had a baby, and I still do. Of course, it is absolutely necessary for a healthy recovery and for attachment to your new child. However, I felt the extreme isolation.

I have always worked, which has shaped my self-image. The absence of work, coupled with new associations with non-working mothers, made me feel like a stranger in a strange land. What made it worse was that I felt guilty for wanting to put my child in another person's care so I could return to work, even though this was undoubtedly the right choice for me. I had to brave comments wondering why I'd had children if I hadn't planned on raising them — a heartless statement! I had to hide my excitement that my husband would soon be arriving home to give me some time away from the baby. I didn't talk about how I longed to have an adult conversation that doesn't centre on baby issues of any kind.

Maternity leave isn't relaxing or magical for me. I am never more than a few feet from a helpless, crying baby. I do love children, though, and the fact that babies grow up is one reason I chose to be a parent. But I look forward to returning to work — and I look forward to showing my kids that mothers work just as much as fathers. ■

**Moir Sheehan is a postdoc in plant breeding and genetics at Cornell University.**

# And on gloomy Sunday...

There goes the neighbourhood.

**Anthony S. Haines**

Dave rang the doorbell of the small terraced house. After a few moments, a man in a dressing-gown opened the door.

"Hello, I'd like to talk to you about God," Dave began.

"Sure," the man interrupted. "What would you like to know about me?"

After a few moments of confusion, Dave's mind-wave collapsed to a plausible model, and he said: "I'm sorry, I've never met anyone actually called God before."

"No," said the man. "I meant I am the creator of your universe. Why don't you come in?"

Dave mutely followed God into his dingy apartment. "How can I know you are God?" he wondered aloud.

"Really," said God. "I thought you were the one to work on faith. But I don't have time to argue the point. Here, taste this." He handed Dave a glass of clear liquid. A sip told Dave that it was water. "Now try it again." The liquid was now red, and tasted of wine. "An old favourite, but these days a mere parlour trick, perhaps? Try this on for size." Suddenly, Dave was standing in a field of flowers, under an azure sky. "Before you ask; no this isn't heaven," said God. "It's Devon."

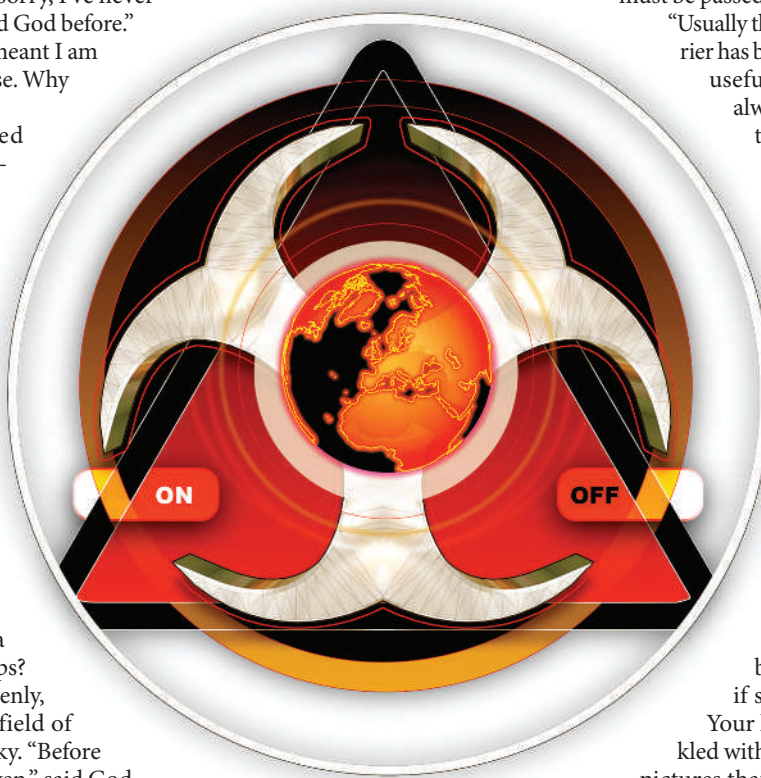
A moment later they were back in God's living room. "Would you like to sit down? I'll make you a cup of tea."

"Why have you revealed yourself to me?" Dave asked while God rinsed out a pair of grubby-looking mugs.

"You came to me, remember? And I thought — why not? Let me explain my problem. Your philosophers have struggled with the existence of the world for a long time. But the truth is that it was an accident. I invented a way of representing a simple universe using much less processing than normal. You'll have heard of cellular automata? It's something like that. Quantum mechanics is in there to reduce the processing load.

"Anyway, after a bit of tweaking of the parameters, interesting stuff started to

happen. I got atoms, molecules, stars, everything. And, eventually, life arose — here and there, where conditions were just right. Just three usable dimensions, and all of this..." God looked misty eyed for a moment. "Then, suddenly, wham! The speed of time slowed right down. And looking into it I found this tiny planet where quantum effects had suddenly become much more intensive to process."



God brought the tea over, which He seemed to have brewed in the usual way. "You'd developed civilization and started investigating quantum entanglement, and experimenting with quantum computing. In the process you were generating important states where precision mattered, so my shortcuts couldn't be applied. This wouldn't be a problem except that it brought you to my attention."

"So," said Dave, mind racing. "You're not the God?"

"If you mean the Judaeo-Christian God, then no. Sorry. You made that up by yourselves. I just set things up, lit the blue touch-paper and watched what happened. It worked out quite well at first, too," God mused. "I got a paper out of

it in quite a respectable journal."

Dave's tea was untouched. "What are you doing here in Birmingham?" He asked.

"Oh, I've been watching for so long," God said. "I just wanted to see what this world felt like..."

God leaned forward. "Have you heard about memes? There are good ideas and bad ideas, and they are passed on almost independently of whether they are true. To be successful, an idea, that is, a 'meme', must be passed from brain to brain.

"Usually this happens because the carrier has benefited, and wishes to pass useful information on. But not always. Memes may persuade their host to propagate them.

And unrelated memes can merge together, and may then transfer more effectively. This is what is happening when children whisper gossip to each other followed by the phrase 'and pass it on'.

"Generally we think of ideas as little additions to the mind. But ideas affect the mind. I'm sure you'll have heard a song that you don't like but can't stop your brain from singing? What if something worse existed?

Your literature is already sprinkled with stories about the concept: pictures that kill the viewer, games so addictive no one could stop playing; the format isn't important. And Douglas Hofstadter described how it is impossible to create a perfect gramophone, because if it reproduces every sound perfectly there will be a noise that destroys it.

"The same must be true of consciousness. So there is good reason to believe that lethal conceptually transmitted diseases can exist. And moreover, that they may be highly infectious, or have a carrier phase. Discovering you has led to something of a backlash I'm afraid. There are forces that even God must answer to. The Research Council has spoken. I have to switch your universe off."

As a microbiologist and hobbyist programmer, Tony Haines can create and destroy worlds both at work and in his spare time.

JACEY